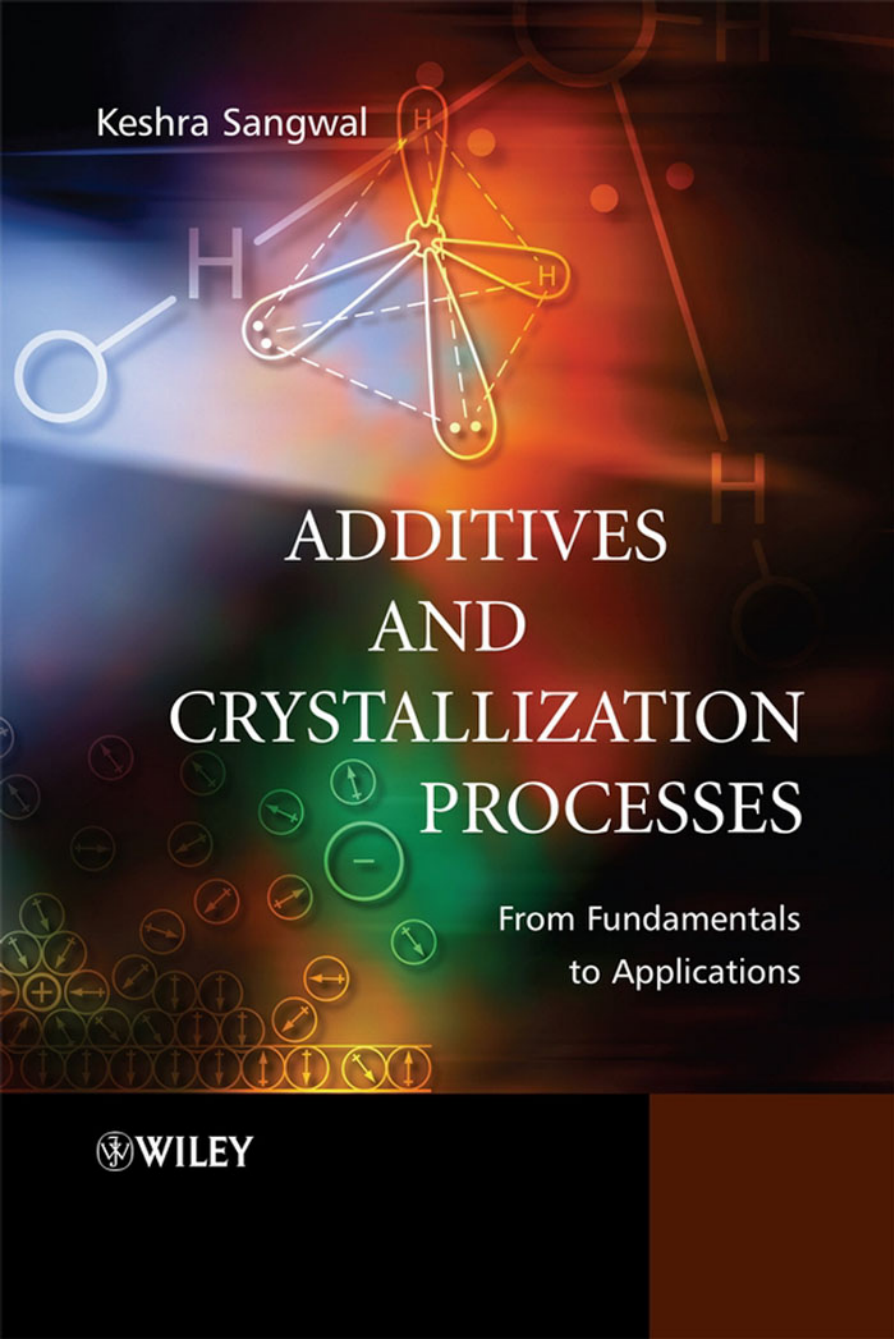


Keshra Sangwal



ADDITIVES AND CRYSTALLIZATION PROCESSES

From Fundamentals
to Applications

 WILEY

Additives and Crystallization Processes

Additives and Crystallization Processes

From Fundamentals to Applications

KESHRA SANGWAL

Department of Applied Physics, Institute of Physics, Lublin University of Technology, Poland



John Wiley & Sons, Ltd

Copyright © 2007

John Wiley & Sons Ltd, The Atrium, Southern Gate, Chichester,
West Sussex PO19 8SQ, England

Telephone (+44) 1243 779777

Email (for orders and customer service enquiries): cs-books@wiley.co.uk

Visit our Home Page on www.wiley.com

All Rights Reserved. No part of this publication may be reproduced, stored in a retrieval system or transmitted in any form or by any means, electronic, mechanical, photocopying, recording, scanning or otherwise, except under the terms of the Copyright, Designs and Patents Act 1988 or under the terms of a licence issued by the Copyright Licensing Agency Ltd, 90 Tottenham Court Road, London W1T 4LP, UK, without the permission in writing of the Publisher. Requests to the Publisher should be addressed to the Permissions Department, John Wiley & Sons Ltd, The Atrium, Southern Gate, Chichester, West Sussex PO19 8SQ, England, or emailed to permreq@wiley.co.uk, or faxed to (+44) 1243 770620.

Designations used by companies to distinguish their products are often claimed as trademarks. All brand names and product names used in this book are trade names, service marks, trademarks or registered trademarks of their respective owners. The Publisher is not associated with any product or vendor mentioned in this book.

This publication is designed to provide accurate and authoritative information in regard to the subject matter covered. It is sold on the understanding that the Publisher is not engaged in rendering professional services. If professional advice or other expert assistance is required, the services of a competent professional should be sought.

The Publisher and the Author make no representations or warranties with respect to the accuracy or completeness of the contents of this work and specifically disclaim all warranties, including without limitation any implied warranties of fitness for a particular purpose. The advice and strategies contained herein may not be suitable for every situation. In view of ongoing research, equipment modifications, changes in governmental regulations, and the constant flow of information relating to the use of experimental reagents, equipment, and devices, the reader is urged to review and evaluate the information provided in the package insert or instructions for each chemical, piece of equipment, reagent, or device for, among other things, any changes in the instructions or indication of usage and for added warnings and precautions. The fact that an organization or Website is referred to in this work as a citation and/or a potential source of further information does not mean that the author or the publisher endorses the information the organization or Website may provide or recommendations it may make. Further, readers should be aware that Internet Websites listed in this work may have changed or disappeared between when this work was written and when it is read. No warranty may be created or extended by any promotional statements for this work. Neither the Publisher nor the Author shall be liable for any damages arising herefrom.

Other Wiley Editorial Offices

John Wiley & Sons Inc., 111 River Street, Hoboken, NJ 07030, USA

Jossey-Bass, 989 Market Street, San Francisco, CA 94103-1741, USA

Wiley-VCH Verlag GmbH, Boschstr. 12, D-69469 Weinheim, Germany

John Wiley & Sons Australia Ltd, 42 McDougall Street, Milton, Queensland 4064, Australia

John Wiley & Sons (Asia) Pte Ltd, 2 Clementi Loop #02-01, Jin Xing Distripark, Singapore 129809

John Wiley & Sons Ltd, 6045 Freemont Blvd, Mississauga, Ontario L5R 4J3, Canada

Wiley also publishes its books in a variety of electronic formats. Some content that appears in print may not be available in electronic books.

Anniversary Logo Design: Richard J. Pacifico

Library of Congress Cataloging in Publication Data

Sangwal, Keshra.

Additives and crystallization processes : from fundamentals to applications / Keshra Sangwal.

p. cm.

ISBN 978-0-470-06153-4 (cloth)

1. Crystal growth. 2. Nucleation. 3. Additives. 4. Crystallization. I. Title.

QD921.S25 2007

660'.284298—dc22

2007014618

British Library Cataloguing in Publication Data

A catalogue record for this book is available from the British Library

ISBN 978-0-470-06153-4

Type-set in 10/12pt Times by Integra Software Services Pvt. Ltd, Pondicherry, India

Printed and bound in Great Britain by Antony Rowe Ltd, Chippenham, Wiltshire

This book is printed on acid-free paper responsibly manufactured from sustainable forestry in which at least two trees are planted for each one used for paper production.

To my parents and teachers

*Learn knowledge by humble reverence,
by enquiry and by service.
The men of wisdom, who have seen the truth,
will instruct thee in knowledge.*

The Bhagavadgita

Contents

<i>Preface</i>	xiii
1 Complexes in Solutions	1
1.1 Structure of Common Solvents	2
1.2 Structure of Pure Aqueous Electrolyte Solutions	4
1.2.1 Solvation of Electrolyte Ions in Solutions	4
1.2.2 Concentrated and Saturated Electrolyte Solutions	6
1.2.3 Formation of Aquo and Partially Aquo Complexes	8
1.3 Structure of Aqueous Electrolyte Solutions Containing Additives	10
1.4 Polyelectrolytes and Surfactants in Solutions	16
1.5 Polydentate Ligands and Molecular Additives	18
1.6 Crystal–Additive Interactions	19
References	19
2 Three-Dimensional Nucleation and Metastable Zone Width	21
2.1 Driving Force for Phase Transition	22
2.2 Three-Dimensional Nucleation of Crystals	25
2.2.1 Three-Dimensional Nucleation Rate	25
2.2.2 Three-Dimensional Heterogeneous Nucleation	30
2.3 Metastable Zone Width	35
2.4 Nucleation and Transformation of Metastable Phases	38
2.4.1 Crystallization of Metastable Phases	38
2.4.2 Overall Crystallization	41
2.5 Induction Period for Crystallization	47
2.6 Effects of Additives	52
2.6.1 Solubility	52
2.6.2 Three-Dimensional Nucleation Rate	56
2.6.3 Metastable Zone Width	56
References	62

3 Kinetics and Mechanism of Crystal Growth: An Overview	65
3.1 Crystal Growth as a Kinetic Process	66
3.2 Types of Crystal–Medium Interfaces	67
3.3 Roughening of Steps and Surfaces	69
3.3.1 Thermodynamic Roughening and the Surface Entropy Factor	70
3.3.2 Kinetic Roughening	72
3.4 Growth Kinetics of Rough Faces	73
3.5 Growth Kinetics of Perfect Smooth Faces	75
3.6 Growth Kinetics of Imperfect Smooth Faces	78
3.6.1 Surface Diffusion and Direct Integration Models	78
3.6.2 Bulk Diffusion Models	80
3.6.3 Growth by a Group of Cooperating Screw Dislocations	82
3.6.4 Preferential Growth at Edge Dislocations	84
3.7 Effect of Foreign Substances on Growth Kinetics	85
3.7.1 Some General Considerations	87
3.7.2 Growth Kinetics by Heterogeneous Two-Dimensional Nucleation	90
3.8 Real Crystal Growth Mechanisms	96
3.8.1 Structure of Interfacial Layer	96
3.8.2 Sources of Growth Steps	100
3.9 Techniques for Studying Growth Kinetics	104
References	105
4 Effect of Impurities on Crystal Growth Kinetics	109
4.1 Mobile and Immobile Impurities	109
4.2 Surface Coverage and Adsorption Isotherms	112
4.2.1 Adsorption Isotherms	113
4.2.2 Changes in Surface Free Energy by Adsorption of Impurities	115
4.3 Kinetic Models of Impurity Adsorption	115
4.3.1 Earlier Models	115
4.3.2 Velocity of Curved Steps	116
4.3.3 Impurity Adsorption at Kinks in Steps: Kubota–Mullin Model	118
4.3.4 Impurity Adsorption at Surface Terrace: Cabrera–Vermilyea Model	119
4.3.5 Effectiveness Factor for Impurity Adsorption	121
4.3.6 Adsorption of Two Competing Impurities	124
4.4 Confrontation of Impurity Adsorption Mechanisms with Experimental Data	127
4.5 Time-Dependent Impurity Adsorption	132
4.6 Growth Kinetics in the Presence of Impurities	136
4.6.1 Basic Kinetic Equations	136
4.6.2 Time Dependence of Face Displacement	141
4.6.3 Dependence of Kinetic Coefficient for Step Motion on Impurity Concentration	142
4.7 Tapering of KDP-Type Crystals	143

4.8	Growth-Promoting Effects of Impurities	146
4.8.1	Decrease in Step Free Energy and Roughening of Steps	147
4.8.2	Formation of Surface Macroclusters	152
4.9	Impurity Adsorption on Rough Faces	157
4.10	Formation of Two-Dimensional Adsorption Layer	158
4.11	Interactions Between Additives and Crystal Interface	160
4.11.1	Nature of Impurity–Crystal Interactions	160
4.11.2	Chemical Aspects of Impurity–Crystal Interactions	166
4.12	Tailor-Made Additives	172
	References	174
5	Dead Supersaturation Zone and Threshold Supersaturations for Growth	177
5.1	Origin of Threshold Supersaturations for Growth	179
5.1.1	Basic Kinetic Equations	179
5.1.2	Three Different Distances Between Impurity Particles	182
5.2	Determination of Threshold Supersaturations from $v(\sigma)$ and $R(\sigma)$ Data	184
5.2.1	Relationship Between the Model Involving Cooperating Spirals and the Power-Law Approach	185
5.2.2	Relationship Between the Power-Law Approach and an Empirical Expression with Corrected Supersaturation	185
5.2.3	Determination of σ^*	186
5.3	Dependence of Threshold Supersaturations on Impurity Concentration: Basic Theoretical Equations and Linear Approximations	187
5.4	Confrontation of Theoretical Equations with Experimental Data	190
5.4.1	Impurity Adsorption at Kinks and Surface Terrace	190
5.4.2	Threshold Supersaturations and Impurity Adsorption Isotherms	193
5.5	Impurity Adsorption and Solution Supersaturation	197
5.6	Dependence of Ratios σ_d/σ^* and σ^*/σ^{**} on c_i	198
	References	202
6	Mineralization in Natural and Artificial Systems	205
6.1	Biomineralization as a Process	205
6.1.1	Structure and Composition of Biominerals	205
6.1.2	Humans and Animals	206
6.1.3	Plants	209
6.1.4	Mollusk Shells and Avian Eggshells	211
6.2	Pathological Mineralization	216
6.3	Effect of Biologically Active Additives on Crystallization Processes	222
6.3.1	Overall Precipitation Kinetics	222
6.3.2	Overall Growth Kinetics	230
6.3.3	Phases and Polymorphs of Crystallizing Calcium Salts	242
6.3.4	Transformation of Metastable Phases	247

6.4 Scale Formation and Salt Weathering	258
References	262
7 Morphology and Size Distribution of Crystals	265
7.1 Growth Morphology of Crystals	266
7.1.1 General Concepts	266
7.1.2 Effect of Additives on Surface Morphology	273
7.1.3 Effect of Solvent on Crystal Morphology	275
7.1.4 Growth Morphodroms	276
7.2 Ostwald Ripening and Crystal Size Dispersion	282
7.3 Crystal Size Distribution	284
7.3.1 Population Balance Approach	285
7.3.2 Balanced Nucleation-Growth Approach	289
7.3.3 Approach Based on Law of Proportionate Effect	291
7.3.4 Effect of Additives on Crystal Size Distribution	295
7.4 Control of Shape and Size of Particles	298
7.4.1 Growth-Directed Synthesis	298
7.4.2 Template-Directed Synthesis	307
7.5 Biological Tissue Engineering	311
References	314
8 Additives and Crystallization Processes in Industries	319
8.1 Pharmaceutical Industry	320
8.1.1 Nucleation, Growth and Morphology of Drug Crystals	321
8.1.2 Preparation and Size Distribution of Drug Particles	324
8.2 Petroleum Industry	330
8.2.1 Some Basic Concepts	331
8.2.2 Crystallization Behavior of Linear Long-Chain <i>n</i> -Alkanes	332
8.2.3 Biodiesels and their Crystallization Behavior	338
8.3 Food Industry	348
8.3.1 Some Basic Concepts	351
8.3.2 Crystallization of Food Fats in the Bulk	356
8.3.3 Crystallization of Polymorphs	361
8.3.4 Crystallization of Fats and Oils in Emulsion Droplets	366
8.3.5 Number of Nucleation Centers and Overall Crystallization in Emulsion Systems	372
References	377
9 Incorporation of Impurities in Crystals	381
9.1 Types of Impurity Incorporation and the Segregation Coefficient	382
9.2 Equilibrium Segregation Coefficient	386
9.2.1 Binary Mixture Approach	386
9.2.2 Thermodynamic Approach	388
9.2.3 Theoretical Predictions and their Comparison with Experimental Data on Segregation Coefficient	389
9.3 Effective Segregation Coefficient	396

9.3.1 Volume Diffusion Model	396
9.3.2 Diffusional Relaxation Approach	397
9.3.3 Statistical Selection Approach	401
9.3.4 Surface Adsorption Approach	402
9.4 Relationship Between Effective Segregation Coefficient and Face Growth Rate	410
9.5 Threshold Supersaturation for Trapping of Impurities During Growth	413
9.6 Effective Segregation Coefficient and Internal Stresses Caused by Impurities	416
References	418
<i>List of Symbols</i>	421
<i>Subject Index</i>	427
<i>Author Index</i>	437

Preface

Impurities play an important role in different spheres of our day-to-day life. For example, trace amounts of impurities present in crystalline solids have a profound influence on their mechanical, electrical, thermal and optical properties. Consequently, the performance of different types of devices based on these solids depends on the nature and concentration of impurities present in them. Trace amounts of impurities present in a growth medium also have a strong influence on the processes of nucleation of crystallizing phases of the same substance and the subsequent growth of the nucleated phase. Typical examples of such processes are: (1) beneficial mineralization such as the formation of bone and tooth, and pathological mineralization such as formation of human kidney stones, (2) scale formation in domestic appliances and industrial plants, and (3) crystallization of saturated fatty acid methyl ester components of biodiesel during cold seasons, clogging fuel lines and filters of engines.

Any foreign substance other than the crystallizing compound is considered as an impurity. Thus, a solvent used for growth and any other compound deliberately added to the growth medium or inherently present in it is an impurity. Different terms, such as additive, admixture, inhibitor and poison, are used in the literature for foreign substances other than the solvent used for obtaining supersaturated solutions. Irrespective of its concentration, a deliberately added impurity is called an *additive*, but by the term *admixture* we mean an impurity added in relatively large amounts (up to several percent). A *surfactant* may be any chemical compound active on the surface in changing its growth behavior. An impurity can accelerate or decelerate the growth process. The impurity that decelerates growth is called a *poison* or an *inhibitor*, while one that accelerates growth is said to be a growth *promoter*.

Foreign substances present in the aqueous solutions used for the crystallization of substances can be as diverse as simple ions of common bivalent metals and proteinaceous compounds such as aspartic and glutamic acids in the crystallization of different phases of calcium carbonate and calcium phosphate, and the same impurity can modify the crystallization behavior of both highly and sparingly soluble compounds. For example, bivalent cations of various metals modify the crystallization behavior of highly soluble compounds such as sodium chloride and potassium dihydrogenphosphate and also sparingly soluble compounds such as calcium carbonate.

In different industries, the important requirements that a crystallized solid-state product has to fulfill are its phase or polymorph, thermodynamic and kinetic stability during its storage life, growth morphology and size distribution, which ultimately determine the product solid-state properties such as separation, flow, compaction, dissolution, and packing. The above requirements are met by controlling crystallization conditions which determine various processes such as nucleation, crystal growth, aggregation, Ostwald ripening, and phase transformation. Additives have a profound effect on the course of the above processes. In beneficial and pathological biomineratization, an intimate relationship between crystallizing compound and protein matrix is well known. Interactions of natural polymeric impurities with ionic crystals are the causes of the formation of pathological crystal aggregates such as kidney stones, dental calculus and deposits in gout and atherosclerosis. Similarly, the aragonite form of calcium carbonate layers covering the inner surface of some popular mollusk shells, known as mother of pearl or nacre, has a higher fracture toughness due to small amounts of protein matrix than aragonite obtained artificially by chemical precipitation. In industrial plants, water-soluble synthetic poly-electrolytes are used as scale inhibitors and/or dispersants for the prevention of scale deposits in cooling water systems.

Additives affect different processes involved during crystallization. Therefore, the understanding of interactions between additives and crystallizing phase is important in different crystallization processes encountered in the laboratory, in nature and in such diverse industries as the pharmaceutical, food and biodiesel industries. Moreover, the knowledge of polymer–crystal interactions gathered so far is a very useful guide for materials scientists to design low-temperature technologies for the preparation of novel composite materials for biomedical applications.

Foreign substances present in the medium used for the growth of a variety of various substances have long been recognized to have a profound influence on the external appearance (usually called growth habits or growth morphology) of crystals. The literature existing prior to 1950 on the habit modification of crystals by impurities has been surveyed in the classical monograph by Buckley [Crystal Growth, John Wiley & Sons, New York (1951)]. After the publication of this monograph, efforts were diverted to understanding the basic mechanisms responsible for changes in the growth habit of crystals caused by impurities on the microscopic level. The first important work in this direction was published during the late 1950s and 1960s when kinetic models describing the motion of ledges across the surface of a crystal were formulated theoretically in terms of adsorption of impurity particles at surface terrace (Cabrera–Vermilyea model), ledges (Sears model) and kinks (Bliznakov model). During this period, on the basis of their experimental results on the growth forms of alkali metal halides as a function of supersaturation and impurity concentration, Kern and his associates advanced the structural interpretation of habit modification in terms of the formation of two-dimensional adsorbed-impurity layers similar to epitaxial relationships in epitaxial growth. The second phase of investigations on impurity effects, spanning between the 1970s and early 1980s, concentrated on the experimental investigation of growth kinetics in the presence of additives, and started from the work of Boistelle and Simon and of Davey and Mullin. These authors studied face growth rates and layer displacement rates as a function of impurity concentration, and confronted the experimental data with different kinetic models of impurity adsorption. The last phase of the studies on impurities began from the early 1980s with the work of

Berkovitch-Yellin and co-workers on the design of structurally specific additives, called tailor-made impurities, in inhibiting the growth of preselected faces of crystals.

Since the publication of Buckley's monograph, the literature on the effects of impurities on crystal growth has been growing enormously, and is scattered in various scientific journals. The published literature addresses the following topics: habit modification and morphodroms, kinetic data on face growth rates and layer displacement rates, observation of the presence of dead supersaturation zones at low impurity concentrations, *ex situ* and *in situ* observation of the morphology of crystal faces, nucleation and precipitation kinetics, segregation coefficient of impurities, and chemical constitution of impurity species and chemistry of adsorption in solution growth. The literature on the mechanism of action of impurities on growth kinetics has been reviewed several times since 1970 (Boistelle, 1976; Davey, 1979; Simon and Boistelle, 1981; Chernov, 1984; van Rosmalen and Bennema, 1990; Klug, 1993; Sangwal, 1996; Füredi-Milhofer and Sarig, 1996; Kubota, 2001). However, until now there has been no monograph devoted exclusively to the role of additives in crystallization processes. This present text is an attempt to fill this gap.

This work presents a generalized description of the mechanisms of action of additives during nucleation, growth and aggregation of crystals during various types of crystallization. The subject matter of the book reflects my own choice. Some of the topics discussed here fall in the domains of specialized fields such as industrial crystallization, crystal growth technology, and biomimetic mineralization. Such topics are included here especially to expose the reader to the importance of additives in crystallization processes, from a physicist's perspective, in diverse fields of basic research and applied activities such as chemical engineering, industrial crystallization, materials science, and the technology of the growth of crystals. In its present form, this text provides a generalized description of the mechanisms of action of additives during nucleation, growth and aggregation of crystals during crystallization. I have made every effort to make the book self-contained, keeping mathematics to the minimum.

The contents can roughly be divided into four parts. The first is introductory where basic concepts about the nature of complexes in dilute and concentrated solutions (Chapter 1), three-dimensional nucleation and metastable zone width (Chapter 2), and crystal growth processes (Chapter 3) are outlined. The second part consists of two chapters, and addresses the effect of additives on crystal growth kinetics (Chapter 4) and the observation of threshold supersaturations for growth (Chapter 5). The third part gives an overview of processes of mineralization in natural and artificial systems (Chapter 6) and morphology and size distribution of crystals (Chapter 7), with emphasis on the role of additives in these processes. The last part addresses applied aspects of additives in the pharmaceutical, food and petroleum industries (Chapter 8), and processes of segregation during crystallization (Chapter 9).

This text is primarily addressed both to specialists and to graduate students of industrial crystallization, chemical engineering, materials science, and condensed matter physics, who are interested in looking for a comprehensive review of the fundamentals of the processes of nucleation and growth of crystals from pure systems in general and from systems containing a variety of additives in particular both in basic and applied research. However, it will also serve as a ready source of reference for practical materials scientists interested in using the basic principles of additive–material interactions to design and prepare novel composite materials.

It is practically impossible to write a scientific book without referring to the published works of other authors. The present text is not an exception in this regard. In fact, I have leaned heavily on the work of numerous other authors during the writing of this book. Their studies have served as an unending reservoir of concepts and ideas for the nucleation and development of the network of the book during various stages of its progress. I have also generously used in the text a number of photographs and graphs published by various authors in different journals. I have selected such photographs and graphs from the literature easily accessible to me. I extend my apologies to the authors whose work I have not cited.

A sketchy draft of the manuscript was written during my four-month stay in 2004/2005 at the Venture Business Laboratory, Hiroshima University, Japan. Since then, the contents were constantly updated, and its present version was completed during my recent study leave. I am grateful to the authorities of Hiroshima University for inviting me to work there as a visiting professor during 2004/2005, and to the authorities of my parent institution for the grant of a study leave during the academic year 2006/2007.

I express my profound gratitude to the following authors for sending reprints of their papers and original figures for reproduction: Dr J.J. De Yoreo (Lawrence Livermore National Laboratory, USA), Dr I. Foubert (Ghent University, Belgium), Prof. M. Kitamura (University of Hyogo, Himeji, Japan), Prof. N. Kubota (Iwate University, Morioka, Japan), Dr A.J. Malkin (Lawrence Livermore National Laboratory, USA), Dr J. Prywer (Łódź University of Technology, Poland), Dr R.I. Ristić (University of Sheffield, UK), Prof. A.L. Rodgers (University of Cape Town, South Africa), Prof. K. Sato (Hiroshima University, Japan), Prof. K. Tsukamoto (Tohoku University, Sendai, Japan), Dr S. Ueno (Hiroshima University, Japan), and Prof. E. Vlieg (University of Nijmegen, The Netherlands). I am also grateful to the following publishers for their kind permission to use and reproduce various figures from books and journals published by them: American Chemical Society, American Institute of Physics, Elsevier Science, Japan Oil Chemists' Society, S. Karger AG, Basel, Springer, Heidelberg, Springer, Dordrecht, Taylor and Francis, John Wiley & Sons, and Wiley-VCH. The sources of the illustrations used in the monograph are duly cited wherever they appear in the text.

I owe my indebtedness to Prof. Kyo Sato (Hiroshima University, Japan), Prof. Dimo Kashchiev (Institute of Physical Chemistry, Bulgarian Academy of Sciences, Sofia, Bulgaria), Emeritus Prof. Nori Kubota (Iwate University, Morioka, Japan), and Dr Rile Ristić (Sheffield University, UK) for discussions and advice during the preparation of the manuscript. I am also grateful to Dr Ewa Mielniczek-Brzóska for her scientific collaboration over the years, and to Dr Kazimierz Wójcik, Dr Jarosław Borc, and Mr Satoshi Arima (Hiroshima University) for their assistance with the preparation of figures and the final version of the manuscript for publication. I bless my son, Sunil, for checking the manuscript. Finally, I thank my wife, Marta, for her support and patience.

Keshra Sangwal
Lublin
March, 2007

1

Complexes in Solutions

Water is a popular solvent for the growth of a variety of inorganic and organic compounds. It is not toxic and is less volatile than organic solvents, which are, in general, toxic, volatile and flammable. In comparison with organic solvents, it is also easily available in the pure state and is cheap. Because of its higher boiling point than most of the organic solvents commonly used for growth, it provides a reasonably wide range for the selection of growth temperature. Moreover, it is chemically inert to a variety of glasses, plastics and metals used in crystal growth equipment. However, water is not a reversible solvent for some materials. It hydrolyzes some materials and introduces water of crystallization to others which may be desired in the anhydrous form. Therefore, for the growth of crystals of a compound from solution, the selection of a solvent is critical. A simple rule of thumb in the proper selection of a solvent is chemical similarity between the solvent and the compound to be grown. For example, crystals of nonpolar organic compounds can be grown easily from nonpolar organic solvents. Chemical similarity also determines solute solubility in the solvent (Chapter 2).

Experiments reveal that a solvent in which the compound has a solubility between 10 and 60% at a given temperature is economically suitable for crystal growth. Very low and very high solubility of a solute provide low growth rates due to low solute concentration and increased viscosity, respectively. Therefore, in both of these cases it is desirable to use additives to change the solute solubility in a solvent or solution viscosity. Additives not only change the properties of solutions, but also lead to changes in the growth habits of crystals (Section 7.1).

Molecules of an additive, as described by the chemical formula of the latter, rarely participate in adsorption processes on a growing or dissolving surface of a crystal from solution containing the additive. Generally, the species adsorbing on a surface are ions of the additive formed by its dissociation in the solution or complexes formed by chemical reactions between additive ions or molecules and the solvent. In the processes of formation

of ions and complexes, the concentration of the main solute intended for crystallization plays a significant role.

Foreign substances which influence the processes of nucleation and growth of crystals can be divided into simple electrolyte (single-functional), polyelectrolyte and surfactants (multifunctional), and tailor-made (adsorption site-specific) impurities (van Rosmalen and Bennema, 1990). Ions and molecules of simple electrolytes have small dimensions. Therefore, they are capable of moving over the surface or can remain immobile after being adsorbed on the surface, depending on whether the bonds formed by additive molecules with the surface molecules are weak or strong. However, because of their large dimensions, there is a higher possibility of formation of several bonds between the molecules of polyelectrolyte and tailor-made impurities and the surface molecules. Consequently, their molecules adsorbed on the surface remain practically immobile due to the need for simultaneous rupture of the bonds with the surface. The physical concepts of the nature of mobile and immobile impurities are discussed in Chapter 4.

In this chapter, the structures of solvents, solutions of pure electrolytes and solutions of an electrolyte containing additives are described. After a short account of the structure of common solvents in the next section, general features of formation of complexes in dilute and concentrated aqueous solutions of simple electrolytes are outlined in Section 1.2. The nature of complexes of additives in simple electrolyte solutions is then discussed in Section 1.3. Finally, some features of the structure of complexes of polyelectrolyte and molecular additives in aqueous solution are described in Sections 1.4 and 1.5.

1.1 Structure of Common Solvents

Among liquids, water has unusual properties. It has a high boiling point, a high thermal conductivity, dielectric constant and surface tension, a low enthalpy of fusion, a maximum density at 4 °C, etc. These properties are due to the existence of the hydrogen bond.

A water molecule is composed of an oxygen atom at the center of a regular tetrahedron having hydrogen nuclei (i.e. protons) at two of its vertices and lone-pair electrons in orbitals directed towards the other two (Figure 1.1a). Because of the repulsion of the electron pairs, the H–O–H angle is not exactly equal to the tetrahedron angle 109° 28' but is 105°. Consequently, the center of gravity of the oxygen atom does not coincide with the center of gravity of the positive charge, and the neutral water molecule can be considered as an electrical dipole. The nature of the proton and the exposed positions of the lone-pair electrons enable two water molecules to be held together by a special interaction, some 17–25 kJ/mol in strength, known as the hydrogen bond (Figure 1.1b). The properties of the hydrogen bond determine the structural features of crystalline form of *water ice*, in which oxygen atoms lie in layers with each layer consisting of a network of open, puckered hexagonal rings. Such a network structure of associated water molecules contains interstitial regions between the tetrahedra, which are larger than the dimensions of a water molecule. Therefore, a free unassociated water molecule can enter the interstitial regions without disrupting the network structure.

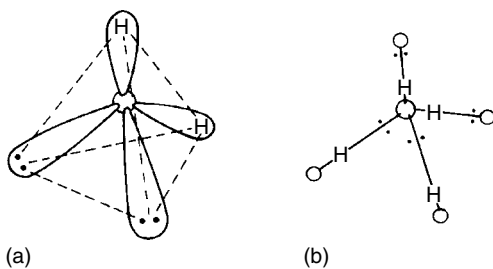


Figure 1.1 (a) Geometric representation of nucleus and electron charge distribution in a water molecule. (b) Hydrogen bond formed as a result of attraction of a proton from one water molecule to a lone pair of another

There is no uniform theory to explain the properties of *liquid water*, but several models have been proposed, which may be classified into three groups. The first group consists of *physical models*, assuming the existence of an equilibrium between various structural entities, which may be small or large clusters. These clusters may be composed of monomeric molecules, hexameric rings in different packing, a hydrogen-bonded framework and interstitial molecules, and distorted or broken hydrogen-bonded structures. In the group of *liquid-lattice models*, it is assumed that a local ordering exists in the liquid because of the tetrahedral orientation of hydrogen-bonded molecules. In some cases an additional hypothesis regarding the molecular packing is used. The third group is formed by the *molecular dynamic approach* (or continuum approach), which does not *a priori* assume any structure or ordering. In this case, based on a simple picture of the molecular structure and of nearest-neighbor intermolecular interactions, the behavior of an ensemble of water molecules is simulated.

The physical and liquid-like models describe liquid water as an equilibrium mixture of species that are distinguishable in an instantaneous picture, while the continuum model describes water as essentially hydrogen bonded, but with a distribution of angles, distances and bond energies. While experimental evidence is always available to justify the assumptions used in various models, experiments and molecular orbital calculations show that hydroxonium and hydroxide ions of water are hydrated, the hydrogen bond in H_3O_2^- being weaker than in H_5O_2^+ . The higher hydrated species of H_3O^+ (H_5O_2^+ , H_7O_3^+ , H_9O_4^+ , etc.) and HO^- (H_5O_3^- , H_7O_4^- , etc.) show a gradual decrease in hydrogen bond energy. These trends are due to the cooperativity of the hydrogen bond(s).

The structure of organic liquids may also be considered to be similar. For example, in the case of the alcohol ROH, there is a favorable configuration of molecules for the formation of bonds in series between the hydrogen atom of the OH group of one ROH molecule and the oxygen atom of the OH group of another ROH molecule, but there is an unfavorable configuration for the formation of bonds between the R group of one ROH molecule and the hydrogen or oxygen atom of another ROH molecule. These configurations may form large, closed complexes (ring configurations). However, in comparison with the cooperativity of water molecules in series, in organic solvents the cooperativity is poor because of a much smaller dipole moment.

1.2 Structure of Pure Aqueous Electrolyte Solutions

1.2.1 Solvation of Electrolyte Ions in Solutions

Extremely dilute solutions of electrolytes may be considered to be composed of the solvent in which ions of the solute are randomly distributed at large distances. The spherically symmetrical electrical field of an individual ion may tear water dipoles out of the liquid water structure and orient their charged ends towards the center of the ion. The ion–dipole forces are the basis of ion–solvent interactions. Due to the ion–dipole forces, a certain number of water molecules in the immediate vicinity of the ion are trapped and oriented in the ionic field. The oriented water molecules cease to associate with other water molecules of the liquid water network and form a firmly held (immobilized) sheath around the ion. This region is called the primary solvation (or hydration) sheath. The water molecules of the primary sheath move with the ion as a single kinetic entity.

At a sufficient distance away from the ion, its influence becomes negligible because the ionic field approaches zero. Here, the water structure remains undisturbed and is that of bulk water. However, in the region between the solvent sheath and the bulk water, the orienting effects of the ion and the ordering effect of water network are operative. In this region, the normal structure of bulk water is partly broken. The water molecules of this secondary solvation (or hydration) sheath do not move with the ion.

Several methods as diverse as mobilities, reaction kinetics, thermodynamics (density, solubility, activity, boiling and melting points, etc.), spectroscopy (visible, ultraviolet, infrared Raman, nuclear magnetic resonance, and Mössbauer) diffraction (X-ray, neutron and electron), X-ray absorption, and computer simulations (molecular dynamics and Monte Carlo) have been employed for the determination of hydration numbers of ions (Ohtaki, 2001). Diffraction methods reveal that the hydration number for different mono-, bi- and trivalent cations and mono- and bivalent anions/radicals are usually 6 ± 2 . In general, these results on hydration number for bi- and trivalent cations obtained by nuclear magnetic resonance (NMR) spectroscopy agree with those by diffraction methods, but the hydration number of most monovalent cations and anions is about 3 and 1, respectively. These differences in the hydration number result from the fact that diffraction methods do not always expose water molecules firmly attached to central ions, while NMR detects water molecules strongly combined with the ions and moving slowly with respect to the NMR measurement time-scale exceeding about 10^{-9} s.

The observed bond length between an ion and a water molecule is roughly the sum of the bare ion radius and the van der Waals radius of a water molecule (0.140 nm). Water molecules around an ion are not directed towards the dipole of the water molecule but are tilted by an angle θ due to hydrogen bonding of water molecules of the first shell with those on the second shell. A tilt angle $\theta > 0^\circ$ enables to form three hydrogen bonds while $\theta = 0^\circ$ forms only two hydrogen bonds. Consequently, in contrast to the latter situation, in the former case a more stable hydration sphere is formed. The weak solvation of anions, for example, is due to a value of the tilt angle close to 0° .

The structure of hydrated ions gives information about energetics of ions in water and represents the static behavior of water molecules in the solvation shells of the ions. There is always some residence time and rotation of water molecules in the solvation shells of ions. The experimental data show (Ohtaki, 2001) that the average residence time $\tau_{\text{H}_2\text{O}}$ of a water molecule in the bulk is $(4.6 \pm 0.3) \times 10^{-12}$ s. The residence time τ_{O} of oxygen

atoms of a water molecule in the first solvation shell of alkali metal ions and halide ions is close to that of bulk water, but its value for most of the bi- and trivalent cations lies between about 10^{-8} and 10^{-2} s, the highest values belonging to ions such as Al^{3+} , Cr^{3+} and Fe^{3+} . It is a general trend that, for ions in the same group of the periodic table, the larger the ionic radius, the smaller is the value of τ_o . The residence time τ_H of hydrogen atoms of a water molecule in the first solvation shell of cations is smaller than τ_o due to the proton transfer reaction between the first hydration shell and the nearest neighbor water molecule. However, as expected, τ_H is greater than τ_o for halide ions.

From the above discussion, it follows that the ions of a salt in dilute solutions are not bare, having radii corresponding to their crystallographic radii. Although various methods indicate different numbers of water molecules bound to the ions in solution, the number of water molecules involved during the solvation of different ions in water is intimately connected with the surface charge density and the type of charge of an ion. The surface charge density of an ion decreases with increase in its valency and decreases with increase in its size. Therefore, the smaller the size or higher the charge of an ion, the greater is the number of water molecules involved in solvation due to stronger ion-solvent interactions. Anions are less solvated than cations. This difference is due to the weaker interactions between water dipoles and anions than those between water dipoles and cations.

During the dissolution of ionic lattices in water, the ions composing the surface layer of the lattice and the dipoles of solvent molecules attract each other. This attraction is responsible for the solvation of ions. The work of interaction W_{I-D} , per mole of ions, between N_A ions and n_s water molecules involved in the primary solvation sheath of each ion is given by (see, for example, Bockris and Reddy, 1970)

$$W_{I-D} = -\frac{N_A n_s z_i e \mu_s}{(r_i + r_s)^2} \quad (1.1)$$

where N_A is the number of ions per mole, z_i is the valency of the ion, e is the elementary charge, μ_s is the dipole moment of a water molecule, and r_i and r_s are the radii of an ion and a water molecule, respectively. During dissolution, the bonds holding the ions together are broken and the ions go into solution. For the rupture of one mole of the crystalline substance into ions and the transfer of the ruptured ions to infinity, it is necessary to expend an energy equal to the lattice energy, which is given by Born's equation:

$$U = \alpha_m N_A \frac{z_1 z_2 e^2}{a_0} \left(1 - \frac{1}{n} \right) \quad (1.2)$$

where z_1 and z_2 are the ionic valencies, a_0 is the distance between ions in the crystalline lattice, which is equal to the sum of their crystallographic radii, n is the Born exponent, which lies between 8 and 12, and α_m is the Madelung constant, which depends on the crystal structure.

The solubility of an electrolyte in a solvent is associated with the heat of solution ΔH , of the electrolyte, which is determined by solvation processes. To understand this, one may consider that the crystal ions are first taken apart into vacuum by expending energy U and then placed into the solvent one by one such that in this process they become

6 Additives and Crystallization Processes

solvated. With reference to the energy of an ion in vacuum, the process of solvation of the ions is accompanied by a change in its energy by ΔH_{solv} . Solvation of ions is associated with solute–solvent interactions, and is always accompanied by a release of heat (i.e. $\Delta H_{\text{solv}} > 0$), and an ion in the solvent has a radius $R_i = r_i + 2r_s$. The process of transfer of ions from the lattice to the solution is solvation and is associated with the heat of solution ΔH_s , given by

$$\Delta H_s = U - \Delta H_{\text{solv}} \quad (1.3)$$

From Equation (1.3), it follows that, depending on the values of U and ΔH_s , the heat of solution of an electrolyte $\Delta H_s > 0$ and $\Delta H_s < 0$. When $U > \Delta H_{\text{solv}}$, $\Delta H_s > 0$ and the system absorbs heat (i.e. the reaction is endothermic). However, when $U < \Delta H_{\text{solv}}$, $\Delta H_s < 0$ and the system releases heat (i.e. the reaction is exothermic).

1.2.2 Concentrated and Saturated Electrolyte Solutions

All ions and molecules in solutions are more or less solvated, and the solvated ions are the most fundamental species for ionic reactions in solutions. In dilute solutions of electrolytes, ions may be assumed to undergo random motion due to their thermal energy and, therefore, are in random positions. The electrostatic force F between the ions is given by

$$F = z_1 z_2 e^2 / \epsilon r^2 \quad (1.4)$$

where ϵ is the dielectric constant of the solvent and r is the average distance between the ions. At very low solute concentrations, the positively and negatively charged ions are at large distances, a positive ion of charge $+z_1 e$ may be surrounded by a cloud of excess negative charge $-z_2 e$, and vice versa. Despite this possible temporary interaction, the cations and anions remain as separate entities.

When the solute concentration is increased, the positively and negatively charged ions may be trapped in the coulombic field of each other, thus forming ion pairs. The ion pairs are dipoles with net zero charge. The coulombic fields of other ions do not act on these uncharged pairs. When the solute concentration is increased further, the electrostatic force between the ions and the ion-pair ‘dipoles’ becomes sufficiently strong. Then the ion pairs and individual ions are able to form charged triple ions. Further increase in solute concentration may lead to the formation of still larger clusters composed of four, five or more ions.

It is well known that the dielectric constant ϵ of aqueous solutions of electrolytes decreases with increase in solute concentration c . Similarly, the activity coefficient f of an aqueous electrolyte solution decreases with increasing solute concentration c . These observations are a consequence of association of ions into ion pairs, triple ions and clusters composed of four or more ions.

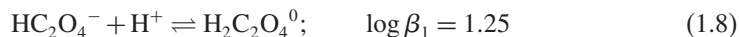
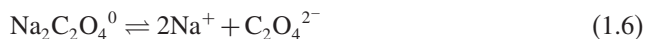
Many electrolytes dissolve in water, but they are usually poorly soluble in nonaqueous solvents. In several cases this low solubility of the electrolytes in nonaqueous solvents is associated with their dielectric constant ϵ . The relation between solubility c for poorly soluble salts in different solvents and their dielectric constant ϵ is given by (Izmailov, 1976)

$$\log c = C + (B_1 \mu - B_2) / \epsilon \quad (1.5)$$

where C , B_1 and B_2 are constants, and $B_2 \gg B_1$. Since for different solvents $\mu > 1$, the factor $(B_1\mu - B_2) < 0$. Consequently, the solubility of a salt decreases with a decrease in ϵ of the solvent.

From the above, it may be concluded that the formation of ion pairs, triple ions and clusters composed of an increasing number of ions is favored in nonaqueous solvents of low dielectric constant ϵ , because the coulombic force is inversely proportional to ϵ [see Equation (1.4)]. It has been suggested (for example, see Bockris and Reddy, 1970) that triple ions are formed in solvent for which $\epsilon < 15$, whereas clusters of four, five, or more ions are formed in solvents with $\epsilon < 10$.

The above picture of the dissociation of solute molecules into ions and the association of ions into large entities may be illustrated by the example of concentrated solutions of sodium oxalate ($\text{Na}_2\text{C}_2\text{O}_4$) in water. Figure 1.2 illustrates the dependence of pH of aqueous solutions of sodium oxalate on its solubility c_0 at temperatures between 20 and 60°C. As seen from the figure, the solution pH increases with the solute concentration c . This $\text{pH}(c_0)$ dependence is associated with the concentration of various species formed in saturated solutions according to different chemical equilibria involving dissociation of $\text{Na}_2\text{C}_2\text{O}_4$:



where β_1 and β_2 are the first- and the second-order equilibrium dissociation constants corresponding to dissociation Reactions (1.7) and (1.8). The equilibrium dissociation constant β is related to the standard Gibbs free energy ΔG_0 involved in the dissociation:

$$\Delta G_0 = -R_G T \ln \beta = -2.3026 R_G T \log \beta \quad (1.10)$$

where R_G is the gas constant and T is the temperature in Kelvin. Reactions (1.7) and (1.8) shift to the right with decreasing pH, producing more neutral $\text{H}_2\text{C}_2\text{O}_4^0$ species and Na^+ ions. This situation corresponds to pure, natural sodium oxalate solution saturated at 30°C, which has a pH of 6.4. However, Reaction (1.9) shifts to the right with increasing pH, producing more $\text{C}_2\text{O}_4^{2-}$ ions and neutral NaOH^0 species. This example shows that there exists a wide spectrum of charged and uncharged species in concentrated solutions of electrolytes and the concentration of individual species depends on solute concentration and solution temperature.

It should be mentioned that the concept of dissociation of electrolyte molecules into isolated ions and their subsequent association into ion pairs, triple ions and clusters composed of more ions is useful for our understanding of the structure of solutions. However, this picture is too simple to account for the structure of species formed in aqueous solutions between metal cations and bi- or trivalent acid ligands. In these solutions aqueous complexes are formed.

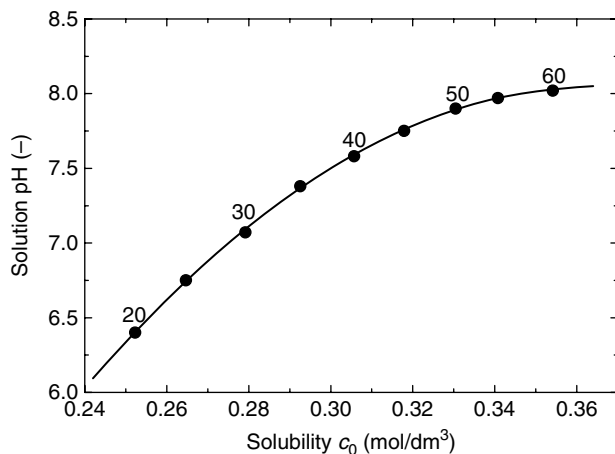
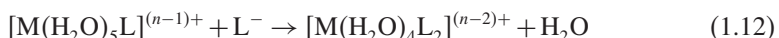
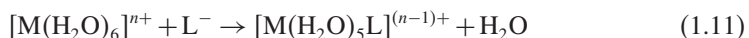


Figure 1.2 Dependence of pH of aqueous solutions of sodium oxalate on its solubility c_0 . Solubility was measured at temperatures between 20 and 60 °C at temperature intervals of 5 °C. Reproduced from R. Misztal, PhD Thesis, Jagiellonian University, Cracow. Copyright (2004), with permission of R. Misztal

1.2.3 Formation of Aquo and Partially Aquo Complexes

As mentioned above, all ions undergo solvation during their dissolution and a solvation shell of solvent water molecules, the number of which depends on the solvating ion is formed around the ion. Bi- and trivalent cations are usually surrounded by a layer of 4–6 firmly attached water molecules. These solvated ions are frequently referred to as *aquo complexes*. Depending on the number of water molecules attached to the ion, coordination between water molecules and the central ion is assumed.

In the presence of monovalent acid ligands L^- , the ligands replace the water molecules of an aquo complex, say $[M(H_2O)_6]^{n+}$, successively, forming higher (or successive) complexes according to the reactions



and so on, with equilibrium dissociation constants β_1 , β_2 , etc.

While describing chemical reactions between an aquo complex and a ligand, the water molecules contained in the complex and the valency of the complex are not mentioned. For example, the complexes in Equations (1.11) and (1.12) are represented as M, ML, ML_2 , ..., ML_{n-1} and ML_n , while the equilibrium dissociation constants are given by equations of the following type:

$$\beta_n = \frac{[ML_n]}{[ML_{n-1}][L]} \quad (1.13)$$

where M is a metal ion, L is a ligand, and the complete dissociation of ML_n gives



with the solubility product

$$K_s = [M^{n+}][L]^n \quad (1.15)$$

The successive equilibrium dissociation constants usually follow the relation

$$\beta_1 > \beta_2 > \dots > \beta_{n-1} > \beta_n \quad (1.16)$$

Between β_1 and β_2 the following empirical correlation has been found (Shock and Koretski, 1993, 1995; Sassani and Shock, 1998; Prapaipong *et al.*, 1999):

$$\log \beta_2 = A - B \log \beta_1 \quad (1.17)$$

where A and B are constants. The constant B is 1.83, 2.13 and 1.76 for monovalent inorganic and organic ligands, oxalate and malonate complexes, respectively, and has been attributed to the number of groups available to bind with metal cation (Prapaipong *et al.*, 1999).

The above complexes formed by the cation M and the ligand L can be neutral, positively charged or negatively charged. This may be understood better when the charges on the cation and the ligand are taken into account. If z_1 and z_2 denote the valencies of the cation M and the ligand L, the ligand L^{z_2-} and the cation M^{z_1+} form the complexes $ML^{(z_1-z_2)+}$, $(ML_2)^{(z_1-2z_2)+}$ and $(ML_3)^{(z_1-3z_2)+}$. For example, trivalent Fe^{3+} and bivalent $C_2O_4^{2-}$ form the following complexes: $Fe(C_2O_4)^+$, $Fe(C_2O_4)_2^-$ and $Fe(C_2O_4)_3^{3-}$ with $\log \beta_1 = -7.53$, $\log \beta_2 = -13.64$ and $\log \beta_3 = -18.4$.

It is well known that several cations undergo hydrolysis when their concentration in the solution is increased. The stability of different hydroxyl complexes of a metal is determined by the solution pH. Figure 1.3 illustrates the speciation of Cu(II) complexes formed in aqueous solutions of $CuCl_2$ as a function of solution pH. It may be seen that

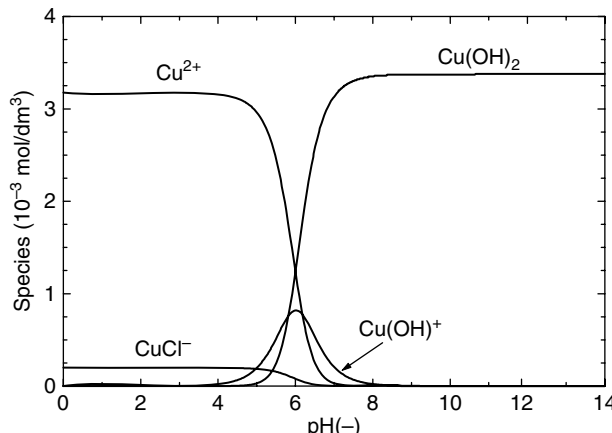


Figure 1.3 Speciation of different Cu(II) species in aqueous solution of $3.375 \times 10^{-3} \text{ mol}/\text{dm}^3$ $CuCl_2$ as a function of solution pH. Courtesy of E. Mielniczek-Brzóska (2005)

only Cu^{2+} ions (as solvated species) are present at pH below 4, while only $\text{Cu}(\text{OH})_2$ is formed at pH exceeding 8. In the pH range 5.4–6.6, three species Cu^{2+} , $\text{Cu}(\text{OH})^+$ and $\text{Cu}(\text{OH})_2$ coexist, but Cu^{2+} and $\text{Cu}(\text{OH})^+$ exist at pH between 4 and 5.4 and $\text{Cu}(\text{OH})^+$ and $\text{Cu}(\text{OH})_2$ at pH between 6.6 and 8. These curves are determined by the stability constants of the complexes.

1.3 Structure of Aqueous Electrolyte Solutions Containing Additives

When an electrolyte additive is added to an aqueous solution of an electrolyte, the complexes formed represent the characteristics of complexes due to both the solute and the additive. In this case, in addition to the aquo complexes formed by the dissociation of the solute, the solution contains a mixture of complexes formed by the equilibrium dissociation reactions between the solute ligand and the additive cation. The main complexes formed now are $\text{ML}^{(z_1-z_2)+}$, $(\text{ML}_2)^{(z_1-2z_2)+}$ and $(\text{ML}_3)^{(z_1-3z_2)+}$. For example, in the presence of Cu^{2+} ions, they are $\text{Cu}(\text{C}_2\text{O}_4)$ and $\text{Cu}(\text{C}_2\text{O}_4)_2^{2-}$, and the solution pH is determined by the latter charged complex.

The pH of a solution depends on the concentrations of both solute and additive present in it. This feature is shown in Figure 1.4a and b, which illustrate the dependence of solution pH on $\ln c$ (where c is the ammonium oxalate concentration) for different concentrations c_i of Cu(II) and Cr(III) ions, respectively. The plots in both figures may be divided into well-defined regions of linear plots of solution pH against ammonium oxalate concentration c , where the transition of one region to another may be defined by either solution pH or solute c . In the case of Cu(II) ions, for example, these regions are (I) $\text{pH} < \text{pH}_1$, (II) $\text{pH}_1 < \text{pH} < \text{pH}_2$, and (III) $\text{pH} > \text{pH}_2$, where the value of pH_2 depends

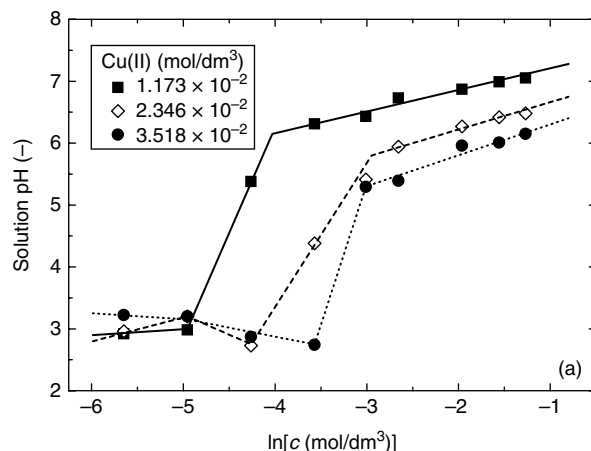


Figure 1.4 Relationship between solution pH and $\ln c$ of ammonium oxalate concentration for different concentrations c_i of two additives: (a) Cu(II) and (b) Cr(III). The plots may be divided into well-defined regions of linear plots. Reproduced from (a) K. Sangwal and E. Mielniczek-Brzóska. Fluid Phase Equilibria, in press. Copyright (2007a), with permission from Elsevier; and (b) K. Sangwal and E. Mielniczek-Brzóska (2005), unpublished work

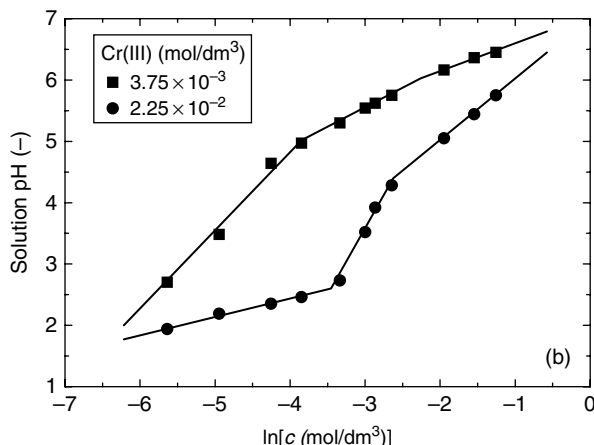


Figure 1.4 (Continued)

on solute concentration c . Alternatively, the solute concentrations corresponding to the transitions are c_1 and c_2 . The values of c_1 and c_2 are determined by additive concentration c_i . Hence it may be argued that these three regions correspond to the predominance of three different complexes.

The concentrations of different copper complexes formed in aqueous ammonium oxalate AO solutions for Cu(II) concentration of 1.173×10^{-2} mol/dm³ is presented as plots of $\ln[\text{species}]$ against $\ln c$ in Figure 1.5. It is clearly seen that Cu^{2+} and $\text{Cu}(\text{C}_2\text{O}_4)$, $\text{Cu}(\text{C}_2\text{O}_4)^{2-}$ and $\text{Cu}(\text{C}_2\text{O}_4)_2^{2-}$, and $\text{Cu}(\text{C}_2\text{O}_4)$ complexes are predominant for

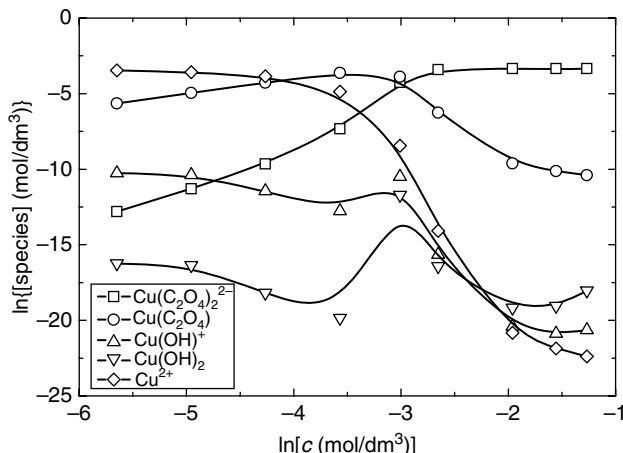


Figure 1.5 Plots of concentrations of different copper complexes formed in aqueous ammonium oxalate solutions for Cu(II) concentration of 1.173×10^{-2} mol/dm³. Reproduced from K. Sangwal and E. Mielniczek-Brzóska. Fluid Phase Equilibria, in press. Copyright (2007a), with permission from Elsevier

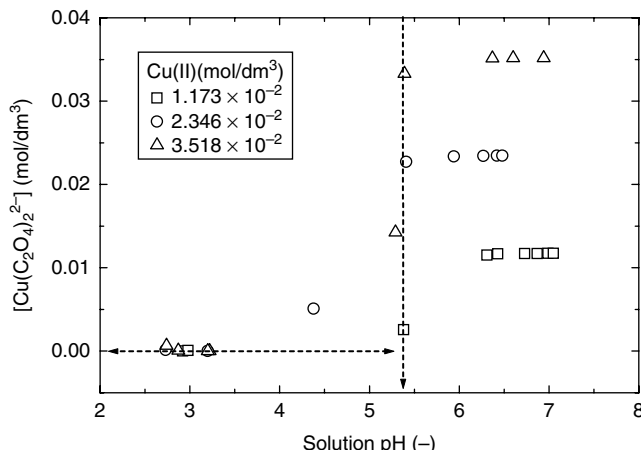


Figure 1.6 Dependence of concentration of $\text{Cu}(\text{C}_2\text{O}_4)_2^{2-}$ on solution pH for three Cu(II) concentrations in the starting solutions. Note that concentration of $\text{Cu}(\text{C}_2\text{O}_4)_2^{2-}$ suddenly increases when solution pH exceeds 5.3. Reproduced from K. Sangwal and E. Mielniczek-Brzóska. Fluid Phase Equilibria, in press. Copyright (2007a), with permission from Elsevier

$\ln c < -4.5$, $-4.5 < \ln c < -3$, and $\ln c > -3$, respectively. The values of $\ln c = -4.5$ and -3 correspond to the transition concentrations $c_1 \approx 0.01 \text{ mol}/\text{dm}^3$ and $c_2 \approx 0.03 \text{ mol}/\text{dm}^3$. The solute concentration interval $c_1 < c < c_2$ indicates the pH range when precipitation of $\text{Cu}(\text{OH})_2$ takes place. The dependence of concentration of $\text{Cu}(\text{C}_2\text{O}_4)_2^{2-}$ complex formed in ammonium oxalate in the presence of three Cu^{2+} concentrations on solution pH is shown in Figure 1.6. It can be clearly seen that the precipitation of $\text{Cu}(\text{OH})_2$ is completely suppressed for $\text{pH} > 5.4$ and $\text{Cu}(\text{C}_2\text{O}_4)_2^{2-}$ complexes begin to prevail in every solution.

Speciation analysis of complexes in saturated and unsaturated electrolyte solutions containing additive cations can be carried out using specially written computer programs based on chemical equilibria of complexes. In the calculations of concentrations of different complexes, one requires data on the stability constant β of various possible complexes, solution composition (i.e. concentrations c_i of additive cations and c of solute) and solution pH. In a recent study of speciation of complex species in saturated aqueous solutions of ammonium oxalate at 30 °C containing bivalent [i.e. Cu(II), Mn(II), Zn(II), Co(II) and Ni(II)] and trivalent [Fe(III) and Cr(III)] cationic additives, it was found (Sangwal and Mielniczek-Brzóska, 2007b) that the concentrations of various complex species increase whereas those of $\text{C}_2\text{O}_4^{2-}$ and H^+ decrease with increase in the concentration of an additive in the saturated solutions. As an example, Figure 1.7 illustrates the concentrations of different complexes, denoted here as [species], formed with increasing concentrations c_i of Cu(II) additive in saturated solutions containing increasing solute concentration c_0 as plots of $\ln[\text{species}]$ against $\ln(c_i/c_0)$.

Speciation analysis also revealed that the dominant complexes present in saturated solutions are $\text{Cu}(\text{C}_2\text{O}_4)_2^{2-}$ for Cu(II), $\text{M}_{\text{II}}(\text{C}_2\text{O}_4)_3^{4-}$ for the other bivalent cations M(II), and $\text{M}_{\text{III}}(\text{C}_2\text{O}_4)_3^{3-}$ for Cr(III) and Fe(III) additives. It may be noted from Figure 1.8 that, irrespective of the type of the impurity and the value of the ratio c_i/c_0 , the concentrations

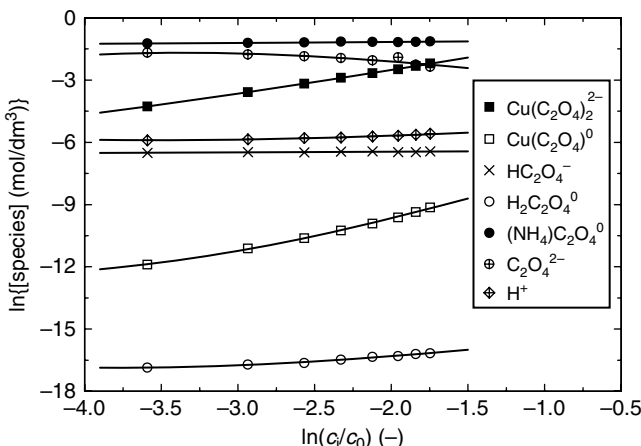


Figure 1.7 Dependence of logarithm of concentration of various complexes (denoted $\ln[\text{species}]$) on $\ln(c_i/c_0)$ for Cu(II) additive. Concentrations are in mol/dm^3 . Continuous curves are drawn according to a cubic relations but they can equally well be described by a quadratic relation. Reproduced from K. Sangwal and E. Mielniczek-Brzóska. Cryst. Res. Technol. **42**, 531. Copyright (2007b), with permission from Wiley-VCH

of dominating complexes are practically the same in the saturated solutions. Consequently, the data of $\ln[\text{species}]$ against $\ln(c_i/c_0)$ for various complexes predominantly present in saturated solutions containing different additives fall on the same plot (see Figure 1.8). However, a careful examination of the experimental data reveals that the points for Mn(II) impurity lie somewhat below the data points for the remaining impurities. This difference is associated with the fact that in the saturated solutions of the latter additives practically 99% of the metal ions form dominant complexes and the remaining about 1% form other complexes, whereas in the solutions containing Mn(II) about 72% of the metal ions form $\text{Mn}(\text{C}_2\text{O}_4)_3^{4-}$ complex and the remaining 28% $\text{Mn}(\text{C}_2\text{O}_4)_2^{2-}$ and $\text{Mn}(\text{C}_2\text{O}_4)^0$ complexes.

It should be mentioned that the plots of $\ln[\text{species}]$ against $\ln(c_i/c_0)$ for various complexes of different impurities show similar trends, which may be described by empirical relations. In a narrow range of $\ln(c_i/c_0)$ between about -4.5 and -2, the data for various complexes of different impurities may be represented reasonably well by a linear dependence (Figure 1.8), but in the entire $\ln(c_i/c_0)$ interval, the data are better described by quadratic or cubic relations (see Figure 1.8). The physical basis of these empirical relations remains unclear.

The formation of chemical species in solutions of electrolytes involves strong chemical interactions in the form of bonds between metal ions and ligands. These chemical bonds provide permanent association between cations and anions in adjacent positions and are not separated by neutral solvent molecules. The chemical bonds differ from electrostatic interactions, which are temporary affairs. The different units of a species are not static, but change their positions by bending, stretching or twisting relative to each other. These changes in the bonds within the species are related to the chemical constitution.

Information about the constitution and concentrations of various species in an electrolyte solution can be obtained by employing various kinds of absorption spectroscopy.

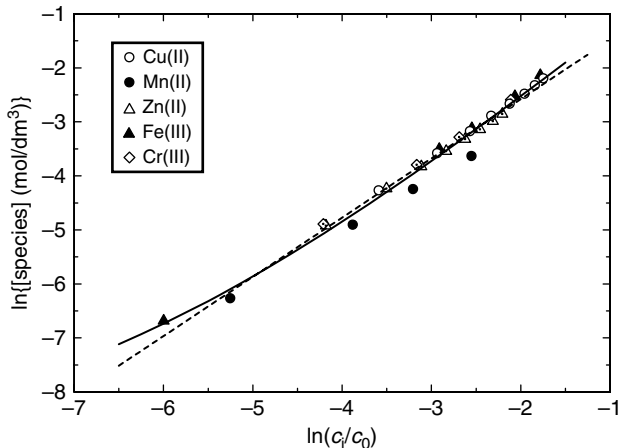


Figure 1.8 Dependence of logarithm of concentration of dominant complexes (denoted $\ln[\text{species}]$) on $\ln(c_i/c_0)$ for various additives. Concentrations are in mol/dm³. The continuous curve is drawn according to a cubic relation and the dashed curve represents a linear dependence. Reproduced from K. Sangwal and E. Mielniczek-Brzóska. Cryst. Res. Technol. **42**, 531. Copyright (2007b), with permission from Wiley-VCH

The commonly used techniques are ultraviolet and visible (UV-vis), infrared Raman, nuclear magnetic resonance, and electron spin resonance absorption spectroscopy. For instance, in UV-vis spectroscopy, the intensity I of the peak in an absorption spectrum is associated with the concentration of particular species present in the solution, while the wavenumber $\nu/c_{\text{light}} = 1/\lambda$ corresponding to the position of the peak is characteristic of the chemical constitution of the species. Here ν and λ are the frequency and the wavelength of the absorbed light and c_{light} is the velocity of light.

Information on changes in the chemical constitution of various species present in solutions composed of a given additive concentration c_i and changing concentration of solute c is reflected in the plots of molar absorptivity ε_{abs} (calculated from the light intensity I) and λ , as a function of solute concentration c . For example, based on data obtained from the spectra of aqueous solutions of different concentrations c of ammonium oxalate containing a predefined concentration c_i of Cu(II) additive recorded in the visible wavelength region, the plots of $\varepsilon_{\text{abs}}(c)$ and $\lambda(c)$ reveal three distinct regions of AO concentration c defined by different values of ε_{abs} and λ (Sangwal and Mielniczek-Brzóska, 2007a). The values of the transition concentrations c_1 and c_2 characterizing the three regions were found to be similar to those obtained from Figure 1.5.

Sangwal and Mielniczek-Brzóska (2007a) observed an empirical relation between λ and c :

$$\lambda = \lambda_0(1 - \theta) \quad (1.18)$$

where λ is the value of wavelength of absorbed light corresponding to the coverage θ , λ_0 is the value of λ when $\theta = 0$, and θ is the fractional coverage of the surface of a complex by the solute and is given by the usual adsorption isotherms (see Section 4.2). Physically,

$0 \leq \theta \leq 1$ is the interval of the ratio c_i/c of concentrations of Cu(II) and AO corresponding to a given c_i , when a particular complex is stable in the solution. Obviously, $\theta = 0$ and $\theta = 1$ are the limits of the appearance and disappearance of the complex formed in the interval of the concentration ratio c_i/c . The results also showed that the value of $\lambda_0 = 790$ nm agrees well with the value of 794 nm for $\text{Cu}(\text{H}_2\text{O})_6^{2+}$ complex, whereas the values 790 and 710 nm are associated with the formation of $\text{Cu}(\text{OH})_2$ and $\text{Cu}(\text{C}_2\text{O}_4)_2^{2-}$ species formed in regions II and III, respectively. The values of about 15 kJ/mol for the differential heat of adsorption Q_{diff} are roughly half of the values for several adsorption processes on crystal surfaces (see Chapter 4).

It should be mentioned that the value of differential heat of adsorption Q_{diff} , given above, is lower by a factor between about 0.05 and 0.3 of the standard heat of formation of a variety of inorganic ions in aqueous solutions (Lide, 1996/1997). Instead, the value of Q_{diff} is comparable with the values of integral heats of solution to form compounds from their ions (Lide, 1996/1997). This implies that Q_{diff} is directly connected neither with the strength of bonds between the atoms of the complex species nor with the standard enthalpy of their formation. This is mainly due to the fact Q_{diff} is not equal to the energy of adsorption (i.e. chemical association or formation); see Section 4.2.

Knowledge of the presence and concentration of various species by speciation analysis is essential for identifying the species that interact with the surface of a crystal during its growth and dissolution. Therefore, after knowing the species present in a growth or dissolution medium, one should determine the possible candidates which can ensure attractive interactions with the ions/radicals at the crystal interface. Obviously, the most

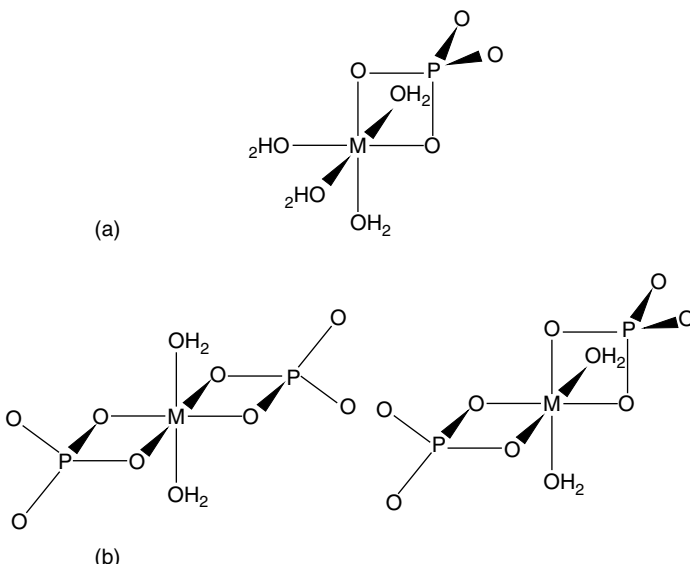
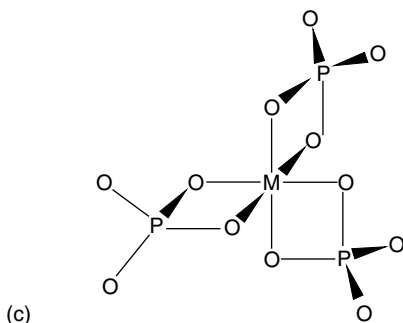


Figure 1.9 Spatial structure of phosphate complexes: (a) MHPo_4^+ , (b) $\text{M}(\text{HPO}_4)_2^-$ and (c) $\text{M}(\text{HPO}_4)_3^{3-}$. Hydrogen atoms are not shown. Reproduced from S. Veintemillas-Verdaguer and R. Rodriguez-Clemente. J. Cryst. Growth 79, 198. Copyright (1986), with permission from Elsevier

**Figure 1.9** (Continued)

strongly adsorbing complex is the most effective. However, the overall effect of a somewhat less effective complex can be more than that of the most effective complex, depending on the relative concentration of the two or more complexes.

Adsorption of a metal complex with the ions/radicals at the crystal interface is related with the structure of the complex, and is determined by the spatial coordination of ligands with the metal ion. Figure 1.9 illustrates the spatial structure of phosphate complexes MHPo_4^+ , $\text{M}(\text{HPO}_4)_2^-$ and $\text{M}(\text{HPO}_4)_3^{3-}$, composed of M(III) ions coordinated with one, two and three phosphate groups, respectively. Evidently, complexes in which ligands lie in the same plane are likely to adsorb more strongly than others (see Section 4.11).

1.4 Polyelectrolytes and Surfactants in Solutions

Polyelectrolytes are charged polymers in aqueous solutions. Based on their nature, polyelectrolytes may be divided into three main groups (Füredi-Milhofer and Sarig, 1996): (1) soluble polymers, (2) proteins, and (3) polysaccharides. The first group may be divided further into (i) synthetic soluble polymers and (ii) polypeptides, the second group into (i) proteins and (ii) proteoglycans, and the third group into (i) polysaccharides and (ii) mucopolysaccharides. Both proteoglycans and mucopolysaccharides contain a protein and a polysaccharide moiety, with the difference that in proteoglycans the protein fraction dominates. Polyelectrolytes possess an array of polar (basic and/or acidic) groups on an open chain (for example, most of the synthetic polymers and some polypeptides) or have a tertiary structure. Some polypeptides, and most of the proteins and proteoglycans, have carboxylic arrays which may fold in a planar beta-sheet configuration.

Polyelectrolyte (multifunctional) impurities are phosphonic acids, polycarboxylic acids, polysulfonic acids, and different low and high molecular weight copolymers with various acidic groups. In aqueous solutions, at low concentrations the molecules of a polyelectrolyte are arranged in a linear array due to the electric field concentrated along the polyelectrolyte chain. However, with increasing polyelectrolyte concentration screening of the electric field due to the proximity of the polyelectrolyte ions the molecular chain becomes bent. In saturated electrolyte solutions, negative polyelectrolyte ions may be coordinated to the solute cations forming complexes.

Surfactants are amphiphilic molecules having a hydrophobic part and a hydrophilic ionic group (see also Section 4.2.2). The hydrophilic (polar) part has a high affinity for water, whereas the hydrophobic (nonpolar) part has a high affinity for fat molecules. Most surfactants can be represented by the formula RX, where R is the hydrophilic head group and X is the lipophilic (hydrophobic) tail group. The head group may be anionic, cationic, zwitterionic or nonionic. The tail group usually consists of one or more hydrocarbon chains having between 10 and 20 carbon atoms per chain. The chains may be saturated or unsaturated, linear or branched, aliphatic and/or aromatic. Surfactants used in the food industry have mainly nonionic (monoglycerides, Tweens and Spans) or zwitterionic head groups (e.g. lecithin) and one or two linear aliphatic chains, saturated or unsaturated, in tail groups (Dickinson and McClements, 1995).

The overall affinity of surfactants for an oil phase or an aqueous phase is usually defined on the basis of their hydrophile–lipophile balance (HLB) number (Dickinson and McClements, 1995). A surfactant with a low HLB number (between 4 and 6) is predominantly hydrophobic, dissolves preferentially in oil, stabilizes water-in-oil emulsions and forms reverse micelles (see below). A surfactant with a high HLB number (between 8 and 18) is predominantly hydrophilic, dissolves preferentially in water, stabilizes oil-in-water emulsions and forms micelles in water. A surfactant with an intermediate HLB number (about 7) has no preference for either solvent. The HLB number is, therefore, an important factor when selecting a surfactant for a specified application. However, other factors, such as molecular geometry and intermolecular interactions, also influence the overall physico-chemical properties of surfactant solutions.

Surfactant molecules aggregate spontaneously in aqueous solutions to form micelles, bilayers, vesicles and reverse micelles (Figure 1.10). The formation of these thermodynamically stable structures is a consequence of the asymmetric nature of the surfactant molecules. Their formation minimizes the contact area between nonpolar tail groups and water, thereby reducing the positive free energy associated with the nonpolar groups (i.e. hydrophobic effect).

Electrostatic repulsion between charged head groups, partial dehydration of head groups and constrained translation of surfactant molecules are the main factors opposing the formation of the stable structures. Above a certain surfactant concentration, the hydrophobic effect prevails against the above factors and stable micelles are formed. At this surfactant concentration, there is an abrupt change in the solution properties such as surface tension, conductivity and turbidity. The surfactant concentration when micellar formation occurs is usually referred to as the critical micelle concentration (CMC). The value of the CMC of a surfactant is determined by its chemical properties and the composition and temperature of the solvent. For more details on micelles and CMCs of a variety of natural and synthetic surfactants, the reader is referred to monographs by Jones and Chapman (1995) and Dickinson and McClements (1995).

Micelles may be spherical or non-spherical, depending on the molecular geometry of the surfactant molecules. Usually, micelles contain between 10 and 100 molecules and have diameters of about 5 nm (i.e. about twice the diameters of individual molecules). At concentrations below the CMC, ionic surfactants behave like simple electrolytes. For example, their conductivity increases linearly with surfactant concentration. Thus, the active concentration of the surfactant is equal to the real value only below the CMC and

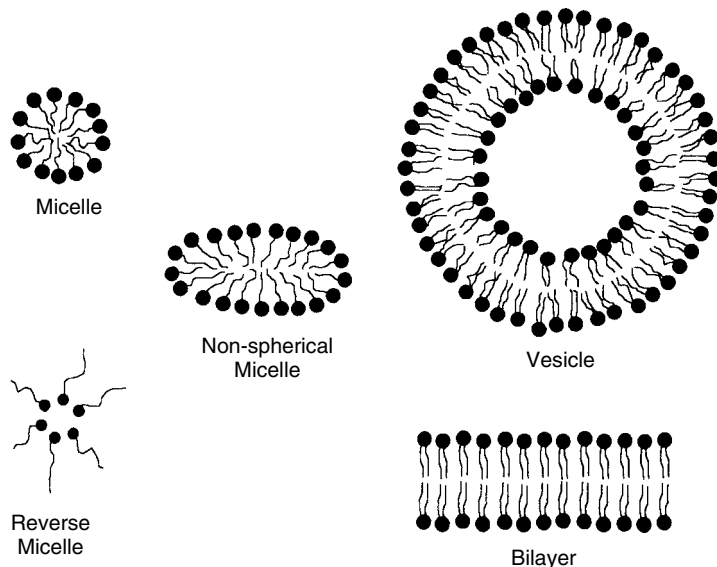


Figure 1.10 Schematic illustration of different types of stable aggregates of surfactant molecules. Reproduced from E. Dickinson and D.J. McClements. Advances in Food Colloids. Copyright (1995), with permission from Springer Science and Business Media

the micelle formation is related to the insufficiency of water molecules to solvate the surfactant molecules.

In concentrated aqueous solutions, the state of surfactants is determined by micelle formation and precipitation of the surfactants with some ions of the salt. Since the micelle formation is related to the insufficiency of water molecules to solvate the surfactant, the solvation of a dissolved electrolyte reduces the concentration of free water molecules. Consequently, the value of the CMC decreases with increase in the electrolyte solution. However, exceptions to this general trend are also known (König and Emons, 1988). For example, clustering takes place in aqueous MgSO_4 solutions above a 2 molal concentration. This clustering liberates water molecules above a 2 molal concentration. Consequently, a progressive increase in CMC for sodium dodecyl sulfate is observed in MgSO_4 solutions.

1.5 Polydentate Ligands and Molecular Additives

Polydentate ligands are substances, which coordinate mainly with cations available in the solution or of the crystal surface, forming complexes. Typical substances of this type are EDTA (ethylenediaminetetraacetic acid), polyphosphates and many organophosphorus compounds. Other molecular additives include soluble organic dyes, amino acids, organic ions and molecules in aqueous solutions, and small organic molecules and polymers in organic solutions. In aqueous solutions, the behavior of molecular additives is explained by using the concepts of electrolytic dissociation, solvation, complexation, etc.

Since the hydrogen bond is stronger than van der Waals type interactions and is usually distributed in specific directions rather than a few strong ionic bonds responsible for the effect of ionic additives during the growth of inorganic salts, the action of hydrogen bonding additives can be selective to certain faces of a crystal. Such substances are called tailor-made additives or impurities. Tailor-made additives are usually composed of giant molecules whose molecular structure is similar to that of the substrate molecules comprising the crystal. They have their structure specifically modified with respect to the substrate only at one site of the additive molecules.

1.6 Crystal–Additive Interactions

During nucleation and growth of crystals, different types of interactions are involved between growth species (molecules or ions) and the growing surface. These interactions include van der Waals, ionic and hydrogen bonding. Van der Waals interactions are important during the growth of simple organic compounds such as *n*-alkanes and ionic interactions during the crystallization of simple ionic crystals, while hydrogen bonding is important during the growth of both organic and inorganic compounds. During growth in the presence of additives also, similar chemical interactions occur at the interface between the additive species and the solid phase.

The effect of simple electrolyte additives is due to electrostatic interaction between the additive species (hydrated ions or metal complexes) and the crystal ions of opposite charge at kinks or surface terrace, followed by chemical reactions on the surface. The inhibiting action of polyelectrolyte additives is essentially due to the long-distance electrostatic interaction between the polyelectrolyte groups or negatively charged ligands and cations of the crystal surface, followed by the formation of bonds with possible substitution of surface anions by the ligands.

Different types of chemical interactions involved during growth are discussed in Chapter 4.

References

- Bockris, J. O'M., and A.K.N. Reddy (1970). *Modern Electrochemistry*, Vols 1 and 2, Plenum Press, New York.
- Dickinson, E., and D.J. McClements (1995). *Advances in Food Colloids*, Chapman and Hall, London.
- Füredi-Milhofer, H., and S. Sarig (1996). *Prog. Cryst. Growth Charact. Mater.* **32**, 45.
- Izmailov, N.A. (1976). *Elektrokhimiya Rastvorov* (*Electrochemistry of Solutions*), 3rd ed., Khimiya, Moscow.
- Jones, M.N., and D. Chapman (1995). *Micelles, Monolayers, and Biomembranes*, Wiley-Liss, New York.
- König, A., and H.H. Emmons (1988). *Cryst. Res. Technol.* **23**, 319.
- Lide, D.R. (Ed.) (1996/1997). *Handbook of Chemistry and Physics*, 77th ed., CRC Press, Boca Raton, FL.
- Mielniczek-Brzóska, E. (2005). Unpublished work.
- Misztal, R. (2004). *PhD Thesis*, Jagiellonian University, Cracow.

- Ohtaki, H. (2001). *Monatsh. Chem.* **132**, 1237.
- Prapaipong, P., E.L. Shock, and C.M. Koretsky (1999). *Geochim. Cosmochim. Acta* **63**, 2547.
- Sangwal, K., and E. Mielniczek-Brzóyska (2005). Unpublished work.
- Sangwal, K., and E. Mielniczek-Brzóyska (2007a). *Fluid Phase Equilibria*, in press.
- Sangwal, K., and E. Mielniczek-Brzóyska (2007b). *Cryst. Res. Technol.* **42**, 531.
- Sassani, D.C., and E.L. Shock (1998). *Geochim Cosmochim. Acta* **62**, 2671.
- Shock, E.L., and C.M. Koretsky (1993). *Geochim. Cosmochim. Acta* **57**, 4899.
- Shock, E.L., and C.M. Koretsky (1995). *Geochim. Cosmochim. Acta* **59**, 1497.
- van Rosmalen, G.M., and P. Bennema (1990). *J. Cryst. Growth* **99**, 1053.
- Veintemillas-Verdaguer, S., and R. Rodriguez-Clemente (1986). *J. Cryst. Growth* **79**, 198.

2

Three-Dimensional Nucleation and Metastable Zone Width

Physical (e.g. condensation, crystallization, phase transitions in the solid phase) and chemical processes (e.g. heterogeneous reactions) in the vapor, melt or solution phases of every system take place through the formation of three-dimensional (3D) nuclei of a new phase and occur only when the medium is supersaturated. The formation of the nuclei is associated with a change in the free energy of the system. In homogeneous systems, nuclei of the new phase are not formed as soon as the system becomes supersaturated even though thermodynamically such a situation is possible. The system is said to be in a state of metastable equilibrium, and it can remain in that state without attaining the minimum free energy corresponding to the equilibrium state. In other words, in such cases nucleation of the new phase sets in after some period (called the induction period), the value of which depends on such factors as the temperature and pressure of the system, the presence of chemical phases (impurities) different from the nucleating phase and mechanical disturbances. Introduction of seeds of the nucleating phase and increased supersaturation level facilitate the process of nucleation of the new phase. However, there is always a supersaturation level when the new phase nucleates instantaneously, i.e. the new phase precipitates. This supersaturation level corresponds to the upper limit of the state of metastable equilibrium and defines the width of the metastable zone width.

Nuclei, which can attain a size greater than that of a critical nucleus, develop into crystals of visible size by the attachment of growth species (i.e. molecules, atoms or ions) at energetically favorable growth sites such as kinks in the ledges of a surface. At a given supersaturation and temperature, there is a critical value of the free energy when stable 3D nuclei of critical size are formed. Thus, the process of growth of crystals of visible

size involves at least two stages: (1) formation of stable 3D nuclei and (2) development of the stable 3D nuclei into crystals with well-developed faces.

In this chapter, the basic concepts of driving force for nucleation and growth of crystals and of the process of 3D nucleation are first outlined. Using the expressions for 3D nucleation, the metastable zone width is then described. Finally, the effects of additives on nucleation rates, nucleation of polymorphs, solubility of ionic salts, and metastable zone width are discussed.

2.1 Driving Force for Phase Transition

In order to understand the conditions when nuclei of phase II are formed from a homogeneous phase I such as vapor, melt or solution, we refer to Figure 2.1. The solid curve shows the situation when the two phases are in equilibrium conditions. A vapor–crystal phase change is characterized by a p – T diagram, and a solution–crystal phase change by a c – T diagram. Here p is the vapor pressure, c the solute concentration, and p_0 and c_0 denote the saturation vapor pressure and the equilibrium solute concentration at temperature T_0 , respectively.

We consider the change from vapor to crystalline phase during the cooling of the vapor, as shown by the line ABCD in the p – T diagram in Figure 2.1. Points B and D represent the equilibrium state in the two phases. At a constant vapor pressure p_1 , a decrease in the temperature along the curve BC means passing through the equilibrium curve, with phase I becoming metastable (i.e. supersaturated). The supersaturation of the vapor phase is represented by the difference $\Delta p = p_1 - p_0$. At a constant temperature T_0 , the change takes place along the curve CD as a result of decreasing supersaturation to the point D, where Δp becomes zero. Thus, the supersaturated state of the vapor phase may be represented either with reference to a constant temperature T_0 by the difference Δp or with reference to a constant vapor pressure p_1 by the difference $\Delta T = T_1 - T_0$.

In the case of a c – T diagram, at a constant temperature T supersaturation is represented by $\Delta c = c - c_0$, where c and c_0 denote the actual and the equilibrium concentration of solute in the solution. In the case of a melt, its supercooling is denoted by $\Delta T = T - T_0$, where T is the temperature of the supercooled melt and T_0 is the melting point of the solute (with $T > T_0$). The supersaturation σ is defined by the ratios $\Delta p/p_0$ and $\Delta c/c_0$, while the ratio $S = p/p_0$ or c/c_0 .

It should be noted that a system becomes metastable only when $\Delta p = p - p_0$ or $\Delta c = c - c_0 > 0$. Under these conditions, only nucleation, precipitation, deposition and growth of new phase II are possible. Spontaneous nucleation (i.e. precipitation) of phase II occurs when Δp or Δc exceed certain values Δp^* or Δc^* . These values of Δp^* or Δc^* characterize the width of the metastable zone width, and is shown by the dotted curve in Figure 2.1. When Δp or $\Delta c < 0$, the system is always stable. In this case, if phase II is present in the system, it undergoes evaporation or dissolution.

The driving force for the processes of crystallization (i.e. nucleation, precipitation, growth, deposition, etc.) is the difference in the free energy of supersaturated or supercooled mother phase and the free energy of the newly forming phase. Under constant temperature and pressure conditions, any change in a system proceeds from a state of higher to a state of lower Gibbs free energy. Consequently, the Gibbs function G is taken

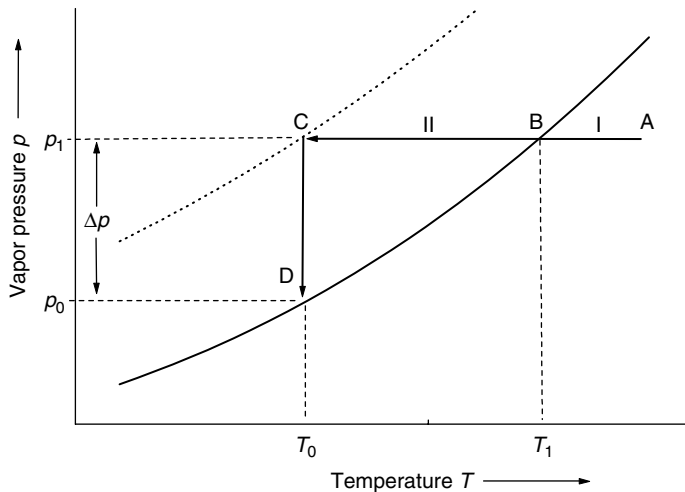


Figure 2.1 Schematic illustration of the dependence of vapor pressure p of a system on temperature. The solid curve shows the state when vapor phase I is in equilibrium with solid phase II and the dotted curve shows the upper limit of the metastable zone when precipitation of phase II occurs in the system

as a thermodynamic potential, and the change in the system as a passage from a state of higher to a state of lower potential. Thus, the reaction



is thermodynamically possible if the change in the free energy

$$\Delta G = (cG_C + dG_D) - (aG_A + bG_B) < 0 \quad (2.2)$$

where A and B are the reactants, C and D are the reaction products, and a , b , c and d denote the number of moles of A, B, C and D, respectively, participating in the reaction.

The change in the Gibbs free energy ΔG may be expressed by

$$\Delta G = G_{II} - G_I = \Delta H - T\Delta S \quad (2.3)$$

where H and S denote the enthalpy and entropy of a phase and $\Delta H = H_{II} - H_I$ and $\Delta S = S_{II} - S_I$. The dependence of the free energy G_I of vapor, melt or solution phase I, and G_{II} of solid phase II on temperature T and the free-energy change ΔG with respect to temperature are shown schematically in Figure 2.2. Obviously, formation of phase II is possible when $\Delta G > 0$ and occurs for $T < T_0$.

In the case of crystallization from the melt and the solution, the free-energy change may be expressed in terms of temperature difference ΔT . In the state of thermodynamic equilibrium when $\Delta G = 0$ (and $T = T_0$), from Equation (2.3) one has

$$\Delta S = \Delta H/T_0 \quad (2.4)$$

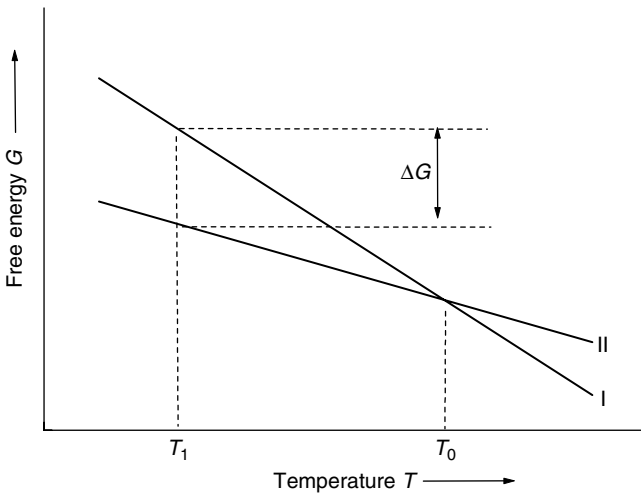


Figure 2.2 Change in Gibbs free energy G of vapor, melt or solution (phase I) and solid (phase II) as a function of temperature of a system

which, for nonequilibrium conditions, gives

$$\Delta G = \Delta H - T\Delta H/T_0 = \Delta H\Delta T/T_0 \quad (2.5)$$

where $\Delta T = T - T_0$.

If n_1, n_2, \dots, n_i represent the number of moles of components 1, 2, ..., i in a particular phase, the relationship between differences in thermodynamic potential ΔG and chemical potential μ may be expressed by

$$\Delta G = \sum_i \Delta \mu_i n_i \quad (2.6)$$

Here the difference in the chemical potentials of a given phase corresponding to the vapor pressures p and p_0 is given by

$$\Delta \mu = k_B T \ln(p/p_0) \quad (2.7)$$

where k_B is the Boltzmann constant and T is the temperature in kelvin. In the case of solutions, the chemical potential difference may be given by

$$\Delta \mu = k_B T \ln(a/a_0) = k_B T [\ln(f/f_0) + \ln(c/c_0)] \quad (2.8)$$

where a and a_0 are the activities of supersaturated and saturated solutions, respectively, f and f_0 are the corresponding activity coefficients, and c and c_0 are the concentrations of the solute in supersaturated and saturated solutions, respectively. For small values of supersaturations when $f/f_0 \approx 1$, Equation (2.8) may be written in the form

$$\Delta \mu = k_B T \ln(c/c_0) \quad (2.9)$$

In terms of temperature difference ΔT , from Equation (2.5) one may write

$$\Delta\mu = \Delta H \Delta T / T_0 n \quad (2.10)$$

where n is the number of particles produced by the dissociation of molecules in the liquid phase. Denoting the supersaturation ratio p/p_0 and c/c_0 by S and the supersaturation by $\sigma = (S - 1)$, Equations (2.8) and (2.9) may be written in the form

$$\Delta\mu = k_B T \ln(1 + \sigma) \quad (2.11)$$

and for small values of σ when $\ln(1 + \sigma) \approx \sigma$,

$$\Delta\mu = k_B T \sigma \quad (2.12)$$

For sparingly soluble salts, the supersaturation is given by

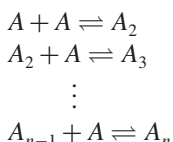
$$\Delta\mu/k_B T = \ln S = \ln(a/a_0) = \ln[(a_{\text{cation}} a_{\text{anion}})/K_s] \quad (2.13)$$

where a_{cation} and a_{anion} are the activities of free cations and anions, respectively, and $K_s = (a_{\text{cation}} a_{\text{anion}})$ is the solubility product of the electrolyte. Thus, supersaturation here is defined as the ratio between formation product and solubility product.

2.2 Three-Dimensional Nucleation of Crystals

2.2.1 Three-Dimensional Nucleation Rate

The formation of three-dimensional (3D) nuclei from atomic or molecular entities existing in the volume of a growth medium involves their aggregation in an ordered phase. The details of the process of aggregation of atoms or molecules in the supersaturated medium and the order in the structure of the nuclei are not well known. However, the process is usually envisaged to occur as a result of collision of individual atoms or molecules in such a way that the collisions yield a sequence of aggregates of increasing size such as dimers, trimers, tetramers, etc., according to the reactions



where A_2, A_3, \dots, A_n are the resulting aggregates formed by the additions of individual atoms/molecules to the preceding ones. Aggregates such as A_2, A_3, \dots, A_n are usually called embryos, sub-nuclei or clusters. The formation of sub-nuclei of large size is, therefore, a statistical process and the formation of such sub-nuclei by the collision of a large number of atoms/molecules simultaneously is highly improbable. Since the surface tension of a sphere is the lowest, the sub-nuclei prefer to attain a rounded shape. Since the process of formation of sub-nuclei is in dynamic equilibrium, some of them grow

larger whereas others simply disintegrate with time. However, the statistical addition of individual atoms/molecules to some of the sub-nuclei leads to their development into a size when they no longer disintegrate. Such nuclei are said to attain a critical size and are called three-dimensional stable nuclei.

The reduction in the Gibbs free energy of the system due to the formation of a spherical nucleus of radius r is equal to the sum of the surface excess free energy, ΔG_S , and the volume excess free energy, ΔG_V . The surface free energy, ΔG_S , is associated with the creation of the surface of the solid phase in the growth medium and is equal to the product of the surface area of the developing nucleus and the interfacial tension γ between the surface of the nucleus and the supersaturated medium surrounding it. Similarly, the volume excess free energy, ΔG_V , is a result of the creation of the volume of the nucleus in the medium and is equal to the product of the volume of the nucleus and the free energy change, ΔG_v , per unit volume. Then one may write the free energy change as

$$\Delta G = \Delta G_S + \Delta G_V = 4\pi r^2 \gamma + \frac{4}{3}\pi r^3 \Delta G_v \quad (2.14)$$

In a supersaturated medium, ΔG_v is a negative quantity. Therefore, the two terms on the right-hand side of Equation (2.13) depend differently on r . This behavior of the free energy change, ΔG , associated with the formation of the nucleus is shown in Figure 2.3 as a function of nucleus radius r . As can be seen, ΔG passes through a maximum and the maximum value ΔG_{3D}^* corresponds to the critical radius r_{3D}^* . The value of r_{3D}^* may be obtained by maximizing Equation (2.14), taking $d\Delta G/dr = 0$, i.e.

$$\frac{d\Delta G}{dr} = 8\pi r\gamma + 4\pi r^2 \Delta G_v = 0 \quad (2.15)$$

or

$$r_{3D}^* = -2\gamma/\Delta G_v \quad (2.16)$$

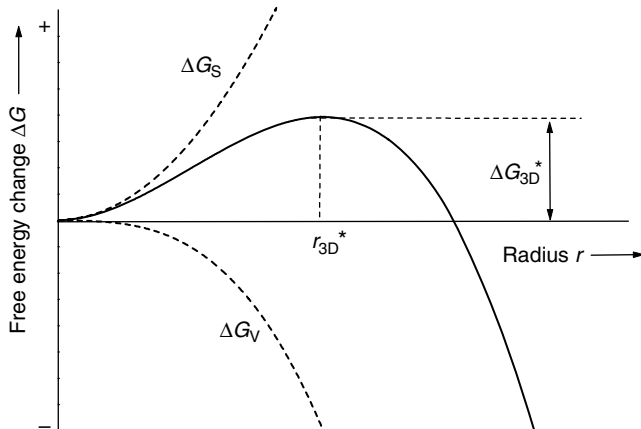


Figure 2.3 Change in Gibbs free energy ΔG as a function of radius r of nucleus formed in a supersaturated medium. Dashed curves show energy contributions ΔG_S and ΔG_V

where ΔG_v is a negative quantity. Substituting the value of r from Equation (2.16) into Equation (2.14), one obtains

$$\Delta G_{3D}^* = \frac{16\pi}{3} \frac{\gamma^3}{(\Delta G_v)^2} = \frac{4\pi}{3} \gamma r_{3D}^{*2} \quad (2.17)$$

It should be noted that in Equation (2.16), r_{3D}^{*2} is always positive because ΔG_v is a negative quantity.

The occurrence of a crystalline phase in a supersaturated medium depends on the radius r of the nuclei forming in it. When the radius r of the nuclei is smaller than r_{3D}^* , the nuclei dissolve. However, when $r > r_{3D}^*$, the nuclei are stable and grow. As can be seen from Figure 2.3, ΔG_{3D}^* is a barrier for 3D nucleation, and only when $r > r_{3D}^*$ is there a reduction in the free energy of the nucleus with an increase in its size. The critical radius r_{3D}^* is the minimum size of a stable nucleus.

Equation (2.17) may be expressed in a more practical form using the Gibbs–Thomson relation. According to the Gibbs–Thomson relation, the supersaturation ratio S and nucleus radius r are related by

$$\ln S = 2\gamma\Omega/k_B T r \quad (2.18)$$

where Ω is the molecular volume. Then

$$-\Delta G_v = 2\gamma/r = k_B T \ln S/\Omega \quad (2.19)$$

and from Equations (2.16), (2.17) and (2.19) one may write

$$r_{3D}^* = 2\gamma\Omega/k_B T \ln S \quad (2.20)$$

$$\Delta G_{3D}^* = \frac{16\pi}{3} \frac{\gamma^3 \Omega^2}{(k_B T \ln S)^2} \quad (2.21)$$

Obviously, increasing supersaturation and temperature and decreasing interfacial tension facilitate the formation of 3D nuclei.

It should be mentioned that every phase transition is associated with two energy changes: the overall change in the free energy ΔG , given by Equation (2.2), and the activation barrier ΔG_{3D}^* , given by Equation (2.21). The overall change in the free energy ΔG determines the stability of the 3D nuclei formed in the growth system, while the value of the activation barrier ΔG_{3D}^* determines the process of occurrence of 3D nucleation. The greater the change in ΔG , the higher is the stability of the phase formed (nuclei). Similarly, the higher the activation barrier ΔG_{3D}^* , the more difficult it is to attain stable nuclei. These energies may be represented schematically in the form of plot of free energy G as a function of reaction coordinate, as shown in Figure 2.4.

The activation barrier ΔG_{3D}^* , which is a measure of the ‘difficulty’ for embryos to attain the radius r_{3D}^* of the stable nuclei, defines the nucleation rate J . The nucleation

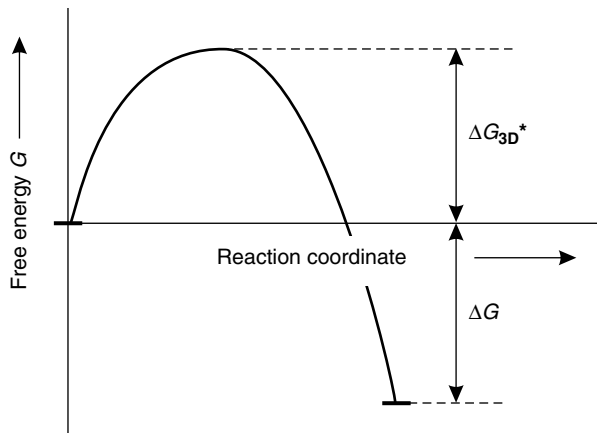


Figure 2.4 Free energy G as a function of reaction coordinate, illustrating schematically evolution of the energies ΔG_{3D}^* [Equation (2.21)] and ΔG [Equation (2.2)]

rate J is defined as the number of nuclei formed per unit volume per unit time, and is customarily described by an Arrhenius-type relation:

$$J = AS \exp(-\Delta G_{3D}^*/k_B T) \quad (2.22)$$

where A is a kinetic parameter determined by the attachment of atoms/molecules to the nucleus and ΔG_{3D}^* is given by Equation (2.21). However, the free energy change $\Delta G_{3D}^* = \Delta G_{3D}(i^*)$ corresponding to the stable nuclei composed of i^* molecules is achieved when the number $n(i^*)$ of critically sized clusters are in equilibrium with the number n of molecules per unit volume in the medium. The condition for this equilibrium is

$$n(i^*) = n \exp(-\Delta G_{3D}(i^*)/k_B T) \quad (2.23)$$

where i^* is a number.

In Equation (2.21), the factor $16\pi/3$ is a result of the geometry of a spherical nucleus. For nuclei of other geometries this geometric factor has other appropriate values. For a cube, for example, it is 32.

The behavior of the nucleation rate J on the supersaturation ratio S of systems is well described by Equation (2.22) at low solute concentrations. At high concentrations the viscosity of the system increases. Then the nucleation rate J begins to decrease with increasing S such that the nucleation rate J shows a maximum at a particular value of S . This behavior is shown in Figure 2.5. In this case the nucleation rate is given by

$$J = AS \exp\left(-\frac{\Delta G_{3D}^*}{kT} + \frac{\Delta G'}{kT}\right) \quad (2.24)$$

where $\Delta G'$ is the activation energy for the motion of atoms/molecules across the nucleus–medium interface. At low values of S when ΔG_{3D}^* dominates, the rate increases with

increase in S . However, at very high values of S when ΔG_{3D}^* becomes negligible in comparison with $\Delta G'$, the latter term begins to dominate. Consequently, at very high values of S when ΔG_{3D}^* becomes relatively small in comparison with $\Delta G'$, the nucleation rate J is decreased. Absence of nucleation means that the system is in the glassy state.

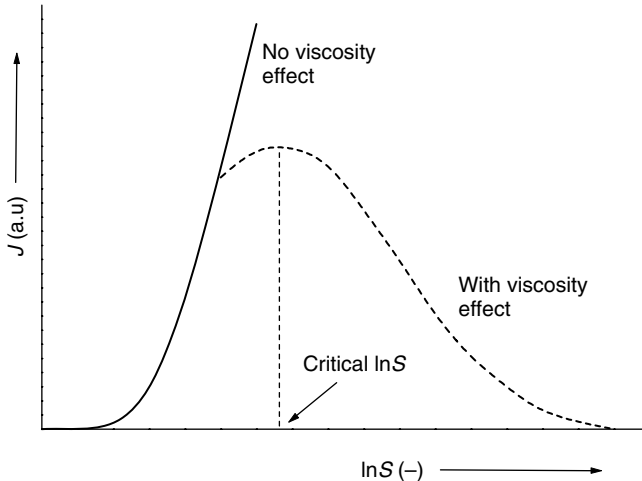


Figure 2.5 Dependence of 3D nucleation rate J on supersaturation ratio $\ln S$. Note that there is a critical value of supersaturation above which increased viscosity of the medium leads to a decrease in J

The treatment of 3D nucleation described above is based on the thermodynamic approach given by Gibbs and Volmer, and later modified by Becker, Döring and other workers. It is usually referred to as the classical theory of homogeneous three-dimensional nucleation. The main criticism of this approach is that it assumes that the interfacial energy γ of a critically sized nucleus is the same as that of a large bulk crystal of the crystallizing compound. Since the number of atoms/molecules in a critical nucleus probably varies from a few to less than about 1000, there is no justification for the above assumption. However, this assumption is justified when

$$n(i) = n(1) \exp\{-[\Delta G_{3D}(i) - \Delta G_{3D}(1)]/k_B T\} \quad (2.25)$$

where $\Delta G_{3D}(i)$ and $\Delta G_{3D}(1)$ are the values of the reversible work required to form an embryo of size i and a monomer, respectively. Different functions of i may be used for $\{\Delta G_{3D}(i) - \Delta G_{3D}(1)\}$. For spherical nuclei the following relation holds (Katz *et al.*, 1992):

$$\Delta G_{3D}(i) - \Delta G_{3D}(1) = \kappa(i^{2/3} - 1) \quad (2.26)$$

where

$$\kappa = 4\pi(3\Omega/4\pi)^{2/3}\gamma/k_B T \quad (2.27)$$

The assumption of the size dependence of the surface free energy introduces a correction factor $(\exp \kappa)/S$, where S is the supersaturation ratio.

In the limit $i^* \rightarrow 1$, the atomistic theory of nucleation provides a more adequate description of the nucleation rate (Kashchiev, 2000):

$$J = A \exp(-F^*/k_B T) \exp(i^* \ln S) \quad (2.28)$$

where F^* is the effective excess energy of the nucleus.

2.2.2 Three-Dimensional Heterogeneous Nucleation

Homogeneous 3D nucleation is possible when there is no external source that alters either the value of the kinetic parameter A or the interfacial energy γ . It is well known that foreign particles present in bulk media as well as cracks and scratches on the walls of crystallizers frequently catalyze 3D nucleation. This type of nucleation is referred to as heterogeneous 3D nucleation.

Depending on the shape of the embryos forming on the foreign substrate, the embryos develop in two or three dimensions. For example, a cap-shaped embryo changes its size in three dimensions, whereas a disk-shaped embryo grows laterally with its height remaining fixed. In the former case the nucleation is three-dimensional, whereas in the latter case it is two-dimensional. Therefore, in principle, nucleation on a foreign substrate can be either two- or three-dimensional.

We consider here the former case, where the embryo forms on a flat substrate. In this case the shape of the crystal embryo is essentially a spherical cap (see Figure 2.6a), with the equilibrium wetting (contact) angle θ defined from 0 and π by

$$\cos \theta = (\gamma_{sf} - \gamma_{cs}) / \gamma_{cf} = m \quad (2.29)$$

where γ_{cs} , γ_{sf} and γ_{cf} denote the interfacial energy between crystalline solid phase (c) and foreign particle surface (s), foreign particle surface (s) and mother fluid phase (f), and crystalline solid phase (c) and fluid phase (f), respectively. For a sufficiently large nucleus, $\gamma_{cf} = \gamma$. The contact angle θ defines a numerical factor ϕ , given by

$$\phi = (2 + \cos \theta)(1 - \cos \theta)^2 / 4 \quad (2.30)$$

The value of ϕ lies between 0 and 1, depending on the value of $m = \cos \theta$, as shown in Figure 2.6b. Obviously, heterogeneous nucleation occurs when $-1 < m < 1$, and the situation $m = -1$ corresponds to homogeneous nucleation. When $\theta = 0$, $\phi = 0$; when $\theta = \pi/2$, $\phi = 1/2$; and when $\theta = \pi$, $\phi = 1$. The cases of $\theta = 0$ and $\theta = \pi$ are usually referred to as complete wetting and complete non-wetting, respectively.

Regardless of whether nucleation is homogeneous or heterogeneous, the above treatment of three-dimensional nucleation can be represented by unified formulae if the interfacial energy γ of nucleus formed by homogeneous nucleation is replaced by an effective interfacial energy γ_{eff} , given by

$$\gamma_{\text{eff}} = \Phi \gamma \quad (2.31)$$

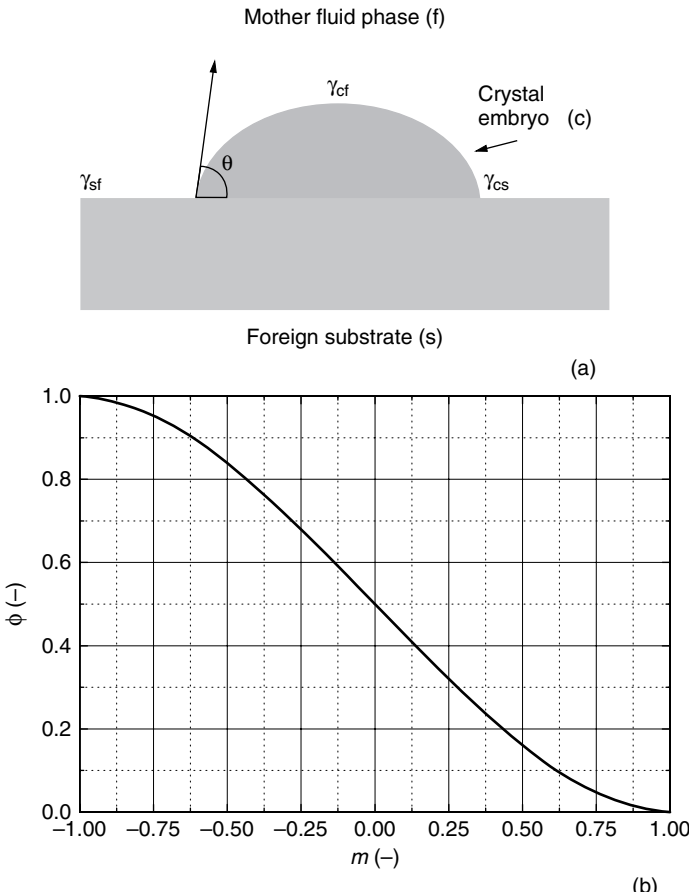


Figure 2.6 Cross-section of a cap-shaped nucleus on the surface of a substrate; crystalline embryo (c), foreign substrate particle (s) and mother phase (f). (b) Dependence of the factor ϕ on $m = \cos \theta$ according to Equation (2.30)

where the activity factor Φ is a number between 0 and 1, and is related to the numerical factor ϕ [see Equation (2.30)]. For cap-shaped nuclei, $\Phi = \phi^{1/3}$.

The above treatment of heterogeneous 3D nucleation considers only changes in the interfacial energy of the nucleus, and does not take into account the process of integration of growth species into the embryos during nucleation on foreign particles. Figure 2.7a shows this effect. It can be seen that nucleation on a foreign substrate body (s) of radius R_s reduces the effective surface of collision of embryos, where growth species are incorporated into embryos. This leads to a decrease in the value of the kinetic parameter A , thereby decreasing the nucleation rate J [see Equation (2.22)]. This effect is opposite to that of the predicted decrease in the nucleation barrier ΔG_{3D}^* due to a decrease in the interfacial energy γ [see Equations (2.21) and (2.31)]. The effect of decrease in the

effective surface area for collision of embryos due to nucleation on foreign bodies is determined by the following parameters (Liu *et al.*, 2000):

$$\phi(m, R') = \frac{1}{2} + \frac{1}{2} \left(\frac{1-mR'}{q} \right)^3 + \frac{1}{2} (R')^3 \left[2 - 3 \left(\frac{R'-m}{q} \right) + \left(\frac{R'-m}{q} \right)^3 \right] + \frac{3}{2} m(R')^2 \left(\frac{R'-m}{q} - 1 \right) \quad (2.32)$$

$$\phi'(m, R') = \frac{1 + (1-R'm)/q}{2} \quad (2.33)$$

where

$$q = [1 + (R')^2 - 2(R')m]^{1/2} \quad (2.34)$$

and

$$R' = R_s/r_{3D}^* \quad (2.35)$$

with the radius of critical nucleus r_{3D}^* given by Equation (2.20).

The plots of $\phi(m, R')$ as a function of m and R' are shown in Figure 2.7b. When $R' \rightarrow 0$ or $m = -1$, $\phi(m, R') \rightarrow 1$. This case corresponds to the situation where the size of foreign solid substrate (s) is very small in comparison with the critical nuclei. In other words, here the interactions and structural match between the nuclei and the substrates are negligible. This is the case of homogeneous nucleation. For the case when $R' \rightarrow \infty$ or $m \rightarrow 1$, $\phi(m, R') \rightarrow 0$. This corresponds to perfect interactions and structural match between the nuclei and the substrates, and foreign particles act as seed crystals and the activation barrier $\Delta G_{3D}^* = 0$. It follows from Figure 2.7b that when $R' \geq 1$ and $\phi(m, R') = 0$, growth of nuclei takes place on foreign particles. Thus, heterogeneous nucleation occurs for $-1 < m < 1$ or $0 < \phi(m, R') < 1$, depending on the nature of the substrate surface and on supersaturation. It should be noted that $\phi'(m, R')$ gives plots similar to those in Figure 2.7b for $\phi(m, R')$.

When $R' \gg 1$, nuclei may be considered to form on a planar substrate (see Figure 2.7a) and Equation (2.22) describes the nucleation rate J . However, when the effective surface area for the collision of embryos is considered, the nucleation rate is given by (cf. Liu, 1999, Liu *et al.*, 2000)

$$J = 4\pi a R_s^2 N_0 \phi'(m, R') [\phi(m, R')]^{1/2} AS \times \exp\{-\phi(m, R')[B/\ln S]^2\} \quad (2.36)$$

where

$$B = \left(\frac{16\pi}{3} \right)^{1/2} \left(\frac{\gamma}{k_B T} \right)^{3/2} \Omega \quad (2.37)$$

N_0 is the number of nuclei per unit area on the surface, and a is the dimension of growth species. Note that for homogeneous nucleation when $\phi(m, R') = \phi'(m, R') = 1$ and $4\pi a R_s^2 N_0 \rightarrow 1$, Equation (2.36) reduces to Equation (2.22).

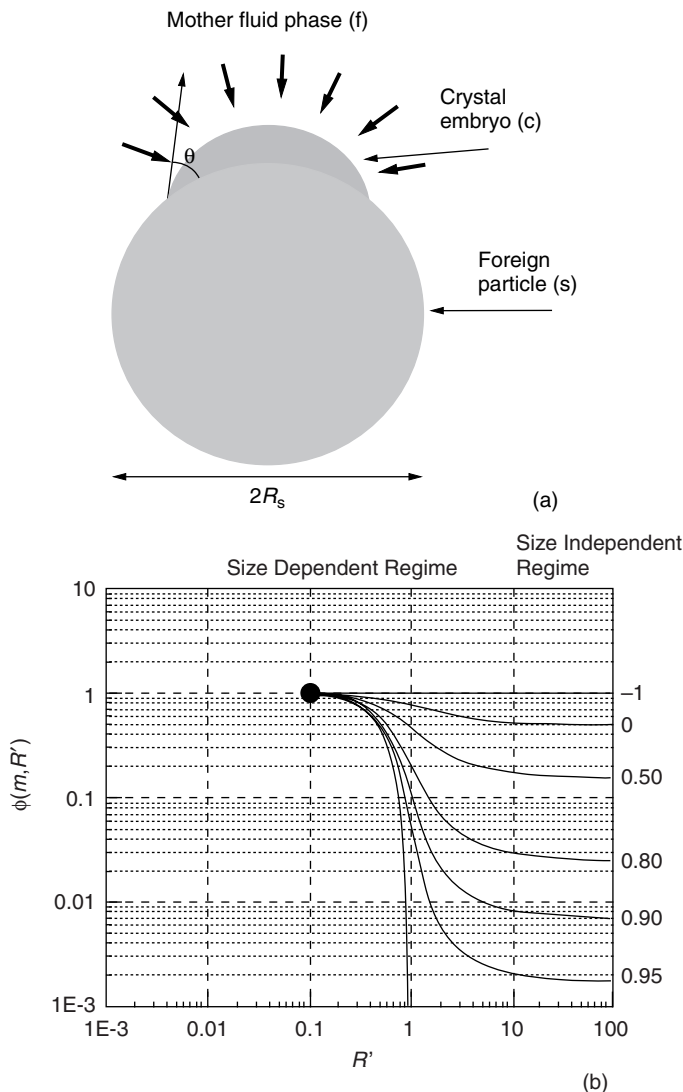


Figure 2.7 (a) Schematic illustration of heterogeneous 3D nucleation on a foreign particle of radius R_s ; crystal embryo (c), foreign substrate particle (s) and mother phase (f). (b) Dependence of factor $\phi(m, R')$ on the relative particle size $R' = R_s/r_{3D}^*$ and m . Adapted from X.Y. Liu, K. Tsukamoto, and M. Sorai. Langmuir **16**, 5499. Copyright (2000), with permission from American Chemical Society

According to Equation (2.36), the factors $\phi(m, R')$ and $\phi'(m, R')$ play different roles in different supersaturations. At low supersaturations, the nucleation barrier is very high [see Equation (2.21)]. Consequently, the exponential term associated with the nucleation barrier is dominant over contribution from collisions of embryos due to the available effective surface area on the substrate, represented by the factors $\phi(m, R')$ and

$\phi'(m, R')$. Thus, the nucleation rate is controlled by heterogeneous nucleation. However, at higher supersaturations, the pre-exponential term involving factors associated with effective collisions becomes dominant over the exponential term. Figure 2.8 shows the plots of nucleation rate J against supersaturation $\ln S$ according to Equation (2.36) for different values of m due to foreign particles. It can be seen that nucleation on foreign particles with small $\phi(m, R')$ and $\phi'(m, R')$, corresponding to a large m and/or a large radius R_s , is dominant at low supersaturations. In contrast, nucleation on particles with large $\phi(m, R')$ and $\phi'(m, R')$, corresponding to a small m and/or a small radius R_s , is governed by kinetics at high supersaturations. For any two sets of m and $\phi(m, R')$ there is always a critical value of supersaturation when heterogeneous nucleation occurring at low supersaturation undergoes transition to homogeneous nucleation, as indicated by points A, B and C. Thus, it may be concluded that, for a given system, different foreign particles having distinct surface properties and/or different sizes control nucleation in different supersaturation regimes. Homogeneous nucleation occurs only when $\phi(m, R') = \phi'(m, R') = 1$, and this occurs at very high supersaturations.

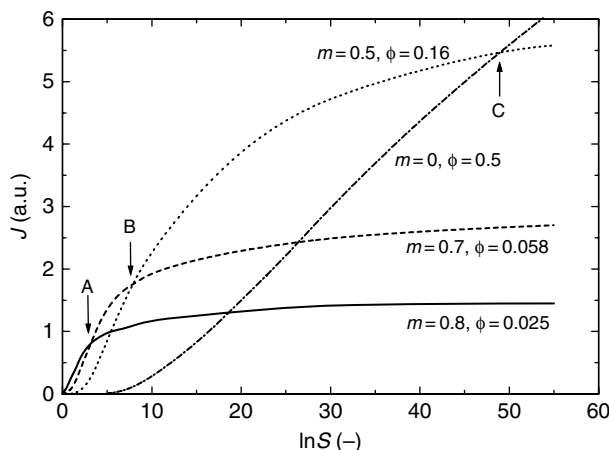


Figure 2.8 Dependence of nucleation rate J on supersaturation $\ln S$ according to Equation (2.36) for different values of m due to foreign particles. The plots are drawn for $R_s = 1000a$ and $\gamma_{sf}\Omega^{2/3}/k_B T = 1.5$. Adapted from X.Y. Liu, K. Tsukamoto, and M. Sorai. Langmuir **16**, 5499. Copyright (2000), with permission from American Chemical Society

The nature of the curves of Figure 2.8 may be reproduced by the following simple empirical function:

$$J = A''\phi^{1/2} \exp\{-\phi(B/\ln S)^2\} \quad (2.38)$$

where the symbols have the same meaning as before. The plots of J against $\ln S$ predicted by Equation (2.38) for different values of ϕ , $A'' = 1$ and $\gamma\Omega^{2/3}/k_B T = 2.5$ are shown in Figure 2.9. With increasing value of $\gamma\Omega^{2/3}/k_B T$, the plots are shifted to higher values of $\ln S$. The similarity of the plots in Figures 2.8 and 2.9 suggests that in Equation (2.36) the quantity $4\pi aR_s^2 N_0 \phi'(m, R') \approx 1$.

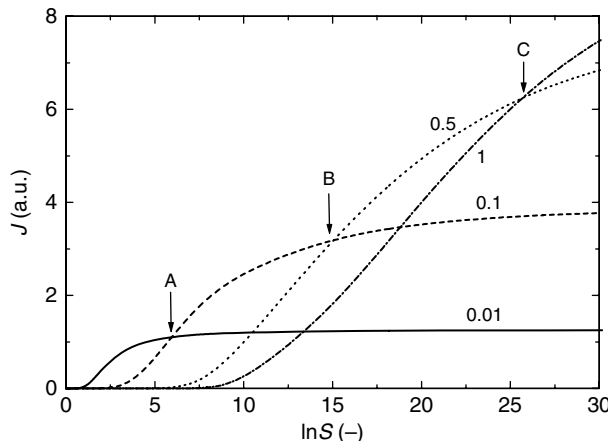


Figure 2.9 Dependence of nucleation rate J on supersaturation $\ln S$ predicted by Equation (2.38) for different values of ϕ , $A'' = 1$ and $\gamma_{\text{sf}} \Omega^{2/3} / k_{\text{B}} T = 2.5$

2.3 Metastable Zone Width

The kinetic factor A in Equations (2.22) and (2.36) usually lies between 10^{14} and $10^{41} \text{ m}^{-3} \text{ s}^{-1}$, where the lower values indicate the presence of foreign active centers, seeds, etc., in the system and/or a lower frequency of monomer attachment to the nuclei (Kashchiev, 2000). The supersaturation in crystal nucleation normally does not exceed 10^2 and is frequently below 10. Therefore, it may be assumed that the quantity AS is a constant. It is reasonable to take an intermediate value of AS as $10^{26} \text{ m}^{-3} \text{ s}^{-1}$. Using this value, one may calculate and compare the nucleation rate J for a chemical compound crystallizing in different solvents or for different compounds, different polymorphs of the same chemical compound, or different phases nucleating in the same solvent under the same conditions. For this purpose, one requires the values of solid–fluid interfacial energy γ_{cf} , denoted hereafter γ . For aqueous solutions, γ may be estimated from the following relation (Sangwal, 1989):

$$\gamma/k_{\text{B}} T = \xi[(\Delta H_{\text{m}}/R_{\text{G}} T_{\text{m}}) - f_1 \ln c_0]/4a^2 \quad (2.39)$$

where ΔH_{m} is the enthalpy of melting of the compound, ξ is the crystallographic anisotropy factor, the constant $f_1 = 1$, R_{G} is the gas constant, T_{m} is its melting point, c_0 is its solubility, in molar fraction, at temperature T , and a is the interionic distance in the solid state. The value of ξ lies between 0 and 1, and is a measure of the roughness of the surfaces of a crystal (Elwenspoek, 1986a,b; Bennema and van der Eerden, 1987; Sangwal, 1989). The lower the value of ξ , the rougher is the surface. From an analysis of experimental data reported for different compounds, it was found that $\xi = 1/2$ (Sangwal, 1989). For different inorganic compounds, the following empirical relation holds:

$$\Delta H_{\text{m}}/R_{\text{G}} T_{\text{m}} = 3 + 6n/z_{\text{c}}^2 \quad (2.40)$$

where n is the number of water molecules and z_c is the number of cation charge in the formula unit of a salt. From a survey of the interfacial energy of different compounds, Nielsen and Söhnel (1971) and Söhnel (1982) reported a similar relation:

$$\gamma/k_B T = [\ln c_x - \ln c_0]/ha^2 = \ln(c_x/c_0)/ha^2 \quad (2.41)$$

where $c_x = \rho/M$ (ρ is the crystal density and M is the molecular weight), c_0 is the solid solubility in mol/dm³, and h is the average hydration number per ion. The analysis gives the average values $c_x = 0.011$ and $h \approx 3$. Mersmann (1990) also found a relation similar to Equation (2.41), where $(1/h)a^{-2} = 0.414\Omega^{-2/3}$. The above relationships between crystal solubility and interfacial tension are associated with crystal–fluid interactions. A high solubility implies strong crystal–fluid interactions and a low interfacial tension.

Supersaturation has a dominating effect on the nucleation rate J . This effect can be analyzed conveniently from Equation (2.22) rewritten in the form

$$J = A' \exp[-(B/\ln S)^2] \quad (2.42)$$

where B is given by Equation (2.37) and A' denotes the pre-exponential term in Equations (2.27) and (2.36), given by

$$A' = 4\pi a R_s^2 N_0 \phi'(m, R') [\phi(m, R')]^{1/2} AS \quad (2.43)$$

in Equation (2.36), and $A' = AS$ in Equation (2.27). Since the quantity $\Omega^{2/3}/k_B T$ is constant at a given temperature, different values of $\gamma\Omega^{2/3}/k_B T$ imply that they refer to proportional changes in γ .

Figure 2.10 illustrates the dependence of J on supersaturation $\ln S$ for the following situations: (1) two different γ and a constant A' and (2) a constant value of γ and two values of A' . The plots show that, for a given value of γ , the nucleation rate depends strongly on supersaturation. There is a critical supersaturation S_c below which $J = 0$ but J increases abruptly as soon as this value of the critical supersaturation is exceeded. The nucleation rate $J = 0$ means that statistically the time τ required for the formation of one nucleus per m³ of the supersaturated medium is infinite. The period required for nucleation is called the induction period and customarily it is assumed that $\tau = 1/J$. The induction period τ decreases with increase in supersaturation S . For example, for $(\gamma\Omega^{2/3}/k_B T) = 1$, at $\ln S = 0.2$, $J = 3.61 \times 10^{-19}$ nuclei m⁻³ s⁻¹ or $\tau = 2.77 \times 10^{18}$ s, i.e. 8.8×10^{10} years. However, when $\ln S = 0.5$, $J = 7.7 \times 10^{18}$ nuclei m⁻³ s⁻¹ or $\tau = 1.29 \times 10^{-19}$ s. Obviously, the time required for nucleation is negligibly small and the medium is essentially close to the state of spontaneous nucleation (i.e. precipitation). The value of supersaturation when $J = 1$ nucleus m⁻³ s⁻¹ is the limit of supersaturation up to which the medium is metastable and defines the metastable zone width.

For a given supersaturation, the nucleation rate also depends strongly on the crystal–fluid interfacial tension γ . For example, instead of unity when $(\gamma\Omega^{2/3}/k_B T) = 3$, $J = 4.7 \times 10^4$ nuclei m⁻³ s⁻¹ or $\tau = 2.1 \times 10^{-5}$ s for $\ln S = 0.5$. This means that a solvent which results in a high solid–fluid interfacial energy leads to an increase in the metastable zone width.

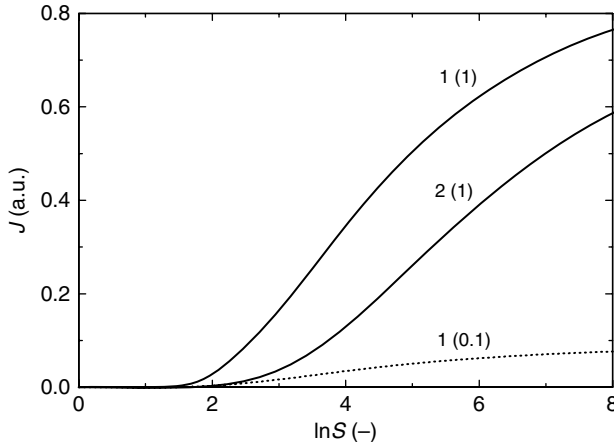


Figure 2.10 Plots of nucleation rate J on supersaturation $\ln S$ for different γ , as indicated by $(\gamma\Omega^{2/3}/k_B T)$ and A' . Solid curves represent J for $(\gamma\Omega^{2/3}/k_B T) = 1$ and 2, and $A' = 1$ nucleus $m^{-3} s^{-1}$; the dashed curve represents J for $(\gamma\Omega^{2/3}/k_B T) = 1$ and $A' = 0.1$ nuclei $m^{-3} s^{-1}$. Numerals in parentheses denote A' and those before the parentheses denote $(\gamma\Omega^{2/3}/k_B T)$. Note that the nucleation rate J depends strongly on $\ln S$ and γ .

From Equation (2.36), one may calculate the critical supersaturation S_c corresponding to a given value of nucleation rate J . When $J = 1$ nucleus $m^{-3} s^{-1}$, Equation (2.36) may be written in the form

$$S_c = \exp[B/\ln^{1/2}(A'/J)] \quad (2.44)$$

where A' is the pre-exponential term of Equations (2.22) and (2.36). When $B/\ln^{1/2}(A'/J) \ll 1$, Equation (2.44) may be written as

$$S_c \approx 1 + B/\ln^{1/2}(A'/J) \quad (2.45)$$

Figure 2.11 shows the dependence of S_c on $\gamma\Omega^{2/3}/k_B T$ for different values of A' . Since the general expression in Equation (2.36) applies to both homogeneous and heterogeneous 3D nucleation, from Figure 2.11 it follows that the quantities distinguishing heterogeneous from homogeneous nucleation are the values of interfacial energy γ and the properties and size of foreign particles, which ultimately determine the values of $\phi(m, R')$ and $\phi'(m, R')$. A low value of A' or a high value of γ leads to an increase in S_c .

Nucleation and growth occur in the metastable zone. Consequently, for practical purposes, the supersaturation for these processes can be controlled more reliably when the metastable zone width is relatively wide. Therefore, from the standpoint of applications, one is always interested in enlarging the metastable zone width. One of the possible means to achieve this is to add specific additives to the growth medium. This aspect is discussed in Section 2.6.3.

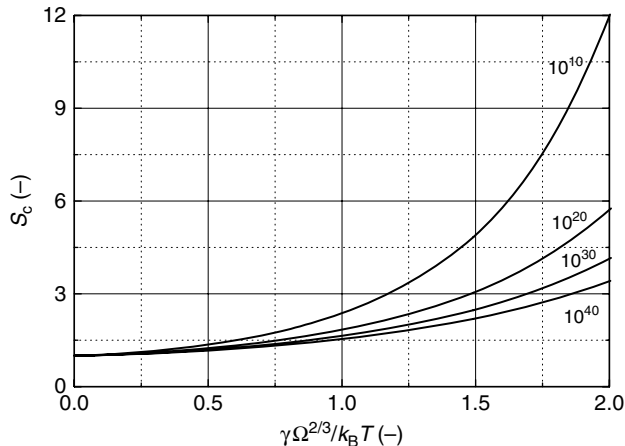


Figure 2.11 Plots of S_c against $\gamma \Omega^{2/3} / k_B T$ for different values of A'

2.4 Nucleation and Transformation of Metastable Phases

2.4.1 Crystallization of Metastable Phases

Any solid may exist in different forms: amorphous phases, solvates and polymorphs. Solvates are chemical compounds for which the ratio between solvent and solute molecules is constant. Usually, they crystallize in different structures. Different solids with the same chemical composition are called polymorphs or polymorphic modifications. In contrast to polymorphism, there is also a phenomenon called isomerism, where the atoms are arranged in different ways, giving rise to different molecules. In the solid state both polymorphs and isomers have different properties, but in the solution only the isomers have different properties.

Under the same conditions several phases can coexist, but the phase which is characterized by the lowest free energy $G = H - TS$ at a given temperature T is the stable one. This may be explained in terms of the thermodynamic stability of different phases. Figure 2.12 shows the temperature dependence of the Gibbs free energy for two phases I and II, crystallizing from, for example, the same solution, and for the equilibrium concentration (i.e. solubility). Figure 2.12 is an extension of Figure 2.2. It illustrates that thermodynamically phases II and I are stable only below temperatures T_{II} and T_I , respectively, and that phase I is more stable than phase II, because for $T < T_I$ the transformation of phase I from the solution is accompanied by a higher change in the Gibbs free energy, i.e. $\Delta G_I > \Delta G_{II}$. However, if phase II coexists with phase I at a temperature, for example, between T_{II} and T_I , it is thermodynamically unstable (i.e. it is metastable). A higher stability of phase I with respect to phase II means that the former phase is less soluble than the latter. Consequently, the solid–fluid interfacial energy γ of phase I is higher than that of phase II [see Equation (2.39)].

At temperatures below T_I , the higher stability of phase I does not mean that it should nucleate first. This may be explained by the dependence of the nucleation rate J on the nucleation barrier ΔG_{3D}^* of each phase and the pre-exponential factor A' associated

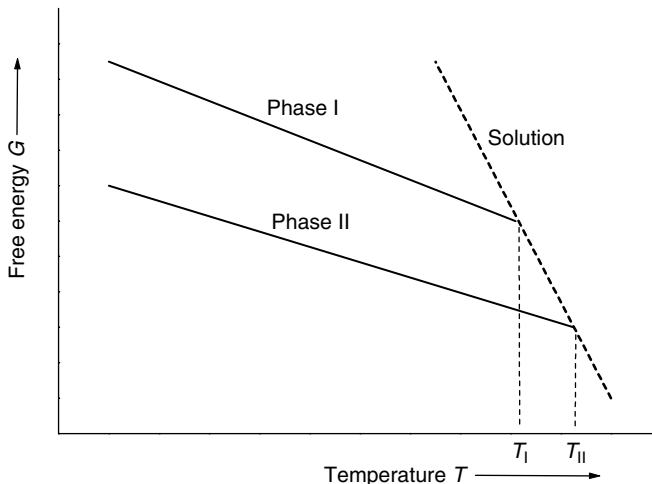


Figure 2.12 Dependence of Gibbs free energy G for two phases I and II, crystallizing from solution, on temperature T . The dashed line shows the $G(T)$ dependence for the equilibrium concentration

with the kinetics of attachment of atoms/molecules to the developing embryos [see Equations (2.22) and (2.36)]. The higher solubility of phase II than that of phase I has two effects: (1) the nucleation barrier ΔG_{3D}^* for the nucleation of phase II is lower than that for phase I because the interfacial tension γ for phase II is lower than that for phase I, and (2) the concentration of atoms/molecules available for their attachment to developing nuclei is higher for phase II than for phase I. Both of these factors lead to an increase in the nucleation rate of phase II. Since the interfacial energy appears in the exponential term, its effect is much more pronounced at low supersaturations.

It should be noted that the solubilities of phases I and II are also different. This means that the concentrations of ions/molecules responsible for the difference in the solubility of the two phases are also different. Consequently, unless the enthalpies of dissolution of the two phases are drastically different, it may be assumed that the supersaturation $\ln S$ available for their nucleation at a particular temperature is essentially the same.

The supersaturation dependence of the nucleation rate J of two phases may be understood qualitatively from Figure 2.8, assuming that nucleation of the two phases occurs on particles of different radius R_s and the radius of these particles corresponds to their critical radius r_{3D}^* . Since $\gamma(I) > \gamma(II)$, $R_s(I) > R_s(II)$ for the same supersaturation S . As pointed out above, nucleation on particles of large radius is governed by the nucleation barrier at low supersaturations, whereas nucleation on particles with small radius is governed by the kinetics of integration of growth species at high supersaturations. Consequently, nucleation of stable phase I is favored at low S and that of metastable phase II at high S .

It is well known that calcium oxalate crystallizes in two forms, monohydrate (COM) and dihydrate (COD), and the COD form is thermodynamically more stable. Consequently, nucleation of metastable COM is a possible source of urinary and kidney stones (see Chapter 6). Figure 2.13 illustrates the dependence of the nucleation and morphology of

COM and COD on the initial supersaturation $S_i = ([\text{Ca}^{2+}][\text{C}_2\text{O}_4^{2-}]/K_s)^{1/2}$ and reactant ratio $R_i = [\text{Ca}^{2+}]/[\text{C}_2\text{O}_4^{2-}]$. In the figure, eCOD denotes an elongated octahedral shape of COD crystals. With reference to stoichiometric composition $R_i \approx 1$, it can be seen that the metastable COM form appears predominantly at high supersaturations $S_i > 20$. However, the formation of crystals of the stable COD form strongly depends on the ratio R_i . In general, excess Ca^{2+} ions in the solution favor the formation of COD whereas crystals of the COM form are favorably nucleated from Ca^{2+} -deficient solutions. It seems that the difference in the formation of COD and COM from solutions containing excess and deficient Ca^{2+} ions is associated with the overall number of water molecules in the first solvation shell of ions. Ions containing a higher number of water molecules in their solvation shell favor the nucleation of compounds containing a higher number of water of hydration.

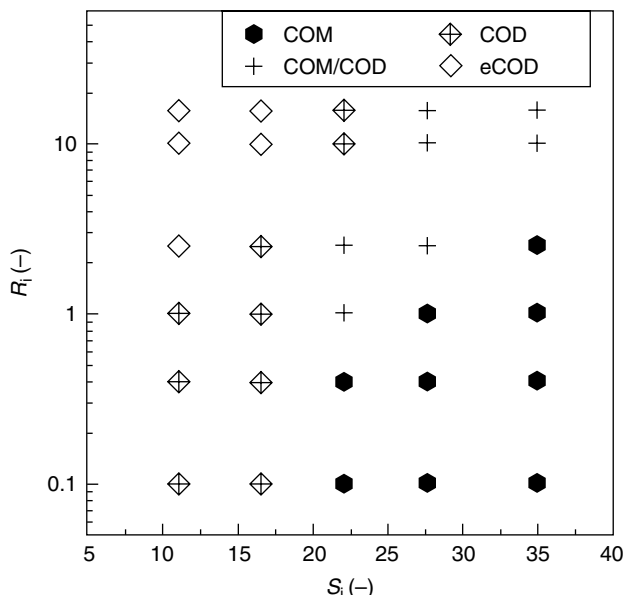


Figure 2.13 Dependence of nucleation and morphology of calcium oxalate monohydrate (COM) and dihydrate (COD) polymorphs on initial supersaturation S_i and reactant ratio $R_i = [\text{Ca}^{2+}]/[\text{C}_2\text{O}_4^{2-}]$. eCOD denotes an elongated octahedral shape of COD crystals. Reproduced from T. Jung, W.-S. Kim, and C.K. Choi. Mater. Sci Eng. C **24**, 31. Copyright (2004), with permission from Elsevier

Although the metastable phase II nucleates first, after nucleation it undergoes transformation into the stable phase I. This happens both in the solid state and in the solution. The former occurs when the two phases nucleate in the solid state. The general concepts and equations describing this type of transformation are the same as those given in Section 2.2. However, in the solution-mediated transformation, the kinetics depend on the dissolution rates of the metastable phase and on the nucleation and growth rates of the stable phase. These rates depend on several factors, such as the difference in solubility, crystal size, temperature, impurities, and stirring. In the latter case the transformation

kinetics are followed by measuring the evolution of solute concentration or fractional concentration of the powder crystals in contact with the solution.

Solution-mediated transformation process can, in general, be divided into three stages, as shown in Figure 2.14. Crystals of metastable phase II are initially present in the solution of certain volume, and up to a certain time the solution concentration remains practically constant. In this stage the number of nuclei of phase I is small. In the second stage, the number of nuclei of phase I increases and these new nuclei grow into crystals. The solution concentration decreases because dissolution of the decreasing phase II is able to supply the necessary solute for the crystallization of phase I. When all crystals of phase II have dissolved, the solution concentration asymptotically approaches the equilibrium concentration of the stable phase I.

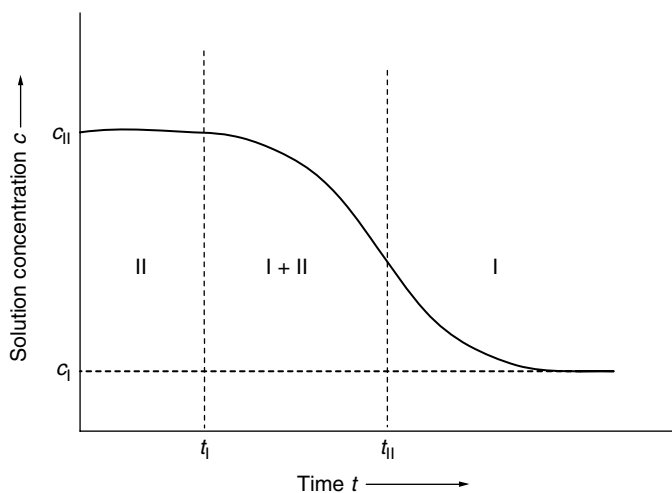


Figure 2.14 Evolution of solution concentration during solution-mediated transformation of metastable phase II into phase I. Adapted from R. Boistelle. In: N. Garti and K. Sato (Eds.), Crystallization and Polymorphism of Fats and Fatty Acids, Chap. 5, p. 189. Copyright (1988), with permission from Taylor & Francis

2.4.2 Overall Crystallization

Overall crystallization of a phase in a closed system occurs by nucleation and growth of crystallites in the volume. The overall crystallization may occur by a mononuclear or polynuclear mechanism involving the formation of one or many nuclei in the volume, respectively. There are two routes to the formation of many nuclei in the volume. In the first case, the nuclei may be formed in the system at the initial moment $t = 0$ and thereafter they grow irreversibly until the completion of crystallization in the entire volume. In the second case, the nuclei form continuously during the crystallization process. These two processes are known as instantaneous and progressive nucleation mechanisms, respectively. However, during progressive nucleation the nucleation rate can be time independent (stationary nucleation) or time dependent (nonstationary nucleation).

As discussed above, nucleation may be homogeneous or heterogeneous. Homogeneous nucleation occurs in ideally pure liquids, whereas heterogeneous nucleation occurs when the system contains nanoparticles (e.g. seeds) and/or impurity particles. The theoretical expressions for the mononuclear and polynuclear mechanisms, and for instantaneous and progressive nucleation, are different from each other. In terms of mass $w(t)$ crystallized in volume V at time t , the fraction y of crystalline phase (frequently called overall crystallization of a phase) in a closed system may be defined as

$$y = w(t)/w_0 \quad (2.46)$$

where w_0 is the maximum mass of the crystallizing phase.

When nucleation occurs on active centers, the total number N_0 of nuclei in the system cannot exceed the total number N_a of active centers present in it. The active centers thus determine both the maximum number of nuclei formed in the system and the duration of nucleation. During the nucleation process, the number of active centers is exhausted progressively during crystallization. Therefore, the time dependence of the kinetics of nucleation on active centers determines the overall crystallization kinetics.

When nucleation of crystallites in the volume occurs by the polynuclear mechanism and all active centers have the same activity, in the case of nonstationary nucleation, for $\tau > 4t$ the number of nuclei per unit volume in the system may be written in the form (cf. Kashchiev, 2000; Chapters 15 and 25)

$$N(t) = N_a [1 - \exp(-J_{a,s} t / \zeta)] \quad (2.47)$$

where the factor

$$\zeta = (t/\tau)^{-1/2} \pi^{-3/2} \exp(-\pi^2 \tau / 4t) \quad (2.48)$$

$J_{a,s}$ is the stationary nucleation rate per active center, N_a is the total number of active nucleation centers, and τ is the time lag for nucleation. Taking $J_{a,s} = 1/\tau$, Equation (2.47) may be written in the approximate form

$$N(t) = N_a \{1 - \exp[-(t/\tau)^p]\} \quad (2.49)$$

where the exponent $p > 3/2$. In the case of stationary nucleation the factor $\zeta = 1$ [Equation (2.47)], and the exponent $p = 1$ [Equation (2.49)].

Stationary and non-stationary nucleation may be distinguished from each other from the shape of the $N(t)$ curves (cf. Kashchiev, 2000). In stationary nucleation, the $N(t)$ curve passes through the origin, whereas in non-stationary nucleation it shows a sigmoidal shape involving a time lag when a significant number of active centers participate in crystallization.

When nucleation occurs by the progressive polynuclear mechanism, the crystallized mass during overall crystallization may be given by (Kashchiev, 2000)

$$w(t) = w_0 \{1 - \exp[-(t/\Theta)^q]\} \quad (2.50)$$

where w_0 is the total mass for crystallization, the time constant

$$\Theta = (q/c_g k^{q-1} J_s)^{1/q} \quad (2.51)$$

and the exponent

$$q = 1 + \nu d \quad (2.52)$$

In the above equations, J_s is the rate of stationary nucleation, k is the growth constant defined as $k = r^{1/\nu}/t$ (r is the radius of growing crystal), c_g is the shape factor for nuclei (e.g. $4\pi/3$ for spherical nuclei), ν is a number equal to 1/2 and 1 for growth controlled by volume diffusion and mass transfer, respectively, and d is the dimensionality of growth. For the growth of needles, plates and polyhedra, d is 1, 2 and 3, respectively. The above treatment is usually referred to as the Kolmogorov–Johnson–Mehl–Avrami (KJMA) theory.

In the case of instantaneous nucleation, the overall crystallization may also be given by Equation (2.50) with the constant $q = \nu d$ (Kashchiev, 2000). Then the time constant Θ has a value different from that for progressive nucleation mechanism [see Equation (2.51)].

During crystallization, it is frequently observed that the newly formed phase in the supersaturated mother phase is a metastable one rather than the thermodynamically most stable one. However, under conditions favorable for the formation of a metastable phase, with time the system tends to attain the minimum free energy state by transformation of the metastable crystallization phase into the thermodynamically stable phase (Section 2.4.1). The process of transformation occurs by nucleation and growth of the thermodynamically stable crystallites in the metastable phase rather than in the old mother phase. This means that when direct formation of the stable phase is not possible, the overall crystallization becomes a two-stage process in which the formation of the first stage precedes the appearance of the second stage. This is described by the Oswald rule of stages (also called Oswald step rule).

The nucleation and growth of the stable (s) phase within the metastable (m_u) phase makes the kinetics of formation of the former depend on those of the latter, and may be described by (Kashchiev, 2000)

$$y_s(t) = y_{m_u}(t) \{1 - \exp[-(\Theta_{m_u}/\Theta_s)^s][(t/\Theta_{m_u}) - b']^s\} \quad (2.53)$$

or, alternatively, in the form

$$y_s(t) = y_{m_u}(t) (1 - \exp\{-[(t/\Theta_s) - (\Theta_{m_u}/\Theta_s)b']^s\}) \quad (2.54)$$

where $b' = (m_u - 1/m_u)^{1/m_u}$, $y_{m_u}(t)$ is given by Equation (2.50), m_u and s denote the value of q for the crystallization of metastable and stable phase, respectively, and Θ_{m_u} and Θ_s are the corresponding time constants. We recall that $q = \nu d$ and $1 + \nu d$ for instantaneous and progressive nucleation mechanisms, respectively. Obviously, when the quantity $(\Theta_{m_u}/\Theta_s)b' = 0$, Equation (2.54) reduces to Equation (2.50). However, since the ratio $\Theta_{m_u}/\Theta_s > 0$ and the constant $b' > 0$, the dependence predicted by Equation (2.54) differs significantly from that of Equation (2.50).

As a typical example, Figure 2.15 shows the percentage transformation y of COM from COT and COD at 37°C as a function of time. It can be seen that the process is faster for COT than for COD, and there are well-defined different stages of evolution of the stable phase from the metastable phase, as described in Figure 2.14. In general, the transformation of a metastable phase into a stable phase is determined by temperature, ionic strength (i.e. supersaturation ratio S), and medium composition, including additives.

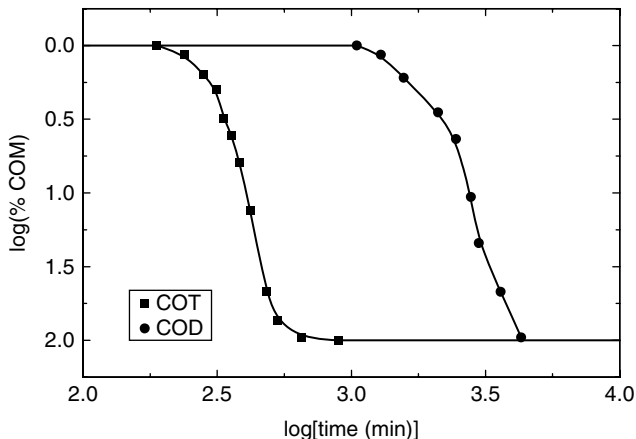


Figure 2.15 Percentage transformation y of COM from COT and COD at 37°C as a function of time t . Adapted from G.H. Nancollas. In: G.H. Nancollas (Ed.), Biological Mineralization and Demineralization, Springer, Berlin, p. 79. Copyright (1982), with permission from Springer Science and Business Media

It should be pointed out that Figure 2.15 illustrates the evolution of the stable phase due to decrease in the concentration of metastable phases in a way similar to that in Figure 2.14. Traditionally, however, the time dependence of the transformation y of a new phase is shown as an increasing function. This is presented in Figure 2.16, which shows the data of Figure 2.15 for the transformation of COD and COT into COM. The best-fit plots for the data according to Equations (2.50) and (2.53) with the exponents $q = m_u = s = 4$ are shown by dashed and solid lines, respectively.

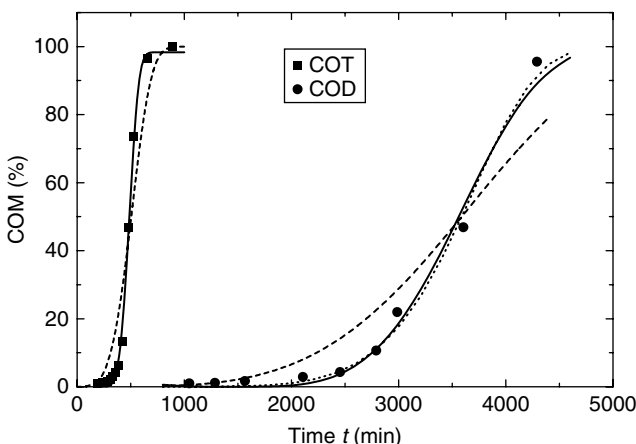


Figure 2.16 Transformation y of COM from COT and COD at 37°C as a function of time, and the best-fit plots of the data according to Equations (2.50) and (2.53), with the exponents $q = m_u = s = 4$. Original data from Nancollas (1982)

It can be seen from Figure 2.16 that, with $q = m_u = s = 4$, the fit of the experimental data by Equation (2.53) is much superior to that by Equation (2.50). However, Equation (2.50) also describes the experimental data equally well for a variable q such that $q > 4$. The best-fit constants then are $\Theta_{m_u} = 508$ min and $q = 9.2$ for COT, and $\Theta_{m_u} = 3780$ min and $q = 7.1$ for COD. This type of dependence is shown by the dotted curve for the COD data.

The ratio Θ_{m_u}/Θ_s , the time constant Θ_{m_u} and the constant b' depend on the chosen value of $s = m_u$ in Equation (2.53). This behavior is shown in Figure 2.17 for the best-fit values of the above constants as a function of $s = m_u$, say q , of Equation (2.50). From this figure, it follows that for a particular value of q the constants Θ_{m_u}/Θ_s , Θ_{m_u} and b' are mutually related. Since the maximum value of $q = 4$ in Equation (2.52), it is useful to determine the unique values of Θ_{m_u}/Θ_s and Θ_{m_u} for $s = m_u = q = 4$.

The reproducibility of the experimental data by the best fit according to Equations (2.50) and (2.53) implies that

$$[(t/\Theta_s) - (\Theta_{m_u}/\Theta_s)b']^s = (t/\Theta_s)^q \quad (2.55)$$

where $s = 4$ and $q > 4$. This equality enables one to find a relation between $(\Theta_{m_u}/\Theta_s)b'$ and q . Equation (2.55) may be expressed in the form

$$x^n - x + c = 0 \quad (2.56)$$

where $(t/\Theta_s) = x$, $(\Theta_{m_u}/\Theta_s)b' = c$ and $q/4 = n$. Taking its derivative $x' = 0$, one obtains

$$x_c = (1/n)^{1/(n-1)} \quad (2.57)$$

On substituting this value of x_c in Equation (2.56), one obtains an expression relating n and c in the form

$$(1/n)^{n/(n-1)} - (1/n)^{1/(n-1)} + c = 0 \quad (2.58)$$

which, upon substituting the values of n and c , gives

$$(\Theta_{m_u}/\Theta_s)b' = (4/q)^{4/(q-4)} - (4/q)^{q/(q-4)} \quad (2.59)$$

This equation can be solved only numerically and may be approximated by the empirical relation

$$(\Theta_{m_u}/\Theta_s)b' = A - Bq^{-p} \quad (2.60)$$

where the constants are $A = 1.564 \pm 0.0566$, $B = 2.253 \pm 0.040$ and $p = 0.2605 \pm 0.0125$. The numerical data predicted by Equation (2.59) are shown in Figure 2.18 for different values of q , while the solid curve represents the approximation Equation (2.60).

Equation (2.60) not only represents a relationship between $(\Theta_{m_u}/\Theta_s)b'$ and q , but also a condition for the occurrence of any transformation between successive phases in terms of the constancy of the ratio $\Theta_{m_u}/\Theta_s = 0$ when $s = m_u = 4$ and $b' = (m_u - 1/m_u)^{1/m_u} \approx 1.39$. However, a close examination of the values of Θ_{m_u}/Θ_s and Θ_{m_u} for the transformation

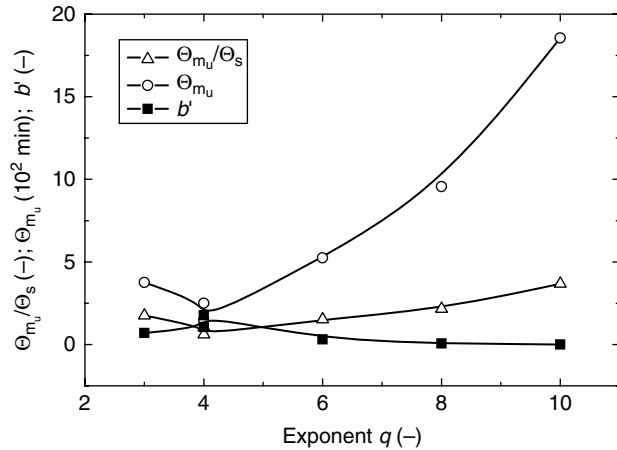


Figure 2.17 Dependence of ratio Θ_{m_u}/Θ_s , time constant Θ_{m_u} and constant b' of Equation (2.53) for the transformation of COT into COM on the exponent q of Equation (2.50) at 37°C

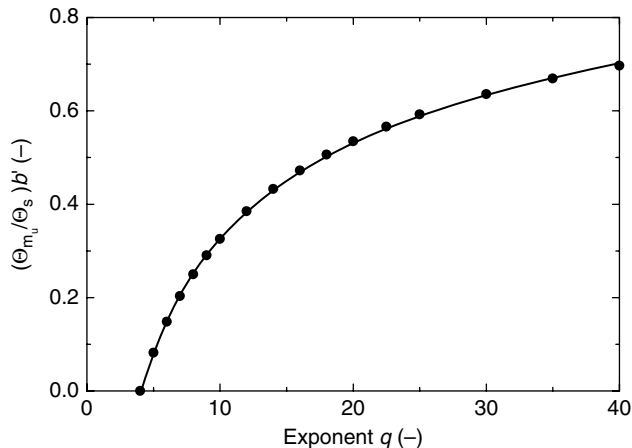


Figure 2.18 Numerical values of $(\Theta_{m_u}/\Theta_s)b'$, predicted by Equation (2.59), as a function of q . The solid curve represents the best fit of numerical data with $A = 1.564$, $B = 2.253$ and $p = 0.2605$ of Equation (2.60)

of COT into COM as a function of q (see Figure 2.17) shows that, for $q \geq 4$, they obey the following empirical relations:

$$4(\Theta_{m_u}/\Theta_s)/q = 1; \quad \Theta_s = \Theta_{m_u}(4/q)^2 = 1 \quad (2.61)$$

Relations (2.61) may be used to estimate Θ_s from a simple fit of the experimental data according to Equation (2.50).

2.5 Induction Period for Crystallization

As discussed above, according to the nucleation theories the nucleation rate J depends on supersaturation S , and there is a threshold value of supersaturation S_{\max} when the metastable phase precipitates spontaneously into the new stable phase. This means that after the initial moment $t = 0$ of attaining supersaturation in the old phase, formation of an appreciable amount of the new phase requires a certain time t_i , called the induction period or induction time. This time is an experimentally measurable quantity and is a measure of the ability of the system to remain in the metastable state, and is composed of two parts: (1) the time t_s required to form stable nuclei and (2) the time t_g required for the subsequent growth of the stable nuclei to observable size.

As discussed in Section 2.4.2, there are two possibilities for the formation and growth of nuclei in the mother phase. In the first case, one nucleus is formed in the system within a time t and then it grows to visible dimensions at an infinitely fast growth rate R . In the second case, while the first nucleus grows to visible dimensions, new nuclei have time to form. These cases are referred to as the mononuclear (MN) and polynuclear (PN) mechanisms, respectively. The above mechanisms describe two extreme case of formation of detectable nuclei. Therefore, they may be united into a single expression for induction period (Kashchiev *et al.*, 1991; Kashchiev, 2000):

$$t_i = t_{\text{MN}} + t_{\text{PN}} = 1/JV + [qy/(c_g JR^3)]^{1/q} \quad (2.62)$$

where y is the smallest experimentally detectable fraction of overall crystallization [see Equation (2.46)], c_g is the shape factor, V is the volume of the parent phase, the growth rate R is related to supersaturation $\sigma = (S - 1)$ by $R = A\sigma^n$ (A being the growth rate constant and $1 < n < 2$), and the exponent $q = (1 + \nu d)$ in Equation (2.52).

When the MN mechanism applies, one has

$$t_i = t_{\text{MN}} = (J_0 V)^{-1} S^{-1} \exp[B/(\ln S)^2] \quad (2.63)$$

and for PN mechanism

$$t_i = t_{\text{PN}} = [qy/(c_g J_0 A^{q-1})]^{1/q} [S(S - 1)^{q-1}]^{-1/q} \exp[B/4(\ln S)^2] \quad (2.64)$$

where B is given by Equation (2.37). These equations may be expressed in the form

$$\ln(t_i S) = B/(\ln S)^2 - \ln(J_0 V) \quad (2.65)$$

$$\ln\{t_i [S(S - 1)^{q-1}]^{1/q}\} = B/4(\ln S)^2 + \ln\{[qy/(c_g J_0 A^{q-1})]^{1/q}\} \quad (2.66)$$

According to these dependences, the plots of $\ln(t_i S)$ against $(\ln S)^{-2}$ and $\ln\{t_i [S(S - 1)^{q-1}]^{1/q}\}$ against $(\ln S)^{-2}$ are straight lines with slopes B and $B/4$, respectively. For spherical nuclei the shape factor $c_g = 16\pi/3$. When the PN mechanism holds, $q = 4$.

When the atomistic model of nucleation applies, from Equation (2.28) one obtains

$$\ln t_i = -\ln A + F^*/k_B T - i^* \ln S \quad (2.67)$$

A plot of $\ln t_i$ against $\ln S$ gives a slope equal to the number i of molecules in the critical nucleus.

From experimental data on the induction period t_i for nucleation as a function of relative supersaturation S for systems with or without an additive, one can verify the validity of the above models. However, it should be noted that the value of the interfacial energy γ predicted by Equation (2.64) of the PN model is higher by a factor $4^{1/3} = 1.5874$ than that by Equation (2.63) of the MN model. Moreover, these equations apply to three-dimensional homogeneous nucleation.

Figure 2.19a and b show the plots of $\ln t_i$ and $\ln[t_i[S^{1/4}(S - 1)^{3/2}]$ against $(\ln S)^{-2}$, respectively, for vaterite nucleation from aqueous solutions at 25 °C at pH between 8.35 and 9.2. The plots indicate that a better fit is obtained for the MN mechanism. The better fit with the MN mechanism suggests that $t_s \gg t_g$. However, as pointed out by Verdoso *et al.* (1992), the MN mechanism holds for small volumes and low supersaturations. A reasonably good fit for the PN mechanism also indicates that this mechanism cannot be rejected outright. Kashchiev *et al.* (1991) suggested that a transition from the MN to the PN mechanism may be observed in the plot of $\ln t_i$ against $\ln S$, as shown in Figure 2.19c. From this figure, one obtains i equal to about 8 and 2 at low and high supersaturations, respectively. These low values of i suggest that the concept of interfacial energy is only formal.

Figure 2.19a and b show plots with one slope B in the entire range of supersaturation. This implies that one value of the interfacial energy is involved in the formation of nuclei. However, the nucleation may equally well be homogeneous or heterogeneous, depending on the value of supersaturation and solvent composition. In heterogeneous nucleation, the induction period corresponding to a given value of supersaturation of a system is reduced due to a decrease in the interfacial energy [see Equation (2.31)]. This feature may be deduced from data on the induction period t_i for a system in a large range of supersaturation S . Figure 2.20a

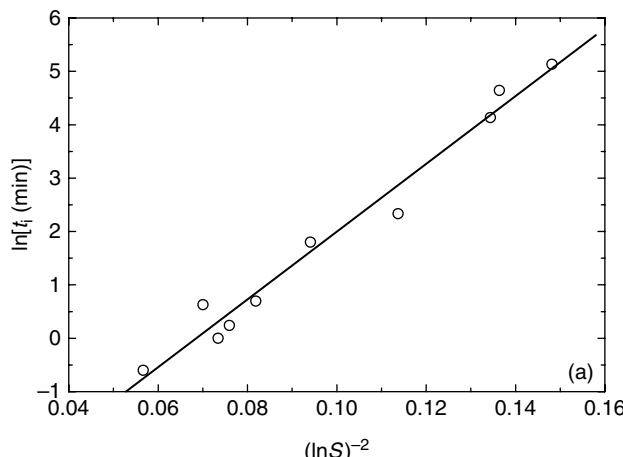


Figure 2.19 Plots of data of induction period t_i as a function of supersaturation S for vaterite nucleation according to different models: (a) $\ln t_i$ against $(\ln S)^{-2}$ (MN mechanism), (b) $\ln[t_i S^{1/4}(S - 1)^{3/4}]$ against $(\ln S)^{-2}$ (PN mechanism), and (c) $\ln t_i$ against $\ln S$ (atomistic model). Original data from Gomez-Morales *et al.* (1996)

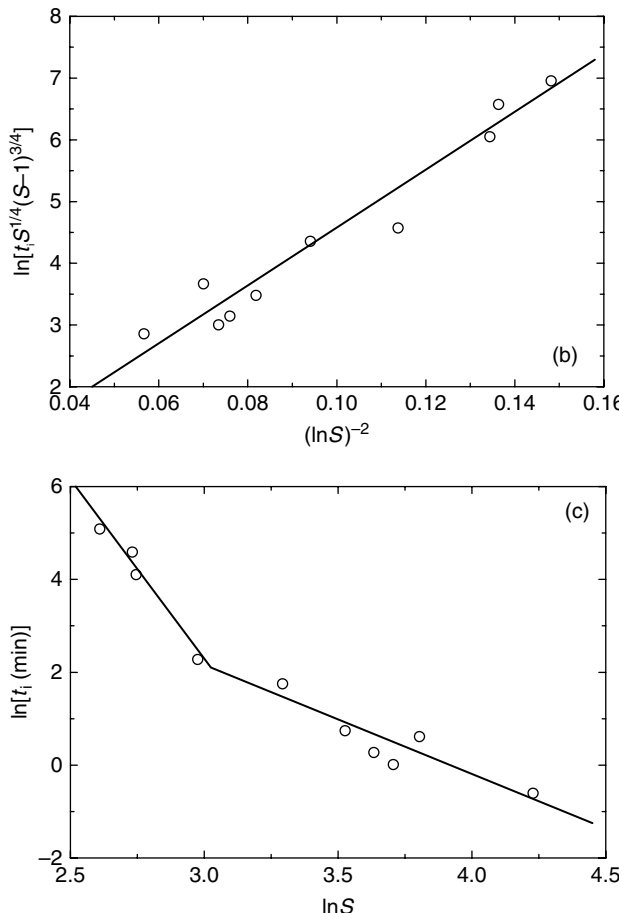


Figure 2.19 (Continued)

shows the plots of $\ln t_i$ against $(\ln S)^{-2}$ according to Equation (2.65) for dexamethasone sodium phosphate in aqueous solutions with different acetone contents. It can be seen that the slope of the plot increases steeply with increase in the acetone content. The figure also shows that for solutions containing more than 50% acetone, the slope of the plot consists of at least two parts. The slope is smaller for $(\ln S)^{-2} > 1$ (i.e. $S > 1$) than for $(\ln S)^{-2} < 1$, implying that at low supersaturations nucleation is probably predominantly heterogeneous in comparison with that at $S > 1$. This is due to an increase in the interfacial energy γ with increasing acetone content. This increase in γ is directly connected with decreasing solubility of the compound in the solvent water with increasing acetone content [see Section 2.6.1; Equation (2.39)]. Figure 2.20b shows the dependence of the experimentally determined γ for dexamethasone sodium phosphate on acetone content. In this figure are also shown two values of γ obtained for $(\ln S)^{-2} < 1$ and $(\ln S)^{-2} > 1$ in the case of solvent containing 68.8% acetone. In these two supersaturation intervals, the experimentally determined values of γ differ by about 40%, the higher value corresponding to the high supersaturation interval.

However, at both low and high supersaturations these values of γ are lower by about 50% than those predicted by Mersmann's relation. This discrepancy may be attributed partly to the occurrence of polynuclear nucleation and partly to the persistence of heterogeneous and/or secondary nucleation.

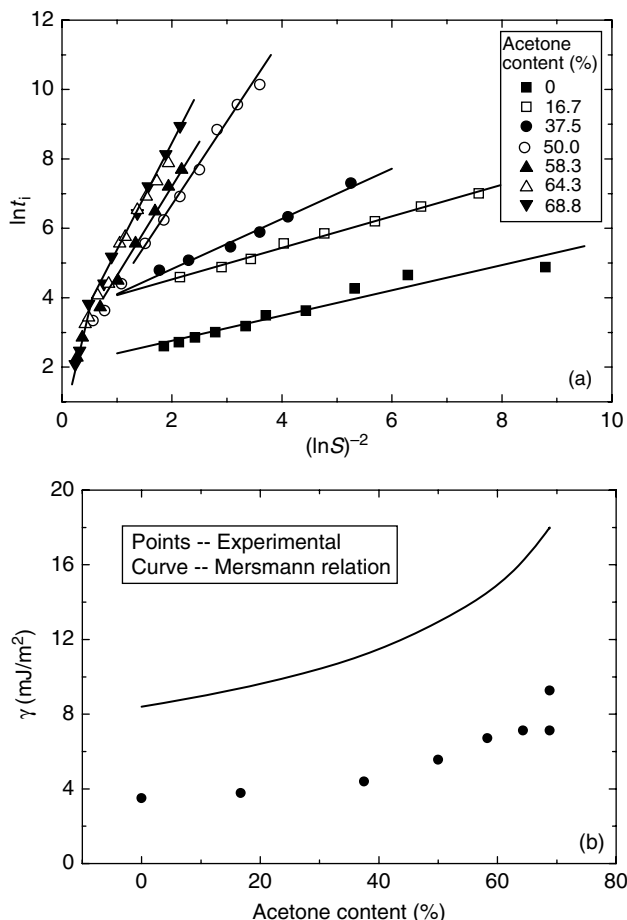


Figure 2.20 Plots of $\ln t_i$ against $(\ln S)^{-2}$ according to Equation (2.65) for dexamethasone sodium phosphate in aqueous solutions with different acetone contents. It can be seen that for $(\ln S)^{-2} < 1$ the slope is higher than that for $(\ln S)^{-2} > 1$. (b) Dependence of interfacial energy γ on acetone content. Experimental data are shown by points and the curve shows the theoretically predicted dependence from Mersmann's relation [see Equation (2.41)]. Note that γ increases with increase in acetone content. Original data from Hao et al. (2005)

Figure 2.21 presents the plot of $\ln t_i$ as a function of $(\ln S)^{-2}$ according to Equation (2.65) for the nucleation of calcium carbonate from aqueous solutions in gravity (i.e. terrestrial) and microgravity conditions. It can be seen that in the investigated range of supersaturation in the experiments under gravity conditions three straight lines of

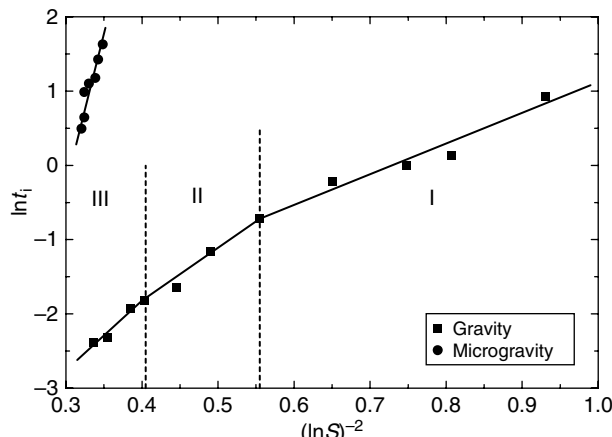


Figure 2.21 Plots of $\ln t_i$ against $(\ln S)^{-2}$ according to Equation (2.65) for the nucleation of calcium carbonate from aqueous solutions in gravity and microgravity conditions. In gravity three straight lines of different slopes meet each other, forming three supersaturation regimes. Under gravity conditions the slope in regime III is about four times larger than that in regime I. Reproduced from X.Y. Liu, K. Tsukamoto, and M. Sorai. Langmuir **16**, 5499. Copyright (2000), with permission from American Chemical Society

different slopes meet each other, forming three supersaturation regimes. Under gravity conditions the slope in regime III is about four times and that in regime II is about two times larger with respect to the slope in regime I. In contrast, the slope under microgravity conditions is about 3.5 times higher than that in regime III of comparable supersaturation level. This observation implies that the measured interfacial energy of calcium carbonate is about 1.5 times higher in microgravity than in gravity conditions.

The above observations may be explained in terms of the supersaturation dependence of nucleation rate discussed in Section 2.2.2 in terms of nucleation on foreign particles. As can be seen from Figure 2.8, depending on the values of m and $\phi(m, R')$, under gravity conditions three intersecting straight lines with different slopes suggest that three different types of foreign bodies control the nucleation of calcium carbonate in three different supersaturation regimes. The microgravity effect on nucleation may be explained by considering convection due to temperature or the concentration gradient caused by nucleation and growth. Convection ensures the transport of growth units to the surface of the growing crystal, thereby compensating for depletion of the concentration (or supersaturation) during nucleation. Convection also substantially promotes the effect of foreign bodies such as tiny particles and organic species on the walls of the crystallization vessels. Moreover, convection promotes the transport of new seed crystals from the surface of walls of the crystallization vessels to the bulk. The number of effective foreign bodies for heterogeneous nucleation is thus increased. Once heterogeneous nucleation occurs at relatively low supersaturation, the nucleating material is consumed quickly, thereby leading to a drop in the bulk supersaturation.

Convection of the solution in gravity conditions leads to the development of gravitational sinks associated with drop in the bulk supersaturation. The gravitational sinks

disappear soon after microgravity is introduced and the convection due to the concentration and temperature gradient is eliminated. Consequently, microgravity will greatly slow the transport of growth units towards the substrate surface, causing concentration (supersaturation) depression during nucleation on the surfaces of substrates. This implies that a much higher supersaturation is necessary to achieve a similar nucleation rate for heterogeneous nucleation. From this inference, it follows that in microgravity heterogeneous nucleation is suppressed and homogeneous nucleation is favored. This explains a high value of interfacial energy in microgravity conditions.

2.6 Effects of Additives

Additives present in a growth medium always lead to a change in the solubility of the solute. A natural consequence of the change in the solubility of the compound is that the concentration of ions/molecules of the solute present in the medium and the solute–fluid interfacial energy γ are altered. These changes lead to changes in the metastable zone width S_c [see Equation (2.44)] and the three-dimensional nucleation rate J [Equations (2.22) and 2.36)]. These issues are discussed below.

2.6.1 Solubility

Experiments show that additives lead to changes in the solubility of compounds and the metastability zone width for their growth. These observations imply that the parameters such as supersaturation used for the study of the growth kinetics of crystals and for the growth of large crystals for applications should be correctly determined. However, in the published literature dealing with growth kinetics and study of the metastable zone width, attention has rarely been paid to changes in the solubility of compounds in the presence of impurities and additives. In this section, the effect of additives on the solubility of electrolytes is described. The examples presented here are from recent work carried out on aqueous solutions of ammonium and sodium oxalates in the presence of bi- and trivalent cationic additives at 30 and 40 °C (Misztal, 2004; Sangwal and Mielniczek-Brzóska, 2007a,b).

The solubility c_0 of a solute in a solvent depends on temperature. For an ideal solution it follows the relation (Berg, 1963; Eggers *et al.*, 1964; Izmailov, 1976)

$$\ln c_0 = \frac{\Delta H_m}{R_G T_m} \left(1 - \frac{T_m}{T} \right) \quad (2.68)$$

where the solubility c_0 is expressed in mole fraction, ΔH_m is the enthalpy of melting and T_m is the melting point of the solute in kelvin. A similar relation holds in the case of real systems, where one obtains the enthalpy of solution ΔH_s instead of ΔH_m . The value of ΔH_s depends on the solvent used. This relation is usually referred to as the solubility for regular or real systems. A typical plot of the temperature dependence of the solubility of a solute in a solvent following ideal solution behavior is shown in Figure 2.22. In drawing the plot it is assumed that $\Delta H_m/R_G T_m = 3$ [see Equation (2.40)] and $T_m = 550$ K. This system corresponds to a compound similar to sodium oxalate.

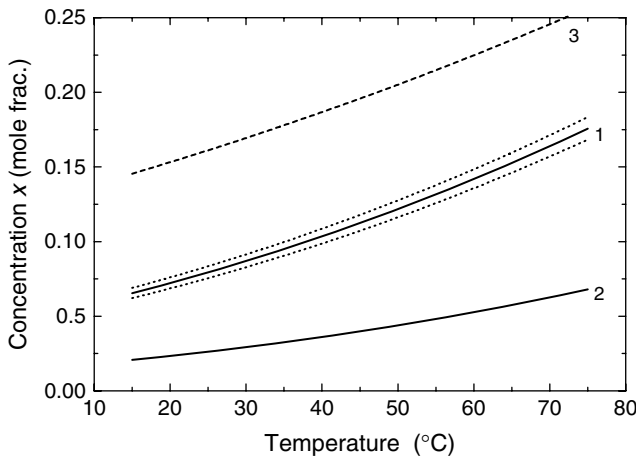


Figure 2.22 Dependence of solubility c_0 of a solute (curve 1, solid line) in an imaginary solvent on temperature according to Equation (2.68). Curves 1 and 2 show ideal and real solubility, respectively. Curve 1 is drawn with $\Delta H_m/R_G T_m = 3$ and $T_m = 550\text{ K}$ and curve 2 with $T_m = 660\text{ K}$. Dotted curves are drawn for $T_m = 555\text{ K}$ (lower curve) and 545 K (upper curve). Curve 3 represents the metastable zone curve according to Equation (2.44) with $\gamma_{cf} \Omega^{2/3}/kT^* = 2.4$, where the reference temperature $T^* = 300\text{ K}$

In the case of regular solutions, deviations from ideal solubility behavior are due to the nature of the interactions between solute ions and solvent molecules. If $\phi_{b(ss)}$, $\phi_{b(ff)}$ and $\phi_{b(sf)}$ denote solid–solid, fluid–fluid and solid–fluid bonds per pair of molecules/ions, respectively, the change in the bond energy ϕ_b during dissolution may be given by (see, for example, Dekker, 1969)

$$Z\phi_b/2 = Z[\phi_{b(ss)} + \phi_{b(ff)} - 2\phi_{b(sf)}]/2 \quad (2.69)$$

where Z is the number of nearest neighbors. Since the enthalpy of solution $\Delta H_s = Z\phi_b/2$ and enthalpy of melting $\Delta H_m = Z[\phi_{b(ss)} - \phi_{b(sf)}]/2$, Equation (2.69) may be expressed in the form

$$\Delta H_s = \Delta H_m + \Delta H_{\text{mix}} \quad (2.70)$$

where the enthalpy of mixing

$$\Delta H_{\text{mix}} = Z[\phi_{b(ff)} - \phi_{b(sf)}] \quad (2.71)$$

Obviously, $\Delta H_{\text{mix}} \neq 0$ for regular solutions and $\Delta H_{\text{mix}} = 0$ for ideal solutions. In other words, in regular solutions $\Delta H_s \geq \Delta H_m$. Moreover, the ideal solution relationship approximates the behavior of real systems only for mixtures of chemically similar substances and applies at low solute concentrations. However, in general, the higher the change in the enthalpy of mixing ΔH_{mix} due to the impurity, the higher is the solubility of the solute. Curve 2 in Figure 2.22 illustrates the solubility of a real system predicted by

Equation (2.68) with the enthalpy of mixing $\Delta H_{\text{mix}} = \Delta H_m/5$. The curve corresponds to $T_m = 660$ K.

Apart from the effect of temperature, several factors are known to affect the solubilities of different compounds. Among the well-known ones are (Berg, 1963; Margolis, 1966; Charlot, 1976; Pataki and Zapp, 1980) the common-ion effect, effect of foreign ions, effect of pH and formation of complexes. The presence of common ions always decreases the solubility of a solute, while foreign ions and complex formation lead to an increase in the solubility. Most of these observations can be interpreted in terms of changes in the values of ΔH_s or T_m caused by these factors. Since ΔH_s and T_m are mutually related [cf. Equation (2.40)], the ultimate consequence of the above factors may be explained from consideration of changes in the enthalpy of mixing ΔH_{mix} , determined by the bond energy $\phi_{b(\text{sf})}$ [see Equation (2.71)]. For example, if a given factor leads to a decrease or increase in T_m , the solubility predicted by Equation (2.68) is changed accordingly. Figure 2.22 shows the solubility curves of the system when one of the above factors leads to a change in T_m of the compound by 5 K. An increase in T_m leads to a decrease in solubility x and a decrease in T_m to an increase in c_0 . In the above example, a change in T_m by 5 K changes the solute solubility up to 10% of the additive-free solubility.

At a particular temperature, the solubility c_0 of ammonium and sodium oxalates in aqueous solutions containing bi- and trivalent cationic additives changes with the concentration c_i of an additive. Usually, the solubility of a compound increases with increase in additive concentration c_i , but, depending on the properties of the additive and solution temperature, it can also decrease. A typical example of the plots of the solubility c_0 of ammonium oxalate against the concentration c_i of several bi- and trivalent cationic additives in aqueous solutions at 30°C is illustrated in Figure 2.23. The experimental data may be fitted reasonably well according to the empirical relation

$$c_0 = c_0^* + A_s c_i \quad (2.72)$$

where c_0^* is the solubility of ammonium oxalate in water in the absence of additives, and the value of the slope A_s is determined by the chemical properties of the additives. It can be seen from these plots that the value of the slope A_s of $c_0(c_i)$ plots does not depend on the valency of a cationic additive alone. For example, bivalent Cu(II), Co(II) and Ni(II) give very different values of A_s .

The empirical linear dependence in Equation (2.72) of the solubility c_0 of ammonium oxalate on the concentration c_i of different impurities is associated with the stability of dominant complexes formed by additive cations with oxalate ions. Figure 2.24 shows the dependence of $-\log \beta_l$ of different impurity complexes containing an increasing number l of oxalate ligands on the parameter A_s for saturated solutions. Here the ligand number $l = 1, 2$ and 3 . Except for Mn(II) and Ni(II) impurities, the data may be represented reasonably well by the empirical relation

$$-\log \beta_l = -\log \beta_l^* + X_1 A_s \quad (2.73)$$

where the constant $-\log \beta_l^*$ is the extrapolated value of $-\log \beta_l$ for $A_s = 0$, and the constant X_1 is the slope related to changes in $-\log \beta_l$ with A_s . Since the standard Gibbs

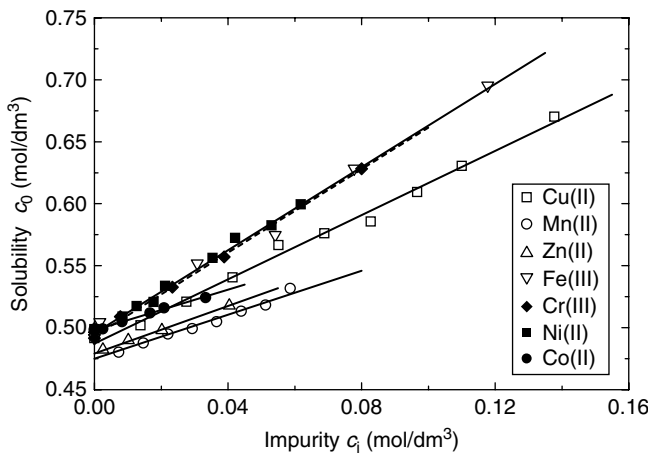


Figure 2.23 Dependence of solubility c_0 of ammonium oxalate in water at 30°C on concentration c_i of different bi- and trivalent cationic additives. The solubility of pure ammonium oxalate was omitted when fitting the experimental data in the presence of Zn(II) and Mn(II) impurities according to Equation (2.72). Reproduced from K. Sangwal and E. Mielniczek-Brzóska. Cryst. Res. Technol. **42**, 531. Copyright (2007b), Wiley-VCH

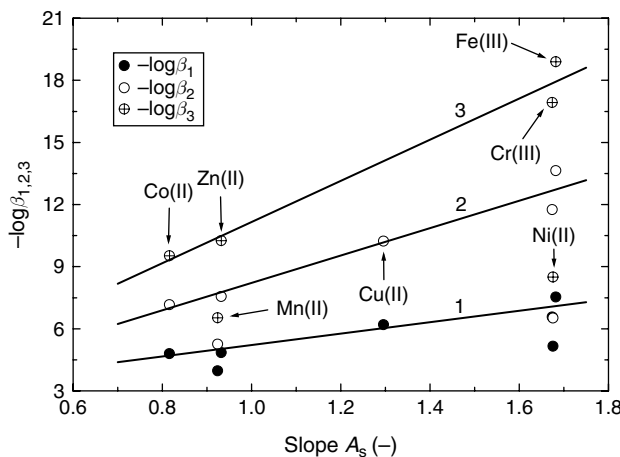


Figure 2.24 Dependence of $-\log \beta_1$ (i.e. $-\log \beta_1$, $-\log \beta_2$ and $-\log \beta_3$) for impurity complexes containing one, two and three oxalate ligands on the parameter A_s^{-1} . Data for Mn(II) and Ni(II) were excluded from the analysis. Reproduced from K. Sangwal and E. Mielniczek-Brzóska. Cryst. Res. Technol. **42**, 531. Copyright (2007b), Wiley-VCH

free energy ΔG_{0s} involved in the formation of dominant complexes in the saturated solutions from their corresponding lower complexes is related to their corresponding stability constants (i.e. $\ln \beta_s = -\Delta G_0 / R_G T$) and their successive equilibrium (stability) constants are mutually related (see Section 1.2.3), it may be concluded that the relationship between

$-\log \beta_s$ and A_s is associated with the dependence of the standard Gibbs free energy ΔG_{0s} involved in the formation of dominant complexes in the saturated solutions on the slope A_s . However, as seen in the case of Mn(II) additive, a lower relative concentration of the dominant complex of an additive present in the saturated solution may lead to deviations from the linear relation in Equation (2.73).

2.6.2 Three-Dimensional Nucleation Rate

The presence of an impurity in the solution may affect the nucleation rate J by causing changes in the solid–liquid interfacial energy γ_{eff} and/or the kinetic factor A' (Kashchiev and Firoozabadi, 2002). When impurity molecules adsorb on the nucleus surface, they lead to a decrease in γ_{eff} [see Equation (2.31)], thereby leading to an increase in J . However, the lifetime of nuclei is very short and the impurity molecules cannot reach them by diffusion in the solution. Therefore, an impurity in the solution can either promote nucleation through a decrease in γ_{eff} as a result of adsorption on the nucleus or has no effect on J when there is no adsorption. All these changes in J due to γ_{eff} are caused via ΔG_{3D}^* [Equation (2.21)] and the critical nucleus radius r_{3D}^* [Equation (2.20)].

An impurity that does not change γ_{eff} may change the value of A' by physically blocking the existing active sites for the attachment of growth units. If θ is the fraction of blocked active sites, then the kinetic factor becomes $A'(1 - \theta)$. Assuming that the impurity adsorption on these active sites obeys the Langmuir adsorption isotherm [see Equation (4.5)], the dependence of nucleation rate J on impurity concentration c_i may be given by (Kashchiev and Firoozabadi, 2002; Sangwal and Mielniczek-Brzóska, 2004)

$$J = [A'/(1 + Kc_i)] \exp(-\Delta G_{3D}^*/kT) \quad (2.74)$$

where the Langmuir constant K is given by [see Equation (4.6)]

$$K = \exp(Q_{\text{diff}}/R_G T) \quad (2.75)$$

where R_G is the gas constant and Q_{diff} is the differential heat of adsorption corresponding to the impurity coverage θ of the available adsorption sites. When $c_i = 0$, Equation (2.72) reduces to Equation (2.22).

2.6.3 Metastable Zone Width

Several authors (Shimomura and Suzuki, 1989; Srinivasan *et al.* 1999, 2000; Rajesh *et al.* 2000, 2001; Sayan and Ulrich, 2001; Gürbüz and Ozdemar, 2003; Omar and Ulrich, 2003; Sangwal and Mielniczek-Brzóska, 2004) have reported that the metastable zone width for the crystallization of a variety of compounds growing from solutions changes with the addition of different impurities. It was also observed (Srinivasan *et al.* 1999, 2000; Rajesh *et al.* 2000, 2001) that organic compounds, such as EDTA, urea and thiourea, lead to an increase in the metastable zone width and improvement in the quality of several crystals. Shimomura and Suzuki (1989) reported similar results in the case of KDP crystals growing from aqueous solutions containing Cr(III) additive, as shown in Figure 2.25. In most of the cases, an increase in the metastable zone width with the concentration of impurities has been reported. However, in the papers dealing

with the metastable zone width (Srinivasan *et al.* 1999, 2000; Rajesh *et al.* 2000, 2001; Sayan and Ulrich, 2001; Gürbüz and Ozdemar, 2003) attention is rarely paid (Omar and Ulrich, 2003; Sangwal and Mielniczek-Brzóska, 2004) to changes in the solubility of compounds in the presence of impurities. Therefore, it may be argued that probably most of the data on the dependence of metastable zone width on the concentration c_i of impurities, published in the above papers, are erratic, and cannot be used to verify theoretical predictions of the effect of an impurity on the metastable zone width for the crystallization of a compound.

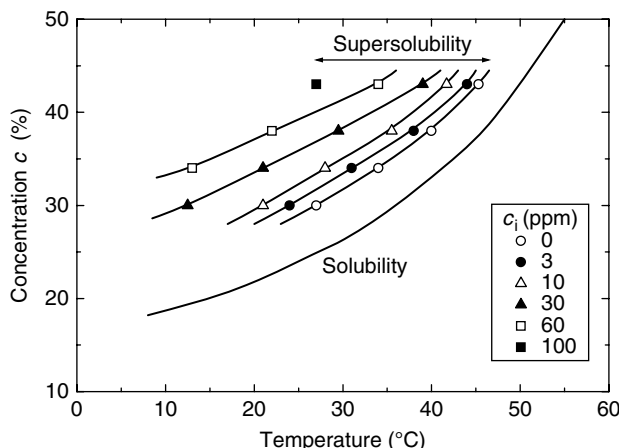


Figure 2.25 Effect of Cr(III) ions on the metastable zone (supersolubility) of KDP solution. No effect of Cr(III) ions was found on solubility. Reproduced from O. Shimomura and M. Suzuki. J. Cryst. Growth **98**, 850. Copyright (1989), with permission from Elsevier

In order to understand the effect of additives on the metastable zone width, we refer to Figure 2.22. As explained above, the dashed curves below and above the ideal solubility curve 1 show the effect of an additive on the solubility when the additive leads to an increase and decrease, respectively, in the value of melting point T_m from 550 K by only 5 K, but the ratio $\Delta H_m / R_G T_m = 3$ and is constant for both additive-free and additive-containing systems. Recalling that the assumption that the quantity $\gamma_{sf} \Omega^{2/3} / k_B T$ is constant implies incorrectly that solid–liquid interfacial energy is independent of temperature T . Therefore, in the calculations of the metastable zone curve it is necessary to take some reference temperature T^* . Curve 3 represents the metastable zone curve predicted by Equation (2.38) with $\gamma_{sf} \Omega^{2/3} / k_B T^* = 2.4$, where the reference temperature $T^* = 300\text{K}$.

Comparison of metastability curve 3 with dashed curves of solubility in the presence of additives and curve 1 for additive-free system shows that changes in solubility by an additive can lead to large changes in the metastable zone width. Therefore, to study the influence of additives on the metastable zone width, it is necessary to obtain data on the equilibrium concentration c_0 and concentration c^* for the metastable zone width for a system under the same conditions of temperature and additive concentration.

Effect of Chemical Nature of Additives on Metastable Zone Width

Sangwal and Mielniczek-Brzóska (2004) reported experimental data on the effect of six different bi- and trivalent cations on the metastable zone width for the growth of ammonium oxalate monohydrate crystals from aqueous solutions obtained at 30°C as a function of impurity concentration c_i . These data are presented in Figure 2.26. It can be seen that there is a negligible effect of Cu(II), Fe(III) and Cr(III) impurities on the metastable zone width, but Mn(II), Co(II) and Ni(II) lead to a significant increase in the value of S_{\max} . Among the latter impurities, the effect of Co(II) and Ni(II) is much more pronounced than that of Mn(II). These results may be explained by using Equations (2.22) and (2.31) for three-dimensional nucleation rate J [see Equation (2.74) and Section 2.6.2].

Substituting the value of ΔG_{3D}^* from Equation (2.21) in Equation (2.74), one obtains after rearrangement the maximum supersaturation ratio S_{\max} :

$$S_{\max} = \exp \left\{ \frac{B}{[\ln(A'/J) - \ln(1 + Kc_i)]^{1/2}} \right\} \quad (2.76)$$

where B is given by Equation (2.37). When $\ln(1 + Kc_i)/\ln(A'/J) \ll 1$ and $\ln(1 + Kc_i) \approx Kc_i$, Equation (2.76) can be written as

$$S_{\max} = \exp\{B_1[1 + Kc_i/2\ln(A'/J)] \approx (1 + B_1) + B_2c_i \quad (2.77)$$

where

$$B_1 = B/\ln^{1/2}(A'/J) \quad (2.78)$$

and

$$B_2 = B_1K/2\ln(AS/J) = BK/2\ln^{3/2}(A'/J) \quad (2.79)$$

When $c_i = 0$, from Equations (2.76) and (2.77), one obtains S_{\max} for impurity-free system in the form of Equations (2.44) and (2.45).

Best-fit plots of the experimental $S_{\max}(c_i)$ data for different additives according to Equation (2.76) are presented by solid lines in Figure 2.26a and b. The values of the Langmuir constant K and the differential heat of adsorption Q_{diff} [cf. Equation (2.76)] for different additives are given in Table 2.1. It can be seen that the trends in the changes in K and Q_{diff} remain unchanged when the values of B and $\ln(A'/J)$ for different additives are different according to the best fit of the data or are kept fixed equal to 0.25 and 7.5, respectively, for all impurities (dashed curves in Figure 2.26b).

From Table 2.1, it can be seen that the values of B and $\ln^{1/2}(A'/J)$ depend on the chemical nature of an additive, but the ratio $B/\ln^{1/2}(A'/J)$ is a constant quantity equal to about 0.096 such that a change in B is accompanied by a proportional change in $\ln^{1/2}(A'/J)$. Simultaneous changes in B and $\ln^{1/2}(A'/J)$ suggest that the effective interfacial energy γ_{eff} [cf. Equation (2.39)], the kinetic parameter A' related to the attachment of growth units to the embryos and the nucleation rate J are interrelated. Decreases in B and $\ln^{1/2}(A'/J)$ occur when an impurity leads to a decrease in the differential heat of adsorption Q_{diff} . The above features suggest that the increase in the values of S_{\max} is caused by the blocking of active nucleation sites by Mn(II), Co(II) and

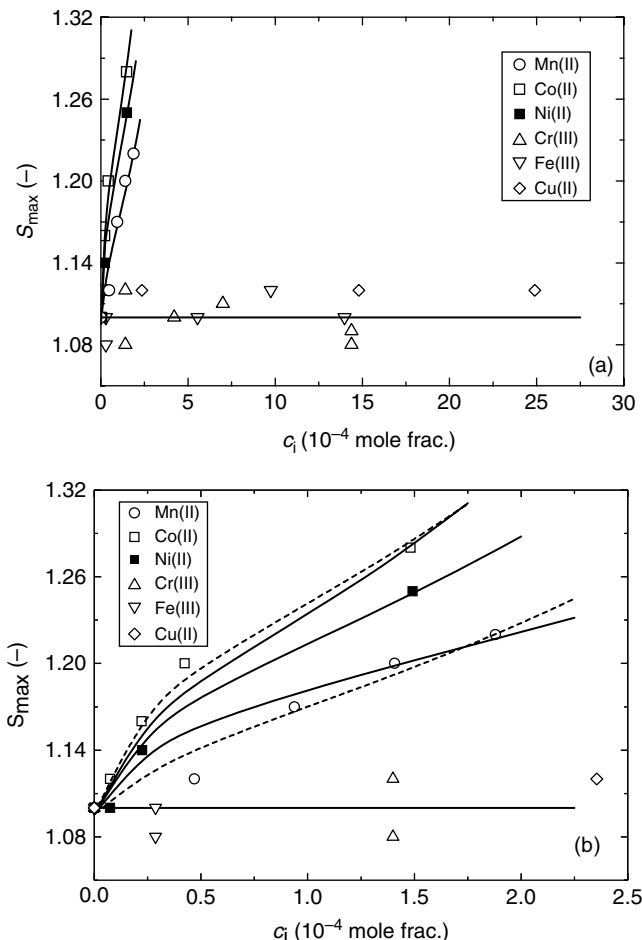


Figure 2.26 Plots of metastable zone width $S_{\max} = 1 + \sigma_{\max}$ against the concentration c_i of different impurities according to Equation (2.76). In (a) and (b) solid curves represent data fitted with different values of constants B and $\ln(A'/J)$, and in (b) dashed curves represent data with $B = 0.25$ and $\ln(A'/S) = 7.5$. The values of B , $\ln(A'/J)$ and K given in Table 2.1. Reproduced from K. Sangwal and E. Mielniczek-Brzóska. J. Cryst. Growth **267**, 662. Copyright (2004), with permission from Elsevier

Ni(II) additives, whereas no such blocking phenomenon occurs in the presence of Cu(II), Cr(III) and Fe(III) additives.

It should be mentioned that the linear dependence of S_{\max} on c_i predicted by Equation (2.77) is followed in the case of ammonium oxalate monohydrate by Co(II) and Ni(II) additives only for $c_i \ll 5 \times 10^{-5}$ mole fraction (see Figure 2.26b). For Mn(II) additive, the $S_{\max}(c_i)$ plot appears linear because the term Kc_i is close to unity. However, in contrast to the $S_{\max}(c_i)$ data for ammonium oxalate monohydrate in the presence of Mn(II), Co(II) and Ni(II) additives, the experimental data on the metastable zone width, measured as the temperature difference $\Delta T_{\max} = T_0 - T_{\max}$ (where the T_0 is the saturation

Table 2.1 Constants of Equation (2.76) for different additives. Adapted from K. Sangwal and E. Mielniczek-Brzóska. J. Cryst. Growth **267**, 662. Copyright (2004), with permission from Elsevier

Additive	Figure	Curve	B	$\ln(A'/J)$	$K(\times 10^5)$	Q_{diff} (kJ/mol)
Mn(II)	2.25b	Dashed	0.25	7.5	19	36.4
	2.25a,b	Solid	0.20	4.8	2.3	31.1
Co(II)	2.25b	Dashed	0.25	7.5	44	38.5
	2.25a,b	Solid	0.27	8.75	133	41.3
Ni(II)	2.25a,b	Solid	0.25	7.5	34	37.9
Others	2.25a,b	Solid	0.25	7.5	0	0

temperature and T_{\max} is the temperature up to which the solution is stable), for KDP (Shimomura and Suzuki, 1989), NaCl (Omar and Ulrich, 2003) and borax (Gürbüz and Özdemar, 2003) follow the linear relation in Equation (2.77), suggesting that $Kc_i \ll 1$.

Effect of Solubility on Metastable Zone Width

In Equations (2.76) and (2.77), relating the supersaturation zone width S_{\max} with the concentration c_i of impurities, and for systems without impurities, the important quantities are the interfacial tension γ_{eff} (contained in B) and the ratio J/A' . The values of these quantities may be obtained from the experimental data using the above equations. As discussed above, in the case of ammonium oxalate monohydrate the value of γ_{eff} calculated from the value of $B = 0.25$, obtained from the experimental $S_{\max}(c_i)$ data, is about 8.4 mJ/mol, for example, in the case of Ni(II) additive (assuming that molecular volume $\Omega = 2.12 \times 10^{-29} \text{ m}^3$ and $k_B T = 2.52 \text{ kJ/mol}$). This value of γ_{eff} is very low in comparison with the interfacial energy of crystals similar to ammonium oxalate monohydrate. For example, $\gamma = 40 \text{ mJ/m}^2$ for potassium acid phthalate (Borc and Sangwal, 2004). The low value of γ_{eff} is associated with, *inter alia*, the effect of solvent. Since the value of the interfacial tension γ_{eff} of inorganic compounds depends on their solubility c_0 [see Equations (2.39) and (2.41)], it is expected that the solubility c_0 of AO in the presence of impurities and without impurities affects the value of S_{\max} .

The above analysis of $S_{\max}(c_i)$ data for ammonium oxalate monohydrate in aqueous solutions containing various additives does not take into consideration the role of solubility. To analyze the role of solubility, using Equation (2.39) from Equation (2.76), one obtains

$$\ln^{2/3} S_{\max} = 0.64 \left\{ \frac{\xi}{[\ln(A'/J) - \ln(1 + Kc_i)]^{1/3}} \right\} \left(\frac{\Delta H_m}{R_G T_m} - f \ln c_0 \right) \quad (2.80)$$

where the constant $f = 1$. For ammonium oxalate monohydrate, the ratio $\Delta H_m / R_G T_m \approx 4.5$ [see Equation (2.40)]. From Equation (2.80), it may be noted that, for a constant value of c_i , $\ln^{2/3} S_{\max}$ decreases linearly with increasing $\ln c_0$. However, when $\ln^{2/3} S_{\max}$ does not depend on c_0 (i.e. when $f = 0$), $\ln^{2/3} S_{\max}$ is a constant quantity, whose value is determined by the term $\xi / \ln^{1/3}(A'/J)$. The constancy of $\ln^{2/3} S_{\max}$ implies that S_{\max} remains unaltered, irrespective of the temperature dependence of solubility c_0 for impurity-free systems and the concentration c_i of additives contained in a system.

The plots of $\ln^{2/3} S_{\max}$, based on the experimental data obtained during the study of growth kinetics of AO in the presence of different impurities (see Figure 2.26a) and

obtained at different temperatures during the measurement of density and viscosity of concentrated AO aqueous solutions in the absence of impurities (Frej *et al.*, 2000), against $\ln c_0$ and the theoretically predicted dependence in Equation (2.80) are shown in Figure 2.27. While plotting the $S_{\max}(c_0)$ data in the presence of different impurities according to Equation (2.80), Equation (2.72) was used to calculate the solubility c_0 of ammonium oxalate in solution containing a concentration c_i of an impurity.

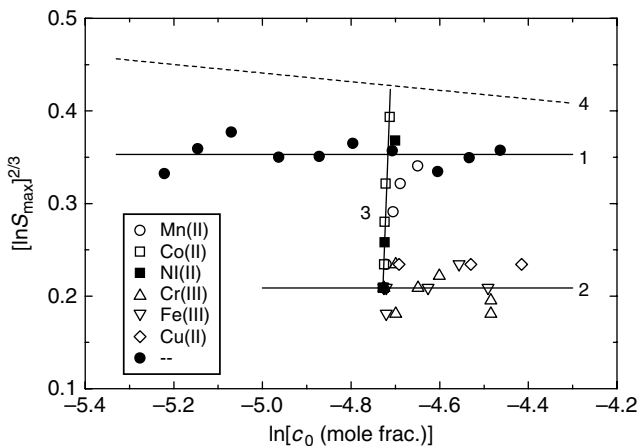


Figure 2.27 Plot of $(\ln S_{\max})^{2/3}$ against solubility $\ln c_0$ of ammonium oxalate in the presence of different impurities (curves 1–3) and the theoretically predicted dependence (curve 4). The constants of different curves are: (1) $\xi = 0.24$ and $f = 0$, (2) $\xi = 0.14$ and $f = 0$, (3) $\xi = 0.14$, $f = 0$ and $K = 2.5 \times 10^6$, and (4) $\xi = 0.14$ and $f = 1$. In all cases $\ln(A'/J) = 7.5$. The $S_{\max}(c_0)$ data obtained during density and viscosity measurements of pure solutions at different temperatures are shown by solid circles. Reproduced from K. Sangwal and E. Mielniczek-Brzóska. J. Cryst. Growth **267**, 662. Copyright (2004), with permission from Elsevier

It can be seen from Figure 2.27 that S_{\max} does not depend on changes in the solubility c_0 of AO associated with changes in temperature (curve 1). A similar behavior is observed in the presence of Cu(II), Fe(III) and Cr(III) impurities (curve 2), where the changes in c_0 are caused by the impurity and not by changes in temperature. However, the values of S_{\max} in the presence of Cu(II), Fe(III) and Cr(III) impurities are much lower than those noted during viscosity measurements. These features of Figure 2.27 are consistent with the predictions of Equation (2.80).

The lower values of S_{\max} in the presence of Cu(II), Fe(III) and Cr(III) impurities than those observed during viscosity measurements are associated with the difference in the value of the term $\xi/\ln^{1/3}(A'/J)$, equal to 0.0725 and 0.1226, respectively. Taking $\ln(A'/J) = 7.5$ for Ni(II), for example (see above), one finds that $\xi = 0.14$ (i.e. 1/7.05) and $\xi = 0.24$ (i.e. 1/4.17), respectively. The factor ξ characterizes the state of the faces composing 3D nuclei in terms of their smoothness or roughness. A low value of ξ implies a high density of active nucleation sites due to roughening of the faces of the 3D nuclei (Elwenspoek, 1986a,b; Bennema and van der Eerden, 1987; Sangwal, 1989). Therefore, it may be concluded that the critically sized 3D nuclei formed during viscosity

measurements are relatively smooth in comparison with those formed during growth experiments containing Cu(II), Fe(III) and Cr(III) impurities. The constant value of S_{\max} in the presence of the above impurities implies that the active nucleation sites are not blocked and the density of the active sites remains constant.

In contrast to the effect of Cu(II), Fe(III) and Cr(III) impurities, Mn(II), Co(II) and Ni(II) impurities lead to a steep increase in the metastable zone width S_{\max} with increasing solubility c_0 of ammonium oxalate (i.e. with an increase in c_i), such that ultimately at high impurity concentrations S_{\max} approaches or even exceeds the highest value recorded during viscosity measurements. Equation (2.80) explains this observation with three variables: impurity concentration c_i , solubility c_0 in the presence of impurity, and $\xi/\ln^{1/3}(A'/J) = 0.0725$. The values of the constant K determined in this case are comparable to those given in Table 2.1. For example, for Co(II) impurity $K = 2.5 \times 10^6$ (curve 3, Figure 2.27).

As inferred above, the increase in S_{\max} with increasing solubility c_0 is associated with the process of physical blocking of active growth sites by the above impurities. As expected, the ultimate effect of this physical blocking of active growth sites with increasing concentration c_i of these impurities is to render the critically sized growth nuclei smoother due to the increasing value of ξ in the term $\xi/\ln^{1/3}(A'/J)$. Using the values of $\ln^{1/3}(A'/J)$ for different additives (see Table 2.1), one finds that ξ changes in the order: $\xi[\text{Mn(II)}] < \xi[\text{Ni(II)}] < \xi[\text{Co(II)}]$, and lies between 0.122 and 0.142. The highest value of ξ attained is about 0.25 for nuclei developed during viscosity measurements of pure solutions.

In the above analysis of $S_{\max}(c_i)$ and $S_{\max}(c_i, c_0)$ data, it was assumed that spherical nuclei are formed. Consequently, the value of ξ is an average value for all possible planes composing stable critically sized 3D nuclei. An increase in the average value of ξ suggests that the stable nuclei are not spherical and adsorption of an impurity occurs preferentially on specific planes composing the nuclei.

Finally, it should be mentioned that the metastable zone width S_{\max} observed for ammonium oxalate monohydrate is relatively low in comparison with the theoretical value of over 0.5 at 30 °C. The low value of S_{\max} can be due to secondary nucleation induced by the presence of seeds and stirring of the solution during the measurement (Nývlt *et al.*, 1985). The relatively low values of γ_{eff} and ξ for systems with and without additives are consistent with this possibility.

References

- Bennema, P. and J.P. van der Eerden (1987). In: I. Sunagawa (Ed.), *Morphology of Crystals*, Terrapub, Tokyo, p. 1.
- Berg, E.W. (1963). *Physical and Chemical Methods of Separation*, McGraw-Hill, New York.
- Boistelle, R. (1988). In: N. Garti and K. Sato (Eds.), *Crystallization and Polymorphism of Fats and Fatty Acids*, Marcel Dekker, New York, Chap. 5, p. 189.
- Borc, J., and K. Sangwal (2004). *Surf. Sci.* **555**, 1.
- Charlot, G., *Analiza Nieorganiczna Jakościowa (Quantitative Inorganic Analysis)*, PWN, Warsaw, 1976.
- Dekker, A.J. (1969). *Solid State Physics*, Macmillan, New York.

- Eggers, D.F., N.W. Gregory, G.D. Halsey, and B.S. Rabinovitch (1964). *Physical Chemistry*, John Wiley & Sons, Inc., New York.
- Elwenspoek, M. (1986a). *J. Cryst. Growth* **78**, 353.
- Elwenspoek, M. (1986b). *Appl. Phys. A* **41**, 123.
- Frej, H., A. Balicka, and M. Jakubczyk (2000). *J. Chem. Eng. Data* **45**, 415.
- Gomez-Morales, J., J. Torrent-Burgues, and R. Rodriguez-Clemente (1996). *J. Cryst. Growth* **169**, 331.
- Gürbüz, H., and B. Özdemar (2003). *J. Cryst. Growth* **252**, 343.
- Hao, H., J. Wang, and Y. Wang (2005). *J. Cryst. Growth* **274**, 545.
- Izmailov, N.A. (1976). *Elektrokhimiya Rastvorov (Electrochemistry of Solutions)*, 3rd ed., Khimiya, Moscow.
- Jung, T., W.-S. Kim, and C.K. Choi (2004). *Mater. Sci. Eng. C* **24**, 31.
- Kashchiev, D. (2000). *Nucleation: Basic Theory and Applications*, Butterworth-Heinemann, Oxford.
- Kashchiev, D., and A. Firoozabadi (2002). *J. Cryst. Growth* **243**, 476.
- Kashchiev, D., D. Verdoes, and G.M. van Rosmalen (1991). *J. Cryst. Growth* **110**, 373.
- Katz, J.L., J.A. Fisk, and V. Chakarov (1992). In: N. Fukuta, and P.E. Wagner (Eds.), *Nucleation and Atmospheric Aerosols*, A. Deepak, Hompton, p. 83.
- Liu, X.Y. (1999). *J. Chem. Phys.* **111**, 1624.
- Liu, X.Y., K. Tsukamoto, and M. Sorai (2000). *Langmuir* **16**, 5499.
- Margolis, E.J. (1966). *Chemical Principles in Calculations of Ionic Equilibria*, Macmillan, New York.
- Mersmann, A. (1990). *J. Cryst. Growth* **102**, 841.
- Misztal, R. (2004). *PhD Thesis*, Jagiellonian University, Cracow.
- Nancollas, G.H. (1982). In: G.H. Nancollas (Ed.), *Biological Mineralization and Demineralization*, Springer, Berlin, p. 79.
- Nielsen, A.E., and O. Söhnel (1971). *J. Cryst. Growth* **11**, 233.
- Nývlt, J., O. Söhnel, M. Matuchova, and M. Broul, *The Kinetics of Industrial Crystallization from Solution*, Academia, Prague, 1985.
- Omar, W., and R. Ulrich (2003). *Cryst. Res. Technol.* **38**, 34.
- Pataki, L., and E. Zapp (1980). *Basic Analytical Chemistry*, Akadémiai Kiadó, Budapest.
- Rajesh, N.P., K. Meera, K. Srinivasan, P. Santhana Raghavan, and P. Ramasamy (2000). *J. Cryst. Growth* **213**, 389.
- Rajesh, N.P., C.K. Lakshmana Perumal, P. Santhana Raghavan, and P. Ramasamy (2001). *Cryst. Res. Technol.* **36**, 55.
- Sangwal, K. (1989). *J. Cryst. Growth* **97**, 393.
- Sangwal, K., and E. Mielniczek-Brzóska (2004). *J. Cryst. Growth* **267**, 662.
- Sangwal, K., and E. Mielniczek-Brzóska (2007a). *Fluid Phase Equilibria*, in press.
- Sangwal, K., and E. Mielniczek-Brzóska (2007b). *Cryst. Res. Technol.* **42**, 531.
- Sayan, P., and R. Ulrich (2001). *Cryst. Res. Technol.* **36**, 411.
- Shimomura, O., and M. Suzuki (1989). *J. Cryst. Growth* **98**, 850.
- Söhnel, O. (1982). *J. Cryst. Growth* **57**, 101.
- Srinivasan, K., K. Meera, and P. Ramasamy (1999). *J. Cryst. Growth* **205**, 457.
- Srinivasan, K., K. Meera, and P. Ramasamy (2000). *Cryst. Res. Technol.* **35**, 291.
- Verdos, D., D. Kashchiev, and G.M. van Rosmalen (1992). *J. Cryst. Growth* **118**, 401.

3

Kinetics and Mechanism of Crystal Growth: An Overview

The art of crystallization is much older than the written history of mankind, but the beauty of crystals in terms of their external regularity and symmetry began to be appreciated in the second half of the second millennium. In 1669, Steno recognized that the angles between two neighboring faces of the crystals of a substance differing in their external appearance (morphology) are constant. In 1782, Haüy observed that each chemical substance has a characteristic group of external crystalline shape. These findings led to the idea that each crystal is made up of a particular type of ‘building blocks’ arranged regularly side by side in three dimensions.

Since the first theory of crystal growth was advanced by Curie in 1885, three different approaches have been followed to describe crystal morphology. The first of these, the thermodynamic approach, initiated by Curie and extended by Wulff and others, deals with the construction of crystal morphology from crystallographic structural and, closely related, minimum energy considerations. The second approach, initially formulated between 1922 and 1928 by Volmer, Kossel and Stranski, considers crystal growth in terms of attachment of atoms or molecules at the surface of a crystal thought to be free from internal imperfections. Initially in this approach, growth was considered to start from two-dimensional nuclei developed on a surface, but in 1949 Frank pointed out the role of screw dislocations in the growth of imperfect crystals. The third approach, introduced by Noyes and Whitney in 1897, treats crystal growth as a process of the transport of crystallizing substance by diffusion.

It is obvious that the thermodynamic approach involves macroscopic parameters whereas the second approach treats crystal growth at atomic or molecular level. In the initial version of the diffusion approach, macroscopic parameters such as bulk diffusion constant and thickness of diffusion layer were used, but modern diffusion theories also treat crystal growth at the atomic level. This chapter describes these atomic-level theories

of crystal growth. However, in view of the vast literature existing on the subject, only the basic ideas of these theories are presented. The contents of the chapter are based on the reviews published previously by the author (Sangwal, 1994, 1998a). For further details on crystal growth processes the reader is referred to, *inter alia*, Brice (1973), Chernov (1984) and van der Eerden (1993).

3.1 Crystal Growth as a Kinetic Process

The development of three-dimensional stable nuclei by the attachment of growth species leads to the formation of macroscopic entities with well-developed surfaces. Figure 3.1 shows different positions for the attachment of growth units at a flat crystal–medium interface of a simple cubic lattice. A growth unit attached at the surface terrace, a smooth ledge and a kink site, has one, two and three out of the six nearest neighbors, respectively. Therefore, a growth unit arriving on the surface terrace, at the terrace ledge and at the kink simply loses one, two and three degrees of freedom, respectively. If ϕ_b is the binding energy per pair, the corresponding binding energy of a growth unit attached at these sites is ϕ_b , $2\phi_b$ and $3\phi_b$, respectively.

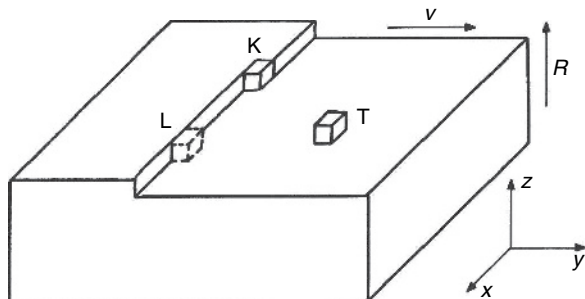


Figure 3.1 Different positions for the attachment of growth units at a flat crystal–medium interface of a simple cubic lattice

The probability of capture of a growth unit at a given site depends through terms $\exp(n\phi_b/k_B T)$ (where n is the number of bonds formed, k_B is the Boltzmann constant and T is the temperature in kelvin). Therefore, the growth unit has a much higher probability of becoming a part of the crystal at the kink site rather than at the ledge or at the surface terrace. Consequently, in contrast to ledges, the contribution of kinks is overwhelmingly high in the rate v of displacement of a step along the surface and in the rate R of displacement of the surface normal to it. Similarly, the contribution to the face growth rate R by the direct attachment of growth units at the terrace is negligible.

From the above, it may be concluded that the kinetics of crystal growth may, in general, be considered to occur in the following stages:

- (1) transport of growth units to the growing surface by bulk diffusion and their capture on the surface terrace;
- (2) migration of growth units adsorbed on the terrace to the step by surface diffusion and their capture at the step;
- (3) migration of growth units adsorbed on the step to the kink site and their integration into the kink;
- (4) transport of the released heat of the reaction and solvent molecules from the solvated atoms/molecules.

One or more of the above steps may control the growth rate, but the slowest one is always the rate-limiting step. However, the growth kinetics, as characterized by rates v and R , depend on crystal structure, structure of crystal–medium interface (i.e. rough or smooth), presence of dislocations emerging on the growing face, supersaturation of the growth medium, growth temperature, stirring and impurities present in the growth medium. The difference in the growth rates R of different faces of a crystal determines its external shape (macromorphology). Growth kinetics also influence the topography of a growing surface and the stability of a growth interface.

Using the above background of crystal growth processes, various models for the growth of smooth flat (i.e. singular) faces are described (Section 3.4). Growth on these faces is possible if two-dimensional nucleation or the presence of dislocations emerging on the surface provides steps and kinks on it. However, in contrast to growth units of the same dimensions in the x , y and z directions, as has been assumed *a priori* in the crystal growth theories, we may also consider that they are parallelepiped-shaped with dimensions a , b and c in the x , y and z directions, respectively, and are incorporated in kinks of steps parallel to the x direction in the (001) face, as shown in Figure 3.2.

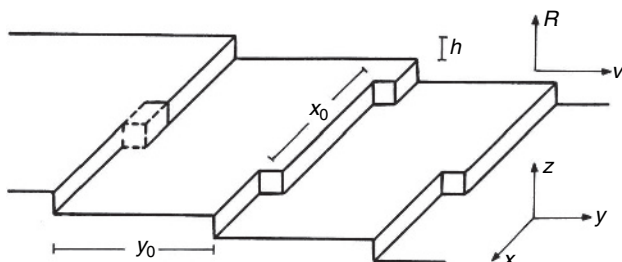


Figure 3.2 Incorporation of growth units of dimensions a , b and c in the x , y and z directions, respectively, in kinks of steps parallel to the x direction in the (001) face

3.2 Types of Crystal–Medium Interfaces

Crystals are usually bounded by plane faces. In accordance with the surface free energy per unit area, as shown by a Gibbs–Wulff plot, these faces may be divided into singular and nonsingular. Singular faces correspond to cusps whereas nonsingular faces show maxima on the Wulff plots. Faces which are misoriented by a small angle from singular

faces are called vicinal faces (Figure 3.3). This classification was introduced by Burton *et al.* (1951). Cahn (1960) treated the solid–fluid interface as a set of successive atomic layers during transition from the solid phase to the fluid phase. This transition may be abrupt such that a fluid layer follows the solid layer, or it may be gradual and in this sense it is difficult to define precisely the boundary between the solid and fluid layers. These interfaces are called sharp and diffuse interfaces, respectively.

Hartman and Perdok (1955) classified the faces of a crystal into F (flat), S (stepped) and K (kinked) faces. F-type faces possess at least two sets of chains of periodically bonded atoms, molecules or radicals [called periodic bond chains (PBCs)], S faces have one such PBC and K faces do not have any PBC (see Figure 3.4). Thus, singular faces with minimum surface free energy are F faces, whereas S and K faces correspond to vicinal and nonsingular faces, respectively.

An ideally flat face is like a terrace, whereas an S face is composed of equally spaced kink-free ledges. However, depending on the environment conditions (for example, temperature and supersaturation), the ledges can have a varying density of kinks. Growth, evaporation and dissolution processes of vicinal faces of crystals composed of terraces between ledges and kinks in the ledges are discussed in terms of terrace, ledge and kink sites. Surfaces composed of terrace, ledge and kink sites are called terrace–ledge–kink (TLK) surfaces.

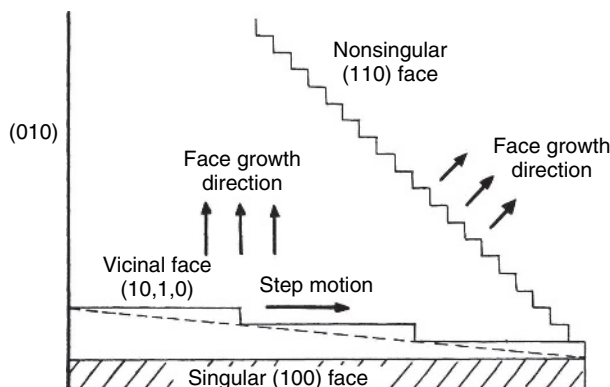


Figure 3.3 Cross-sectional view of the faces of different orientations of a simple cubic crystal. Adapted from E. Kaldus. In: C.H.L. Goodman (Ed.), *Crystal Growth: Theory and Techniques*, Vol. 1, p. 49. Copyright (1976), with permission from Springer Science and Business Media

Sharp interfaces may also be classified in terms of their smoothness. They can be ideally smooth or rough on the atomic scale. Growth on smooth interfaces is possible if two-dimensional nucleation (perfect interface) or presence of dislocations emerging on the surface (imperfect interface) supply kinks necessary for the attachment of growth units. This is shown in Figure 3.4. In the case of a rough interface, a large number of kinks are always present on the surface and individual atoms/molecules can be added to the growing surface statistically.

It should be mentioned that our present understanding of the thermodynamics of roughening of steps and surfaces dates back to the period before 1990.

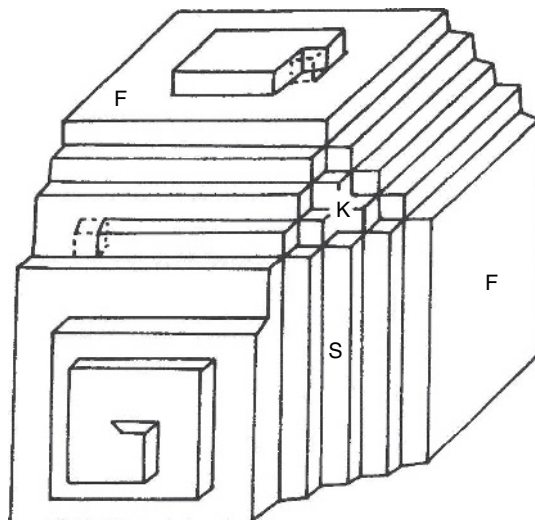


Figure 3.4 Classification of different types of faces of a simple cubic crystal according to the periodic bond chains (PBC): F (flat), S (stepped) and K (kinked). Adapted from R. Boistelle and J.P. Astier. *J. Cryst. Growth* **90**, 14. Copyright (1988), with permission from Elsevier

3.3 Roughening of Steps and Surfaces

As mentioned in Section 3.1, atoms adsorbed on a surface terrace may migrate to the step ledge and join it. The atoms forming the step ledge may also leave their positions because of thermal vibrations, forming ‘gaps’ in the step, i.e. a pair of adjoining kinks of opposite sign. Thus, a straight step no longer remains straight and possesses a certain number of kinks. In other words, an otherwise smooth step becomes rough due to the escape of atoms from it to the surface and the attachment of migrating atoms from the surface to the step. The degree of roughness increases with increasing temperature, and is accompanied by a decrease in the specific free linear energy of the step, γ_l . If N_+ and N_- are the numbers of positive and negative kinks of atomic size per unit length, and N_0 is the number of smooth sites on the step without kinks, then

$$N_+ + N_- + N_0 = N_l = 1/a \quad (3.1)$$

where N_l is the linear density of atoms on the step and a is the atomic diameter. The decrease in free linear energy, γ_l , of the step is given by (Chernov, 1984)

$$\begin{aligned} \gamma_l &= U_l - TS_l \\ &= N_l\omega - N_l k_B T \ln(1 + 2\eta) = -N_l k_B T \ln[\eta(1 + 2\eta)] \end{aligned} \quad (3.2)$$

where

$$\eta = \exp(-\omega/k_B T), \quad \eta^2 = N_+ N_- / N_0^2 \quad (3.3)$$

and ω is the increase in the step energy due to the formation of a kink.

Equation (3.2) shows that $\gamma_l = 0$ at $\eta = \eta_R = 1/2$, i.e. $\omega/k_B T = \ln 2 \simeq 0.69$. At higher temperatures γ_l becomes negative and a step cannot exist. Evidence in favor of this conclusion has been obtained from both computer simulation and growth experiments. Figure 3.5 illustrates the computer-simulated step configurations for the (101) face of a Kossel crystal.

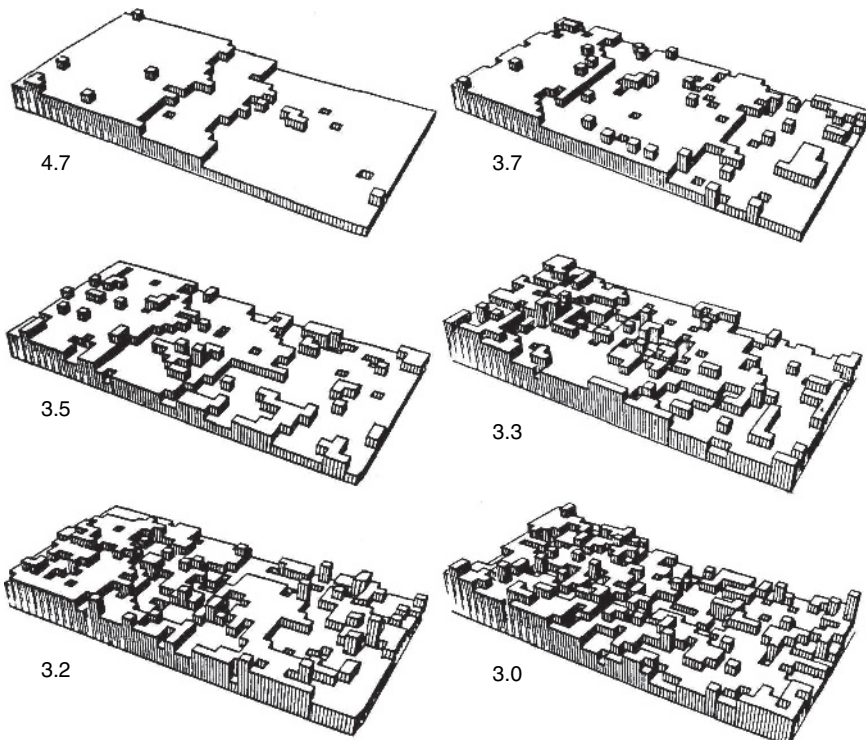


Figure 3.5 Configuration of a ledge step on the surface of a crystal, obtained by computer simulation for different values of α . Reproduced from G.H. Gilmer and K.A. Jackson. In: E. Kaldus and H.J. Scheel (Eds.), Current Topics in Materials Science, Vol. 1, p. 79. Copyright (1976), with permission from Elsevier

3.3.1 Thermodynamic Roughening and the Surface Entropy Factor

The above discussion of the roughness of a step was for a crystal–vapor system, but the arguments are equally valid for the case of crystal–melt and crystal–solution interfaces. However, in these cases normally the so-called lattice gas model is used. In this model, it is assumed that the fluid atoms are packed in the same lattice as in the crystal, but the binding energies in the two phases are different. Then the increase in the interface energy is given by (Bennema and Gilmer, 1973; Chernov, 1984)

$$\omega = [(\phi_{b(ss)} + \phi_{b(ff)})/2] - \phi_{b(sf)} \quad (3.4)$$

where $\phi_{b(ss)}$, $\phi_{b(ff)}$ and $\phi_{b(sf)}$ are the bond energies between neighboring solid–solid, fluid–fluid and solid–fluid atoms (cells), respectively, and ω is given by Equation (3.3).

Returning to the vanishing of γ_l , one finds a situation when $U_l = TS_l$. Physically, this means that with an increase in temperature the step fluctuations become increasingly stronger such that the step smears out in an increasingly wider band near its average position. Finally, at some critical temperature T_R , this width becomes infinitely large such that there is homogenization of the two phases. Above the temperature T_R , the step no longer exists and the F face is not smooth on an atomic scale but consists of random atomic clusters and separate atoms.

Equation (3.2) represents the free linear energy of a step with kinks of monoatomic height. In the absence of this restriction, the specific surface free energy γ is given by (Chernov, 1984)

$$a^2 \gamma = \gamma_l = \omega - k_B T \ln \left[\frac{(1+\eta)}{(1-\eta)} \right] \quad (3.5)$$

In this case, $\gamma_l = 0$ for $\eta_R = \sqrt{2} - 1$ and $\omega/k_B T_R = 0.88$. The value $\eta_R = \sqrt{2} - 1$ corresponds to the exact Onsager's solution for the critical transition temperature in the two-dimensional Ising model (Burton *et al.*, 1951). T_R is the roughening temperature. At $T < T_R$ the surface is smooth on an atomic scale, and at $T > T_R$ it is rough. From the value $\omega/k_B T_R = 0.88$, Burton *et al.* (1951) concluded that thermal roughening for solid–vapor interfaces takes place above the melting point of the solid and will rarely be encountered in practice.

Considering an initially plane interface on which adatoms in a single layer are allowed to occupy randomly lattice sites (single layer model), Jackson (1958) calculated the change in the free energy on adding atoms (molecules) to a fraction x of the N possible sites at equilibrium temperature T_0 :

$$\Delta F/Nk_B T_0 = \alpha x(1-x) + x \ln x + (1-x) \ln(1-x) \quad (3.6)$$

with the so-called surface entropy factor α given by

$$\alpha = z\omega/k_B T = \xi \Delta H_m/k_B T \quad (3.7)$$

where z is the possible number of bonds with the first nearest neighbors in a plane parallel to the surface under consideration, ξ is the ratio of the binding energy of an atom in the slice to the total crystallization energy being defined with reference to vacuum, and ΔH_m is the latent heat of melting.

From an analysis of Equation (3.6) for different values of α , Jackson showed that surfaces with $\alpha < 2$ are rough whereas those with $\alpha > 2$ are smooth. When applied to the solid–vapor interface, this model predicts atomically smooth interfaces.

In the language of the lattice gas model, the surface entropy factor α is defined by [cf. Equations (3.4) and (3.7)]

$$\alpha = 4\omega/k_B T = \{2[\phi_{b(ss)} + \phi_{b(ff)}] - 4\phi_{b(sf)}\} / k_B T \quad (3.8)$$

In the case when complete wetting is assumed, i.e. when $\phi_{b(ff)} = \phi_{b(ss)}$, this equation reduces to Equation (3.7) because $\Delta H_m = (\phi_{b(ss)} - \phi_{b(ff)})/2$. However, depending on

whether $\phi_{b(sf)} > \phi_{b(ff)}$ or $\phi_{b(sf)} < \phi_{b(ff)}$, deviations in the values of α predicted by Equation (3.7) may be expected. In terms of solubility x_0 (expressed as mole fraction), α is given by (Elwenspoek, 1986a; Bennema and van der Eerden, 1987)

$$\alpha = \xi [(\Delta H_m / k_B T_m) - \ln x_0] \quad (3.9)$$

where T_m is the melting point of the crystal. This equation is valid for growth from ideal and regular solutions containing two or more components (Elwenspoek, 1986a). Equation (3.9) reveals that the lower the saturation concentration, the higher is the value of α . In other words, α decreases for substances with a positive temperature coefficient of solubility and increases for substances with a negative value.

The α factor may also be defined in terms of the free linear energy γ_l of a step [Equations (3.2) and (3.5)] by

$$\frac{\alpha}{z} = \frac{\omega}{k_B T} = \frac{\gamma_l}{k_B T} + \ln(1 + 2\eta)$$

or

$$\frac{\alpha}{z} = \frac{\omega}{k_B T} = \frac{\gamma_l}{k_B T} + \ln\left(\frac{1 + \eta}{1 - \eta}\right) \quad (3.10)$$

which for small values of η reduce to the form

$$\alpha/z = \gamma_l/k_B T \quad (3.11)$$

The logarithmic terms in Equations (3.10) represent the increase in entropy.

For the (001) face of a Kossel crystal, computer simulation shows (van der Eerden *et al.*, 1978) that when $\alpha < 3$ the solid–fluid interface is rough, and a linear (continuous) growth takes place. When α rises above 3 the interface becomes smoother on a molecular level, so that for $3 < \alpha < 4$ growth by surface nucleation is possible in the absence of steps, whereas for $\alpha > 4$ observable growth requires the presence of dislocations.

3.3.2 Kinetic Roughening

Supersaturation (or supercooling) has a significant influence on the surface roughening. The roughening of a surface with an increase in the value of the driving force is called kinetic roughening. Kinetic roughening is connected with the size of the critical two-dimensional nucleus, which approaches the size of an atom or molecule on the surface. This is possible for a small value of linear free energy of a step when the supersaturation is increased to a critical value σ [see Equation (3.31)]. In this case, there is no activation barrier for two-dimensional growth and every atom landing on the surface may become part of the surface without surface diffusion processes (continuous growth).

Kinetic roughening is often observed in organic crystals and, above a critical supersaturation at an equilibrium temperature, the growth rate of a face depends linearly on the supersaturation (see Figure 3.6) and the face becomes round. The critical value of supersaturation, σ_{cr} , above which kinetic roughening takes place is related to a dimensionless free

energy per growth unit in a step on crystal surfaces, γ_f ($\gamma_f = \gamma_l/k_B T = a^2 \gamma/k_B T$, where a is the step length), by the relation (Elwenspoek, 1986a; Elwenspoek and van der Eerden, 1987)

$$\sigma_{cr} = 2\pi\gamma_f^2 \quad (3.12)$$

for spherical nuclei. In the region of kinetic roughening, the linear dependence of R on supersaturation, σ , is described by (Elwenspoek, 1986a; Elwenspoek and van der Eerden, 1987)

$$R = R_0(\sigma - \sigma_{cr}) \quad \text{for } \sigma > \sigma_{cr} \quad (3.13)$$

where R_0 is the growth rate extrapolated to supersaturation σ_{cr} . The temperature dependence of the extrapolated growth rate R_0 in toluene follows the relation (Elwenspoek, 1986b)

$$R_0 = x_0 \frac{k_B T}{h_p} \exp\left(-\frac{\Delta H_v}{R_G T}\right) \quad (3.14)$$

where x_0 is the solubility of the compound in mole fraction, h_p is Planck's constant, ΔH_v is the enthalpy of evaporation and R_G is the gas constant. The validity of Equation (3.14) implies that the solvent is inert and the solution is ideal. Moreover, one notes that this equation is exactly of the form predicted for rough faces [see Equations (3.18) and (3.21)].

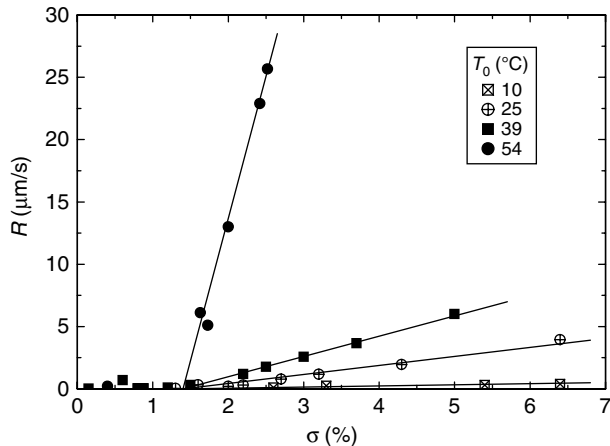


Figure 3.6 Dependence of growth rate R of the (110) face of naphthalene crystals on supersaturation σ for different equilibrium temperatures T_0 . Note that above a certain value of supersaturation σ_{cr} the rate linearly increases with σ . Adapted from M. Elwenspoek. *Appl. Phys. A* **41**, 123. Copyright (1986b), with permission from Springer Science and Business Media

3.4 Growth Kinetics of Rough Faces

Rough faces are characterized by a large number of inherent kink sites and, therefore, there is no need for two-dimensional nucleation on them. Atoms or molecules are added

to them randomly after overcoming an activation barrier (Figure 3.7). Following Brice (1973), if $\Delta\phi_L$ and $\Delta\phi_S$ are the activation energies for the movement of an atom in the liquid and the solid, respectively, then using Eyring's formalism the numbers of atoms entering the solid J_{LS} and the liquid J_{SL} per unit time may be represented by

$$J_{LS} = \frac{k_B T}{h_p} \exp\left(-\frac{\Delta\phi_I}{k_B T}\right) \quad (3.15)$$

$$J_{SL} = \frac{k_B T}{h_p} \exp\left(-\frac{\Delta\phi_I + \Delta\phi}{k_B T}\right) \quad (3.16)$$

where $\Delta\phi$ is the free energy difference between atoms in the solid and the liquid at their equilibrium positions, and $\Delta\phi_I$ is the activation energy required to transfer an atom from the liquid to the solid. From Equations (3.15) and (3.16), at equilibrium the net number of atoms entering the solid may be given by

$$J = J_{LS} - J_{SL} = \frac{k_B T}{h_p} \exp\left(-\frac{\Delta\phi_I}{k_B T}\right) \left[1 - \exp\left(-\frac{\Delta\phi}{k_B T}\right)\right] \quad (3.17)$$

If a is the diameter of the depositing atoms, x_0 is the average distance between kinks on the surface such that the probability of finding a kink on the surface is $(a/x_0)^2$, the free energy differences $\Delta\phi_I$ and $\Delta\phi$ are expressed in molar units (e.g. $\Delta\phi = \Delta G/N_A$, where N_A is Avogadro's number), and the term in square brackets can be approximated to $\Delta\phi/k_B T$, the linear growth rate of the face is given by

$$R = (a/x_0)^2 a J = \beta_{\text{surf}} \sigma \quad (3.18)$$

where the supersaturation is defined in terms of the free energy change ΔG_v by the relation (see Section 2.1)

$$\sigma = \frac{\Delta G_v}{R_G T} \quad (3.19)$$

and the kinetic coefficient for growth of the rough interface

$$\beta_{\text{surf}} = a \frac{k_B T}{h_p} \exp\left(-\frac{\Delta G_I}{k_B T}\right) \quad (3.20)$$

In the case of growth from viscous liquids, the growth rate in Equation (3.18) is divided by the diffusion coefficient D of atoms in the liquid, and is given by

$$R = \eta' \sigma \exp\left(-\frac{\Delta G_I - \Delta G_L}{R_G T}\right) \quad (3.21)$$

where ΔG_L is the activation energy for diffusion and η' is the dynamic viscosity of the liquid.

According to Equations (3.18) and (3.21), the growth rate of a crystal face growing by the continuous growth mechanism exhibits a linear dependence on supersaturation. The linear dependence of interface growth rate on supersaturation was presented independently by Wilson in 1900 and by Frenkel in 1932, and is usually referred to as the Wilson–Frenkel law for normal growth.

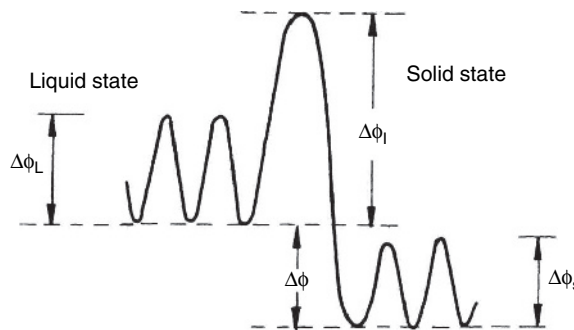


Figure 3.7 Change in the free energy involved in the growth of a crystal on its rough solid-liquid interface

3.5 Growth Kinetics of Perfect Smooth Faces

Growth of perfect faces devoid of dislocations is possible by the incorporation of growth units at the kinks of steps supplied by two-dimensional (2D) nucleation. Depending on the rate v of displacement of steps of the nuclei, three versions of growth by 2D nucleation are possible. When the 2D nuclei spread over the surface with $v = \infty$ and $v = 0$, we have mononuclear and polynuclear models, respectively. However, to account for the fact that a finite v is also possible, a model involving simultaneous birth and spread of nuclei (B+S model), also called the multiple nucleation model, is frequently used. In the case of a finite step velocity, for small and large areas of the surface growing by 2D nucleation one has only two models, the polynuclear and multiple nucleation models (Figure 3.8).

The normal growth rate R of a face of area P due to the formation of 2D nucleation at a rate J may be written as follows:

(a) *Polynuclear model when $P^{1/2} < (v/J)^{1/3}$:*

$$R = hPJ \quad (3.22)$$

(b) *Multiple nucleation model when $P^{1/2} > (v/J)^{1/3}$:*

$$R = hJ^{1/3}v^{2/3} \quad (3.23)$$

where h is the height of steps of the nuclei.

Integration of atoms/molecules adsorbed on the surface into kinks in the steps can occur either by their migration over the surface an average distance λ_s or by their direct exchange at the step edge. The former mechanism, called the surface diffusion mechanism, holds when the surface diffusion distance λ_s for the adsorbed atoms/molecules is relatively large and is comparable to the average distance y_0 between growth steps containing the kinks (i.e. $\lambda_s \geq y_0$). However, when the adsorbed atoms/molecules are relatively immobile (i.e. $\lambda_s \ll y_0$), their diffusion over the surface will not contribute significantly to growth. Instead, due to their high concentration in the mother phase, the growth units landing on the surface will be captured directly at kinks in the steps. This is the

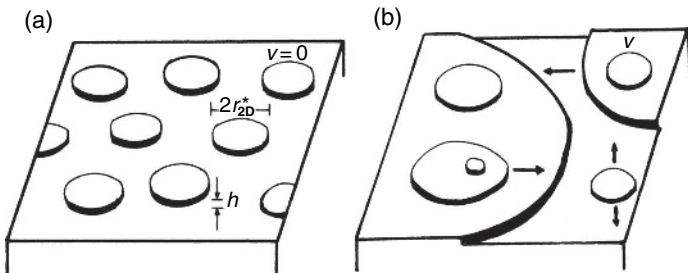


Figure 3.8 Two-dimensional nucleation models of growth based on finite step velocity v : (a) polynuclear model and (b) multiple nucleation model

direct integration mechanism. However, in both of these mechanisms, the transport of the growth atoms/molecules is faster than their surface diffusion or direct integration.

The difference between the equations for R based on surface diffusion and direct integration of growth units lies mainly in the expressions for v . In the case of surface diffusion, the velocity of a straight step may be given by (Burton *et al.*, 1951; Sangwal, 1994)

$$v = 2\sigma(\lambda_s/a)\beta_l \quad (3.24)$$

where the kinetic coefficient β_l for the step is given by

$$\beta_l = a\nu \exp(-\Delta G_{\text{att}}/k_B T) \quad (3.25)$$

λ_s is the diffusion distance on the surface, a is the size of the growth unit, $\nu = k_B T/h_p$ is the frequency of vibration of atoms on the surface, ΔG_{att} is the energy required for the integration of a molecule/atom into the crystal, and the supersaturation (see Section 2.1)

$$\ln S \approx \sigma = (c - c_0)/c_0 \quad (3.26)$$

where c and c_0 denote, respectively, the actual and equilibrium solute concentrations expressed in mole fraction.

Equation (3.24) is the extreme case of Equation (3.41) when both the retardation factors β and Λ , related to the density of kinks in the steps and the density of steps on the surface terrace, respectively, are unity, and only a part of the adsorbed atoms/molecules reach the kinks in the steps of the 2D nuclei. Equation (3.24) represents the maximum step velocity corresponding to the capture of all atoms/molecules arriving by surface diffusion into the kinks in the steps. In solution growth, ΔG_{att} is equal to the energy ΔG_{dehyd} required for the dehydration of molecule/atom during its integration into the crystal.

In the case of growth by the direct integration of growth units, for not very concentrated solutions when $\Omega c_0 \leq 0.2$, the step velocity may be given by (Chernov, 1961, 1984, 1986b)

$$v = \beta_l \frac{c - c_0}{\rho - c} = \beta_l \Omega c_0 \sigma \quad (3.27)$$

where ρ is the crystal density and has units of concentration c and c_0 , Ω is the specific molecular volume of molecules/atoms, and the kinetic coefficient β_l for steps is given by Equation (3.25) in which the activation energy ΔG_{att} is now equal to the activation energy for the integration of molecule/atoms into the kink and is usually denoted by W .

The rate of nucleation is given by (Ohara and Reid, 1973; Chernov, 1984; Sangwal, 1994)

$$J = C_1 \sigma^{1/2} \exp(-\Delta G_{2D}^*/k_B T) \quad (3.28)$$

where

$$C_1 = \pi h n_1 c_0 \beta_l \quad (3.29)$$

the free energy change corresponding to the formation of a stable disc-shaped 2D nucleus of critical radius r_{2D}^* of height h on the perfect surface

$$\Delta G_{2D}^* = \pi h \gamma^2 \Omega / k_B T \sigma \quad (3.30)$$

and the critical radius r_{2D}^* of the 2D nucleus

$$r_{2D}^* = \gamma \Omega / k_B T \sigma \quad (3.31)$$

In Equations (3.30)–(3.32), γ is the surface free energy, and the concentration of adsorbed molecules/atoms (i.e. the number of molecules/atoms per unit area) on the surface is given by

$$n_1 = h c_0 \exp(-E_{\text{ad}}/k_B T) \quad (3.32)$$

where E_{ad} is the energy of adsorption of the molecules/atoms on the surface.

Using Equations (3.24) and (3.28) for step velocity v , and Equation (3.29) for nucleation rate J , Equations (3.22) and (3.23) may be written in the following form:

(a) *Polynuclear model:*

$$R = h P C_1 \sigma^{1/2} \exp(-\Delta G_{2D}^*/k_B T) \quad (3.33)$$

(b) *Multiple nucleation model:*

$$R = h C_2^{2/3} C_1^{1/3} \sigma^{5/6} \exp(-\Delta G_{2D}^*/3k_B T) \quad (3.34)$$

where the constant $C_2 = 2\lambda_s/a$ and $C_1 = \Omega c_0$ for growth by surface diffusion and direct integration mechanisms, respectively.

Thus, the forms of rate expressions for polynuclear and multiple nuclear models based on surface diffusion and direct integration are essentially the same. Both models predict an exponential dependence on supersaturation at low σ and $R \propto \sigma^{1/2}$ or $R \propto \sigma^{5/6}$ at high σ . However, according to the polynuclear model, the growth rate R increases with the area P of the growing crystal, whereas no dependence of R on P is predicted by the multiple nucleation model. In fact, in the polynuclear model it is expected that the exponent exceeds 1/2 due to contributions from the surface area P .

3.6 Growth Kinetics of Imperfect Smooth Faces

The main postulate of these models is that steps on a growing surface are provided by the presence of a screw dislocation and that there is no need for 2D nucleation involving an activation barrier ΔG_{2D}^* [see Equation (3.30)]. If an array of steps of height h and interstep distance y_0 , forming a spiral hillock of inclination $p = h/y_0$, traverses across a growing surface at a rate v , then the normal growth rate R is given by (see Figure 3.2)

$$R = hv/y_0 = pv \quad (3.35)$$

where the interstep distance y_0 is related with the radius r_{2D}^* of the critically sized circular nucleus corresponding to activation barrier ΔG_{2D}^* [see Equation (3.30)] by [cf. Equation (3.31)]

$$y_0 = 19r_{2D}^* = 19\gamma\Omega/k_B T\sigma \quad (3.36)$$

In this relation, it is assumed that the hillock inclination p is constant and the supersaturation σ_s available on the surface is equal to the bulk supersaturation σ_b in the solution.

As mentioned in Section 3.8, the frequently observed growth steps on the surfaces of crystals have thickness ih , which is a multiple of the height h of elementary steps (where the integer $i \geq 1$). However, the above equations are also valid for such multiple-height steps.

3.6.1 Surface Diffusion and Direct Integration Models

According to the surface diffusion model (Burton *et al.*, 1951; Bennema and Gilmer, 1973), the step velocity v and the face growth rate R are given by

$$v = 2\sigma(\lambda_s/a)\beta\Lambda\beta_l \tanh(y_0/2\lambda_s) \quad (3.37)$$

and

$$R = C^* \frac{\sigma^2}{\sigma_1} \tanh\left(\frac{\sigma_1}{\sigma}\right) \quad (3.38)$$

where

$$C^* = \frac{\beta\Lambda\Omega N_0}{a} \beta_l \quad (3.39)$$

and

$$\sigma_1 = \frac{19\gamma\Omega}{2k_B T \lambda_s} \quad (3.40)$$

where N_0 is the concentration of growth units on the surface, β is the kink retardation factor related to the density of kinks in the steps and Λ is the step retardation factor related to the density of steps on the surface terrace.

Equation (3.37) represents the general expression for v for a situation in which the mean kink distance $x_0 \ll \lambda_s$. The step kinetic coefficient β_l is given by Equation (3.25). When $y_0 \gg \lambda_s$ (i.e. $\sigma \ll \sigma_1$),

$$v = 2\sigma(\lambda_s/a)\beta\Lambda\beta_l \quad (3.41)$$

and the face growth rate

$$R = C^* \frac{\sigma^2}{\sigma_1} \quad (3.42)$$

However, when $y_0 \ll \lambda_s$ (i.e. $\sigma \gg \sigma_1$)

$$v = \sigma(y_0/a)\beta\Lambda\beta_l \quad (3.43)$$

and

$$R = C^*\sigma \quad (3.44)$$

Equations (3.42) and (3.44) represent the ideal parabolic and linear laws, respectively.

According to Equations (3.24) and (3.27), $\beta_l = v/\sigma$ when $2\lambda_s/a = 1$ and $\Omega c_0 = 1$ [i.e. the constant $C_2 = 1$ in Equation (3.34)]. Equation (3.37) thus implies that $(\lambda_s/a)\beta\Lambda\tanh(y_0/2\lambda_s) = 1/2$. This condition means that the step velocity v depends on σ through β , Λ and y_0 at low σ [Equation (3.41)] while only through β and Λ at high σ [Equation (3.43)]. However, the values the kink retardation factor β and the step retardation factor Λ depend on σ but their relationships with σ are complicated.

According to Equations (3.41) and (3.43), two distinct relationships between v and σ may be distinguished for β and Λ equal to unity. At low σ when y_0 is very large and the condition $y_0 \gg \lambda_s$ holds, Equation (3.41) reduces to Equation (3.24) and $v \propto \sigma$. At high σ when the condition $y_0 \ll \lambda_s$ holds, Equation (3.41) predicts a supersaturation-independent v , because $y_0 \propto 1/\sigma$.

The factor β is determined by the exchange between the kinks and the adsorbed molecules. When this exchange is slow such that the surface supersaturation near the kinks exceeds zero ($\sigma_s > 0$), $\beta < 1$. However, when the exchange between them is rapid, $\beta = 1$. The value of Λ is determined by the relation between the surface diffusion distance λ_s and the mean interkink distance x_0 . When $\lambda_s \gg x_0$, $\Lambda = 1$; in contrast, when $\lambda_s \leq x_0$, $\Lambda < 1$. These cases correspond to low σ when $y_0 > \lambda_s$. At high supersaturations, on the other hand, when $y_0 \ll \lambda_s$, both $\beta \approx 1$ and $\Lambda \approx 1$ for $\lambda_s \gg x_0$ and $\sigma_s \geq 0$. The distances x_0 and y_0 are explained in Figure 3.2.

According to the direct integration model (Chernov, 1961; Chernov *et al.*, 1986a,b), the step velocity v is given by Equation (3.27) while the face growth rate

$$R = C\sigma^2 \quad (3.45)$$

where the constant

$$C = \frac{k_B T}{19\gamma} hc_0 \beta_l \quad (3.46)$$

with β_l given by Equation (3.25). According to Equation (3.45), the face growth rate $R \propto h/\gamma$.

The form of Equations (3.42) and (3.45) for R is essentially the same at low σ when $\sigma \ll \sigma_1$ and $\tanh(\sigma_1/\sigma) = 1$.

3.6.2 Bulk Diffusion Models

In these models, it is assumed that diffusion of growth units in the bulk medium is slower than their diffusion on the surface and integration into kinks. Considering low or high density of kinks in the steps, two bulk diffusion models have been developed. Burton *et al.* (1951) considered the situation when the distance between kinks in a step is large such that diffusion fields develop around the kinks and on the surface. On the other hand, Chernov (1961) treated the case when the distance between kinks is so small that a step can be considered as a line sink.

BCF Model

According to the BCF model, if the thickness of the unstirred diffusion layer at the surface is δ and when supersaturation is large, the rate of displacement of a step in a set of parallel steps is given by

$$v = 2\pi D\beta' c_0 \sigma(x_0)/x_0 \quad (3.47)$$

where D is the bulk diffusion constant of the solute, β' is a new retardation factor for the entry of growth units in the kinks, and the supersaturation $\sigma(x_0)$ is given by

$$\sigma(x_0) = \sigma \left\{ 1 + \left[\frac{2h\pi(\delta - y_0)}{x_0 y_0} \right] + \left(\frac{2y_0}{x_0} \right) \ln \left(\frac{y_0}{x_0} \right) \right\}^{-1} \quad (3.48)$$

Then the linear growth rate

$$R = C_3 \sigma \sigma(x_0) \quad (3.49)$$

where

$$C_3 = \frac{2\pi\beta' D n_0 h k_B T}{19 x_0 y_0} \quad (3.50)$$

with n_0 equal to the concentration of growth units in the bulk.

From Equation (3.48) one has two cases. For small σ when y_0 is large, $y_0 \gg 2\pi h\delta/x_0$, which defines a critical supersaturation

$$\sigma_{c1} = \frac{19\gamma\Omega x_0}{2\pi h\delta k_B T} \quad (3.51)$$

For $\sigma \ll \sigma_{c1}$, one obtains the parabolic law

$$R = C_4\sigma^2 \quad (3.52)$$

where $C_4 < C_3$ [cf. Equation (3.48)], in which R is practically independent of δ . For $\sigma \gg \sigma_{c1}$, one obtains the linear law

$$R = C_5\sigma \quad (3.53)$$

where

$$C_5 = Dn_0\Omega/\delta \quad (3.54)$$

Here R is inversely proportional to δ .

Chernov's Model

In this model, the rate of motion of steps is given by

$$v = \Omega c_0 \beta_l \sigma(y_0) \quad (3.55)$$

where the kinetic coefficient β_l for step motion is given by Equation (3.25), and the supersaturation

$$\sigma(y_0) = \sigma \left\{ 1 + (\beta_l h / \pi D) \ln[(y_0/h) \sinh(\pi\delta/y_0)] \right\}^{-1} \quad (3.56)$$

Then the linear growth rate

$$R = \frac{\beta_l \Omega c_0 h \sigma^2}{\sigma_{c2} \delta \left[1 + (\beta_l h / \pi D) \ln \{ (\sigma_{c2} \delta / \sigma h) \sinh(\sigma / \sigma_{c2}) \} \right]} \quad (3.57)$$

where the critical transition supersaturation

$$\sigma_{c2} = \frac{19\gamma\Omega}{\pi k_B T \delta} \quad (3.58)$$

Two cases follow from Equation (3.57). At supersaturations $\sigma \ll \sigma_{c2}$,

$$R = B_3 \sigma^2 \quad (3.59)$$

where the constant

$$B_3 = \frac{h \beta_l \Omega c_0}{\sigma_{c2} \delta \left[1 + (\beta_l h / \pi D) \right]} \quad (3.60)$$

Obviously here R is inversely proportional to δ .

For $\sigma \gg \sigma_{c2}$,

$$R \approx D\Omega c_0 \sigma / \delta \quad (3.61)$$

Thus, R is proportional to σ but inversely proportional to δ .

It should be noted from Equations (3.47) and (3.55) that the step velocity v decreases continuously with decreasing interstep spacing y_0 , and no impurity is required for this process.

3.6.3 Growth by a Group of Cooperating Screw Dislocations

When a group of equally spaced screw dislocations arranged along a line of length L participates in growth, the inclination p of a hillock formed around the dislocation source with a total Burgers vector ih on the face occupying the region with a perimeter $2L$ is given by (Burton *et al.*, 1951; Bennema and Gilmer, 1973; Chernov *et al.*, 1986a,b)

$$p = \frac{ih}{19r_{2D}^* + 2L} \quad (3.62)$$

where the term in the denominator of the right-hand side denotes the new interstep distance. Since $r_{2D}^* \propto 1/\sigma$, it follows from Equation (3.62) that the inclination p depends nonlinearly on σ . Rearranging Equation (3.62), one obtains

$$\frac{1}{p} = \frac{2L}{ih} + \frac{19\gamma\Omega}{ihk_B T \sigma} \quad (3.63)$$

which yields a linear relationship between $1/p$ and $1/\sigma$.

Using Equation (3.62), we may express the linear growth rate by [cf. Equation (3.35)]

$$R = pv = \frac{ihv}{19(\gamma\Omega/k_B T \sigma) + 2L} \quad (3.64)$$

where v is described by Equations (3.24), (3.27), (3.37), (3.47) and (3.55) of the BCF and Chernov's models. Equation (3.64) may be rewritten in the form

$$R = \sigma^2 / (X + Y\sigma) \quad (3.65)$$

where

$$Y = \frac{2La}{ih\Omega N_0 \beta_l} \quad (3.66)$$

and

$$X = \frac{19\gamma\Omega}{k_B T} \frac{a}{ih\Omega N_0 \beta_l} = \frac{19\gamma_l a}{2k_B T L} Y = GY \quad (3.67)$$

In the above equations, the interfacial energy $\gamma = \gamma_l a^2$, where γ_l is the linear free energy of a step and β_l is the kinetic coefficient for step motion.

Equation (3.65) is easy to handle for the determination of dead supersaturation zone (i.e. supersaturation barrier σ_d) from the experimental $R(\sigma)$ data. This topic is discussed in Chapter 5. However, for the purpose of the determination of growth mechanism and participation of composite dislocation sources from the $R(\sigma)$ data, Equation (3.65) is frequently written in the form

$$\frac{\sigma^2}{R} = \frac{19\gamma\Omega}{k_B T} \frac{a}{ih\Omega N_0 \beta_l} + \frac{2L\sigma}{ih\Omega N_0 \beta_l} \quad (3.68)$$

For a unit dislocation emitting a step of height h , $L = 0$. Then Equations (3.62) and (3.64) reduce to the corresponding expressions given by the surface diffusion, direct integration and bulk diffusion models described above. Then p and v increase strictly linearly with σ , and the face growth rate R may be expressed by the so-called power law:

$$R \propto \sigma^n \quad (3.69)$$

where $n = 2$ and 1 at relatively low and high σ , respectively.

The strength of a composite dislocation source is given by

$$\varepsilon = \frac{p}{h/y_0} = \frac{i}{1 + 2L/(19\gamma\Omega/k_B T\sigma)} \quad (3.70)$$

It may be noted from this equation that the strength ε is essentially a constant equal to i only for $1 \gg 2L/(19\gamma\Omega/k_B T\sigma)$, i.e. when $L \rightarrow 0$ or $\sigma \rightarrow 0$. Physically, this condition means that in the range of low supersaturations σ an ideal parabolic dependence is possible only for a point source with $L = 0$. For $L > 0$ the source strength decreases with increasing σ and depends on the value of L . In the case of growth controlled by surface diffusion, one obtains the linear law

$$R = C'\sigma \quad (3.71)$$

with the constant

$$C' = C^*(\lambda_s/s) \tanh(s/\lambda_s) \quad (3.72)$$

where C^* is given by Equation (3.44), λ_s is the mean diffusion distance for growth units, and s is the average distance between an array of screw dislocations of unit strength participating in growth. Depending on the value of λ_s/s , one has $0 \leq C' \leq C^*$. The $R(\sigma)$ dependence for two arbitrary values of C' of Equation (3.72) and different values of σ_1 of Equation (3.44) is shown in Figure 3.9.

Using a power-law approach for the analysis of the dependences of slopes p of hillocks and velocities v of steps on the surfaces of some crystals growing from solutions, it was shown (Sangwal, 1998a, b) that the face growth rate R may also be expressed in the form

$$R = A\sigma^n \quad (3.73)$$

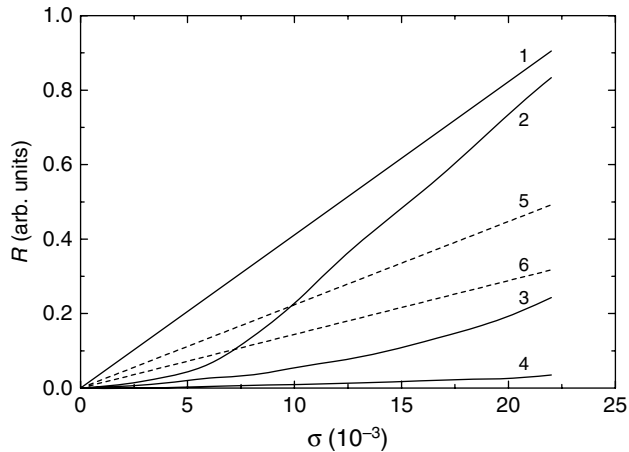


Figure 3.9 Theoretical BCF curves (1–6) with an arbitrary C^* for different values of σ_1 : (1) 10^{-3} , (2) 10^{-2} , (3) 10^{-1} , (4) 1; curves 5 and 6 correspond to two linear laws with arbitrary values of C' , where $0 \leq C' \leq C^*$. Adapted from P. Bennema and G.H. Gilmer. In: P. Hartman (Ed.), Crystal Growth: an Introduction, Chap. 10, p. 263. Copyright (1973), with permission from Elsevier

where the exponent n lies between $11/12$ and 2, and the value of the constant A is related to the activation energy W for growth. The power-law approach holds when $L > 0$.

It should be noted that, for a unit dislocation when $L = 0$, Equations (3.65) and (3.73) reduce to the classical BCF parabolic law, $R = A_0\sigma^2$, where $A_0 = C^*/\sigma_1 = 1/X$ of Equation (3.67).

Finally, it should be mentioned that a value lower than 2 is possible for the exponent n due to the influence of surface or volume diffusion and to $L > 0$.

3.6.4 Preferential Growth at Edge Dislocations

The role of screw dislocations in the growth of F faces of crystals is well established from the observation of growth spirals on them and from studies of growth kinetics (Verma, 1953; Chernov, 1984; Sangwal, 1994, 1998a; Sangwal and Rodriguez-Clemente, 1991). However, after 1962 several workers reported (Keller, 1975; Bauser and Strunk, 1981, 1984) that edge dislocations act as persistent sources of monomolecular steps in the form of concentric closed-loop patterns. It was also reported (Sherwood and Shripathi, 1988) that, at a given supersaturation, the growth rate R of F faces of potash alum crystals increases with increase in the density of edge dislocations.

For geometric reasons, an edge dislocation is not expected to provide sources of steps for crystal growth because its Burgers vector is parallel to the growing surface. The origin of activity of edge dislocations has been explained in terms of Coulomb interactions, impurity segregation at dislocations, dissociation of edge dislocation into partial dislocations, and surface relaxation. According to the surface relaxation mechanism advanced by Frank (1981), crystals have surface stresses of the order of their surface free energies, but these stresses can be either tensile or compressive. Due to its geometry, an edge dislocation always has a region compressed on one side and dilated on the

other side of the site of its emergence on the surface, leading to compressive and tensile surface stresses in its vicinity. Irrespective of whether the surface stress is compressive or tensile, they decrease the energy of a surface nucleus. Therefore, the region near the emergence point of a dislocation is always more favorable than the unstrained surface for the formation of a 2D nucleus on the surface.

Assuming that changes in surface stresses due to edge dislocations emerging on a growing surface and due to externally applied stresses on a crystal facilitate 2D nucleation on a surface through changes in surface energy γ , from the multiple nucleation model one may write [see Equation (3.34)]

$$\ln(R/\sigma^{5/6}) = K_1 - K_2 \Delta\gamma^2/\sigma \quad (3.74)$$

$$R/R_0 = \exp[-B'(\gamma^2 - \gamma_0^2)] \quad (3.75)$$

respectively. In Equation (3.74), $\Delta\gamma$ is the changes in the surface energy γ caused by an edge dislocation and K_1 and K_2 are constants. In Equation (3.75), γ and γ_0 are the values of the surface energy in the presence and absence of externally applied stresses, respectively, and B' is a constant. The experimental results obtained by Sherwood and Shripathi (1988) can be explained by using the above expressions.

3.7 Effect of Foreign Substances on Growth Kinetics

It is well known that foreign substances added to growth media can lead to dramatic changes in the growth kinetics of crystals. Figure 3.10 illustrates a typical example of the dependence of the experimental growth rate R of the {100} face of ammonium oxalate

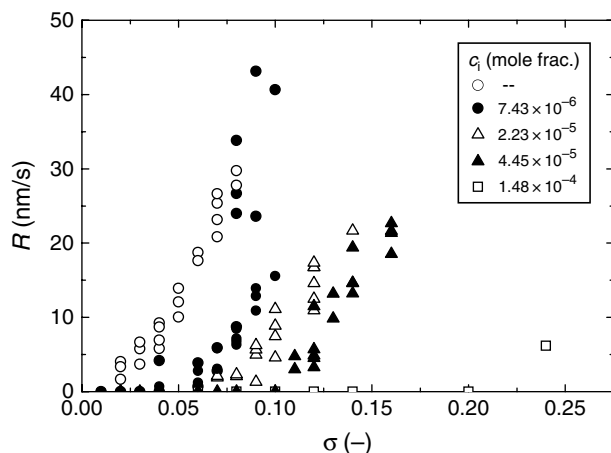


Figure 3.10 Example of the dependence of growth rate R of the {100} face of ammonium oxalate monohydrate crystals on supersaturation σ for different concentration c_i of Co(II) impurity. Reproduced from E. Miśniczek-Brzóska and K. Sangwal. Cryst. Res. Technol. **39**, 993. Copyright (2004), Wiley-VCH

monohydrate crystals on solution supersaturation σ for different concentrations c_i of Co(II) ions. It may be noted that addition of the Co(II) ions to the solution leads to a decrease in the growth rates R of the crystal, and the decrease is higher with increasing additive concentration c_i . Moreover, for every concentration c_i of the additive there is a particular value of supersaturation σ , hereafter denoted σ_d , below which the face growth rate R is zero and does not increase with increasing σ . Apart from a supersaturation barrier σ_d when $R = 0$, there is a critical supersaturation σ^* when the growth rate exhibits a sudden marked increase with increasing σ .

The example in Figure 3.10 refers to growth by the screw dislocation mechanism, where it is implied that the activity of the dislocation source does not change with change in supersaturation σ and the step velocity v increases linearly with σ . However, it is found (van Erk *et al.*, 1980; Chernov *et al.*, 1986b; Onuma *et al.*, 1990) that trace amounts of foreign substances present in the growth medium cause deviations from the theoretical $R(\sigma)$ dependence at low supersaturations. Therefore, the effect of foreign substances, intentionally added to the growth medium or inherently present in it, on the $R(\sigma)$ dependence remains unclear in the precise determination of the threshold supersaturation σ_d .

The effect of trace amounts of inherently present foreign substances on growth kinetics at low values of σ has been demonstrated in the case of the growth of dislocation-free crystals from aqueous solutions (Malkin *et al.*, 1989; Onuma *et al.*, 1994). Figure 3.11 shows the dependence of R of the dislocation-free (100) face of $\text{Ba}(\text{NO}_3)_2$ crystals. It can be seen that not only does the growth rate R depend nonlinearly on supersaturation σ , but also there is an inflection point on the $R(\sigma)$ curve at $\sigma = \sigma^*$.

It is observed that foreign substances, frequently called impurities, can also lead to increases in the growth rate of crystals, and even the same foreign substance can decrease the growth rate of some faces of a crystal while increasing the growth rate of other

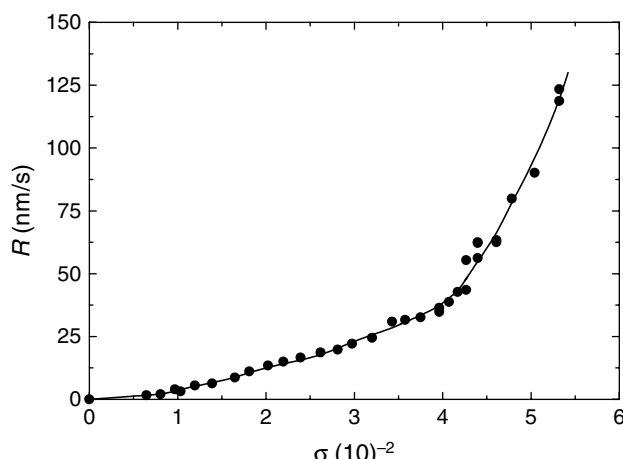


Figure 3.11 Dependence of R of the dislocation-free (100) face of $\text{Ba}(\text{NO}_3)_2$ crystals on supersaturation σ . After K. Onuma, T. Kameyama and K. Tsukamoto. J. Cryst. Growth **137**, 610. Copyright (1994), with permission from Elsevier

faces. In general, however, the effect of foreign substances on the growth of F faces of crystals may be considered to be two-fold: (1) they retard the velocity of motion of steps by adsorbing at kinks or at the surface, and (2) they decrease the value of surface free energy by adsorbing on the growing surface. These are usually called kinetic and thermodynamic effects of impurities, and are associated with decreases in the values of the kinetic coefficient β_l for steps and the free energy γ of the growing surface, respectively. These aspects are discussed below.

3.7.1 Some General Considerations

Foreign substances may affect crystal growth rates in different ways. They can change the properties of the growth medium, whereby the equilibrium saturation concentration (i.e. solubility) of the solute and, hence, the supersaturation available for nucleation and growth, are altered (see Chapter 2). Foreign substances can also affect the thermodynamic and kinetic terms involved in the growth models. The thermodynamic parameter in the growth models is the interfacial energy γ , whereas the kinetic parameters are associated with the density of kinks and obstructions provided in the movement of steps on the surface by impurity particles (see Chapter 4).

Adsorption of foreign substances can change the properties of the crystal–medium interface such that the interfacial energy γ of the growing crystal is changed. The change in the value of γ results in a change in the nucleation rate J in the two-dimensional nucleation models [the exponential term in Equation (3.28)], and the radius r_{2D}^* of critical two-dimensional nucleus [Equation (3.31)] and hence the spacing y_0 between the spiral steps in the BCF theory [Equation (3.36)]. Therefore, the growth rate R based on these theories is changed (see Section 3.6). Since the commonly observed effect of foreign substances is to retard growth rates, it is usually assumed that adsorption of an impurity particles increases the value of γ . However, consideration of the adsorption process in terms of adsorption isotherms and reversible adsorption equilibrium shows that adsorption of foreign substances decreases the value of γ (Kern, 1967; Davey, 1979). This decrease in γ will, consequently, cause an increase in R (Ohara and Reid, 1973).

The kinetic term in the growth theories is directly related to the velocity v of movement of steps on the crystal surface. Foreign substances adsorbed on the surface decrease this velocity by decreasing the values of the kink retardation factor β and the step retardation factor Λ [see Equation (3.37)]. Adsorption of foreign particles at kink sites also decreases their density, which results in a decrease in v .

The above general considerations show that, at relatively low concentration of an additive, the theoretical models of growth predict their opposite effects on growth kinetics. The thermodynamic parameter tends to increase the step velocity v and face growth rate R , whereas the kinetic effect tends to decrease them. At relatively high supersaturations when a high density of kinks is available at the ledges, additive adsorption always decreases the rates v and R for all values of additive concentrations. However, at low supersaturations which ensure a low density of kinks at the ledges, the rates increase for small additive concentrations and decrease as the additive concentration is increased. This behavior is illustrated in Figure 3.12 for the linear growth rates of the (100) and (111) faces of $\text{Pb}(\text{NO}_3)_2$ grown from aqueous solutions in the presence of Methyl Blue.

As discussed in Chapter 4, particles of a foreign substance can adsorb on the surface terrace nonselectively and can diffuse over large distances between the neighboring ledges

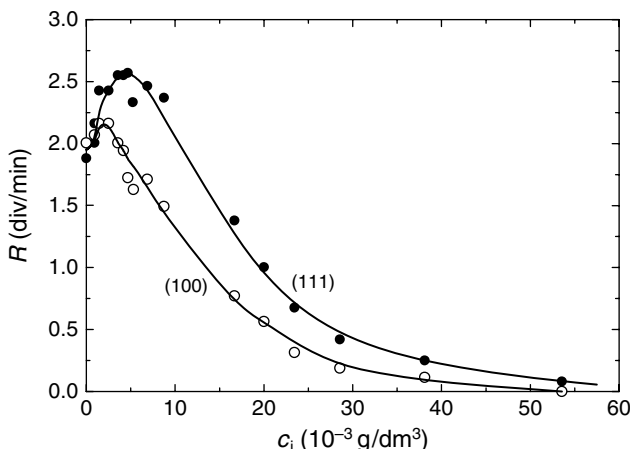


Figure 3.12 Dependence of linear growth rates R of (100) and (111) faces of $\text{Pb}(\text{NO}_3)_2$ grown from aqueous supersaturated solutions on concentration c_i of Methyl Blue. Adapted from G.M. Bliznakov and E.K. Kirkova. Z. Phys. Chem. **206**, 271. Copyright (1957), with permission from Oldenbourg Wissenschaftsverlag

on the surface. They can adsorb preferentially at kinks in the ledges. There are also foreign substances which adsorb selectively on the surface terrace and remain immobile there for long durations. Such foreign substances are called immobile impurities. However, the above considerations of the simultaneous effects of thermodynamic and kinetic parameters are valid for any foreign substance which is capable of adsorbing at both kinks and the surface terrace.

The value of the concentration of an additive, at which a peak in the $v(c_i)$ and $R(c_i)$ curves is observed, depends on the supersaturation used for growth, the temperature of growth, the nature of the adsorbing particles of the additive, and the nature of the crystal face. For example, in the case of growth of the (100) faces of KDP in the presence of organic additives (Barsukova *et al.*, 1992), the peaks at $\sigma = 1.5\%$ appear at 0.27 mol%, 0.07 mol% and 0.0005 mol% of glycerine, ethyleneglycol and EDTA, respectively. The corresponding concentrations are 0.006 mol% and 0.0001 mol% for polyethyleneglycol of molecular weights of 300 and 2000, respectively. The inhibiting effect of the above additives is negligible on the (101) faces of KDP, which grow about 8 times faster than the (100) faces. Barsukova *et al.* (1992) suggested that the initial increase in R is due to the ability for formation of inactive complexes by the additives with inorganic foreign substances present in the solution. In any case, these results reveal that the effect of an additive is related to the size of inhibiting species and to the rate of growth (i.e. the nature of the growing face).

The experimental results on growth kinetics of different crystals show that the maxima in the curves of growth rate R against the concentration c_i of additives appear at relatively low additive concentrations in the case of inorganic salts growing in the presence of additives adsorbing nonselectively on the surface (Bliznakov and Kirkova, 1957; Kirkova and Nikolaeva, 1973). However, such maxima are not observed in the $R(c_i)$ curves in

the case of tailor-made impurities, which adsorb selectively on the surface (Black *et al.*, 1986; Davey *et al.*, 1986; Chu *et al.*, 1989; Ristić *et al.*, 1994).

Differences in the rates of exchange of additive particles (k_{ad}) and growth species (k_{gs}) present in the growth medium with the integration sites (e.g. kinks in steps) on the surface determine the nature of adsorption during growth. In the case of immobile impurities, the exchange rate k_{ad} for additive particles is usually small in comparison with the exchange rate k_{gs} for growth entities (i.e. $k_{\text{ad}} < k_{\text{gs}}$) and, therefore, adsorption mainly affects the thermodynamic parameter. However, in the case of mobile impurities when $k_{\text{ad}} > k_{\text{gs}}$, additive adsorption has a dominant effect on kinetic parameters. The rate constant is given by

$$k_a = (k_B T / h_p) C_a \exp(-\Delta G_a / k_B T) \quad (3.76)$$

where the suffix ‘a’ denotes the processes of capture of impurity and growth species, C_a is a constant related to their concentration in the medium, and ΔG_a is the corresponding activation energy. Therefore, $\Delta G_{\text{ad}} > \Delta G_{\text{gs}}$ and $\Delta G_{\text{ad}} < \Delta G_{\text{gs}}$ for immobile and mobile impurities, respectively. These cases follow from the adsorption times of the additive particles and growth species (see Section 4.1), while Equation (3.76) can be obtained as Equation (3.17).

In contrast to the growth of F faces by the displacement of ledges on the surface terrace, growth of S and K faces takes place by the so-called normal growth involving statistical deposition of growth molecules at growth sites (i.e. kinks) without their diffusion on the surface (Section 3.4). Therefore, adsorption of impurity particles at kinks on S and K faces decreases the density of kinks and hinders the access of growth entities to them, leading to a decrease in the growth rates of these faces. These faces thus behave like F faces.

Typical plots of the $v(c_i)$ and $R(c_i)$ dependences for the {111} and $\{\overline{1}\overline{1}\}$ faces of NaClO_3 crystals grown in the presence of $\text{Na}_2\text{S}_2\text{O}_7$ additive are illustrated in Figure 3.13.

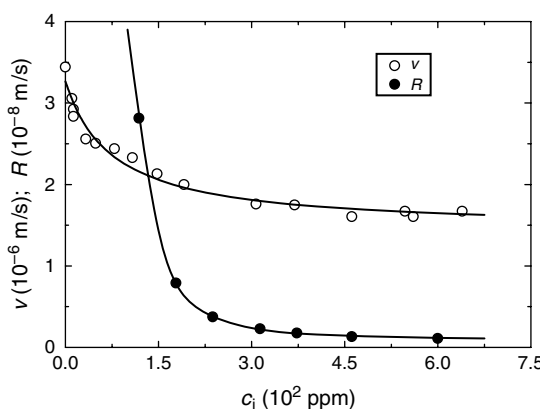


Figure 3.13 Examples of dependence of step velocity v on the {111} face and growth rate R of the $\{\overline{1}\overline{1}\}$ faces of NaClO_3 crystals on the concentration c_i of $\text{Na}_2\text{S}_2\text{O}_7$ additive. Note that {111} and $\{\overline{1}\overline{1}\}$ faces refer to growth of smooth and rough F faces, respectively. See the text for details. Original data from Ristić *et al.* (1994)

The {111} and $\{\overline{1}\overline{1}\}$ faces of NaClO₃ crystals are smooth and rough, respectively, on molecular level (Ristić *et al.*, 1994). The curve representing the $v(c_i)$ data is drawn according to Equation (4.30), whereas the solid curve describing the $R(c_i)$ data is drawn according to Equation (4.110). The physical interpretation of these expressions is given in the next chapter.

3.7.2 Growth Kinetics by Heterogeneous Two-Dimensional Nucleation

When describing the effect of interfacial energy γ above, it was assumed *a priori* that foreign substances lead to an increase or decrease in its value, which subsequently changes the value of the nucleation barrier ΔG_{2D}^* [Equation (3.30)] and the nucleation rate J [Equation (3.28)]. However, the actual mechanism of these changes remains unclear. Liu *et al.* (1997) advanced a model of heterogeneous two-dimensional nucleation for a perfect F face, and examined the free energy barrier for two-dimensional nucleation in the presence of impurity particles and the kinetics of nucleation and growth. In their model, they made the following assumptions: (1) the impurity particles adsorbed on the crystal surface are cylindrical with an average radius R_s and an average density N_s , and (2) R_s and N_s remain constant during growth. The schematic illustration of the mechanism of heterogeneous 2D nucleation on such impurity particles is similar to that shown in Figure 2.6a.

2D nucleation on a perfect surface occurs when the free energy barrier ΔG_{2D}^* is surpassed. As in the case of 3D nucleation, when the impurity particles are present on the surface, they serve as substrates for 2D nucleation and decrease the nucleation barrier. Let us consider the formation of a solute embryo of radius r of volume V and surface area P on a nucleating impurity particle of radius R_s . Then following Liu *et al.* (1997), the free energy for the formation of a crystal embryo of radius r is given by

$$\Delta G_{2D} = -\Delta\mu V/\Omega + \gamma_{cf} P_{cf} + (\gamma_{sf} - \gamma_{sc})P_{sc} \quad (3.77)$$

where $\Delta\mu$ is the chemical potential difference between crystalline solid (solute) and fluid, γ_{ij} is the linear free energy of the step edge between phases i and j (see Figure 2.7a), and Ω is the molecular volume. Then the contact angle θ is given by [see Equation (2.29)]

$$\cos\theta = (\gamma_{sf} - \gamma_{sc})/\gamma_{cf} = m \quad (3.78)$$

Using appropriate values for V , P_{cf} and P_{sc} from Figure 2.6, one may write

$$\Delta G_{2D(het)}^* = \Delta G_{2D(hom)}^* \Phi'(m, x) \quad (3.79)$$

where [cf. Equation (3.30)]

$$\Delta G_{2D(hom)}^* = \frac{\pi h \gamma_{cf}^2 \Omega}{k_B T \ln S} \quad (3.80)$$

$$\begin{aligned} \Phi'(m, x) = & \frac{1}{\pi} \left\{ \arccos[(xm - 1)/w] + (x^2 - 2xm) \arccos[(x - m)/w] \right. \\ & -(1 - xm)[w^2 - (1 - xm)^2]^{1/2}/w^2 \\ & \left. -x^2(x - m) \times [w^2 - (x - m)^2]^{1/2}/w^2 \right\} \end{aligned} \quad (3.81)$$

$$w = (1 + x^2 - 2xm)^{1/2} \quad (3.82)$$

and

$$x = R_s/r_{2D}^* \quad (3.83)$$

The factor $\Phi'(m, x)$ has values from 0 to 1.

The dependence of the factor $\Phi'(m, x)$ on x for different values of m is similar to that of $\phi(m, R')$ of three-dimensional nucleation on R' for different values of m , as shown in Figure 2.7b. In Figure 2.7b, taking $\phi(m, R') = \Phi'(m, x)$ as a function of $R' = x$ for different values of the parameter m , one notes that when $x = 0$ or $m = -1$, $\Phi'(m, x) = 1$. The situation $x \rightarrow 1$ means that solid particles do not behave as the nucleating substrate. The case $m = -1$ corresponds to the situation when there is no wetting between solid impurity particles and the embryo. The situations when $x = 0$ or $m = -1$ [i.e. $\Phi'(m, x) = 1$] correspond to the case of homogeneous 2D nucleation. With increasing x and decreasing m ($-1 \leq m \leq 1$), $\Phi'(m, x)$ decreases from 1 to 0, implying that the nucleation barrier $\Delta G_{2D(het)}^*$ decreases from $\Delta G_{2D(hom)}^*$ to 0 ($0 \leq \Delta G_{2D(het)}^* \leq \Delta G_{2D(hom)}^*$). In this regime, impurity particles play a critical role in 2D nucleation. In the case when $m \rightarrow 1$, impurity particles reduce to the embryos of the crystallizing phase. When $x \geq 1$, $\Phi'(m, x)$ and $\Delta G_{2D(het)}^* \rightarrow 0$. When $x \rightarrow \infty$, a round nucleating particle reduces to a plane, and Equation (3.80) describes 2D nucleation on a plane surface.

The rate of 2D nucleation is given by (Liu *et al.*, 1997)

$$J_{2D} = C_1 (\ln S)^{1/2} \exp \left[-\frac{\pi h \gamma_{sf}^2 \Omega}{(k_B T)^2 \ln S} \Phi'(m, x) \right] \beta'_{st} \delta(m, x, R_s, N_s) \quad (3.84)$$

where C_1 is given by Equation (3.30), β'_{st} is the sticking probability, and the factor $\delta(m, x, R_s, N_s)$ lies between 0 and 1. In the factor $\delta(m, x, R_s, N_s)$, N_s is the concentration of growth units equal to $1/a^2$, where a is the size of growth species. In heterogeneous 2D nucleation, only part of the circumference of the embryo is available to the collision of growth species. For heterogeneous 2D nucleation $0 < N_s \pi a R_s < 1$, whereas for homogeneous 2D nucleation $N_s \pi a R_s = 1$. Therefore, the value of the factor $\delta(m, x, R_s, N_s)$ is determined by the proportion of the surface which can effectively cause heterogeneous 2D nucleation.

It can be seen from Equation (3.84) that the factor $\Phi'(m, x)$ included in the exponential term lowers the energy barrier for nucleation, thereby increasing the nucleation rate J_{2D} , while the factor $N_s \pi a R_s$ in the pre-exponential term leads to a decrease in J_{2D} . Therefore, the ultimate nucleation rate J_{2D} is determined by these two factors.

Substituting the values of J_{2D} from Equation (3.84) and step velocity v for growth of a perfect surface [Equations (3.24) and (3.27)], one can calculate the growth rate R of a perfect smooth face for polynuclear and multiple nucleation (birth-and-spread) models, respectively. It is well known that the steps of nuclei move with a certain velocity v . Therefore, the multiple nucleation model is close to reality. We discuss below the expressions for growth kinetics according to the multiple nucleation model [Equation (3.23)].

Surface Diffusion-Controlled Growth

From Equations (3.23), (3.24) and (3.84), the face growth rate is given by

$$R = C_6 \sigma^{2/3} (\ln S)^{1/6} \exp[-C_7 \Phi'(m, x)/(T^2 \ln S)] [\delta(m, x, R_s, N_s)]^{1/3} \quad (3.85)$$

where

$$C_6 = h(2\lambda_s/a)^{2/3}\beta_l^{2/3}C_1^{1/3} \quad (3.86)$$

and

$$C_7 = \pi h \gamma_{\text{cf}}^2 \Omega / 3k_B^2 \quad (3.87)$$

When $\sigma \ll 1$, Equation (3.85) reduces to

$$R = C_6 \sigma^{5/6} \exp[-C_7 \Phi'(m, x)/T^2 \sigma] [\delta(m, x, R_s, N_s)]^{1/3} \quad (3.88)$$

A similar expression can be given for growth by direct integration of growth units.

Volume Diffusion-Controlled Growth

Substituting the values of v from Equation (3.55) and J_{2D} from Equation (3.84) in Equation (3.23), one obtains

$$R = C_8 \sigma^{2/3} (\ln S)^{1/6} \exp[-C_7 \Phi'(m, x)/(T^2 \ln S)] [\delta(m, x, R_s, N_s)]^{1/3} \quad (3.89)$$

where

$$C_8 = (h\Omega)^{5/6} \beta_l [2D_s \pi / av]^{1/3} (n_1^2 \zeta)^{2/3} \quad (3.90)$$

with [cf. Equation (3.56)]

$$\zeta = [1 + (\beta_l h / \pi D) \ln(y_0/h)]^{-1} \quad (3.91)$$

and C_7 given by Equation (3.87). When $\sigma \ll 1$, Equation (3.89) reduces to the form

$$R = C_8 \sigma^{5/6} \exp[-C_2 \Phi'(m, x)/(T^2 \sigma)] [\delta(m, x, R_s, N_s)]^{1/3} \quad (3.92)$$

Equations (3.85), (3.88), (3.89) and (3.92) describe the growth kinetics of a perfect smooth face by multiple nucleation model both for heterogeneous and homogeneous 2D nucleation. However, when $\Phi'(m, x) = \delta(m, x, R_s, N_s) = 1$, these equations describe homogeneous 2D nucleation.

From the above, it follows that the presence of impurity particles in a system can decrease the nucleation barrier, depending on the values of m and x . Physically, this means the critical supersaturation σ_{cr} when the radius of the 2D nucleus approaches the size of an atom or molecule on the surface. This phenomenon is known as kinetic roughening (see Section 3.3.2), and occurs when $\Delta G_{2D}^* \leq k_B T$. Using Equations (3.79) and (3.80), one obtains the critical supersaturation for kinetic roughening in the form

$$\sigma_{\text{cr}} = \sigma_{\text{cr(hom)}} \Phi'(m, x) \quad (3.93)$$

where the critical supersaturation $\sigma_{\text{cr(hom)}}$ for kinetic roughening of a surface in impurity-free system is given by

$$\sigma_{\text{cr(hom)}} = \frac{\pi h \gamma_{\text{cf}}^2 \Omega}{(k_B T)^2} \quad (3.94)$$

According to Equation (3.93), σ_{cr} is determined by $\Phi'(m, x)$ and γ_{cf} .

It may be concluded that for a given system, the presence of impurities can lead to a substantial decrease in the 2D nucleation barrier in terms of $\Phi'(m, x)$, and, consequently, the critical supersaturation σ_{cr} for kinetic roughening. The effect is pronounced when m is close to unity and the impurity radius R_s is relatively large.

As noted above, for homogeneous 2D nucleation both $\Phi'(m, x)$ and $\delta(m, x, R_s, N_s)$ are unity, but for heterogeneous 2D nucleation both $\Phi'(m, x)$ and $\delta(m, x, R_s, N_s)$ are less than unity. However, in the latter case the two factors $\Phi'(m, x)$ and $\delta(m, x, R_s, N_s)$ have opposite effects on the growth rate of the crystal face. The factor $\Phi'(m, x)$ leads to a reduction in the 2D nucleation barrier, resulting in an increase in the growth rate R , while the factor $\delta(m, x, R_s, N_s)$ leads to a reduction in the growth rate. These are essentially the thermodynamic and kinetic parameters, respectively.

At low supersaturations, the effect of the factor $\Phi'(m, x)$ is dominant and growth by heterogeneous 2D nucleation is kinetically more favorable than growth by homogeneous 2D nucleation. However, with an increase in supersaturation, the exponential term associated with heterogeneous 2D nucleation barrier becomes unimportant and the factor $\delta(m, x, R_s, N_s)$ approaches unity. Then growth becomes controlled by homogeneous 2D nucleation rather than by heterogeneous 2D nucleation, with a transition occurring at supersaturation σ^* given by

$$\sigma^* = 3[\Phi'(m, x) - 1]C_7/[T^2 \ln \delta(m, x, R_s, N_s)] \quad (3.95)$$

Obviously, for $\sigma < \sigma^*$ the growth rate due to heterogeneous 2D nucleation will be higher than that due to homogeneous 2D nucleation, whereas for $\sigma > \sigma^*$ the growth rate due to homogeneous 2D nucleation will be higher than that due to heterogeneous 2D nucleation. Moreover, Equation (3.95) shows that an increase in $\Phi'(m, x)$ and a decrease in $\delta(m, x, R_s, N_s)$ lead to a decrease in the value of σ^* . However, changes in $\Phi'(m, x)$ lead to more pronounced changes in σ^* than the $\ln \delta(m, x, R_s, N_s)$ term in the denominator. For example, an increase in $\Phi'(m, x)$ from 0.1 to 0.5 causes a decrease in σ^* by 45%, whereas a similar decrease in σ^* is caused when $\delta(m, x, R_s, N_s)$ decreases by about four orders of magnitude from 10^{-5} to 10^{-9} . Therefore, it may be assumed that for a given growth system, σ^* is relatively insensitive to the value of the term $\ln \delta(m, x, R_s, N_s)$ in Equation (3.95).

Figure 3.14 shows the plots of $\ln(R/\sigma^{5/6})$ against $1/\sigma$, predicted by Equations (3.88) and (3.92), for the (100) face of dislocation-free $\text{Ba}(\text{NO}_3)_2$ crystals grown from aqueous solutions. The original $R(\sigma)$ data are presented in Figure 3.11. It can be seen that there is indeed a transition supersaturation $\sigma^* \approx 4\%$, and growth by homogeneous and heterogeneous 2D nucleation occurs for $1/\sigma < 1/\sigma^*$ and $1/\sigma > 1/\sigma^*$, respectively. The experimental data for growth due to dislocations are also shown in Figure 3.14. As expected for this mechanism [for example, see Equations (3.45) and 3.52)], here a nonlinear relation between $\ln(R/\sigma^{5/6})$ and $1/\sigma$ is obtained. Moreover, one notes that in the supersaturation range $1/\sigma \geq 18$ (i.e. $\sigma \leq 5\%$), the rate R due to 2D nucleation-controlled growth is always lower than that for dislocation-controlled growth, whereas for $\sigma > 5\%$ they are equal. The former observation is associated with the nature of the activation barrier involved in the generation of steps required for growth.

It should be mentioned that $\Phi'(m, x)$ is a function of σ . Therefore, in the case of heterogeneous 2D nucleation, the dependence of $\ln(R/\sigma^{5/6})$ on $1/\sigma$ is not expected to

be strictly linear unless x is very large [see Equation (3.88)]. The plot in Figure 3.14 suggests that x is large.

Liu *et al.* (1997) found that for the growth of the (100) face of $\text{Ba}(\text{NO}_3)_2$ crystals controlled by heterogeneous 2D nucleation, $\gamma_l/k_B T = 0.371$, $\Phi'(m, x) \approx 0.101$, $m \approx 0.65$, and $\theta \approx 0.86$. From the data reported by Malkin *et al.* (1989) for the growth of the dislocation-free (101) face of ADP crystals, Liu *et al.* (1997) obtained similar values of the above parameters, i.e. $\Phi'(m, x) \approx 0.127$, $m \approx 0.6$, and $\theta \approx 0.93$.

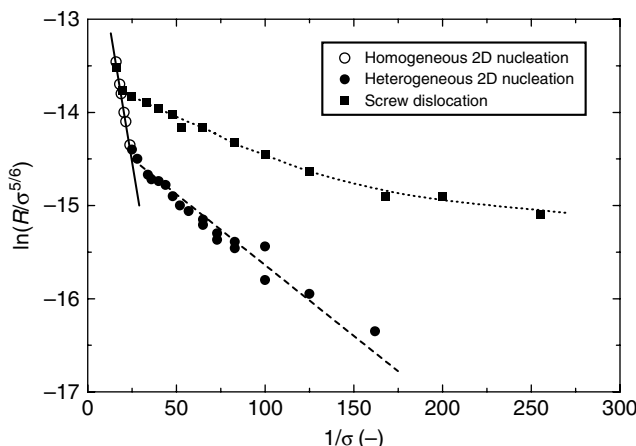


Figure 3.14 Plots of $\ln(R/\sigma^{5/6})$ against $1/\sigma$ for the (100) face of $\text{Ba}(\text{NO}_3)_2$ crystals grown from aqueous solutions. Reproduced from X.Y. Liu, K. Maiwa, and K. Tsukamoto. J. Chem. Phys. **106**, 1870. Copyright (1997), with permission from American Institute of Physics

As mentioned above, the presence of impurity particles results in the reduction of the 2D nucleation barrier $\Delta G_{2\text{D}}^*$ in terms of $\Phi'(m, x)$. However, as seen from Figure 2.7b, the maximum effect of the impurity is expected when $m \rightarrow 1$. This implies that interactions between adsorbed impurity particles and growth species are fairly strong. Moreover, the size of impurity particles should be similar to or larger than that of the critical nucleus (i.e. $x = R_s/r_{2\text{D}}^* \geq 1$). This means that growth can occur when

$$R_s = r_{2\text{D}}^* = \gamma_{\text{cf}} \Omega / k_B T \ln S \quad (3.96)$$

Equation (3.96) shows that the greater the size of the impurity particle, the lower is the value of supersaturation σ for the occurrence of growth in the presence of an impurity. As an example, assuming that $\gamma_l/k_B T = 0.5$ ($\gamma_{\text{cf}} \Omega \approx \gamma_l a$), one finds $R_s \approx 50a$ for a realistic value of $\sigma = 0.01$. Therefore, in practice, polymer molecules and dust particles have sufficient size to cause growth on them.

From the above, it follows that the growth promoting effect of an impurity as a result of reduction in 2D nucleation barrier does not occur when the impurity particles yield m close to -1 and $R_s \ll r_{2\text{D}}^*$. This situation means that the interactions between impurity particles and growth species should be repulsive, whereas the $R_s > r_{2\text{D}}^*$ condition means that the impurity particles should be small.

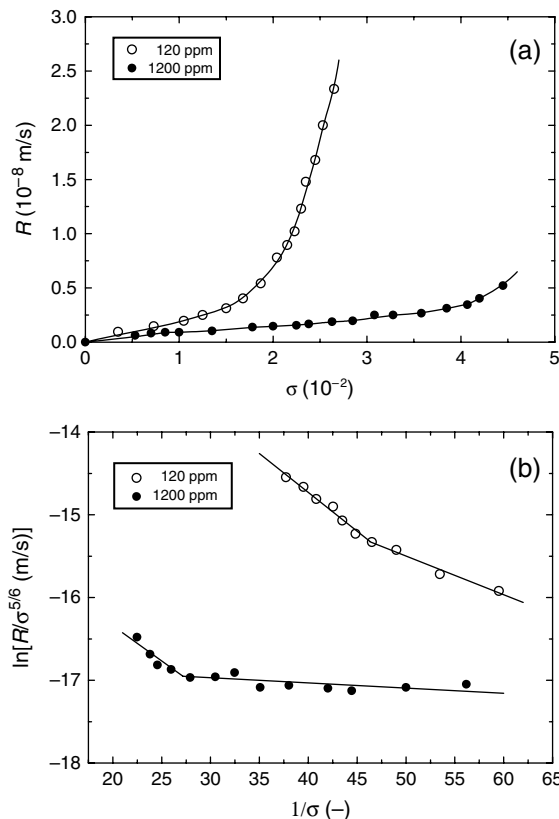


Figure 3.15 (a) Dependence of R of the $\{\overline{1}\overline{1}\overline{1}\}$ face of NaClO_3 crystals from aqueous solutions on supersaturation σ for two different concentrations of $\text{S}_2\text{O}_6^{2-}$ ions. (b) Plots of $\ln[R/\sigma^{5/6}]$ against $1/\sigma$ based on the data in (a). Original data from Ristić et al. (1994)

The kinetic data for the dependence of growth rate R of the $\{\overline{1}\overline{1}\overline{1}\}$ face of NaClO_3 crystals from aqueous solutions on supersaturation σ for two different concentrations of $\text{S}_2\text{O}_6^{2-}$ ions, shown in Figure 3.15a, is another example illustrating the existence of transition supersaturation σ^* . Figure 3.15b presents the $R(\sigma)$ data of Figure 3.15a as plots of $\ln(R/\sigma^{5/6})$ against $1/\sigma$. From Figure 3.15, it may be noted the $R(\sigma)$ data are described satisfactorily by the multiple nucleation model. This means that the presence of dislocations is unimportant during the growth of the $\{\overline{1}\overline{1}\overline{1}\}$ faces of NaClO_3 crystals. This inference is consistent with the fact that the $\{\overline{1}\overline{1}\overline{1}\}$ faces of NaClO_3 crystals are rough F faces.

Irrespective of the value of impurity concentration c_i , the slope $C_7\Phi'(m, x)/T^2$ [cf. Equations (3.92) and (3.87)] of the plots in Figure 3.15b is practically the same (equal to 0.094, and $\gamma_l/k_B T = 0.3$) in the supersaturation interval $\sigma^* > \sigma$, as expected for homogeneous nucleation. However, in the interval $\sigma^* < \sigma$ when heterogeneous nucleation takes place, the slope decreases from 0.047 to 0.006 [corresponding to $\Phi'(m, x)$ equal to 0.5 and 0.067] with an increase in c_i from 120 to 1200 ppm, respectively.

The transition value of supersaturation σ^* increases from 2.2 to 3.7% with an increase in impurity concentration c_i from 120 to 1200 ppm. Using Equation (3.96) and the values

of σ^* , one can estimate the value of the radius R_s of impurity particles when transition from heterogeneous to homogeneous nucleation takes place and deduce the relationship, if any, between R_s and c_i . Taking $\gamma_l/k_B T = 0.3$ given above, one obtains R_s equal to $13.8a$ and $7.8a$, corresponding to impurity concentrations c_i of 120 and 1200 ppm, respectively. In the case of ionic interactions involved between impurity particles and the crystal interface, the above distances are indeed realistic (see Section 3.8). Moreover, it is interesting to observe that the impurity radius R_s inducing heterogeneous nucleation is inversely proportional to the one-third power of impurity concentration c_i (i.e. $R_s \propto c_i^{-1/3}$).

The transition from heterogeneous to homogeneous 2D nucleation is not confined to ionic crystals alone, but is also encountered during the growth of complex organic crystals and macromolecules (Malkin *et al.*, 1999). The values of $\Phi'(m, x)$ estimated from the $\ln(R/\sigma^{5/6})$ plots are similar to those obtained in the case of growth of small-molecule crystals described above. However, the values of transition supersaturation σ^* during the growth of complex organic and macromolecular crystals are one to two orders of magnitude higher than those obtained for inorganic crystals. For example, for the growth of the {001} face of catalase crystals and the {101} face of thaumatin crystals, the values of $1/\sigma^*$ are 0.48 and 1.2, respectively (Malkin *et al.*, 1999). Since the values of the slope for the above crystals are 0.52 and 0.39, using Equation (3.96) one obtains $R_s = 0.35a$ and $0.75a$, respectively. Obviously, in these cases the impurity molecules are essentially immobile and involve short-range interactions with the crystal interface.

3.8 Real Crystal Growth Mechanisms

The above description of the final theoretical expressions of crystal growth kinetics of F faces is relatively idealized and represents extreme situations of (a) the possible type of growth entities in the form of atoms, ions or molecules that enter growth sites on the growing surface, (b) the possible sources of growth sites (kinks) in the step ledges produced by dislocations generated in the crystal surface or by 2D nucleation occurring on the already existing surface, and (c) the possible modes of supply of the growth entities to kinks in the steps of a growing surface by surface diffusion, direct integration and bulk diffusion. In practice, crystal growth is a complex phenomenon involving (i) a wide spectrum of entities present in the growth medium, which are not simple atoms, ions or molecules, (ii) simultaneous occurrence of growth by the participation of dislocations and 2D nucleation as sources of steps, and (iii) difficulties in separating the contribution of individual modes of supply of growth entities. The nature of growth entities present in solutions was discussed in Chapter 1. In this section, the nature of the growth interface between the crystal terminal surface and the growth medium and some general features of the sources of steps on growing crystals are presented. Since most of the growth systems described in this monograph deal with ionic compounds and proteins, the discussion is confined to such systems.

3.8.1 Structure of Interfacial Layer

When an ionic crystal is brought in contact with its supersaturated aqueous solution, growth does not start instantaneously. In fact, in a small fraction of time, an electrical double layer is developed on the solution side of the boundary separating the crystal from

the solution, frequently referred to as crystal–medium interface, as a consequence of the difference in chemical potential of the ions (i.e. entities) in the crystal and in the solution, as shown in Figure 3.16. The double layer is composed of solvent ions and the solvated growth species present in the solution. It is the result of a dynamic equilibrium involving continuous transfer of solvent ions and growth entities across the boundary separating the crystal from the solution interface. Crystal growth takes place by the diffusion of growth entities in the double layer to active growth sites at the crystal–medium interface. However, because of restrictions imposed by the underlying crystal lattice, diffusion of solvent molecules and growth entities in the interfacial layer close to the crystal–medium interface is slower than that in the bulk medium.

On the solution side of the interface in the immediate neighborhood of the crystal, an inner compact and rigid Helmholtz–Stern layer (also called Stern layer) of specifically adsorbed solvent molecules and partially solvated ions (growth species) is formed. This layer has a thickness of only a few molecular diameters. Since all the solvent molecules are electron donors by oxygen, they tend to coordinate with the positive ions belonging to the ionic surface of the crystal. Therefore, the dipoles are oriented with their oxygen atoms towards the crystal surface. Consequently, a positive space-charge region appears on the crystal surface. Solvated anions (or negatively charged growth entities) penetrate into the inner layer, partially lose their solvation sheath and are specifically adsorbed on the crystal surface due to short-range chemical interactions and Coulomb interactions. Solvated cations (or positively charged species) can equally well penetrate into the inner layer and, after partially losing their solvation sheath, bond chemically with some ions of the crystal surface.

At very low supersaturations (i.e. small chemical potential differences) when the rate of surface reactions is small, most of the solvated ions may be accommodated in the Helmholtz–Stern layer. However, with an increase in supersaturation, the concentration of solvated ions (or charged entities) increases, and so does the thickness of the interfacial layer. Due to mutual attractive and repulsive interactions between charged entities of different types, the interfacial layer extends thicknesses on the order of thousands of molecular distances (Sunagawa *et al.*, 1995). However, because of the presence of the growth medium, the mutual interactions are not strong enough to keep the charged species in close proximity. Consequently, after a few molecular distances from the crystal–medium interface, the interfacial layer is diffuse. This layer, extending from the Helmholtz–Stern layer into the bulk of the solution, is usually called the diffuse layer.

The presence of a diffuse layer is possible in stagnant solutions. In this case, at the growth interface the available supersaturation σ_s (i.e. interface or surface supersaturation) is lower than the supersaturation σ_b in the bulk medium. In stirred solutions, when the ions have the opportunity to be transferred into the bulk medium, the thickness of the diffuse layer decreases. Therefore, it is expected that at a particular stirring rate the thickness of the interfacial layer attains a constant value on the order of a few molecular distances. In principle, this situation is possible when $\sigma_s = \sigma_b$. However, in practice it is difficult to achieve $\sigma_s = \sigma_b$ and to attain interfacial layers of a few molecular distances. For example, as reported by Sunagawa *et al.* (1995), the best results for $\sigma_s/\sigma_s \approx 0.95$ and interfacial layer thickness $\delta \approx 30 \mu\text{m}$ during the growth of the {111} face of potash alum crystals, and $\delta \approx 200 \mu\text{m}$ for the growth of the {111} faces of BaNO_3 .

Since many physical and chemical processes, such as catalysis and crystal growth, occur at the solid–liquid interface, understanding of the interface structure has attracted

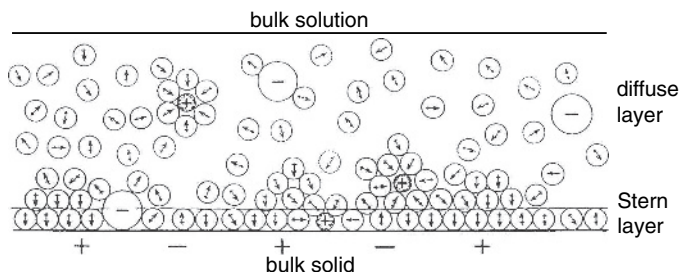


Figure 3.16 Schematic illustration of development of an electrical double layer at the interface of an ionic crystal with its solution. Water dipoles are represented by arrow-containing circles where the arrow indicates the position of oxygen charge in the water dipole. The surface is unevenly solvated due to the different affinities of cations and anions against the solvent. Reproduced from S. Veintemillas-Verdaguer. Prog. Cryst. Growth Charact. Mater. **32**, 75. Copyright (1996), with permission from Elsevier

considerable interest during the last decade. These investigations essentially provide a molecular level picture of the nature of the electrical double layer described above. Here, rather than surveying the literature on the subject, the recent results of investigations carried out by using surface X-ray diffraction techniques of the structure of the {100} and {101} faces of KDP crystals in contact with its aqueous growth solution are presented. These are the main faces appearing in the morphology of KDP crystals. The growth rate of the {101} face depends strongly on the solution pH, but the growth rate of the {100} face is practically independent of solution pH. For the literature on the subject, the reader is referred to recent papers by Kaminski *et al.* (2005, 2006) and Fenter *et al.* (2000).

Figure 3.17 illustrates schematically the interface structure of the {100} face of KDP crystals. Because of the two-fold axes perpendicular to the surface, each unit cell contains two symmetry-equivalent O1 atoms. The O1 occupancy is close to unity, implying that this position is occupied by an oxygen atom of the water molecule and not by solute ions. The O1 position is close to two phosphate groups and a potassium ion with distances between 1.9 and 2.6 Å, as shown in Figure 3.17. The distance between the O1 atom and the O^{*} atom of the phosphate group with the broken H-bonds is the shortest, thus ensuring the strongest interaction. The O1 layer is well ordered in both the lateral and perpendicular directions, but the O2 layer has no in-plane order and contains PO₄ and K ions. The O2 layer and the additional layers above it have perpendicular order alone.

It was found (Kaminski *et al.*, 2006) that the atoms at the crystal surface show no relaxation, and the internal structure is the same for all pH values. This means that the first liquid layer is essentially chemisorbed at the surface through an H-bond and a PO₄ group in the crystal surface. The H-bond is insensitive to the solution pH.

In contrast to the {100} face, the {101} face exhibits lateral order in two and perpendicular order in four layers (Kaminski *et al.*, 2005). This order is twice the amount for the {100} faces. However, the structure of the {101} face is such that the bonding of positive ions is important for this face, and this results in a changing balance between K⁺ and H₃O⁺ ions as a function of pH. Thus, the nature of the order in the interfacial layer on

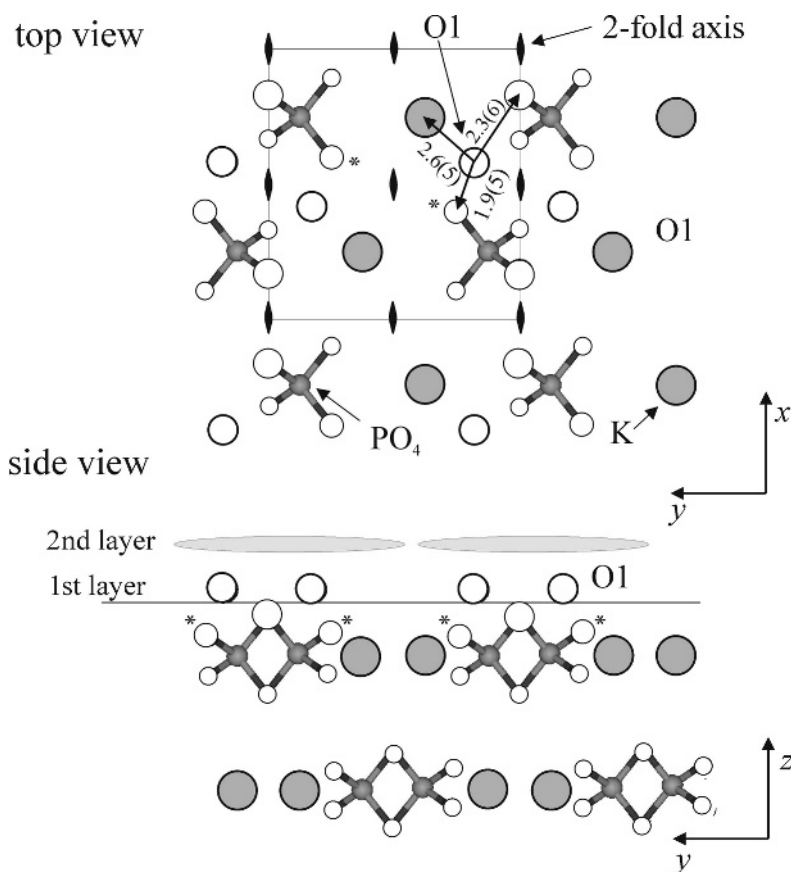


Figure 3.17 Schematic of the interface structure of the $\{100\}$ face of KDP. Each unit cell contains two symmetry equivalent ‘liquid’ $\text{O}1$ atoms because of the two-fold axes perpendicular to the surface. The asterisks indicate O atoms with broken H-bonds due to the surface termination. Reproduced from D. Kaminski, N. Radenović, M.A. Deij, W.J.P. van Enckevort, and E. Vlieg. Cryst. Growth Des. **6**, 588. Copyright (2006), with permission from American Chemical Society

the two faces depends on their crystallographic structure and the resulting bonding with the solution. The difference in the bonding leads to different kinetic barriers for growth and different growth behavior of the two faces.

The atomic structure of the $\{010\}$ interface of brushite ($\text{CaHPO}_4 \cdot 2\text{H}_2\text{O}$) with water is another example of a similar order in the interfacial layer (Arsić *et al.*, 2004). The solution side of the interface consists of two water bilayers with different ordering properties. The first water bilayer is highly ordered and is essentially part of the brushite crystal structure. The second water bilayer has no in-plane order, but shows layering in the perpendicular direction.

Kaminski *et al.* (2006) cite examples of several systems involving relatively strong bonding between solvent and crystal surface: water at RuO₂(110), water at mica surfaces, and amide cosolvents at the {100} face of benzamide. In such systems, crystal growth requires the rupture of these bonds before the attachment of new growth units. This means that the solvent can have a strong influence on the growth kinetics and the resulting morphology of the crystals. The formation of an electrochemical double layer on the polar {111} face of NaCl crystals is also responsible for their stabilization (Radenović *et al.*, 2006). The results show that level of order in the adsorbed water layer at the interface is correlated with the solubility of the compound in the solvent, a low ordering being associated with low solubility. However, the level of order in the water layer for different faces of a crystal depends on their crystallographic structure.

Electrical double layers are characteristic of all phases, and there is voluminous literature on the subject. The reader is referred to standard books on electrochemistry for a description of the basic concepts (for example, Bockris and Reddy, 1970), while a recent review has been devoted to the developments in the theory of diffuse double layer (Fawcett and Smagala, 2006).

3.8.2 Sources of Growth Steps

The idealized presentation of crystal growth is based on the assumption that transport of growth entities occurs either by surface or volume diffusion, while growth sites are ensured by step ledges generated by dislocations emerging on the growing surface or by two-dimensional nucleation on it. Although there may remain problems in attaining entirely surface diffusion-controlled growth by stirring due to the persistence of supersaturation gradient along the growing surface and an inability to achieve surface supersaturation σ_s equal to bulk supersaturation σ_b (cf. Sunagawa *et al.*, 1995), one can fairly satisfactorily obtain experimentally data on growth kinetics under surface and bulk diffusion-controlled conditions. Subsequently, from an analysis of the data so obtained, one can draw conclusions about the possible growth mechanism, namely whether growth proceeds by the participation of dislocations or 2D nucleation. This approach has been followed in numerous studies reported in the literature (for example, see Sunagawa *et al.*, 1995; Sangwal, 1998a).

It is a common observation that the same data on growth kinetics for small-molecule ionic salts can be described equally well by both spiral growth and 2D nucleation mechanisms, and there is little to choose between the two mechanisms. The problem is particularly severe at relatively low supersaturations, where measurement errors are large and trace amounts of impurities inherently present in the medium affect the growth rates. In such cases, direct observation of the growing surfaces provides the final clue to the governing growth mechanism for the system under investigation. There is a preponderance of literature on the observation of growth surfaces of a variety of substances by optical microscopy (van Enckevort, 1984; Sangwal and Rodrigues-Clemente, 1991), but the last two decades have witnessed the growth of atomic force microscopy (AFM) as a very useful technique for the *ex situ* and *in situ* investigation of growth and dissolution processes of sparingly soluble compounds such as calcite and gypsum (Teng *et al.*, 2000; Dove *et al.*, 2004) and macromolecular crystals such as proteins and viruses (Land *et al.*, 1997; Malkin *et al.*, 1999; McPherson *et al.*, 2003), which have low growth rates in comparison with those of most low-molecule ionic compounds such as KDP. Thanks to

their heights, which are typically between 10 and 40 nm, in contrast to less than about 1 nm on the growth surfaces of small-molecule crystals, the *in situ* study of proteins by AFM provides especially invaluable information on growth processes because growth steps on their surfaces can be easily observed and, in favorable cases, even individual protein molecules can be observed as they are integrated into advancing steps (McPherson *et al.*, 2003; Kuznetsov *et al.*, 2005).

For understanding the growth kinetics of F faces of crystals, it is of interest to know the ranges of supersaturation where the classical crystal growth theory involving dislocation sources and two-dimensional nucleation theories are applicable. Practically all crystals have dislocations emerging on their main faces appearing in their growth morphology. Therefore, it is expected that at low supersaturations growth occurs mainly by spiral growth, but the contribution of 2D nucleation to growth kinetics becomes increasingly significant with increasing supersaturation because of the decreasing energy barrier for 2D nucleation [see Equation (3.30)]. Teng *et al.* (2000) observed this trend during an *in situ* investigation by AFM of the growth kinetics of the {10̄14} face of calcite crystals from pure aqueous solutions over a wide range of supersaturation σ up to about 1.5.

The observations (Teng *et al.*, 2000) revealed that, at lower values of σ from 0 to 0.8, calcite growth is initiated entirely by screw dislocations and grain boundaries. It was found that most of the hillocks (more than 80%) are multiple spirals produced by individual dislocations with multiple Burgers vectors, groups of randomly scattered dislocations, and closed loops emitted by a single source. The remaining hillocks (less than 20%) are single spirals, and were less common. In the areas free from single spirals, growth occurs only at the existing steps and no new sources of steps (e.g. by 2D nucleation) are generated. Single spirals are devoured by multiple spirals on continued growth. In the range of supersaturation $\sigma > 0.8$, 2D surface nucleation becomes increasingly important with increasing supersaturation. With an increase in σ , first 2D nucleation, favored by lattice defects such as grain boundaries, occurs, but at higher supersaturations growth occurs entirely by the multiple nucleation mechanism. Examples of the observation of spiral growth and 2D nucleation on the {10̄14} face of calcite crystals are shown in Figure 3.18.

The above results are consistent with our general understanding that the classical parabolic growth law involving single spirals, formed at screw dislocations with unit Burgers vector, holds only at very low supersaturations close to the equilibrium. In general, since multiple spirals are the main sources for growth steps, a parabolic growth law is not followed. The observation of 2D nucleation only after exceeding a critical supersaturation is also expected in the case of homogeneous 2D nucleation when impurities do not facilitate nucleation.

The formation of single and multiple spirals and 2D nuclei (islands) is a common feature observed on a variety of crystals. Thick steps, usually referred to as bunched steps formed as a result of joining of tens, hundreds and even thousands of elementary growth steps, are also frequently observed. Figure 3.19 illustrates typical examples of 2D nucleation (a, b), spiral growth (c) and macrosteps (d) on the growing faces of macromolecular crystals. In many cases, the shapes of growth spirals and 2D nuclei reflect the geometries of the face on which they are formed. Here, following McPherson *et al.* (2003), some important observations made during the growth of macromolecular crystals are described.

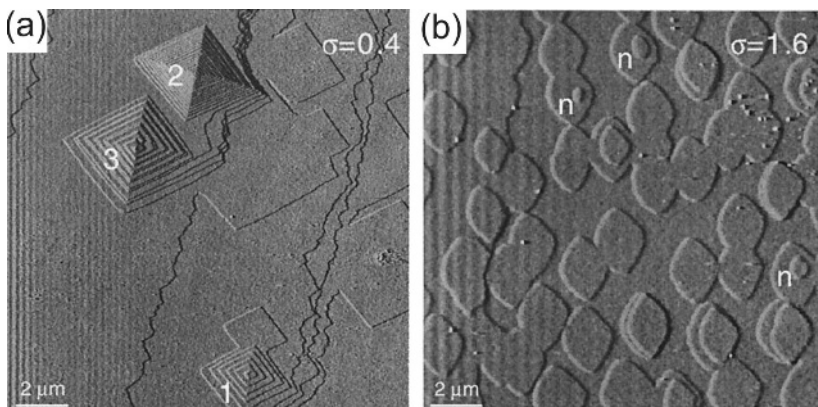


Figure 3.18 Observation of (a) spiral growth and (b) 2D nucleation on the $\{10\bar{1}4\}$ face of calcite crystals; supersaturation σ : (a) 0.4 and (b) 1.6. In (a) spirals 1 and 3 are single spirals whereas spiral 2 is composed of two double spirals. In (b) some nuclei formed by successive nucleation are indicated by n . Reproduced from H.H. Teng, P.M. Dove, and J.J. De Yoreo. Geochim. Cosmochim. Acta **64**, 2255. Copyright (2000), with permission from Elsevier.

The height of elementary steps of growth spirals and 2D nuclei on the surfaces of macromolecular crystals usually corresponds to a single unit cell dimension (Figure 3.19a and c), but it depends on the symmetry elements of the underlying face. For example, the height of layers of 2D nuclei formed on the orthorhombic crystals of beef liver catalase corresponds to exactly one half-unit cell, and the layers of molecules are composed of bottom halves and top halves of unit cells. The shape of 2D nuclei depends on the surface free energies of their various edges, and their orientation is determined by the symmetry of the crystal. For example, when a 2_1 axis is present perpendicular to the face, the orientations of successively stacking growth nuclei are changed by π relative to one and another (Figure 3.19b). At high supersaturations when the growth rate is high, successive steps accumulate to form a thick step (i.e. macrostep) and move like a single identity (Figure 3.19d). The displacement velocity of these macrosteps is different from that of elementary steps. All the above features of growth structures observed on the surfaces of macromolecular crystals are similar to those on the surfaces of small-molecule crystals.

Macromolecular crystals often exhibit spontaneous appearance of vast, multilayer stacks of growth layers on their surfaces, as shown in Figure 3.20. These elevated structures appear to be formed from liquid-phase droplets existing in concentrated macromolecular solutions (McPherson *et al.*, 2003). The liquid-phase droplets are large, disorganized aggregates composed of high concentrations of molecules. When these droplets come in contact with the crystal surface, the lattice serves as an epitaxial substrate for the crystallization of the molecules on it, forming a crystal layer. The newly formed layer subsequently serves as another substrate, which induces the development of another layer on the previous layer. The process continues, yielding a multilayer stack. This type of growth by three-dimensional nucleation ensures tangential spreading of layers, and is a dominant mechanism during the growth of some macromolecules.

In addition to dust particles and other foreign inorganic materials, incorporation of foreign macromolecules, denatured or degraded macromolecules and their aggregates

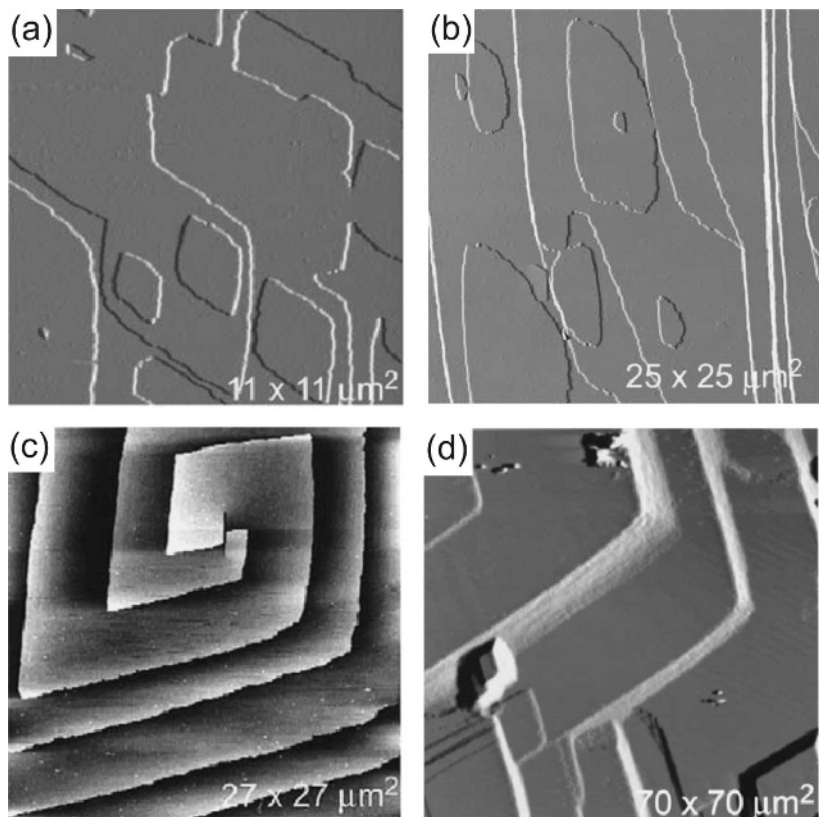


Figure 3.19 Typical examples of (a, b) 2D nucleation, (c) spiral growth and (d) macrosteps on the growing faces of macromolecular crystals: (a, c, d) glucose isomerase; (b) beef catalase. Reproduced from A. McPherson, Yu.G. Kuznetsov, A. Malkin, and M. Plomp. *J. Struct. Biol.* **142**, 32. Copyright (2003), with permission from Elsevier

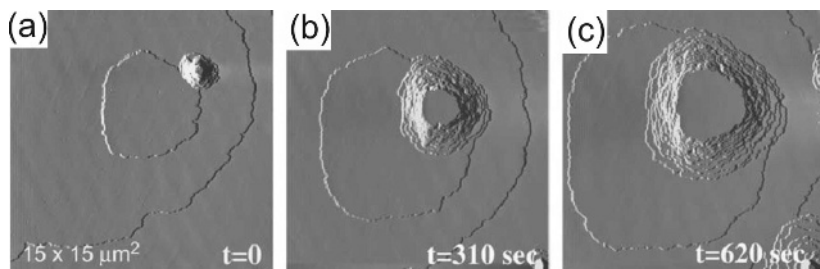


Figure 3.20 Example of tangential development of three-dimensional nuclei into a stack of tangentially expanding two-dimensional nuclei on a cubic satellite tobacco mosaic virus (STMV) crystal. Reproduced from A. McPherson, Yu.G. Kuznetsov, A. Malkin, and M. Plomp. *J. Struct. Biol.* **142**, 32. Copyright (2003), with permission from Elsevier

and microcrystals has been observed in growing protein, nucleic acid or virus crystals (McPherson *et al.*, 2003; Kuznetsov *et al.*, 2005). This type of growth occurs in the case of crystal lattices which are tolerant in terms of molecular size and conformation. In these crystal lattices, the macromolecules form sparse, weak, and geometrically imprecise bonds. The crystals have a low surface free energy γ and a poor long-range order between the macromolecules. In contrast, there are crystal lattices with a high surface free energy γ and a precise long-range order. The macromolecules form numerous strong, geometrically well-defined bonds in three dimensions. Consequently, their lattices are highly selective in terms of particle size, integrity and conformation.

3.9 Techniques for Studying Growth Kinetics

During the last four decades, growth kinetics of crystals from solutions have been extensively investigated by different techniques. Sangwal (1998a) briefly surveyed the literature on the subject up to 1997.

The first data on growth kinetics of crystals grown from solution were obtained by the weighing technique. This technique may be considered fairly reliable for the study of the kinetics of crystals containing the same group of faces. Typical examples of compounds crystallizing with the same groups of faces are alkali metal halides, potash alum and barium nitrate. However, even in these compounds it is observed that additional faces appear with a change in supersaturation. Therefore, for the determination of the growth mechanism of crystals exhibiting a variety of faces in their growth habit, it is desirable to obtain data on growth kinetics of individual faces.

Data on the supersaturation and temperature dependence of R are usually obtained by measurement of the displacement of a given face either *ex situ* with an optical microscope from the position of seed interfaces for different crystals grown separately, or *in situ* with an optical microscope from the position of the interface of a small crystal growing in a growth cell. For the *in situ* study of growth kinetics in a growth cell, Michelson interferometry (Rashkovich *et al.*, 1985) enables one to measure precisely the supersaturation dependence of the growth rate R of a face and the inclination p of hillocks developing on it due to dislocations directly from the interference fringes produced around them, and the velocity of steps $v = R/p$ indirectly. The method does not give the height h of steps directly. This shortcoming is overcome in real-time phase shift interferometry, which is capable of imaging interfacial morphology with a depth resolution of about 3 nm and lateral resolution of about 0.5 μm over an area of 2×2 mm (Onuma *et al.*, 1994; Booth *et al.*, 2002a,b). Phase shift interferometry is based on Michelson interferometry with two main modifications (Booth *et al.*, 2002a,b): (1) the mirror in one of the two reference arms is replaced by a growing crystal surface, and (2) a liquid-crystal variable waveplate, or phase shifter, is placed in the reference arm. The three-dimensional representation of the surface morphology in terms of the height difference between surface features is obtained by a phase-shift algorithm using five interferograms and image processing. These *in situ* observations were made mainly on inorganic crystals.

Conventional transmission- and reflection-type optical microscopy has also been used for the observation of elementary steps on protein crystals (Sazaki *et al.*, 2004). Using

laser confocal microscopy combined with differential interference contrast microscopy, 2D nucleation and subsequent growth of 2D nuclei of elementary height on the {110} faces of tetragonal lysozyme crystals in real time have been observed (Sazaki *et al.*, 2004).

During the *in situ* investigation of growth kinetics by optical microscopy techniques, the morphology of surfaces is not disturbed or damaged and the temperature and supersaturation can be controlled reasonably well. However, the main disadvantage of these techniques is limited lateral resolution in the sub-micron range and vertical resolution of about 1 nm. In contrast to optical microscopy techniques, atomic force microscopy (AFM) enables one to scan areas in size from about 20 nm to about 200 μm , and achieve a lateral resolution of several nanometers and a vertical resolution better than 1 nm. AFM is ideal for the *in situ* study of growth kinetics of macromolecules because of relatively large particles (with diameter between 3 and 10 nm) and a slow displacement rate of growth steps. However, the technique is less suited for the measurement of R and is limited to the study of growth kinetics of sparingly soluble ionic compounds (Kipp *et al.* 1994; Onuma *et al.*, 1995a,b; Kipp and Lacmann, 1996; Land *et al.*, 1997) and macromolecules (Land *et al.*, 1997; McPherson *et al.*, 2003).

Using Michelson interferometry and AFM, it has been established (see, for example, Land *et al.*, 1997; Kurihara *et al.*, 1996; Malkin *et al.*, 1999) that the growth of inorganic and macromolecular crystals occurs by similar mechanisms. The essential difference lies in the value of the kinetic coefficient β_l . A typical value of β_l for fairly soluble inorganic crystals such as KDP grown from aqueous solutions is of the order of 10^{-4} – 10^{-3} m/s, whereas that for the growth of macromolecules, such as catalase, thaumatin and canavalin, is 10^{-7} – 10^{-5} m/s, which is 2–3 orders of magnitude lower than that for inorganic compounds. The low value of β_l for macromolecular crystals is mainly due to steric factors associated with the improper orientation of incoming molecules for their incorporation into the crystal. The values of $\gamma_l/k_B T$, as determined from the slopes of the plots of $\ln(R/\sigma^{5/6})$ against $1/\sigma$, are approximately the same for inorganic and macromolecular crystals, and typically lie between 0.3 and 0.7. However, the typical values of the surface free energy γ are 10–40 and 0.1–0.5 mJ/m² for inorganic and macromolecular crystals, respectively. The lower values of γ of macromolecular crystals (by 1–2 orders of magnitude) than that of inorganic crystals are mainly due to their high solvent content and the relatively sparse intermolecular interactions per lattice unit.

Since the introduction of Michelson interferometry (Rashkovich *et al.*, 1985), our understanding of the elementary processes of growth from solutions has increased enormously. With the advent of AFM, not only have direct *in situ* measurements of step velocity become possible, but also the observation of individual macromolecules, foreign protein macromolecules and their aggregates and microcrystals, as they are incorporated into advancing steps (McPherson *et al.*, 2003). However, despite enormous progress in the experimental techniques, determination of the growth mechanism of crystals from kinetic data is still a challenging problem (Teng *et al.*, 2000).

References

- Arsić, J., D. Kaminski, P. Poodt, and E. Vlieg (2004). *Phys. Rev. B* **69** (24), art. no. 245406.
 Barsukova, M.I., V.A. Kuznetsov, T.M. Okhrimenko, V.S. Naumov, O.V. Kachalov, A. Yu. Klimova, M.I. Kolybaeva, and V.I. Salo (1992). *Kristallografiya* **37**, 1003.

- Bauser, E., and H. Strunk (1981). *J. Cryst. Growth* **51**, 362.
- Bauser, E., and H. Strunk (1984). *J. Cryst. Growth* **69**, 561.
- Bennema, P., and G.H. Gilmer (1973). In: P. Hartman (Ed.), *Crystal Growth: an Introduction*, North-Holland, Amsterdam, Chap. 10, p. 263.
- Bennema, P., and J.P. van der Eerden (1987). In: I. Sunagawa (Ed.), *Morphology of Crystals*, Terrapub, Tokyo, p. 1.
- Black, S.N., R.J. Davey, and M. Halcrow (1986). *J. Cryst. Growth* **79**, 785.
- Bliznakov, G.M., and E.K. Kirkova (1957). *Z. Phys. Chem.* **206**, 271.
- Bockris, J. O'M., and A.K.N. Reddy (1970). *Modern Electrochemistry*, Vols 1 and 2, Plenum Press, New York.
- Boistelle, R. and J.P. Astier (1988). *J. Cryst. Growth* **90**, 14.
- Booth, N.A., A.A. Chernov and P.G. Vekilov (2002a). *J. Cryst. Growth* **273/239**, 1818.
- Booth, N.A., B. Stanojev, A.A. Chernov, and P.G. Vekilov (2002b). *Rev. Sci. Instrum.* **73**, 3540.
- Brice, J.C. (1973). *The Growth of Crystals from Liquids*, North-Holland, Amsterdam.
- Burton, W.K., N. Cabrera, and F.C. Frank (1951). *Philos Trans. Ry. Soc. London A* **243**, 299.
- Cahn, J.W. (1960). *Acta Metall.* **8**, 556.
- Chernov, A.A. (1961). *Usp. Fiz. Nauk* **73**, 277; Engl. Transl.: *Sov. Phys. Usp.* **4**, 116.
- Chernov, A.A. (1984). *Modern Crystallography III: Crystal Growth*, Springer, Berlin.
- Chernov, A.A., L.N. Rashkovich, and A.A. Mkrtchyan (1986a). *J. Cryst. Growth* **74**, 101.
- Chernov, A.A., L.N. Rashkovich, I.L. Smol'ski, Yu.G. Kuznetsov, A.A. Mkrtchyan, and A.I. Malkin (1986b). *Rost. Krist.* **15**, 43.
- Chu, Y.D., L.D. Shiau, and K.A. Berglund (1989). *J. Cryst. Growth* **97**, 689.
- Davey, R.J. (1979). In: E.J. de Jong and S.J. Jančić, (Eds.), *Industrial Crystallization* 78, North-Holland, Amsterdam, p. 169.
- Davey, R.J., W. Fila, and J. Garside (1986). *J. Cryst. Growth* **79**, 607.
- Dove, P.M., J.J. De Yoreo, and K.J. Davis (2004). In: X.Y. Liu and J.J. De Yoreo (Eds.), *Nanoscale Structure and Assembly at Solid–Fluid Interfaces, Vol. II: Assembly at Hybrid and Biological Systems*, Kluwer, Boston, Chap. 2, p. 55.
- Elwenspoek, M. (1986a). *J. Cryst. Growth* **78**, 353.
- Elwenspoek, M. (1986b). *Appl. Phys. A* **41**, 123.
- Elwenspoek, M., and J.P. van der Eerden (1987). *J. Phys. A: Math. Gen.* **20**, 669.
- Fawcett, W.R., and T.G. Smagala (2006). *Langmuir* **22**, 10635.
- Fenter, P., P. Geissbühler, E. DiMasi, G. Srager, L.B. Sorensen, and N.C. Sturchio (2000). *Geochim. Cosmochim. Acta* **64**, 1221.
- Frank, F.C. (1981). *J. Cryst. Growth* **51**, 367.
- Gilmer, G.H., and K.A. Jackson (1976). In: E. Kaldis and H.J. Scheel (Eds.), *Current Topics in Materials Science*, Vol. 1, North-Holland, Amsterdam, p. 79.
- Hartman, P., and W.G. Perdok (1955). *Acta Crystallogr* **8**, 49, 521.
- Jackson, K.A. (1958). In: M. Madden (Ed.), *Liquid Metals and Solidification*, ASM, Cleveland OH, p. 174.
- Kaldis, E. (1976). In: C.H.L. Goodman (Ed.), *Crystal Growth: Theory and Techniques*, Vol. 1, Plenum Press, London, p. 49.
- Kaminski, D., N. Radenović, M.A. Deij, W.J.P. van Enckevort, and E. Vlieg (2005). *Phys. Rev. B* **72**, art. no. 245404.
- Kaminski, D., N. Radenović, M.A. Deij, W.J.P. van Enckevort, and E. Vlieg (2006). *Cryst. Growth Des.* **6**, 588.
- Keller, K.W. (1975). In: R. Ueda and J.B. Mullin (Eds.), *Crystal Growth and Characterization*, North-Holland, Amsterdam, p. 361.
- Kern, R. (1967). In: N.N. Sheftal (Ed.), *Rost Kristallov (Growth of Crystals)*, Vol. 8, Nauka, Moscow, 1967, p. 5.

- Kipp, S., and R. Lacmann (1996). *J. Cryst. Growth* **160**, 320.
- Kipp, S., R. Lacmann, and M.A. Schneeweiss (1994). *J. Cryst. Growth* **141**, 291.
- Kirkova, E.K., and R.D. Nikolaeva (1973). *Krist. Tech.* **8**, 463.
- Kurihara, K., S. Miyashita, G. Sazaki, T. Nakada, Y. Suzuki, and H. Komatsu, (1996). *J. Cryst. Growth* **166**, 904.
- Kuznetsov, Yu.G., D.L. Makino, A.J. Malkin, and A. McPherson (2005). *Acta Crystallogr. D* **61**, 720.
- Land, T.A., J.J. De Yoreo, and J.D. Lee (1997). *Surf. Sci.* **384**, 137.
- Liu, X.Y., K. Maiwa, and K. Tsukamoto (1997). *J. Chem. Phys.* **106**, 1870.
- Malkin, A.I., A.A. Chernov, and I.V. Alexeev (1989). *J. Cryst. Growth* **97**, 765.
- Malkin, A.J., Y.G. Kuznetsov, and A. McPherson (1999). *J. Cryst. Growth* **196**, 471.
- McPherson, A., Yu.G. Kuznetsov, A. Malkin, and M. Plomp (2003). *J. Struct. Biol.* **142**, 32.
- Mielniczek-Brzóska, E., and K. Sangwal (2004). *Cryst. Res. Technol.* **39**, 993.
- Ohara, M., and R.C. Reid (1973). *Modeling Crystal Growth Rates from Solutions*. Prentice-Hall, Englewood Cliffs, NJ.
- Onuma, K., T. Kameyama, and K. Tsukamoto, (1994). *J. Cryst. Growth* **137**, 610.
- Onuma, K., K. Tsukamoto, and I. Sunagawa (1990). *J. Cryst. Growth* **100**, 125.
- Onuma, K., A. Ito, T. Tateishi, and T. Kameyama (1995a). *J. Cryst. Growth* **148**, 201.
- Onuma, K., A. Ito, T. Tateishi, and T. Kameyama (1995b). *J. Cryst. Growth* **154**, 118.
- Radenović, N., D. Kaminski, W. van Enckevort, S. Graswinckel, I. Shah, M.I. t'Velt, and E. Vlieg (2006). *J. Chem. Phys.* **124**, art. no. 164706.
- Rashkovich, L.N., A.A. Mkrtchyan, and A.A. Chernov (1985). *Kristallografiya* **30**, 380.
- Ristić, R., B.Yu. Shekunov, and J.N. Sherwood (1994). *J. Cryst. Growth* **139**, 336.
- Sangwal, K. (1994). In: K. Sangwal (Ed.), *Elementary Crystal Growth*, Saan, Lublin, Chap. 4, p. 83.
- Sangwal, K. (1998a). *Prog. Cryst. Growth Charact. Mater.* **36**, 163.
- Sangwal, K. (1998b). *J. Cryst. Growth* **192**, 200.
- Sangwal, K., and R. Rodriguez-Clemente (1991). *Surface Morphology of Crystalline Solids*, Trans Tech, Zurich.
- Sasaki, G., T. Matsui, Tsukamoto, K., N. Usami, T. Ujihara, K. Fujiwara, and K. Nakajima (2004). *J. Cryst. Growth* **264**, 536.
- Sherwood, J.N., and T. Shripathi (1988). *J. Cryst. Growth* **88**, 358.
- Sunagawa, I., K. Tsukamoto, K. Maiwa, and K. Onuma (1995). *Prog. Cryst. Growth Charact. Mater.* **30**, 153.
- Teng, H.H., P.M. Dove, and J.J. De Yoreo (2000). *Geochim. Cosmochim. Acta* **64**, 2255.
- van der Erden, J.P. (1993). In: D.T.J. Hurle (Ed.), *Handbook of Crystal Growth*, Vol. 1, Elsevier, Amsterdam, Chap. 6, p. 307.
- van der Eerden, J.P., P. Bennema, and T.A. Cherpanova (1978). *Prog. Cryst. Growth Charact.* **1**, 219.
- van Enckevort, W.J.P. (1984). *Prog. Cryst. Growth Charact.* **9**, 1.
- van Erk, W., H.J.G.J. van Hoek-Martens, and G. Bartles (1980). *J. Cryst. Growth* **48**, 621.
- Veintemillas-Verdaguer, S. (1996). *Prog. Cryst. Growth Charact. Mater.* **32**, 75.
- Verma, A.R. (1953). *Crystal Growth and Dislocations*, Butterworth, London.

4

Effect of Impurities on Crystal Growth Kinetics

When the growth rates of F faces of a crystal are studied as a function of supersaturation σ in a growth medium containing impurities, it is found that, even at the same value of concentration, some impurities retard the face growth rate R of the crystal, whereas others lead to an increase in R . A similar behavior is observed in the case of displacement velocities v of steps on the F faces of crystals as a function of σ . In this chapter, our present understanding of the kinetics of growth of crystals in the presence of impurities is surveyed. The effects of impurities on three-dimensional nucleation and metastable zone width are discussed in Chapter 2, the appearance of threshold supersaturations associated with sudden changes in step velocity v and face growth rate R in $v(\sigma)$ and $R(\sigma)$ plots in the presence of impurities and their dependence on the concentration and chemical nature of impurities are described in Chapter 5, and the mechanisms of capture of impurities by a growing crystal and the dependence of the effective segregation coefficient k_{eff} of impurities on supersaturation σ and impurity concentration c_i are presented in Chapter 9. Here the term ‘impurities’ means any foreign substance other than the solute deliberately added to or inherently present in a growth medium. The role of solvent is discussed in Chapter 7 on the morphology of crystals.

4.1 Mobile and Immobile Impurities

The kinetic picture of adsorption of particles from a growth medium on the flat (F) face of a crystal is similar to that of adsorption of gas atoms/molecules (de Boer, 1953; Sangwal, 1999). For example, during growth solute molecules reach the surface and stay there for

a certain length of time, after which they redissolve in the supersaturated medium. The time τ_{ad} of adsorption is given by the Frenkel equation:

$$\tau_{\text{ad}} = \tau_0 \exp(Q_{\text{ad}}/R_G T) \quad (4.1)$$

where τ_0 is the time of oscillation of the molecules in the adsorbed state and is usually called as adsorption or residence time, R_G is the gas constant, T is the temperature in kelvin and Q_{ad} is the heat of adsorption, which is the amount of heat liberated when the molecule is brought from the bulk medium to the adsorbed state. Obviously, at a given temperature τ_{ad} strongly depends on Q_{ad} .

The adsorbed molecules undergo migration along the surface during the time τ_{ad} . The process of migration involves the hopping of a molecule with an average time τ_{smig} when it picks up an energy ΔQ_{smig} , from one adsorption site to another on the surface. The residence time τ_{smig} for the adsorbed molecules is related with ΔQ_{smig} by

$$\tau_{\text{smig}} = \tau'_0 \exp(Q_{\text{smig}}/R_G T) \quad (4.2)$$

where the time τ'_0 is of the order of τ_0 .

From Equations (4.1) and (4.2), one can obtain an expression for the surface diffusion distance λ_s for the adsorbed molecule in the form

$$\lambda_s = a \tau_{\text{ad}} / \tau_{\text{smig}} = a \exp[(Q_{\text{ad}} - \Delta Q_{\text{smig}})/R_G T] \quad (4.3)$$

where a is the distance between equivalent adsorption sites on the surface. From Equation (4.3), it follows that when $Q_{\text{ad}} > \Delta Q_{\text{smig}}$, $\lambda_s > a$ and the solute molecules are mobile. However, when $Q_{\text{ad}} = \Delta Q_{\text{smig}}$, $\lambda_s = a$ and the solute molecules remain immobile.

The above ideas of adsorption of solute molecules on the surface and their diffusion may equally be applied to the adsorption of impurity particles during the growth of crystals from a supersaturated medium containing an impurity. However, during the processes of adsorption of impurity molecules on, and their migration over, the surface the impurity molecules constantly collide with solute molecules on the surface and, therefore, their movement is somewhat restricted. This restricted motion affects the value of λ_s but the basic picture of adsorption remains practically unchanged.

A growing F face consists of steps (ledges) and the steps have kinks on them (Section 3.2). Therefore, as in the case of solute molecules, during growth kinks and steps are preferential sites for the capture of impurity particles wandering over the growing surface (Figure 4.1). Consequently, the kinetic effect of an impurity on step velocity v and face growth rate R may be considered to involve three stages:

- (1) Adsorption (temporary capture) at the surface of impurity particles diffusing from the bulk growth medium (adsorption heat Q_{ad}).
- (2) Migration of impurity admolecules on the surface terrace (energy ΔQ_{smig}).
- (3) Adsorption of impurity molecules, migrating on the surface, at kink-free areas of steps (free energy change Q_{step}) and at kinks in steps (free energy Q_{kink}).

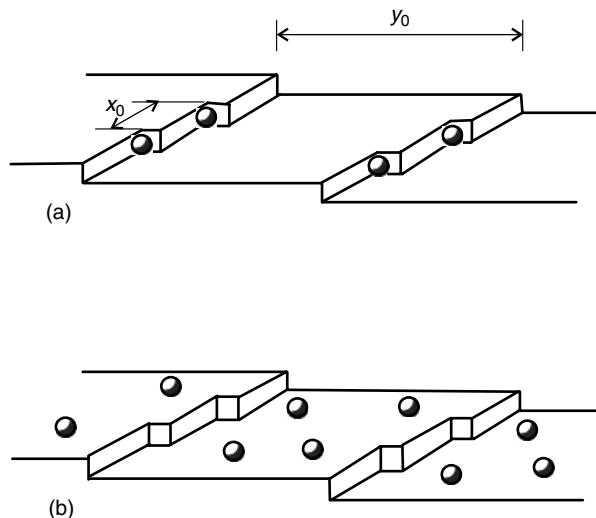


Figure 4.1 Illustration of adsorption of impurity particles at (a) kinks and (b) surface terrace on the F face of a crystal. In (a) y_0 denotes the average distance between steps on a surface terrace and x_0 is the average distance between kinks in a step

The relative values of the above three energies determine the site and mode of adsorption of impurities (Figure 4.1). The following situations are possible:

- (1) When Q_{ad} is comparable to ΔQ_{smig} irrespective of the values of Q_{step} or Q_{kink} , impurity adsorption occurs at the surface terrace.
- (2) When Q_{ad} is relatively high in comparison with ΔQ_{smig} , the adsorbed impurity molecules are mobile on the surface and can be subsequently adsorbed at kink-free areas of steps and also at their kinks with free energy changes Q_{step} and Q_{kink} , respectively. Since $Q_{\text{step}} < Q_{\text{kink}}$, adsorption of migrating impurity molecules is always favored at kinks.
- (3) When $Q_{\text{kink}} \gg Q_{\text{step}}$, the impurity molecules directly diffuse to the kinks and adsorb there instead of adsorbing on the surface.

During an analysis of the kinetics of the growth of crystals from solutions in the absence of impurities, Sangwal (1998a, b) concluded that BCF surface diffusion model applies for such systems. Therefore, it may be believed that surface diffusion is also important during growth from solutions containing impurities. Consequently, situation (3) involving direct integration of impurity particles to kinks may be neglected, at least in the case of growth from solutions.

It should be noted that Kubota–Mullin model essentially describes situations (2) and (3) of adsorption of impurity particles (see Section 4.3.3). However, their model does not consider explicitly impurity adsorption at kinks. Instead, it assumes that impurity particles are firmly adsorbed along the steps and act as stoppers for their displacement. The above considerations show that the Kubota–Mullin model is physically possible in the case of mobile impurities adsorbing at kinks in steps. The Cabrera–Vermilyea model, on the other hand, describes impurity adsorption on the surface terrace (immobile

impurities). The so-called tailor-made impurities are an extreme case of adsorption on the surface terrace when $Q_{\text{ad}} \leq \Delta Q_{\text{smig}}$, $\lambda_s \leq a$. The models of impurity adsorption are described in Section 4.3.4.

4.2 Surface Coverage and Adsorption Isotherms

In order to discuss the effect of impurities on growth kinetics, it is useful to introduce a parameter θ characterizing the coverage of the surface sites available for adsorption. Here, it is assumed that the adsorption of impurity molecules is confined to the layer in the immediate vicinity of the crystal surface. It is assumed that there are no vertical and horizontal interactions between the adsorbing impurity molecules.

The number n_{max} of sites available for adsorption per unit area of a surface at given growth conditions is constant, but, for a particular concentration of impurity, a fraction θ of the n_{max} sites available for adsorption is occupied by the impurity particles. Corresponding to a given concentration c_i of the impurity, if the number of adsorption sites occupied per unit area on the surface at a particular temperature is n_{ad} , the coverage of adsorption sites θ may be expressed by

$$\theta = n_{\text{ad}} / n_{\text{max}} \quad (4.4)$$

In the absence of an impurity, the available adsorption sites on the surface are empty, i.e. $n_{\text{ad}} = 0$ and $\theta = 0$. With an increase in impurity concentration, θ increases until $\theta = 1$, when all adsorption sites are occupied.

When vertical and horizontal interactions occur between adsorbing impurity molecules, the impurity particles form pairs, trimers and larger aggregates around some adsorption sites. In this case, depending on the concentration of impurity particles adsorbed at the possible adsorption sites, n_{ad} can exceed n_{max} and $\theta > 1$. Such a process can lead to the formation of a two-dimensional layer of the adsorbed impurity. Thus, with increasing impurity concentration, one has two situations, namely $\theta < 1$ and $\theta > 1$.

Usually a small amount of an impurity is sufficient to modify the growth habit and growth kinetics of crystals. Therefore, it can be understood that $\theta < 1$ for such low concentrations of impurities.

The parameter θ is essentially similar to the surface coverage θ of adsorption isotherms and the conventional adsorption isotherms can be used to describe the dependence of θ on impurity concentration c_i . Usually Langmuir, Temkin and Freundlich isotherms are used to describe and analyze the data on growth kinetics in the presence of impurities, but because of its simplicity, the Langmuir adsorption isotherm is traditionally employed. These isotherms are frequently used to describe chemical adsorption, which is highly localized and is restricted to the monomolecular adsorption layer. However, they are also valid for physical adsorption processes.

In the literature dealing with the growth kinetics of crystals in the presence of impurities, simple adsorption isotherms involving the adsorption of impurity particles alone on potential adsorption sites are considered, although solute molecules also adsorb on the growing surface. The main cause of this approach is associated with the fact that it is easy to handle growth rate expressions based on simple adsorption isotherms

because they contain one parameter characterizing the adsorption behavior of the impurity (Sections 4.3.3 and 4.3.4). An additional problem lies when two different impurities are present in a growth medium: then both impurities compete with each other to occupy the same adsorption sites (Section 4.3.6).

Recently, Martins *et al.* (2006) have developed theoretical expressions based on the competitive adsorption of solute and impurity molecules to describe the growth kinetics of crystals growing from solutions. In fact, the concept of competitive adsorption has been used earlier to describe the segregation of impurities in growing crystals (Guzman *et al.*, 1998; Sangwal and Palczyńska, 2000; Sangwal *et al.*, 2000) (see Chapter 9). However, in the present monograph simple adsorption isotherms are used when describing the kinetic effects of impurities.

4.2.1 Adsorption Isotherms

Langmuir Isotherm

The Langmuir adsorption isotherm is based on the postulate that the adsorption sites have the same activity and the differential heat of adsorption Q_{diff} does not depend on surface coverage θ . According to the Langmuir isotherm, the surface coverage θ is given by (see, for example, Eggers *et al.*, 1964; Oćcik, 1982)

$$\theta = K c_i / (1 + K c_i) \quad (4.5)$$

where the Langmuir constant K is given by (Davey and Mullin, 1974; Oćcik, 1982)

$$K = \exp(Q_{\text{diff}}/R_G T) \quad (4.6)$$

and Q_{diff} is the differential heat of adsorption corresponding to the coverage θ . At small impurity concentrations or for small K when $K c_i \ll 1$,

$$\theta = K c_i \quad (4.7)$$

This linear relationship is Henry's equation.

The differential heat of adsorption Q_{diff} is equal to the heat of adsorption of molecules adsorbed on the surface directly minus the heat of dissolution of the adsorbed molecules (i.e. $Q_{\text{diff}} = Q_{\text{ad}} - Q_{\text{des}}$). Note that $Q_{\text{diff}} \neq Q_{\text{ad}}$, where the heat of adsorption Q_{ad} is given by Equation (4.1).

Temkin Isotherm

The Temkin isotherm assumes that the differential heat of adsorption Q_{diff} depends on the surface coverage θ . It satisfactorily describes chemical adsorption processes at intermediate coverages (i.e. $\theta \approx 0.5$). According to the Temkin adsorption isotherm (Eggers *et al.*, 1964)

$$\theta = Z \ln C_0 + Z \ln c_i \quad (4.8)$$

where

$$C_0 = \exp(Q_{\text{diff}}^0/R_G T) \quad (4.9)$$

and

$$Z = R_G T / b Q_{\text{diff}}^0 = 1 / b \ln C_0 \quad (4.10)$$

In Equation (4.9), Q_{diff}^0 is the initial heat of adsorption corresponding to $\theta \rightarrow 0$, and is related to Q_{diff} by

$$Q_{\text{diff}} = Q_{\text{diff}}^0 (1 - b\theta) \quad (4.11)$$

where the constant $b < 1$.

Freundlich Isotherm

When the active adsorption sites are of different adsorption energy, the total coverage is the sum of coverage on each type of sites, i.e.

$$\theta = \sum_i f_i \theta_i \quad (4.12)$$

where f_i is the fraction of sites i corresponding to the coverage θ_i . For an exponential distribution of adsorption sites as a function of adsorption energy, the total coverage is given by (Eggers *et al.*, 1964)

$$\theta = m (c_i / c_i^*)^m \quad (4.13)$$

where

$$m = k_B T / \varepsilon_m \quad (4.14)$$

and c_i^* is the impurity concentration corresponding to $\theta = 1$. In Equation (4.14), ε_m is a measure of the distribution of energies of adsorption sites. The differential heat of adsorption Q_{diff} and the energy constant ε_m are related by (Eggers *et al.*, 1964)

$$Q_{\text{diff}} = -\varepsilon_m \ln \theta \quad (4.15)$$

Since $\theta < 1$ and $m > 0$, Q_{diff} given by Equation (4.15) is always a positive quantity.

Equation (4.13) may be given in a more practical form:

$$\theta = K_1 c_i^m \quad (4.16)$$

where

$$K_1 = m / c_i^{*m} \quad (4.17)$$

When $m = 1$, Equation (4.16) reduces to Henry's equation [see Equation (4.7)] with $K = K_1 = 1/c_i^*$ and Q_{diff} is given by Equation (4.6).

4.2.2 Changes in Surface Free Energy by Adsorption of Impurities

It is well known (see, for example, Eggers *et al.*, 1964; Oćcik, 1982) that the surface free energy (precisely: surface tension) of a liquid (solvent) undergoes a change when another liquid is added to it, and even small amounts c_i of the latter liquid lead to dramatic changes when the surface energies of the two liquids differ significantly. In the case of aqueous solutions of organic solutes, the decrease in the surface energy is given by Szyszkowski's empirical equation:

$$(\gamma_0 - \gamma)/\gamma_0 = B \ln(1 + Ac_i) \quad (4.18)$$

where γ_0 is the surface free energy of the pure liquid (solvent) and γ is that of the solution (i.e. the solvent containing the solute), and A and B are constants. Substances which lead to a change in the surface tension of the solution are called *surface active* or *surfactants*. Depending on whether the surface tension γ_0 of the solvent is higher or lower than that of the added substance, the added substances can decrease or increase the surface tension γ of the solution [i.e. the difference $\Delta\gamma = (\gamma_0 - \gamma) > 0$ or $\Delta\gamma < 0$, respectively]. This means that the surface activity of an added substance depends on its property and also the nature of the solvent. Surface-active substances have asymmetric molecules composed of polar groups such as $-OH$, $-COOH$, $-NH_2$ and $-SO_3H$, which undergo easy solvation in water, and also nonpolar molecules composed of, for example, long hydrocarbon chains.

The constant A is called the specific capillary activity and is characteristic of the additive, and B is given by (Oćcik, 1982)

$$B = \Gamma_{2\infty} R_G T / \gamma_0 \quad (4.19)$$

where $\Gamma_{2\infty}$ is the excess surface concentration of the adsorbing substance corresponding to complete coverage in the surface layer, and is related to the constant $\omega_m = 1/\Gamma_{2\infty} N_A \approx 0.3 \text{ nm}^2$ for various surface-active molecules of asymmetric structure.

The above concept can equally well be extended to the adsorption of impurities on the surfaces of crystals. In the solvent used for growth, if the impurity molecules undergo easy solvation in it, the impurity leads to a decrease in the solid–liquid interfacial tension ($\gamma_0 > \gamma$). However, if the impurity molecules do not undergo solvation in it, the impurity leads to an increase in the solid–liquid interfacial tension ($\gamma_0 < \gamma$). The latter situation is especially true in the case of tailor-made impurities. Moreover, it should be noted that a change in the solid–liquid interfacial tension caused by an impurity is accompanied by a change in the solubility of the solute (see Section 2.3).

4.3 Kinetic Models of Impurity Adsorption

4.3.1 Earlier Models

In order to explain the decrease in face growth rates R of crystals in the presence of impurities, Bliznakov considered that during growth a part of the possible adsorption sites on the surface is occupied by impurity particles whereas the remaining sites remain

unoccupied (Bliznakov, 1954, 1958, 1965; Bliznakov and Kirkova, 1957). If the face growth rates are R_0 and R_i in the absence and presence of the impurity, respectively, the resulting growth rate R in the presence of an impurity with coverage θ of adsorption sites may be written in the form

$$R = R_0(1 - \theta) + R_i\theta \quad (4.20)$$

or

$$\frac{R}{R_0} = 1 - \left(\frac{R_0 - R_i}{R_0} \right) \theta \quad (4.21)$$

where the fractional surface coverage θ is given by the usual adsorption isotherms.

Chernov (1961, 1984) treated the adsorption of foreign substances in terms of density of kinks in a ledge. According to Chernov, when impurity particles adsorb at kinks, they render them ineffective. Thus, the average distance x_0 between kinks is increased (i.e. their density is decreased), which leads to a decrease in the layer displacement rate v and the linear growth rate R with an increase in impurity concentration. In this case, following the same arguments as those of Bliznakov, one may write

$$\frac{v}{v_0} = 1 - \left(\frac{v_0 - v_i}{v_0} \right) \theta \quad (4.22)$$

where it is assumed that an impurity particle adsorbed at a kink site renders it only partly ineffective. If it is assumed that the face growth rate R is proportional to v , from Equation (4.22) one obtains Bliznakov's Equation (4.21). The face growth rate R is indeed proportional to v in the case of spiral growth mechanism at relatively large supersaturations (Burton *et al.*, 1951; Sangwal, 1994, 1996); Section 3.6.

It should be noted that $0 \leq R_i \leq R_0$ and $0 \leq v_i \leq v_0$ in Equations (4.21) and (4.22). Therefore, depending on the values of R_i and v_i , the factors $(R_0 - R_i)/R_0$ and $(v_0 - v_i)/v_0$ in Equations (4.21) and (4.22) can have values between 0 and 1.

4.3.2 Velocity of Curved Steps

In order to describe the effect of the adsorption of impurity particles on growth kinetics, we consider a train of parallel steps with an average step distance y_0 and an average distance x_0 between kinks in a step (see Figure 3.2). Depending on how the impurity particles pin the motion of steps, there are two extreme possibilities: (1) if the impurity particles are firmly adsorbed on to the surface terrace (i.e. they are immobile), they will physically block the movement of the step, and (2) if the impurity particles are mobile, they will move to the kinks and not only block the integration of solute molecules to the kinks but also block the movement of advancing steps by the pinning mechanism. When the advancing step contacts an impurity particle, it tends to curl around it. The step will stop when the average distance between the adsorbed particles $L < 2r_{2D}^*$ [where r_{2D}^* is the radius of the critically sized two-dimensional nucleus on the surface; see Equations (3.28) and (4.31)], while it will squeeze between a pair of neighboring impurity particles when $L > 2r_{2D}^*$. The configuration of advancing straight steps is thus modified by the adsorbed

impurity particles and their average velocity v in the presence of the impurity becomes smaller than the velocity v_0 in the absence of the impurity. The mechanism of blocking of the movement of a step ledge by two firmly attached impurity particles is illustrated in Figure 4.2.

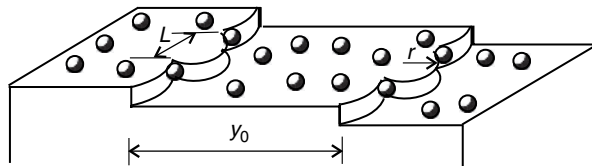


Figure 4.2 Blocking of the movement of a step ledge by two firmly attached impurity particles

The above general ideas may be quantified by considering the relationship between the advancement velocity v_r of a curved step and the radius r of the curvature of the step (Burton *et al.*, 1951):

$$v_r/v_0 = 1 - r_{2D}^*/r \quad (4.23)$$

where the critical radius of a two-dimensional nucleus given by [see Equation (3.31)]

$$r_{2D}^* = \gamma_l a / k_B T \sigma \quad (4.24)$$

and v_0 is the velocity of a linear step. In Equation (4.24) γ_l is the linear edge free energy ($\gamma_l \approx \gamma a^2$, where γ is the surface free energy and $a \approx \Omega^{1/3}$ is the diameter of the host particle), k_B is the Boltzmann constant, and T is the temperature in kelvin. When the step squeezes out between two neighboring impurity particles adsorbed at an average distance L , its radius of curvature changes with time. This leads to a decrease in the instantaneous velocity of the step with time. The minimum velocity v_{\min} corresponding to the curvature $r = L/2$ is given by

$$v_{\min}/v_0 = 1 - 2r_{2D}^*/L \quad (4.25)$$

In the absence of impurity, $L \rightarrow \infty$, and there is a maximum velocity $v_{\max} = v_0$. Thus, in the presence of an impurity, there is an average step velocity v over time.

The time-averaged step velocity can be taken in two ways: (1) $v = (v_{\min}v_0)^{1/2}$ and $v = (v_0 + v_{\min})/2$. The former average velocity is the basis of the model of impurity adsorption proposed by Cabrera and Vermilyea (1958), whereas the latter is connected with the model advanced by Kubota and Mullin (1995). However, it should be emphasized that both of these models deal only with the kinetic aspect of the adsorption of impurities on F faces of crystals and entirely neglect the thermodynamic aspect.

4.3.3 Impurity Adsorption at Kinks in Steps: Kubota–Mullin Model

Here we take the arithmetic mean velocity. Then from Equations (4.23) and (4.25), one obtains (Kubota *et al.*, 2000; Sangwal, 1999, 2002)

$$v/v_0 = 1 - r_{2D}^*/L \quad (4.26)$$

while $v = 0$ for $L \leq r_{2D}^*$.

When adsorption occurs at kinks, the linear coverage θ_l of kink sites in the ledges by impurity particles is equal to the fractional coverage θ_s of the surface, and may be expressed by

$$\theta_l = x_0/L \quad (4.27)$$

where the average distance x_0 between active adsorption sites (i.e. between kinks) in a step, $x_0 = a/n_{\max}$, and the average distance L between adsorbed impurity particles, $L = a/n_{\text{ad}}$. Then Equation (4.26) may be written in the form

$$v/v_0 = 1 - \alpha_l \theta_l \quad (4.28)$$

where the impurity effectiveness parameter α_l is given by

$$\alpha_l = \frac{\sigma_l^0}{\sigma} = \left(\frac{\gamma_l a}{k_B T x_0} \right) \frac{1}{\sigma} \quad (4.29)$$

In Equation (4.28), the surface coverage θ by the impurity may be described by the usual adsorption isotherms (see Section 4.2). Then the final expressions are as follows.

Langmuir isotherm:

$$\frac{v}{v_0} = 1 - \alpha_l \left(\frac{Kc_i}{1 + Kc_i} \right) \quad (4.30)$$

or

$$\frac{v_0 - v}{v_0} = \frac{1}{\alpha_l} \left(1 + \frac{1}{Kc_i} \right) \quad (4.31)$$

When $Kc_i \ll 1$,

$$v/v_0 = 1 - \alpha_l Kc_i \quad (4.32)$$

Temkin isotherm:

$$v/v_0 = 1 - \alpha_l Z(\ln C_0 + \ln c_i) \quad (4.33)$$

or

$$(v_0 - v)/v_0 = \alpha_l Z(\ln C_0 + \ln c_i) \quad (4.34)$$

When $\ln(c_i/C_0) \approx (c_i/C_0) - 1$, Equation (4.34) reduces to the linear form:

$$v/v_0 = 1 - (\alpha_l/bC_0)c_i \quad (4.35)$$

where the constant $b < 1$ [see Equation (4.11)]. This equation is of the same form as Equation (4.32), and the constant $1/bC_0 = K$.

Freundlich isotherm:

$$v/v_0 = 1 - Bc_i^m \quad (4.36)$$

where

$$B = \alpha_l m / c_i^{*m} \quad (4.37)$$

Equation (4.36) reduces to Equation (4.32) when $m = 1$. Then $1/c_i^* = K$.

It should be noted that Equation (4.28) is similar to Equation (4.21) given by Bliznakov, where the impurity effectiveness parameter

$$\alpha_l = (R_0 - R_i)/R_0 \quad (4.38)$$

However, the two models differ from each other in the following respects:

- (1) In Bliznakov's equation $0 \leq R_i \leq R_0$. Therefore, depending on the value of R_i , the impurity effectiveness parameter can have values between 0 and 1.
- (2) In the Kubota–Mullin model, $0 \leq \alpha_l \leq \infty$. When $\sigma_l^0 \ll \sigma$, $\alpha_l \rightarrow 0$; when $\sigma_l^0 \gg \sigma$, $\alpha_l \rightarrow \infty$. The former situation is possible when the ratio $a/x_0 \ll 1$ and σ is relatively high, while the latter situation is achieved when $a/x_0 \rightarrow 1$ and σ is low.

From the above discussion, it may be concluded that Bliznakov's model is a special case of the Kubota–Mullin model involving adsorption of impurity particles at kinks in the ledges of an F face.

4.3.4 Impurity Adsorption at Surface Terrace: Cabrera–Vermilyea Model

We assume that the adsorbed particles are immobile in comparison with the mobility of step ledges and the adsorbed particles have an average separation L on a two-dimensional lattice having the possible adsorbed sites with an average distance λ between them. Then the surface coverage may be given by (Sangwal, 1996, 1999)

$$\theta_s = n_{\text{ad}}/n_{\text{max}} = (\lambda/L)^2 \quad (4.39)$$

From this equation, we take the value of L and substitute in the expression for the time-averaged step velocity v . However, there are two possibilities to calculate the time-averaged step velocity v :

- (a) $v = (v_0 + v_{\min})/2$ as in the Kubota–Mullin model. Then v is given by Equation (4.26).
- (b) $v = (v_0 v_{\min})^{1/2}$ as in Cabrera–Vermilyea model. Then

$$v/v_0 = (1 - 2r_{2D}^*/L)^{1/2} \quad (4.40)$$

We consider these cases below.

Case (a). When v is given by Equation (4.26), one may write (Sangwal, 1999)

$$v/v_0 = 1 - r_{2D}^* \theta_s^{1/2} / \lambda = 1 - \alpha_s \theta_s^{1/2} \quad (4.41)$$

where the new impurity effectiveness parameter α_s is given by

$$\alpha_s = \frac{\sigma_s^0}{\sigma} = \left(\frac{\gamma_l a}{k_B T \lambda} \right) \frac{1}{\sigma} \quad (4.42)$$

When the Langmuir, Temkin and Freundlich adsorption isotherms hold, Equation (4.41) may be written as

$$\left(\frac{v_0}{v_0 - v} \right)^2 = \left(\frac{1}{\alpha_s} \right)^2 \left(1 + \frac{1}{K c_i} \right) \quad (4.43)$$

$$\left(\frac{v_0 - v}{v_0} \right)^2 = \alpha_s^2 Z (\ln C_0 + \ln c_i) \quad (4.44)$$

and

$$\left(\frac{v_0 - v}{v_0} \right)^2 = B_{s1} c_i^m \quad (4.45)$$

respectively. In Equation (4.45), the constant

$$B_{s1} = \alpha_s^2 m / c_i^{*m} \quad (4.46)$$

Obviously, the forms of these equations differ from those of the Kubota–Mullin model by the square-root term originating from the definition of coverage θ_s [see Equation (4.39)].

Case (b). When v is given by Equation (4.40), we have (Sangwal, 1996)

$$v/v_0 = (1 - 2r_{2D}^* \theta_s^{1/2} / \lambda)^{1/2} = (1 - 2\alpha_s \theta_s^{1/2})^{1/2} \quad (4.47)$$

where α_s is given by Equation (4.42). In the case of the Langmuir, Temkin and Freundlich isotherms, Equation (3.47) may be expressed as

$$\left(\frac{v_0^2}{v_0^2 - v^2} \right)^2 = \left(\frac{1}{2\alpha_s} \right)^2 \left(1 + \frac{1}{K c_i} \right) \quad (4.48)$$

$$\left(\frac{v_0^2 - v^2}{v_0^2} \right)^2 = (2\alpha_s)^2 Z (\ln C_0 + \ln c_i) \quad (4.49)$$

and

$$\left(\frac{v_0^2 - v^2}{v_0^2} \right)^2 = (2\alpha_s)^2 m (c_i / c_i^*)^m \quad (4.50)$$

respectively. When $2\alpha_s\theta_s^{1/2} \ll 1$, Equations (4.48), (4.49) and (4.50) transform to Equations (4.43), (4.44) and (4.45), respectively.

Equations (4.43) and (4.44) were derived more recently (Sangwal, 1999), whereas Equations (4.48) and (4.49) were reported earlier (Sangwal, 1996). However, it can be seen that the expressions in cases (a) and (b) differ significantly from each other for relatively high values of $2\alpha_s\theta_s^{1/2}$.

It should be mentioned that the above kinetic equations were obtained for the adsorbed impurity particles forming a roughly square lattice on the surface. Then $L = 2r$ when the curvature is at the minimum. However, in more realistic cases, the adsorbed impurity particles form polygonal lattices. Then the condition for the curvature at the minimum is $L = \xi r$, where $1.5 < \xi < 1.8$ for regular polygons of various geometries (Potapenko, 1993). This correction increases σ_s^0 [see Equation (4.42)] by a factor of $2/\xi$ in the above expressions, but the general conclusions following from them remain unchanged.

4.3.5 Effectiveness Factor for Impurity Adsorption

Equations (4.28), (4.41) and (4.47) contain the impurity effectiveness adsorption factor α_l or α_s that has a deciding effect on the course of the dependence of the relative step velocity v/v_0 on impurity concentration c_i . To illustrate the role of the impurity effectiveness factor, first we consider the nature of $v/v_0(c_i)$ plots for its different values using Equation (4.30), and then discuss the difference between the values of impurity effectiveness factor for adsorption at kinks and surface terrace using Equations (4.28), (4.41) and (4.47).

The plots of the calculated relative step velocities v/v_0 for different values of α_l against a dimensionless impurity concentration Kc_i are shown in Figure 4.3. Three situations may be distinguished. When $\alpha_l > 0$, the step velocity decreases rapidly with increasing impurity concentration, reaching zero even at low values of impurity concentration. When

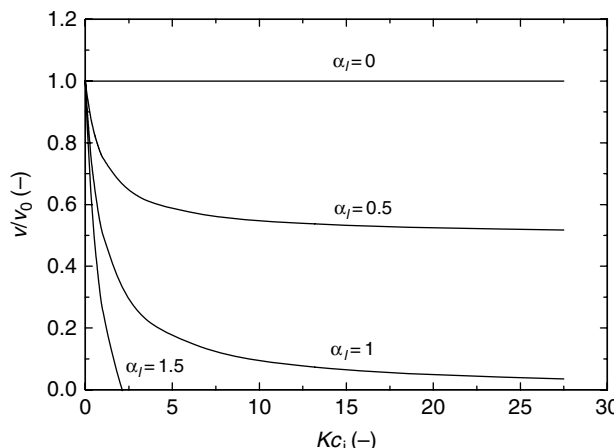


Figure 4.3 Relative step velocities v/v_0 , calculated by Equation (4.30), for different values of α_l against dimensionless impurity concentration Kc_i

$\alpha_l = 1$, the step velocity approaches zero asymptotically. However, when $\alpha_l < 1$, the step velocity never reaches zero as the impurity concentration is increased. These features of α_l are associated with its relationship with fractional coverage θ_l , and with the fact that $\theta_l \leq 1$. When $\alpha_l = 1$ and $\theta_l = 1$, $v = 0$. In other words, growth stops completely at complete fractional coverage. When $\alpha_l > 1$, v approaches zero even for $\theta_l < 1$. However, when $\alpha_l < 1$, v never approaches zero even for $\theta_l = 1$.

The behavior of the impurity effectiveness factor for kink and surface terrace adsorption is compared in Figure 4.4, which shows the plots of relative step velocity v/v_0 versus dimensionless impurity concentration Kc_i . It may be noted that impurity adsorption on a surface terrace (Cabrera–Vermilyea model) predicts more pronounced reduction in v/v_0 in comparison with adsorption at kinks in the steps (Kubota–Mullin model). Moreover, in the case of adsorption at a surface terrace Equation (4.47), based on the geometric mean velocity $(v_{\min} v_0)^{1/2}$, predicts a steeper reduction in step velocity than Equation (4.41) based on the arithmetic velocity $(v_{\min} + v_0)/2$. In the former case, $v/v_0 \rightarrow 0$ at dimensionless impurity concentration $Kc_i = 0.33$. Irrespective of whether one considers the geometric or arithmetic time-averaged velocity, Figure 4.4 clearly shows that surface terrace adsorption is more effective.

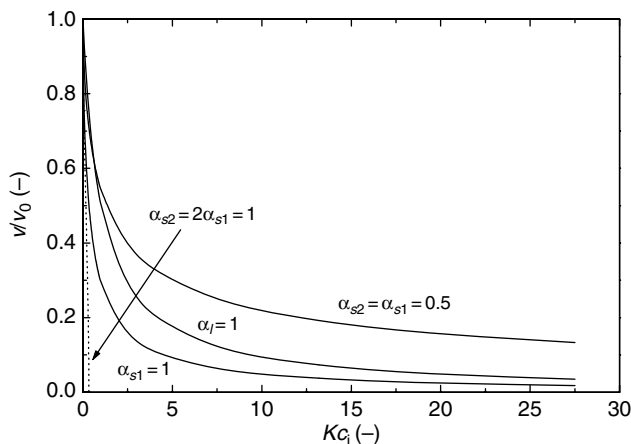


Figure 4.4 Relative step velocities v/v_0 , calculated by Equations (4.28), (4.41) and (4.47), for α_l and α_s against dimensionless impurity concentration Kc_i . α_{s1} and α_{s2} refer to Equations (4.41) and (4.47), respectively

From Equations (4.28), (4.41) and (4.47), it follows that the value of the impurity effectiveness factor α decreases with increase in supersaturation σ and growth temperature T and the quantity $\alpha T \sigma = \gamma_l a / k T x$ is constant for a growth system, where x denotes x_0 or λ . It is found that for a given supersaturation the quantity $\alpha_l T$ for adsorption at kinks is indeed a constant (Sangwal, 1999); for example, see Figure 4.10a. However, at a constant temperature the quantity $\alpha \sigma$ is not always a constant. Figure 4.5 shows the data on α as a function of $1/\sigma$ for three different growth systems, i.e. sucrose containing raffinose, potassium acid phthalate containing Cr(III), and ammonium oxalate monohydrate

containing Cu(II) impurity. It can be seen that the linear dependence of α on $1/\sigma$ is followed only in the case of sucrose. For the other systems, there are deviations from the linear dependence. The linear dependence between α on $1/\sigma$ implies that in the range supersaturation used for the growth of sucrose the step free energy γ_l is independent of supersaturation. However, in the other cases γ_l increases with increase in supersaturation (see below).

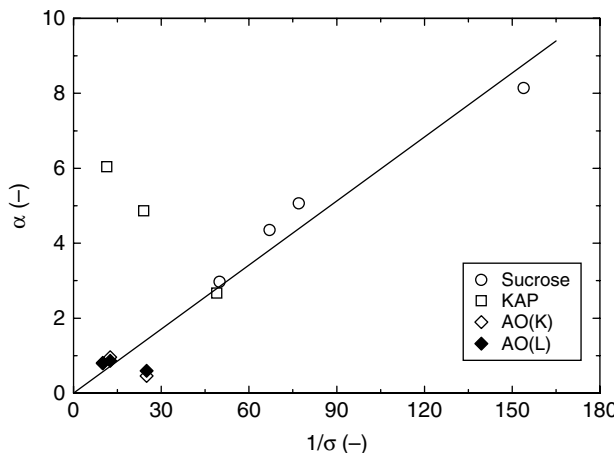


Figure 4.5 Data on impurity effectiveness parameter α plotted as a function of $1/\sigma$ for three different growth systems, i.e. sucrose containing raffinose, potassium acid phthalate (KAP) containing Cr(III), and ammonium oxalate monohydrate (AO) containing Cu(II) impurity. Data from Kubota (2001) and Mielniczek-Brzóska et al. (2000). Values of α for adsorption at kinks and ledges are denoted by K and L , respectively

In the case of crystallization and transformation of polymorphic phases, instead of x_0 and λ , the average separation L between impurity particles is an important parameter. The separation L is related to the average spacing x (i.e. x_0 or λ) between possible adsorption sites and the growth supersaturation σ by [see Equation (4.29)]

$$L = \alpha x = \gamma_l a / k_B T \sigma \quad (4.51)$$

With increasing supersaturation, three cases can be distinguished from this equation for the relationship between L and x . At low σ when $\alpha > 0$, $L > x$. Since $L > 2r_{2D}^*$ in this case, growth will continue. When $\alpha \rightarrow 1$ with an increase in σ , $L \rightarrow x$, and growth stops. However, when $\alpha < 1$ at still higher supersaturations, $L < x$. This apparent impossible situation corresponds to an increase in the linear step free energy γ_l with increasing σ , which leads to the roughening of steps and surface terrace (Bennema and van der Eerden, 1987; Sangwal, 1999). This roughening occurs at a particular supersaturation σ_{cr} given by Equation (3.12). In this situation, the condition $L \rightarrow 2r_{2D}^*$ is always satisfied and there is no growth.

The above arguments are equally valid for adsorption of impurity particles on a surface terrace. From these considerations, it may be concluded that the relationship between the average distance L between impurity particles adsorbed at kinks in steps or on surface terrace and the average distance x_0 between kinks or λ between active surface sites is determined by the supersaturation dependence of the impurity effectiveness factor α_l or α_s .

4.3.6 Adsorption of Two Competing Impurities

In the above cases, it was implicitly considered that only one type of impurity is present in the growth medium. However, in practice it is possible that the number of impurities present in the growth medium is more than one, and they adsorb simultaneously on the growing surface of a crystal. Then one has to consider the simultaneous adsorption of these impurities in the growth kinetics.

For simplicity, we consider only two different types of impurities, say A and B, which compete with each other to adsorb either at kinks or at the surface terrace. We assume that their adsorption follows a mixed Langmuir adsorption isotherm given in the form (Eggers *et al.*, 1964; Oćcik, 1982)

$$\theta_A = (1 - \theta_B) \left(\frac{K_A c_A}{1 + K_A c_A} \right), \quad \theta_B = (1 - \theta_A) \left(\frac{K_B c_B}{1 + K_B c_B} \right) \quad (4.52)$$

where θ_A and θ_B are the coverages of A and B impurities, respectively, c_A and c_B are their concentrations, and K_A and K_B are their adsorption constants given by Equation (4.6).

The average distance L between two neighboring adsorbed impurity particles of A or B along a step per unit length on the surface or on the surface terrace per unit area is given by

$$1/L = 1/L_A + 1/L_B \quad (4.53)$$

where L_A and L_B are the average distances between A and B impurity particles, respectively. Now, depending on whether adsorption occurs at kinks or surface terraces, the relationships between distance L and surface coverage θ are different. In the case of adsorption at kinks,

$$1/L = (\theta_{lA} + \theta_{lB})/x_0 \quad (4.54)$$

whereas in the case of adsorption at a surface terrace,

$$1/L = (\theta_{sA}^{1/2} + \theta_{sB}^{1/2})/\lambda \quad (4.55)$$

where x_0 is the average distance between kinks along a step and λ is the average distance between possible adsorption sites on the surface terrace. Then, using Equations (4.28), (4.41) and (4.47) in combination with Equations (4.54) and (4.55), one may write expressions relating step velocity v and concentration of impurity A or B. Since the expressions in the case of adsorption of two impurities are somewhat complicated due to the sum of

$\theta_A^{1/2}$ and $\theta_B^{1/2}$, we consider here adsorption at kinks only. Then, for the impurity A one obtains

$$\frac{v}{v_0} = 1 - \frac{\sigma_l^0}{\sigma} \left(\frac{K_A c_A + \theta_B}{1 + K_A c_A} \right) \quad (4.56)$$

or, in a more practical form,

$$\frac{v_0}{v_0 - v} = \frac{\sigma}{\sigma_l^0} \left(1 + \frac{1 - \theta_B}{K_A c_A + \theta_B} \right) \quad (4.57)$$

For $\theta_B = 0$, these equations reduce to Equations (4.30) and (4.31), respectively. In Equation (4.56), σ_l^0 is given by Equation (4.29). A similar equation may be written for impurity B.

The influence of the presence of a second impurity, say B, on the relative step velocity v/v_0 , calculated by using Equation (4.56), as a function of dimensionless impurity concentration $K_A c_A$ is shown in Figure 4.6 at different fractional coverages θ_B . It may be noted that the rates for $\theta_B < \text{ca. } 0.05$ differ by less than 3% from the rates for only A impurity but begin to differ substantially for $\theta_B > \text{ca. } 1\%$. The poorly differing relative step rates at $\theta_B < \text{ca. } 0.05$ are vividly recognized when, instead of $v/v_0(K_A c_A)$ plots, $v_0/(v_0 - v)$ is plotted against $(K_A c_A)^{-1}$ [cf. Equation (4.57)], as shown in Figure 4.7. The deviations from the linear dependence predicted for one-impurity systems [i.e. when $\theta_B = 0$ in Equation (4.57); see also Equation (4.31)] appear substantial at low values of $K_A c_A$, and the intercept $1/\alpha_l$ approaches a value of about 2 for $\theta_B = 0.1$ instead of unity for a one-impurity system. These deviations from the linear relation due to the presence of even small concentrations of impurity B become clear when the data in Figure 4.7a are analyzed at high impurity concentrations $K_A c_A$ [i.e. low $(K_A c_A)^{-1}$], as shown in Figure 4.7b.

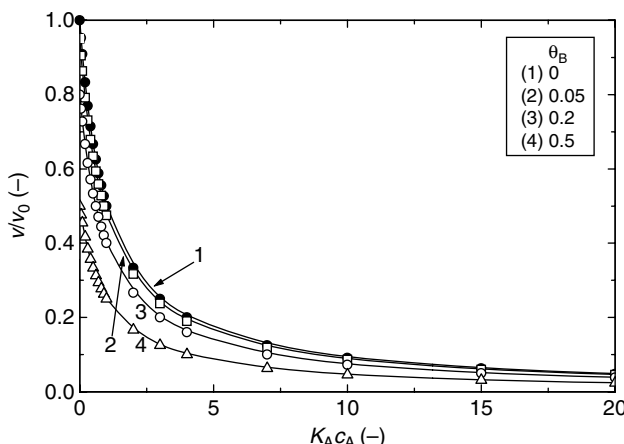


Figure 4.6 Relative step velocities v/v_0 , calculated by Equation (4.56), for different values of θ_B against dimensionless concentration $K_A c_A$ of impurity A

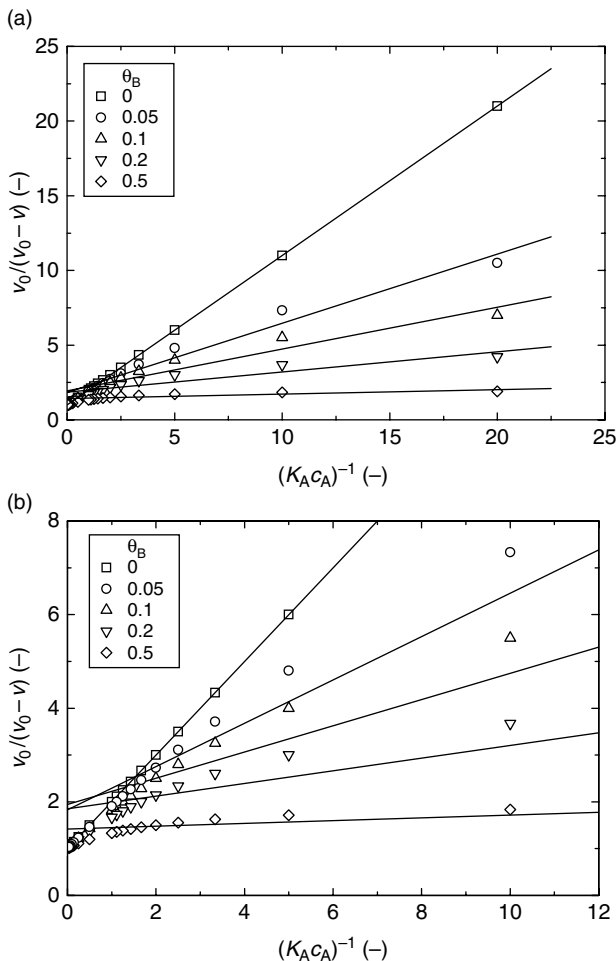


Figure 4.7 (a, b) Plots of $v_0/(v_0 - v)$, calculated by Equation (4.57), for different values of θ_B against $1/K_A c_B$. Linear plots represent the best-fit values of the intercept $1/\alpha_l$ and the slope $(1 - \theta_B)/[\alpha_l(\theta_B + K_A c_A)]$. (b) Enlarged part of (a) in the ranges of low values of $v_0/(v_0 - v)$ and $1/K_A c_B$

It can be seen from Figure 4.7b that the slope of the plot of $v_0/(v_0 - v)$ against $(K_A c_A)^{-1}$ is not constant over the entire range of concentration of impurity A when the system contains another impurity B, and the value of the deviation of the intercept $1/\alpha_l$ from unity is a consequence of this trend. The dependence of the intercept $1/\alpha_l$ and the slope $(1 - \theta_B)/[\alpha_l(\theta_B + K_A c_A)]$ on the surface coverage θ_B is shown in Figure 4.8. Obviously, although the greatest deviation from the linear dependence occurs at $\theta_B = 0.1$, the effect of impurity B on growth rate is very large even at θ_B as low as 0.01. This is so because at $c_i = 1$ ppm, B can adsorb very strongly since $K_B = 10^4$ and $Q_{\text{diff}} = 23$ kJ/mol.

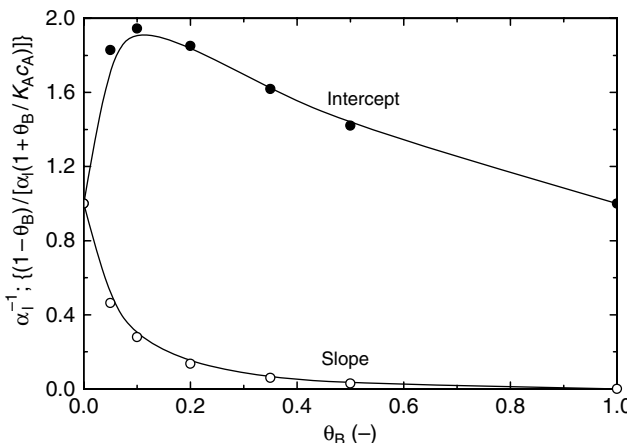


Figure 4.8 Dependence of the best-fit values of the intercept $1/\alpha_i$ and the slope $(1 - \theta_B)/[\alpha_i(\theta_B + K_A C_A)]$ on θ_B , demonstrating that large deviations from the linear dependence occur at $\theta_B < 0.1$.

4.4 Confrontation of Impurity Adsorption Mechanisms with Experimental Data

In the preceding section, the growth kinetics of crystals in the presence of an impurity were described in terms of the dependence of step velocity v on the F faces of crystals on impurity concentration c_i . As mentioned in Section 3.9, experimental investigation of the $v(c_i)$ dependence is relatively difficult due to problems associated with the resolution of steps on the surfaces of crystals, but there are numerous publications devoted to the experimental investigation of the dependence of growth rate R on supersaturation σ for a variety of crystals growing from solutions both in the absence and presence of impurities. When analyzing the experimental $R(\sigma, c_i)$ data from the standpoint of different kinetic models, it is *always* assumed that the growth rate R of a face is proportional to the step velocity v on it.

From the treatment of growth kinetics of crystals in the presence of impurities in Section 4.3 in terms of different isotherms, it is obvious that different relationships between v or R and c_i are possible, depending on the values of the adsorption constants K , C_0 and m of these isotherms and impurity concentration c_i (see Section 4.2.1). The various theoretical relationships indicate that, apart from the distinction between the validity of different isotherms, the dependences of rates v or R on c_i and σ and of the supersaturation barrier $\sigma_{l,s}^*$ on c_i can be used to determine whether a growth system involves impurity adsorption at kinks or at the surface terrace.

Ristić *et al.* (1994) reported experimental data on the step velocity v , determined by Michelson interferometry, on the {111} faces of NaClO₃ crystals at a constant supersaturation $\sigma = 4 \times 10^{-3}$ as a function of c_i of dithionite impurity (S₂O₆²⁻ ions). Figure 4.9a and c show the plots of the dependence of their $v(c_i)$ data, as predicted by using the Langmuir and Temkin isotherms, respectively. Figure 4.9a illustrates the plot of $v_0/(v_0 - v)$ and $v_0^2/(v_0 - v)^2$ against c_i^{-1} and Figure 4.9c presents the plots of $(v_0 - v)/v_0$ and

$[(v_0 - v)/v_0]^2$ against $\ln c_i$ according to the models involving impurity adsorption at kinks and the surface terrace, respectively.

Figure 4.9a reveals that, despite a large scatter in the data at $c_i^{-1} > 0.03 \text{ ppm}^{-1}$, both curves for the kink and surface terrace adsorption may be approximated to two linear parts below and above a transition impurity concentration c_i^{tr} of about 100 ppm ($c_i^{-1} \approx 0.01 \text{ ppm}^{-1}$). This feature may be noted at relatively low c_i^{-1} (i.e. high c_i) in Figure 4.9b, which shows the initial part of Figure 4.9a (close to the origin) at a higher magnification. However, in contrast to the dependences followed in Figure 4.9a and b

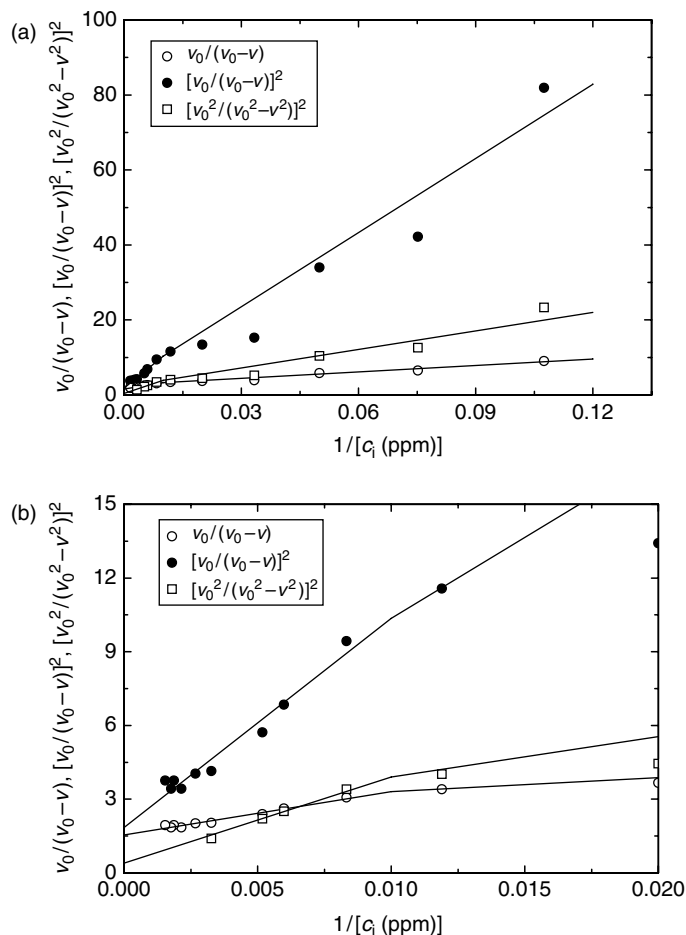


Figure 4.9 Data on step velocity v on the $\{111\}$ faces of NaClO_3 crystals at $\sigma = 4 \times 10^{-3}$ as a function of c_i of dithionite impurity replotted in terms of dependences predicted by (a, b) Langmuir [Equations (4.31), (4.43) and (4.48)] and (c) Temkin isotherms [Equations (4.34) and (4.44)]. Plots of (a, b) $v_0/(v_0 - v)$, $[v_0/(v_0 - v)]^2$ and $[v_0^2/(v_0^2 - v^2)]^2$ against c_i^{-1} and (c) $(v_0 - v)/v_0$ and $[(v_0 - v)/v_0]^2$ against $\ln c_i$. (b) is an enlarged part of (a) close to the origin. Note that in (a, b) the three curves have two linear parts below and above about 100 ppm. Data from Ristić et al. (1994). Adapted from K. Sangwal. J. Cryst. Growth **203**, 197. Copyright (1999), with permission from Elsevier

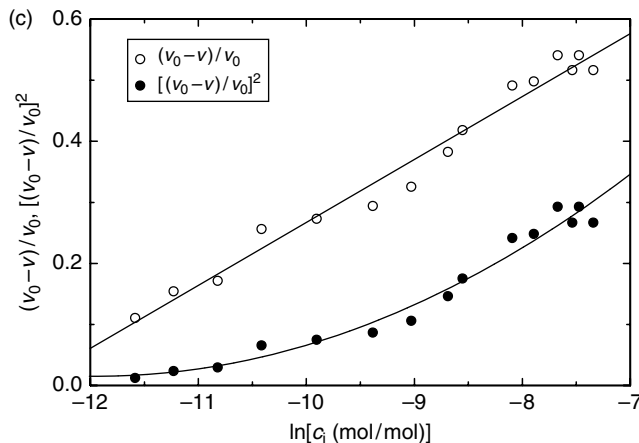


Figure 4.9 (Continued)

for the Langmuir isotherm, Figure 4.9c shows that the plot of $(v_0 - v)/v_0$ against $\ln c_i$ is linear over the entire range of impurity concentration c_i whereas the slope of the plot of $(v_0 - v)^2/v_0^2$ against $\ln c_i$ increases continuously with increasing c_i . Assuming that $\gamma_l/k_B T = 1$, the calculated adsorption parameters for this growth system are given in Table 4.1.

As can be seen from Table 4.1, the correlation coefficients for the two dependences below and above c_i^{tr} are similar. This means that there is little to choose between the kink and surface terrace adsorption mechanisms in the case of the Langmuir adsorption isotherm. Moreover, if one assumes that the Langmuir isotherm holds good in the present system and only one impurity is involved in adsorption, one cannot explain the origin

Table 4.1 Adsorption parameters for the growth of different crystals. Reproduced from K. Sangwal. J. Cryst. Growth **203**, 197. Copyright (1999), with permission from Elsevier

Crystal	Impurity	c_i	Isotherm	Adsorption mechanism	K or C_0 (mol/mol)	Q_{diff} or Q_{diff}^0 ($\times 10^{-3}$) (kJ/mol)	$\sigma_{l,s}^0$ ($\times 10^{-3}$) (kJ/mol)	x_0 or λ	CC
NaClO ₃ S ₂ O ₆ ²⁻	< 100 ppm	Langmuir	Kink		4.1×10^4	26.8	1.64	305a	0.984
			Kink		8.8×10^3	22.9	2.59	193a	0.986
	< 100 ppm	Langmuir	Terrace		3.7×10^5	32.3	2.58	193a	0.970
			Terrace		2.2×10^5	30.0	2.95	170a	0.980
			Kink		2.9×10^5	31.7	—	—	0.987
L-Asp	L-Glu	< 1.2 mmf ^a	Temkin	Kink	5.1×10^4	27.3	—	—	0.939
			Temkin	Terrace	2.1×10^4	25.1	—	—	0.924
TNT	Stilbene	< 0.16 mmf	Langmuir	Kink	2.6×10^5	31.4	< 99.4	10a	0.996
			Langmuir	Terrace	1.2×10^5	29.5	< 99.6	10a	0.997
		Temkin	Kink		2.4×10^{11}	66.0	—	—	0.989
			Terrace		6.2×10^7	45.2	—	—	0.991

^aMillimole fraction (10^{-3} mole fraction).

of the appearance of two linear parts below and above c_i^{tr} (Figure 4.9a and b) and a continuously increasing slope of the plot of $(v_0 - v)^2/v_0^2$ against $\ln c_i$ (Figure 4.9c). These features of the plots may be explained in two ways:

- (1) In the case of growth of the {111} faces of NaClO_3 in the presence of dithionite impurity, the kink adsorption mechanism with the Temkin isotherm holds good.
- (2) As shown in Section 4.3.6, the presence of a trace amount of an unknown impurity in the solution can also lead to the of a transition value of c_i^{tr} .

Bliznakov and Kirkova (1969) reported $R(c_i)$ data for the {100} and {111} faces of NaClO_3 crystals growing from aqueous solutions in the presence of Na_2SO_4 impurity at different temperatures between 10 and 27°C. Figure 4.10a and b show their $R(c_i)$ data in the form of plots of $(R_0 - R)^{-1}$ against c_i^{-1} [Equation (4.31)] for the {100} face and $(R_0 - R)$ against $\log c_i$ [Equation (4.34)] for the {111} face, as predicted by the Langmuir and Temkin isotherms, respectively. Figure 4.10 reveals that the $R(c_i)$ data for the two faces follow the kink adsorption mechanism with different adsorption isotherms.

The examples in Figures 4.9 and 4.10 show that the experimental $v(c_i)$ and $R(c_i)$ data for different faces of the same crystal may follow different isotherms. For example, in the case NaClO_3 crystals growing in the presence of Na_2SO_4 impurity, the {100} faces follow the Langmuir isotherm, whereas the {111} of faces obey the Temkin isotherm. No breaks in the plots are observed for these faces over the entire range of impurity concentration.

Examination of the plots of $R_0/(R_0 - R)$ against $1/c_i$ in Figure 4.10a reveals that their intercept $\sigma/\sigma_l^0 (= 1/\alpha_l)$ increases with temperature and the product $\sigma_l^0 T$ is practically a constant, equal to 10.5 K for $\sigma = 7.17\%$. Since for compounds such as NaClO_3 , $\gamma_l/k_B T \approx 1$ at 300 K, from Equation (4.29) one obtains the interkink distance $x_0 \approx 29a$, which is a reasonable value for the kink adsorption mechanism.

Now some examples of the growth kinetics of organic compounds in the presence of tailor-made impurities are presented. For this purpose, the data for (a) L-asparagine monohydrate (L-Asp) in the presence of L-glutamic acid (L-Glu) (Black *et al.*, 1986), (b) trinitrotoluene (TNT, $n\text{-C}_{36}\text{H}_{74}$) growing in the presence of 2-chloro-2,4,6-trinitrostilbene (stilbene) (Grey *et al.*, 1956; Black *et al.*, 1986), and (c) hexatriacontane (HTC) in the presence of dioctadecylamine (DODA) (Simon *et al.*, 1974) are chosen. In order to deduce the applicability of an adsorption isotherm to describe the growth rate data, the values of correlation coefficient (Table 4.1) and constant $\sigma/\sigma_{l,s}^0$ are considered. Typical plots of $R(c_i)$ data for TNT crystals according to the dependencies predicted by Langmuir and Temkin isotherms are presented in Figure 4.11a and b, respectively.

Analysis of the experimental data revealed (Sangwal, 1999) that the Langmuir isotherm is better followed by TNT crystals (see Figure 4.11a) and the Temkin isotherm by the {110} face of HTC and the {012} faces of L-Asp crystals. Moreover, it was found that in the case of the Langmuir isotherm the impurity effectiveness parameter $\alpha_{l,s} = \sigma_{l,s}^0/\sigma$ is negative for HTC crystals. The physically impossible negative value of $\alpha_{l,s}$ suggests that the Langmuir isotherm does not hold for HTC crystals. In terms of the correlation coefficient, from Table 4.1 one may conclude that impurity adsorption occurs at the surface terrace on the TNT surface but at kink sites on the {012} faces of L-Asp crystals.

Black *et al.* (1986) reported a linear dependence of $(R_0 - R)/R_0$ on impurity concentration c_i for the {101} faces of L-Asp crystals. This dependence follows from

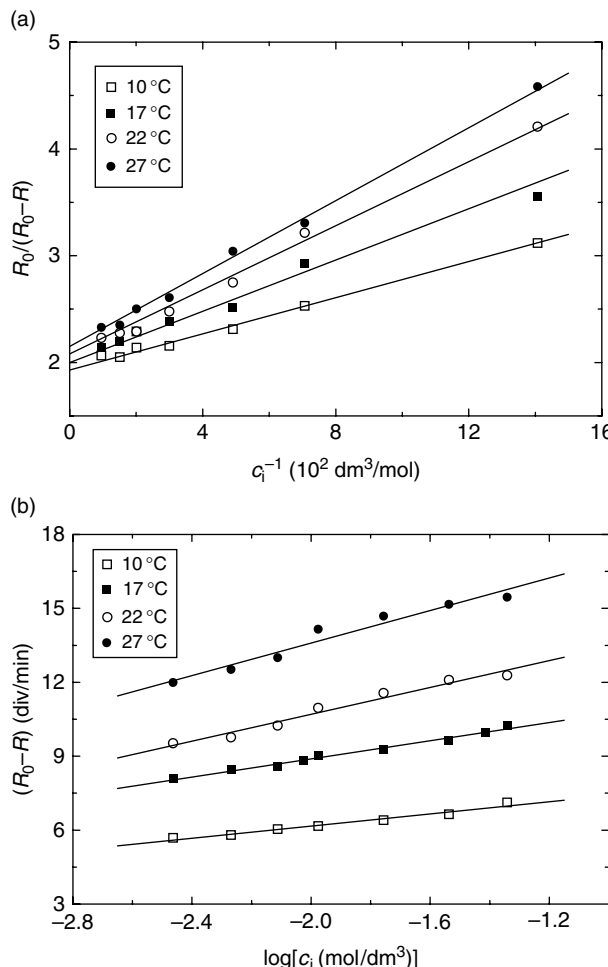


Figure 4.10 Plots of (a) $R_0/(R_0 - R)$ against c_i^{-1} and (b) $(R_0 - R)$ against $\log c_i$ for the $\{100\}$ and $\{111\}$ faces of NaClO_3 crystals grown from aqueous solutions at $\sigma = 7.17\%$, respectively, at different temperature. Adapted from G.M. Bliznakov and E.K. Kirkova. Krist. Tech. **4**, 331. Copyright (1969), with permission from Wiley-VCH

impurity adsorption at kinks in conjunction with the Langmuir adsorption isotherm when $Kc_i \ll 1$ [see Equation (4.32)]. This behavior is different from that on the $\{012\}$ faces.

From the above examples of the growth kinetics of different faces of L-Asp and sodium chlorate crystals, it may be concluded that it is impossible to predict the isotherm that would explain the data for different crystals or for different faces of a crystal. Moreover, as shown by the kinetic data on the $\{012\}$ faces of L-Asp crystals, the correlation coefficient is not a true indicator of the operating adsorption mechanism when a large scatter is involved in the experimental data.

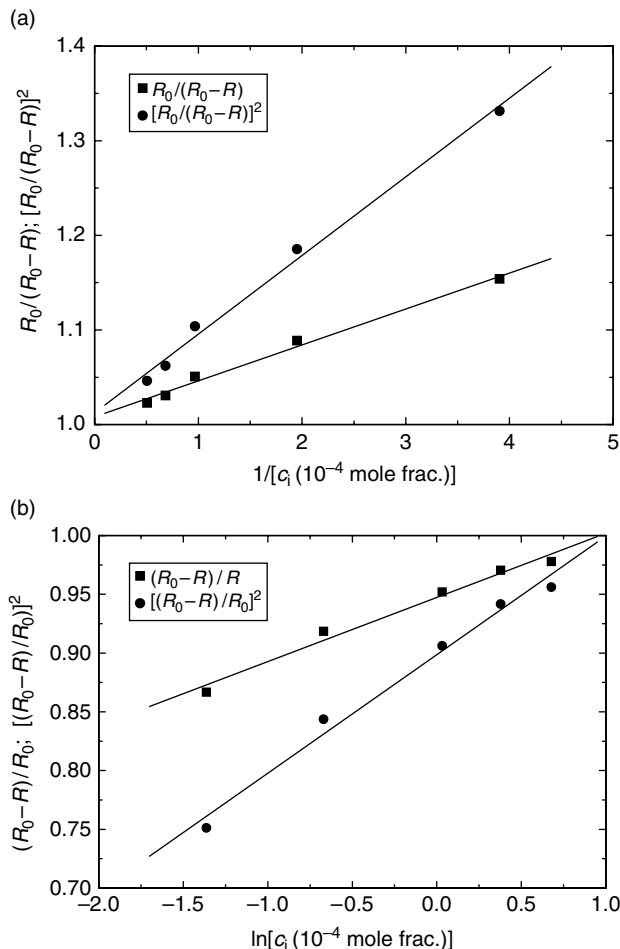


Figure 4.11 $R(c_i)$ data for TNT crystals according to the dependences predicted by (a) Langmuir and (b) Temkin isotherms. See text for details. Data from Grey et al. (1956)

From Table 4.1, it is interesting that the value of $\sigma_{l,s}^0$ is roughly an order of magnitude higher and x_0 or λ are an order of magnitude lower for tailor-made impurities than that for ionic impurities.

4.5 Time-Dependent Impurity Adsorption

The above mechanisms for the adsorption of impurity particles are based on the premise that the entire surface is exposed to the impurity molecules. This means that the adsorption of the impurity is uniform over the available surface. This type of adsorption is said to be equilibrium adsorption and the fractional coverage θ (i.e. θ_l or θ_s in our case) should be replaced by θ_{eq} . This situation is possible only at low supersaturations when

the average distance between steps is large and the displacement velocity v of steps is small. However, when the step velocity becomes high with increasing supersaturation, the concentration of impurity particles adsorbed between two advancing steps becomes nonuniform because the terrace area in front of the step at the upper level remains exposed for a longer time than the terrace area above the advancing step at the lower level. This type of adsorption is said to be time dependent. With a further increase in supersaturation when the interstep distance is small, the impurity concentration between two steps may be considered as uniform. This results in time-independent impurity adsorption.

Equilibrium or instantaneous impurity adsorption essentially refers to static surfaces and all adsorption isotherms describe this type of adsorption. The concept of time-dependent adsorption is also known in the growth and dissolution of crystals where formation of thick steps is often observed. It was introduced by Burton *et al.* (1951) and employed by Frank (1958) and Cabrera and Vermilyea (1958) to explain the origin of kinematic waves and step bunching in terms of relationships between flux of steps passing across a point and the density of steps on a surface. The concept of time-independent impurity adsorption was proposed later by van der Putte *et al.* (1978) to explain the smoothing of etched surfaces at high impurity concentrations. However, Kubota (2001), Kubota and Mullin (1995), and Kubota *et al.* (1997, 2000) used the concepts of equilibrium and time-dependent adsorption of impurities during crystal growth.

It is clear that the fractional surface coverage during instantaneous adsorption is different from that during time-dependent and time-independent adsorption of an impurity. Therefore, below we denote equilibrium fractional surface coverage by θ_{eq} and time-dependent surface coverage by θ . The net adsorption rate may be written as (Kubota *et al.*, 2000)

$$\frac{d\theta}{dt} = k_1(1 - \theta)c_i - k_2\theta \quad (4.58)$$

where k_1 and k_2 are constants, and the impurity concentration c_i is also assumed to be constant. Integrating Equation (4.58) and taking the initial condition that $\theta = 0$ when $t = 0$ for a given c_i , one obtains

$$\theta = \theta_{\text{eq}}[1 - \exp(-t/\tau)] \quad (4.59)$$

where the time constant $\tau = (k_1 c_i + k_2)^{-1}$.

For simplicity we consider the Kubota–Mullin model. Then, substituting for θ from Equation (4.59) in Equation (4.28) one obtains

$$v/v_0 = 1 - \alpha_l \theta_{\text{eq}}[1 - \exp(-t/\tau)] \quad (4.60)$$

Since the impurity effectiveness parameter $\alpha_l = \sigma_l^0/\sigma$ [see Equation (4.29)], Equation (4.60) may be written in the form

$$\begin{aligned} v/v_0 &= 1 - (\sigma_d/\sigma)[1 - \exp(-t/\tau)] \\ &= 1 - \sigma_c/\sigma \end{aligned} \quad (4.61)$$

where the threshold supersaturation σ_c corresponding to $0 < v/v_0 < 1$ is given by

$$\sigma_c = \sigma_d[1 - \exp(-t/\tau)] \quad (4.62)$$

with [cf. Equation (4.29)]

$$\sigma_d = \frac{\gamma_i a}{k_B T L} = \sigma_i \theta_{eq} \quad (4.63)$$

Obviously, σ_c increases with an increase in τ (i.e. with σ), whereas v/v_0 decreases with increase in the value of threshold supersaturation σ_c .

In the case of weakly adsorbing impurities (i.e. for $\alpha_l \leq 1$), Equation (4.60) is valid for all values of t from 0 to ∞ . However, in the case of strongly adsorbing impurities (i.e. for $\alpha_l > 1$), it is valid up to a characteristic time t_c when $v = 0$. The time t_c is given by

$$t_c = \ln \left(\frac{\alpha_l \theta_{eq}}{\alpha_l \theta_{eq} - 1} \right) \tau \quad (4.64)$$

When $\exp(t/\tau) = 1$ or $t/\tau = 0$, $v = v_0$ irrespective of the value of $\alpha_l \theta_{eq}$.

From Equation (4.60), it follows that with an increase in supersaturation σ the adsorption kinetics change from instantaneous adsorption at some value of $\sigma = \sigma_0$ to time dependent and the time constant τ increases with σ from 0 to ∞ . When $\tau = \infty$, impurity adsorption becomes time independent and $v = v_0$. However, impurity adsorption can become time dependent for both $\sigma_c < \sigma_0$ and $\sigma_c > \sigma_0$. Experiments suggest that $\sigma_c \leq \sigma_0$.

For the supersaturation dependence of step velocity v , from Equation (4.60) several cases can be distinguished (Kubota *et al.*, 2000), as described below.

Case 1. When impurity adsorption is instantaneous ($\tau = 0$). This case corresponds to $\tau = 0$ in Equation (4.60). When $\tau = 0$, impurity adsorption occurs instantaneously, and Equation (4.61) reduces to the form

$$v/v_0 = 1 - \sigma_d/\sigma \quad (4.65)$$

for $\sigma_d < \sigma \ll 1$. The displacement velocity v of steps on an F face is given by [see Equations (3.24) and (3.27)]

$$v = \beta_l \sigma \quad (4.66)$$

where the kinetic coefficient β_l for the growth step is given by [cf. Equation (3.25)]

$$\beta_l = a \nu \exp(-W/k_B T) \quad (4.67)$$

where ν is the frequency of vibration of molecules/atoms on the surface and W is the activation energy for growth. Using Equation (4.65) for v_0 , one may write Equation (4.66) in the form

$$v = \beta_{l0}(\sigma - \sigma_d) \quad (4.68)$$

for $\sigma > \sigma_d$. In this equation, the kinetic coefficient for step velocity $\beta_{l0} = v_0/\sigma$ corresponds to an impurity-free system. Figure 4.12a shows the $v(\sigma)$ plots according to Equations (4.66) and (4.68) (i.e. when $\sigma_d = 0$ and $\sigma_d > 0$). The step movement occurs when $\sigma > \sigma_d$.

Case 2. When impurity adsorption is extremely slow ($\tau = \infty$). When the time constant $\tau = \infty$, then $v = v_0$ [see Equation (4.61)]. There is no effect of impurity on step velocity, and the step velocity increases linearly with increase in supersaturation (Figure 4.12a).

Case 3. When adsorption decreases abruptly from instantaneous to very slow ($\tau = 0$ to ∞). The time constant τ increases steadily from 0 to ∞ such that the adsorption becomes time dependent abruptly at a transition supersaturation σ_0 . Depending on the value of σ_0 , two cases are expected in the growth behavior: $\sigma \leq \sigma_0$ and $\sigma \geq \sigma_0$.

Case 4. When the adsorption rate decreases steadily with growth time. This case refers to the situation when impurity adsorption is instantaneous initially (i.e. $\tau = 0$), but it becomes time dependent as growth proceeds ($\tau = \infty$). In this case, there is a supersaturation σ_0 when the step velocity becomes time dependent and follows Equation (4.61). Then the step velocity v gradually increases from an initial value when $\tau = 0$ to a final value when $\tau = \infty$. However, depending on the value of σ , two situations are possible: $\sigma_c \geq \sigma_0$ and $\sigma_c \leq \sigma_0$. These $v(\sigma)$ plots are shown schematically in Figure 4.12b and c.

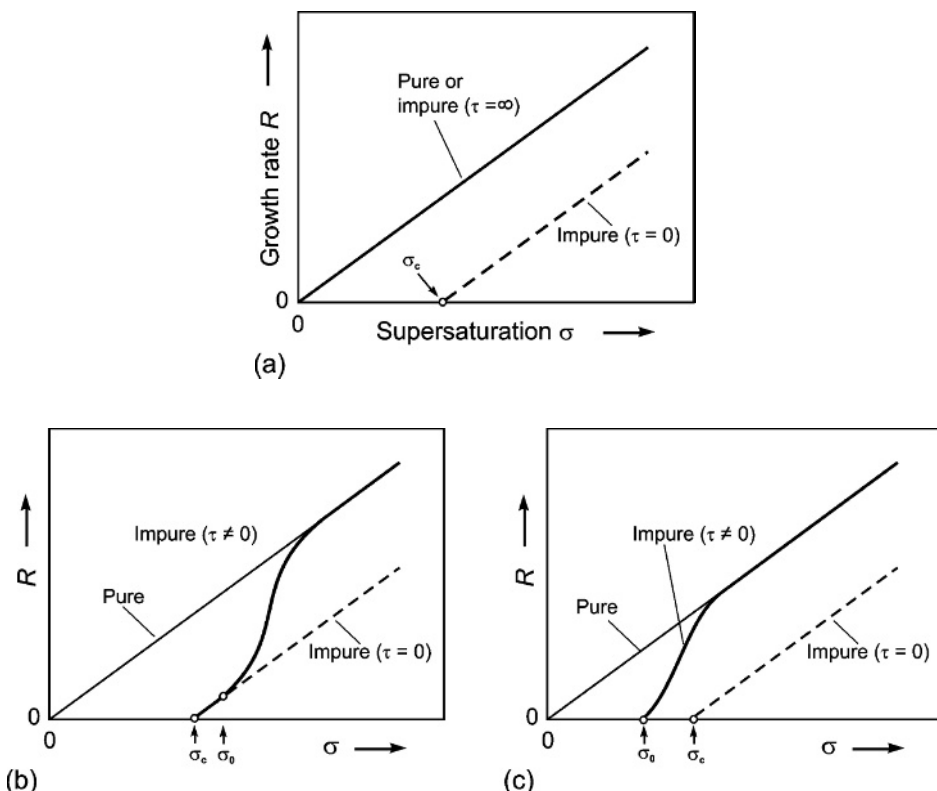


Figure 4.12 Schematic representation of step velocity v on supersaturation σ for (a) instantaneous and (b, c) time-dependent impurity adsorption; (b, c) show situations when $\sigma_c \geq \sigma_0$ and $\sigma_c \leq \sigma_0$, respectively. Reproduced from N. Kubota, M. Yokota, and J.W. Mullin. *J. Cryst. Growth* **212**, 480. Copyright (2000), with permission from Elsevier

4.6 Growth Kinetics in the Presence of Impurities

4.6.1 Basic Kinetic Equations

In the above cases of impurity adsorption, the supersaturation dependence of step velocity v , described by Equation (4.61), may be written in the general form

$$v = \beta_{l0}(\sigma - \sigma_d) - \beta_{l0}(\sigma - \sigma_d) \exp(-t/\tau) \quad (4.69)$$

or alternatively

$$v = \beta_{l0}(\sigma - \sigma_d) \quad \text{for } \sigma_d < \sigma < \sigma^* \quad (4.70)$$

$$v = \beta_{l0}(\sigma - \sigma_d) \exp(-t/\tau) \quad \text{for } \sigma^* < \sigma < \sigma^{**} \quad (4.71)$$

Note that Equation (4.70) refers to growth kinetics controlled by instantaneous impurity adsorption, whereas Equation (4.71) refers to growth controlled by time-dependent adsorption. Equations (4.70) and (4.71) are the basic equations for the analysis of $v(\sigma)$ on crystal growth.

In contrast to $v(\sigma)$ data, $R(\sigma)$ data are abundantly available in the literature. Therefore, it is necessary to derive kinetic equations for growth rate R in the presence of impurities. Here growth mechanisms involving screw dislocations and two-dimensional nucleation are considered. We begin with the model involving a complex source of cooperating screw dislocations, because well-developed macroscopic growth hillocks are usually formed on the morphologically important faces of the crystals grown from solutions both in the presence and absence of impurities. Following Sangwal (2002) and Sangwal and Mielińczek-Brzóska (2003), below are given the expressions for the supersaturation dependence of face growth rate in the presence of impurities.

When a group of equally spaced screw dislocations arranged along a line of length l participate in growth, the dependence of the growth rate R of an F face on supersaturation σ is given by (see Section 3.6.3)

$$R = \sigma^2 / (X + Y\sigma) \quad (4.72)$$

where

$$Y = \frac{2la}{ih\Omega N_0 \beta_l} \quad (4.73)$$

and

$$X = \frac{19\gamma\Omega}{k_B T} \frac{a}{ih\Omega N_0 \beta_l} = \frac{19\gamma_l a}{2k_B T l} Y = GY \quad (4.74)$$

where i is the number of dislocations participating in growth, h is the height of elementary steps and N_0 is the concentration of growth units on the surface, Ω is the specific molecular volume of molecules/atoms, the linear free energy of the step $\gamma_l \approx \gamma a^2$ (where γ is the interfacial energy of the growing face), a is the dimension of growth units

perpendicular to the step, k_B is the Boltzmann constant, T is the temperature in kelvin, and the kinetic coefficient β_l for the growth step is given by Equation (4.67). When the face growth rate R is proportional to the step velocity v , one may write

$$R = A_1 \sigma \exp(-W/k_B T) \quad (4.75)$$

where A_1 is a constant related with the term $a\nu$ in Equation (4.67).

From an analysis of the dependences of slopes p of hillocks and velocities v of steps on the surfaces of some crystals growing from solutions, Sangwal (1998a, b) showed that the face growth rate R may also be described by

$$R = A\sigma^n \quad (4.76)$$

where the exponent n lies between 11/12 and 2, and the value of the constant A is related with the activation energy W for growth. The power-law approach applies when $l > 0$, but for a unit dislocation when $l = 0$, Equations (4.72) and (4.76) reduce to the classical BCF parabolic law:

$$R = C\sigma^2 \quad (4.77)$$

where the constant $C = 1/X$.

When a face grows according to the multiple nucleation model, the face growth rate is given by [see Equation (3.34)]

$$R = C_8 \sigma^{5/6} \exp(-F/\sigma) \quad (4.78)$$

where C_8 and F are constants of these equations.

Assuming that the face growth rate R is proportional to the step velocity v , Equation (4.70) for the system containing an impurity may be written as

$$R = R_0(1 - \sigma_d/\sigma) \quad (4.79)$$

where R_0 is the growth rate in the absence of the impurity and the constant σ_d is given by Equation (4.63). This equation may be applied to the above growth rate equations.

Upon substituting the value of R from Equation (4.79) in Equations (4.72), (4.76) and (4.77), one obtains

$$R = \frac{\sigma}{Y(G + \sigma)}(\sigma - \sigma_d) \quad (4.80)$$

$$R = A\sigma^{n-1}(\sigma - \sigma_d) \quad (4.81)$$

and

$$R = C_8 \sigma^{(5/6)-1}(\sigma - \sigma_d) \exp(-F/\sigma) \quad (4.82)$$

respectively. In the case of the traditional BCF parabolic law, Equations (4.80) and (4.81) may be written in the form

$$R = C\sigma(\sigma - \sigma_d) \quad (4.83)$$

where $G \gg \sigma$ and $n = 2$, respectively.

In the case of time-dependent impurity adsorption, Equations (4.80)–(4.83) should be multiplied by the factor $1 - \exp(t/\tau)$. For example, Equation (4.83) may be given in the form

$$R = C\sigma(\sigma - \sigma_d)[1 - \exp(-t/\tau)] \quad (4.84)$$

where the first term $C\sigma(\sigma - \sigma_d)$ denotes the growth rate corresponding to instantaneous impurity adsorption and is valid for $\sigma < \sigma^*$, and the second term represents the case of time-dependent adsorption.

Simon *et al.* (1974) reported that the $R(\sigma)$ curves of the (110) face of paraffin crystals grown from petroleum ether containing increasing concentration of dioctadecylamine impurity are similar and are displaced relative to each other by increasing values of supersaturation barrier σ_d . They pointed out that these $R(\sigma)$ curves may be described by the usual growth rate equations with corrected supersaturation $(\sigma - \sigma_d)$ instead of applied supersaturation σ . Bredikhin *et al.* (1987) observed that, for the growth rate R of the (100) face of KDP in the presence of Fe(III) and Al(III) ions, in the range $\sigma < \sigma_d$ there is no growth, for $\sigma_d < \sigma < \sigma^*$ the growth rate follows the classical BCF parabolic law, and for $\sigma > \sigma^*$ the growth rate follows the relation

$$R = A'(\sigma - \sigma^*)^{n'} \quad (4.85)$$

where A' is a constant and the exponent $n' = 5/4$. These authors attributed the experimental $R(\sigma)$ data in $\sigma > \sigma^*$ region to mass transfer processes in the solution. Rashkovich and Kronske (1997) reported that the displacement velocity v of steps on the (100) face of KDP between $\sigma_d < \sigma < \sigma^*$ in the presence of Fe(III) and Al(III) ions follows the parabolic relation

$$v = b_l(\sigma - \sigma_d)^2 \quad (4.86)$$

where b_l is an empirical constant similar to the kinetic coefficient β_{l0} in Equation (4.68), but $b_l \neq \beta_{l0}$.

Empirical Equations (4.85) and (4.86) are similar to Equation (4.83), but are not exactly predicted by the above theoretical considerations. This discrepancy is mainly associated with the scatter in the determination of experimental data at low supersaturations. This topic is discussed in Section 5.2. Figure 4.13 illustrates the experimental $R(\sigma)$ data for the (110) face of paraffin crystals grown from petroleum ether containing different concentrations of dioctadecylamine impurity. The face growth rate decreases as the impurity concentration is increased, and in all cases there is a critical supersaturation σ_d beyond which growth takes place. The best-fit plots for the experimental data according to Equation (4.82) of growth by the polynuclear model are shown as solid curves. As can be seen, the experimental data are well reproduced by the theoretical equation.

It is usually found (see, for example, Bredikhin *et al.*, 1987; Kitamura *et al.*, 1992; Guzman and Kubota, 2004; Guzman *et al.*, 2001; Kubota *et al.*, 2003; Rashkovich and Kronske, 1997; Sangwal and Mielniczek-Brzóska, 2003; Simon and Boistelle, 1981) that

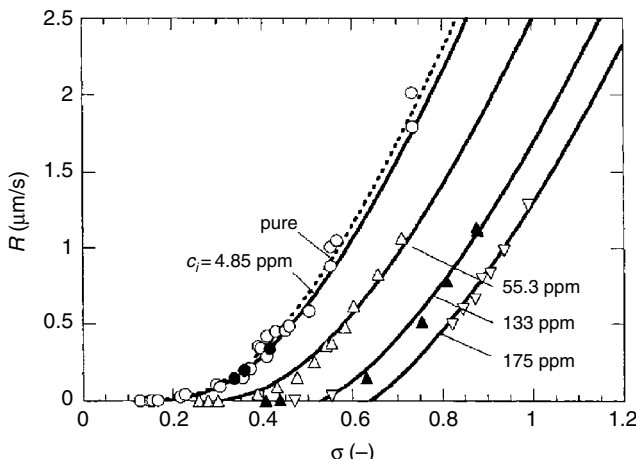


Figure 4.13 Experimental $R(\sigma)$ data for the (110) face of paraffin crystals grown at 292 K from petroleum ether containing different concentrations of dioctadecylamine impurity. Solid curves show the best-fit plots according to Equation (4.82). Reproduced from N. Kubota, M. Yokota, and J.W. Mullin. *J. Cryst. Growth* **212**, 480. Copyright (2000), with permission from Elsevier

there is a steep increase in the step velocity v and face growth rate R . Figure 4.14 shows the effect of Cr(III) ions on the growth rate R of the (100) face of an ammonium sulfate crystal as a function of supersaturation, and Figure 4.15 presents the experimental $v(\sigma)$ data on the (100) face of KDP in the presence of different concentrations of Fe(III) impurity. The theoretically predicted curves are drawn in the figures.

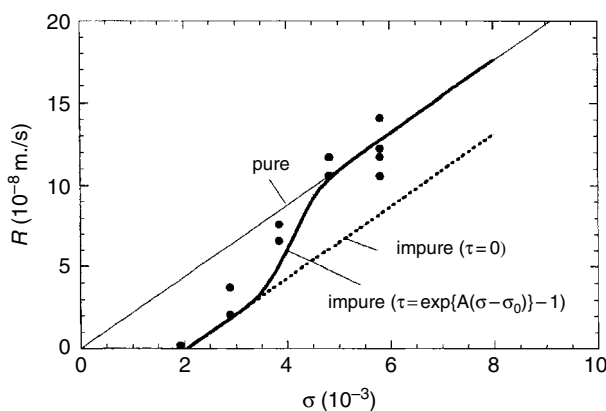


Figure 4.14 Growth rate R of the (100) face of an ammonium sulfate crystal as a function of supersaturation σ from aqueous solutions containing Cr(III) ions. The solid line is drawn according to Equation (4.60), assuming that $v \propto R$. Reproduced from N. Kubota, M. Yokota, and J.W. Mullin. *J. Cryst. Growth* **212**, 480. Copyright (2000), with permission from Elsevier

In order to confront the experimental $v(\sigma)$ and $R(\sigma)$ data with the theoretical expression in Equation (4.61), one requires two parameters: $\alpha_i \theta_{eq}$ and τ . These parameters can be

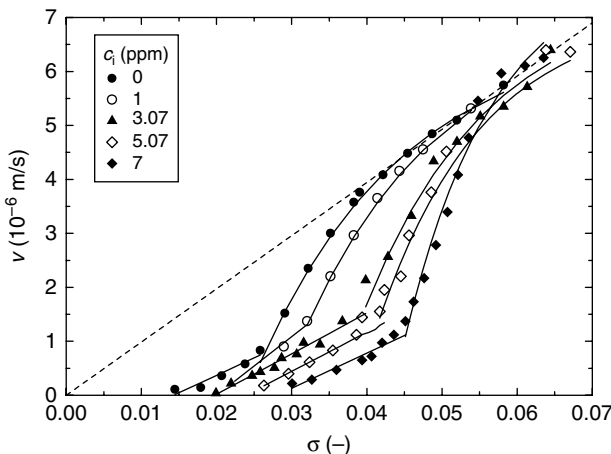


Figure 4.15 Experimental $v(\sigma)$ data on the (100) face of KDP in the presence of different concentrations of Fe(III) impurity. The curves are drawn according to Equations (4.70) and (4.71) in the supersaturation regions $\sigma_d < \sigma < \sigma^*$ and $\sigma > \sigma^*$, respectively. Reproduced from K. Sangwal. J. Cryst. Growth **203**, 197. Copyright (1999), with permission from Elsevier

determined from the best fit of experimental data in the range of supersaturation when there is an abrupt increase in v or R at the transition supersaturation σ_0 (see Figure 4.15). In our terminology, $\sigma_0 = \sigma^*$. There is no independent way to calculate the value of τ . Kubota *et al.* (2000) assumed the following exponential function:

$$\tau = \exp[p_1(\sigma - \sigma^*)] - 1 \quad (4.87)$$

where p_1 is an empirical constant and σ_d corresponds to the supersaturation when $v = 0$ and $R = 0$. However, it was found (Sangwal, 2002; Sangwal and Mielińczek-Brzóska, 2003) that the $v(\sigma)$ data, reported by Rashkovich and Kronske (1997), for the growth of KDP crystals in the presence of different trivalent cations and the $R(\sigma)$ data, reported by Sangwal and Mielińczek-Brzóska (2003) and Mielińczek-Brzóska and Sangwal (2004), for ammonium oxalate single crystals in the presence of Mn(II), Co(II) and Ni(II) ions, are satisfactorily reproduced when

$$\tau^{-1} = -p_2(\sigma - \sigma^*) \quad (4.88)$$

where p_2 is a constant.

There are two difficulties with the above theory of time-dependent impurity adsorption:

- (1) Equations (4.87) and (4.88) describing the dependence of time constant τ on σ are empirical. Moreover, it is found (Kubota *et al.*, 2000) that in some cases the time constant τ has an unusually high value (see below). These observations remain unexplained.
- (2) In the interval $\sigma_d < \sigma < \sigma^*$, the value of the kinetic coefficients for the displacement of step and face, denoted by $\beta_{l0} = v_0/\sigma$ [cf. Equation (4.66)] and $\beta_{f0} = C = R_0/\sigma^2$ (where R_0 is the growth rate in impurity-free solution), respectively, obtained from

the fit of the experimental $v(\sigma)$ and $R(\sigma)$ data according to Equation (4.61) decreases with increase in impurity concentration c_i (Sangwal, 2002; Sangwal and Mielniczek-Brzóyska, 2003). However, as discussed in Section 4.4.4, this observation can be explained in terms of the effect of an impurity on the activation energy required for integration of growth units.

4.6.2 Time Dependence of Face Displacement

Assuming that the growth rate R of a face is proportional to the step velocity v on it and the face displacement Δl is a function of time, integration of Equation (4.60) gives (Kubota *et al.*, 2000)

$$\Delta l = (1 - \alpha_l \theta_{\text{eq}}) v_0 t + \alpha_l \theta_{\text{eq}} v_0 \tau [1 - \exp(t/\tau)] \quad (4.89)$$

for $t \leq t_c$. For $t \geq t_c$, Δl becomes independent of time, i.e.

$$\Delta l = v_0 \tau - \frac{\exp(-t_c/\tau)}{1 - \exp(-t_c/\tau)} v_0 t_c \quad (4.90)$$

The experimental data for the dependence of face displacement Δl on growth time t at different concentrations c_i of Cr(III) impurity for the (100) face of ammonium sulfate crystals grown at $\sigma = 3.85 \times 10^{-3}$ and 298.2 K are shown in Figure 4.16. The curves represent the best fit, according to Equations (4.89) and (4.90), for the data, with time constant $\tau = 3.7 \times 10^3$ s and the values of $\alpha_l \theta_{\text{eq}}$ plotted as a function of impurity concentration c_i in Figure 4.17. The linear dependence of $\alpha_l \theta_{\text{eq}}$ on c_i implies that a linear isotherm $\theta_{\text{eq}} = K c_i$ holds in this case.

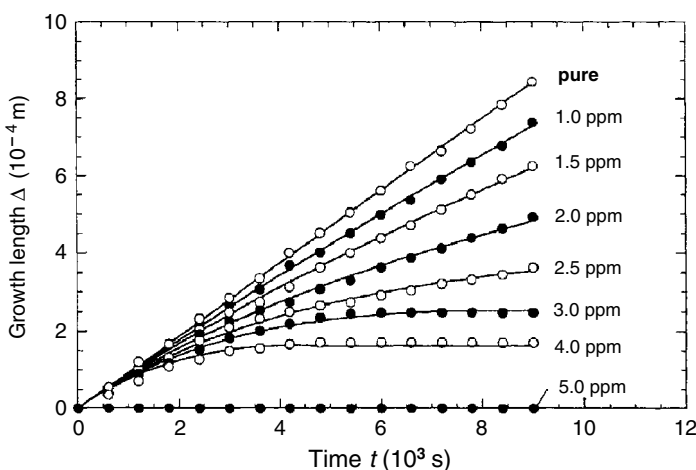


Figure 4.16 Dependence of face displacement Δl on growth time t at different concentrations c_i of Cr(III) impurity for the (100) face of ammonium sulfate crystals grown at $\sigma = 3.85 \times 10^{-3}$ and 298.2 K. Curves represent the best fit according to Equations (4.89) and (4.90). Reproduced from N. Kubota, M. Yokota, and J.W. Mullin. *J. Cryst. Growth* **212**, 480. Copyright (2000), with permission from Elsevier

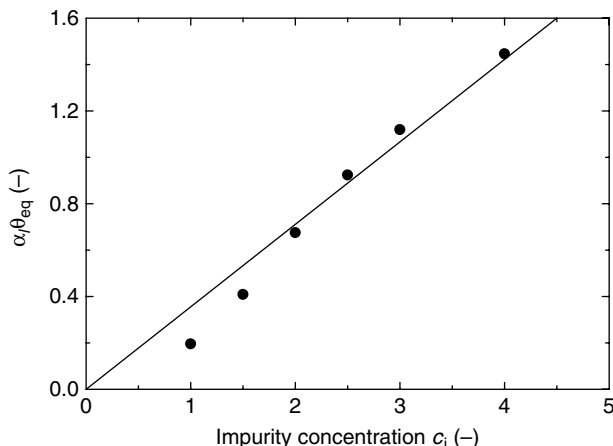


Figure 4.17 Plot of $\alpha_l \theta_{eq}$ as a function of concentration c_i of Cr(III) impurity for growth of the (100) face of ammonium sulfate crystals. Reproduced from N. Kubota, M. Yokota, and J.W. Mullin. *J. Cryst. Growth* **212**, 480. Copyright (2000), with permission from Elsevier

It may be noted from Figure 4.17 that its slope is 3.7×10^5 . Assuming that $\alpha_l = 1$, one may estimate the differential heat of adsorption $Q_{\text{diff}} = 32.3 \text{ kJ/mol}$. This is indeed a realistic value for impurity adsorption.

4.6.3 Dependence of Kinetic Coefficient for Step Motion on Impurity Concentration

In the interval $\sigma_d < \sigma < \sigma^*$, the values of kinetic coefficients for the displacement of step and face, denoted by $\beta_{l0} = v_0/\sigma$ and $\beta_{f0} = C = R_0/\sigma^2$, respectively [cf. Equation (4.66)], decrease with increase in impurity concentration c_i . We refer to Equation (4.67) for the kinetic coefficient for step motion β_l on c_i , and define the step kinetic coefficient for pure system by

$$\beta_{l0} = v_0/\sigma = a\nu \exp(-W_0/k_B T) \quad (4.91)$$

where W_0 is the activation energy for growth in pure system (i.e. $W = W_0$ when $c_i = 0$). Then it is expected that $\beta_l = \beta_{l0}$ is independent of impurity concentration c_i .

Usually, $\beta_l < \beta_{l0}$, which implies that

$$W = W_0 + \Delta W \quad (4.92)$$

where ΔW is an additional activation energy contribution due to the presence of impurity. Since a and ν are constants, it follows from this equation that the decrease in β is possible with an increase in the activation energy W . This behavior is associated with competition between solute and impurity particles during growth in the presence of impurities.

4.7 Tapering of KDP-Type Crystals

It is well known that the presence of trivalent metal ions, such as Fe^{3+} , Cr^{3+} and Al^{3+} , affects the growth rate, morphology and quality of KDP-type crystals grown from aqueous solutions. The effect of impurities is particularly marked on the growth kinetics of the crystals along the x (y) and z directions (Mullin *et al.*, 1970; Veintemillas-Verdaguer and Rodriguez-Clemente, 1986; Owczarek and Sangwal, 1990a,b; Sasaki and Yokotani, 1990; Sangwal, 1996). Additional high-index faces (called tapered faces) also appear between the $\{100\}$ and $\{101\}$ faces of the crystals during their growth (Figure 4.18). The tapered faces are inclined with respect to the $\{100\}$ face by an average angle ϕ , the value of which depends on supersaturation, growth temperature, stirring, solution pH and the impurities present in the solution.

During the growth of ADP and KDP crystals from aqueous solutions without intentionally added impurities, tapering occurs at relatively low supersaturations immediately after crossing the dead supersaturation barrier σ_d (Mullin *et al.*, 1970). However, as can be seen from Figure 4.19, at a given supersaturation σ tapering of the $\{101\}$ faces of these crystals is caused only above a certain concentration c_i^* of impurity and the value of impurity concentration c_i^* increases with supersaturation σ used for growth (see, for example, Mullin *et al.*, 1970; Sasaki and Yokotani, 1990; Owczarek and Sangwal, 1990a). The best-fit plot for the experimental data is drawn according to Equation (4.30) with the constants $R_0 = 2.19 \times 10^{-7} \text{ m/s}$, $\alpha_l = 0.77$ and $K = 1.1 \times 10^3 \text{ dm}^3/\text{g ion}$.

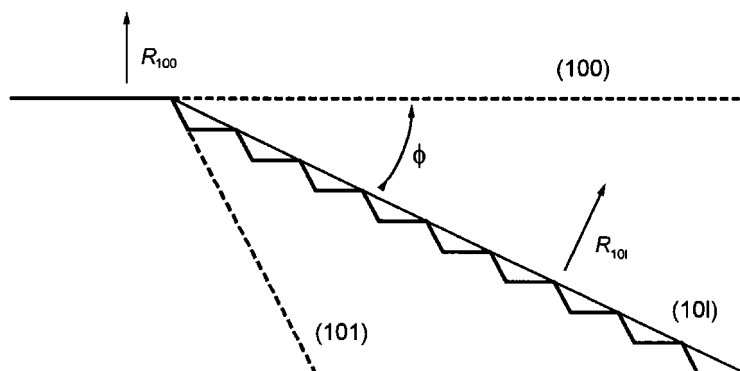


Figure 4.18 Schematic presentation of the tapering process. The tapered high-index face is $\{101\}$ and is inclined by an angle ϕ with respect to the $\{100\}$ face

The appearance of tapered faces is associated with a decrease in the rate of movement of growth layers by the adsorption of impurities on the $\{100\}$ faces, which results in the accumulation of growth steps spreading on the $\{100\}$ face. Consequently, the value of tapering angle ϕ is directly connected with adsorption processes taking place on this surface. The process of tapering is shown schematically in Figure 4.18. If R_0 and R are the growth rates of the $\{100\}$ faces in the absence and presence of an impurity, respectively, the tapering angle ϕ is given by

$$\cos \phi = R/R_0 \quad (4.93)$$

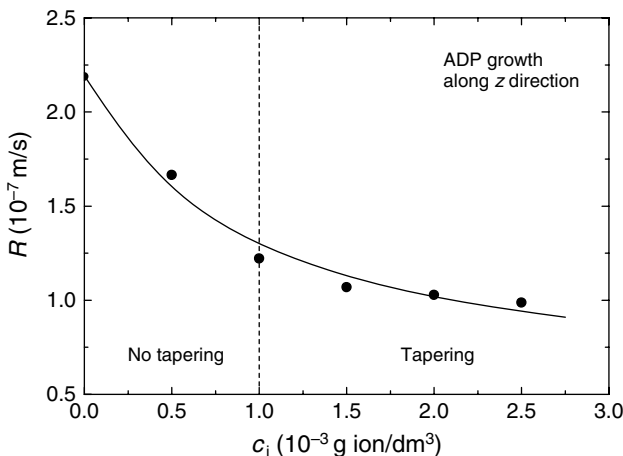


Figure 4.19 Dependence of growth rate R along the z direction of ADP crystals on the concentration c_i of Fe^{3+} impurity. Growth temperature 25°C and supersaturation $\sigma \approx 7.5\%$. The plot represents Equation (4.30). Adapted from J.W. Mullin, A. Amataivadhma, and M. Chakraborty. *J. Appl. Chem.* **20**, 153. Copyright (1970), International Academic Publishing Company

with $0 < \phi < 45^\circ$. Using Equations (4.31) and (4.43), Equation (4.93) may be expressed in the form (cf. Figure 4.18)

$$(1/\cos \phi)^n = (1/\alpha)^n (1 + Kc_i) \quad (4.94)$$

where the exponent $n = 1$ and 2 for adsorption at kinks in steps and at the surface terrace, respectively. Here it is assumed that the growth rate R of a face is proportional to the step velocity v on it.

Owczarek and Sangwal (1990a) reported reliable and extensive experimental data on the tapering of KDP crystals grown at supersaturations of 4.2, 6.3 and 13.0% at 30°C in the presence of Fe^{3+} impurity. Sangwal (1999) analyzed these data using Equation (4.94). A typical example of the dependence of tapering angle ϕ on impurity concentration c_i at $\sigma = 4.2\%$ is shown in Figure 4.20a. From the intercepts and slopes of the plots of $1/\cos \phi$ and $(1/\cos \phi)^2$ against c_i the values of constant K , $\sigma_{l,s}^0$, the heat of adsorption Q_{diff} , and the average separation x_0 or λ between adsorption sites can be estimated. For the estimation of x_0 or λ it was assumed that $\gamma_l/k_B T = 1$. The values of the above parameters are collected in Table 4.2.

Figure 4.20a shows that there is essentially no difference between the plots for the exponents $n = 1$ and 2. Table 4.2 reveals that the value of the average distance between active adsorption sites (i.e. x_0 or λ) decreases with increasing supersaturation. This feature is associated with the roughening of steps or surface with increasing supersaturation.

As mentioned above, at a given supersaturation σ , tapering is caused only above a certain concentration c_i^* of impurity and the value of impurity concentration c_i^* increases with supersaturation σ used for growth. Thus, from a study of tapering of KDP-type

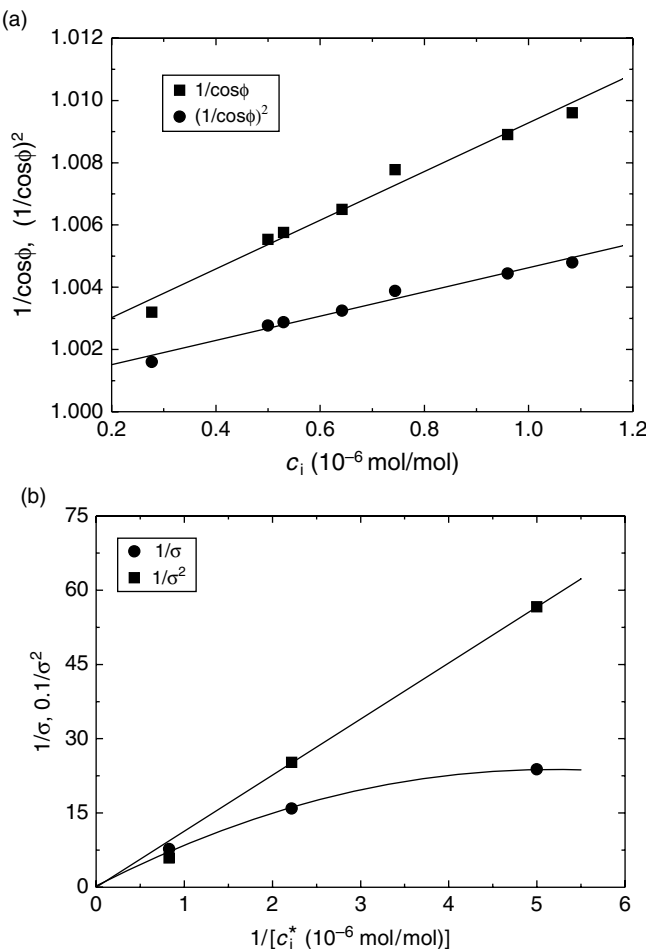


Figure 4.20 Plots of (a) $1/\cos\phi$ and $(1/\cos\phi)^2$ against c_i of Fe^{3+} for KDP growth at $\sigma = 4.2\%$ and (b) $1/\sigma$ and $1/\sigma^2$ against $1/c_i^*$ for Fe^{3+} impurity. Reproduced from K. Sangwal. J. Cryst. Growth **203**, 197. Copyright (1999), with permission from Elsevier

Table 4.2 Estimated values of K , Q_{diff} , $\sigma_{l,s}^0$ and x_0 or λ for Fe^{3+} adsorption on {100} face of KDP from tapering data. Reproduced from K. Sangwal. J. Cryst. Growth **203**, 197. Copyright (1999), with permission from Elsevier

σ (%)	Adsorption mechanism	K (mol/mol)	Q_{diff} (kJ/mol)	$\sigma_{l,s}^0$	x_0 or λ
4.2	Kink	3.90×10^3	20.8	4.2×10^{-2}	24a
	Terrace	7.81×10^3	22.6	4.3×10^{-2}	23a
6.3	Kink	5.16×10^3	21.5	6.3×10^{-2}	16a
	Terrace	1.04×10^4	22.6	6.3×10^{-2}	16a
13.0	Kink	5.33×10^3	21.6	0.13	8a
	Terrace	1.08×10^3	23.4	0.13	8a

crystals, one can also obtain the following data: (1) the dependence of threshold supersaturation σ^* on c_i when growth is stopped, and (2) the dependence of c_i^* on σ when tapering sets in (i.e. $\phi = 0$). To explain the $c_i^*(\sigma)$ data for the occurrence of tapering, one may use plots of $1/\sigma$ and $1/\sigma^2$ against $1/c_i^*$, predicted by the models involving impurity adsorption at kinks and the surface terrace, respectively; see Equation (5.23). These plots are shown in Figure 4.20b for the occurrence of tapering on the {100} faces of KDP in the presence of Fe^{3+} ions. It can be seen that the plot of $1/\sigma^2$ on $1/c_i^*$, based on impurity adsorption on the surface terrace, is indeed linear for this system.

As can be seen from Table 4.2, the values of x_0 or λ are practically similar and cannot be taken as a measure to differentiate between adsorption at kinks and at the surface terrace. However, the linear plot of $1/\sigma^2$ on $1/c_i^*$ for the occurrence of tapering implies that adsorption occurs at the surface terrace.

The structure of possible metal ion species and their chemical interactions with the surface ions, which cause tapering of KDP-type crystals, are discussed in Section 4.11.

4.8 Growth-Promoting Effects of Impurities

The effect of impurities on the growth of F faces of crystals is two-fold: (1) they retard the velocity of steps by adsorbing at kinks or at the surface (kinetic effect), and (2) they decrease the value of the surface free energy by adsorbing on the growing surface (thermodynamic effect). The kinetic effect of impurities is associated with a decreases in the values of the kinetic coefficient β_l for steps and is discussed in Section 4.3. The thermodynamic effect, on the other hand, is connected with changes in the free energy γ of the growing surface. This issue was discussed in Section 3.7. In the literature, there are several papers devoted to the kinetic effects of impurities but relatively little attention has been paid to the thermodynamic effects.

It was mentioned in Section 4.2 that impurity particles arriving on a crystal surface are adsorbed on it at active sites. However, when the impurity concentration is increased, the impurity molecules can be preferentially attached to the adsorbed molecules both laterally and vertically, thereby forming three- or two-dimensional impurity clusters, respectively. These localized impurity clusters are relatively stable because of their lower solubility than that of the growing crystal. If the clusters formed on the surface of a crystal are composed of tiny three-dimensional impurity clusters, both the impurity particles and the impurity clusters act as obstacles for the motion of growth layers. This situation corresponds to the growth of a face in the presence of two impurities, where the added impurity is A and the impurity clusters are impurity B. Here both the small impurity particles and the three-dimensional impurity clusters act as growth inhibitors and there is an overall decrease in the face growth rate R . Then Equation (4.57) for the step velocity in the presence of two impurities may be applied.

When the three-dimensional clusters are relatively large, growth is entirely stopped on those parts of the surface where impurity clusters are formed, but the remaining parts of the face continue to grow according to the usual growth mechanisms involving two-dimensional nucleation or dislocations with or without impurity adsorption. This process leads to the so-called irregular growth for supersaturations σ exceeding some

critical value (Simon *et al.*, 1974; Simon and Boistelle, 1981; Owczarek and Sangwal, 1990b).

In this section, the growth-promoting effects of impurities are described.

4.8.1 Decrease in Step Free Energy and Roughening of Steps

The growth-promoting effects of impurities due to a decrease in the step free energy were discussed in Section 3.7 for the case of the multiple nucleation model. According to this model, the growth rate R may be given by [see Equation (3.89)]

$$R = A_0 \sigma^{5/6} \exp[-F/\sigma] \quad (4.95)$$

where

$$\begin{aligned} A_0 &= C_8 [\delta(m, x, R_s, N_s)]^{1/3} \\ &= [\delta(m, x, R_s, N_s)]^{1/3} (h\Omega)^{5/6} \beta_l (2D_s \pi / av)^{1/3} (n_1^2 \zeta)^{2/3} \end{aligned} \quad (4.96)$$

$$\begin{aligned} F &= C_7 \Phi'(m, x) / T^2 \\ &= \Phi'(m, x) \Delta G_{2D(hom)}^* / k_B T \end{aligned} \quad (4.97)$$

In the above equations, $\delta(m, x, R_s, N_s)$ and $\Phi'(m, x)$ are two parameters characterizing the effect of an impurity, ζ is a supersaturation-dependent constant, $\Delta G_{2D(hom)}^*$ is the free energy change required for the formation of stable two-dimensional nuclei on a perfect surface, i.e.

$$\Delta G_{2D(hom)}^* = \pi h \gamma^2 \Omega / (k_B T)^2 \sigma \quad (4.98)$$

and the concentration n_1 of adsorbed molecules on the surface is given by [see Equation (3.32)]

$$n_1 = hc_0 \exp(-E_{ad}/k_B T) \quad (4.99)$$

where E_{ad} is the energy of adsorption of molecules/atoms on the surface and c_0 is the solubility of the solute at temperature T .

Equation (4.95) describes the growth kinetics of a perfect smooth face by the multiple nucleation model for both heterogeneous and homogeneous 2D nucleation. However, when $\Phi'(m, x) = \delta(m, x, R_s, N_s) = 1$, this equation describes growth kinetics by homogeneous 2D nucleation. According to Equation (4.95), the effects of an impurity on growth kinetics are included in the parameters A_0 and F . Similarly, if one considers growth to occur by the participation of a group of dislocations, an impurity affects the parameters X and G of Equation (4.74). Therefore, the BCF theory and the two-dimensional nucleation mechanism, expressed in the form of dependence of face growth R on supersaturation σ , are appropriate to analyze the effects of kinetic and thermodynamic parameters simultaneously (Sangwal and Mielniczek-Brzóska, 2001a,b).

In the literature on growth kinetics in the presence of impurities, it has also been reported that in some growth systems impurities lead to an increase in the growth rate (see, for example, Owczarek and Sangwal, 1990b; Kuznetsov *et al.*, 1998; Sangwal and Mielniczek-Brzóska, 2001a,b; Eremina *et al.*, 2005). Figure 4.21 shows schematically the typical growth morphology of an ammonium oxalate monohydrate (AO) crystal grown at 30 °C from ‘pure’ aqueous solutions of supersaturation about 4%. The growth rates of the AO crystals were measured along the $\langle 100 \rangle$, $\langle 010 \rangle$ and $\langle 001 \rangle$ directions from the displacement of the growth interface under an optical microscope. The $\langle 100 \rangle$ and $\langle 010 \rangle$ directions represent the growth of the (100) and (010) faces while the $\langle 001 \rangle$ corresponds to the growth of the morphologically important $\{021\}$ faces. For the sake of convenience, the growth rates are expressed for the (100) , (010) and (001) faces instead of directions.

Figure 4.22 illustrates a typical example of the dependence of the experimental growth rate R of the (010) face of crystals on solution supersaturation σ at 30 °C for different concentrations c_i of Fe(III) ions. As can be seen, for c_i up to 9.75×10^{-4} mole fraction the rate R increases with σ . A similar increase in R with σ is also observed at the highest $c_i = 1.4 \times 10^{-3}$ mole fraction for $\sigma \leq 5\%$ beyond which the rate steadily decreases with increasing σ . It was found (Sangwal and Mielniczek-Brzóska, 2001a) that the dependence of R of the (100) and (001) faces on σ in the presence of Fe(III) impurity is also similar to that for the (010) face, but in these cases the decrease in the growth rate R with an increase in σ for $\sigma \leq 5\%$ at the highest $c_i = 1.4 \times 10^{-3}$ was relatively weak. However, as found for Cu(II) impurity, even for the same crystal the same impurity can lead to an increase in the growth rate R of one face and to a decrease in R of another face.

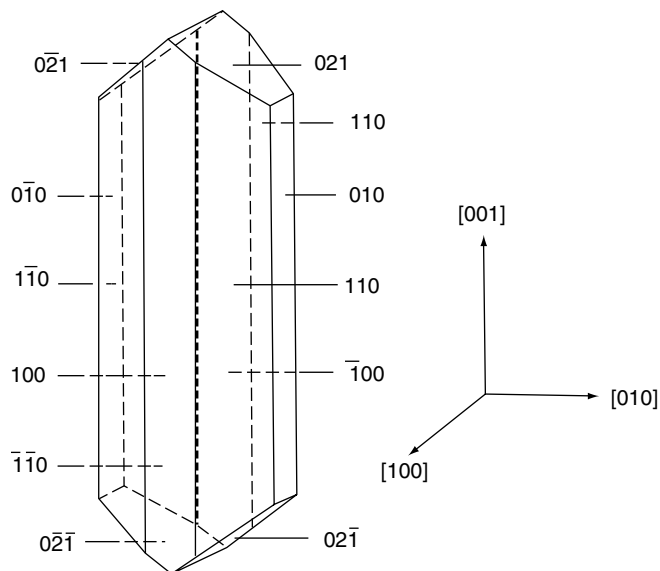


Figure 4.21 Schematic illustration of the typical growth morphology of an AO crystal grown at 30 °C from ‘pure’ aqueous solutions of supersaturation about 4%. Reproduced from E. Mielniczek-Brzóska and K. Sangwal. Cryst. Res. Technol. **29**, 1027. Copyright (1994), with permission from Wiley-VCH

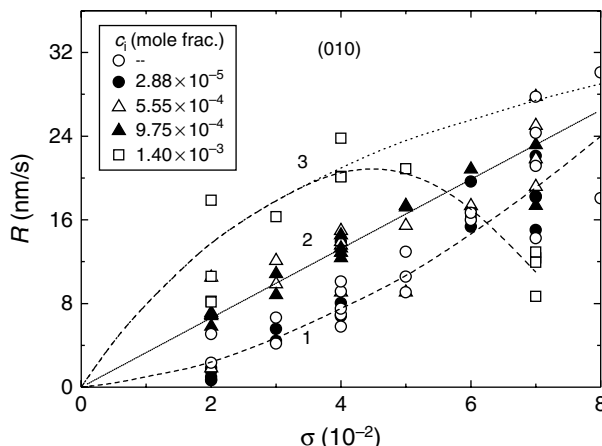


Figure 4.22 Typical example of the dependence of growth rate R of the (010) face of AO crystals on supersaturation σ for different concentrations c_i of Fe(III) ions in aqueous solutions at 30°C. The dotted part of curve (3) shows schematically situations of $R(\sigma)$ dependence for the (100) and (001) faces. Reproduced from K. Sangwal and E. Mielniczek-Brzóska. J. Cryst. Growth 233, 343. Copyright (2001b), with permission from Elsevier

Examination of the $R(\sigma)$ plots in Figure 4.22 at different impurity concentrations c_i shows that the $R(\sigma)$ plots are essentially linear at c_i of 5.55×10^{-4} and 9.75×10^{-4} mole fraction. However, the $R(\sigma)$ plots show positive deviations (downward curvatures) from linearity in pure solutions and at $c_i = 2.88 \times 10^{-5}$ mole fraction and negative deviations (upward curvature) at $c_i = 1.4 \times 10^{-3}$ mole fraction. Moreover, there is a large dispersion (scatter) in the growth rate of a particular face even at the same value of supersaturation used for the growth of the crystal. This growth rate dispersion is mainly associated with the difference in the activity of dominant sources of steps (dislocations) produced in the regeneration stage of new crystal on a seed (Chernov *et al.*, 1986a,b; Sangwal, 1994, 1998a).

Sangwal and Mielniczek-Brzóska (2001a,b) analyzed their $R(\sigma)$ data for the growth of ammonium oxalate monohydrate crystals in the presence of impurities using three models: (1) BCF surface diffusion model, (2) model involving complex source of cooperating screw dislocations, and (3) multiple nucleation model. The use of the first two models is justified in view of the fact that well-developed macroscopic growth hillocks are formed on the morphologically important faces of the crystals grown in both the absence and presence of the impurity. The use of the multiple nucleation model is also justified for the analysis of growth kinetics because, except for very low supersaturations, it also gives a fit comparable to the surface diffusion model. Moreover, among different fitting functions, a simple exponential function typical of two-dimensional surface nucleation models is frequently found to represent the trend of the dependence of $R(\sigma)$ data for growth from impure solutions, as shown by the dotted curve in Figure 4.22. It was found that the above models satisfactorily describe the experimental $R(\sigma)$ data on the growth kinetics of AO crystals.

Figure 4.23a shows the plots of $\ln(R/\sigma^{5/6})$ against $1/\sigma$ for the (100) face of AO crystals according to Equation (4.95) of the multiple nucleation model, and the dependences of

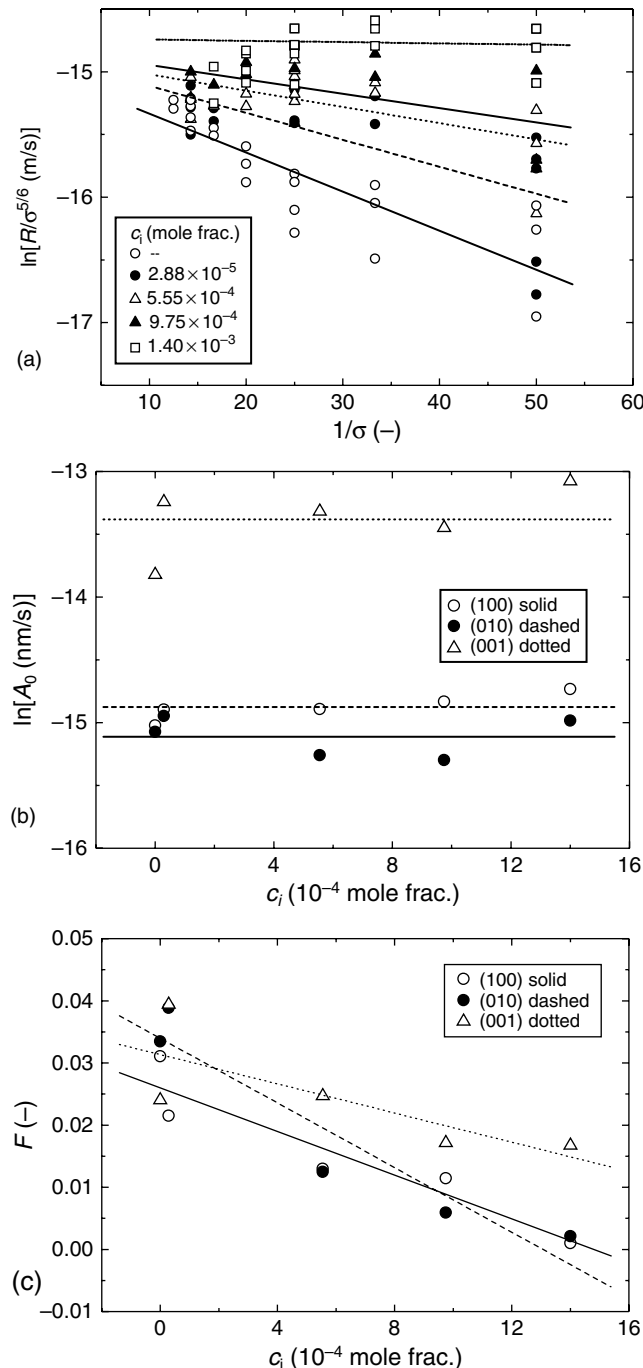


Figure 4.23 (a) Plots of the dependence of $\ln[R/\sigma^{5/6}]$ on $1/\sigma$ for the (100) face of AO grown from solutions containing different concentrations of Fe(III) impurity. The linear dependence of the plot for $c_i = 1.4 \times 10^{-3}$ is drawn for data with $1/\sigma > 25$ (i.e. $\sigma < 4\%$). (b, c) Plots of (b) $\ln A_0$ and (c) F against c_i for different faces. Reproduced from K. Sangwal and E. Mielniczek-Brzóska. J. Cryst. Growth **233**, 343. Copyright (2001b), with permission from Elsevier

Table 4.3 Values of A_0 , $F_0^{1/2}$, b' and Q_{diff} from multiple nucleation model for different AO faces. Reproduced from K. Sangwal and E. Mielniczek-Brzóska, J. Cryst. Growth **233**, 343. Copyright (2001b), with permission from Elsevier

Face	h (nm)	A_0 (m/s)	$F_0^{1/2}$	b'	K	Q_{diff} (kJ/mol)
(100)	0.8035	3.47×10^{-7}	0.161	677	1.016×10^4	23.2
(010)	1.0309	2.73×10^{-7}	0.184	766	1.149×10^4	23.6
(001)	0.3795	1.54×10^{-6}	0.177	373	5.602×10^3	21.7

the corresponding best-fit values of $\ln A_0$ and F on c_i are presented in Figure 4.23b and c, respectively. One observes from Figure 4.23b that for a given face the quantity $\ln A_0$ is practically independent of c_i , but F decreases with an increase in c_i following the relation

$$F = F_0(1 - b'c_i) \quad (4.100)$$

where F_0 is the value of F when $c_i = 0$ and b' is a constant. The calculated values of average A_0 , $F_0^{1/2}$ and b' for different faces are given in Table 4.3.

Using Equation (4.97) and the fact that $\Phi'(m, x) = 1$ for homogeneous 2D nucleation, from Equation (4.100) one obtains

$$\Phi'(m, x) = (1 - b'c_i) \quad (4.101)$$

Obviously, in the range of concentration c_i of Fe(III) impurity used, $\Phi'(m, x)$ decreases linearly with increase in c_i . Using Equation (3.93) from Equation (4.101) it may be concluded that there is a decrease in critical supersaturation σ_{cr} with increase in c_i , and is associated with the kinetic roughening of steps (also see below).

Using Equations (4.97) and (4.98) and rewriting F in terms of the surface free energy γ [i.e. $\gamma(h\Omega)^{1/2}/k_B T = F^{1/2}$], for $bc_i \ll 1$, Equation (4.100) may be expressed in the form

$$\gamma_l = \gamma_{l0}(1 - bc_i) \quad (4.102)$$

where γ_l and γ_{l0} are the linear step free energy for growth from impurity-containing and pure solutions, respectively, and the constant $b = b'/2$.

Equation (4.102) is similar to Szyszkowski's empirical relation, Equation (4.18), rewritten in the form

$$\gamma = \gamma_0\{1 - B'\theta\} \quad (4.103)$$

when the surface coverage $\theta = Kc_i \ll 1$ and the constant $B' = (h\Omega)^{1/2}/\omega_m$ (cf. Equation (4.19)). Then the constant

$$b' = 2b = 2B'K \approx K/15 \quad (4.104)$$

where the Langmuir constant K is given by Equation (4.6). The values of K calculated from b' using Equations (4.104) and (4.6) and Q_{diff} are included in Table 4.3.

A decrease in the surface free energy with increase in impurity concentration is a consequence of roughening of steps similar to kinetic roughening associated with increase in supersaturation, discussed in Section 3.3.2. However, the plots of $\ln(R/\sigma^{5/6})$ against $1/\sigma$ for different faces shown in Figure 4.23 reveal that for $1/\sigma < 25$ (i.e. $\sigma > 4\%$) the slopes $F = \partial[\ln(R/\sigma^{5/6})]/\partial(1/\sigma)$ of the plots for $c_i > 9.75 \times 10^{-4}$ have negative values. This means that in these cases the linear step free energy γ_l/kT increases with increase in σ [cf. Equation (4.98)]. A similar feature was observed in the case of plots of σ^2/R against σ (Sangwal and Mielniczek-Brzóska, 2001b). This feature may be explained in two ways:

- (1) An impurity facilitates the formation of kinks up to a maximum value of their density (i.e. number of kinks per unit length), and corresponding to a given concentration of a growth-promoting impurity, there is a maximum density of kinks that is produced by the impurity. This maximum density of kinks in a step defines the conditions of its roughening.
- (2) The impurity particles begin to inhibit the formation of kinks and lead to the bunching of steps emitted by the dislocation sources. Since the velocity of bunched steps is lower than that of unbunched steps, the growth rate of the face decreases with increasing supersaturation.

In order to explain the observation that A_0 for a face is independent of c_i , we use Equation (4.96) and assume that $\delta(m, x, R_s, N^0) = 1$. Then, upon substituting the values of different quantities for AO in Equation (4.96), one obtains

$$A_0 \approx 0.03\beta_l = 0.03a\nu \exp(-W/k_B T) \quad (4.105)$$

This means that the kinetic coefficient β_l of steps on a face does not depend on the Fe(III) impurity concentration c_i , and that an increase in A_0 caused by c_i at a given supersaturation σ or by σ at a given c_i is associated with a decrease in the activation energy for growth W . Obviously, when either σ or c_i approaches ∞ , the activation energy $W \rightarrow 0$.

From Table 4.3, it may also be noted that the quantity $A_0 h_{hkl}^{-2}$ for the three faces of AO crystals is a constant equal to $2.46 \times 10^{-25} \text{ m}^3/\text{s}$. Then, taking $h_{hkl}^{-2}a = \Omega = 1.6 \times 10^{-28} \text{ m}^3$ for the molecular volume of AO, one obtains $A_0/a = 1534 \text{ s}^{-1}$. This constancy again shows that the activation energy W for growth decreases with increase in σ and c_i [cf. Equation (4.67)]. However, now W is independent of the nature of the crystal face. Taking $\nu = 10^{13} \text{ s}^{-1}$ and $A_0/a = 1534 \text{ s}^{-1}$ in Equation (4.105), one finds that W is 48 kJ/mol at 303 K. This value of W is similar to that obtained for other crystals (Malkin *et al.*, 1989; Sangwal, 1998a).

It should be mentioned that from the surface area ω_m per adsorbed molecule [cf. Equation (4.19)] one obtains a distance l between 0.5 and 0.7 nm. This distance l corresponds to the lower limit of the diffusion distance λ_s given in Section 4.1.

4.8.2 Formation of Surface Macroclusters

An increase in the growth rate of an F face can also occur when impurity particles form localized two-dimensional impurity clusters which provide additional kinks for growth. The localized two-dimensional impurity clusters may be produced by lateral

attachment of more impurity molecules from the growth medium to firmly adsorbed (i.e. immobile) impurity molecules at some adsorption sites on the growing surface. If P is the ratio of the surface area where impurity clusters promote growth, and $(1 - P)$ is the surface area where growth occurs according to Equation (4.95), the resulting face growth rate may be expressed as a sum of contributions of growth rates R_i and R_{clust} in areas where the impurity acts as inhibitor and promoter of growth, respectively, i.e.

$$\begin{aligned} R &= R_i(1 - P) + R_{\text{clust}}P \\ &= R_0(1 - \sigma^0\theta/\sigma)(1 - P) + P\kappa_1\theta A_0\sigma^{5/6}\exp[-(F/\sigma)\kappa_2\theta] \end{aligned} \quad (4.106)$$

where R_0 is the growth rate by two-dimensional nucleation or dislocation source in the absence of the impurity, A_0 and F are given by Equations (4.96) and (4.97), respectively, and κ_1 and κ_2 are constants characterizing the effectiveness of the impurity in generating kinks at the nucleus diameter where solute molecules are attached and in increasing the activation energy ΔG_{2D}^* for 2D nucleation, respectively. The increase in ΔG_{2D}^* is associated with an increase in the step free energy γ_l according to Equation (4.18). When $(F/\sigma)\kappa_2\theta \ll 1$, Equation (4.106) may be written as

$$R = R_i(1 - P) + P\kappa_1\theta A_0\sigma^{5/6}[1 - (F/\sigma)\kappa_2\theta] \quad (4.107)$$

When the contribution of clusters to growth rate is much greater than that of the usual surface kinks [i.e. $R_i(1 - P) \ll R_{\text{clust}}P$], the exponential term is a constant, and the fractional coverage θ is described by Freundlich adsorption isotherm, Equation (4.106) reduces to

$$R = K_1 c_i^m \quad (4.108)$$

where the constant

$$K_1 = (P\kappa_1 A_0\sigma^{5/6} m / c_i^{*m}) \exp[-(F/\sigma)\kappa_2\theta] \quad (4.109)$$

Figure 4.24 shows the growth rate R as a function of dimensionless impurity concentration Kc_i predicted according to Equation (4.106) for different combinations of the parameters P , σ^0 , F and σ . When drawing the plots, it was assumed that $R_0 = A_0$, $\theta = Kc_i$, $\kappa_1 = 10^4$ and $\kappa_2 = 2$. From Figure 4.24, the following points may be noted:

- (1) At very low values of P the growth rate R decreases continuously with increase in the dimensionless impurity concentration Kc_i .
- (2) At relatively high values of P the growth rate first increases and then decreases with increase in Kc_i , exhibiting a maximum growth rate the value of which depends on the choice of the parameters P , σ^0 , F and σ . However, the effect of changes in σ^0 are relatively small, but the values of P , F and σ on the plots have a dominant effect on the growth rate.
- (3) At P close to unity, the growth rate increases continuously and approaches a plateau.

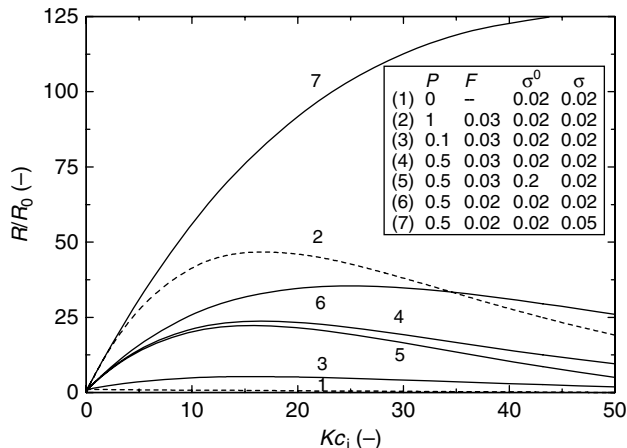


Figure 4.24 Relative growth rate R/R_0 predicted according to Equation (4.106) for different combinations of the parameters P , σ^0 , F and σ . When drawing the plots, it was assumed that $R_0 = A_0$, $\theta = Kc_i$, $\kappa_1 = 10^4$ and $\kappa_2 = 2$

It should be emphasized that Equations (4.106) and (4.108) describe the case when two-dimensional impurity clusters act as growth promoters. However, similar equations can be derived for the case when the growth promoters are three-dimensional impurity clusters. Owczarek and Sangwal (1990b) considered this case. In fact, their consideration refers to the surface area ratio $P = 1/2$.

Figure 4.25 shows typical examples of the $R(Kc_i)$ data, generated from the plots of Figure 4.24 for different values of P , σ^0 , F and σ , in the form of the dependence of $\ln R$ on $\ln(Kc_i)$. It can be seen that in all cases the data for $\ln R$ against $\ln(Kc_i)$ can be represented

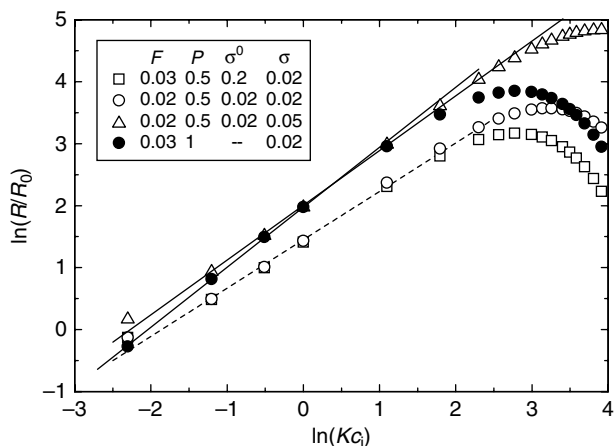


Figure 4.25 Typical plots of the dependence of $\ln(R/R_0)$ on $\ln(Kc_i)$ for different values of P , σ^0 , F and σ . Data were generated from the plots in Figure 4.24

by linear plots with a slope m close to unity. However, in some of the plots the slope deviates from unity. This deviation is associated with the values of the parameters P , σ^0 , F and σ . In general, the slope $m \rightarrow 1$ when $P \rightarrow 1$, and the value of m decreases with decrease in P , F and σ and increase in σ^0 .

Equations (4.106) and (4.108) can be used to verify the validity of the model of surface clusters acting as growth promoters. However, the simplest way to verify it is to use Equation (4.108), which predicts a maximum value of growth rate R_{\max} for $c_i \rightarrow 1$. Figure 4.26a presents the data for the growth rate of the $(10\bar{1}1)$ face of NaNO_3 crystals grown from aqueous solutions containing Co^{2+} ions at supersaturations of

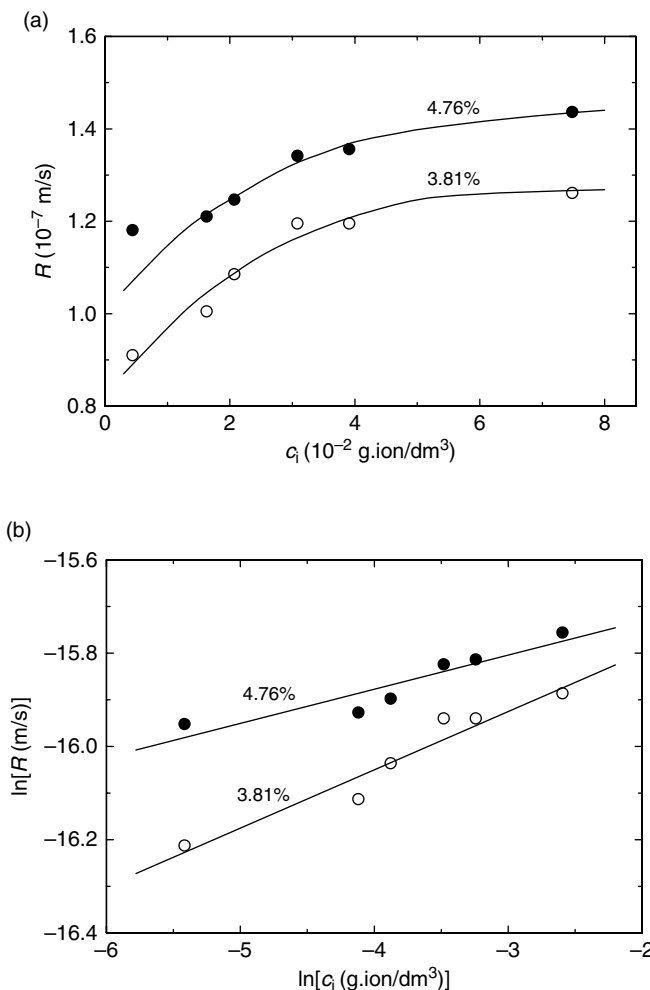


Figure 4.26 (a) Dependence of R of the $(10\bar{1}1)$ face of NaNO_3 crystals grown from aqueous solutions containing Co^{2+} ions at two different σ . Reproduced from E.K. Kirkova and R.D. Nikolaeva. Krist. Tech. **6**, 741. Copyright (1971), with permission from Wiley-VCH. (b) Data for (a) replotted as $\ln R$ against $\ln c_i$

3.81 and 4.76% (Kirkova and Nikolaeva, 1971). As expected from the nature of Equation (4.108), from Figure 4.26a it can be seen that the rate asymptotically attains a constant maximum value. The same data are replotted in Figure 4.26b according to the dependence in Equation (4.108). The curves give the maximum growth rate $R_{\max} = 1.7 \times 10^{-7}$ m/s and the exponent $m = 0.12$ and 0.08 for supersaturations of 3.81 and 4.76%, respectively.

The growth data for NaNO_3 from aqueous solutions containing Co^{2+} ions, presented in Figure 4.26, imply that the exponent m decreases with increase in supersaturation σ . This observation is contrary to the prediction of the above model. However, this apparent contradiction can be reconciled because the slope m also depends on other parameters (for example, interfacial energy and impurity adsorption process).

An increase in the growth rate R of KDP along the $\langle 001 \rangle$ direction at a high supersaturation of 13% with increasing concentration c_i of Cr^{3+} and Fe^{3+} ions is another example of the growth-promoting effect of impurities (Owczarek and Sangwal, 1990b). However, at relatively low supersaturations the growth rate R along the $\langle 001 \rangle$ direction decreases with increase in the concentration c_i of these impurities (see Figure 4.19; Mullin *et al.*, 1970; Owczarek and Sangwal, 1990b). The growth rate of KDP-type crystals along the $\langle 001 \rangle$ direction is related to the growth rate of the pyramidal (101) faces. Therefore, it may be argued that the increase in the growth rate of KDP-type crystals along the $\langle 001 \rangle$ direction is associated with the formation of impurity clusters on the (101) faces.

Figure 4.27 illustrates a dependence similar to that in Figure 4.26b for the linear growth rate along $\langle 001 \rangle$ directions of KDP crystals grown at 30 °C and supersaturation $\sigma = 13\%$ from aqueous solutions containing Cr^{3+} and Fe^{3+} ions. As expected from this model of

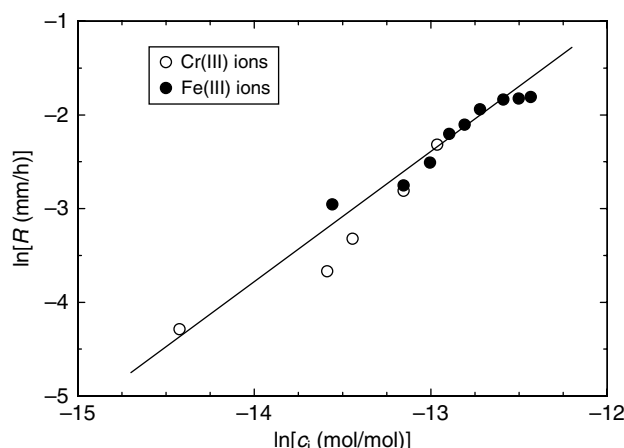


Figure 4.27 Dependence of linear growth rate R along $\langle 001 \rangle$ directions of KDP crystals grown from aqueous solutions at $\sigma = 13\%$ on the concentration c_i of Cr^{3+} and Fe^{3+} ions. Note that both impurities follow the same dependence. Reproduced from I. Owczarek and K. Sangwal. J. Cryst. Growth **102**, 574. Copyright (1990b), with permission from Elsevier

the growth-promoting effect of an impurity, all data for both Cr^{3+} and Fe^{3+} ions follow the same curve with the values of constants $R_{\max} = 2.45 \times 10^{-6} \text{ mm/h} = 8.8 \times 10^{-6} \text{ m/s}$ and $m = 1.33$.

4.9 Impurity Adsorption on Rough Faces

As mentioned in Section 3.4, the growth of rough faces (such as S and K faces) takes place by statistical deposition of growth molecules at growth sites (i.e. kinks), resulting in the displacement of a face in a direction normal to it. Because of the statistical nature of deposition and the high density of kinks present on them, the concentration of an impurity required to inhibit the growth rates of these faces is much higher than that required to inhibit the growth rates of F faces. In order to describe the effect of impurities on the growth rate R of rough faces, Equation (4.106) in conjunction with an appropriate adsorption isotherm may be used.

Figure 4.28 illustrates the dependence of growth rate R of the $\{\overline{1}\overline{1}\overline{1}\}$ faces, which are rough F faces, of NaClO_3 on the concentration of $\text{S}_2\text{O}_6^{2-}$ ions added to aqueous solutions. It was found that the $R(c_i)$ data can be represented satisfactorily by the following relations:

$$R = R_0[1 + b \exp(-k_1 c_i)] \quad (4.110)$$

$$R = R'_0(1 + b_1 c_i^m) \quad (4.111)$$

where R_0 , b and k_1 , and R'_0 , b_1 and m are constants, as follows:

$$R_0 = 1.6 \text{ nm/s}, b = 267 \text{ and } k_1 = 2.3 \text{ ppm}^{-1} \text{ for Equation (4.110).}$$

$$R_0 = 1.6 \text{ nm/s}, b_1 = 2.9 \times 10^8 \text{ ppm}^m \text{ and } m = -3.85 \text{ for Equation (4.111).}$$

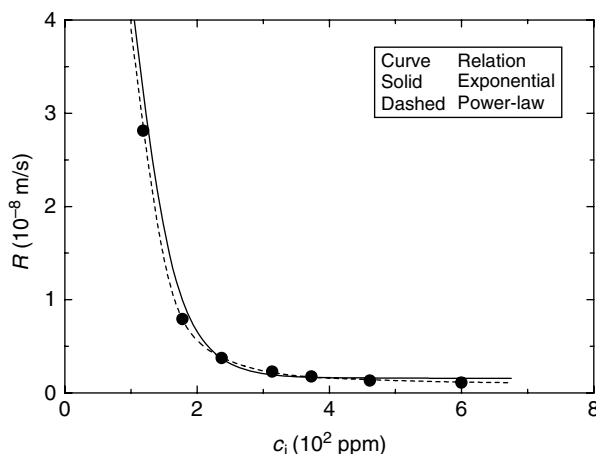


Figure 4.28 Growth rate R of $\{\overline{1}\overline{1}\overline{1}\}$ faces of NaClO_3 crystals as a function of concentration c_i of dithionite ions. Solid and dashed curves represent the best-fit plots according to Equations (4.110) and (4.111), respectively. Data from Ristić et al. (1994); see Figure 3.13

The form of Equation (4.110) is similar to that of Equation (4.69) describing the growth rate involving time-dependent impurity adsorption, and Equation (4.111) is similar to Equation (4.36) describing the growth rate when the Freundlich adsorption applies.

A comparison of Equation (4.110) with Equation (4.69) shows that $b = -1$ and $t/\tau = k_1 c_i > 0$. The negative value of b may be attributed to $\gamma_l < 0$, a phenomenon associated with the roughening of growth steps (see Section 4.8.1). However, the latter equality means that the time

$$t = k_1 c_i \tau \propto \theta_{\text{eq}} \tau \quad (4.112)$$

This relation is similar to Equation (4.64) for the characteristic time t_c and is valid for strongly adsorbed impurities (i.e. when $\alpha > 1$).

In Equation (4.111), both b_1 and m are negative quantities, in contrast to $B > 0$ and $0 < m < 1$ of Equation (4.36). Moreover, $|m|$ is unusually high. These observations suggest that the similarity between Equations (4.36) and (4.111) is a mere coincidence. The term c_i^m in the denominator implies that the following relation holds between R and θ :

$$R = R'_0 (1 + b_2/\theta) \quad (4.113)$$

where b_2 is another constant. Physically, R_0 and R'_0 correspond to the growth rate when $c_i \rightarrow 0$, the constant b is related with the impurity concentration c_i^* when $\theta \rightarrow 1$. If one assumes that the face growth rate R is determined by the surface free energy γ according to the generally observed trend that the lower the surface energy, the higher is the growth rate R , then Equation (4.111) yields

$$\gamma = \gamma'_0 (1 + b_1 c_i^{-m}) \quad (4.114)$$

This equation is essentially another version of Szyszkowski's relation [Equation (4.18)].

4.10 Formation of Two-Dimensional Adsorption Layer

A decrease in the growth rate of a face is possible due to the inaccessibility of growth units to the surface caused by the formation of a uniform two-dimensional layer of the adsorbing impurity. The appearance of the polar {111} surfaces on NaCl crystals during their growth from aqueous solutions containing CdCl₂ additive has been reported to occur by the formation of such 2D layers. Hartman (1965) and Bienfait *et al.* (1965) assumed that the {111} surfaces of NaCl are covered by an epitaxial layer (two-dimensional compound), where a Cd²⁺ ion interacts with three Cl⁻ ions from the crystal side and with three Cl⁻ ions or three H₂O molecules from the solution side. This epitaxial CdCl₂ layer is identical with pure CdCl₂ with a layer thickness d_{0003} , where the hexagonal unit cell has parameters $a = b = 0.385$ nm, $c = 1.746$ nm. The $a = b$ axes of this hexagonal unit cell are close to the a and b axes of the two-dimensional, trigonal, unit cell of {111} NaCl. However, based on adsorption isotherms, Boistelle and Simon (1974)

proposed that the adsorption layer consists of $\text{CdCl}_2 \cdot 2\text{NaCl} \cdot 3\text{H}_2\text{O}$ instead of CdCl_2 . The geometric fit between the adsorption compound and the {111} face of NaCl is shown in Figure 4.29.

In a recent study of the structure of the {111} faces of NaCl crystals grown from aqueous solutions by optical microscopy, AFM and surface X-ray diffraction (SXRD), Radenović *et al.* (2005) found that these surfaces are atomically smooth without surface reconstruction. *In situ* SXRD observation also showed that on an atomic scale the {111} NaCl surface is similar to its bulk face terminated along the {111} plane. Analysis based on the SXRD observations and electrical double-layer theory revealed that the polar {111} NaCl is stabilized by a mixed monolayer of Cd^{2+} (occupancy 0.25) and water (occupancy 0.75) in direct contact with the top Cl^- layer of the {111} surface of bulk NaCl underneath. This result implies that the $\text{Cd}^{2+}/\text{H}_2\text{O}$ layer does not exhibit lateral strong ordering.

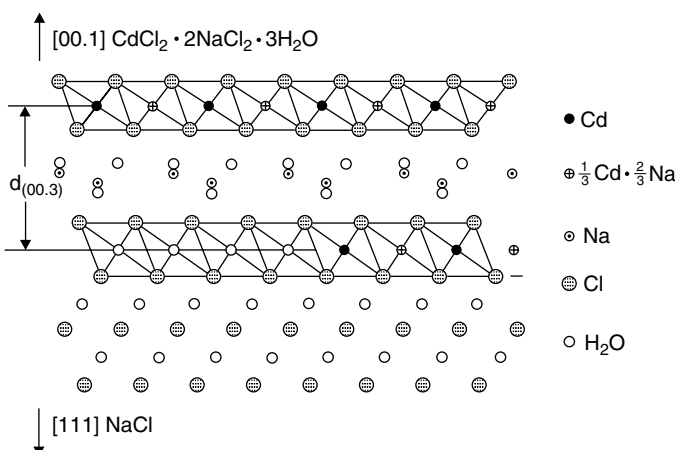


Figure 4.29 Projection of successive {111} planes of an NaCl lattice on the (1-10) plane and the two-dimensional adsorption layer of $\text{CdCl}_2 \cdot 2\text{NaCl} \cdot 3\text{H}_2\text{O}$. Reproduced from R. Boistelle and B. Simon. J. Cryst. Growth **26**, 140. Copyright (1974), with permission from Elsevier

Stabilization of the {111} faces of NaCl crystals growing from aqueous solutions is not confined to CdCl_2 additive alone. Both inorganic additives like Mn^{2+} and Zn^{2+} , and organic compounds like urea and formamide stabilize the {111} surfaces of NaCl crystals (Radenović *et al.*, 2003). However, larger molecules such as dimethylformamide and benzamide, with a charge distribution similar to that of urea and formamide, do not stabilize the {111} surfaces of NaCl. Similarly, the phenomenon of stabilization of the {111} faces is also observed on several NaCl-type crystals (Li *et al.*, 1990; Radenović *et al.*, 2004).

Radenović *et al.* (2004) observed that the appearance of the {111} faces in the presence of formamide is intimately connected with the unit cell size of NaCl-type crystals, and is observed from NaF crystals with unit cell size 0.462 nm up to KCl with a unit cell size 0.628 nm. According to them, this feature is associated with the fitting of the formamide

molecules to the {111} surface, where the ionic resonance structure of the formamide molecules is responsible for their adsorption on the surface. The ionic resonance structure of formamide molecules is associated with the bonds between the negatively charged oxygen and the positively charged nitrogen atoms. The distance between the negatively charged oxygen and the positively charged nitrogen in the formamide molecules is similar to the distance between the positively charged sodium sublayer and the negatively charged chloride sublayer of the NaCl {111} face. These considerations suggest that the stabilization of the {111} surfaces of NaCl-type crystals is due to the ionic resonance structure of formamide molecules. Thus, it may be concluded that dipole–ion interactions in the electrical double layer and the shape and size of additive molecules are important factors for the stabilization of the {111} surfaces of NaCl-type crystals by the adsorption of additives.

Another example of the stabilization of rough faces of the morphology of crystals is the appearance of the {001} faces of AO crystals grown from aqueous solutions containing Mn²⁺ ions (Sangwal *et al.*, 2003). The main features of the surface morphology of the stabilized {001} faces of AO crystals are similar to those observed on the {111} faces of NaCl crystals grown in the presence of Cd²⁺ ions (Radenović *et al.*, 2005) and urea and formamide (Radenović *et al.* 2003).

4.11 Interactions Between Additives and Crystal Interface

4.11.1 Nature of Impurity–Crystal Interactions

Growth of a crystal from its growth medium takes place by the integration of growth entities at kink sites in step ledges on the crystal surface (see Section 3.1). The growing surface of the crystal is separated from the bulk growth medium by an electrical double layer composed of a Helmholtz–Stern layer in the immediate vicinity of the solid crystal and a diffusion layer separating the Helmholtz–Stern layer from the bulk medium (Section 3.8.1). As discussed in Section 3.8.1, there is a strong lateral ordering between solute atoms/molecules of the Helmholtz–Stern layer, which is essentially a two-dimensional adsorption layer whose chemical composition is reminiscent of the structure of the crystal surface underneath. However, there is mainly vertical ordering between solute atoms/molecules in the subsequent molecular layers. This means that interactions between atoms/molecules somewhat away from the Helmholtz–Stern layer are not strong enough to yield lateral or vertical ordering between solute atoms/molecules. Thus, it can be assumed that the concentration of solute atoms/molecules in the diffuse layer decreases with an increase in distance beyond the Helmholtz–Stern layer.

During the growth of different crystals, all types of chemical interactions occur in the electrical double layer. The nature of interactions between solute atom/molecules depends on the chemical properties of the atoms/molecules of growing crystal. For instance, Coulomb interactions are dominant during the growth of ionic salts, whereas van der Waals interactions occur mainly during the growth of molecular crystals.

In growth systems containing impurities, all types of chemical interactions also occur in the electrical double layer. However, chemical interactions commonly occurring at the crystal interface during the adsorption of impurities are van der Waals, ionic, and

hydrogen bonding (Klug, 1993). Among these interactions, van der Waals interactions are important both as an independent adsorption and as a supplementary mechanism in all types of adsorption. Van der Waals interactions are partly responsible for the pronounced ability of long-chain ionic surfactant molecules to displace similarly charged simple inorganic ions from solid substrates. Several crystalline systems are influenced by surfactants, often by van der Waals adsorption of hydrocarbon ends of surfactants on the crystal surface.

Formation of hydrogen bonds often plays a primary role during the adsorption of impurities in the growth of both inorganic and ionic crystals (Klug, 1993; Weissbuch *et al.*, 1995). As in the case of covalent bonds, hydrogen forms a strong bond mainly with oxygen, nitrogen and fluorine atoms. Hydrogen bonds are stronger than van der Waals bonds and usually directionally more specific. Therefore, the effect of impurities forming hydrogen bonds with certain crystal faces can be very selective. Figure 4.30 illustrates the formation of hydrogen bonds by two different additive molecules on the growth interface of a molecular crystal.

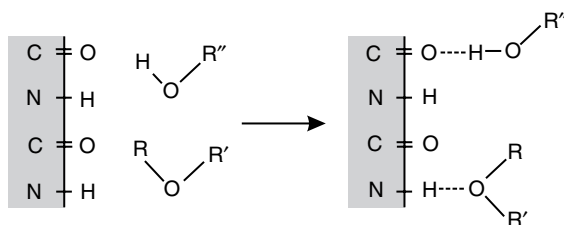


Figure 4.30 Formation of hydrogen bonds on the growth interface of a molecular crystal. Adapted from D.L. Klug. In: A.S. Myerson (Ed.), Handbook of Industrial Crystallization, p. 65. Copyright (1993), with permission from Elsevier

Ionic interactions are very important in the crystallization of ionic salts from aqueous solutions. For instance, highly polarizable ions such as Cr^{3+} , Al^{3+} and Fe^{3+} , an important group of simple cationic impurities, form predominantly ionic bonds at the crystal–solution interface, thereby having a pronounced effect on the growth of KDP-type and simple inorganic crystals from aqueous solutions. Tapering of the {100} face of KDP-type crystals is a manifestation of this effect (Section 4.7). The so-called multifunctional impurities such as phosphonic acids, polycarboxylic acids and polysulfonic acid, and high molecular weight copolymers having various acidic groups, are also capable of forming bonds with cationic species at crystal–solution interfaces.

The nature of the interactions of an impurity with the growth surfaces of ionic crystals may be understood from the crystal structure. As an example, we consider ammonium oxalate monohydrate (AO) crystals (Sangwal *et al.*, 2003). This compound crystallizes in an orthorhombic structure with space group $P2_12_12$ and lattice parameters $a = 0.8035 \text{ nm}$, $b = 1.0309 \text{ nm}$, $c = 0.3795 \text{ nm}$. Figure 4.31 shows the arrangement of $\text{C}_2\text{O}_4^{2-}$ ions, NH_4^+ ions and H_2O molecules in the [010] and [001] projections of the structure of AO crystals. The main features of the AO structure are the following:

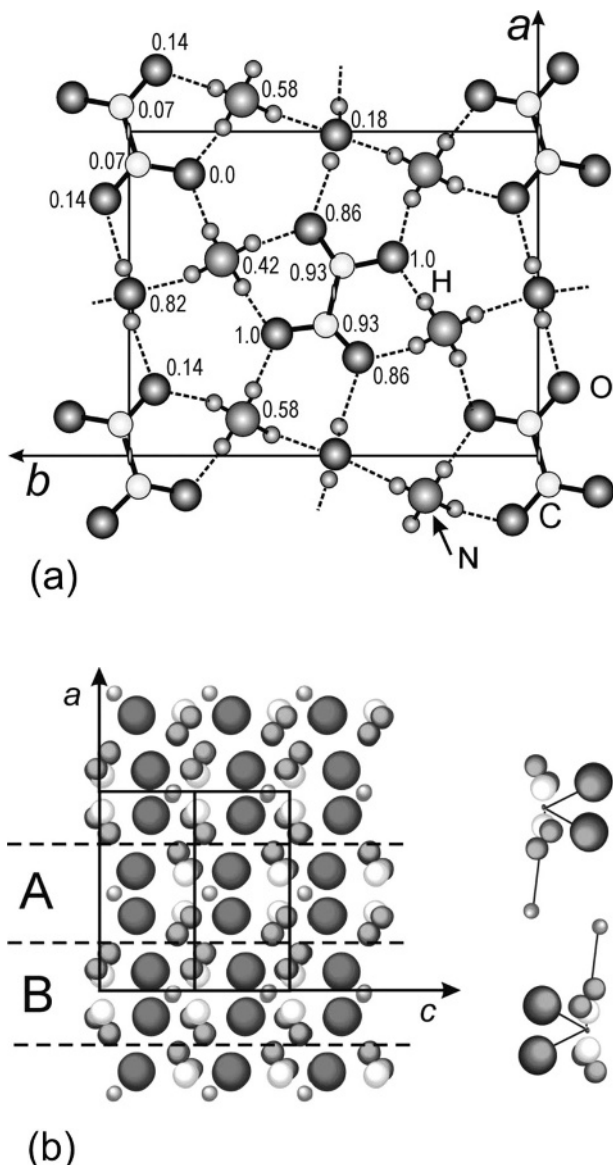


Figure 4.31 Different projections of the structure of AO crystals: (a) [001] and (b) [010] projection. Note that the [010] projection (b) consists of two different growth units in layers A and B, which are related by a two-fold symmetry. Projection (a) shows interatomic distances and basic bonds. In (b) large dark, medium-sized dark, medium-sized gray and small more gray spheres denote NH_4^+ ions, oxygen atoms, carbon atoms and water molecules, respectively, and each growth units consists of an $(\text{NH}_4)_2\text{C}_2\text{O}_4 \cdot \text{H}_2\text{O}$ molecule shown on the right. Reproduced from K. Sangwal, E. Mielniczek-Brzóska, and J. Borc. Cryst. Res. Technol. **38**, 103. Copyright (2003), Wiley-VCH

- (1) NH_4^+ ions are joined with $\text{C}_2\text{O}_4^{2-}$ ions by ionic bonds in the $\langle 110 \rangle$ direction and with H_2O molecules by strong hydrogen bonds in the $\langle 010 \rangle$ direction, whereas H_2O molecules are held in the bridges above two oxalate ions by hydrogen bonds, thereby forming chains along the $\langle 100 \rangle$ direction. This feature may be seen from the [001] projection (Figure 4.31a).
- (2) There are van der Waals interactions between successive stacking of the (001) planes, and the successive (001) layers may also be viewed as composed of alternate layers of negatively charged $\text{C}_2\text{O}_4^{2-}$ ions and positively charged NH_4^+ ion pairs (see Figure 4.31b).
- (3) An oxalate ion has a two-fold axis of symmetry parallel to the z axis, passing through the center of the C–C bond perpendicular to it. The COO plane makes an angle of 13° with the (001) plane symmetrical with respect to the z axis, leading to the twisting of the C–C bond.

As can be seen from Figure 4.31b, in the [010] projection the parallel (001) sheets have a stoichiometric composition involving one unit composed of one $\text{C}_2\text{O}_4^{2-}$ ion per pair of NH_4^+ ions and one water molecule. In this case, the symmetry-related two different types of $\text{C}_2\text{O}_4^{2-}$ ions lie in the same (001) sheets. However, the NH_4^+ ions may be in the same (001) sheet or in neighboring sheets, depending on their distance from the $\text{C}_2\text{O}_4^{2-}$ ions. Since a $\text{C}_2\text{O}_4^{2-}$ ion has a two-fold axial symmetry around the center of its two C atoms, we may assume that the center of a $\text{C}_2\text{O}_4^{2-}$ ion lies in the C–C center. Then, considering ionic interactions between nearest pair of NH_4^+ ions and a $\text{C}_2\text{O}_4^{2-}$ ion, one may choose a growth unit composed of one $\text{C}_2\text{O}_4^{2-}$ ion, two NH_4^+ ions and one water molecule in a projection. However, if the nearest distance between the centers of NH_4^+ and $\text{C}_2\text{O}_4^{2-}$ ions are taken, they appear as a dipole. Since $\text{C}_2\text{O}_4^{2-}$ ions in a projection are related by a two-fold axial symmetry, the neighboring growth units in the [010] projection of the (001) face are also different. This feature is clearly seen in Figure 4.31b, where the two types of growth units compose A and B layers of thickness d_{200} . The two types of growth units in the [010] projection of the (100) face are arranged alternately and form only one type of the outer A or B layers of thickness d_{001} . Similarly, one may find from the [001] projection that there are different growth units in successive layers of the (100) and (010) faces.

In terms of consistency in the nature of building units in the [010] and [001] projections of the structure of AO crystals, it follows that the growth units of AO crystals consist of single $(\text{NH}_4)_2\text{C}_2\text{O}_4 \cdot \text{H}_2\text{O}$ molecules. Typical examples of the arrangement of growth units in the [010] and [001] projections and the bonds between them are shown in Figure 4.32a and b, respectively. The arrangement of growth units in the (100) projection is similar to that in the (010) projection. With reference to Figure 4.31a, it should be noted that the identical growth units in the [001] direction are held together by van der Waals-type interactions, in the [100] direction by hydrogen bonds, and in the [010] direction by a mixture of ionic and hydrogen bonds. Moreover, the bond energies ϕ between nearest growth units, irrespective of the difference in their stacking, in the $\langle 100 \rangle$, $\langle 100 \rangle$ and $\langle 100 \rangle$ directions are the same (see Figures 4.31a and 4.32a and b).

Projections such as Figures 4.32a and b may be used to deduce connected nets for different orientations, and from the connected nets the growth habit and surface morphology of crystals may be explained in terms of the strength of bonds between the

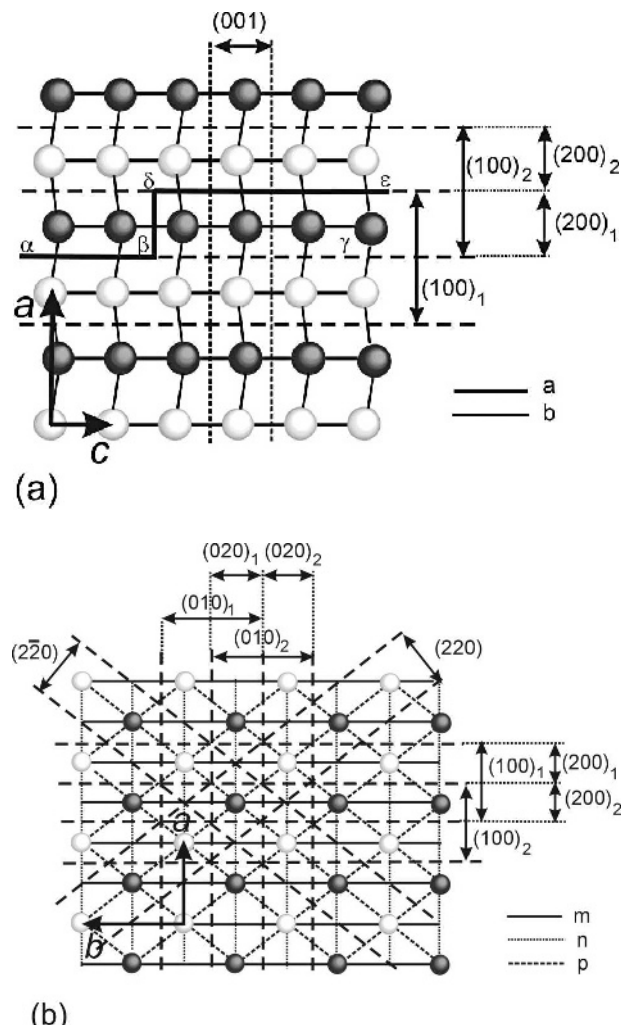


Figure 4.32 (a) [010] projection of the (001) and (100) faces with symmetry-related $(\text{NH}_4)_2\text{C}_2\text{O}_4 \cdot \text{H}_2\text{O}$ molecules as building units in layers A and B of Figure 4.31b; (b) [001] projection of (100), (010), (110) and ($1\bar{1}0$) faces with symmetry-related $(\text{NH}_4)_2\text{C}_2\text{O}_4 \cdot \text{H}_2\text{O}$ molecules as building units. Some bonds between the building units are also shown in these projections. Reproduced from K. Sangwal, E. Mielińczek-Brzóska, and J. Borc. Cryst. Res. Technol. **38**, 103. Copyright (2003), Wiley-VCH

growth units (Grimbergen *et al.*, 1998; Sangwal *et al.*, 2003). In the connected net analysis, individual building units like A and B in Figure 4.31b should form direct chains composed of similar bonds (cf. Strom, 1980, 1985). When this condition is not satisfied, one considers pairs of building units lying in a particular direction to form the basic building units. This situation may be visualized, for example, by taking two nearest

building units such as A and B in the [100] direction to form basic units AB or BA in Figure 4.32a.

Projections such as Figure 4.32a or b may also be used to deduce the energy of a step from the bonds broken between the building units. For example, in Figure 4.32a, the step energy for the (200) step is half of the bond energy ϕ_a between building units A and A (or B and B) in the $\langle 001 \rangle$ direction (denoted by bonds a) and may be calculated by comparing the surface energy of a flat surface bounded by $\alpha\beta\gamma$ with that of a surface with a step bounded by $\alpha\beta\delta\epsilon$. Similarly, the step energy for the (001) step is half of the bond energy ϕ_c between the building units A and B (or B and A) in the $\langle 100 \rangle$ direction (denoted by bonds b).

Two more features follow from Figure 4.32a:

- (1) Stacking of two successive layers of the [010] projection in such a way that the building units above the line $\alpha\beta\delta\epsilon$ form the upper partially completed layer forms a kink in the ledge oriented in the c direction. Attachment of a building unit A or B [i.e. $(\text{NH}_4)_2\text{C}_2\text{O}_4 \cdot \text{H}_2\text{O}$ molecule] singly involves the formation of a bond of strength a. Similarly, kink in a ledge oriented in the a direction may be imagined. In this case, the attachment of a building unit involves the formation of a bond of strength b.
- (2) When the basic building units involved are AB or BA {i.e. $[(\text{NH}_4)_2\text{C}_2\text{O}_4 \cdot \text{H}_2\text{O}]_2$ pairs}, the kinks are composed of AB pairs in the ledges oriented in the c and a directions. In these cases, the attachment of building units AB or BA in a kink involves the formation of bonds of strength 2a and 2b, respectively.

Obviously, the main issues involved in the application of connected net analysis to real experimental situations are knowledge of the constitution and composition of building units in the growth medium and interactions of the building units with the ions/molecules composing kinks in steps. Here it is implied that building units are composed of solute and impurity particles. Some of these aspects are discussed in Section 4.11.2.

According to the connected net analysis, the $\{001\}$ face of AO is expected to be an F face (see Figure 4.32b). The absence of the $\{001\}$ face in the morphology of AO crystals grown from pure aqueous solutions is due to the fact that its growth occurs below the kinetic roughening transition because of weak connected nets in the $\{001\}$ face. The origin of the formation of weak connected nets is mainly associated with the structure of the $\{001\}$ face, which is composed of growth units in the form of dipoles with NH_4^+ ions protruding out on the $\{001\}$ plane (Figure 4.31b).

On the $\{001\}$ face, electrostatic interactions mainly determine the strength of p and m bonds whereas relatively weak hydrogen bonding determines the strength of n bonds (Figure 4.32b). Therefore, the strength of these bonds decreases in the order m, p and n. As mentioned above, since NH_4^+ ions protrude out on the $\{001\}$ face, it may be supposed that Mn^{2+} ions substitute the protruding NH_4^+ ions and increase the strength of the above bonds in the same order. Increase in the strengths of bonds m, p and n between the normal growth units C and D and the corresponding units, say C' and D', composed of Mn(II) ions (see Figure 4.32b), leads to an overall increase in the strength of the bonds of the corresponding connected nets. This increase in the bond strength of the connected nets of the $\{001\}$ face of AO crystals is responsible for its stabilization in the presence of Mn^{2+} impurity.

It should be emphasized that the assumption of an overall increase in the strength of the bonds of the corresponding connected nets by growth units containing impurity ions does not mean that all bonds become stronger equally. Since the adsorption of such ‘impure’ growth units involves the formation of new bonds between the basic ‘pure’ growth units on the surface, in fact some bonds become stronger whereas the others are weakened. Consequently, it is possible that the connected nets composing some faces of the crystal are weakened by the adsorbing impurity. This can explain the increased growth rates, and hence disappearance, of some faces, such as the {100} of AO, from the growth morphology in the presence of a number of bivalent cations, including Mn^{2+} ions (Sangwal *et al.*, 2003).

4.11.2 Chemical Aspects of Impurity–Crystal Interactions

As discussed in Section 2.6.1, at a given temperature, impurities lead to a change in the solubility of electrolytes. In the case of ammonium oxalate, for example, its solubility c_0 increases practically linearly with increase in the concentration c_i of the impurity and the slope A_s of the $c_0(c_i)$ plots depends on the chemical nature of the impurity (Sangwal and Mielniczek-Brzóska, 2007).

Figure 4.33 shows the data for stability constants $-\log \beta_1$ of the complexes composed of first ligand of different impurities as a function of A_s (cf. Figure 2.24). We consider the first-ligand complexes simply because their stability constants are more accurate than those of complexes with higher ligands. Obviously, except for Cu(II) and Fe(III) impurities having relatively high values of $-\log \beta_1$, all the other impurities lead to the appearance of dead supersaturation zones. In fact, in the plot of $-\log \beta_1$ against A_s one

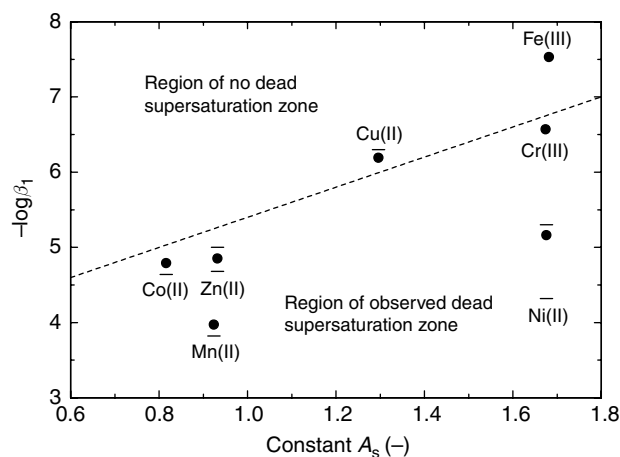


Figure 4.33 Dependence of $-\log \beta_1$ on A_s for different impurities. Horizontal bars indicate the upper and lower values for $-\log \beta_1$ of a complex and the points indicate their most probable value. The dashed line represents the linear dependence according to Equation (4.115), with constants $-\log \beta_{cr}^* = 3.4$ and $X_1 = 2$. Reproduced from K. Sangwal and E. Mielniczek-Brzóska. Cryst. Res. Technol. **42**, 531, Copyright (2007), Wiley-VCH

can identify the ranges of $-\log \beta_1$ for the effect of different impurities. Impurities for which $-\log \beta_1 < -\log \beta_{\text{cr}}$ lead to the appearance of dead supersaturation zones. Dead supersaturation zones do not appear when $-\log \beta_1 > -\log \beta_{\text{cr}}$ for an impurity. This behavior is shown in Figure 4.33 by the dashed line, and may be represented by an empirical linear relation [see Equation (2.73)]:

$$-\log \beta_{\text{cr}} = -\log \beta_{\text{cr}}^* + X_1 A_s \quad (4.115)$$

with constants $-\log \beta_{\text{cr}}^* \approx 3.4$ and $X_1 \approx 2$. The value of $-\log \beta_{\text{cr}}^*$ is close to the value of $-\log \beta = 3.8$ for HC_2O_4^- ions and refers to the species involved during growth from pure solutions (see below).

Figure 4.34 shows the projection of the ammonium oxalate monohydrate (AO) structure on the (100) plane. The projection shows the stacking of NH_4^+ ions, $\text{C}_2\text{O}_4^{2-}$ ions and H_2O molecules in two successive layers. The upper layer is represented by dark ammonium and oxalate ions and water molecules, while the lower layer is denoted by gray ions and molecules. In the upper layer one may also discern a kink relative to the lower layer by joining oxalate ions 2 and 1 with 3 and 4. Oxalate ions 3 and 4 are oriented along the [010] direction whereas ions 1 and 2 are oriented along the [001] direction. Similarly, kinks containing NH_4^+ pairs may be identified. Thus, the kink may be considered as a part of elementary steps oriented along the [010] or [001] directions. Consequently, in the case of predominantly electrostatic interactions occurring between the ions of the upper layer and migrating species from the solutions, growth of AO crystals from impurity-free solutions occurs by the integration of species present in the solution into the kinks.

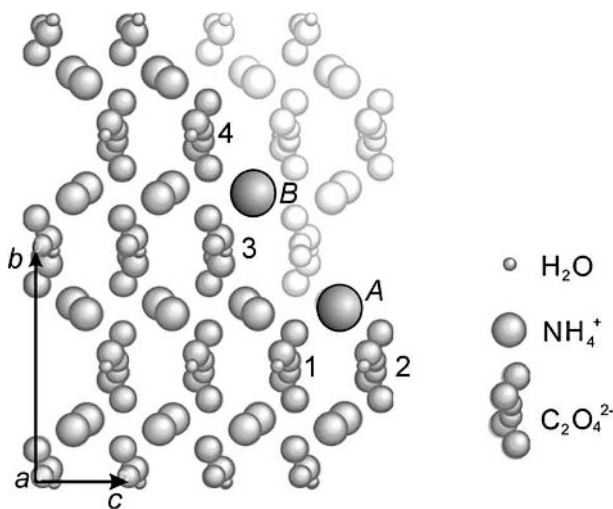


Figure 4.34 Projections of the AO structure on the (100) plane, showing the arrangement of NH_4^+ ions, $\text{C}_2\text{O}_4^{2-}$ ions and H_2O molecules in two successive layers. Adsorption sites for positively charged complexes are indicated as A and B. See text for details. Reproduced from K. Sangwal, E. Miśniczek-Brzóska, and J. Borc. *J. Cryst. Growth* **244**, 183. Copyright (2002), with permission from Elsevier

The formation of various species in pure aqueous saturated AO solutions may be explained by the dissociation of ammonium oxalate in water according to the equilibrium reaction



After dissociation, NH_4^+ and $C_2O_4^{2-}$ ions undergo hydrolysis according to the following equilibrium reactions:



Reactions (4.117)–(4.119) are equivalent to Reactions (1.7)–(1.9).

In pure AO solutions saturated at 30 °C, the solution pH is 6.1. This means that in natural solutions there is equilibrium between $(NH_4)_2C_2O_4^0$ neutral species and NH_4^+ and $C_2O_4^{2-}$ ions, while Reactions (4.118) and (4.119) shift to the right with increasing pH, producing undissociated $H_2C_2O_4^0$ and NH_4OH^0 species. Hence it may be argued that the species involved during the growth of AO crystals from pure solutions are NH_4^+ and $C_2O_4^{2-}$ ions. This implies that growth of AO crystals from impurity-free solutions occurs by the attachment of $C_2O_4^{2-}$ and NH_4^+ ions to the lattice positions in kinks on the growing surface, and that, except for their desolvation, the attachment of these ions to the kinks does not involve any chemical reaction. At low pH when Reactions (4.117) and (4.118) shift to the right, AO growth is controlled by the attachment of $C_2O_4^{2-}$ ions. However, at high pH when Reaction (4.119) shifts to the right, attachment of NH_4^+ ions controls the growth of AO crystals. This is so because the concentration of ions which are in deficiency determines the growth kinetics. From the above discussion, it may be concluded that growth of AO crystals from pure aqueous solutions is controlled by the attachment of $C_2O_4^{2-}$ ions because the pH is 6.1.

The mechanism of adsorption of complexes on the surface of a growing crystal is basically similar to that of integration of growth species at kink sites. However, during growth from solutions containing impurity complexes, the dominant complexes compete with NH_4^+ pairs and $C_2O_4^{2-}$ ions in occupying their usual lattice positions in the growing crystal surface. Since the dominant impurity complexes are negatively charged, it can be argued that they compete with $C_2O_4^{2-}$ ions inherently present or formed by hydrolysis reactions of bi- or trivalent metal oxalate complexes.

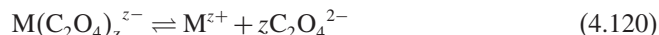
It should be mentioned that according to the connected net analysis the growth units are electrically neutral $(NH_4)_2C_2O_4 \cdot H_2O$ single molecules and $[(NH_4)_2C_2O_4 \cdot H_2O]_2$ paired molecules (see Section 4.11.1). However, the above discussion implies that, during growth from solutions containing impurities, charged impurity complexes compete with NH_4^+ and $C_2O_4^{2-}$ ions in occupying their usual lattice positions in the growing crystal surface. Basically, these two approaches are complementary, since the neutral single molecules or their pairs may be considered as reservoirs of basic NH_4^+ and $C_2O_4^{2-}$ units [cf. Equations (4.116)–(4.119)].

The dominant cation-containing species present in saturated aqueous solutions of ammonium oxalate are negatively charged, most stable oxalato complexes such as

$\text{Cu}(\text{C}_2\text{O}_4)_2^{2-}$, $\text{Mn}(\text{C}_2\text{O}_4)_3^{4-}$, $\text{Zn}(\text{C}_2\text{O}_4)_3^{4-}$, $\text{Cr}(\text{C}_2\text{O}_4)_3^{3-}$ and $\text{Fe}(\text{C}_2\text{O}_4)_3^{3-}$. These dominant impurity complexes differ in stability, electric charge and mass. Therefore, it may be supposed that electrostatic interactions predominantly occurring between ligands of these dominant complexes and pairs of adjoining NH_4^+ ions composing the growth surface are responsible for their adsorption at growth sites (i.e. kinks) on F faces. For example, in Figure 4.34 the adsorbing complexes consist of metal ions such as A and B, and at least two oxalate ligands capable of occupying positions 1 and 2, and 3 and 4, respectively. After reaching the surface, particles adsorb on it for some adsorption time τ_{ad} , followed by their redissolution into the growth medium, and may be given by the Frenkel equation [see Equation (4.1)]. Obviously, retardation of growth involves exchange of ligands of the adsorbed complex with the growing surface such that partially solvated impurity cations are left behind as a result of decomposition of the impurity complex. Depending on the nature of post-decomposition reactions, the impurity cation is either captured by the growing crystal or is pushed away into the bulk growth medium.

From Equation (4.1), it follows that the value of the adsorption time τ_{ad} increases with increasing τ_0 and Q_{ad} . Assuming that the time constant τ_0 is the same for all complexes and the heat of adsorption is proportional to the standard Gibbs free energy change ΔG_{0s} for the complexes, Equation (4.1) suggests that dead supersaturation zones are observed for impurities which form dominant complexes with a high number of $\text{C}_2\text{O}_4^{2-}$ radicals and/or smaller change in ΔG_{0s} (i.e. low $-\log \beta_s$). This inference means that a higher charge of the dominant complex and a smaller change in ΔG_{0s} lead to a short adsorption time τ_{ad} . In the former case, the shorter adsorption time is associated with weaker electrostatic interactions of complex species with the surface ions.

After the adsorption time τ_{ad} , the complex adsorbed on the surface dissociates (desorbs). For example, in the case of Cu^{2+} and Cr^{3+} ions, the adsorbed charged $\text{M}(\text{C}_2\text{O}_4)_z^{z-}$ complex dissociates according to the reaction



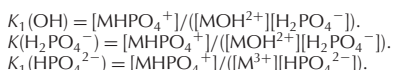
where M^{z+} denotes a cation which is probably partially solvated and z is the charge on it. Reaction (4.120) occurs in steps, with each dissociation product behaving as an adsorbing complex with its own adsorption time such that the total adsorption time is the sum of τ_{ad} of all adsorbing complexes. The $\text{C}_2\text{O}_4^{2-}$ ions are integrated into the crystal, while the M^{z+} ions are either pushed away into the solution or are captured into the crystal, depending on the chemical properties of the incorporating ions. Physically, a shorter adsorption time means that complex species quickly inhibit all possible kink sites. In other words, this situation corresponds to the instantaneous adsorption (and inhibition) of all growth sites. In instantaneous adsorption, adsorbed impurity species are in equilibrium (i.e. steady-state adsorption) and the suppressed growth rate is explained by Cabrera-Vermilyea or Kubota-Mullin model of impurity adsorption. Threshold supersaturation σ_d , corresponding to the upper limit of the dead supersaturation zone, appears until the adsorption time τ_{ad} is less than a critical time τ_{ad}^* . When τ_{ad} exceeds τ_{ad}^* , the surface-adsorbed complex is able to undergo dissociation on the surface and, under favorable circumstances, become integrated into the growing crystal. Hence it may be concluded that the appearance of a dead supersaturation zone in the $v(\sigma)$ and $R(\sigma)$ plots is associated with the stability of surface-adsorbed complexes formed by interactions between the species present in the bulk medium and the surface ions.

It should be noted that the relation $\tau_{\text{ad}} > \tau_{\text{ad}}^*$ is a necessary but not a sufficient condition. In order to become part of the growing crystal, the impurity ion has to meet size and charge requirements. The incorporation of impurities during crystal growth is discussed in Chapter 9.

Now we explain the tapering of KDP-type crystals following the above approach. It is well known that the tapering effect decreases in the order $\text{Cr}^{3+} > \text{Fe}^{3+} > \text{Al}^{3+}$. Since the effect of trivalent cations on the growth of KDP-type crystals has drawn considerable interest for over four decades, different approaches advanced to explain their effectiveness in producing tapering are briefly presented below. In these approaches it has been proposed that complexes like MHPO_4^+ , $\text{M}(\text{H}_2\text{O})_6^{3+}$ or $\text{M}(\text{H}_2\text{O})_4(\text{OH})_2^+$ (where M denotes a trivalent cation), present in the saturated solution, interact with the crystal surface. In principle, this concept of interactions on the growth surface is correct, but the basic problem lies in the identification of the interacting complexes, which diffuse to the crystal surface from the bulk medium. Various thermodynamic properties of the above ions are given in Table 4.4.

Table 4.4 Thermodynamic properties of Cr^{3+} , Fe^{3+} and Al^{3+} ions. Adapted from S. Veintemillas-Verdaguer and R. Rodriguez-Clemente. J. Cryst. Growth **79**, 198. Copyright (1996), with permission from Elsevier

Property	Cr^{3+}	Fe^{3+}	Al^{3+}
Ionic radius (nm)	0.063	0.064	0.051
Hydration enthalpy (kJ/mol)	4627	4489	4698
Bond energy (kJ/mol)	83	80.9	78.1
Hydrolysis constant K_1 (25 °C)	1.26×10^{-4}	6.3×10^{-3}	1.12×10^{-5}
Solubility product of $\text{M}(\text{OH})_3$ (25 °C)	6.7×10^{-30}	4×10^{-38}	1.9×10^{-33}
Stability constant $K(\text{MHPO}_4^+)$ (25 °C)	3×10^8	5×10^8	1.9×10^7
Stability constant $K_1(\text{MH}_2\text{PO}_4^{2+})$ (25 °C)	3.6×10^2	4×10^3	1×10^3
Solubility product of phosphates (25 °C)	10^{-18}	1.25×10^{-22}	10^{-17}



None of the properties listed in Table 4.4 explains the effect of different cations in a simple way. For example, Al^{3+} , with the smallest radius, should have a strong electrostatic interaction with the crystal and produce maximum tapering. However, the other ions are more effective. The bond energies have the correct order, but they differ from each other insignificantly to show great differences in their effectiveness. The stability constants of hydrolysis product $\text{M}(\text{H}_2\text{O})_4(\text{OH})_2^+$ and of formation of complexes such as MHPO_4^+ and $\text{MH}_2\text{PO}_4^{2+}$ also do not predict the right order. Hence it may be concluded that, in addition to thermodynamic properties of the above cations, kinetic factors should also be taken into account to explain the observed trend of their effectiveness.

As pointed out in Section 1.3, the chemical constitution of complexes present in concentrated solutions of electrolytes depends on the solution pH. Since the pH of supersaturated ADP and KDP solutions is about 4, the possible phosphate complexes interacting with the

ADP and KDP surface are $M(H_2O)_4(HPO_4)^+$, $M(H_2O)_2(HPO_4)_2^-$ and $M(HPO_4)_3^{3-}$ (see Figure 1.9). However, it can be supposed that the phosphate complexes interacting with the ADP and KDP surface are simple ones because adsorption of complicated species is difficult due to steric hindrance. The impurity complex $M(H_2O)_2(HPO_4)_2^-$, with the structure shown on the left of Figure 1.9b, is such a candidate.

The effect of an impurity on processes of adsorption and desorption of impurity complexes on the {100} growth surfaces of KDP crystal is presented in Figure 4.35. The complex, formed in the bulk solution (stage 1), adsorbs on the step by interacting with the step through the phosphate ligand (stage 2), thereby retarding the movement of the step (stage 3). At this stage, depending on whether the residence time τ_{ad} is less than or greater than a critical time τ_{ad}^* , the adsorbed complex either leaves the surface or is integrated into the crystals. According to this mechanism, the M^{3+} ion is incorporated in the KDP crystal in an interstitial position. In Figure 4.35 the dehydration of the adsorbed surface complex determines its capture into the {100} face of the KDP crystal, provided that the step period τ_{step} , defined as the time when a succeeding step replaces its preceding neighbor, exceeds the residence time τ_{ad} . This point is discussed in Section 5.1.2.

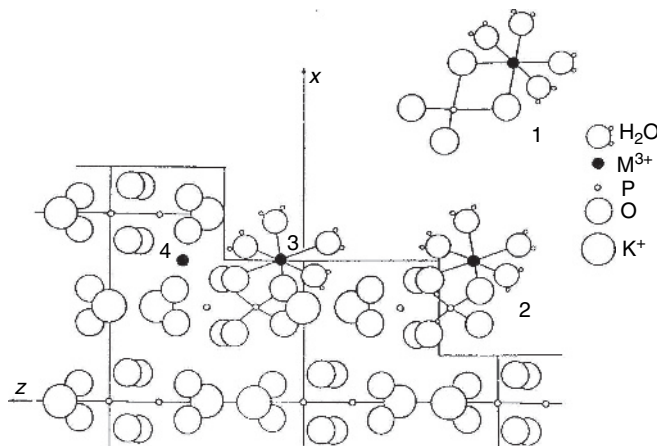


Figure 4.35 Schematic illustration of the mechanism of adsorption of $M(HPO_4)_2^-$ complex on the {100} face of a KDP crystal. Reproduced from S. Veintemillas-Verdaguer. Prog. Cryst. Growth Charact. Mater. **32**, 75. Copyright (1996), with permission from Elsevier

The mechanism of adsorption of impurities on the surfaces of AO and KDP crystals is relatively complex because of the constitution of solute and impurity species participating in growth. For a better understanding of interactions involved in the adsorption of impurity on the surfaces of crystals during growth, it is advantageous to investigate growth systems in which solute and impurities are simple ions or molecules. Sparingly soluble salts are good candidates for such studies. In recent years, *in situ* investigation of the inhibitory effect of several impurities, identified in both urine and kidney stones, on the growth of calcium oxalate monohydrate (COM) crystals has drawn considerable interest (see, for example, Wang *et al.*, 2006a,b). The results show (Wang *et al.*, 2006b) that citrate ions

significantly change the morphology and kinetics of the $(\bar{1}01)$ face but have little effect on the (010) face, the fast-moving $[101]$ step on the $(\bar{1}01)$ face becomes highly rough, and, according to molecular modeling calculations, the binding energy for citrate ions to the fast-moving $[101]$ step on this face is 165 kJ/mol. Somewhat similar results were obtained in the case of osteopontin impurity, but this impurity caused major changes in the morphology and kinetics on the (010) face. The authors attributed these results to the Cabrera–Vermilyea mechanism of adsorption of impurities.

The above discussion of interactions between additives and crystal interface is essentially phenomenological. In actual practice, for a proper understanding of the interactions involved, it is necessary to calculate the actual values of the interaction energies involved in the adsorption of additive molecules on the surface of a crystal in terms of crystal structure. This aspect is covered by molecular modeling of adsorption of additives on crystal surface, which has played a profound role in our present understanding of the fundamentals of adsorption processes (Braybrook *et al.*, 2002). For a survey of the literature devoted to developments in the field of molecular modeling of adsorption at crystal surfaces and interfaces, the reader is referred to a recent review by Wierzbicki and Madura (2004).

4.12 Tailor-Made Additives

Tailor-made additives are designed to interact in specific ways with selected faces of crystalline materials. The molecules of tailor-made additives are composed of two parts. One part (for example, chemical groups or moieties) is identical with that of the substrate molecules undergoing crystallization. When such molecules are added to a solution undergoing crystallization, by virtue of their moieties identical with the substrate these parts of the additive mimic the solute molecule and are, therefore, readily adsorbed at growth sites on the crystal surface. The second part of the additives is modified and is designed in such a way that the ends of these parts are chemically or structurally different from the host molecules, thereby disrupting subsequent attachment of solute molecules. This effect is achieved by tailoring the additive molecules to introduce steric hindrance, for example, by replacing methyl or chlorine substituents for hydrogen atoms in the host molecules or by substituting planar molecules with twisted ones (Berkovitch-Yellin *et al.*, 1985). In contrast to the above structural differences associated with replacing atoms or groups of host molecules by structurally different groups in additive molecules, chemical differences are achieved by replacing host molecules (for example, replacing amide molecules $RCONH_2$) with their derivatives in the modified part of the additive molecules (for example, by carboxylic acid derivatives RCO_2H) (Weisinger-Lewin *et al.*, 1989).

The specificity of tailor-made additives for certain faces of crystals is due to selective binding of identical parts of additive molecules on them while the modified part emerges from the crystal surface. This selective adsorption of additive molecules inhibits growth perpendicular to these faces, but the growth on other faces is not changed at all or only slightly. Thus, the morphology of the crystals is modified by tailoring additives that adsorb and inhibit at preselected faces. In their excellent review, Weissbuch *et al.*

(1995) give several examples of the use of tailor-made additives for morphology engineering, dissolution and etching of a variety of crystals. In their examples, they mainly discuss the effect of chiral additives characterized by left- (L) or right-handed (D) configurations. In a more recent review, Weissbuch *et al.* (2001) discuss the use of tailor-made inhibitors for various purposes such as crystal morphology engineering, kinetic resolution of racemates, reduction of crystal symmetry, assignment of absolute configuration of chiral molecules and polar crystals, and control of crystal polymorphism. Tailor-made additives, which self-assemble at the air–aqueous solution interface due to their intrinsic hydrophobic properties, may also be used to induce oriented crystallization by means of a structural match.

The effect of tailor-made impurities can be illustrated by the example of benzoic acid (C_6H_5COOH) additive on the crystallization of benzamide ($C_6H_5CONH_2$) from ethanol (Berkovitch-Yellin *et al.*, 1982; Addadi *et al.*, 1986). In the absence of the benzoic acid additive, benzamide crystallizes from ethanol, in the monoclinic space group $P2_1/c$, as

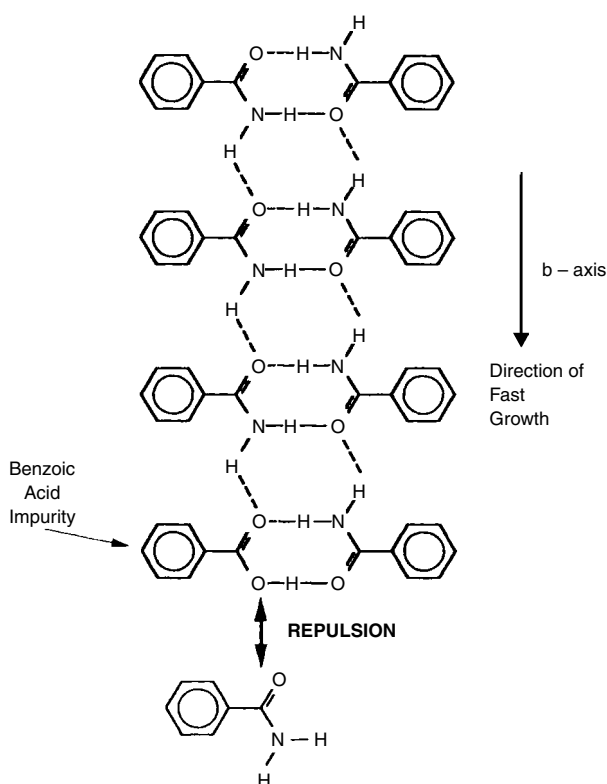


Figure 4.36 Inhibition of growth of benzamide crystals along the *b* direction by adsorption of benzoic acid molecule of the additive. Reproduced from L. Addadi, Z. Berkovitch-Yellin, I. Weissbuch, M. Lahav, and L. Leiserowitz. In: E.L. Eliel, S.H. Wilen, and N.L. Allinger (Eds.), Topics in Stereochemistry, Vol. 16, p. 1. Copyright (1986), with the permission from John Wiley & Sons, Inc., New York

platelets elongated along the *b* direction, as shown in Figure 4.36. The molecules in the crystal form hydrogen-bonded cyclic dimers, which are subsequently interlinked by hydrogen bonds to form ribbons parallel to the *b*-axis. The ribbons are stacked along the 0.5-nm *a*-axis in an arrangement involving mainly Coulomb interactions. The ribbon and stack motifs form stable {001} layers. Successive stacking of these layers along the *c* direction, via weak van der Waals interactions between phenyl groups, is responsible for the {001} platelet crystals. A benzoic acid molecule of the additive can replace a benzamide molecule at the end of a ribbon. However, at the outer side of the additive molecule where a new benzamide molecule is expected to be attached for growth, repulsive interaction takes place between additive and host molecules due to the adjacent lone-pair electrons of oxygens of the two molecules. This repulsion inhibits growth of benzamide crystals in the *b* direction, thereby changing the plate-like crystals to needles elongated along the *a* direction.

Tailor-made additives are effective during the growth of both organic and inorganic crystals. For example, α -amino acids induce habit changes in sodium chloride (Fenimore and Thraikill, 1949) and gypsum ($\text{CaSO}_4 \cdot 2\text{H}_2\text{O}$) crystals (Cody and Cody, 1991). In the case of NaCl, the positively (NH_3^+) and negatively (CO_3^-) charged moieties of α -amino acids fit at the {110} faces but not at the {100} and {111} faces. Consequently, the less stable {110} faces become more important in the growth morphology of NaCl crystals.

Investigations of interactions between organic impurities and inorganic crystals have profound importance for our understanding of biomineralization processes. For example, gypsum crystals grown in the presence of optically pure α -amino acids demonstrate enantioselective interactions between the crystal faces and the additive as a result of stereospecificity of interactions between α -amino acid molecules and gypsum crystal lattice (Cody and Cody, 1991). Among the α -amino acids, L-glutamic acid exhibits morphological changes at the {111} faces, whereas D-glutamic acid modifies the {111} faces of gypsum.

References

- Addadi, L., Z. Berkovitch-Yellin, I. Weissbuch, M. Lahav, and L. Leiserowitz (1986). In: E.L. Eliel, S.H. Wilen, and N.L. Allinger (Eds.), *Topics in Stereochemistry*, Vol. 16, John Wiley & Sons, Inc., New York, p. 1.
- Bennema, P. and J.P. van der Eerden (1987). In: I. Sunagawa (Ed.), *Morphology of Crystals*, Terrapub, Tokyo, p. 1.
- Berkovitch-Yellin, Z., L. Addadi, M. Idelson, M. Lahav, and L. Leiserowitz (1982). *Angew. Chem. Suppl.*, 1336.
- Berkovitch-Yellin, Z., J. van Mil, L. Addadi, M. Lahav, and L. Leiserowitz (1985). *J. Am. Chem. Soc.* **107**, 3111.
- Bienfait, M.R., R. Boistelle, and R. Kern (1965). In: R. Kern (Ed.), *Adsorption et Croissance Cristalline*, CNRS, Paris, p. 577.
- Black, S.N., R.J. Davey, and M. Halcrow (1986). *J. Cryst. Growth* **79**, 785.
- Bliznakov, G.M. (1954). *Bull. Acad. Sci. Bulg. Ser. Phys.* **4**, 135.
- Bliznakov, G.M. (1958). *Fortschr. Min.* **36**, 149.
- Bliznakov, G.M. (1965). In: R. Kern, (Ed.), *Adsorption et Croissance Cristalline*, CNRS, Paris, p. 291.
- Bliznakov, G.M., and E.K. Kirkova (1957). *Z. Phys. Chem.* **206**, 271.

- Bliznakov, G.M., and E.K. Kirkova (1969). *Krist. Tech.* **4**, 331.
- Boistelle, R., and B. Simon (1974). *J. Cryst. Growth* **26**, 140.
- Braybrook, A.L., B.R. Heywood, R.A. Jackson, and K. Pitt (2002). *J. Cryst. Growth* **242**, 336.
- Bredikhin, V.I., V.I. Ershov, V.V. Korolikhin, V.N. Lizyakina, S.Yu. Potapenko, and N.V. Khlyunev (1987). *J. Cryst. Growth* **84**, 509.
- Burton, W.K., N. Cabrera, and F.C. Frank (1951). *Philos Trans. Ry. Soc. London A* **243**, 299.
- Cabrera, N., and D.A. Vermilyea (1958). In: R.H. Doremus, B.W. Roberts, and D. Turnbull (Eds.), *Growth and Perfection of Crystals*, John Wiley & Sons, Inc., New York, p. 393.
- Chernov, A.A. (1961). *Usp. Fiz. Nauk* **73**, 277; Engl. Transl.: *Sov. Phys. Usp.* **4**, 116.
- Chernov, A.A. (1984). *Modern Crystallography III: Crystal Growth*. Springer, Berlin.
- Chernov, A.A., L.N. Rashkovich, and A.A. Mkrtchyan (1986a). *J. Cryst. Growth* **74**, 101.
- Chernov, A.A., L.N. Rashkovich, I.L. Smol'ski, Yu.G. Kuznetsov, A.A. Mkrtchyan, and A.I. Malkin (1986b). *Rost. Krist.* **15**, 43.
- Cody, A.M., and R.D. Cody (1991). *J. Cryst. Growth* **113**, 508.
- Davey, R.J., and J.W. Mullin (1974). *J. Cryst. Growth* **26**, 45.
- de Boer, J.H. (1953). *The Dynamical Character of Adsorption*, Oxford University Press, Oxford.
- Eggers, D.F., N.W. Gregory, G.D. Halsey, and B.S. Rabinovitch (1964). *Physical Chemistry*, John Wiley & Sons, Inc., New York.
- Eremina, T.A., V.A. Kuznetsov, N.N. Eremin, T.M. Okhrimenko, N.G. Furmanova, E.P. Efremova, and M. Rak (2005). *J. Cryst. Growth* **273**, 586.
- Fenimore, C.P., and A. Thraikill (1949). *J. Am. Chem. Soc.* **71**, 2714; cited by Weissbuch et al. (1995).
- Frank, F.C. (1958). In: R.H. Doremus, B.W. Roberts, and D. Turnbull (Eds.), *Growth and Perfection of Crystals*, John Wiley & Sons, Inc., New York. p. 411.
- Grey, W.A., E.R. Dalbey, and R.W. van Dolah (1956). *J. Am. Chem. Soc.* **78**, 1803.
- Grimbergen, R.F.P., H. Meekes, P. Bennema, C.S. Strom, and L.J.P. Vogels (1998). *Acta Crystallogr. A* **54**, 491.
- Guzman, L.A., and N. Kubota (2004). *J. Cryst. Growth* **275**, e237.
- Guzman, L.A., K. Maeda, S. Hirota, and N. Kubota (1998). *J. Cryst. Growth* **186**, 438.
- Guzman, L.A., N. Kubota, M. Yokota, A. Sato, and K. Ando (2001). *Cryst. Growth Des.* **1**, 225.
- Hartman, P. (1965). In: R. Kern (Ed.), *Adsorption et Croissance Cristalline*, CNRS, Paris, p. 477.
- Kirkova, E.K., and R.D. Nikolaeva (1971). *Krist. Tech.* **6**, 741.
- Kitamura, M., K. Ikemoto, Y. Kawamura, and T. Nakai (1992). *Int. Chem. Eng.* **32**, 157.
- Klug, D.L. (1993). In: A.S. Myerson (Ed.), *Handbook of Industrial Crystallization*, Butterworth-Heinemann, Boston, p. 65.
- Kubota, N. (2001). *Cryst. Res. Technol.* **36**, 749.
- Kubota, N., and J.W. Mullin (1995). *J. Cryst. Growth* **152**, 203.
- Kubota, N., M. Yokota, and J.W. Mullin (1997). *J. Cryst. Growth* **182**, 86.
- Kubota, N., M. Yokota, and J.W. Mullin (2000). *J. Cryst. Growth* **212**, 480.
- Kubota, N., M. Yokota, N. Doki, L.A. Guzman, and S. Sasaki (2003). *Cryst. Growth Des.* **3**, 397.
- Kuznetsov, V.A., T.M. Okhrimenko, and M. Rak (1998). *J. Cryst. Growth* **193**, 164.
- Li, L., K. Tsukamoto, and I. Sunagawa (1990). *J. Cryst. Growth* **99**, 150.
- Malkin, A.I., A.A. Chernov, and I.V. Alexeev (1989). *J. Cryst. Growth* **97**, 765.
- Martins, P.M., F.A. Rocha, and P. Rein (2006). *Cryst. Growth Des.* **6**, 2814.
- Mielniczek-Brzóska, E., and K. Sangwal (1994). *Cryst. Res. Technol.* **29**, 1027.
- Mielniczek-Brzóska, E., and K. Sangwal (2004). *Cryst. Res. Technol.* **39**, 993.
- Mielniczek-Brzóska, E., K. Gielzak-Koćwin, and K. Sangwal (2000). *J. Cryst. Growth* **212**, 532.
- Mullin, J.W., A. Amatavivadhama, and M. Chakraborty (1970). *J. Appl. Chem.* **20**, 153.
- Ościk, J. (1982). *Adsorption*, PWN, Warsaw.
- Owczarek, I., and K. Sangwal (1990a). *J. Cryst. Growth* **99**, 827.

- Owczarek, I., and K. Sangwal (1990b). *J. Cryst. Growth* **102**, 574.
- Potapenko, S.Yu. (1993). *J. Cryst. Growth* **133**, 141.
- Radenović, N., W. van Enckevort, P. Verwer, and E. Vlieg (2003). *Surf. Sci.* **523**, 307.
- Radenović, N., W. van Enckevort, and E. Vlieg (2004). *J. Cryst. Growth* **263**, 544.
- Radenović, N., W. van Enckevort, D. Kaminski, M. Heijna, and E. Vlieg (2005). *Surf. Sci.* **599**, 196.
- Rashkovich, L.N., and N.V. Kronsky (1997). *J. Cryst. Growth* **182**, 434.
- Ristić, R., B.Yu. Shekunov, and J.N. Sherwood (1994). *J. Cryst. Growth* **139**, 336.
- Sangwal, K. (1994). In: K. Sangwal (Ed.), *Elementary Crystal Growth*, Saan, Lublin, Chap. 4, p. 83.
- Sangwal, K. (1996). *Prog. Cryst. Growth Charact. Mater.* **32**, 3.
- Sangwal, K. (1998a). *Prog. Cryst. Growth Charact. Mater.* **36**, 163.
- Sangwal, K. (1998b). *J. Cryst. Growth* **192**, 200.
- Sangwal, K. (1999). *J. Cryst. Growth* **203**, 197.
- Sangwal, K. (2002). *J. Cryst. Growth* **242**, 215.
- Sangwal, K., and E. Miłniczek-Brzóska (2001a). *Cryst. Res. Technol.* **36**, 837.
- Sangwal, K., and E. Miłniczek-Brzóska (2001b). *J. Cryst. Growth* **233**, 343.
- Sangwal, K., and E. Miłniczek-Brzóska (2003). *Cryst. Res. Technol.* **38**, 133.
- Sangwal, K., and E. Miłniczek-Brzóska (2007). *Cryst. Res. Technol.* **42**, 531.
- Sangwal, K., E. Miłniczek-Brzóska, and J. Borc (2002). *J. Cryst. Growth* **244**, 183.
- Sangwal, K., E. Miłniczek-Brzóska, and J. Borc (2003). *Cryst. Res. Technol.* **38**, 103.
- Sangwal, K., and T. Pałczyńska (2000). *J. Cryst. Growth* **212**, 522.
- Sasaki, T., and A. Yokotani (1990). *J. Cryst. Growth* **99**, 820.
- Simon, B., and R. Boistelle (1981). *J. Cryst. Growth* **52**, 779.
- Simon, B., A. Grassi, and R. Boistelle (1974). *J. Cryst. Growth* **26**, 90.
- Strom, C.S. (1980). *Z. Kristallogr.* **153**, 99.
- Strom, C.S. (1985). *Z. Kristallogr.* **171**, 11.
- van der Putte, P., W.J.P. van Enckevort, L.J. Giling, and J. Bloem (1978). *J. Cryst. Growth* **43**, 659.
- Veintemillas-Verdaguer, S. (1996). *Prog. Cryst. Growth Charact. Mater.* **32**, 75.
- Veintemillas-Verdaguer, S., and R. Rodriguez-Clemente (1986). *J. Cryst. Growth* **79** 198.
- Wang, L., J.J. De Yoreo, X. Guan, S.R. Qui, J.R. Hoyer, and G.H. Nancollas (2006a). *Cryst. Growth Des.* **6**, 1768.
- Wang, L., W. Zhang, S.R. Qui, W.J. Zachowicz, X. Guan, R. Tang, J.R. Hoyer, J.J. De Yoreo, and G.H. Nancollas (2006b). *J. Cryst. Growth* **291**, 160.
- Weisinger-Lewin, Y., F. Frolov, R.K. McMullan, T.F. Koetzle, M. Lahav, and L. Leiserowitz (1989). *J. Am. Chem. Soc.* **111**, 1035.
- Weissbuch, I., L. Leiserowitz, and M. Lahav (1995). In: A. Mersmann (Ed.), *Crystallization Technology Handbook*, Marcel Dekker, New York, p. 401.
- Weissbuch, I., M. Lahav, and L. Leiserowitz (2001). In: K. Sato, Y. Furukawa, and K. Nakajima (Eds.), *Advances in Crystal Growth Research*, Elsevier, Amsterdam, Chap. 22, p. 381.
- Wierzbicki, A., and J.D. Madura (2004). In: X.Y. Liu and J.J. De Yoreo (Eds.), *Nanostructure and Assembly at Solid–Fluid Interfaces, Vol. II: Assembly in Hybrid and Biological Systems*, Kluwer, Boston, Chap. 1, p. 1.

5

Dead Supersaturation Zone and Threshold Supersaturations for Growth

The dependence of the displacement rate v of steps on the F faces and face growth rate R of crystals growing from solutions containing a certain amount of impurity on supersaturation σ frequently reveals that there is a threshold supersaturation σ_d below which no growth takes place, and the value of σ_d increases with increasing impurity concentration c_i in the solution. The supersaturation range in which no growth takes place is usually called the dead supersaturation zone. The existence of dead supersaturation zones has been reported for a variety of systems (for the literature, see Sangwal, 1996, 1998; Kubota, 2001; Dove *et al.*, 2004).

Since 1986, two different supersaturation barriers σ_d and σ^* have been reported in $v(\sigma)$ and $R(\sigma)$ plots for different crystals growing from aqueous solutions containing bi- and trivalent cationic impurities (Bredikhin *et al.*, 1987; Chernov *et al.*, 1986a,b; Rashkovich and Shekunov, 1991; Rashkovich and Kronske, 1997; Sangwal and Mielniczek-Brzóska, 2003; Mielniczek-Brzóska and Sangwal, 2004). Bredikhin *et al.* (1987) reported that for $\sigma_d < \sigma < \sigma^*$, the growth rate R of the {100} faces of potassium dihydrogenphosphate (KDP) in the presence of Fe(III) and Al(III) ions slowly increases following the classical BCF parabolic law, whereas for $\sigma > \sigma^*$, the growth rate rapidly increases following an $R[(\sigma - \sigma^*)^{5/4}]$ dependence. Rashkovich and Kronske (1997) reported that the initial parts of their $v(\sigma)$ data obtained on the {100} faces of KDP in the presence of Cr(III), Fe(III), and Al(III) additives follow the empirical relation $v = \beta'(\sigma - \sigma_d)^2$ (where β' is a constant), whereas for $\sigma > \sigma^*$ the step velocity v linearly increases with σ . During their studies of the effect of trivalent cations on the displacement velocity v of steps on the {100} and {101} faces of KDP crystals, Chernov *et al.* (1986a,b), Rashkovich and Shekunov (1992), and Rashkovich and Kronske (1997) found that there is also

another value of supersaturation $\sigma > \sigma^{**}$, when the impurity ceases to have an effect on the step velocity v which attains a value equal to that for a system without impurities. Sangwal and Mielniczek-Brzóska (2003) and Mielniczek-Brzóska and Sangwal (2004) also observed that, for a given concentration of Co(II), Ni(II) and Mn(II) impurities, the face growth rate R of ammonium oxalate monohydrate $[(\text{NH}_4)_2\text{C}_2\text{O}_4 \cdot \text{H}_2\text{O}; \text{AO}]$ crystals from aqueous solutions containing impurities approaches a value corresponding to pure solutions for supersaturation $\sigma > \sigma^{**}$. The appearance of different threshold supersaturations is illustrated schematically in Figure 5.1.

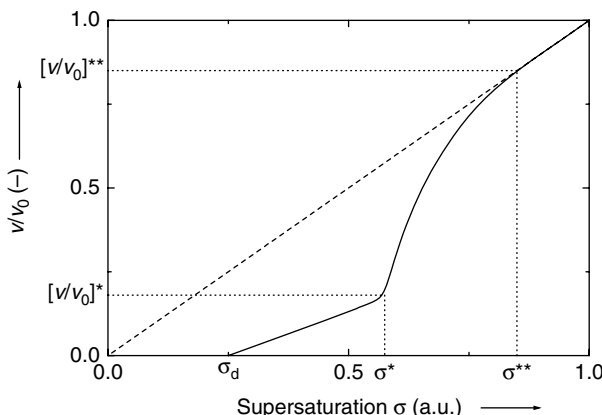


Figure 5.1 Schematic presentation of $v(\sigma)$ data illustrating the appearance of different threshold supersaturations at a hypothetical concentration c_i of an impurity

Recent extensive studies of the growth kinetics of AO crystals from aqueous solutions containing various bi- and trivalent impurities have revealed that no supersaturation barrier occurs in the case of Cu(II) (Mielniczek-Brzóska *et al.*, 2000; Sangwal and Mielniczek-Brzóska, 2001a) and Fe(III) impurities (Sangwal and Mielniczek-Brzóska, 2001b), one threshold supersaturation σ_d occurs in the case of Cr(III) impurity (Sangwal and Mielniczek-Brzóska, 2002), while two different threshold supersaturations σ_d and σ^* appear in the presence of Mn(II) (Sangwal and Mielniczek-Brzóska, 2003) and Co(II) and Ni(II) impurities (Mielniczek-Brzóska and Sangwal, 2004). These results mean that the effect of different impurities on the growth of even the same compound under identical growth conditions may differ enormously.

In this chapter, the origin of the appearance of threshold values of supersaturation σ_d , σ^* and σ^{**} is discussed first in the framework of the models of impurity adsorption described in Chapter 4. The final expressions for the dependence of step velocity v and face growth rate R on impurity concentration c_i are then used to interpret the experimental data on threshold supersaturations σ_d , σ^* and σ^{**} and the ratios σ_d/σ^* and σ^*/σ^{**} of successive threshold supersaturations. The chapter is based on the contents of papers by Sangwal (1999, 2002, 2005).

5.1 Origin of Threshold Supersaturations for Growth

5.1.1 Basic Kinetic Equations

The basic kinetic equations for growth in the presence of impurities are derived in Chapter 4. These equations describe situations when impurity particles adsorb at kinks in step ledges (i.e. Kubota–Mullin model) and on the surface terrace between successive ledges (Cabrera–Vermilyea model).

In the case of time-dependent impurity adsorption at kinks, the time-averaged step velocity v may be given by [see Equation (4.61)]

$$\begin{aligned} v/v_0 &= 1 - (\sigma_{dl}/\sigma)[1 - \exp(-t/\tau)] \\ &= 1 - \sigma_{cl}/\sigma \end{aligned} \quad (5.1)$$

where

$$\sigma_{cl} = \sigma_{dl}[1 - \exp(-t/\tau)] \quad (5.2)$$

with

$$\sigma_{dl} = \frac{\gamma_l a}{k_B TL} = \sigma_l^0 \theta_{eql} \quad (5.3)$$

Similarly, in the case of impurity adsorption at the surface terrace, from Equations (4.41) and (4.39) one may write

$$\begin{aligned} v/v_0 &= 1 - (\sigma_{ds}/\sigma)[1 - \exp(-t/\tau)]^{1/2} \\ &= 1 - \sigma_{cs}/\sigma \end{aligned} \quad (5.4)$$

where

$$\sigma_{cs} = \sigma_{ds}[1 - \exp(-t/\tau)]^{1/2} \quad (5.5)$$

with

$$\sigma_{ds} = \frac{\gamma_l a}{k_B TL} = \sigma_s^0 \theta_{eqs}^{1/2} \quad (5.6)$$

In the above equations, the indices l and s refer to adsorption at kinks and on the surface terrace, τ is a time constant for adsorption, t is the time, γ_l is the step free energy, a is the diameter of molecules, k_B is the Boltzmann constant, T is the temperature in kelvin, and L is the average distance between adsorbed impurity particles, which is related to the fractional coverage θ_{eq} corresponding to instantaneous impurity adsorption, defined by Equations (4.27) and (4.39).

As in the case of Equations (4.28) and (4.41), Equations (5.2) and (5.5) hold when $0 \leq \sigma_c/\sigma \leq 1$. Then $1 \geq v/v_0 \geq 0$. However, from Equations (5.2) and (5.5), one finds that they are essentially similar. Since $0 \leq 1 - \exp(-t/\tau) \leq 1$, $1 \geq v/v_0 \geq 0$. Therefore,

in the discussion below we omit the indices l and s and skip the distinction between adsorption at kinks and on the surface terrace.

In order to understand the role of the time-dependent term included in the square brackets, i.e. $[1 - \exp(-t/\tau)]$, in Equations (5.2) and (5.5) of threshold supersaturations, it is useful to consider the dependence of $1 - \exp(-t/\tau)$ on adsorption time t or adsorption time constant τ , as shown in Figure 5.2 for adsorption at kinks (i.e. $\rho = 1$). Depending on the value of τ in Equations (5.2) and (5.5), three situations can be considered:

- (1) When $\tau = 0$, the term $1 - \exp(-t/\tau) = 1$, $\sigma_c = \sigma_d$ and $v/v_0 = 0$. This is the case of instantaneous impurity adsorption and occurs at $\sigma < \sigma_d$ (Figure 5.1).
- (2) When $\tau \rightarrow \infty$, $\sigma_c = 0$ and $v/v_0 = 1$. Here the impurity adsorption becomes time independent, i.e. the flux of impurity particles adsorbing along the surface terrace becomes uniform (i.e. $\Delta c_i/\Delta y = 0$) in the direction y of motion of steps. Assume that this situation occurs at another threshold supersaturation σ^{**} .
- (3) When $0 < \tau < \infty$, the term $1 - \exp(-t/\tau)$ lies between 0 and 1, $0 < \sigma_c < \sigma_d$ and $0 < v/v_0 < 1$. This case corresponds to the onset of time-dependent impurity adsorption on the terrace between successive steps. Physically, the flux of the impurity particles adsorbing on the surface terrace shows a positive gradient ($\Delta c_i/\Delta y > 0$) in the direction y of motion of steps. Let us assume that this occurs at a threshold supersaturation σ^* .

With reference to Equations (5.2) and (5.5), one finds that $\sigma_d > \sigma^* > \sigma^{**}$ such that $\sigma^{**} \rightarrow 0$. This inference is a consequence of the condition that $v/v_0 = 0$. However, the plots of v/v_0 against σ for particular values of σ_d and time-dependent adsorption as governed by the time constant τ always predict the correct order: $\sigma_d < \sigma^* < \sigma^{**}$. Figure 5.3 illustrates the dependence of v/v_0 on σ according to Equation (5.1), assuming that τ is described by

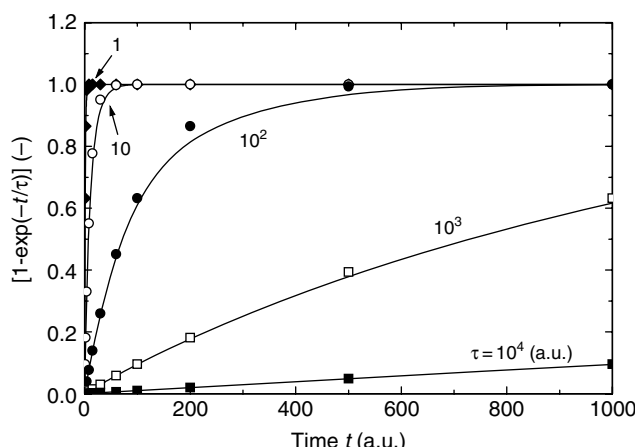


Figure 5.2 Dependence of $1 - \exp(-t/\tau)$ on adsorption time t for different values of adsorption time constant τ . Values of τ are indicated on the plots

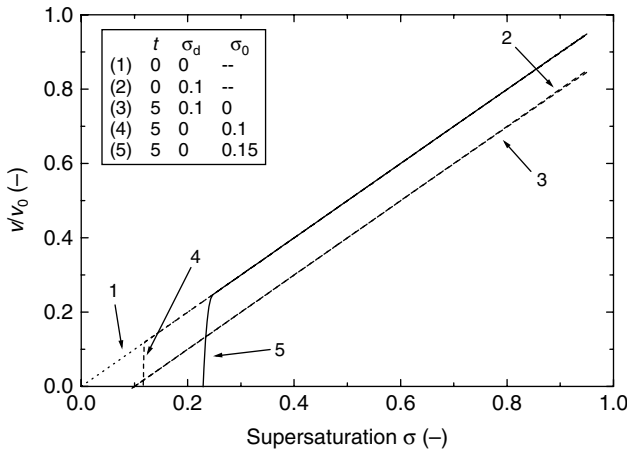


Figure 5.3 Dependence of v/v_0 against σ for different values of constant t (with $k_1 = 1$) and σ_0 according to Equation (5.1)

$$\tau = k_1(\sigma - \sigma_0) \quad (5.7)$$

where σ_0 and k_1 is a constant. This relation is a simplified form of the relation given by Kubota *et al.* (2000). The dependence of τ on σ is associated with the kinetic roughening of steps. As described by Kubota *et al.* (2000), a sudden transition is possible due to the time-dependent adsorption of an impurity.

In the present case, kinetic roughening of steps involves two processes: (1) increase in the density of kinks in a step and (2) increase in the density of steps emitted by a dislocation source with an increase in supersaturation σ . Following Nielsen (1981, 1984), the relationship between the density N_k of kinks (i.e. the number of kinks per unit area) on the surface of a crystal growing by spiral growth mechanism and the supersaturation used for growth is given by

$$N_k = \frac{a^2}{x_0 y_0} = \frac{S^{1/2} \ln S}{19(\gamma_l/k_B T) \exp(\gamma_l/k_B T)} \quad (5.8)$$

Since for fairly soluble compounds $\gamma_l/k_B T$ is between 0.3 and 0.5, Equation (5.8) may be written as

$$N_k = \kappa \sigma \quad (5.9)$$

where $\sigma \approx S^{1/2} \ln S$ and the constant κ is equal to 0.064 and 0.215 for $\gamma_l/k_B T = 0.5$ and 0.2, respectively. Thus, the time constant τ is intimately connected with the kinetic roughening due to an increase in supersaturation σ .

With reference to Equation (5.7), two remarks should be made:

- (1) It assumes that σ_d is a constant quantity independent of σ . Since the reasonable values for L are between $10a$ and $100a$, it is obvious that σ_d lies between 0.005 and 0.05, as is usually found for fairly soluble compounds.
- (2) The value of $\sigma_0 \neq \sigma_d$, because σ_0 is associated with the onset of kinetic roughening, while σ_d is determined by thermodynamic parameter γ_l . This implies that $\sigma_0 > \sigma_d$.

5.1.2 Three Different Distances Between Impurity Particles

Assuming that the value of the step free energy γ_l does not depend on σ , for a given equilibrium fractional coverage θ_{eq} corresponding to the observed threshold supersaturations σ_d , σ^* and σ^{**} , one can define average effective distances between adsorbed impurity particles in the sequence $l_d > l^* > l^{**}$. We now discuss the physical basis of this sequence of distances, considering adsorption at kinks.

There is no growth (i.e. $v_{\min}/v_0 = 0$) for $\sigma \leq \sigma_d$ because the average distance l between impurity particles encountering an advancing step does not exceed the diameter $2r_{2D}^*$ of a critical nucleus [see Equation (4.25)]. This situation holds until $\sigma \leq \sigma_d$ when the average distance between steps

$$y_0 = 19r_{2D}^* \geq l_d \quad (5.10)$$

where $l_d = L$ in Equations (5.3) and (5.6). Since the critical nucleus diameter $2r_{2D}^*$ decreases with increase in supersaturation σ [cf. Equation (4.24)], with an increase in σ the step tends to squeeze out through the fence of impurity particles such that the time-averaged step velocity $v < v_0$ [see Equation (4.28)]. At such supersaturations the impurity particles have sufficient time to settle down at adsorption sites on the surface between two steps during the period of their movement through distance y_0 . This is the so-called instantaneous impurity adsorption.

Different stages of crossing of a growth step through an array of impurity particles situated at an average distance l are illustrated in Figure 5.4. Positions 2–6 show different

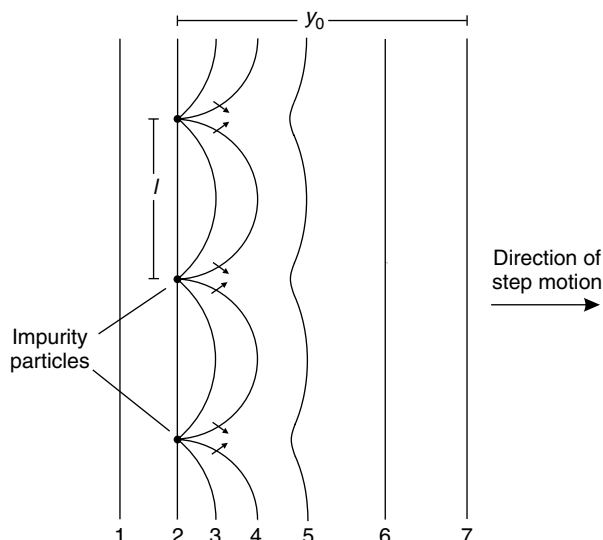


Figure 5.4 Different stages of crossing of a growth step through a fence of impurity particles. Position 2 represents the stage when the step encounters impurity particles and position 6 denotes the stage when it attains a configuration before encountering the impurity particles. Regions of negative curvature are indicated by arrows

configurations of the step after encountering and crossing impurity particles. After penetrating through the fence of impurity particles, the advancing step attains the configuration of minimum line tension by the preferential integration of growth species at regions of negative curvatures involving high density of kinks.

Both of the distances x_0 and y_0 between kinks in a step and between steps decrease with increase in supersaturation σ . Consequently, corresponding to a given fractional coverage θ_{eq} , the contribution of the term $(\sigma^0/\sigma)\theta_{\text{eq}}$ decreases with increasing σ . This facilitates the squeezing out of advancing steps through the fence of impurity particles as a result of decreasing r_{2D}^* with increasing σ . Moreover, when the average distance y_0 between steps becomes less than the distance between impurity particles, after crossing a fence of impurity particles an advancing step encounters new impurity particles ahead of it even before attaining its minimum linear energy (i.e. attaining rectilinearity). This defines another distance given by

$$y_0 = 19r_{2D}^* = l^* \quad (5.11)$$

such that $l_d > l^*$. This stage corresponds to the onset of time-dependent impurity adsorption and occurs at σ^* . In this case there is a decreasing surface concentration of adsorbed impurity molecules on the terrace between neighboring steps. With further increase in supersaturation, the average distance l between impurity particles still increases and the concentration of impurity particles adsorbed on the terrace between neighboring steps shows the tendency to become essentially uniform. This continues until supersaturation σ^{**} is reached, when the impurity adsorption becomes time independent, and is accompanied by another average distance l^{**} between adsorbed impurity particles when $19r_{2D}^* = l^{**}$ such that $l_d > l^* > l^{**}$.

The above idea of an average distance corresponding to a supersaturation barrier is consistent with the concept advanced by Rashkovich and Kronske (1997). According to them, the barrier σ_d occurs at $2r_{2D}^* = l_d$ when there is complete blocking of the movement of steps, while the origin of σ^* is associated with the burial of adsorbed impurity particles as a result of curling of advancing steps around them when the depth of the bent step (indentation) reaches a value δ . The burial of impurity particles occurs when the critical nucleus diameter $2r_{2D}^* \propto \sigma^{-1}$ [see Equation (4.24)] becomes equal to the average distance l^* between adsorbed impurity particles. However, the concept of time-dependent and time-independent impurity adsorption is similar to that of Kubota and Mullin (1995) and Kubota *et al.* (1997, 2000). According to these authors, the origin of σ_d and σ^* is associated with steady-state (instantaneous) impurity adsorption for $\sigma < \sigma^*$ and unsteady-state (i.e. time-dependent) adsorption for $\sigma > \sigma^*$, respectively.

It should be mentioned that the concept of time-dependent adsorption is old and was initially advanced by Frank (1958) and Cabrera and Vermilyea (1958) to explain the origin of kinematic waves and step bunching in terms of relationships between flux of steps passing across a point and the density of steps on the surface. The concept of time-independent impurity adsorption was proposed later by van der Putte *et al.* (1978).

5.2 Determination of Threshold Supersaturations from $v(\sigma)$ and $R(\sigma)$ Data

From Equations (5.1) and (5.4), one obtains [cf. Equation (4.69)]

$$v = \beta_{l0}(\sigma - \sigma_d) - \rho\beta_{l0}(\sigma - \sigma_d)\exp(-t/\tau) \quad (5.12)$$

or alternatively

$$v = A_1(\sigma - \sigma_d) \quad \text{for } \sigma_d < \sigma < \sigma^* \quad (5.13)$$

and

$$v = A_2(\sigma - \sigma_d)\exp(-t/\tau) \quad \text{for } \sigma^* < \sigma < \sigma^{**} \quad (5.14)$$

where $A_1 = \beta_{l0}$ and $A_2 = \rho\beta_{l0}$. While deriving Equation (5.12) from Equation (5.4), it was assumed that $\exp(-t/\tau) \ll 1$. Note that $A_2 = A_1$ or $A_2 = A_1/2$, since $\rho = 1$ or $\frac{1}{2}$ for impurity adsorption at kinks in ledges and on the surface terrace, respectively. Equations (5.12)–(5.14) are the basic equations relating threshold supersaturations σ_d and σ^* with supersaturation σ for crystal growth in the presence of impurities.

From the $v(\sigma)$ and $R(\sigma)$ plots, one can directly read off the values of the different threshold supersaturations. However, the values of σ_d and σ^* read in this way may differ substantially from those determined by using appropriate equations relating the supersaturation dependence of v and R . Since the experimental errors in v and R are greater at low σ , the relative errors in the determination of σ_d are greater than those in σ^* and σ^{**} . Therefore, one should always precisely determine σ_d and σ^* from the experimental $v(\sigma)$ and $R(\sigma)$ data using appropriate equations.

It is difficult to use Equation (5.12) in its present form for the analysis of experimental $v(\sigma)$ or, assuming that $v \propto R$, $R(\sigma)$ data in the entire supersaturation range for the growth of a crystal. However, Equation (5.13) referring to growth kinetics controlled by instantaneous impurity adsorption in the supersaturation intervals $\sigma_d < \sigma < \sigma^*$ and Equation (5.14) referring to growth controlled by time-dependent adsorption in the range $\sigma^* < \sigma < \sigma^{**}$ enable one to determine σ_d and σ^* , respectively, reliably.

It should be mentioned that to describe the $v(\sigma)$ data for the {100} faces of KDP crystals growing from aqueous solutions containing trivalent cationic impurities, Rashkovich and Kronsky (1997) gave an empirical expression in the form

$$v = \beta'(\sigma - \sigma_d)^2 + \frac{\beta'_0\sigma - \beta'(\sigma - \sigma_d)^2}{1 + \exp[d(s - \sigma)]} \quad (5.15)$$

where β' and σ_d are obtained from the initial parts of the $v(\sigma)$ curves, and β'_0 , d and s are empirical constants calculated by considering the data over the entire supersaturation range. The inclusion of an exponential term similar to that in Equation (5.12) is striking, although this term appears in the denominator of Equation (5.15).

5.2.1 Relationship Between the Model Involving Cooperating Spirals and the Power-Law Approach

Assuming that the face growth rate R is proportional to the step velocity v , one obtains the following equations [cf. Equations (4.80) and (4.81)]:

$$R = \frac{\sigma}{Y(G + \sigma)}(\sigma - \sigma_d) \quad (5.16)$$

and

$$R = A\sigma^{n-1}(\sigma - \sigma_d) \quad (5.17)$$

for growth involving cooperating spirals and the power-law approach, respectively. In order to compare the values of supersaturation barrier σ_d determined by using Equations (5.16) and (5.17), it is first necessary to generate $R(\sigma)$ data by one growth rate expression describing at different impurity concentrations c_i for known values of σ_d , and subsequently use these generated $R(\sigma)$ data to determine σ_d by using another growth rate expression.

Sangwal (2002) analyzed the $R(\sigma)$ data generated by Equation (5.17) of the power-law approach by using Equation (5.16) of the model involving a complex source of cooperating screw dislocations. The following situations were considered: (a) n is constant but σ_d increases and (b) n is variable but σ_d is constant. It was found that, for given values of n , the constant $1/Y < A$ and $\sigma_{d_1} < \sigma_{d_2}$, and the difference $(\sigma_{d_1} - \sigma_{d_2})$ decreases with increase in impurity concentration c_i . The threshold supersaturations determined by using Equations (5.16) and (5.17) are denoted σ_{d_1} and σ_{d_2} , respectively. The decreasing difference $(\sigma_{d_1} - \sigma_{d_2})$ and increasing trend in the value of $1/Y$ with increasing c_i is due to a relatively poor fit of the data at low supersaturation σ . In contrast to the above, at a given c_i the value of $1/Y$ initially decreases and then increases with increase in n . The value of $1/Y$ attains a minimum at $n = 1.5$ but it can even exceed unity at n close to 2. The dependence of G also shows a similar behavior. Similar trends in the behavior of $1/Y$ and G with increasing c_i mean that the factor responsible for the changes in these quantities is the same and is related to the data.

5.2.2 Relationship Between the Power-Law Approach and an Empirical Expression with Corrected Supersaturation

In the presence of impurities, in some cases the face growth rate R of crystals may be described (Simon *et al.*, 1974; Bredikhin *et al.*, 1987) by the usual growth rate equations with corrected supersaturation $(\sigma - \sigma_d)$ instead of applied supersaturation σ where the $R(\sigma)$ curves are displaced relative to each other by increasing values of threshold supersaturation σ_d , i.e.

$$R = A'(\sigma - \sigma_d)^{n'} \quad (5.18)$$

where A' and n' are constants. Therefore, it is of interest to compare the $R(\sigma)$ data by using Equations (5.17) and (5.18).

Sangwal (2002) analyzed the general trends of the threshold supersaturation σ_d from the data generated by Equations (5.17) and (5.18). The analysis clearly demonstrated that the main problem in distinguishing the applicability of Equations (5.17) and (5.18) is the lack of reliable data at very low growth rates (i.e. at low supersaturations). Therefore, at low supersaturations the reliability of the empirical parabolic dependence in Equation (5.18) remains questionable; also see Equation (5.15).

5.2.3 Determination of σ^*

In order to determine σ^* , one uses Equation (5.12) with an empirically chosen function for τ . Kubota *et al.* (2000) assumed that the time constant τ is given by Equation (5.7) where $\sigma_0 = \sigma^*$. Sangwal (2002) found that the $v(\sigma)$ data for the growth of the {100} faces of KDP from aqueous solutions containing Cr(III), Fe(III) and Al(III) impurities at $\sigma > \sigma^*$ are satisfactorily reproduced by the expression

$$v = A_2 \{ \exp[-p(\sigma - \sigma^*) - 1] \} \quad (5.19)$$

where A_2 and p are constants. This means that in Equation (5.14) one has

$$t/\tau = -p(\sigma - \sigma^*) - 1 \quad (5.20)$$

and $A_2 = \beta_{l0}\sigma_d = \beta_{l0}\sigma^0\theta_{eq} = v_0[(\sigma^0/\sigma)\theta_{eq}]$, where β_{l0} is the kinetic coefficient for step motion in the absence of impurities.

Sangwal (2002) analyzed the experimental $v(\sigma)$ data, reported by Rashkovich and Kronsky (1997), on the (100) face of KDP crystals in the presence of different trivalent impurities, and obtained the values of constants A_1 and σ_d of Equation (5.13) and A_2 , σ^* and p of Equation (5.14) from the best fit of the experimental data for FeCl_3 impurity. FeCl_3 impurity was selected to illustrate that the linear relation satisfactorily describes the dependence of v on σ for $\sigma_d < \sigma < \sigma^*$, and there is no justification in using the empirical parabolic Equation (5.18), as inferred by Rashkovich and Kronsky (1997). Moreover, for CrCl_3 and AlCl_3 , the plots of v against σ are practically linear in this supersaturation region.

It was observed that the values of the constants A_1 and p in Equations (5.13) and (5.14) change enormously, depending on the number of data points selected during the minimization procedure to obtain the values of the constants of the above equations. The following features were noted:

- (1) A_2 and p are practically constant quantities characteristic of an impurity and are independent of its concentration c_i , while $A_1 < A_2$ and decreases with an increase in c_i of the impurity.
- (2) $A_2 \approx \beta_{lp}$ (where β_{lp} is the step kinetic coefficient for the ‘pure’ growth system) and $A_1 < \beta_{lp}$ for the three impurities.

The dependence of A_1 on the concentration c_i of an impurity is associated with the additional activation barrier ΔW caused by the impurity [see Equation (5.33)]. From the ratio $A_1/\beta_{lp} = \exp k_2$ (where k_2 is a constant, which characterizes the effectiveness of the impurity), Sangwal (2002) observed that the effectiveness of an impurity, as determined by the values of k_2 , decreases in the order FeCl_3 , AlCl_3 and CrCl_3 . This is the order

of increasing solubility product K_s of $M(OH)_3$, where M denotes a trivalent cation. However, this order of the effectiveness of different cations differs from that inferred from tapering data of KDP-type crystals (Section 4.7).

The constancy of A_2 (related to β_{lp}) implies that the term $(\sigma^0/\sigma)\theta_{eq} = 1$ in the case of KDP crystals [cf. Equation (5.20)], and is independent of the nature and concentration of the impurity used during growth at $\sigma > \sigma^*$. The fact that $(\sigma^0/\sigma)\theta_{eq} = 1$ is consistent with the condition that here $v/v_0 = 0$. Since σ^0 is a constant quantity [see Equations (5.3) and (5.6)], the constancy of $(\sigma^0/\sigma)\theta_{eq}$ implies that the fractional coverage θ_{eq} in the case of time-dependent impurity adsorption linearly increases with supersaturation σ used during growth. The above value of $(\sigma^0/\sigma)\theta_{eq}$ is similar to those reported for ammonium sulfate crystals growing in the presence of Cr(III) impurity (Kubota *et al.*, 2000). The average values of the constant p obtained for KDP are lower by about two orders of magnitude than those obtained for ammonium sulfate crystals (Kubota *et al.*, 2000), and depend on the nature of the impurity.

5.3 Dependence of Threshold Supersaturations on Impurity Concentration: Basic Theoretical Equations and Linear Approximations

In order to describe the dependence of threshold supersaturations on the concentration of an impurity, different adsorption isotherms may be used. In this section, Langmuir and Freundlich isotherms are used for the analysis. However, irrespective of whether impurity adsorption is steady state or unsteady state, fractional surface coverage θ refers to all supersaturations.

Assuming that the origin of threshold supersaturations σ_c is associated with particular values of v/v_0 or R/R_0 , the threshold supersaturation σ_c may be given by [cf. Equations (5.1) and (5.4)]

$$\sigma_c = \theta_{eq}^\rho / Q \quad (5.21)$$

where σ_c denotes a threshold supersaturation, and

$$Q = \frac{1 - v/v_0}{\sigma^0 [1 - \exp(-t/\tau)]^\rho} \quad (5.22)$$

In the case of the Langmuir adsorption isotherm, Equation (5.21) may be written as

$$1/\sigma_c^{1/\rho} = Q^{1/\rho} (1 + 1/Kc_i) \quad (5.23)$$

where K is the Langmuir constant [see Equation (4.6)] and σ^0 is given by Equations (4.29) and (4.42). When $Kc_i \ll 1$, Equation (5.23) takes the form

$$\sigma_c^{1/\rho} = Kc_i / Q^{1/\rho} \quad (5.24)$$

Obviously, in this case the threshold supersaturation σ_c increases linearly with increase in c_i^ρ such that $\sigma_c = 0$ when $c_i = 0$.

When impurity adsorption follows the Freundlich isotherm, Equation (5.21) is given by

$$\sigma_c^{1/\rho} = B c_i^m \quad (5.25)$$

where the exponent $m \leq 1$ and the constant B is given by [cf. Equation (4.37)]

$$B = (m/c_i^{*m})/Q^{1/\rho} \quad (5.26)$$

In the case of the Freundlich isotherm, a linear relationship between $\sigma_c^{1/\rho}$ and c_i is also possible. It occurs when the following approximation is valid (see below):

$$A_3 x^{b_1} = A_3 (1 - b_1/A_3)[1 + (b_1/A_3)x] \quad (5.27)$$

where A_3 and b_1 are constants. Then Equation (5.25) may be written in the form

$$\sigma_c^{1/\rho} = B_0 + B' c_i \quad (5.28)$$

where

$$B_0 = (B - m), \quad B' = B_0 m / B = (m - m^2 / B) \quad (5.29)$$

with B given by Equation (5.26).

Approximation (5.27) follows from the first two terms of the expansion of Taylor's series, i.e.

$$f(x) = f(x_0) + f'(x_0)(x - x_0) \quad (5.30)$$

which is valid when

$$x_0 = \left(\frac{1 - b_1/A_3}{1 - b_1} \right)^{1/b_1}; \quad \left(\frac{1 - b_1/A_3}{1 - b_1} \right)^{1/b_1} = \left(\frac{1 - b_1/A_3}{A_3} \right)^{1-b_1} \quad (5.31)$$

where x_0 is the limiting value of the variable x and should not be confused with the interkink distance x_0 . From these relations, it follows that A_3 and b_1 are interrelated, $0 < b_1 < 1$ and $0 < x < 1$. Figure 5.5 shows the plots of $y = A_3 x^{b_1}$ as a function of x (solid lines) and the predicted linear dependence according to the approximation in Equation (5.27) for four different values of b_1 (dotted curves). It can be seen that the linear approximation reproduces satisfactorily the data of the power law in the interval $0.7 < x < 1$. The linear approximation reproduces the power-law curve in a broader range, $0.5 < x < 1$, when the term b_1/A_3 in Equation (5.26) is multiplied by a correction factor of 1.1, as shown by the dashed curves.

Conditions (5.31) imply that, in Equations (5.28) and (5.30), $0 < B < 1$, $B^2 > m$ and the concentration ratio $c_i/c_i^* < 1$. Equation (5.28) has the same form as Equation (5.24), where the constant $B_0 = 0$. However, irrespective of the value of m , $B' < B$. Since $B = K/Q^{1/\rho}$ (see above), it may be concluded that the values of K and Q_{diff} obtained from B' , on the assumption that $B' = B$, are lower than the expected values. These values also depend on the chosen value of Q .

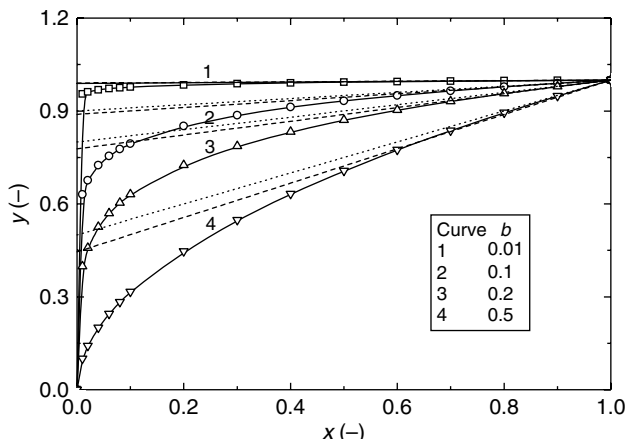


Figure 5.5 Plots of $y = A_3 x^{b_1}$ as a function of x (solid lines) and the predicted linear dependence according to the approximation in Equation (5.29) for four different values of b_1 (dotted curves). Dashed curves represent Equation (5.29) with the term b_1/A_3 multiplied by 1.1. Reproduced from K. Sangwal. Cryst. Res. Technol. **40**, 635. Copyright (2005), with permission from Wiley-VCH

Equation (5.28) has previously been obtained empirically from the experimental $\sigma_d(c_i)$ and $\sigma_d(c_i)$ data (Sangwal, 2002), and is found to hold only in a particular supersaturation range. It was suggested earlier (Sangwal, 2002) that B_0 is a supersaturation barrier likely to be associated with impurities inherently present in the solution. However, in view of the validity of the approximation in Equation (5.27) in reproducing the power-law curve in the interval $0.5 < x < 1$ it may be concluded that the value of B_0 has nothing to do with the impurities inherently present in the solution used for growth.

Equations (5.23) and (5.24) and Equations (5.25) and (5.28), based on the Langmuir and Freundlich adsorption isotherms, respectively, are the basic dependences between threshold supersaturations σ_d and σ^* on impurity concentration c_i . However, for the sake of clarity in the discussion below, we consider the case of adsorption of impurity particles at kinks in step ledges (i.e. $\rho = 1$).

Figure 5.6a and b present the dependence of σ_d and σ^* on c_i predicted according to the Langmuir and Freundlich isotherms, respectively, with the constants given in Table 5.1. From a comparison of curves 3 and 4 in Figure 5.6a and curves 1 and 2 in Figure 5.6b, and curves 1, 4 and 5 in Figure 5.6a, it may be noted that there is an upward shift in the plots with a decrease in the values of Q and K . Similarly, as seen from a comparison of curves 3 and 4 in Figure 5.6b, the plots shift upwards with an increase in B and a decrease in m .

From Figure 5.6a and b, it can be seen that, if the impurity concentration is defined as Kc_i , there is good agreement between the predictions of the Langmuir and Freundlich adsorption isotherms in the interval $0.4 < Kc_i < 1$. Moreover, the plots predicted by a given set of B and m in Equation (5.25) may be reproduced reasonably well with properly selected values of B_0 and B' in Equation (5.28) in the interval $0.5 < Kc_i < 1$ (cf. Figure 5.5).

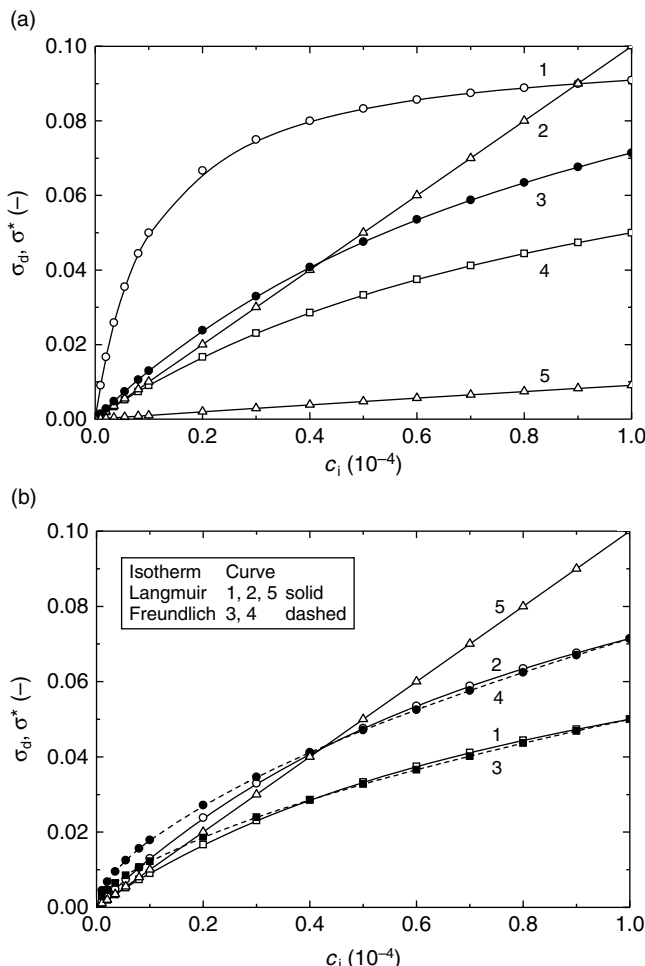


Figure 5.6 Dependence of σ_d and σ^* on c_i predicted according to (a) Langmuir and (b) Freundlich isotherms. The corresponding constants are given in Table 5.1. Note that the plots predicted by a given set of B and m in Equation (5.25) may be reproduced reasonably well with properly selected values of B_0 and B' in Equation (5.28) in the interval $0.5 < Kc_i < 1$. Reproduced from K. Sangwal. Cryst. Res. Technol. **40**, 635. Copyright (2005), with permission from Wiley-VCH

5.4 Confrontation of Theoretical Equations with Experimental Data

5.4.1 Impurity Adsorption at Kinks and Surface Terrace

After obtaining the data on threshold supersaturations σ_d , σ^* and σ^{**} as a function of concentration c_i of an impurity, one is interested in confronting the experimental data with the theoretical predictions and in inferring whether impurity adsorption takes place

Table 5.1 Constants of Equations (5.25) and (5.28) for the curves in Figure 5.6. Reproduced from K. Sangwal. Cryst. Res. Technol. **40**, 635. Copyright (2005), with permission from Wiley-VCH

Figure	Curve	Isotherm	Constants
5.6a	1	Langmuir	$Q = 10, K = 10^5$
	2		$Q = 10^{-3}, K = 1$
	3		$Q = 7, K = 10^4$
	4		$Q = 10, K = 10^4$
	5		$Q = 10, K = 10^3$
5.6b	1	Langmuir	$Q = 10, K = 10^4$
	2		$Q = 7, K = 10^4$
	3	Freundlich	$B = 0.05, m = 0.61$
	4		$B = 0.0714, m = 0.60$
	5	Langmuir	$B = 10^3, m = 1$
			$Q = 10^{-3}, K = 1$

at kinks in ledges and on the surface terrace. In this section some examples are presented with this purpose.

Figure 5.7a and b show the plots of $1/\sigma_d$ and $1/\sigma^*$, and of $1/\sigma_d^2$ and $1/\sigma^{*2}$, respectively, versus $1/c_i$ for the growth of the {100} face of KDP crystals in the presence of Fe(III) and Al(III) impurities, according to the predictions of impurity adsorption at kinks in ledges and on the surface terrace, respectively [cf. Equation (5.23); also see Sections 4.3 and 4.4]. The experimental $\sigma_d(c_i)$ and $\sigma^*(c_i)$ data are taken from the paper by Bredikhin *et al.* (1987). The values of the adsorption parameters K and Q_{diff} for growth in Al(III) impurity according to adsorption at kinks in ledges and on the surface terrace are given in Table 5.2. In the calculations it was assumed that $Q = 1/\sigma^0$ and $\gamma_l/k_B T = 0.5$. The values of these parameters for Fe(III) impurity were similar to those for Al(III) impurity.

Figure 5.8a presents the experimental $\sigma_d(c_i)$ data on the growth of sucrose crystals in the presence of raffinose impurity, and Figure 5.8b shows the plot of $1/\sigma_d$ versus $1/c_i$ from the same data according to Equation (5.23) based on the Langmuir adsorption isotherm. It can be seen that the plots of σ_d versus c_i and of $1/\sigma_d$ versus $1/c_i$ essentially pass through the origin. These plots imply that a linear adsorption isotherm applies in this case, and from the plot of $1/\sigma_d$ versus $1/c_i$ one cannot obtain reliable information about adsorption parameters.

From Table 5.2, it can be seen that the value of the differential heat of adsorption Q_{diff} is lower whereas that of the average distance x_0 or λ between adsorption sites is higher for σ_d than those for σ^* . These results are expected from the model. However, Figure 5.7 and Table 5.2 show that in this case there is little to choose between the mechanisms of impurity adsorption at kinks in ledges and on the surface terrace. Figure 5.8, on the other hand, reveals that reliable information about adsorption processes cannot be obtained by using the traditional Langmuir adsorption isotherm when $Kc_i \ll 1$ and the linear isotherm is valid.

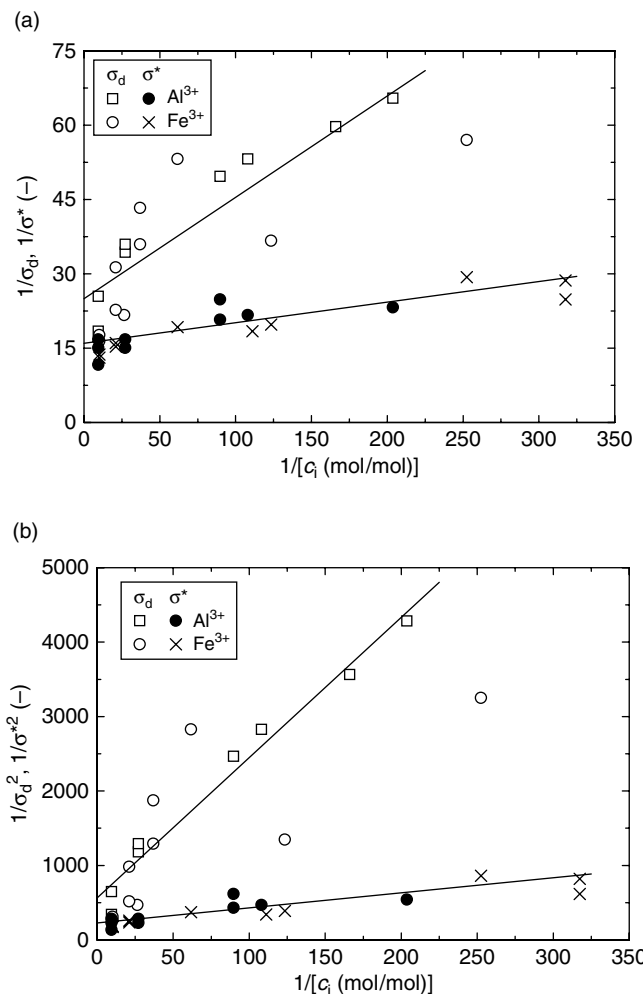


Figure 5.7 Plots of (a) $1/\sigma_d$ and $1/\sigma^*$ versus $1/c_i$, and (b) $1/\sigma_d^2$ and $1/\sigma^{\ast 2}$ versus $1/c_i$ for the growth of the (100) face of KDP crystals in the presence of Fe(III) and Al(III) impurities. Original data after Bredikhin et al. (1987)

Table 5.2 Adsorption parameters K and Q_{diff} for growth of KDP in the presence of Al(III) ions

Barrier	Adsorption mechanism	K (mol/mol) $^{-1}$	Q_{diff} (kJ/mol)	x_0 or λ
σ_d	Kink	122	12.1	50a
	Terrace	30	8.6	48a
σ^*	Kink	385	15.0	32a
	Terrace	112	11.9	30a

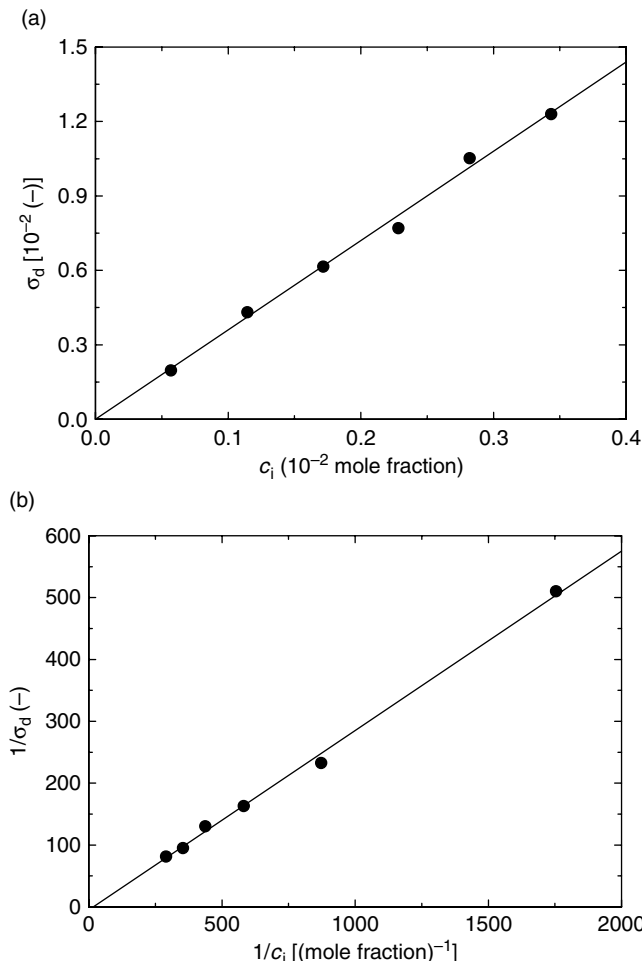


Figure 5.8 Plots of (a) σ_d versus c_i , and (b) $1/\sigma_d$ versus $1/c_i$ for the growth of sucrose crystals in the presence of raffinose impurity. Original data were reported by Kubota et al. (1997) from analysis of growth kinetics obtained by Albon and Dunning (1962)

5.4.2 Threshold Supersaturations and Impurity Adsorption Isotherms

Figure 5.9a presents the plots of σ_d and σ^* and the approximate values of σ^{**} read off directly from the $v(\sigma)$ plots of the (100) face of KDP crystals in the presence of different trivalent impurities published by Rashkovich and Kronsky (1997). It can be seen that, if the points corresponding to $c_i = 0$ are not considered, the dependence of σ_d , σ^* and σ^{**} on c_i for different impurities may be described by Equation (5.28), with the constants B_0 and B' given in Table 5.3.

The data in Figure 5.9a are shown in Figure 5.9b as plots of $1/\sigma_d$, $1/\sigma^*$ and $1/\sigma^{**}$ against $1/c_i$ of the impurities. In the range $0.2 < 1/c_i < 1 \text{ ppm}^{-1}$ the plots may be represented by Equation (5.23) with the constants Q and K/Q listed in Table 5.4. The

values of K and Q_{diff} calculated therefrom are also included in the table. It can be seen from Table 5.4 that, except for FeCl_3 where the values of K and Q_{diff} are practically not related to the threshold supersaturations, for other impurities $K(\sigma_d) < K(\sigma^*) \approx K(\sigma^{**})$ and $Q_{\text{diff}}(\sigma_d) < Q_{\text{diff}}(\sigma^*) \approx Q_{\text{diff}}(\sigma^{**})$. It may be noted that this trend of Q_{diff} is similar to that inferred from Table 5.2.

According to Table 5.4, for most of the impurities the value of Q decreases in the order $Q(\sigma_d) > Q(\sigma^*) > Q(\sigma^{**})$. Since $Q \approx 1/\sigma^0 = k_B T x_0 / \gamma_l a$, the above trend

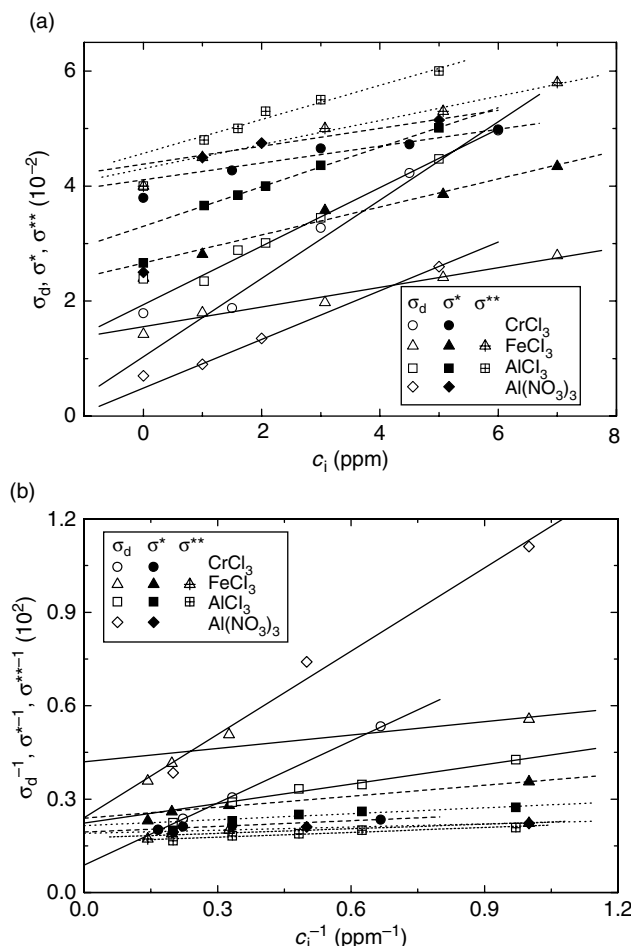


Figure 5.9 Dependence of (a) σ_d , σ^* and σ^{**} on c_i and (b) $1/\sigma_d$, $1/\sigma^*$ and $1/\sigma^{**}$ on $1/c_i$ for different impurities during the growth of KDP crystals. Note that in (a) the data may be described by Equation (5.28), with the constants B_0 and B' given in Table 5.5. In (b) in the range $0.2 < 1/c_i < 1 \text{ ppm}^{-1}$ the plots may be represented satisfactorily by Equation (5.23) with the constants Q and K/Q listed in Table 5.4. Original data obtained from experimental $v(\sigma)$ plots in the paper by Rashkovich and Kronsky (1997). Reproduced from K. Sangwal. Cryst. Res. Technol. **40**, 635. Copyright (2005), with permission from Wiley-VCH

Table 5.3 Values of constants B_0 and B' of Equation (5.28) for KDP growth^a. Reproduced from K. Sangwal. Cryst. Res. Technol. **40**, 635. Copyright (2005), with permission from Wiley-VCH

Impurity	σ_d		σ^*		σ^{**}	
	B_0 ($\times 10^{-2}$)	B' ($\times 10^3$)	B_0 ($\times 10^{-2}$)	B' ($\times 10^3$)	B_0 ($\times 10^{-2}$)	B' ($\times 10^3$)
CrCl ₃	1.0	6.8	4.1	1.5	—	—
FeCl ₃	1.6	1.7	2.7	2.4	4.3	2.1
AlCl ₃	1.9	5.1	3.3	3.4	4.6	3.0
Al(NO ₃) ₃	0.5	4.2	4.4	1.6	—	—

^a In all cases the correlation coefficient lies between 0.968 and 0.999.

Table 5.4 Values of Q and K/Q of Equation (5.23) and K and Q_{diff} for KDP growth^a. Reproduced from K. Sangwal. Cryst. Res. Technol. **40**, 635. Copyright (2005), with permission from Wiley-VCH

Impurity	Barrier	Q	K/Q	K	Q_{diff} (kJ/mol)
CrCl ₃	σ_d	8.8	6.6×10^{-5}	1.3×10^5	29.7
	σ^*	19.4	6.0×10^{-6}	3.2×10^6	37.5
FeCl ₃	σ_d	42	1.4×10^{-5}	2.9×10^6	37.5
	σ^*	23.9	1.2×10^{-5}	2.0×10^6	36.6
	σ^{**}	17.6	4.9×10^{-6}	3.6×10^6	38.0
AlCl ₃	σ_d	22.3	2.1×10^{-5}	1.1×10^6	35.0
	σ^*	21.4	6.4×10^{-6}	3.3×10^6	37.8
	σ^{**}	16.2	5.2×10^{-6}	3.1×10^6	37.7
Al(NO ₃) ₃	σ_d	24.1	8.9×10^{-5}	3.1×10^6	37.7
	σ^*	0.190	5.4×10^{-7}	5.6×10^6	39.2

^a In all cases the correlation coefficient lies between 0.855 and 0.999.

implies that $x_0(\sigma_d) > x_0(\sigma^*) > x_0(\sigma^{**})$. This is the expected trend from the model of three distances: $l_d > l^* > l^{**}$ (Section 5.1.2).

It is observed (Sangwal and Miłniczek-Brzóska, 2003; Miłniczek-Brzóska and Sangwal, 2004) that the values of each of the threshold supersaturations for growth along different directions are essentially similar and are practically independent of the growth direction. The data may be represented by Equations (5.22) and (5.28). This behavior is presented in Figure 5.10a and b, which show the dependence of σ_d and σ^* on the concentration c_i of Mn(II) and Ni(II) impurities, respectively.

Figure 5.11 shows the plots of σ_d and σ^* against c_i of Mn(II) impurity for the growth of ammonium oxalate monohydrate single crystals according to Equation (5.21). The straight-line plots are drawn for growth along $\langle 001 \rangle$. It can be seen that the values of Q and K/Q determined from the straight-line plots show large deviations (up to 30%) due to errors involved in the values of barriers σ_d and σ^* . Therefore, one should be careful when analyzing such data. However, the general observation that the values of the barriers σ_d and σ^* are independent of the growth direction is a useful guide during the analysis.

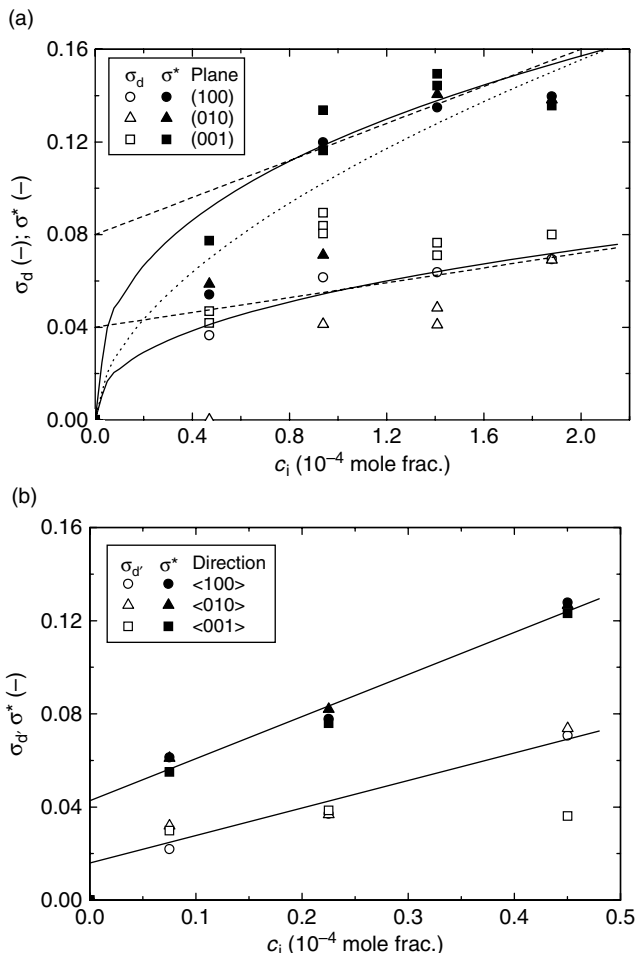


Figure 5.10 Dependence of σ_d and σ^* on c_i of (a) Mn(II) and (b) Ni(II) impurities. Note that the values of the threshold supersaturations for growth along different directions are closely similar and are practically independent of the growth direction. Original data of (a) and (b) from Sangwal and Mielniczek-Brzóska (2003) and Mielniczek-Brzóska and Sangwal (2004), respectively. Reproduced from K. Sangwal. Cryst. Res. Technol. **40**, 635. Copyright (2005), with permission from Wiley-VCH

It should be mentioned that when using the Freundlich adsorption isotherm it is relatively difficult to obtain information about processes of adsorption of impurities from an analysis of the experimental data for growth kinetics of crystals from systems containing impurities. However, the Langmuir adsorption isotherm is convenient for the analysis of the data and provides useful information about adsorption processes. Therefore, the experimental $\sigma_d(c_i)$ and $\sigma^*(c_i)$ data for different impurities are frequently analyzed using Equation (5.23).

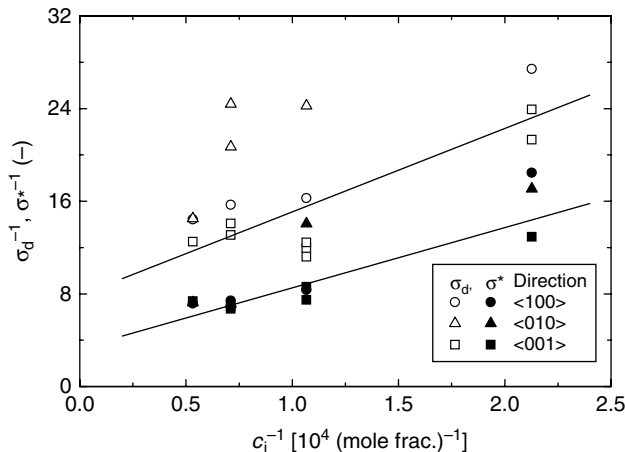


Figure 5.11 Dependence of $1/\sigma_d$ and $1/\sigma^*$ on $1/c_i$ for Mn(II) impurity. Original data from Sangwal and Mielniczek-Brzóyska (2003). Reproduced from K. Sangwal. Cryst. Res. Technol. **40**, 635. Copyright (2005), with permission from Wiley-VCH

5.5 Impurity Adsorption and Solution Supersaturation

Analysis of $\sigma_d(c_i)$, $\sigma^*(c_i)$ and $\sigma^{**}(c_i)$ data for different impurities used during the growth of crystals shows unequivocally that they can be described by the same dependence. A similar dependence followed by different threshold supersaturations implies that the mechanism of adsorption of an impurity involved in their appearance in the $v(\sigma)$ and $R(\sigma)$ plots for different concentration is the same. The difference essentially lies in how the impurity particles adsorbing on the growing surface interact with advancing steps in different supersaturation intervals: $\sigma < \sigma_d$, $\sigma_d < \sigma < \sigma^*$, $\sigma^* < \sigma < \sigma^{**}$ and $\sigma > \sigma^{**}$.

In the supersaturation interval $\sigma < \sigma_d$ there is a barrier for growth where no growth occurs on the surface. Bredikhin *et al.* (1987) suggested that this so-called dead supersaturation zone occurs when the sources of steps composed of pairs of screw dislocations of opposite sign, situated at a distance l , are rendered inactive by the capture of impurity particles. This happens when the diameter $2r_{2D}^*$ of a critical two-dimensional nucleus exceeds the distance l between the dislocations. However, the similarity in the dependence of σ_d on c_i with that of σ^* and σ^{**} excludes this possibility. Therefore, it may be concluded that the appearance of the three barriers occurs as a result of hindrance provided in the motion of steps on the surface by impurity particles adsorbing on the surface or at step ledges moving on it.

Some remarks should be made on growth kinetics in relation to the kinetic coefficient for step motion β_l . The step displacement velocity v is related to the kinetic coefficient β_l by

$$\frac{dv}{d\sigma} = \beta_l = a\nu \exp(-W/kT) \quad (5.32)$$

where W is the activation energy required for the integration of growth units into the step, a is the size of the growth unit and ν is the frequency factor of about 10^{12} per second. Then one may write the ratio of the displacement velocity of the step in the form

$$v/v_0 = \beta_l/\beta_{l0} = (\nu/\nu_0) \exp(-\Delta W/kT) \quad (5.33)$$

where the activation energy difference $\Delta W = (W - W_0)$, and the subscript 0 refers to the values of β_l , ν and W for growth in the absence of an impurity. Equation (5.32) predicts the following situations for $\nu/\nu_0 = 1$:

- (1) When $\beta_l/\beta_{l0} = 0$, $\Delta W = \infty$. This means that there is no growth. This case holds when $\sigma < \sigma_d$.
- (2) When $\beta_l/\beta_{l0} = 1$, $\Delta W = 0$. In this case there is no effect of impurity on growth and it holds for $\sigma > \sigma^{**}$.
- (3) When $0 < \beta_l/\beta_{l0} < 1$, $0 < \Delta W < \infty$. This means that an impurity leads to a reduction in growth rate. This situation corresponds to $\sigma_d < \sigma < \sigma^*$.

All the above situations are indeed observed. However, it should be noted that in the range $\sigma^* < \sigma < \sigma^{**}$ the ratio $\beta_l/\beta_{l0} > 1$. To explain this unusual behavior, one has to take into account changes both in the ratio ν/ν_0 and in the activation energy difference ΔW .

5.6 Dependence of Ratios σ_d/σ^* and σ^*/σ^{**} on c_i

Equations (5.2) and (5.5) relate the ratio σ_d/σ_c of two threshold supersaturations with the ratio v/v_0 of step velocities. Using Equation (5.33) for v/v_0 , one finds that the value of σ_d/σ_c depends on the frequency ratio ν/ν_0 and the activation energy difference $W - W_0$. Since these quantities are related to the adsorption of an impurity on the surface, it is obvious that the ratio σ_d/σ_c is connected with adsorption processes. However, in view of the unknown nature of these quantities as a function of concentration of an impurity in Equation (5.33), the details of the adsorption processes remain unclear. In this section, the relationship between σ_d/σ_c and the impurity concentration c_i is discussed.

For convenience, we denote two successive threshold supersaturations by σ_1 and σ_2 and consider impurity adsorption at kinks. Then, from Equations (5.23) and (5.25) relating the threshold supersaturations σ_1 and σ_2 to c_i , one can obtain the expressions for the dependence of the ratio σ_1/σ_2 on c_i . When the Langmuir adsorption isotherm applies, denoting the constants Q and K corresponding to σ_1 and σ_2 by subscripts 1 and 2, from Equation (5.23) one obtains

$$\frac{\sigma_1}{\sigma_2} = A_r \left(1 + \frac{\alpha_1 K_1 c_i}{1 + K_1 c_i} \right) \quad (5.34)$$

where

$$A_r = Q_2 K_1 / Q_1 K_2 \quad (5.35)$$

$$\alpha_1 = K_2 / K_1 - 1 \quad (5.36)$$

When $K_1 c_i \ll 1$, Equation (5.34) simplifies to

$$\sigma_1/\sigma_2 = A_r(1 + \alpha_1 K_1 c_i) \quad (5.37)$$

where the constants A_r and α_1 are given by Equations (5.35) and (5.36).

As above, denoting the constants Q and m corresponding to σ_1 and σ_2 by subscripts 1 and 2, in the case of the Freundlich isotherm from Equation (5.25) one obtains

$$\sigma_1/\sigma_2 = A_r c_i^{m_1 - m_2} \quad (5.38)$$

where

$$A_r = \frac{B_1}{B_2} = \frac{m_1 Q_2}{m_2 Q_1} \frac{1}{c_i^{*(m_1 - m_2)}} \quad (5.39)$$

When the approximation in Equation (5.27) is valid, Equation (5.38) can be written in the form

$$\sigma_1/\sigma_2 = A_r [1 - (m_1 - m_2)/A_r][1 + (m_1 - m_2)/A_r] c_i \quad (5.40)$$

This expression holds for $0 < A_r < 1$, $A_r > (m_1 - m_2)$, and the concentration ratio $c_i/c_i^* < 1$. Equation (5.40) also has the same form as Equation (5.37). Alternatively, starting from Equation (5.28), one obtains

$$\sigma_1/\sigma_2 = A_r [1 + (B'_1/B_{01} - B'_2/B_{02}) c_i] \quad (5.41)$$

where the subscripts 1 and 2 refer to σ_1 and σ_2 , $A_r = B_{01}/B_{02}$, and the B_0 s and B'_1 s are given by Equation (5.29).

For $K_2 > K_1$, $m_2 > m_1$ and $B'_1/B_{01} > B'_2/B_{02}$, Equations (5.34), (5.37), (5.38), (5.40) and (5.41) predict an increase in σ_1/σ_2 with increasing c_i , while $0 < A_r < 1$, and its value is determined by the constants in the ratios B_1/B_2 , Q_1/Q_2 and B_{01}/B_{02} . The above feature may be noted easily from Equation (5.34) in which $0 < A_r < 1$ because $Q_1 > Q_2$, $K_1 \leq K_2$. In this case, $Q_{\text{diff}}(\sigma_1) \leq Q_{\text{diff}}(\sigma_2)$ [cf. Equation (5.36)].

It may be noted that when $K_2 = K_1$ in Equations (5.34) and (5.37), $m_1 = m_2$ in Equations (5.38) and (5.40), and $B'_1/B_{01} = B'_2/B_{02}$ in Equation (5.41), the ratio $\sigma_1/\sigma_2 = A_r$ and is a constant quantity independent of c_i (see Figure 5.12a). Here $Q_{\text{diff}}(\sigma_1) = Q_{\text{diff}}(\sigma_2)$.

Typical plots illustrating the above features are shown in Figure 5.12, and the constants used to draw the plots are given in Table 5.5. As can be seen from Figure 5.12b, in the interval $0.5 < c_i/c_i^* < 1$ the approximation in Equation (5.27) can be used to reproduce the data predicted by Equation (5.38).

It should be noted that, in contrast to the trends predicted by the theoretical dependence of the ratio σ_1/σ_2 on c_i for an impurity, the dependence of the ratio σ_2/σ_1 on c_i predicts an opposite trend. For example, for the $\sigma_1/\sigma_2(c_i)$ dependence, $A_r < 1$ and the ratio σ_1/σ_2 increases with increasing c_i [see Equation (5.34)]. However, for the $\sigma_2/\sigma_1(c_i)$ dependence, $A_r > 1$ and the ratio σ_2/σ_1 decreases with increasing c_i .

The dependence of σ_d/σ^* and σ^{**}/σ^* on c_i for the growth of the {100} face of KDP crystals in the presence of different trivalent impurities is shown in Figure 5.13. In the

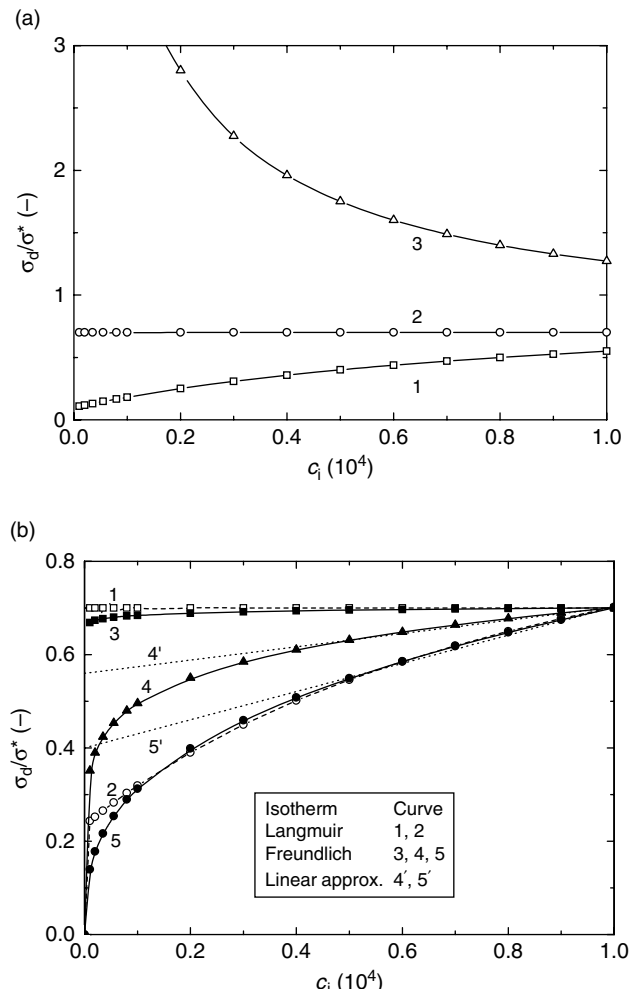


Figure 5.12 Predicted plots of σ_d/σ^* against impurity concentration c_i according to different adsorption isotherms with constants listed in Table 5.5: (a) dependence according to the Langmuir isotherm and (b) dependence according to the Freundlich isotherm and comparison between the dependences predicted by the Langmuir isotherm. In (b) note that the approximation in Equation (5.27) reproduces the data predicted by Equation (5.38) satisfactorily in the interval $0.5 < c_i/c_i^* < 1$. Reproduced from K. Sangwal. Cryst. Res. Technol. **40**, 635. Copyright (2005), with permission from Wiley-VCH

figure the plots are drawn according to Equation (5.37), while the best-fit values of the constants are given in Table 5.6. It can be seen from the table that in the case of FeCl_3 and AlCl_3 impurities the value of $\alpha_1 K_1 \approx 0$ for both σ_d/σ^* and σ^{**}/σ^* , suggesting that A_r is essentially a constant quantity and does not depend on c_i . Moreover, as expected, one finds that $A_r > 1$ for the ratio σ^{**}/σ^* . The value of A_r for σ^*/σ^{**} is simply the inverse of the value for σ^{**}/σ^* . The constant values of A_r are also given in Table 5.6.

Table 5.5 Constants of Equations (5.34), (5.38) and (5.41) in the plots in Figure 5.12. Reproduced from K. Sangwal. Cryst. Res. Technol. **40**, 635. Copyright (2005), with permission from Wiley-VCH

Figure	Curve	Isotherm	Equation	Constants
5.12a	1	Langmuir	(5.34)	$Q_1/Q_2 = 1, \alpha_1 = 9, K_1 = 10^4$
	2		(5.34)	$Q_1/Q_2 = 0.7, \alpha_1 = 0, K_1 = 10^4$
	3		(5.34)	$Q_1/Q_2 = 1.43, \alpha_1 = -9, K_1 = 10^4$
5.12b	1	Langmuir	(5.34)	$Q_1/Q_2 = 0.7, \alpha_1 = 0, K_1 = 10^4$
	2		(5.34)	$Q_1/Q_2 = 0.854, \alpha_1 = 4, K_1 = 10^4$
	3	Freundlich	(5.38)	$B_1/B_2 = 0.7, m = 0.01$
	4		(5.38)	$B_1/B_2 = 0.7, m = 0.15$
	5	Approximation	(5.38)	$B_1/B_2 = 0.7, m = 0.35$
	4'		(5.41)	$A_r = 0.55, \Delta B = 0.27^a$
	5'		(5.41)	$B_0 = 0.40, \Delta B = 0.875^a$

^a $\Delta B = (B'_1/B_{01}) - (B'_2/B_{02})$.

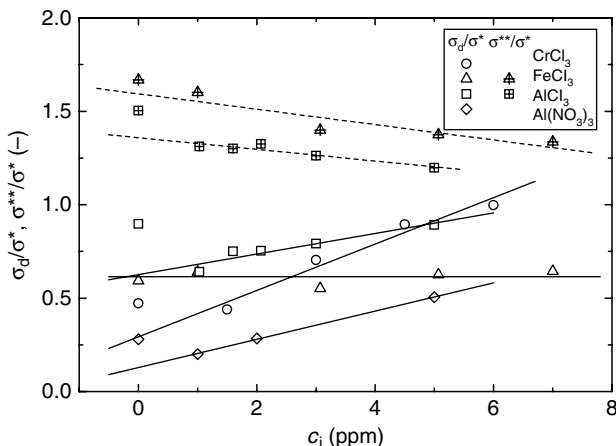


Figure 5.13 Dependence of σ_d/σ^* and σ^{**}/σ^* on c_i for different impurities during KDP growth. Plots are drawn according to Equation (5.37). Reproduced from K. Sangwal. Cryst. Res. Technol. **40**, 635. Copyright (2005), with permission from Wiley-VCH

From Table 5.6, it may be noted that $A_r(\sigma_d/\sigma^*) < A_r(\sigma^{**}/\sigma^{**})$ for FeCl_3 and AlCl_3 impurities. This feature is due to the fact that A_r is related to the relative step velocities v/v_0 because when $K_1 \approx K_2$ and $m_1 \approx m_2$, $A_r \approx Q_1/Q_2$ [see Equations (5.35) and (5.39)]. In contrast to the above impurities, $\alpha_1 > 0$ for CrCl_3 and $\text{Al}(\text{NO}_3)_3$ impurities. Obviously, here $K_2 > K_1$, $m_2 > m_1$ and $B'_1/B_{01} > B'_2/B_{02}$ [cf. Equations (5.37), (5.40) and (5.41), respectively].

Finally, it should be mentioned that Equation (5.34), based on the applicability of the Langmuir adsorption isotherm, enables one to obtain the values of constants K_1 and

Table 5.6 Values of A_r and $\alpha_1 K_1$ for KDP growth. Reproduced from K. Sangwal. *Cryst. Res. Technol.* **40**, 635. Copyright (2005), with permission from Wiley-VCH

Impurity	Ratio	A_r	$\alpha_1 K_1$	CC
CrCl ₃	σ_d/σ^*	0.292	0.424	0.982
FeCl ₃	σ_d/σ^*	0.598	0.007	0.250
		0.615	—	—
	σ^{**}/σ^*	1.593	-0.04	0.899
	σ^*/σ^{**}	0.74	—	—
AlCl ₃	σ_d/σ^*	0.625	0.088	0.948
	σ^{**}/σ^*	1.358	-0.031	0.937
	σ^*/σ^{**}	0.80	—	—
Al(NO ₃) ₃	σ_d/σ^*	0.128	0.590	0.999

K_2 and the corresponding values of Q_{diff} , thus providing an explanation for differences in impurity adsorption processes below and above different supersaturation barriers σ_d , σ^* and σ^{**} . For the analysis one may use $\sigma_d/\sigma^*(c_i)$ and $\sigma^*/\sigma^{**}(c_i)$ data. However, it is difficult to obtain useful information about the adsorption processes from the linear Equations (5.37), (5.40) and (5.41).

References

- Albon, N., and W.J. Dunning (1962). *Acta Crystallogr* **15**, 474.
- Bredikhin, V.I., V.I. Ershov, V.V. Korolikhin, V.N. Lizyakina, S.Yu. Potapenko, and N.V. Khlyunev (1987). *J. Cryst. Growth* **84**, 509.
- Cabrera, N., and D.A. Vermilyea (1958). In: R.H. Doremus, B.W. Roberts, and D. Turnbull (Eds.), *Growth and Perfection of Crystals*, John Wiley & Sons, Inc., New York, p. 393.
- Chernov, A.A., L.N. Rashkovich, and A.A. Mkrtchyan (1986a). *J. Cryst. Growth* **74**, 101.
- Chernov, A.A., L.N. Rashkovich, I.L. Smol'ski, Yu.G. Kuznetsov, A.A. Mkrtchyan, and A.I. Malkin (1986b). *Rost. Krist.* **15**, 43.
- Dove, P.M., J.J. De Yoreo, and K.J. Davis (2004). In: X.Y. Liu and J.J. De Yoreo (Eds.), *Nanoscale Structure and Assembly at Solid–Fluid Interfaces, Vol. II: Assembly at Hybrid and Biological Systems*, Kluwer, Boston, Chap. 2, p. 55.
- Frank, F.C. (1958). In: R.H. Doremus, B.W. Roberts, and D. Turnbull (Eds.), *Growth and Perfection of Crystals*, John Wiley & Sons, Inc., New York. p. 411.
- Kubota, N. (2001). *Cryst. Res. Technol.* **36**, 749.
- Kubota, N., and J.W. Mullin (1995). *J. Cryst. Growth* **152**, 203.
- Kubota, N., M. Yokota, and J.W. Mullin (1997). *J. Cryst. Growth* **182**, 86.
- Kubota, N., M. Yokota, and J.W. Mullin (2000). *J. Cryst. Growth* **212**, 480.
- Mielniczek-Brzóska, E., and K. Sangwal (2004). *Cryst. Res. Technol.* **39**, 993.
- Mielniczek-Brzóska, E., K. Giełzak-Koćwin, and K. Sangwal (2000). *J. Cryst. Growth* **212**, 532.
- Nielsen, A.E. (1981). *Pure Appl. Chem* **53**, 2025.
- Nielsen, A.E. (1984). *J. Cryst. Growth* **67**, 289.
- Rashkovich, L.N., and N.V. Kronsky (1997). *J. Cryst. Growth* **182**, 434.
- Rashkovich, L.N., and B.Yu. Shekunov (1991). *J. Cryst. Growth* **112**, 183.
- Sangwal, K. (1996). *Prog. Cryst. Growth Charact. Mater.* **32**, 3.

- Sangwal, K. (1998). *Prog. Cryst. Growth Charact. Mater.* **36**, 163.
- Sangwal, K. (1999). *J. Cryst. Growth* **203**, 197.
- Sangwal, K. (2002). *J. Cryst. Growth* **242**, 215.
- Sangwal, K. (2005). *Cryst. Res. Technol.* **40**, 635.
- Sangwal, K., and E. Mielniczek-Brzóska (2001a). *Cryst. Res. Technol.* **36**, 837.
- Sangwal, K., and E. Mielniczek-Brzóska (2001b). *J. Cryst. Growth* **233**, 343.
- Sangwal, K., and E. Mielniczek-Brzóska (2002). *J. Cryst. Growth* **242**, 421.
- Sangwal, K., and E. Mielniczek-Brzóska (2003). *Cryst. Res. Technol.* **38**, 113.
- Simon, B., A. Grassi, and R. Boistelle (1974). *J. Cryst. Growth* **26**, 90.
- van der Putte, P., W.J.P. van Enckevort, L.J. Giling, and J. Bloem (1978). *J. Cryst. Growth* **43**, 659.

6

Mineralization in Natural and Artificial Systems

Crystallization in a laboratory or in an industrial plant is carried out in a fluid medium contained in a crystallizer at a predefined temperature. The medium is a homogeneous mixture in the form of solution of a solute dissolved in a suitable solvent, and the solution may or may not contain an impurity. Here the composition of the medium is determined by workers in accordance with the ultimately desired crystalline product they want to obtain. In contrast to this controlled crystallization in the laboratory and in industry, the Earth, humans and animals, plants, mollusk shells, avian eggshells, the exoskeleton of orthopods, pearls and corals constitute a variety of laboratories where crystallization occurs in a complex manner in media the composition of which is determined by Nature. Whereas various minerals in the interior of the Earth are formed at relatively high temperatures and pressures, crystallization in biological systems, usually referred to as biominerization, takes place at normal temperatures.

There is a huge amount of literature devoted to the processes of mineral formation in the Earth's interior. This topic is beyond the scope of this monograph and is entirely neglected. The aim of this chapter is to present a review of the basic mechanisms of biominerization and the effect of additives on the kinetics of biominerization. The basic mechanisms involved in growth morphology of single crystals and deposited layers are discussed in Chapter 7.

6.1 Biominerization as a Process

6.1.1 Structure and Composition of Biominerals

Biominerization is the process by which biological organisms form hard minerals for support, defense and feeding. The minerals are formed in, *inter alia*, cartilage, bones,

teeth, shells, carapaces and spicules, by living organisms under conditions of moderate temperature, pressure and pH. They are usually composites of proteins, polysaccharides and crystals of a variety of inorganic compounds. The inorganic compounds are composed of cations such as Ba, Ca, Cu, Fe, K, Mg, Mn, Na, Pb, Si, Sr and Zn occurring as hydroxides, oxides, sulfates or sulfides, carbonates, oxalates and phosphates (Hunter, 1996; Foo *et al.*, 2004; Wilt, 2005).

Biomineralization processes may be classified into two general types (Hunter, 1996): (i) cell-mediated mineralization, in which mineral formation occurs within membrane-bound vesicles, and (ii) matrix-mediated mineralization, in which mineral formation takes place within extracellular matrices mainly composed of proteins and/or polysaccharides. The complex organic matrix medium forms a porous structure, and contains a solvent, a solute and always an impurity. Diffusion in the porous medium ensures mass transport is involved in the mineralization processes. Thus, biominerization is composed of at least two parts: the precipitating crystalline phase(s) and a supporting structure called the matrix. The types of organic matrix and the mineralizing compounds in different biological systems are summarized in Table 6.1.

Table 6.1 Types of organic matrix and the mineralizing compounds

System	Tissue	Organic matrix	Biomineral
Humans and animals	Cartilage and bones	Proteoglycans and collagen fibres	Calcium oxalate, calcium phosphate, calcium carbonate
	Teeth	Glycoprotein and polysaccharides	As above
	Kidney, bladder and prostate stones	As above	Calcium oxalate, calcium phosphate, calcium carbonate, uric acid
Plants		Cellulose, callose, hemicellulose, pectin	Calcium oxalate, calcium carbonate, silicon dioxide
Mollusk shells and avian eggshells		Conchiolin, proteins, glycoproteins	Calcium carbonate

6.1.2 Humans and Animals

Precipitation of calcium salts is involved in beneficial mineralization such as the formation of bone and tooth and pathological processes such as bone disease, carious lesions and renal stone formation. However, the basic mechanisms of both beneficial and pathological mineralization processes are essentially similar. The mineral is formed in an organic matrix of complex chemical composition (Schenk *et al.*, 1982; Prockop and Williams, 1982; Grover and Ryall, 1995; Walton *et al.*, 2005). The mineral phases formed consist of calcium phosphate and carbonates and some urate and alkali metal phosphate salts. Practically all of these salts precipitate in a number of phases and polymorphs.

The processes involved in the mineralization of bones are briefly outlined below, and pathological mineralization is described in Section 6.2.

The adult skeleton of humans and animals consists of lamellar bone (Schenk *et al.*, 1982). The formation of the bone takes place in two phases (Figure 6.1): (1) deposition of osteoids by osteoblasts and (2) formation of bone. In the first phase, osteoblasts (OB) deposit osteoid (OS), an organic matrix, which shows the characteristic lamellar pattern. Each lamella is composed of a 2–3 µm thick layer of roughly parallel, densely packed collagen fibrils of diameter 60–100 nm. Collagen is the main mammalian protein making up about one-quarter of the total protein content (see below). The orientation of the fibrils changes from lamella to lamella, but a continuous exchange of fibrils takes place. These fibrils, defined as type I collagen, show a periodicity of about 60 nm. The interfibrillar substance amounts to only 5% of the dry organic matrix, the remaining 95% being collagen. The osteoid is separated from the calcified bone by the calcification front (MF). At this interface the osteoid undergoes mineralization. This phase ends with lamellar bone formation, and involves the growth of apatite crystals associated with collagen.

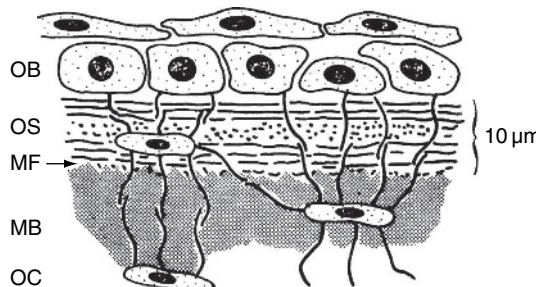


Figure 6.1 Schematic illustration of lamellar bone formation: OB denotes osteoblasts (covered by an endosteal epithelium), OS osteoid, MF mineralization front, MB mineralized bone, and OC osteocyte. Reproduced from R.K. Schenk, E. Hunziker, and W. Herrmann, in G.H. Nancollas (Ed.), Biological Mineralization and Demineralization, Springer, Berlin, p. 143. Copyright (1982), with permission from Springer Science and Business Media

There is a preparation or maturation period for mineralization, which is represented by the thickness of the osteoid seam [i.e. osteoid (OS) interposed between osteoblasts and mineralization front]. In most adult mammals, this thickness is essentially constant (about 10 µm in humans). The mineralization rate is about 1 µm/day for humans and 2 µm/day for the horse and rabbit. This means that for humans, for example, the 10 µm thick osteoid seam represents a time interval of 10 days between osteoid deposition and its subsequent mineralization.

In embryonic and fetal life or in the adult organisms in conditions of rapid and extensive new bone formation, as in fracture repair, woven bone is formed. Its main characteristics are high cellularity, formation of a felt-like web without any preferential orientation by the collagen fibrils and a much smaller osteoid seam. In contrast to lamellar bone, in woven bone a large number of matrix vesicles with all intermediate steps of vesicle-induced initial mineralization are present. Their role is to convert the freshly deposited organic matrix into calcified bone within a couple of days.

A major constituent of the organic matrix of bone is collagen, which accounts for about 30% of its dry weight and 90–95% of its nonmineral content. The function of collagen fibrils is to hold together and give form to the body tissues. Another possible role of collagen is to provide a site for mineralization. Collagen fibrils have about the same strength as steel wires. They consist of highly ordered polymers of rod-like molecule, which contains three peptide chains, called α -chains. Each chain contains about 1000 amino acid residues, and, with the exception of short sequences at the ends of chains, every third amino acid in each chain is glycine. Thus, the molecular formula of an α -chain is $(X - Y - \text{Gly})_n$, where X and Y represent amino acids other than glycine, and n is an integer. In collagen from mammals and birds, about 100 of the X-positions are *proline*, and about 100 of the Y-positions are *hydroxyproline*. In mammalian collagen, about two-thirds of the X- and Y-positions are occupied by a variety of different amino acids. These other amino acids tend to form clusters with groups of hydrophobic and charged residues whose side-chains point out from the center of a triple helix. Thus, collagen is essentially an inside-out protein in which the large number of amino acid side-chains on the surface of the molecule direct precise assembly of the molecules.

A mature human tooth is composed of the following tissues (see Figure 6.2): (1) enamel, the hard outer surface consisting of calcium and phosphate, (2) dentin, the deeper parts in the interior, (3) pulp, the core containing nerves and blood vessels, and (4) cementum, the thin layer around the root and a bone-like material connecting the teeth to the jaw. Both the enamel and the dentin are mineralized. Enamel is produced by cells called ameloblasts (Arends, 1982). The enamel structure is composed of enamel prisms

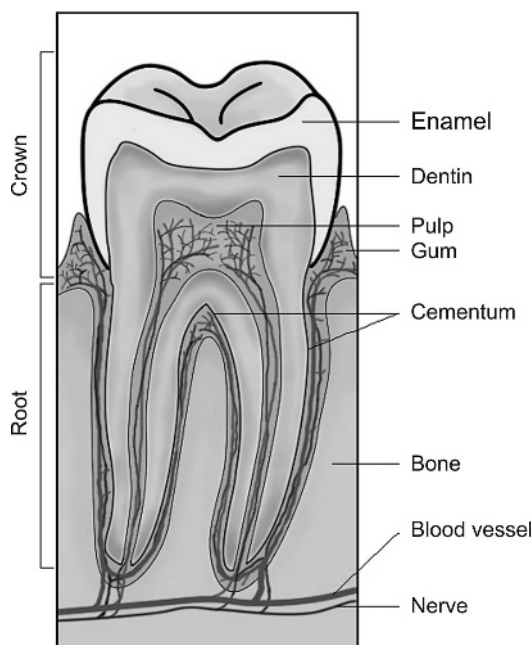


Figure 6.2 Schematic drawing of the structure of an adult human tooth. Adapted from Wikipedia (website: <http://en.wikipedia.org/wiki>)

or rods of 4–5 µm diameter, running from the dentin to the enatomical enamel surface in an organic matrix. Within and between the prisms there are millions of tightly packed minute needle-shaped enamel crystallites about 0.5–10 µm long and 40 nm in diameter. A mature human enamel has the following main components: mineralized nonstoichiometric hydroxyapatite (95% by weight), the organic matrix composed of glycoproteins (1% by weight), and water (4% by weight). Dentin is secreted by the odontoblasts. It contains a microscopic structure called dentinal tubules which are microcanals radiating outwards through the dentin from the pulp cavity to the exterior cementum border. The main components of dentin are proteins in the form of collagen and phosphophoryn, a noncollagenous protein (Saito *et al.*, 2003). Phosphophoryn contains 35–40% phosphoserin residues and 40–50% aspartic acid residues. Phosphophoryn covalently cross-linked to collagen (bound phosphophoryn) induces mineralization of hydroxyapatite (Saito *et al.*, 2003). Hydroxyapatite comprising the dentin is about 50 nm thick and 30 nm in length, and is much smaller than that in enamel. Moreover, it is poorer in crystallinity and alignment than in enamel. Therefore, dentin is softer than enamel, and decays more rapidly. However, it still acts as a protective layer and supports the crown of the tooth.

6.1.3 Plants

In plants, the hard tissue involves biominerization. The common hard tissue, the wood, in plants acquires its hardness and strength from two organic polymers: cellulose and lignin. Most vascular plants are mineralized tissues, and some of the plants, such as certain cacti, contain up to 85% of their dry weight composed of calcium oxalate. Several nonvascular plants, such as marine algae and certain fungi, produce mineralized tissues and cells. Some lichens have as much as 66% of their dry weight formed by calcium oxalate, and some algae contain up to 85% dry weight composed of calcium carbonate.

In higher plants there are three systems of mineralization (Arnott, 1982). The most widely distributed mineralized system in most of the seed plants is calcium oxalate (Arnott, 1982; Nakata, 2003). Calcium oxalate is observed as an intercellular product in virtually all the tissues of a plant, and often accumulates in specialized cells called idioblasts (Figure 6.3). It occurs as calcium oxalate monohydrate (COM; whewellite) and calcium oxalate dihydrate (COD; weddellite). Plants produce calcium oxalate crystals of a variety of shapes and sizes in their cells. Based on their morphology, they are observed in five categories: (i) one or more bundles of acicular crystals in a cell (raphide), (ii) an elongated single or twin crystal in a cell (styloid), (iii) a roughly spherical aggregate of crystals (druse), (iv) rhombohedral single or twinned crystals in a cell (prismatic), and (v) numerous small single and/or twinned crystals in a cell (crystal sand). In different plants the shape, size, number and spatial distribution of crystals vary substantially, but in individual species and tissues the pattern of morphology, size, spatial distribution and hydration state is conserved. Based on such properties of the crystals, the mechanism of formation of calcium oxalate crystals in the idioblast cells is explained. It has been suggested (Nakata, 2003) that intravacuolar matrices composed of macromolecular structures determine the shape and growth of the crystals.

The second system is calcium carbonate in the form of cystoliths, and is found in some families of seed plants (Arnott, 1982). These intracellular deposits occur in a

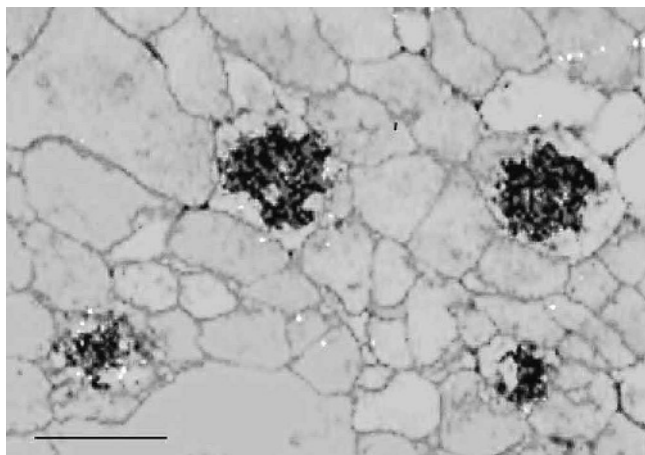


Figure 6.3 Calcium oxalate-accumulating idioblasts observed in the *Pistia stratiotes* leaf section in reflected transmitted light; scale bar, 20 µm. Reproduced from P.A. Nakata. Plant Sci. **164**, 901. Copyright (2003), with permission from Elsevier

large number of genera but are restricted to some families. The usual mineral found in cystoliths is amorphous calcium carbonate (ACC), but vaterite is also known to be present. In *Ficus* the cystoliths are composed of 91.5% calcium carbonate, 4.4% callose, 2.2% cellulose and 1.8% inorganic components. Cystoliths vary in shape from practically spherical to elongated cylinders and may be even branched (Figure 6.4). They also vary in size. In *Ficus* and *Morus*, the internal skeleton consists of radial components extending from the terminal process and are interconnected by concentric bands of similar material (Figure 6.4a and c). The concentric bands follow the external contours of the cystolith body, and result due to changes in the concentration of calcium carbonate and the organic matrix. The organic matrix of the cystolith is composed of cellulose and callose. Callose is a polysaccharide synthesized from D-glucose.

The development of a cystolith begins with the formation of a cell wall process which grows into the cell. The first indication of the formation of the cystolith is the nucleation of a centrally located crystal from which the remainder of the cystolith develops and involves the formation and growth of cell wall surrounding it. The cystolith is connected to the cell wall by many protoplasmic connections which pass through the cell wall into the surrounding cells. As cystolith growth continues, calcium carbonate is deposited in the matrix formed by the cystolith. At the same time, the external cell wall and the cystolith stalk attached to it become silicified.

The third system of biominerization in higher plants involves deposits of hydrated silicon dioxide ($\text{SiO}_2 \cdot n\text{H}_2\text{O}$), as either silica gel or opal. These deposits are generally found within the cellular structure in flowering plant families, the grasses and in some lower vascular plants. The particles produced are called phytoliths, biogenetic opals and silicon bodies. The silicon deposition may occur in the cell lumen, in cell walls or in intercellular spaces. Silica solidifies as phytoliths due to the loss of water from the monosilicic acid in the cell lumen. The organic matrix for silicification is composed of

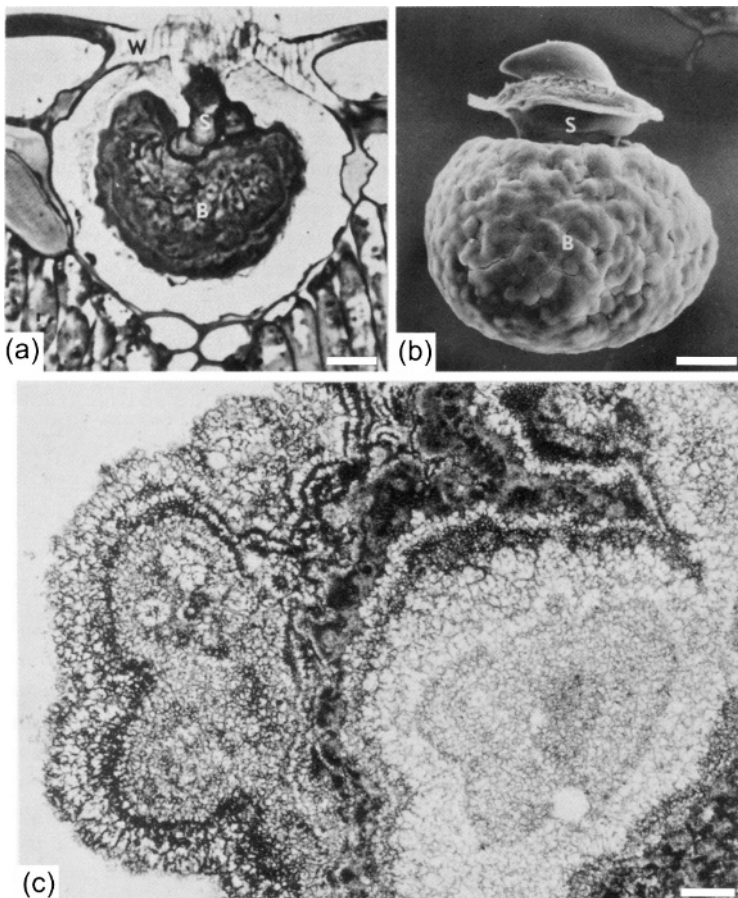


Figure 6.4 Cytholiths of *Morus alba*: (a) longitudinal section showing stalk *S*, cytholith body *B* and siliconized apical cell wall *W*, (b) an isolated cystolith showing stalk *S* and body *B*, and (c) transverse section of a demineralised cystolith showing concentric bands of organic matrix, where the central region is cellulose rich; scale bars: (a) 5, (b) 20 and (c) 2 μm . Reproduced from H.J. Arnott. In: G.H. Nancollas (Ed.), Biological Mineralization and Demineralization, Springer, Berlin, p. 199. Copyright (1982), with permission from Springer Science and Business Media

varying proportions of cellulose, hemicellulose and pectins. Hemicelluloses are composed of xyloglucans, xylans and heteroxylans, while pectins are polysaccharides.

6.1.4 Mollusk Shells and Avian Eggshells

Mollusks are soft-bodied metazoans composed of external calcified structures to support their living tissues. In most cases they have rigid protections as shells. More than 10^5 living mollusk species secrete shells in marine, lacustrine or terrestrial environments. The mollusk shell is a composite biomaterial in which 95–99% per weight mineral is calcium carbonate while the remaining 1–5% is an organic matrix. The topic of mollusk

shells has been discussed by Crenshaw (1982), Chateigner *et al.* (2000), and Marin and Luquet (2004). The growth mechanism, form, and structures of aragonite crystals in the shells of bivalves and snails or in pearls have been well investigated in order to control the quality of cultured pearls (Sunagawa, 2005).

Avian eggshell is mainly composed of the vaterite polymorph of calcium carbonate (Sparks, 1994), whereas chicken eggshell contains large crystals of calcite (Arias *et al.*, 1991). As in mollusks, the main task of the layers of the eggshell is to protect it from flooding with water and bacterial penetration from outside and to maintain a gaseous diffusion pathway against obstruction. The color of an avian eggshell is due to porphin and biliverdin pigments (Sparks, 1994; Mikšík *et al.*, 1996).

The longitudinal section of a mollusk shell consists of two or three layers of calcium carbonate as aragonite or calcite and an external organic layer, the periostracum. The calcified layers have different textures referred to as microstructures. The shells of different mollusks show a variety of microstructures, as shown in Figure 6.5. One of the best known microstructures is mother-of-pearl, or nacre, composed of an iridescent aragonite layer covering the inner surface of the shell of several mollusks. Due to some organic fraction contained in it, nacre has a fracture toughness about three order of magnitude higher than that of aragonite obtained by conventional precipitation. In view of this high mechanical strength, nacre has attracted a great deal of interest from materials scientists, dentists, orthopedists and nanotechnologists.

The construction of a mollusk shell is a biologically controlled mineralization process regulated by an extracellular organic matrix. Figure 6.6 illustrates the physiological process of shell mineralization for a marine bivalve. Shell growth takes place on the border of the shell, where growth occurs in increments by addition of minute layers to adjacent layers. The shell growth requires three components (Figure 6.6): an enclosed compartment (called the extrapallial space) for calcification, membrane-bound ionic pumps, and an extracellular organic matrix, which gives shape to the crystals. The extrapallial space is bound by the growing shell, the leathery periostracum and the calcifying mantle. The role of the periostracum is to provide support for calcium carbonate crystals and to seal the extrapallial space completely in such a way that supersaturation conditions for growth can be attained. Calcium and carbonate ions are taken from the teguments, the gills or the gut, and are transported via the hemolymph to the epithelial cells. They are then pumped to the extrapallial space by calcium and carbonate channels present in the membranes of the calcifying epithelial cells. The third component of the system is the calcifying matrix, which is secreted in the extrapallial space by specialized cells of the calcifying matrix. The matrix is a complex mixture of proteins, glycoproteins, proteoglycans and chitin. The matrix interacts with the mineral ions in such a way that they self-assemble to produce crystallites of well-defined morphologies. The role of the calcifying matrix is to provide sites for nucleation and growth of appropriate calcium carbonate polymorph, and to regulate the shapes and orientation of the crystals.

The shell matrix consists of two fractions, one insoluble and the other soluble. These fractions are usually separated by dissolving the mineral phase with a weak acid or with a calcium-chelating agent such as EDTA, followed by centrifugation. The insoluble shell matrix fraction, called *conchiolin*, is a heterogeneous mixture of proteinaceous substances identified as nacrin, nacrosclerotin, nacroin and chitin. Nacroin is exceptionally rich in

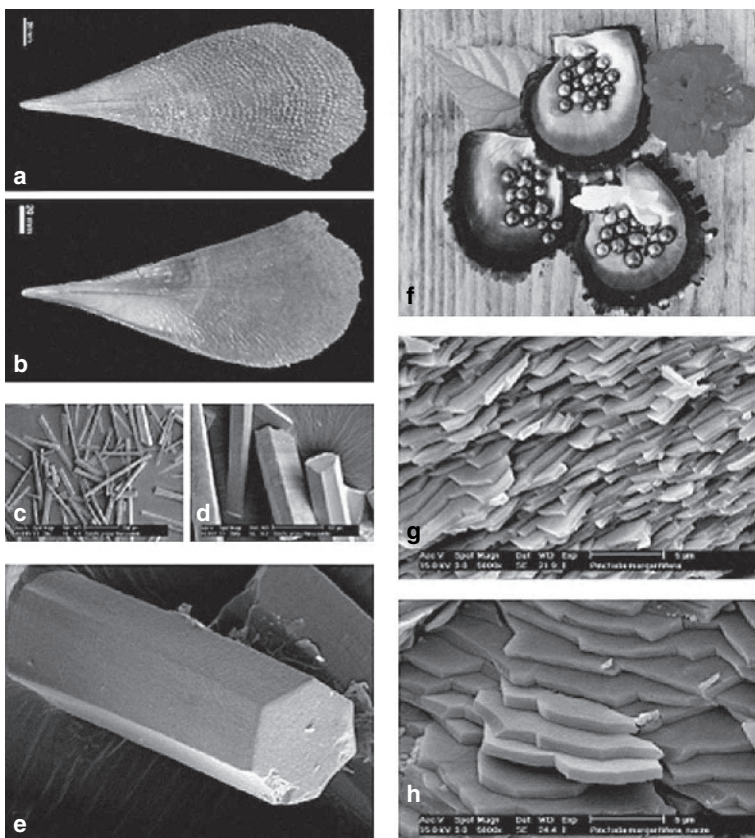


Figure 6.5 Shell of two nacprismatic bivalve genera of mediterranean fan mussel, *Pinna nobilis*, and their microstructures observed by SEM: (a) right valve, external surface showing the prismatic layer, (b) right valve, internal surface, (c) calcite prisms dissociated in the outer layer by sodium hypochlorite, (d) isolated prisms seen at a higher magnification, (e) details of one prism of 40 µm diameter and 100 µm length, (f) shell valves and pearls of the black-lip pearl oyster, *Pinctada margaritifera*, from French Polynesia, (g) necreous layer of *Pinctada margaritifera*, and (h) nacreous layer seen at a higher magnification. In (g) and (h) the nacreous layer is composed of aragonite flat tablets arranged in a brick-wall fashion. Reproduced from F. Marin and G. Luquet. C.R. Palevol. 3, 469. Copyright (2004), with permission from Elsevier

alanine and glycine residues. The proteinaceous nacre matrix resembles silk-fibroin, the main protein of spiders and worm threads. This composition explains the high fracture strength of nacre material. The brick-wall structure in Figure 6.5h is composed of nacre aragonite tablets as bricks glued by hydrophobic proteinaceous matrix surrounding the bricks.

The soluble organic fraction of the matrix is polyanionic and is rich in aspartic acid residues. The role of the polyanionic soluble matrix is two-fold. When adsorbed on an insoluble template, the soluble matrix promotes the nucleation of calcium carbonate

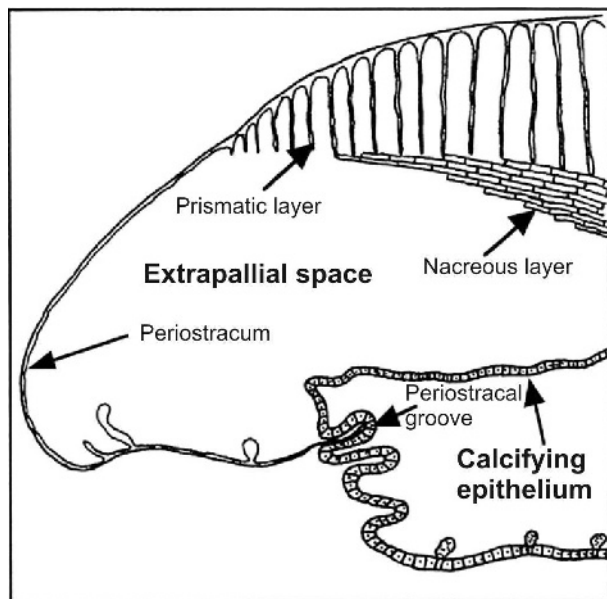


Figure 6.6 Schematic illustration of shell calcification process of a nacoprasimatic bivalve. Calcification of the growing shell occurs in the extrapallial space, which is enclosed by the calcifying epithelium, the periostracum and the shell itself. Reproduced from F. Marin and G. Luquet. C.R. Palevol. 3, 469. Copyright (2004), with permission from Elsevier

crystals on the template surface. However, in the free solution, the same soluble matrix is attached to the cationic surfaces of the growing crystals by electrostatic interaction, thereby inhibiting the growth of the nucleated crystals. Adsorption of the soluble matrix on all sides of the crystals would completely stop their growth. The repetitive brick-wall structure of mollusk nacre is possibly a result of numerous cycles of nucleation, maturation and inhibition. According to the model proposed by Levi-Kalisman *et al.* (2001), the interlamellar framework of the nacre is made of β -chitin, coated with soluble acidic macromolecules.

In the formation of pearls and the nacreous layer in shells, it can be assumed that an organic matrix layer is formed 0.2–0.3 μm away from and between the surfaces of the substrate pearl layer and the pearl epithelium (see the nacreous layer in Figure 6.6), where nucleation and growth of aragonite crystals take place. The thickness of the space controls the thickness of the aragonite crystals, while the separation between neighboring nucleating crystals determines their size. Consequently, aragonite crystals take a platy form with uniform thickness, and the aggregation of crystals produces a brick-wall structure. The {001} face grows large on platy crystals, and takes either a hexagonal form bounded by the {100} and {010} faces or a rhombic form bounded by the {110} faces. The organic matrix sheet is sandwiched between stacks of aragonite crystals, and it is in an epitaxial relation with the aragonite crystals. Therefore, the *c*-axes of the aragonite crystals are aligned perpendicularly to the substrate pearl surface. This results in growth patterns exhibiting closed loops and spirals with step heights corresponding to individual

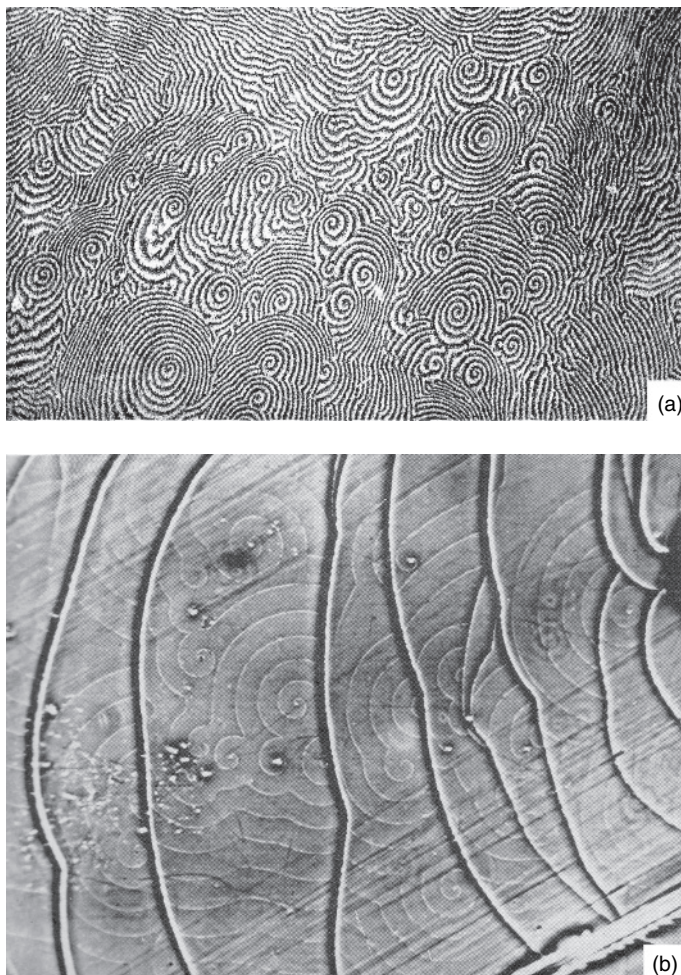


Figure 6.7 Spiral patterns observed on (a) the surface of a pearl and (b) the {0001} faces of a SiC crystal. (a) Reproduced from I. Sunagawa. Crystals: Growth, Morphology and Perfection. Copyright (2005), with permission from Cambridge University Press. (b) Reproduced from A.R. Verma (1953). Crystal Growth and Dislocations, Butterworths, London. Copyright (1953), with permission from Elsevier

crystals (Figure 6.7a). The spiral patterns are formed by twist boundaries composed of screw dislocations introduced by a slight misorientation between neighboring aragonite crystals. These spiral patterns on aragonite platelets are very similar to those observed more than five decades ago on the {0001} faces of SiC crystals (Figure 6.7b).

Finally, it should be mentioned that only one organic matrix sheet is formed at the front in bivalves, but many sheets are formed in snail shells (Sunagawa, 2005). Consequently, in contrast to bivalves which produce platy crystals (Figure 6.8a), snail shells grow as a tower-like pyramidal stacking structure (Figure 6.8b).

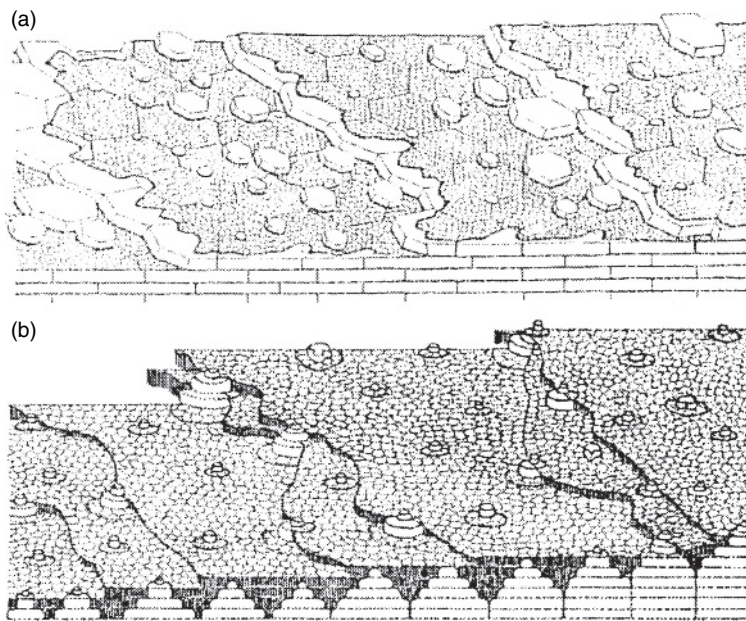


Figure 6.8 Schematic illustration of the formation of nacreous layers in (a) pearl bivalve and (b) a snail. Reproduced from I. Sunagawa. Crystals: Growth, Morphology and Perfection. Copyright (2005), with permission from Cambridge University Press

6.2 Pathological Mineralization

Serum, saliva and urine are the biological fluids involved in the formation of solid mineral phases from supersaturated systems. The composition of these fluids also determines whether mineralization is normal or abnormal. Typical examples of normal mineralization are calcification processes in shells, bones or teeth, while those of abnormal mineralization are bone diseases, carious lesions and the formation of dental and kidney stones. Table 6.2 gives examples of abnormal mineralization and the specific mechanisms involved.

Among the biological fluids, saliva has multifarious functions in the maintenance of oral health and the protection of hard and soft tissues of teeth (Mandel, 1989; van Nieuw Amerongen *et al.*, 2004). The main salivary proteins involved in the protection of the oral cavity are mucins MG1 and MG2 (up to 40%), immunoglobulins (5–15%), proline-rich proteins (1–10%), cystatins (10%) and histatins (5%), but a number of minor glycoproteins (e.g. agglutinin, lactoferrin and lysozyme) and cationic peptides (e.g. defensins and cathelicidin) are also known to have bacteria-killing activity. In general, the functions of saliva are (van Nieuw Amerongen *et al.*, 2004): (1) protection of the tooth surface against wear by a film of salivary mucins and protein-rich glycoprotein, (2) promotion of remineralization of the enamel by pellicle proteins, proline-rich proteins and statherin, which attract calcium ions, (3) retardation of demineralization by pellicle proteins, (4) prevention of adherence of oral microorganisms to the enamel pellicle and inhibit their growth, and (5) rapid neutralization of acids by the salivary bicarbonate/carbonate buffer system.

Table 6.2 Types of abnormal mineralization (after Smith, 1982)

-
- | | |
|----------------------------------|--------------------------------------------------|
| I Abnormal tissue mineralization | |
| A. | Tissue healing following cell death and necrosis |
| B. | Ectopic (metastatic) mineralization |
| C. | Crystal membranolysis |
| II Calculus formation | |
| A. | Sites |
| 1. | Oral |
| (a) | Dental |
| (b) | Salivary glands – sialolithiasis |
| 2. | Gastrointestinal |
| (a) | Gallbladder – cholelithiasis |
| (b) | Pancreas |
| 3. | Urinary |
| (a) | Kidneys and bladder – urolithiasis |
| (b) | Prostate |
| B. | Etiological factors |
| 1. | Supersaturation |
| 2. | Inhibitor deficiency |
| 3. | Matrix |
| 4. | Crystal retention |
-

Saliva is a mixture of proteins secreted by different salivary glands. Therefore, the antimicrobial and protective properties of saliva are a resultant of contributions of various proteins from different glands. When the salivary output is disturbed by some reason, the antimicrobial, buffering, remineralizing and cleansing properties of the saliva are reduced. This leads to a variety of oral diseases, including rapid and severe caries associated with the decay of teeth (Fox, 2004; Twetman, 2004).

Dental caries is the localized progressive decay of teeth, which is initiated by demineralization of the outer tooth surface (i.e. loss of calcium and phosphate ions in the enamel) due to a decrease in the pH in dental plaque by organic acids (mainly lactic acid) produced locally by the bacteria. In human dental plaque, the pH drops from the neutral value of 7 to about 5 for a period of 20 min, for example, during consumption of diet. Subsequently, saliva washes away the acids, bacteria, etc., whereby the plaque pH slowly reaches neutral in the following 40–45 min. Since the dental plaque is composed of dense bacterial masses which adhere strongly to the tooth surface, two properties of the dental plaque are important: (1) only high concentrations of bacteria can produce large quantities of acids in a short period, and (2) the rate of acid formation is faster than the diffusion of the acid because the plaque matrix makes diffusion slow. Evidently, the role of saliva is to suppress tooth decay by washing away acids and bacteria and by acting as

a chemical buffer for $\text{HCO}_3^-/\text{H}_2\text{CO}_3$. Hence the susceptibility to tooth caries cannot be attributed to the concentration of a single component of saliva.

Formation of urinary stones is a major health problem for humans. Among the human urinary stones, a majority are kidney stones (Pak, 1998). In most industrialized countries, about 80% of kidney stones are composed of calcium salts and usually occur as calcium oxalate and less commonly as calcium phosphate in the form of apatite and brushite. The remaining 20% of stones are composed of uric acid, struvite or carbonate apatite, cystine and rare stones.

About 2–5% of the population in Asia, 8–15% in Europe and North America, and 20% in Saudi Arabia develop kidney stones in their lifetime (Robertson, 1993). Kidney stones tend to recur, and the recurrence rate is about 75% during 20 years (Sutherland *et al.*, 1985). The incidence and occurrence rates of kidney stones are affected by genetic, nutritional and environmental factors (Robertson, 1993; Pak, 1998; Siener and Hesse, 2002; Chandrajith *et al.*, 2006). They develop because of abnormalities in urinary composition caused by metabolic and environmental-nutritional factors (Pak 1998; Chandrajith *et al.*, 2006; Grases *et al.*, 2006; Guerra *et al.*, 2006). The metabolic factors are associated with, among others, increasing urinary saturation of calcium ions (hypercalciuria), oxalate ions (hyperoxaluria), uric acid (hyperuricosuria), acid retention causing inhibitor deficiency (hypocitraturia), change in the pH of biological fluid (gouty diathesis and cystinuria), and urea hydrolysis (infection stones). Environmental factors include inappropriate dietary components such as excess of animal protein, salt and alcohol or low fluid intake.

In living organisms, mineralization processes are composed of at least two parts: precipitating crystalline phase(s) and a supporting structure (e.g. matrix). As in the case of crystallization of a compound in the free volume of the medium, for the occurrence of mineralization in a biological system the system has to attain some degree of supersaturation of the precipitating phase. The factors that lead to mineralization of a phase in the complex biological solution are the concentration of precipitating ions, the complexation of ions, the solution pH, crystal growth inhibitors, and the structure and properties of the supporting matrix.

The role of the organic matrix in abnormal mineralization is an especially important problem because it can induce heterogeneous nucleation of the phase by an epitaxy-type mechanism, and contains a variety of chemical components which can act as growth inhibitors. Some of the inhibitors present in biological fluids are listed in Table 6.3.

In order to understand the mechanism of formation of urinary and kidney stones, crystallization of calcium oxalate phases as a function of initial supersaturation S_i , reactant ratio R_i , and nature and concentration of additives have been extensively investigated (Kurutz *et al.*, 2003; Webber *et al.*, 2003; Jung *et al.*, 2004, 2005; Thongboonkerd *et al.*, 2006). It has been found that excess Ca^{2+} conditions favor the formation of thermodynamically metastable COD form but excess $\text{C}_2\text{O}_4^{2-}$ conditions are favorable for the crystallization of COM (see Figure 2.13). In the intermediate range of excess Ca^{2+} conditions, both COD and COM phases are produced. This dependence of crystallization of COM and COD phases on solution stoichiometry and supersaturation conditions is directly connected with the formation of kidney stones in different population groups because of differences in the composition of their urine. For example, South Africa's black population has a significantly low incidence of kidney stones compared with the

Table 6.3 Inhibitors for crystal growth and/or aggregation

Compound	Inhibitor	Source
Calcium carbonate	Polycarboxylic acid anions	Organic matrix
	Collagen	Organic matrix
	Bivalent metal cations	Seawater, organic matrix
	Anionic surfactants	Organic matrix
	Inorganic phosphate ions	Seawater
	Sulfated polysaccharides	Organic matrix
	Lysozyme	Organic matrix
	Stratherin	Saliva
	Proline-rich proteins	Saliva
	Magnesium	Cells and fluids
Calcium phosphate	Citrate	Cells and fluids
	Acid-side amino acids	Organic matrix
	Basic-side amino acids	
	Chitosan	Organic matrix
	Oxy acids (citric, malic, citric)	Urine
	Amino acids (aspartic, glutamic, etc.)	Urine, organic matrix
	Ketoglutaric acid	Urine
Calcium oxalate	Anionic and cationic surfactants	Urine

incidence rate in the white population, the latter being similar to that in Western society (Webber *et al.*, 2003). This difference is associated with the fact that the urine of the black population has a lower citrate concentration, a higher oxalate concentration, and a lower calcium concentration than that of the white population.

The principal component of calcium oxalate kidney stones is COM with urinary proteins and trace amounts of mono-, bi- and trivalent metal cations such as Mg, Na, K, Zn and Fe (Ryall *et al.*, 2005; Chandrajith *et al.*, 2006). The stones are aggregates of COM crystallites held together by urine protein molecules. The degree of occurrence of uric acid crystals in the beginning zone of calcium oxalate renal stones has also been investigated (Grover *et al.*, 2003; Grases *et al.*, 2006). It was found (Grases *et al.*, 2006) that the core of calcium oxalate stones contains uric acid (1.2% of all stones) and organic matter (10.8% of all stones). These results suggest that impurities such as uric acid and sodium urate can induce heterogeneous nucleation of COM as a result of decrease in the metastable zone limit of urine solution, thereby salting out calcium oxalate (Grover *et al.*, 2003). This situation is somewhat similar to that observed in the case of precipitation of aragonite on amorphous magnesian calcium carbonate shown in Figure 7.19d. However, as demonstrated recently by Guerra *et al.* (2006) on the example of supplementation of certain inhibitors, such as citrate and magnesium, for calcium oxalate crystallization the effect of impurities on the reduction in the total amount of calcium oxalate crystals and their aggregates is more pronounced during *in vitro* crystallization in dilute urine. However, in dilute urine the size of the COM crystals increases and their morphology undergoes a change.

Wesson *et al.* (2005) investigated the effect of protein mixture isolated from the urine of normal individuals and stone formers, a number of synthetic homopolymers,

naturally occurring urine macromolecules, and their binary mixtures on the aggregates of previously formed COM crystals. It was observed that protein mixtures isolated from the urine of normal individuals and most stone formers reduce the degree of aggregation of the seed crystals, but the urine protein molecules of less than one-quarter of stone formers either do not disaggregate or promote aggregation. Like normal urine proteins, synthetic and naturally occurring polyanions induce disaggregation whereas polycations have no effect. In contrast, mixing a polyanion, such as polyaspartate or osteopontin, with the polycation polyarginine leads to the promotion of aggregation. These results suggest that the structure and composition of urinary macromolecules are responsible for the formation of kidney stones.

Webber *et al.* (2003) investigated the chemical conditions required for the precipitation of pure COM and COD crystals from the urine of representative black and white populations of South Africa and analyzed the major proteins included in the crystals. The calcium concentration, referred to as the control urine, in the urines of black and white populations was 2.56 and 4.08 mmol/l, respectively. The calcium concentrations of the pooled urine samples were adjusted between 0.5 and 16 mmol/l by titration. The pure COM and COD crystals obtained from the urines in which calcium concentrations had been adjusted and those precipitated from the control urines were used for protein analysis. Figure 6.9a–d and e–h illustrate the scanning electron micrographs of the crystals obtained from the urines of representative black and white populations, respectively, at various calcium concentrations. At 0.5 mmol/l calcium concentration in the urines of both population groups, disc-shaped COM crystals are formed, but they are gradually replaced by bipyramidal COD crystals as the calcium concentration exceeds 12 mmol/l. Moreover, COM crystals are predominantly produced in the control urine of the black group (Figure 6.9c) whereas COD crystals are formed exclusively in the control group of the white group (Figure 6.9g).

From the above observations, it may be concluded that the inherently different urine compositions in different race groups play a decisive role in determining the morphology of urine stones. It is well known (Brown *et al.*, 1989) that citrate, magnesium and potassium stabilize the precipitation of the thermodynamically less stable COD phase. Since the potassium concentration is much lower in the urine of the black than the white population, a relatively low percentage of COD crystals is formed from the urine of the former group.

Comparison of the COM and COD crystals grown from the urines of the two groups also revealed differences in the intracrystalline proteins incorporated in the crystals. Whereas both urinary prothrombin fragment 1 (UPTF1) and osteopontin were in the COM crystals obtained from the urine of the black group, only UPTF1 was contained in crystals grown from the urine of the white group. The COM crystals obtained from the urine of the black group also contained low molecular weight proteins (17–20 kDa), which were not found in the crystals obtained in the urine of the white group. Apart from this, the COM from the urine of the black group contained two- to three-fold more UPTF1 than those from the urine of the white group. The COD crystals precipitated from the urines of the black and white groups also differed in their protein content. The former group's COD crystals contained a large proportion of osteopontin and also an unidentified 56 kDa protein, whereas the latter group's COD crystals contained entirely osteopontin.

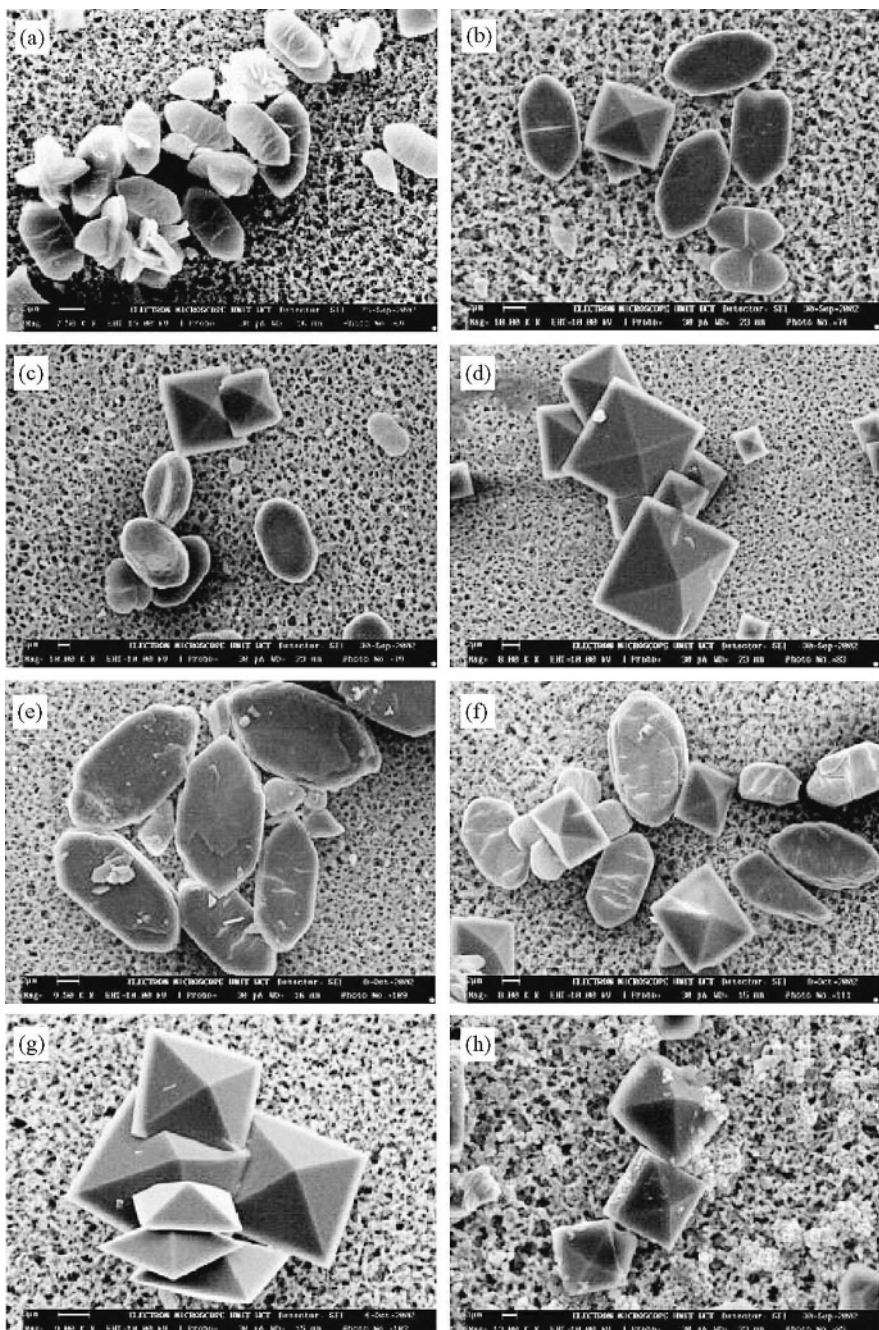


Figure 6.9 Scanning electron micrographs of calcium oxalate crystal phases precipitated from urines of (a–d) black and (e–h) white groups. Calcium concentrations in black group's urine: (a) 0.5, (b) 1.0, (c) 2.56 and (d) 12 mmol/l; calcium concentration in white group's urine: (e) 0.5, (f) 1.0, (g) 4.08 and (h) 12 mmol/l; horizontal edge of photographs is about 6 μm . Reproduced from D. Webber, A.L. Rodgers, and E.D. Sturrock. *J. Cryst. Growth* **259**, 179. Copyright (2003), with permission from Elsevier

The above observations suggest that selective adsorption of UPTF1 and osteopontin is due to the unique crystal structure of COM and COD, and the conformation of proteins at different calcium concentrations at which these phases precipitate. The greater amount of intracrystalline inhibitory protein in the black group may be a cause of the low incidence of stone formation in this group.

In a recent comparison of the ultrastructure and protein content, particularly UPTF1 and osteopontin, of COM and COD crystals precipitated from human urine, and their susceptibility to proteolysis, Ryall *et al.* (2005) found that the ambient calcium concentration mainly determines the binding of protein molecules to calcium oxalate. Each protein may suppress urolithiasis by inhibiting crystallization of preferred growth habit of the crystals, and by facilitating intracrystallite disaggregation and dissolution of crystallites attached to and internalized by renal epithelial cells.

6.3 Effect of Biologically Active Additives on Crystallization Processes

6.3.1 Overall Precipitation Kinetics

Practically all of the calcium salts, such as calcium carbonate, calcium phosphate and calcium oxalate, found as biominerals are sparingly soluble. Their solubility is represented by the solubility product K_s and the supersaturation is given by

$$\ln S = \ln[(IP^{1/\nu} - K_s^{1/\nu})/K_s^{1/\nu}] \quad (6.1)$$

where IP is the ionic activity product and ν is the number of ions in the formula unit of the crystallizing phase. Growth is carried out in different ways:

- (1) Constant composition method from aqueous solutions: (i) by mixing background electrolyte with calculated amounts of reactants, followed by a dilute hydroxide or acid to adjust the pH to a desired value, or (ii) by simultaneously mixing two equal volumes of solutions containing background electrolyte with reactants, followed by addition of seed crystals, lowering of pH, and addition of titrant solutions to restore the concentrations of solutions to their original values (see, for example, Nancollas and Tomson, 1978; Gomez-Morales *et al.*, 1996; Katsifaras and Spanos, 1999; Koutsopoulos and Dalas, 2000; Tsortos and Nancollas, 2002; Wei *et al.*, 2003; Westin and Rasmuson, 2005; Wang *et al.*, 2006a,b).
- (2) Slow diffusion of NH_4HCO_3 vapor into cell-cultured dishes containing CaCl_2 solution in a closed desiccator for the growth of calcium carbonate (Aizenberg *et al.*, 1997; Feng *et al.*, 2000; Shen *et al.*, 2002).
- (3) Double diffusion method involving reaction between two reactants in gel media (Prieto *et al.*, 1989; Wada *et al.*, 1998, 1999).

In method (1), growth kinetics may be studied in both the absence and presence of seeds of specific surface area in the metastable supersaturation zone, i.e. at a supersaturation lower than that which causes spontaneous nucleation but high enough to support growth. The precipitation kinetics are followed either by analysis of the growing seeds or by measurements of ions which are required to be added by automatic pipets as a function of time to maintain the predetermined supersaturation for growth. The growth rate R is

determined from the deposited amount after a known period t . The other methods are more suited for the study of the relative fraction of different polymorphs and the morphology of these polymorphs as a function of reactant compositions, effects of impurities and other growth conditions. In all the above three methods the impurity is mixed with one of the reactants before the onset of an experimental run.

As discussed in Chapter 2, the fraction y of the crystalline phase (frequently called the overall crystallization of a phase) in a closed system when many nuclei occur may be described by an instantaneous nucleation and a progressive nucleation mechanism (Kashchiev, 2000). In terms of mass $w(t)$ crystallized at time t in volume V , overall crystallization is defined as

$$y = w(t)/w_0 \quad (6.2)$$

where w_0 is the maximum mass of the crystallizing phase when $t \rightarrow \infty$. In the case of instantaneous nucleation, all nuclei are formed in the system at the initial moment $t = 0$ and thereafter they grow irreversibly until the completion of the phase transformation. However, in progressive nucleation, nuclei form continuously during the process, and the nucleation rate can be either time independent (stationary nucleation) or time dependent (nonstationary nucleation).

The overall crystallization may be given by the Kolmogorov–Johnson–Mehl–Avrami (KJMA) theory (Kashchiev, 2000; see Section 2.4)

$$y = 1 - \exp[-(t/\Theta)^q] \quad (6.3)$$

where $q = \nu d$ and $1 + \nu d$ for the instantaneous and progressive nucleation mechanisms, respectively (ν is a number equal to 1/2 and 1 for growth controlled by volume diffusion and mass transfer, respectively, and d is the dimensionality of growth), and Θ is the time constant, the value of which is different in the two mechanisms. As shown below, the overall crystallization may equally well be expressed by the following empirical relation:

$$y = 1 - b \exp(-t/\Theta) \quad (6.4)$$

where b is an empirical constant and Θ is a new constant approximately equal to the Θ in Equation (6.3). For $t/\Theta \gg 1$, overall crystallization $y_{\max} = 1$.

The effect of adsorption of impurity particles on overall crystallization may be incorporated in Equation (6.2) by considering instantaneous occupation of fraction θ_{eq} of the total growth sites on the nuclei by additive particles while the remaining $(1 - \theta_{\text{eq}})$ sites remain unoccupied [see Equations (4.20) and (4.21); see also Section 4.3.1]. If the maximum crystallized masses are w_0 and w_i in the absence and presence of the impurity, respectively, the resulting crystallized mass w in the presence of an impurity with coverage θ_{eq} of adsorption sites may be written in the form

$$w = w_0(1 - \theta_{\text{eq}}) + w_i \theta_{\text{eq}} \quad (6.5)$$

or the overall crystallization

$$y = w/w_0 = 1 - \alpha \theta_{\text{eq}} \quad (6.6)$$

where the impurity effectiveness parameter $\alpha = (w_0 - w_i)/w_0 \leq 1$, and y is given by Equation (6.3). When adsorption of impurity particles completely inhibits crystallization at the adsorbed sites, $w_i = 0$, then $\alpha = 1$. The fractional surface coverage θ_{eq} is given by the usual adsorption isotherms. In the case of Langmuir and Temkin adsorption isotherms, θ_{eq} is given by (see Section 4.2)

$$\theta_{\text{eq}} = Kc_i/(1 + Kc_i) \quad (6.7)$$

and

$$\theta_{\text{eq}} = Z(\ln C_0 + \ln c_i) \quad (6.8)$$

respectively, where K , Z and C_0 are constants. In the investigation of precipitation kinetics, the Langmuir constant K is frequently referred to as the adsorption or affinity constant for an impurity. It is defined as the ratio of the rate constants of adsorption and desorption, $k_{\text{ad}}/k_{\text{des}}$, and is a measure of the adsorption affinity of an impurity (see Section 4.1).

For crystallization on seeds, the usual crystal growth theories may be applied. Then the basic concepts of the effect of impurities advanced in Chapter 4 for the growth of single crystals are valid for all impurities irrespective of their type. Moreover, they are valid for cases when (a) all of the faces appearing in the morphology of a crystal are involved and (b) several crystals grow simultaneously in the presence of an impurity. The kinetics of such growth systems yield average values of the fractional coverage θ_{eq} of the impurity and the impurity effective parameter α .

In the case of time-dependent impurity adsorption, the step displacement velocity v is given by [see Equation (4.61)]

$$v/v_0 = 1 - \alpha\theta_{\text{eq}}[1 - \exp(-t/\tau)] \quad (6.9)$$

where τ is a time constant characteristic for an impurity. When the growth rates of individual faces or the average growth rate of a large number of small crystals are involved in a growth system, the step velocity v of the above equations is replaced by R . Then, if the growth rate is defined as the precipitated mass w' , the time dependence of overall crystallization y' may be written from Equation (6.9) in the form

$$y' = w'/w_0 = 1 - \alpha\theta_{\text{eq}}[1 - \exp(-t/\tau)] \quad (6.10)$$

One finds a close similarity between this equation and Equation (6.3). They coincide when $(1 - y')/\alpha\theta_{\text{eq}} = y$, $q = 1$ and the time constant $\tau = \Theta$. However, we note that the derivation of Equation (6.10) is somewhat exaggerated because it can be applied to growth occurring by the movement of growth steps on F faces, and is not expected to hold for precipitation processes. Moreover, this equation holds for both impure and pure systems. Assuming that Equation (6.10) holds for additive-containing systems, for $t/\tau \gg 1$ when the term in the square brackets becomes unity, one may write the overall crystallization corresponding to the maximum value in the form of Equation (6.6), i.e.

$$y'_{\text{max}} = 1 - \alpha_0\theta_{\text{eq}} \quad (6.11)$$

where the new constant $\alpha_0 = \alpha y_{\text{max}}$ and $y_{\text{max}} \leq 1$.

There have been numerous studies on the overall crystallization of important sparingly soluble salts and for a short review on the subject the reader is referred to Füredi-Milhofer and Sarig (1996). A general feature of the crystallization of these salts is that the solution pH, the supersaturation available for growth, the ratio of reactants, the experimental temperature, and the nature and concentration of additive determine the type of crystallizing polymorph and its growth rate. For example, in the case of calcium carbonate, both vaterite and calcite grow at $\text{pH} \geq 9.3$, whereas only vaterite is produced at $\text{pH} \leq 9.2$ (Gómez-Morales *et al.*, 1996).

There have been several studies of the progress of the growth kinetics of sparingly soluble salts both in the absence and in the presence of a variety of impurities. Figure 6.10a

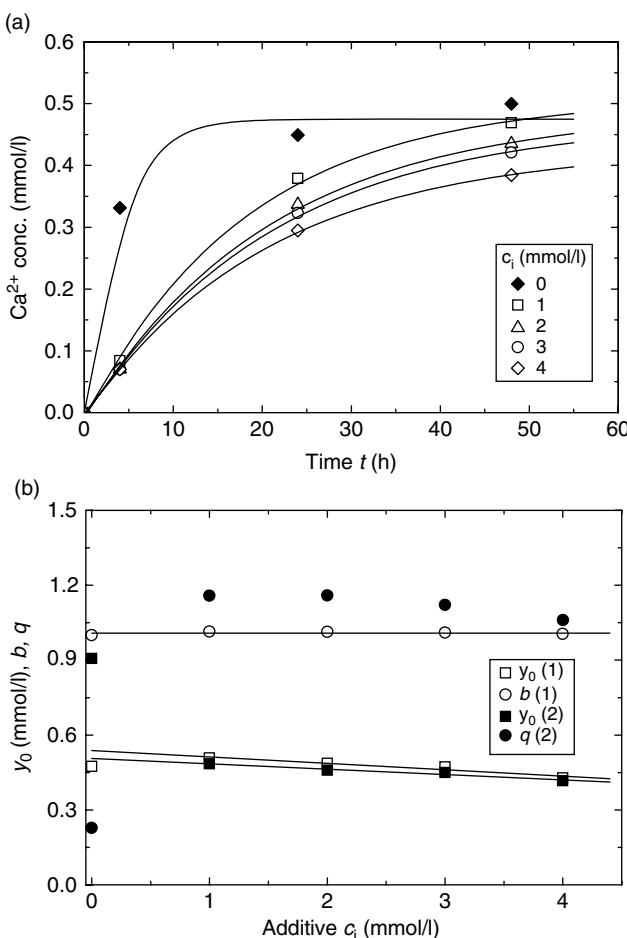


Figure 6.10 (a) Dependence of overall precipitation y of metastable calcium oxalate on time t in the presence of different concentrations of α -ketoglutaric acid. Plots are drawn according to Equation (6.3) with best-fit constants given in (b). Original data from Atanassova *et al.* (1996). (b) Plots of y_0 , $\alpha\theta_{\text{eq}}$ and Θ on impurity concentration c_i . In the inset the numbers (1) and (2) denote Equations (6.4) and (6.3), respectively

illustrates the experimental data, obtained by Atanassova *et al.* (1996), for the overall precipitation y of metastable calcium oxalate as a function of time t in the presence of different concentrations of α -ketoglutaric acid. Overall precipitation y was measured as $[Ca^{2+}]$ and $[Ca^{2+}]_0 = y_0$ at the growth temperature of 37 °C, but the data were recalculated for precipitation. The $y(t)$ data were analyzed by using Equations (6.3) and (6.4). The constants y_0 , q and b of these equations are shown in Figure 6.10b as a function of additive concentration c_i . In the inset, numbers (1) and (2) denote Equations (6.4) and (6.3), respectively.

It may be noted that $q = 0.25$ in the case of pure solutions, but $q = 1$ for systems containing an impurity. This difference in q for pure and additive-containing systems is associated with different nucleation mechanisms. In pure solutions, the observation of $q = 0.25$ suggests that nucleation is instantaneous where growth of the nuclei is controlled by volume diffusion and probably the growth dimensionality $d = 2$ [see Equation (6.3)]. However, in additive-containing solutions, the observation of $q = 1$ implies that nucleation is progressive and $d = 0$ irrespective of whether $\nu = 1/2$ or 1. It can be seen that, except for impurity-free systems, the values of the constant y_0 calculated by the two equations are comparable, because $\alpha\theta_{eq} = 1$ and $q = 1$. The observation that $\alpha\theta_{eq} = 1$ implies that all adsorption site are occupied, while the observation that $q = 1$ means that the dimensionality parameter $d = 0$ [see Equation (6.3)]. It was found that, as expected from $\alpha\theta_{eq} = 1$ and $q = 1$, the values of time constant Θ predicted by the two equations are also comparable for additive-containing solutions.

In Figure 6.10b, one observes a linear dependence of y_0 on c_i with a slope $\alpha K = 2.3 \times 10^5$ [cf. Equation (6.6) and $Kc_i \ll 1$]. Assuming that the impurity effectiveness factor $\alpha = 1$, using Equation (4.6) one finds that the differential heat of adsorption $Q_{diff} = 31.2 \text{ kJ/mol}$ for α -ketoglutaric acid impurity.

Figure 6.11a presents the case of precipitation kinetics of hydroxyapatite (HAP) for two polymer impurities: sodium salts of poly-L-glutamic acid (poly-L-Glu) and poly-L-aspartic acid (poly-L-Asp). The precipitated mass w was determined as $[Ca^{2+}]$ at the growth temperature of 37 °C and pH = 7.4. The plots are drawn according to Equation (6.4), and the best-fit constants w_0 , b and Θ are given in Table 6.4. The dependence of w_0 on the concentration c_i of the impurities is presented in Figure 6.11b, where the plots are drawn according to Equation (6.6) with the constants $w_0(0)$ (i.e. value of w_0 at $c_i = 0$), α , K and Q_{diff} for the polyelectrolytes given in Table 6.5.

The amino acids, glutamic acid (Glu) and aspartic acid (Asp), are known to play an important role in the mineralization of bones and teeth. These two polymers differ in their conformation. Poly-L-Glu molecules are randomly coiled at near-neutral pH values to an α -helical conformation under more acidic conditions, whereas poly-L-Asp shows no such transitions. Calcium ions are known to bind with the carboxyl group of the polymer side-chains. Cations such as Ca^{2+} and Mg^{2+} ($> 10 \text{ mM}$) can induce a coil to helix transition, probably by binding to and neutralizing the side-chain carboxyl group of poly-L-Glu. Some important properties of these polyelectrolytes are given in Table 6.6, where pK_a is the dissociation constant of the acid, l_l is the unit length, l_s is the side-chain length, S_l is the surface area of a molecule with a flat, side-on straight-chain orientation, and S_c is area of the circle composed of chain length l .

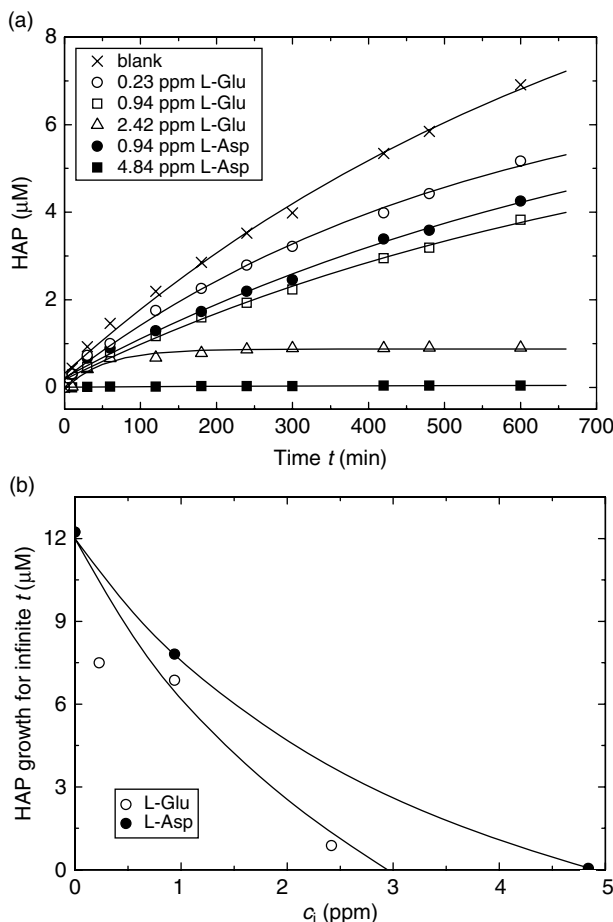


Figure 6.11 (a) Dependence of precipitated mass w of metastable hydroxyapatite on time t in the presence of different concentrations of poly-L-Glu and poly-L-Asp additives. Original data from Tsortos and Nancollas (2002). (b) Plots of initial HAP concentration w_0 on impurity concentration c_i . See text for details

It should be noted from Table 6.6 that the dissociation constant pK_a of a polyelectrolyte increases with increase in its side-chain length l_s and decreases with increase in the surface area S_l of a flat molecule and the area S_c of the circle composed of chain length l_l of a flat molecule. From Tables 6.5 and 6.6, it can be seen that the adsorption characteristics of polyelectrolyte polymers during HAP precipitation, as characterized by the impurity effectiveness parameter α and the Langmuir adsorption constant K , are associated with their dissociation constant pK_a and the surface area S_c of a flat molecule.

Sikirić *et al.* (1999) investigated the transformation of metastable COD phase into the thermodynamically stable phase COM on COM seeds without surfactants and in the presence of critical micellar concentrations (CMC) of $8 \times 10^{-4} \text{ mol}/\text{dm}^3$ sodium dodecyl sulfate (SDS) and $4 \times 10^{-3} \text{ mol}/\text{dm}^3$ dodecylammonium chloride (DDACl) surfactants.

Table 6.4 Best-fit constants of Equation (6.4) for polyelectrolytes

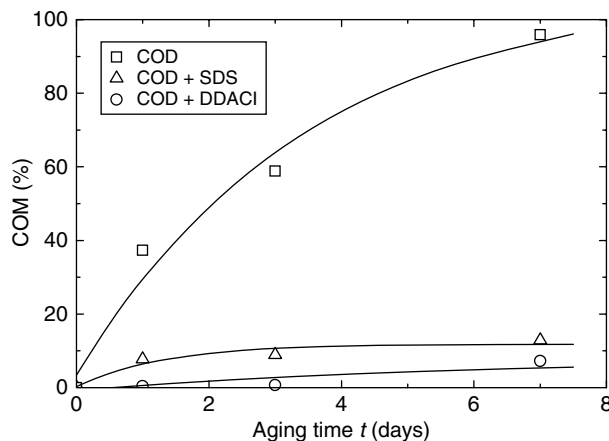
Additive	c_i (ppm)	w_0 (μM)	b	Θ (min)
—	—	12.2 ± 2.1	0.974 ± 0.007	762 ± 187
Poly-L-Asp	0.94	7.8 ± 1.5	0.972 ± 0.008	800 ± 224
	4.84	0.046 ± 0.006	0.971 ± 0.047	273 ± 89
Poly-L-Glu	0.23	7.5 ± 0.7	0.974 ± 0.008	546 ± 85
	0.94	6.9 ± 1.1	0.974 ± 0.007	780 ± 179
	2.42	0.87 ± 0.3	1.048 ± 0.066	52.3 ± 9.6

Table 6.5 Constants $w_0(0)$, α , K and Q_{diff} for polyelectrolytes

Additive	$w_0(0)$ (μM)	α	K ($\times 10^5$)	Q_{diff} (kJ/mol)
Poly-L-Asp	12.2	1.7	2.8	31.6
Poly-L-Glu	11.1	2.1	3.2	31.9

Table 6.6 Some structural properties of polyelectrolytes^{a,b}

Additive	pK_a	l_l (nm)	l_s (nm)	S_l (nm 2 /chain)	S_c (nm 2 /chain)
Poly-L-Asp	4.18	0.334	0.365	21.0	391.7
Poly-L-Glu	4.47	0.334	0.490	16.7	247.7

^a Titrant 0.15 M NaCl.^b Data from Tsotros and Nancollas (2002).**Figure 6.12** Dependence of mass fraction of COM transformed from metastable COD phase with aging time t without additive and in the presence of micellar concentrations of $8 \times 10^{-4} \text{ mol}/\text{dm}^3$ SDS and $4 \times 10^{-3} \text{ mol}/\text{dm}^3$ DDACI surfactants; experimental conditions: amount of COD 0.5 g/dm 3 , CaCl $_2$ concentration 0.01 mol/dm 3 , NaCl concentration 0.3 mol/dm 3 , pH 6.5, and temperature 37°C. Original data from Sikirić et al. (1999)

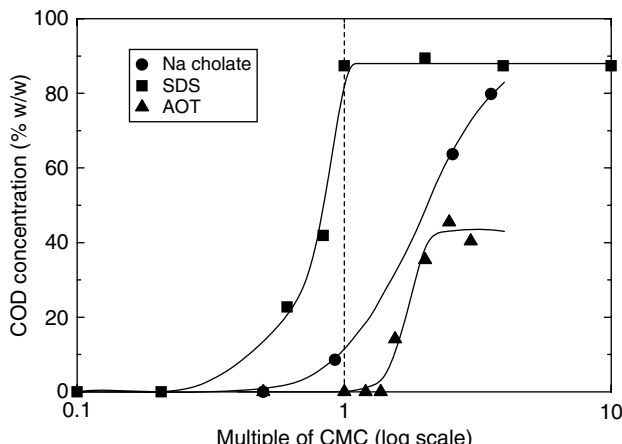


Figure 6.13 Precipitation behavior of calcium oxalate in the presence of three surfactants. Reproduced from H. Füredi-Milhofer, M. Skirić, L. Tunik, N. Filipović, and N. Garti. *Int. J. Mod. Phys.* **16**, 359. Copyright (2002), World Scientific Publishing

Their results are shown in Figure 6.12. The curves are drawn according to Equation (6.4) with the best values of constants b and Θ . The data analysis revealed that $b \approx 1$ (0.968, 0.974 and 1.009 for COM, COM-SDS and COM-DDACl systems, respectively), and $\Theta = 3.4$ days. Optical microscopy observations of COD crystals in the electrolyte solution showed (Sikirić *et al.*, 1999) that at the beginning of an experiment COD crystals were in the form of tetragonal bipyramids, but aging produced pronounced rounding and a decrease in crystal size due to their dissolution. These results mean that Equation (6.3) explains the transformation kinetics of COD into COM in the electrolyte solution, and this is a typical example of solution-mediated transformation.

A profound influence of surfactants as selective inhibitors of the growth of metastable phases of calcium phosphate and calcium oxalate occurs at concentrations above the CMC. Figure 6.13 shows this behavior for the precipitation of calcium oxalate in the presence of three surfactants: single-chained SDS, double-chained sodium diisooctyl sulfosuccinate (AOT) and sodium cholate (Na cholate) (Füredi-Milhofer *et al.*, 2002). As can be seen, SDS and Na cholate almost completely suppress crystallization of COM and cause the crystallization of more than 90% of COD, whereas precipitates formed in the presence of AOT consist of about 50% of either phase.

The above observations are corroborated by the study of the adsorption isotherms of the surfactant AOT on COM and COD crystals (Füredi-Milhofer *et al.*, 2002). The adsorption isotherm of AOT on COM resembles isotherms characterizing the adsorption of surfactant at oxide/water interfaces. The adsorption isotherm reveals a region of low adsorption due to electrostatic interactions of the substrate with surfactant molecules and a region of high adsorption caused by the formation of surface aggregates. The isotherm levels off when the equilibrium surfactant concentration reaches the CMC. Then an equilibrium is reached between free micelles in the solution and the surface aggregates. In contrast to the AOT/COM

system where adsorption starts at a relatively low surfactant concentration of 0.07 CMC, in the AOT/COD system the region of low surfactant adsorption is not apparent because a hydrated layer shields COD surfaces from electrostatic interactions. In this case surfactant adsorption starts at much higher surfactant concentration of about 0.2 CMC and ultimately reaches a surface coverage about half of that for the AOT/COM system. This selective adsorption in the early stage of precipitation is responsible for a reversal in the precipitated phases.

The above examples clearly demonstrate the effect of impurities on crystallization kinetics and the effect is associated with the processes of adsorption of additives at the solid–liquid interfaces of the dissolving (metastable) and the growing (stable) phases. As a result, the additive reduces the dissolution of the dissolving phase and builds up the supersaturation necessary for the crystallization of the stable phase. At the same time, the additive inhibits the growth of crystals of the stable phase by adsorbing on its solid–liquid interface. The adsorption behavior of two different additives on the surfaces of metastable and stable phases is different. Therefore, depending on the adsorption behavior of different additives, they lead to different rates of phase transformation of a metastable phase into its stable phase.

6.3.2 Overall Growth Kinetics

The crystallization rate R is traditionally determined by the constant composition method from plots of titrant addition as a function of time t in the initial stage (for example, for $t < 100$ min in Figure 6.11), normalized for the total surface area of the seed crystals. Then $R = dw/dt \approx w/t$ and $R_0 = dw_0/dt \approx w_0/t$ [cf. Equation (6.3)]. This approach can be justified on the following grounds:

- (1) The contribution of the exponential term in Equation (6.3) to the overall crystallization at a given supersaturation is essentially the same because the contribution of small changes in the time constant Θ to the rates is insignificant.
- (2) The exponent q (equal to 1 or $1 + \nu d$) in Equation (6.3) essentially remains unaltered in systems without and with impurities (see Figure 6.10b).

Figure 6.14a shows the data for the growth rate R of calcite, obtained by Manali and Dalas (2002) at a growth temperature of 25 °C and pH 8.5, on calcite seed crystals as a function of the concentration c_i of sodium alginate impurity. The nature of $R(c_i)$ is similar to that in Figures 4.3 and 4.4, implying that Equations (4.28) and (4.61) of growth kinetics with θ_{eq} given by the usual adsorption isotherms [see Equations (6.7) and (6.8) and Section 4.2], may be applied. Thus, Figure 6.14b presents the plot of $R_0/(R_0 - R)$ against $1/c_i$ using Equation (6.6) in combination with the Langmuir adsorption isotherm [Equation (6.7)]. The plot gives $\alpha = 0.96$, $K = 1.6 \times 10^7$ and $Q_{\text{diff}} = 41.8 \text{ kJ/mol}$.

Figure 6.15 illustrates another example of the dependence of overall growth rate R of calcite, reported by Reddy and Hoch (2001) at 25 °C, pH 8.55 and $S = 4.5$, on calcite seed crystals on the concentration c_i of four polycarboxylic acids: citric (CTRC), tricarballylic (TCBL), cyclopantanetetracarboxylic (TPTCA) and tetrahydrofuranetetracarboxylic acids (THFTCA). The structures of these additive anions are shown schematically shown in Figure 6.16. The plots in Figure 6.15 are drawn according to Equation (6.6) based on the Langmuir adsorption isotherm. The constants α and K and Q_{diff} are listed in Table 6.7. As can be seen, the value of the differential heat of adsorption Q_{diff} for different additives

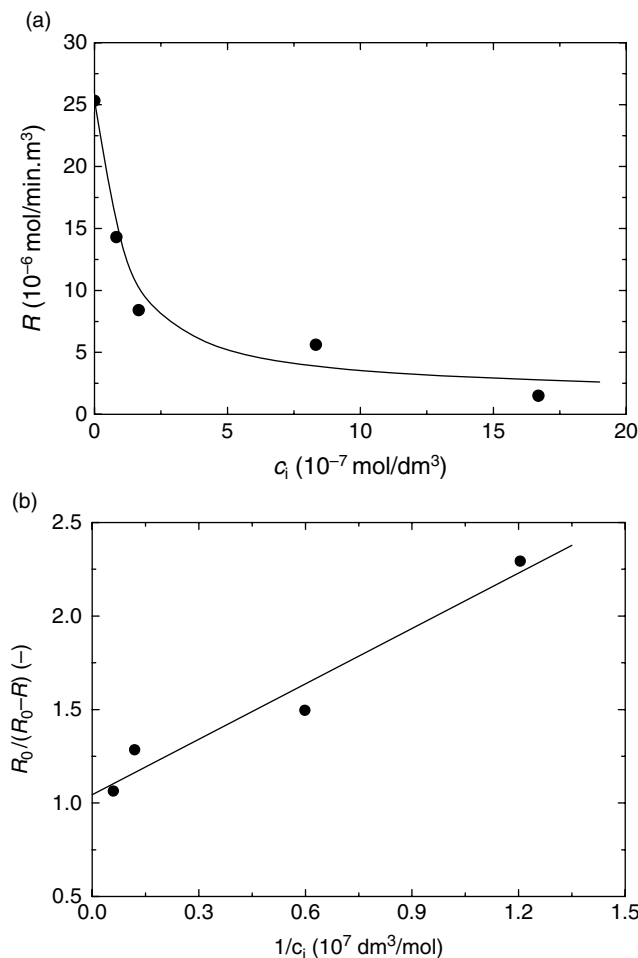


Figure 6.14 (a) Dependence of growth rate R of calcite seed crystals on the concentration c_i of sodium alginate impurity; growth temperature 25 °C and pH 8.5. (b) Plot of $R_0/(R_0 - R)$ on $1/c_i$ according to Equation (6.6). Original data from Manali and Dalas (2002)

is similar and is comparable to that obtained for sodium alginate impurity, but the value of the additive effectiveness parameter α changes in the sequence $\alpha(\text{TCBL}) < \alpha(\text{CTRC}) < \alpha(\text{THFTCA}) < \alpha(\text{CPTCA})$.

CTRC and TCBL are linear whereas TPTCA and THFTCA are cyclic polycarboxylic acids, but at pH 8.55 they have similar degrees of ionization. For all polycarboxylates, the distances between ionized carboxyl groups are similar, and each carboxyl group is separated from an adjacent carboxyl group by two carbon atoms. Because of the fixed distance between carboxylate groups and their orientation in CPTCA and THFTCA, the intramolecular hydrogen bonding between neighboring carboxylic groups stabilizes the ring into a rigid structure for partially ionized acids, whereas the linear polycarboxylic

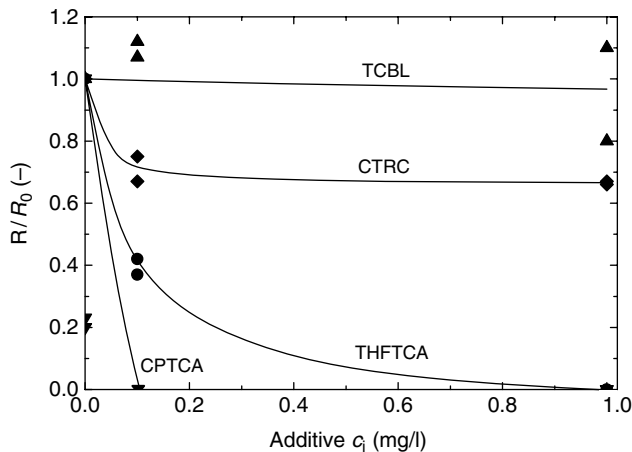


Figure 6.15 Dependence of overall growth rate R of calcite at 25°C , $\text{pH } 8.55$ and $S = 4.5$, on calcite seed crystals on the concentration c_i of four polycarboxylic acids. Data from Reddy and Hoch (2001)

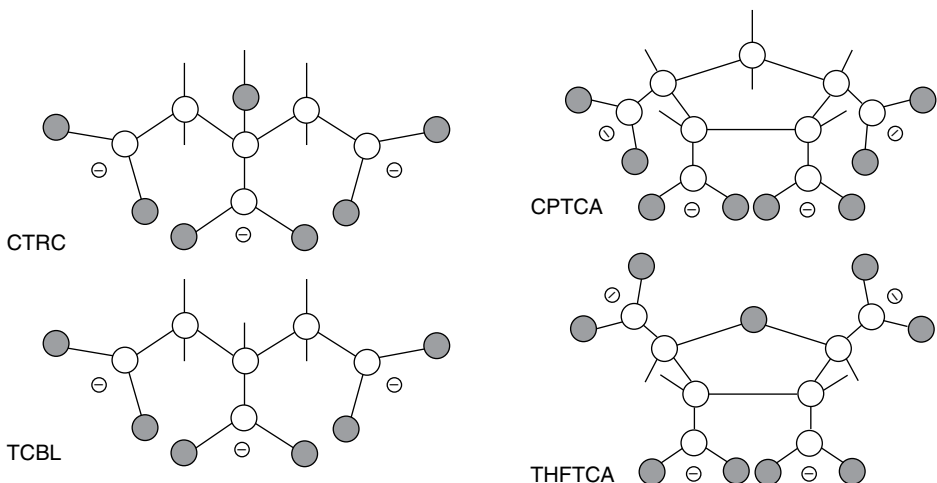


Figure 6.16 Schematic illustration of polycarboxylic acid anions used in Figure 6.15. Reproduced from M.M. Reddy and A.R. Hoch. J. Colloid Interface Sci. **235**, 365. Copyright (2001) with permission from Elsevier

acids (i.e. CTRC and TCBL) have flexible structures. The effectiveness of the above acids as inhibitors of the precipitation of calcite is associated with the match of the distance between carboxylic groups and calcium ions in the calcite lattice. Rigid molecular structures are more specific in inhibition properties than flexible molecules. CPTCA and THFTCA have different inhibiting effectivenesses because their carboxylate groups differ in sterochemical orientation. All carboxyl groups in CPTCA are on the same side of the

Table 6.7 Constants α , K and Q_{diff} for polyelectrolytes

Additive	α	$K (10^4 \text{ l/g})^a$	$Q_{\text{diff}} (\text{kJ/mol})$
TCBL	0.1	0.048	39.6
CTRC	0.34	5.7	51.6
THFTCA	1.08	12.8	53.7
CPTCA	3.57	3.89	50.7

^a $1 \text{ l/g} \approx 1.4 \times 10^8 \text{ (mole fraction)}^{-1}$.

plane of the ring whereas two carboxylates are above and two are below the plane of the ring in THFTCA. Consequently, because CPTCA has more available binding sites with the calcite surface than THFTCA, it is a more effective inhibitor than the latter additive.

Figure 6.17a illustrates the dependence of the overall growth rate R of hydroxyapatite, obtained by Koutsopoulos and Dalas (2000) at 37 °C and pH 7.4, on hydroxyapatite seed crystals on the concentration c_i of two acidic amino acids: L-aspartic acid (L-Asp) and L-glutamic acid (L-Glu). The data in Figure 6.17a are shown in Figure 6.17b as a plot of $R_0/(R_0 - R)$ versus $1/c_i$ according to Equation (6.6) in combination with the Langmuir adsorption isotherm. Assuming that a linear relationship holds between $R_0/(R_0 - R)$ and $1/c_i$, one obtains $\alpha = 1.45$ for both additives, while $K = 3.9 \times 10^3$ and 3.4×10^3 and $Q_{\text{diff}} = 20.8$ and 20.4 kJ/mol for L-Asp and L-Glu, respectively. These values of adsorption parameters differ from those obtained from Figure 6.12, possibly because

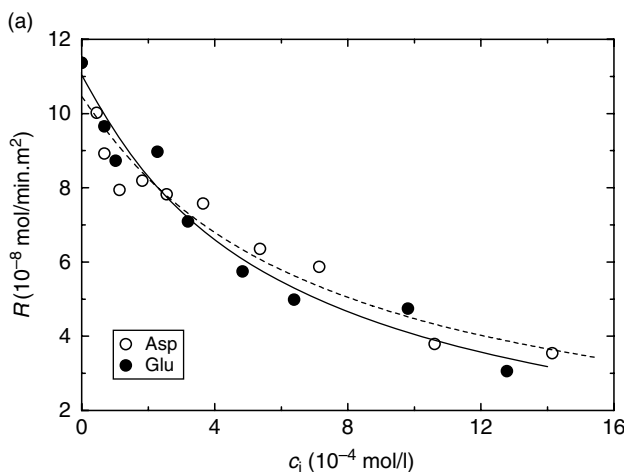


Figure 6.17 (a) Dependence of growth rate R of hydroxyapatite on hydroxyapatite seed crystals on the concentration c_i of acidic amino acid impurities (aspartic and glutamic acids); growth temperature 37 °C and pH = 7.4. Original data from Koutsopoulos and Dalas (2000). Data in (a) shown as (b) a plot of $R_0/(R_0 - R)$ versus $1/c_i$ according to Equation (6.6) in combination with Langmuir adsorption isotherm, and (c) plots of R and R^2 on $\ln c_i$ according to dependences based on Temkin isotherm. In (c) solid and dashed curves represent the best-fit plots according to Kubota-Mullin and Cabrera-Vermilyea models, respectively

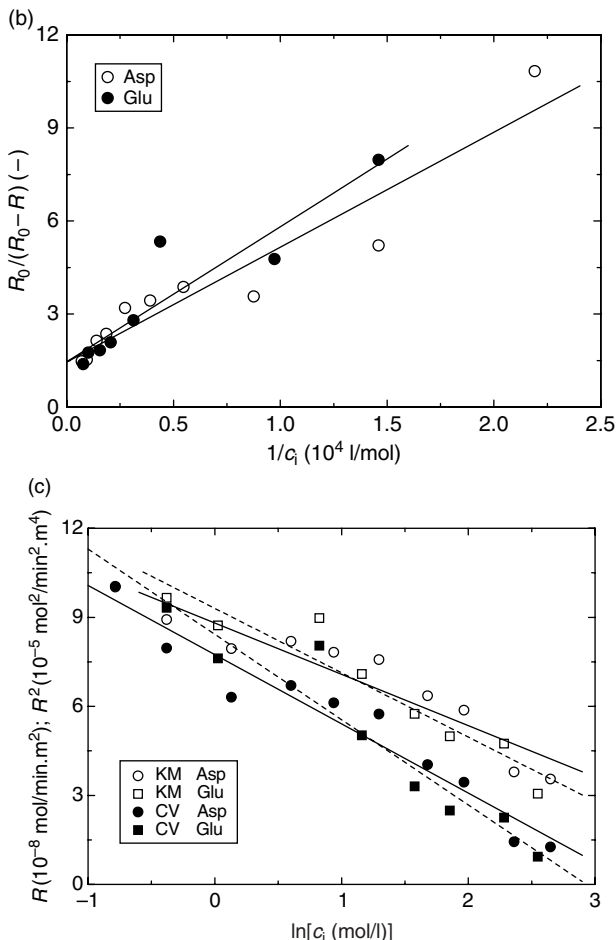


Figure 6.17 (Continued)

of differences in the chemicals and the nonapplicability of the Langmuir adsorption isotherm here. However, one notes that the plot in Figure 6.17b has two slopes with a transition at $1/c_i \approx 0.3 \times 10^4$ l/mol (i.e. $c_i \approx 3 \times 10^{-4}$ mol/l). Figure 6.17c shows the plots of R and R^2 versus $\ln c_i$ according to dependences based on the Temkin isotherm (see Section 4.3). We recall here that the former and latter dependences follow from the Kubota–Mullin and Cabrera–Vermilyea models, respectively. Both models describe the data satisfactorily over the entire impurity concentration range, with a somewhat superior correlation constant in favor of the Kubota–Mullin model.

Growth is essentially a result of integration of growth units into growth sites (i.e. kinks) present on the surface of a crystal. Therefore, for an understanding of the processes involved during growth it is always desirable to investigate the effects of additives on the kinetics of displacement of steps on growing surfaces of crystals. It is indeed a complex area of fundamental scientific interest, where the main problem is the resolution

of growth step during *in situ* observation (Gratz and Hillner, 1993). Since the beginning of the 1990s, several studies have been carried out on the investigation of the effect of additives on the growth of sparingly soluble salts found in biomineralization (Gratz and Hillner, 1993; McCoy and LaFemina, 1997; Teng and Dove, 1997; Walters *et al.*, 1997; Reyhani *et al.*, 2002; Wang *et al.*, 2006a,b). Among these studies, investigations of the morphology of growth hillocks and the kinetics of motion of obtuse (or positive) growth steps on the (1014) cleavage face of calcite crystals have been relatively popular. Some general observations made during these studies are the following:

- (1) The molecules of an additive or related complexes adsorb directly at steps, halting their motion (Gratz and Hillner, 1993). An additive disrupts the relatively straight steps produced in the pure system to form jagged steps (Gratz and Hillner, 1993; Reyhani *et al.*, 2002; Wang *et al.*, 2006a,b). At high additive concentration the steps appear diffuse, topographically high due to the imaging of adsorbed additive molecules (Gratz and Hillner, 1993).
- (2) There exists a threshold concentration of the additive when poisoning of steps takes place (Gratz and Hillner, 1993). This effect is observed for inhibitors such as 1-hydroxyethylidene-1,1-diphosphonic acid (HEDP), sodium triphosphate (NaTP), and sodium hexametaphosphate (SHMP), but no threshold concentration is found for ionic additives, such as NaH_2PO_4 , NaCl and Mg^{2+} ions, although they also reduce the step velocity.
- (3) For HEDP, SHMP and NaTP, adsorption on the steps is rapid initially ($\sim 0.5\text{--}2.5\%$ monolayer coverage), followed by a lower uptake by the enlargement of the poisoned zones.

The above observations may be understood in terms of (a) time-dependent adsorption of an impurity [see Equation (6.9)] and (2) disruption of stability of steps caused by additive, followed by reorganization of the nonequilibrium steps. To illustrate the validity of this explanation, the extensive experimental data on step displacement velocity v in the presence of four inhibitors, HEDP, NTMP, EDTP and DTPP, reported by Reyhani *et al.* (2002), are analyzed and discussed below. The structure of the inhibitors is illustrated in Figure 6.18. They contain different numbers of phosphonic (H_2PO_3) groups bound to N atoms at different positions.

Figure 6.19a and b present the dependence of velocity v of obtuse steps of spirals on the (1014) cleavage face of calcite crystals on time t for different concentrations c_i of HEDP impurity, and for $c_i = 3 \mu\text{M}$ (i.e. 0.6 ppm) of the four investigated additives, respectively. Growth was carried out at room temperature, pH 10.6 and relative supersaturation $S = 7.62$. The plots are drawn according to Equation (6.9) with $v_0 = 4.76 \text{ nm/s}$ and the best-fit constants given in Figure 6.20a and b. Figure 6.20a shows the plots of $\alpha\theta_{\text{eq}}$ and Θ^{-1} as a function of concentration c_i of HEDP impurity, and Figure 6.20b illustrates the interdependence between Θ^{-1} and $\alpha\theta_{\text{eq}}$ for $c_i = 3 \mu\text{M}$ of the four additives. The following features may be noted from Figures 6.19 and 6.20:

- (1) The theoretical Equation (6.9) relating step velocity v with time t satisfactorily describes the experimental $v(t)$ data.
- (2) The constants $\alpha\theta_{\text{eq}}$ and Θ are mutually related (see Figure 6.20a and b). However, for the same impurity, at low concentration c_i the values of both $\alpha\theta_{\text{eq}}$ and Θ are

negative such that for $c_i > c_i^*$ (where c_i^* is the threshold concentration equal to about $3.5 \mu\text{M}$), Θ^{-1} and $\alpha\theta_{\text{eq}}$ increase with an increase in c_i .

- (3) For the same concentration c_i of different impurities, Θ increases with increase in $\alpha\theta_{\text{eq}}$.

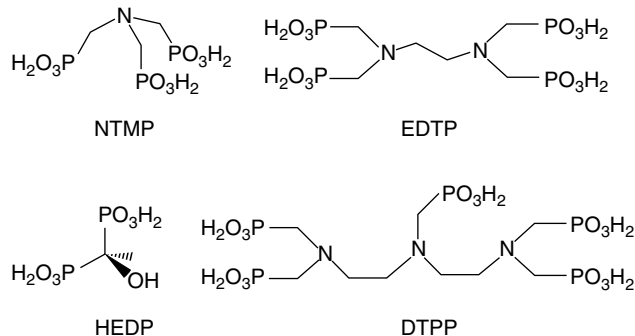


Figure 6.18 Molecular structure of inhibitors used in calcite growth kinetics. Reproduced from M.M. Reyhani, A. Olivier, G.M. Parkinson, F. Jones, A.L. Rohl, and M.I. Ogden. Int. J. Mod. Phys. **16**, 25. Copyright (2002), World Scientific Publishing

Feature (1) is a consequence of time dependent adsorption of the impurity, as implied by Equation (6.9). However, feature (2) that $\alpha\theta_{\text{eq}}$ and Θ are negative is not expected. This is due to the fact that the time constant Θ of Equation (6.9) also takes into account the process of adsorption of the impurity at kinks in steps which are in equilibrium. In other words, before its adsorption on the surface, an equilibrium sets up between an impurity molecule and crystal ions composing a kink. However, adsorption of an impurity molecule on the crystal is essentially a chemical reaction, which can be time dependent with another time constant, say Θ_{in} . Therefore, denoting the time constant Θ corresponding to equilibrium impurity adsorption by Θ_0 , one has the overall time constant Θ composed of two parts, i.e.

$$\Theta = \Theta_{\text{in}} + \Theta_0 \quad (6.12)$$

The initial period Θ_{in} may also include reorganization of the straight step before the onset of adsorption described by Equation (6.9). As judged from Figure 6.20b, the maximum value of Θ_{in} is about 600 s (i.e. about 10 min) for the polyelectrolyte impurities investigated here. This period is indeed fairly long.

From Figure 6.20a it may be noted that for $c_i < 3.5 \mu\text{M}$ a higher deviation from the equilibrium state, as represented by higher negative values of $\alpha\theta_{\text{eq}}$, is accompanied by a higher $1/\Theta_{\text{in}}$. This means that for $c_i < 3.5 \mu\text{M}$ the value of Θ_{in} decreases with increase in c_i , but for $c_i > 3.5 \mu\text{M}$ the value of Θ_0 decreases with increase in c_i . This suggests that the overall time constant Θ of Equation (6.12) is probably a constant quantity for a given impurity and does not depend on impurity concentration c_i . For HEDP the value of Θ is about 850 s.

It should be mentioned that for $c_i > 3.5 \mu\text{M}$ (i.e. $> 0.7 \text{ ppm}$) the dependence of $\alpha\theta$ on c_i appears to follow the Langmuir adsorption isotherm. This is shown in Figure 6.20a

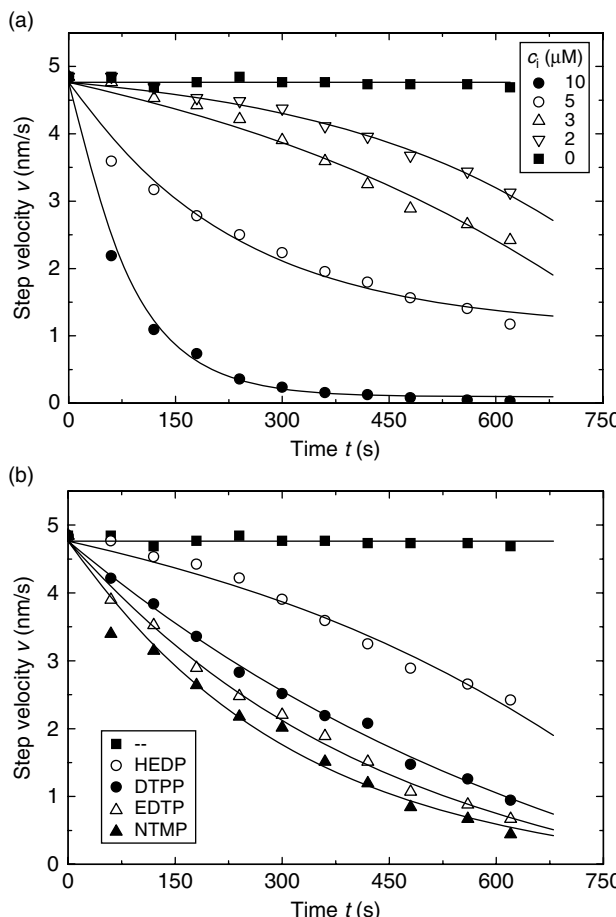


Figure 6.19 Velocity v of obtuse steps of spirals on the $(10\bar{1}4)$ cleavage face of calcite crystals as a function of time t under different conditions: (a) in the presence of different concentrations c_i of HEDP impurity, and (b) in the presence of 3 μM concentration of four different phosphonate-based impurities; growth temperature 273 K and solution pH = 10.6. Plots are drawn according to Equation (6.9). Original data from Reyhani et al. (2002)

by the dashed curve with the value of corrected impurity concentration equal to $(c_i - 3.5 \mu\text{M})$, $\alpha = 1$ and the Langmuir constant $K = 2.5 \mu\text{M}^{-1}$ ($= 1.25 \times 10^7 \text{ ppm}^{-1}$). This K corresponds to the differential heat of adsorption $Q_{\text{diff}} = 41.2 \text{ kJ/mol}$, which is in good agreement with the value obtained from the data of calcite growth reported by Manali and Dalas (2002); see Figure 6.14.

Feature (3) is connected with the adsorption processes and appears to be associated with the number of H_2PO_3 groups present in the impurity (see Figure 6.20). The values of the effectiveness parameter α and Langmuir constants K for some impurities involved in the bimineralization of calcite and aragonite are listed in Table 6.8. These values are

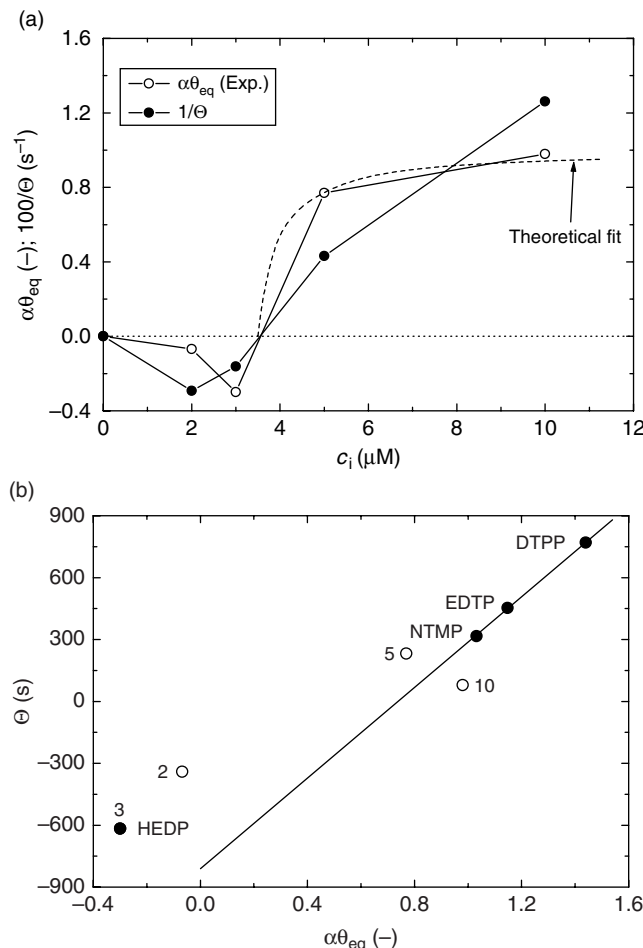


Figure 6.20 (a) Plots of $\alpha\theta_{eq}$ and Θ^{-1} on c_i and (b) plots of time constant Θ against $\alpha\theta_{eq}$ for $c_i = 3 \mu\text{M}$ of different additives (filled circles). Data are from Figure 6.19. In (b) data for other concentrations of HEDP are shown by open circles, and the accompanying numbers are the additive concentrations in μM

either taken directly from the published literature or are based on the analysis of the original data.

It should be mentioned that the property of inhibiting crystallization kinetics in free volume is not confined to relatively large molecules, and simple ions also inhibit growth kinetics. For example, the inhibiting effect of magnesium on the growth of the stable polymorph of calcium carbonate as calcite is well known (Kitamura, 2001; Loste *et al.*, 2003; Dove *et al.*, 2004). It is observed (for example, see Dove *et al.*, 2004) that addition of magnesium to the growth system of a predefined supersaturation σ leads to a pronounced decrease in the step velocity v , as in the case of the effect of other surfactants described earlier. Figure 6.21 shows the dependence of the step velocity v

Table 6.8 Values of constants α and K for calcite and aragonite in the presence of some impurities

Polymorph	Additive ^a	α	K	Source ^b
Calcite	THFTCA	1.08	12.8 l/mg	a
	CPTCA	3.57	3.89 l/mg	a
	TBCl	0.1	0.48 l/mg	a
	CTRC	0.34	57 l/mg	a
	CTRC	0.82	13.55 l/mmol	b
	DTPA	0.99	7.57 l/mmol	b
	EDTA	0.99	7.79 l/mmol	b
	PMA	0.74	148.2 l/mmol	b
	Na alginate	0.96	1055 l/mmol	c
	HEDP	1	2.5 l/ μ mol	b
Aragonite	CTRC	1.01	539.1 l/mmol	b
	DTPA	0.93	1287.2 l/mmol	b
	EDTA	0.87	97.9 l/mmol	b
	PMA	0.94	793.5 l/mmol	b

^a Abbreviations: THFTCA, tetrahydrofuran-tetracarboxylic acid; CPTCA, cyclopentane-tetracarboxylic acid; TBCl, tricarballylic acid; CTRC, citric acid; DTPA, diethylenetriaminepentaacetic acid; EDTA, ethylenediaminetetraacetic acid; PMA, pyromellitic acid.

^b a, Reddy and Hoch (2001); b, Westin and Rasmuson (2005); c, Manoli and Dalas (2002).

on the activity of additive Mg^{2+} ions in the growth solution of calcium carbonate at a constant supersaturation $\sigma = 1.2$. Here the positive and negative steps refer to the obtuse and acute steps described earlier in Figure 6.19. The data in Figure 6.21 can be described by Equation (6.9) with a linear adsorption isotherm [$\theta = Kc_i$ in Equation (6.6)] involving instantaneous additive adsorption [$\exp(-t/\tau) = 0$]. Similarly, at a given concentration of Mg^{2+} , the step velocity v increases with increase in supersaturation σ above a particular threshold supersaturation σ_d , and the value of σ_d increases with increasing additive concentration c_i (Dove *et al.*, 2004). The dependence of threshold supersaturation, defined as threshold Ca(II) activity a_d , on the activity a_i of Mg(II) additive ions is shown in Figure 6.22. The $a_d(a_i)$ plots follow the linear relationship in Equation (5.28).

Gutjahr *et al.* (1996) investigated the effect of the bivalent cations Fe^{2+} , Cu^{2+} , Zn^{2+} , Mg^{2+} , Sr^{2+} and Ba^{2+} on the growth and dissolution rates of calcite and aragonite. They found that (1) cations retard growth and dissolution rates by adsorbing at kinks in accordance with a model which they call the Langmuir–Volmer model and (2) for calcite growth, transition metal ions (e.g. Fe^{2+} , Cu^{2+} and Zn^{2+}) are more effective inhibitors than alkaline earth metal ions (e.g. Sr^{2+} and Ba^{2+}), whereas for aragonite growth alkaline earth metal ions (e.g. Sr^{2+} and Ba^{2+}) are more effective inhibitors than transition metal ions (e.g. Fe^{2+} , Cu^{2+} and Zn^{2+}).

The Langmuir–Volmer model of Gutjahr *et al.* (1996) is basically the same as the Kubota–Mullin model. Regarding the inhibiting effects of cations, they discovered that cations whose carbonates crystallize in the calcite structure are more effective inhibitors during calcite growth, whereas those whose carbonates crystallize in the aragonite structure are more effective during aragonite growth. This feature is illustrated in Figure 6.23, which shows the additive concentrations for halving the growth rates as a function of the

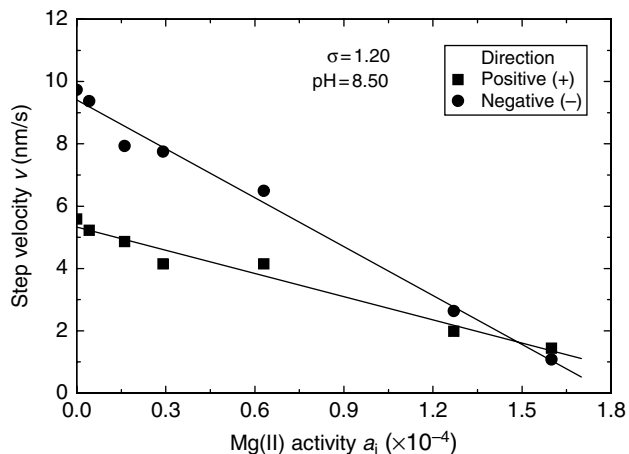


Figure 6.21 Dependence of step velocity v on the activity of additive Mg^{2+} ions in the growth solution of calcium carbonate at a constant supersaturation $\sigma = 1.2$ and $pH = 8.5$. Adapted from Dove et al. (2004)

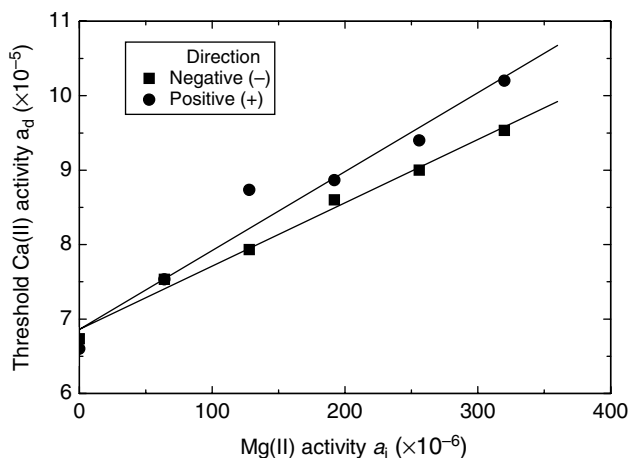


Figure 6.22 Dependence of threshold $Ca^{(II)}$ activity a_d on the activity a_i of $Mg^{(II)}$ additive ions in growth solution. Data from the plots published by Dove et al. (2004)

solubility products of the corresponding carbonates. The inhibitory effect of an additive may be explained in terms of difference in binding energy of the bivalent cation to the CO_3^{2-} neighborhood of the kink sites of the corresponding crystals, thereby leading to different residence times of the additive ion at the kinks, as envisaged in the model of adsorption at kinks (see Sections 4.1 and 4.3).

Wada and Umegaki (1993) and Wada *et al.* (1995) investigated the formation of calcite in the presence of several bivalent cations, e.g. Sr^{2+} , Pb^{2+} and Ba^{2+} , which form carbonates crystallizing in the aragonite structure, and Fe^{2+} , Mg^{2+} , Ni^{2+} , Co^{2+} , Zn^{2+} ,

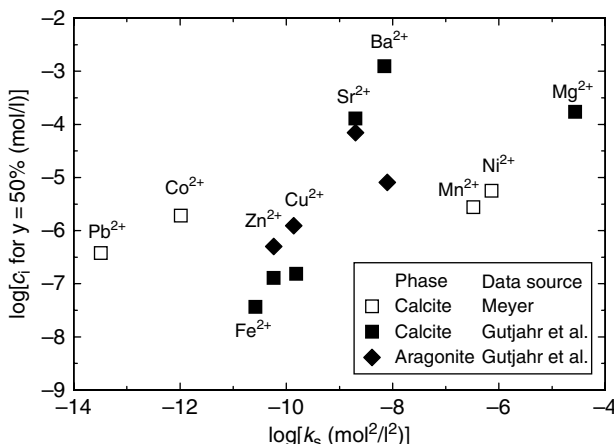


Figure 6.23 Additive concentration for halving the growth rates as a function of the solubility products pK_s of the corresponding carbonates. Open and filled squares denote calcite and filled diamonds denote aragonite. Reproduced from A. Gutjahr, H. Dabringhaus, and R. Lacmann (1996). J. Cryst. Growth **158**, 310. Copyright (1996), with permission from Elsevier

Cu^{2+} and Cd^{2+} , which form calcite-type carbonate. It was found that (1) Sr^{2+} and Pb^{2+} promote aragonite formation, whereas Ba^{2+} promotes the formation of vaterite (Wada and Umegaki, 1993) and (2) except for Cd^{2+} ions, all bivalent ions forming calcite-type carbonate promote the formation of aragonite (Wada *et al.*, 1995). Wada *et al.* (1995) explained the results of formation of aragonite from a consideration of the following two processes:

- (i) The impurities reduce the growth rate of the metastable phase (aragonite here) precipitated at the initial stage of crystallization according to the Ostwald rule of stages, thus producing a high degree of supersaturation in the precipitating system. This applies to impurities forming carbonates crystallizing in the calcite-type structure.
- (ii) The solid solution of calcite, containing a cation carbonate crystallizing in the aragonite phase, formed through the transformation of aragonite becomes thermodynamically less stable than aragonite. This applies to Sr^{2+} and Pb^{2+} .

In a later study, Wada *et al.* (1998) studied the effect of Ag^+ , Al^{3+} and Cr^{3+} on calcium carbonate polymorphs using a double-diffusion (gel) technique. It was observed that (a) all these ions promote aragonite formation, (b) in the presence of Ag^+ the growth of aragonite becomes favorable due to its heterogeneous nucleation on AgCO_3 and (c) in the presence of Al^{3+} and Cr^{3+} ions the growth of aragonite nuclei formed according to the Ostwald rule of stages is inhibited by the additive, and this process ensures a high degree of supersaturation in the precipitating system whereby aragonite crystals grow as a pseudostable phase. The results of this study are described in Section 6.3.3.

Direct evidence of the existence of an initial period Θ_{in} required for the onset of adsorption [see Equation (6.9)] comes from a study, carried out by Saito *et al.* (2003), of the effect of different additives, such as silicate, fluoride, calcium, phosphate, magnesium

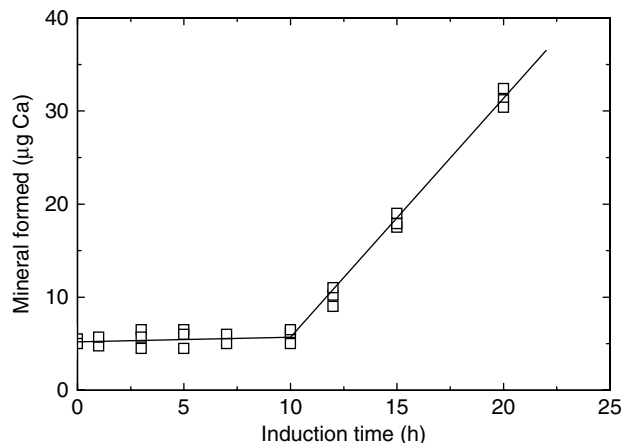


Figure 6.24 Dependence of the amount of calcium bound to insoluble dentin collagen in metastable mineralizing solution on time. Mineral induction time is the time when the amount of calcium bound to the collagen increased suddenly. Reproduced from T. Saito, H. Toyooka, S. Ito, and M.A. Crenshaw (2003). Caries Res. **37**, 445. Copyright (2003), with permission from S. Karger AG, Basel

and silver, on the mineralization of dentin matrix *in vitro*. For the investigation, demineralized dentin matrix was incubated in a metastable calcium phosphate solution with or without the additive. Insoluble dentin matrix induced mineral formation after incubation for 10.2 h in the metastable solution with additive. The mineral induction time by insoluble dentin collagen in the metastable mineralizing solution was determined from the dependence of the amount of calcium bound to insoluble dentin collagen on time, as shown in Figure 6.24. The induction time was taken as the time when the amount of calcium bound to the collagen increased suddenly. Silicate, fluoride, calcium and phosphate significantly decreased whereas magnesium and silver increased the induction time in a dose-dependent manner. This means that the former impurities promoted whereas the latter inhibited the mineralization of dentin matrix. Silicate at 5 μM, fluoride at 40 μM, phosphate at 100 μM and calcium at about 200 μM promoted mineral induction, whereas silver and magnesium at concentrations as low as 2 and 10 μM, respectively, inhibited mineral induction.

6.3.3 Phases and Polymorphs of Crystallizing Calcium Salts

The number of mineral phases involved in biological and other natural systems and in the laboratory is mainly confined to calcium carbonates, oxalates and phosphates. These salts precipitate in a number of different phases and polymorphs, and in many cases mixtures of two or more phases or polymorphs are formed. Here the nature of different precipitated phases and polymorphs of the above calcium salts is briefly described.

The calcium carbonate phases, in order of increasing stability, are (Elfil and Rogues, 2001) calcium carbonate hexahydrate ($\text{CaCO}_3 \cdot 6\text{H}_2\text{O}$; CCH), calcium carbonate monohydrate ($\text{CaCO}_3 \cdot \text{H}_2\text{O}$; CCM), amorphous calcium carbonate (ACC), vaterite,

aragonite and calcite. Most experimental work on calcium carbonate deals with anhydrous crystalline polymorphs (vaterite, aragonite and calcite), because they are stable in a wide temperature range between 0 and 90°C. In contrast, hydrate forms and anhydrous calcium carbonate have been poorly investigated, mainly because of their low stability and narrow temperature range of stability; CCH is stable between 0 and 25°C, CCM between 10 and 50°C, and ACC between 10 and 55°C. It has been suggested (Elfil and Rogues, 2001) that the relatively unstable phases such as CCH, CCM and ACC are stabilized by the presence of Mg^{2+} ions and by inhibitors such as aminopolyphosphate acid. These unstable phases act as precursors for calcium carbonate precipitation at low temperature (Clarkson *et al.*, 1992; Gal *et al.*, 2000; Elfil and Rogues, 2001; Loste *et al.*, 2003).

The transformation process of a metastable phase to a stable phase may be followed *in situ* under an optical microscope in a crystallization cell in which reactants are poured slowly and separately from opposite sides of the cell, and mixed (Kitamura, 2001; Kawano *et al.*, 2002). As an example, Figure 6.25 shows the formation process of calcium carbonate by mixing 0.04 mol/l $CaCl_2$ and 0.06 mol/l Na_2CO_3 aqueous solutions at 20°C. Immediately after the mixing, numerous small particles of amorphous calcium carbonate are precipitated (Figure 6.25a), but later crystals of rhombohedral shape, characteristic of calcite, and spherulites of vaterite phase appear separately and simultaneously (Figure 6.25b and c). The crystals of these latter two crystalline phases grow by forming a precipitation-free zone around them, where the small precipitates of the first phase disappear entirely (Figure 6.25b and c). The formation of a precipitation-free zone around vaterite spherulites and rhombohedral calcite crystals is evidence of solution-mediated phase transformation.

Calcium carbonate precipitates naturally *in vivo* in organisms such as coral reef and shellfish and as scaling occurring in pipes for drainage and circulation of water. It is also used in different industries as an additive in medicines, foods, papers, plastics, printing ink, etc. In nature, control of polymorphous structure is precise. For example, aragonite structure develops in pearls, whereas vaterite structures are formed in avian eggshells. The difference in the structures is determined by the environment (i.e. composition and properties of the medium) in which biomineralization takes place. However, since the physico-chemical properties of different calcium carbonate phases are different, the application of calcium carbonate precipitate is related to the properties of the precipitate phase. For example, properties such as printing characteristics, luster and color are also greatly influenced by polymorphs when calcium carbonate is used as an additive to paper. Therefore, polymorphic control of calcium carbonate precipitates is very important in industrial processes.

Most research on the precipitation behavior of calcium carbonate polymorphs has been carried out by the method of mixing of solutions containing calcium and carbonate ions. In systems involving calcium chloride and sodium carbonate solutions, it is observed that calcite and/or aragonite are usually formed but precipitation of vaterite has also been reported (for the literature, see Kitamura, 2001). It is also known (see, for example, Gutjahr *et al.*, 1996; Katsifaras and Spanos, 1999; Reddy and Hoch, 2001; Abdel-Aal and Sawada, 2003; Hu and Deng, 2003; Wei *et al.*, 2003) that various metal ions and other additives have a strong influence on the precipitation behavior of calcium carbonate polymorphs. Moreover, the precipitation behavior of these polymorphs also depends on

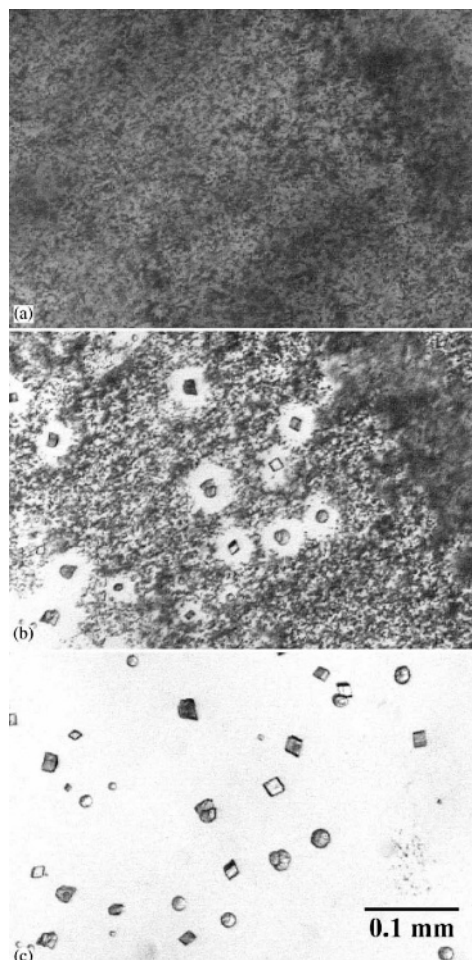


Figure 6.25 Formation of calcium carbonate by mixing 0.04 mol/l CaCl_2 and 0.06 mol/l Na_2CO_3 aqueous solutions at 20°C. Photographs were taken after (a) 2, (b) 23, and 50 min. Reproduced from J. Kawano, N. Shimobayashi, M. Kitamura, K. Shinoda, and N. Aikawa (2002). *J. Cryst. Growth* **237/239**, 419. Copyright (2002), with permission from Elsevier

the crystallization conditions such as solution pH, rate of addition of reactants (i.e. feeding rate), and the concentration of initial reactant solutions (Gomez-Morales *et al.*, 1996; Kitamura, 2001; Kitamura *et al.*, 2002).

In the order of increasing stability (and decreasing solubility), calcium oxalate shows the following phases (Ouyang *et al.*, 2005): calcium oxalate trihydrate [$\text{CaC}_2\text{O}_4 \cdot 3\text{H}_2\text{O}$; COT] calcium oxalate dihydrate [$\text{CaC}_2\text{O}_4 \cdot (2+x)\text{H}_2\text{O}$ with $x < 0.5$; COD] and calcium oxalate monohydrate ($\text{CaC}_2\text{O}_4 \cdot \text{H}_2\text{O}$; COM). From supersaturated solutions of calcium oxalate, obtained by mixing reactants, without additives COM and COT are usually formed, but under different experimental conditions COD is also formed. The form that

prevails depends on the experimental conditions (Skrtić *et al.*, 1987; Brecević *et al.*, 1989; Jung *et al.*, 2004, 2005). Additives also lead to a change in the type of crystallizing form. Among the effective additives are negatively charged organic molecules such as anionic surfactants, acid-rich synthetic polymers, polycarboxylates and several electrolytes with high charge density (Füredi-Milhofer and Sarig, 1996; Jung *et al.*, 2005). A study of the effect of a series of high and low molecular weight synthetic polymers (polyacrylic acid, polymethacrylic acid, an alternating copolymer of styrene sulfonate with maleic anhydride and polyvinylsulfonate) on the crystallizing calcium oxalate polymorphs revealed (Manne *et al.*, 1990) that the concentration of an additive also determines the type and the fraction of the crystallizing phase. COM, COT and COD were found to be the dominant phases at low, intermediate and high concentrations of every additive, respectively. However, in polymeric additives COT is not produced (Jung *et al.*, 2005).

COM and COD are found in kidney stones. Therefore, there have been many reports on the crystallization of calcium oxalate in aqueous solutions, diluted urines and artificial urines (see, for example, Baumann *et al.*, 2003; Grover *et al.*, 2003; Webber *et al.*, 2003; Jung *et al.*, 2004, 2005; Ryall *et al.*, 2005; Ouyang *et al.*, 2005; Walton *et al.*, 2005; Guerra *et al.*, 2006).

In order of increasing stability and decreasing solubility, calcium phosphate phases are (Nancollas, 1982) dicalcium phosphate dihydrate ($\text{CaHPO}_4 \cdot 2\text{H}_2\text{O}$; DCPD), dicalcium phosphate anhydrous (CaHPO_4 ; DCPA), octacalcium phosphate [$\text{Ca}_8\text{H}_2(\text{PO}_4)_6 \cdot 5\text{H}_2\text{O}$; OCP], tricalcium phosphate [$\text{Ca}_3(\text{PO}_4)_2$; TCP], and hydroxyapatite [$\text{Ca}_5(\text{PO}_4)_3\text{OH}$; HAP]. As in the case of calcium carbonate, amorphous calcium phosphate (ACP) phase has also been suggested (Onuma, 2006). As in calcium carbonate and calcium oxalate phases, here also a metastable phase is formed first. Several pieces of evidence indicate that it is usually OCP that crystallizes first, followed by its transformation into HAP. However, phase transition from the amorphous calcium phosphate (ACP) to HAP, involving the participation of $[\text{Ca}_3(\text{PO}_4)_2]_3$ clusters based on $\text{Ca}_3(\text{PO}_4)_2$ of ACP, has also been reported (Onuma, 2006). This aspect of the formation of clusters is also considered further in Section 7.4.

HAP is the most stable calcium phosphate salt under physiological conditions. It is a model compound for the study of hard tissue calcification such as bone and teeth and in many undesirable cases of pathological mineralization.

In the above cases, crystallization was carried from aqueous solutions. However, common aqueous solutions differ from natural biological systems. For example, urinary stones are formed within membrane-bound microspace, and the nucleation and growth of urinary stones are regulated by organic matrix. Mineralization of calcium carbonate as aragonite and vaterite in shellfish and avian eggshells, and calcium phosphate as HAP occurs in a similar way. Therefore, recent studies have been directed to mimic the precipitation of calcium salts which occur as biominerals in natural systems. Because of the presence of channels and microchannels, crystallization of calcium salts in gels is considered to mimic the *in vivo* behavior more closely than in common aqueous solutions (Wada *et al.*, 1999; Eiden-Assman *et al.*, 2002; Ouyang *et al.*, 2004, 2005; Ouyang, 2006).

As shown by the work of Ouyang's group (Ouyang *et al.*, 2004, 2005; Ouyang, 2006), crystallization of different phases of calcium oxalate in gel systems also depends on additives and their concentration in addition to growth temperature. Ouyang *et al.* (2004)

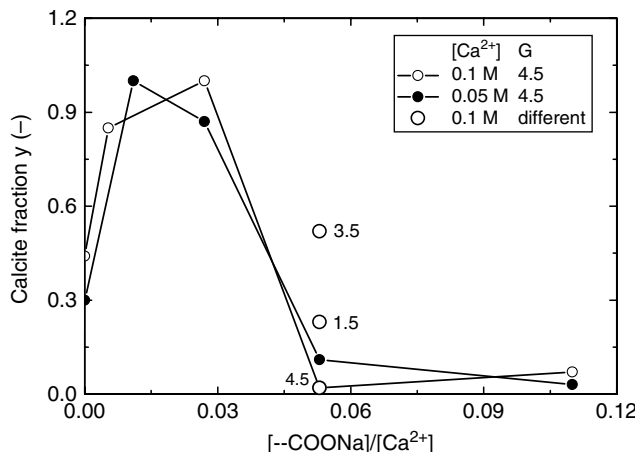


Figure 6.26 Dependence of fraction y of calcite in vaterite–calcite mixture precipitated by the carbonate diffusion method on the ratio $[-\text{COONa}]/[\text{Ca}^{2+}]$ in the presence of poly(adoamino) PAMAM dendrimers of different generations; growth temperature 30°C and $\text{pH } 8.5$. Original data from Naka and Chujo (2003)

studied the effect of different sodium carboxylates on the crystallization of different calcium oxalate hydrates (see Figure 6.26). It was found that:

- (1) As in a control experiment without additive, irrespective of its concentration in the gel, only COM is formed in the presence of sodium acetate additive, but in the presence of disodium tartrate, disodium ethylenediaminetetraacetate and trisodium citrate, COD and COT are also induced.
- (2) Fractions of different crystallized phases depend on the concentration of the multi-functional carboxylates.
- (3) COM, COD and COT are the dominant phases at low, intermediate and high concentrations of every additive, respectively. These results are similar to those reported by Manne *et al.* (1990), but the order of the dominant phases at intermediate and high additive concentrations is reversed.

It should be mentioned that all metastable phases in solution undergo transformation to the least soluble, more stable phase, where the role of the solution is to facilitate the transformation. The transformation of the metastable phase to the stable phase occurs through bulk nucleation and growth of the stable phase or through its surface nucleation and growth on the metastable phase, with dimensionality $d = 3$ and 2, respectively; see below and Section 2.4.2. The metastable phases with very short lifetimes are usually referred to as precursor phases. In the case of calcium carbonate precipitation, for example, hydrates and amorphous phases of calcium carbonate are precursors for the growth of more stable phases such as vaterite, aragonite or calcite, but the observed phase is amorphous calcium carbonate in the form of colloids or aggregates (see, for example, Kitamura, 2001; Kawano *et al.*, 2002). The lifetime of a precursor depends on the operational conditions, such as the addition rate of one of the reactants to the other, in an experiment. The slower the addition rate, the longer is the lifetime of the precursor.

6.3.4 Transformation of Metastable Phases

All metastable phases grown under given crystallization conditions undergo transformation into a thermodynamically more stable phase in accordance with the Oswald rule of stages (see Section 2.4.2). For example, if the thermodynamic stability of a substance increases in the sequence A to B to C, such that phase C is the most stable phase, one observes the transformation of phase A to B first, followed by the subsequent transformation of phase B to C. Transformation of a metastable phase into the next stable one may be described by Equation (2.53) of the overall crystallization, i.e.

$$y_s = y_m \{1 - \exp[-(\Theta_m/\Theta_s)^s(t/\Theta_m - b')^s]\} \quad (6.13)$$

where Θ_m and Θ_s are the time constants for the transformation of the metastable and the stable phases, respectively, the constant $b' = (m - 1/m)^{1/m}$, the exponent $s = \nu d$ (ν is 1/2 or 1 for nucleation controlled by volume and surface diffusion, respectively, and d is the dimensionality for growth), and y_m is given by

$$y_m = 1 - \exp[-(t/\Theta_s)^m] \quad (6.14)$$

where $m = \nu d$ and $1 + \nu d$ for instantaneous and progressive nucleation, respectively. As discussed in Section 2.4.2, a relation equivalent to Equation (6.13) is

$$y_s = 1 - \exp[-(t/\Theta'_s)^{q'}] \quad (6.15)$$

where q' is a fitting parameter exceeding 4, $\Theta'_s \approx \Theta_s(4/q')$, and $y_m = 1$. When $t/\Theta'_s \ll 1$, Equation (6.15) reduces to the linear form

$$y_s = (t/\Theta'_s)^q \approx y_{s0} + y't \quad (6.16)$$

where $y_{s0} = (\Theta'_s)^{-q'} - q'$, and $y' = (q' - q'^2\Theta'_s)^{q'}$; see Section 5.3.

It is convenient to analyze experimental $y_m(t)$ data using Equation (6.15) rewritten in the form

$$\ln\{\ln[1/(1 - y_s)]\} = -q' \ln \Theta'_s + q' \ln t \quad (6.17)$$

From the plots of $\ln\{\ln[1/(1 - y_s)]\}$ of fraction y_s of the precipitated phase as a function of $\ln t$, the values of q' and Θ'_s can be obtained. However, when the approximation $t/\Theta'_s \ll 1$ holds, Equation (6.14) predicts a simple linear relationship between y_s and t .

Data on the time dependence of overall crystallization y may be obtained in terms of crystallized mass w per unit volume or surface area. Then for the analysis one has $y_m = w(t)/w_0$ [see Equation (6.2)] in Equations (6.13) and (6.14). From the values of different constants thus obtained, the nature of processes can be discussed for systems in both the absence and presence of additives. The constants Θ_m/Θ_s , Θ_m , Θ_s , s , m , and q' include the effects of both nucleation and growth of the precipitating phase. However, when crystallization is determined as a $w(t)$ dependence, the value of w_0 almost exclusively gives information about the processes involved in the nucleation stage.

We consider here two examples of the overall crystallization y of transformed phases as a function of composition of the feed solution in gel-like media. Figure 6.26 shows the

dependence of fraction y of calcite in vaterite–calcite mixture precipitated at 30 °C and pH 8.5 by the carbonate diffusion method on the ratio $[-\text{COONa}]/[\text{Ca}^{2+}]$ in the presence of poly(adoamine) PAMAM dendrimers of different generations G. An evident feature of Figure 6.26 is that the overall crystallization y of calcite initially increases and then decreases with increase in the ratio $[-\text{COONa}]/[\text{Ca}^{2+}]$ in the presence of 0.05 and 0.1 M concentration of 4.5G PAMAM dendimer, and there is a maximum value of y for the ratio $[-\text{COONa}]/[\text{Ca}^{2+}]$ of about 0.02. However, in view of the small number of data it is difficult to pinpoint the effect of the physico-chemical properties of the additives of different generations on the trend of the overall transformation of calcite in this system.

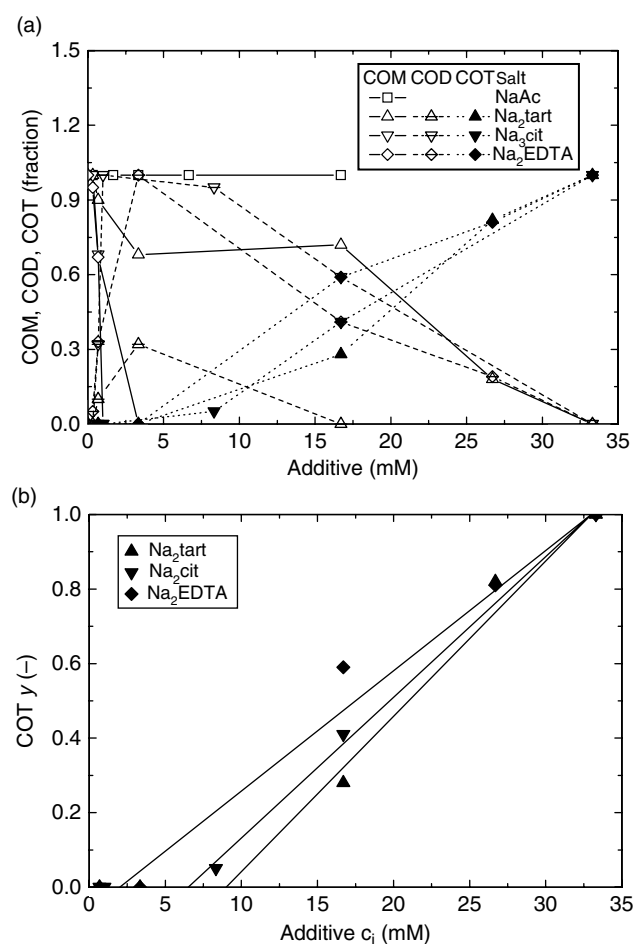


Figure 6.27 (a) Dependence of fractions of different calcium oxalate hydrates COM, COD and COT precipitated in their mixture in lecithin–water liposomes in the presence of sodium salts of some mono- and multifunctional carboxylic acids. Data from Ouyang et al. (2004). (b) Plots of fraction y of COT as a function of c_i . See text for details

Figure 6.27 represents the dependence of fractions of different calcium oxalate hydrates COM, COD and COT precipitated in their mixture in lecithin–water liposomes on the concentration of different sodium salts of some mono- and multifunctional carboxylic acids. Precipitation was carried out by mixing $K_2C_2O_4$ with unilamellar liposomes containing $CaCl_2$ and a known amount of the additive, and the growth conditions were: temperature 25 °C, pH 5.8, reaction time 10 min, and waiting time 3 h. The following features may be noted:

- (1) Two metastable phases subsequently transform to more stable phases (i.e. COT to COD, and COD to COM) simultaneously, but the appearance of COD as the intermediate phase and the effectiveness of an impurity depend strongly on the nature and concentration of an impurity. COD does not form in the presence of NaAc, but in other additives the dependence of COD formation is similar to that of calcite transformation from vaterite seen in Figure 6.26, where the maximum fraction of COD is formed at some value of the concentration c_i^* of an additive.
- (2) With an increase in the concentration of an additive, the formation of COM is inhibited, and the inhibiting effect of an additive, as determined by the additive concentration $c_{i(max)}$ necessary for complete inhibition of COM growth, decreases in the order NaAc, Na_2tart , Na_2cit and Na_2EDTA (see Figure 6.27b).
- (3) For $c_i > c_{i(max)}$, the fraction y of COT increases practically linearly with increasing c_i , such that the slope K_1 of the $y(c_i)$ plots increases in the order NaAc, Na_2tart , Na_2cit and Na_2EDTA (see Figure 6.27b).

The above features are associated with the effect of an additive on two simultaneously occurring different processes: (1) nucleation and growth of more stable phase and (2) dissolution of the metastable phase. When an additive induces the nucleation of a new, more stable phase, its fraction y increases in the total precipitation. However, when the additive suppresses the nucleation of the stable phase, its fraction decreases in the total precipitation. In the former case dissolution of the metastable phase controls the formation of the more stable phase, whereas in the latter case the nucleation of the stable phase controls the precipitation process. Denoting the two processes as a function of impurity concentration c_i , one may write the resulting fraction y as a sum of y_s and y_m in the form

$$y = y_s + y_m = k_s c_i^s - k_m c_i^m \quad (6.18)$$

where k_s and k_m are rate constants corresponding to the nucleation of stable phase s and the dissolution of the metastable phase m, respectively, and s and m are constants. Taking the derivative $dy/dc_i = 0$, one obtains from Equation (6.18) the following relations:

$$c_i^* = (mk_m/sk_s)^{1/(s-m)} \quad (6.19)$$

and

$$k_m = (sk_s/m)c_i^{(s-m)}; \quad k_s = (mk_m/s)c_i^{(m-s)} \quad (6.20)$$

On substituting for k_m and k_s from Equation (6.20) in Equation (6.18) with reference to the stable phase, one obtains the total fraction as

$$y_1 = k_s(1 - s/m)c_i^s \quad (6.21)$$

Equations (6.19) and (6.21) are the basic expressions describing the features observed in Figures 6.26 and 6.27.

Equation (6.19) implies that a peak in the $y(c_i)$ plot at c_i^* is formed only when $s > m$. Then Equation (6.21) predicts $y_1 < 0$. Physically, this means that precipitation is controlled by the dissolution of the metastable phase. When $s < m$, $y_1 > 0$, implying that the nucleation of the stable phase controls the precipitation process. Alternatively, when the value of k_s is substituted in Equation (6.18), one can discuss the precipitation process with reference to the constants of the metastable phase. Instead of Equation (6.21), then the relation is

$$y_2 = k_m(m/s - 1)c_i^m \quad (6.22)$$

This relation is valid when $m \geq s$, and predicts a threshold concentration $c_{i(\max)}$ of the impurity. The value of $c_{i(\max)}$ is determined by the value of s . This explains feature (1) observed above.

Features (2) and (3) follow directly from adsorption processes. Equations (6.21) and (6.22) represent the Freundlich adsorption isotherm. Figure 6.27b suggests that in the case of sodium salts of carboxylic acids, a linear adsorption isotherm holds (i.e. $\theta = Kc_i$, where K is the Langmuir constant), and the constant $k_m = K$. The values of the threshold concentration $c_{i(\max)}$, Langmuir constant K and the differential heat of adsorption Q_{diff} are given in Table 6.9.

Table 6.9 Values of $c_{i(\max)}$, K and Q_{diff} for calcium oxalate growth in the presence of sodium salts of carboxylic acids

Additive	$c_{i(\max)}$ (mM)	$K (10^5 \text{ M}^{-1})$	Q_{diff} (kJ/mol)
NaAc	∞	0	—
Na ₂ tart	2	3.2	32.0
Na ₂ cit	7	3.8	32.4
Na ₂ EDTA	9	4.2	32.6

The linear relation between the fraction y of COT and additive concentration c_i suggests that the values of K and the differential heat of adsorption Q_{diff} are a measure of the inhibiting effectiveness of an additive. The value of Q_{diff} increases in the order Na₂tart, Na₂cit and Na₂EDTA additives. Similarly, a decreasing value of $c_{i(\max)}$ in the order Na₂tart, Na₂cit and Na₂EDTA implies that the effectiveness of these additives in the nucleation of COD and COM increases in that order. The order of the effectiveness of NaAc, Na₂tart, Na₂cit and Na₂EDTA additives may be correlated with the molecular structure of the sodium carboxylates. The more complex the structure of a sodium carboxylate, the higher is its effectiveness.

Figure 6.27 illustrating the above three features of crystallization of calcium oxalate phases is not an isolated case. In fact, in all systems where three phases crystallize simultaneously as a function of solution composition (i.e. reactant ratio, impurity concentration, etc.) reveal these features. Figure 6.28 shows the dependence of fractions of different calcium carbonate phases precipitated in their mixture in a 0.3% agar gel by the

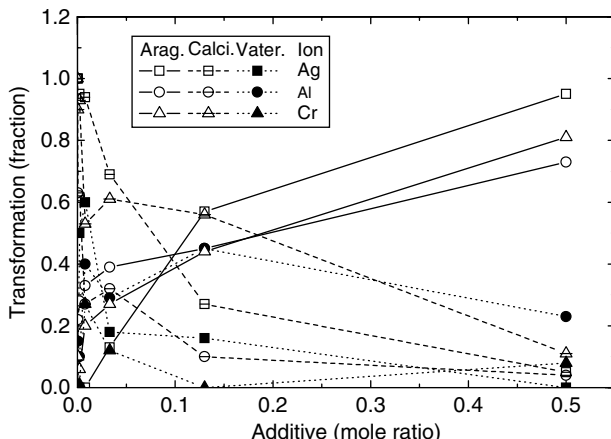


Figure 6.28 Dependence of fractions of different calcium carbonate phases precipitated in their mixture in a 0.3% agar gel by the double-diffusion method on the concentration of Ag^+ , Al^{3+} and Cr^{3+} ions. Precipitation was carried out by the counter diffusion of Ca^{2+} and CO_3^{2-} ions. A known amount of the additive was added to the solution containing Ca^{2+} ions. Growth temperature 15°C. Original data from Wada et al. (1998)

double-diffusion method on the concentration of Ag^+ , Al^{3+} and Cr^{3+} ions. Precipitation was carried out by the counter diffusion of Ca^{2+} and CO_3^{2-} ions. As can be seen from the figure, with an increase in the concentration of each additive the fraction of aragonite increases, that of calcite decreases and the vaterite fraction first increases and then decreases, exhibiting a maximum at a particular impurity concentration $c_{i(\max)}$. In contrast to the calcium oxalate phases where the phase passing through a maximum is COD, now the phase passing through the maximum is vaterite, which is the least stable phase thermodynamically among the observed three phases. This observation implies that kinetics, rather than thermodynamics, control phase transformation. The nature of the plots of fraction y of aragonite or calcite against impurity concentration c_i here is not linear as in the case of calcium oxalate, but follows a Langmuir-type adsorption isotherm with $Kc_i \gg 1$ or a Freundlich-type adsorption with s or $m < 1$ [see Equations (6.21) and (6.22)].

Now some general features of the transformation of a metastable phase into a new stable phase as a function of time are presented. For this purpose, the following examples are considered for analysis and discussion: (i) experimental results of the formation of precursor and the nucleation of polymorphous crystals of calcite and vaterite as a function of time, (ii) experimental $y(t)$ data on the transition of COD and COM into COM in the absence of additive, (iii) experimental $y(t)$ data on the transformation of aragonite into calcite in the presence of seven carboxylic acids, and (iv) experimental $y(t)$ data on the transformation of aragonite into calcite in the presence of Ag^+ , Al^{3+} and Cr^{3+} ions. In examples (ii), (iii) and (iv), the data are analyzed using Equation (6.17), whereas in example (i) $y(t)$ data for calcite are explained by Equation (6.16) and the vaterite–calcite transformation is proposed to occur by a solution-mediated mechanism in which calcite transformation is controlled by dissolution of vaterite in the solution.

In case (i), calcium carbonate precipitation was carried out by feeding 150 ml of aqueous solution of 0.05 or 0.2 M concentration (c_0) of Na_2CO_3 with a pump to the same concentration of CaCl_2 solution, without or with Mg^{2+} ions as an additive, in a crystallizer (Kitamura, 2001). The solution was stirred and the temperature was kept constant at 298 K. After mixing, the solution was neutral and the pH remained constant in an experiment. The feeding rate F of Na_2CO_3 solution was varied between 0.05 and 5 ml/s, and the concentration of Mg^{2+} additive was 5 or 10 mM. In case (ii) precipitation was studied by the constant composition method at 37°C (Nancollas, 1982), in case (iii) the precipitated phase was observed in the presence of Mg^{2+} ions as a precipitation disc in 3% agar gel formed by the double-diffusion method at 15°C after 5 days (Wada *et al.*, 1999), whereas in case (iv) the precipitated phase was observed as a precipitation disc in 0.3% agar gel formed by the double-diffusion method at 15°C (Wada *et al.*, 1998). It should be mentioned that in growth system (iii) containing Mg^{2+} ions (with molar concentration ratio $[\text{Mg}^{2+}]/[\text{Ca}^{2+}]$) aragonite is exclusively formed in the absence of carboxylic acids, but the presence of carboxylic acids in the gel medium favors the formation of magnesian calcite relative to the amount of the additives. Crystallization of calcite phase was investigated as a function of the increase in the induction period t with reference to a control experiment without an additive.

Kitamura (2001) carried out a detailed study of the crystallization of calcium carbonate by mixing sodium carbonate solution at different feeding rates F to CaCl_2 solution containing different concentrations c_{Mg} of MgCl_2 , and investigated the effect of feeding rate and feed concentration on (1) the lifetime of amorphous calcium carbonate and (2) the crystallization fraction of metastable vaterite phase and its transformation to stable calcite phase. Figure 6.29 shows the change in concentration $c_{\text{Ca}^{2+}}$ of Ca^{2+} ions with time t from the start of mixing of solutions of 0.05 mol/l calcium chloride without and with the addition of two concentrations c_{Mg} of MgCl_2 for different feed rates of 0.05 mol/l CaCO_3 solutions. The values of c_{C}^{e} and c_{V}^{e} denote the solubility of calcite and vaterite, respectively. The resulting values of the concentration $c_{\text{Ca}^{2+}}$ are intermediate between the solubilities of calcite and vaterite. The figure shows that, for the different feeding rates F , the Ca^{2+} ion concentration rapidly decreases initially, and then attains a constant value both in the pure system and in systems containing Mg^{2+} ions. A similar behavior of $\text{Ca}^{2+}(t)$ plots was found for $c = 0.2$ mol/l solutions, but the constant value of Ca^{2+} ion concentration attained after the initial period was higher than $c = 0.05$ mol/l. In the presence of Mg^{2+} ions the concentration of Ca^{2+} ions is increased in comparison with that in the pure system. The Ca^{2+} ion concentration also tends to increase with decrease in the feeding rate F of NaCO_3 solutions.

The composition of the polymorphs was found to depend on the concentration c_0 of the solutions, the feeding rate F of sodium carbonate solution, and the crystallization time t . Figure 6.30 shows the change in the composition y_{C} of calcite on time t from pure solutions of 0.2 mol/l concentration c_0 . The $y_{\text{C}}(t)$ dependence is linear with a constant slope y' [see Equation (6.16)]. It was also observed that calcite composition y_{C} for $c_0 = 0.2$ mol/l is smaller than that for $c_0 = 0.05$ mol/l, implying that the crystallization of vaterite is higher with increasing c_0 . Addition of Mg^{2+} ions leads to an increase in the initial values of y_{C} , but the slope of the $y_{\text{C}}(t)$ plots is drastically decreased. The slope approaches zero, especially at high feed rates F . The decrease in the slope of $y_{\text{C}}(t)$ plots implies that the transformation rate of vaterite to calcite is suppressed by the Mg^{2+} ions.

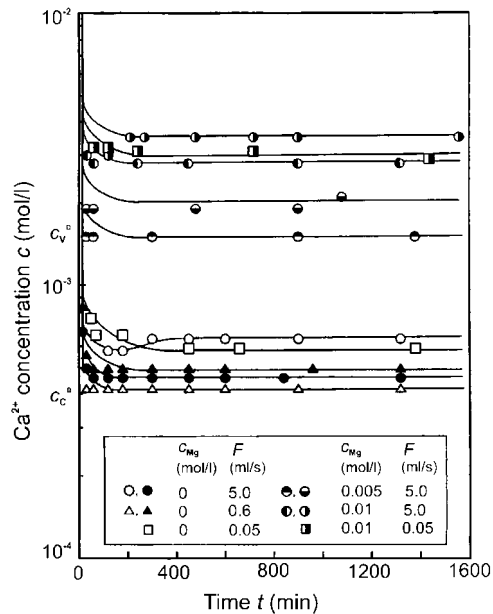


Figure 6.29 Change in concentration c of Ca^{2+} with time t after the start of mixing of solutions of 0.05 mol/l calcium chloride containing different concentrations c_{Mg} of MgCl_2 with the addition of 0.05 mol/l sodium carbonate at different feeding rates F . Adapted from M. Kitamura. J. Colloid Interface Sci. **236**, 318. Copyright (2001), with permission from Elsevier

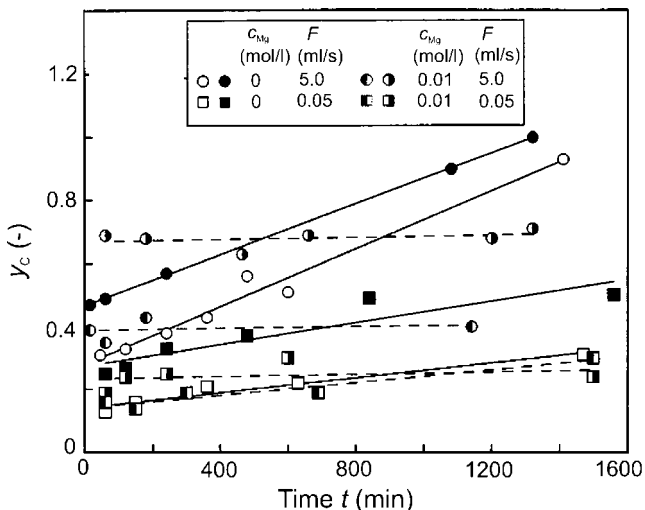


Figure 6.30 Dependence of composition y_C of calcite on time t for 0.2 mol/l solutions. Adapted from M. Kitamura. J. Colloid Interface Sci. **236**, 318. Copyright (2001), with permission from Elsevier

The initial decreasing concentration of Ca^{2+} ions before attaining a constant value is due to the presence of the precursor amorphous calcium carbonate in the form of globular and fibrous particles (Kitamura, 2001; Kawano *et al.*, 2002). The nucleation of polymorphic crystals occurs in the vicinity of the precursor and the polymorphic crystals grow by devouring the precursor particles surrounding the crystals, implying that the solubility of the precursor is higher than that of the polymorphic crystals. Although the lifetime of the precursor is relatively long, it disappears and polymorphic phases nucleate and grow as a result of dissolution of the precursor particles. After the precursor has disappeared completely, calcite crystals grow whereas vaterite dissolves. This indicates that vaterite transforms to calcite by the solution-mediated transformation. The disappearance of the precursor with simultaneous precipitation of vaterite and calcite is also an evidence of solution-mediated transformation.

Following Kitamura (2001), solution-mediated transformation of metastable phase m to stable phase s may be described as a result of dissolution of phase m and growth of phase s:

$$\frac{dM_s}{dt} = k_s M_s^{2/3} (c' - c_s^e) \quad (6.23)$$

$$\frac{dM_m}{dt} = -k_m M_m^{2/3} (c' - c_m^e) \quad (6.24)$$

where M_s and M_m are the masses of stable and metastable phases, respectively, c_s^e and c_m^e are their corresponding solubilities, and k_s and k_m are the rate constants of growth and dissolution of the stable and the metastable phases, respectively. The concentration c' is determined by the relative rates of Equations (6.23) and (6.24). In this case, the solution concentration should decrease with time, approaching the solubility c_s^e of the stable form. When the transformation rate is controlled by the growth of the stable phase, Equation (6.23) describes the rate and $c' = c_m^e$ in Equation (6.24). However, in the dissolution-controlled transformation rate Equation (6.24) can be used, where $c' = c_s^e$. In Figure 6.29, the concentration remains practically constant despite the progress of transformation, implying that the transformation process is dissolution controlled, and the transformation may be described by Equation (6.24).

The concentration of solutions increases with increase in the feed concentration and decreases with increase in the feed rate, while the concentration attains a value c' intermediate between the solubility of metastable (vaterite) and stable (calcite) phases (see Figure 6.29). These results are a consequence of the competition of the two processes described by Equations (6.23) and (6.24). If the solubility difference between metastable and stable phases and the total amount ($M_m + M_s$) of the crystals are constant, the fraction of the metastable phase is

$$y_m = M_m / (M_m + M_s) \quad (6.25)$$

Then, from Equations (6.24) and (6.25) one obtains

$$y_m^{1/3}(t) - y_m^{1/3}(0) = -k't \quad (6.26)$$

where k' is the rate constant of transformation. Figure 6.31 shows the relationship between $y_m = y_V$ of vaterite on time t for 0.2 mol/l solutions according to Equation (6.26).

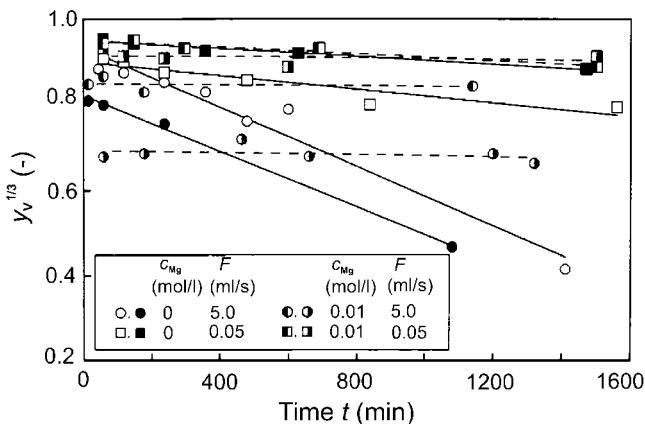


Figure 6.31 Plots of $y_v^{1/3}$ of vaterite on time t for 0.2 mol/l solutions. The linearity predicted by Equation (6.26) is observed. Adapted from M. Kitamura. J. Colloid Interface Sci. **236**, 318. Copyright (2001), with permission from Elsevier

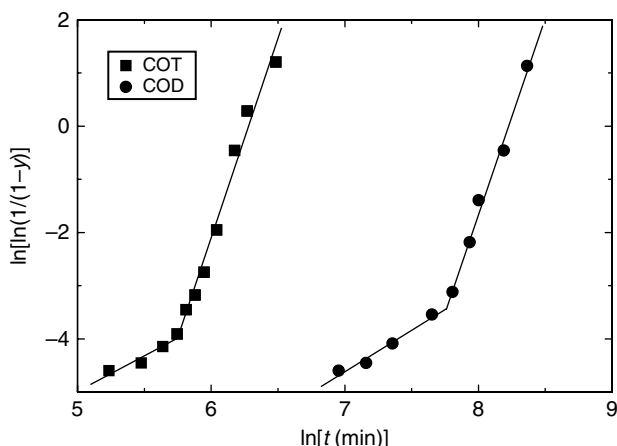


Figure 6.32 Plots of $\ln\{\ln[1/(1-y)]\}$ of fraction y of COM of transformation of COD and COT precipitates as a function of $\ln t$ at 37°C. Data from Nancollas (1982)

Figure 6.32 shows the plots of $\ln\{\ln[1/(1-y)]\}$ of fraction y of COM of transformation of COD and COT precipitates as a function of $\ln t$. These data are shown in Figure 2.15. It can be seen that the dependence is better represented in two parts with a transition value of $\ln\{\ln[1/(1-y)]\} \approx -3.7$. The constants q' and Θ' obtained from the plots in different $\ln\{\ln[1/(1-y)]\}$ range are given in Table 6.10. For $q' > 4$ the Θ' values calculated from the relation $\Theta'_s(\text{calc.}) = (4/q')\Theta'_s(\text{exp.})$ are also given in the parentheses [cf. Equation (6.15)]. Obviously, the calculated Θ'_s values are lower by a factor of 1.85 than the values of Θ'_s obtained by direct fitting of the data by Equation (6.15) with $q' = 4$.

Table 6.10 Constants q' and Θ' in different $\ln\{\ln[1/(1-y)]\}$ ranges

Phase	$\ln\{\ln[1/(1-y)]\}$ range	q'	$\Theta'_s (\Theta_s)$ (min)
COT	< -3.8	1.34	6148
	> -3.8	7.49	534 (285)
COD	< -3.6	1.56	21195
	> -3.6	7.39	3737 (2020)

In the initial stage of crystallization in gels, it may be assumed that the supply of reactants occurs by volume diffusion ($v = 1/2$) and the formation of nuclei takes place by instantaneous nucleation (i.e. $q = 1 + vd$). This means that in the initial stage of crystallization, the growth dimensionality d is about 3. This may be attributed to the growth of nuclei of metastable phases to an appropriate size before their transformation into a stable phase characterized by a higher value of q' of about 7 (i.e. $q = 4$) for $\ln\{\ln[1/(1-y)]\} > -3.7$. This stage is probably associated with progressive nucleation.

Figure 6.33a shows the plots of $\ln\{\ln[1/(1-y)]\}$ of calcite fraction y in aragonite–calcite mixture as a function of logarithm of increase Δt_i in induction time t_i by different carboxylic acids. For all additives the average $q = 1.82 \pm 0.12$, while the time constant Θ [cf. Equation (6.16)] is different for different additives (see Figure 6.33b). Recalling that the supply of reactants in a gel medium is by volume diffusion and instantaneous nucleation is more probable than progressive nucleation in the initial stage of crystallization,

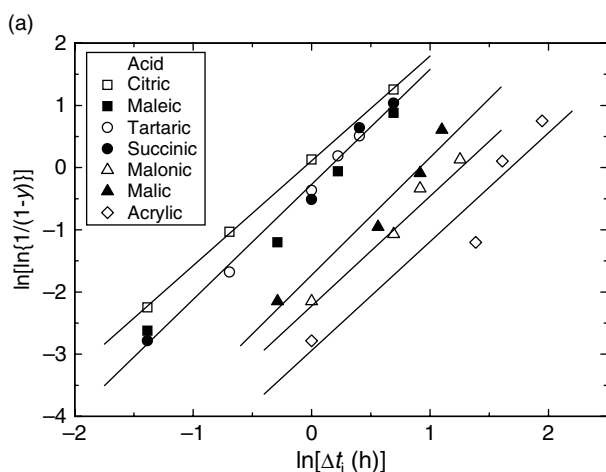


Figure 6.33 (a) Plots of $\ln\{\ln[1/(1-y)]\}$ of calcite fraction y in aragonite–calcite mixture as a function of increase Δt_i in induction time t_i by different carboxylic acids. The precipitated phase was observed as a precipitation disc in 3% agar gel formed by the double-diffusion method; growth temperature 15°C and growth duration 5 days. (b) Relationship between molecular weight MW of additive and time constant Θ . (c) Plots of dissociation constants pK_1 and $p(K_1 + K_2)$ against $\Delta\Theta$. In (b) and (c) the linear plots show the best-fit relations. Original $y(\Delta t_i)$ data and data of MW and pKs are from Wada et al. (1999)

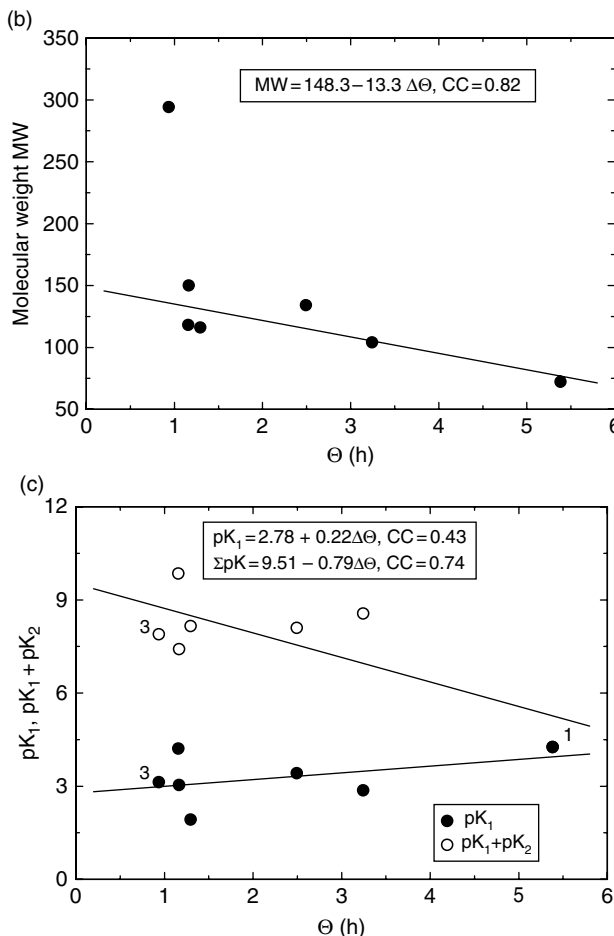


Figure 6.33 (Continued)

the experimental $q = 1.82$ suggests that the crystallizing phase has a dimensionality $d = 3.64$. This value of d indicates that transformation of aragonite into calcite in the gel is associated with solution-mediated phase transformation involving dissolution of metastable aragonite and growth of calcite.

It should be noted that the above inference of solution-mediated phase transformation is inconsistent with the conclusion of Wada *et al.* (1999), who suggested that aragonite–calcite transformation in their gel medium occurs by solid-to-solid reactions. They based their conclusion following the result of $q = 4/3$ in a study of the transformation of aragonite–calcite carried out by Rao (1973) under conditions of solid-to-solid reaction.

The relationship between the time constant Θ and the physico-chemical properties, such as molecular weight MW and dissociation constants pK_1 and $p(K_1 + K_2)$, of the additives was analyzed, as shown in Figure 6.33b and c, respectively. It can be seen that

the time constant Θ decreases with increase in MW of an additive (Figure 6.33b) and its total dissociation constant, i.e. $p(K_1 + K_2 + K_3)$ (Figure 6.33c).

The time constant Θ decreases with increase in the growth constant k and nucleation rate J [see Equation (2.51)]. Hence the above data imply that the effectiveness of different additives decreases in the following order: citric acid (most effective), succinic acid, tartaric acid, maleic acid, malic acid, malonic acid and acrylic acid (least effective). This implies that the effect of tricarboxylic acid on the formation of calcite is greater than that of dicarboxylic acid, while the effect of the latter is greater than that of monocarboxylic acid. This also explains the relationship between Θ and MW and dissociation constant $\sum_i pK_i$ of different acids (Figure 6.33b and c). This suggests that the number of COO^- groups in the molecule of an acid plays an important role in the formation of calcite in the presence of Mg^{2+} ions.

Figure 6.34 presents the plots of $\ln\{\ln[1/(1-y)]\}$ of the fractions y of calcite and aragonite in vaterite–aragonite–calcite mixture as a function of increase Δt_i in induction time t_i by Ag^+ , Al^{3+} and Cr^{3+} ions. The precipitated phase was observed as a precipitation disc in 0.3% agar gel formed by the double-diffusion method at growth temperature 15°C after 5 days. It can be seen that the plots of the kinetics for the three cations have a slope $q \approx 1$ and 3–4 in both Figure 6.34a and b for $\ln \Delta t_i < \ln \Delta t_i^*$ and $\ln \Delta t_i > \ln \Delta t_i^*$, respectively. A value of $q = vd = 1$ suggests that at induction periods $\ln \Delta t_i < \ln \Delta t_i^*$ the precipitation process is controlled by volume diffusion and the growth dimensionality $d = 2$. However, at $\ln \Delta t_i > \ln \Delta t_i^*$ (i.e. for high induction periods) when $q = 3$ –4, crystallization is controlled by solution-mediated phase transformation. These values of q imply that crystallization occurs by instantaneous and progressive nucleation mechanisms in the ranges of low and high induction periods, respectively.

The value of $q \approx 1.8$ for the calcite phase in aragonite–calcite fraction and $q \approx 1$ for calcite and aragonite in vaterite–aragonite–calcite fraction crystallized, respectively, in the presence of different carboxylic acids (Figure 6.33) and cations (Figure 6.34) suggest that the mechanisms of inhibition of unstable phases by the additives are different. In the former case inhibition is predominantly a two-dimensional process, whereas in the latter case it occurs on the entire volume of the nuclei. This difference in the inhibition mechanism of the two types of additives may be due to the structure of the additive molecules.

Concluding this section, it may be said that an additive can stabilize kinetically the thermodynamically metastable phase and suppress the formation of the thermodynamically stable phase. This can occur when an additive favors the nucleation and growth of the stable phase by increasing the value of the kinetic coefficient k_s of the stable phase [Equation (6.23)] and by decreasing the kinetic coefficient k_m of the metastable phase [Equation (6.24)]. The effects of the additives as a function of their concentration are described by the contributions y_s and y_m in Equation (6.18).

6.4 Scale Formation and Salt Weathering

Formation of mineral scales is an important problem in oil-extraction pipelines, heat exchangers, house appliances, water pipes, mining and mineral processing, desalination plants and cane-sugar mill evaporators (Yang *et al.*, 2001; Yu *et al.*, 2002, 2004). The

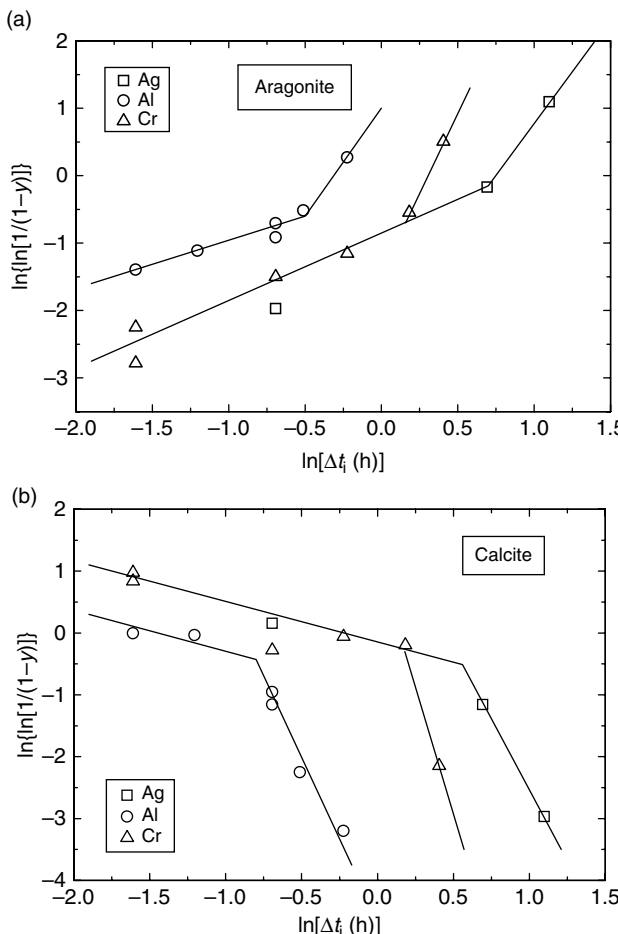


Figure 6.34 Plots of $\ln\{\ln[1/(1-y)]\}$ of fraction y of (a) aragonite and (b) calcite in vaterite–aragonite–calcite mixture as a function of increase Δt_i in induction time t_i by Ag^+ , Al^{3+} and Cr^{3+} ions. For Ag^+ the plots of $\ln\{\ln[1/(1-y)]\}$ against Δt_i were drawn using the absolute values of Δt_i . Original $y(\Delta t_i)$ data from Wada et al. (1998)

presence of a scale layer may lead to a number of problems, such as impedance of heat transfer, increase in energy consumption and unscheduled equipment shutdown. The main component of scales deposited from natural water, especially in cooling water systems, is calcium carbonate, described by the following equilibrium reactions:



A shift of the reaction to the right leads to the precipitation of CaCO_3 as mineral scale, and a shift to the left to the dissolution of the carbonate. In contrast, in cane-sugar mill

evaporators, calcium oxalate monohydrate (COM) and amorphous silica (SiO_2) are major components of scales formed on the calandria tubes (Yu *et al.*, 2002).

Another phenomenon closely related to scale formation is salt weathering associated with damage caused to construction materials (Goudie and Viles, 1997). The problem is severe in the case of sculptural and architectural heritage. Salt weathering occurs due to disruptive pressure exerted by a salt growing in confined volumes, such as pores of stones and bricks of buildings, from solutions where supersaturation may be achieved by solvent evaporation (e.g. from saline water).

Scale formation and salt weathering can be prevented either by taking measures that keep the solution undersaturated or, if the solution becomes supersaturated, by using additives that suppress nucleation and/or growth of crystals. Among the well-known inhibitors of calcite scale formation are polyphosphates, carboxylates, polyacrylic derivatives and benzotriazoles (for the literature, see Yang *et al.*, 2001; Rodriguez-Navarro *et al.*, 2002) while those for COM are water-soluble low molecular weight polymers such as poly(acrylic acid) (PAA) and poly(maleic acid) (Doherty *et al.*, 2004).

Figure 6.35 shows a typical example of the dependence of scale resistance R of calcium carbonate on time t in the presence of poly(acrylic acid) (PAA) and 2-phosphonobutane-1,2,4-tricarboxylic acid (PBTCA) additives. Here the scale resistance is a measure of the thickness of the deposited scale. The experimental conditions used for the scaling were as follows: bulk temperature 41 °C, initial surface temperature 90.5 °C, fluid velocity 0.926 m/s, $[\text{CaCl}_2] = 1.5 \text{ g/l}$, and $[\text{NaHCO}_3] = 1.5 \text{ g/l}$. The plots are drawn according to Equation (6.3), and the number on each curve denotes R_0 , which is the value of R for $t = \infty$. The time constant Θ was found to be 3.2 ± 0.2

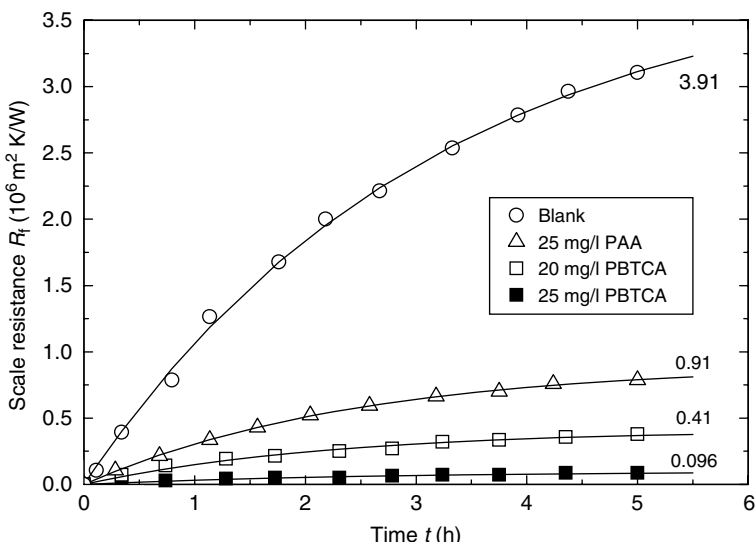


Figure 6.35 Dependence of scale resistance R of calcium carbonate on time t in the presence of PAA and PBTCA additives. Plots are drawn according to Equation (6.3), and the number on each curve denotes R_0 . Original data from Yang *et al.* (2001)

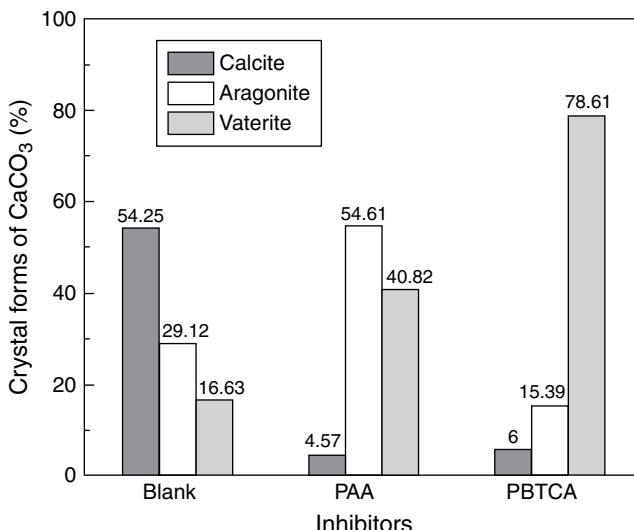


Figure 6.36 Relative composition of different forms of calcium carbonate in deposited scales in the absence and presence of additives. Reproduced from Q. Yang, Y. Liu, A. Gu, J. Ding, and Z. Shen. *J. Colloid Interface Sci.* **240**, 608. Copyright (2001), with permission from Elsevier

and 2.4 ± 0.3 h for scales from pure solutions and from solutions containing additives, respectively.

In the above experiments on scale formation, the three anhydrous forms of calcium carbonate (i.e. vaterite, aragonite and calcite) were deposited, as shown in Figure 6.36. However, it was found that in the absence of inhibitors calcite is the main crystal form, but aragonite and vaterite become the main polymorphs in the presence of PAA, whereas vaterite is the main crystal form in the presence of PBTCA. Moreover, as seen in the case of PBTCA, the vaterite content increases with increase in additive concentration. These results of the effect of additives on scale formation are similar to those of phase transformation from solutions discussed above. Of the two additives used in the above study, PBTCA is more effective than PAA in inhibiting the nucleation of vaterite. These results on the simultaneous formation of polymorphs of thermodynamically different stability are consistent with the Oswald rule of stages. The metastable crystal forms of aragonite and vaterite are stabilized kinetically in the presence of additives. The role of an additive is to promote the nucleation and growth of a more stable phase such as aragonite and/or calcite and to inhibit the dissolution of the metastable vaterite phase.

Yang *et al.* (2001) analyzed the fractal dimensions of the calcite scale surfaces and the average spacing between steps, and found that the increasing inhibiting effect of an additive, as determined by $(R_0 - R'_0)/R_0$ (where R_0 and R'_0 are the values of the initial deposition rates in the absence and presence of an additive, respectively), leads to an increase in the fractal dimension and the step spacing. These relationships are associated with the kinetic effects of additives in polymorphic transformations.

References

- Abdel-Aal, N., and K. Sawada (2003). *J. Cryst. Growth* **256**, 188.
- Aizenberg, J., J. Hanson, T.F. Koetzle, S. Weiner, and L. Addadi (1997). *J. Am. Chem. Soc.* **119**, 881.
- Arends, J. (1982). In: G.H. Nancollas (Ed.), *Biological Mineralization and Demineralization*, Springer, Berlin, 1982, p. 303.
- Arias, J.L., M.S. Fernandez, V.J. Laraia, J. Janicki, A.H. Heuer, and A.I. Caplan (1991). *Mater. Soc. Symp. Proc.* **218**, 193.
- Arnott, H.J. (1982). In: G.H. Nancollas (Ed.), *Biological Mineralization and Demineralization*, Springer, Berlin, p. 199.
- Atanassova, S., K. Neykov, and I. Gutsov (1996). *J. Cryst. Growth* **160**, 148.
- Baumann, J.M., B. Affolter, U. Caprez, and U. Henze (2003). *Eur. Urol.* **43** 421.
- Brećević, Lj., D. Kralj, and J. Garside (1989). *J. Cryst. Growth* **97**, 460.
- Brown, P., D. Ackermann, and B. Finlayson (1989). *J. Cryst. Growth* **98**, 285.
- Chandrajith, R., G. Wijewardana, C.B. Dissanayake, and A. Abegunasekara (2006). *Environ. Geochem. Health* **28**, 393.
- Chateigner, D., C. Hedegaard, and H.-R. Wenk, (2000). *J. Struct. Geol.* **22**, 1723.
- Clarkson, J.R., T. Price, and C. Adams (1992). *J. Chem. Soc., Faraday Trans.* **88**, 243.
- Crenshaw, M.A. (1982). In: G.H. Nancollas (Ed.), *Biological Mineralization and Demineralization*, Springer, Berlin, p. 243.
- Doherty, W.O.S., C.M. Fellows, S. Gorjian, E. Senogles, and W.H. Cheung (2004). *J. Appl. Polym. Sci.* **91**, 2035.
- Dove, P.M., J.J. De Yoreo, and K.J. Davis (2004). In: X.Y. Liu and J.J. De Yoreo (Eds.), *Nanoscale Structure and Assembly at Solid–Fluid Interfaces, Vol. II: Assembly at Hybrid and Biological Systems*, Kluwer, Boston, Chap. 2, p. 55.
- Eiden-Assman, S., M. Viertelhaus, A. Heiss, K.A. Hoetzer, and J. Felsche (2002). *J. Inorg. Biochem.* **91**, 481.
- Elfil, H., and H. Rogues (2001). *Desalination* **137**, 177.
- Feng, Q.L., G. Pu, Y. Pei, F.Z. Cui, H.D. Li, and T.N. Kim (2000). *J. Cryst. Growth* **216**, 459.
- Foo, C.W.P., J. Huang, and D.L. Kaplan (2004). *Trends Biotechnol.* **22**, 577.
- Fox, P.C. (2004). *Caries Res.* **38**, 241.
- Füredi-Milhofer, H., and S. Sarig (1996). *Prog. Cryst. Growth Charact. Mater.* **32**, 45.
- Füredi-Milhofer, H., M. Skirić, L. Tunik, N. Filipović, and N. Garti (2002). *Int. J. Mod. Phys.* **16**, 359.
- Gal, J.Y., N. Gache, and Y. Fovet (2000). *J. Eur. Hydrogeol.* **31**, 47.
- Gomez-Morales, J., J. Torrent-Burgues, and R. Rodriguez-Clemente (1996). *J. Cryst. Growth* **169**, 331.
- Goudie, A.S., and H. Viles (1997). *Salt Weathering Hazards*, John Wiley & Sons, Ltd, Chichester.
- Grases, F., P. Sanchis, J. Parello, and A. Costa-Bauza (2006). *Int. J. Urol.* **13**, 252.
- Gratz, A.J., and P.E. Hillner (1993). *J. Cryst. Growth* **129**, 789.
- Grover, P.K., and R.L. Ryall (1995). In: S.R. Khan (Ed.), *Calcium Oxalate in Biological Systems*, CRC Press, Boca Raton, FL, pp. 305.
- Grover, P.K., V.R. Marshall, and R.L. Ryall (2003). *Chem. Biol.* **10**, 271.
- Guerra, A., T. Meschi, F. Allegri, B. Prati, A. Nouvenne, E. Fiaccadori, and L. Borghi (2006). *Urol. Res.* **34**, 359.
- Gutjahr, A., H. Dabringhaus, and R. Lacmann (1996). *J. Cryst. Growth* **158**, 310.
- Hu, Z., and Y. Deng (2003). *J. Colloid Interface Sci.* **266**, 359.
- Hunter, G.K. (1996). *Curr. Opin. Solid State Mater. Sci.* **1**, 430.
- Jung, T., W.-S. Kim, and C.K. Choi (2004). *Mater. Sci Eng. C* **24**, 31.

- Jung, T., W.-S. Kim, and C.K. Choi (2005). *J. Cryst. Growth* **279**, 154.
- Kashchiev, D. (2000). *Nucleation: Basic Theory and Applications*, Butterworth-Heinemann, Oxford.
- Katsifaras, A., and N. Spanos (1999). *J. Cryst. Growth* **204**, 183.
- Kawano, J., N. Shimobayashi, M. Kitamura, K. Shinoda, and N. Aikawa (2002). *J. Cryst. Growth* **237/239**, 419.
- Kitamura, M. (2001). *J. Colloid Interface Sci.* **236**, 318.
- Kitamura, M., H. Konno, A. Yasui, and H. Masuoka (2002). *J. Cryst. Growth* **236**, 323.
- Koutsopoulos, S., and E. Dalas (2000). *J. Colloid Interface Sci.* **231**, 207.
- Kurutz, J.W., M. Carvalho, and Y. Nakagawa (2003). *J. Cryst. Growth* **255**, 392.
- Levi-Kalisman, Y., G. Falini, L. Addadi, and S. Weiner (2001). *J. Struct. Biol.* **135**, 8.
- Loste, E., R.M. Wilson, R. Sheshadri, and F.C. Meldrum (2003). *J. Cryst. Growth* **254**, 206.
- Manali, F., and E. Dalas (2002). *J. Mater. Sci.: Mater. Med.* **13**, 155.
- Mandel, I.D. (1989). *J. Am. Dental Assoc.* **119**, 298.
- Manne, J., N. Biala, A.D. Smith, and C.C. Gryte (1990). *J. Cryst. Growth* **100**, 627.
- Marin, F., and G. Luquet (2004). *C.R. Palevol.* **3**, 469.
- McCoy, J.M., and P. LaFemina (1997). *Surf. Sci.* **373**, 288.
- Mikšík, I., V. Holán, and Z. Deyl (1996). *Comp. Biochem. Physiol.* **113B**, 607.
- Naka, K., and Y. Chujo (2003). *C.R. Chim.* **6**, 1193.
- Nakata, P.A. (2003). *Plant Sci.* **164**, 901.
- Nancollas, G.H. (1982). In: G.H. Nancollas (Ed.), *Biological Mineralization and Demineralization*, Springer, Berlin, p. 79.
- Nancollas, G.H., and M.B. Tomson (1978). *Science* **200**, 1059.
- Onuma, K. (2006). *Prog. Cryst. Growth Charact. Mater.* **52**, 223.
- Ouyang, H.M. (2006). *Mater. Sci. Eng. C* **26**, 679.
- Ouyang, J.-M., N. Zhou, L. Duan, and B. Tieke (2004). *Colloids Surf. A* **245**, 153.
- Ouyang, J.-M., F. Deng, and L. Duan (2005). *Colloids Surf. A* **257/258**, 215.
- Pak, C.Y.C. (1998). *Lacet* **351**, 1797.
- Prieto, M., L. Fernández-Díaz, and S. López-Andrés (1989). *J. Cryst. Growth* **98**, 447.
- Prokopp, D.J., and C.J. Williams (1982). In: G.H. Nancollas (Ed.), *Biological Mineralization and Demineralization*, Springer, Berlin, p. 161.
- Rao, M.S. (1973). *Indian J. Chem.* **11**, 280.
- Reddy, M.M., and A.R. Hoch (2001). *J. Colloid Interface Sci.* **235**, 365.
- Reyhani, M.M., A. Olivier, G.M. Parkinson, F. Jones, A.L. Rohl, and M.I. Ogden (2002). *Int. J. Mod. Phys.* **16**, 25.
- Robertson, W.G. (1993). In: B.E.C. Nordin, A.G. Need, and M.A. Morris (Eds), *Metabolic Bone and Stone Disease*, Churchill Livingstone, New York, p. 249.
- Rodríguez-Navarro, C., L. Linares-Fernandez, E. Doehe, and E. Sebastian (2002). *J. Cryst. Growth* **243**, 503.
- Ryall, R.L., M.C. Chauvet, and P.K. Grover (2005). *Br. J. Urol. Int.* **96**, 654.
- Saito, T., H. Toyooka, S. Ito, and M.A. Crenshaw (2003). *Caries Res.* **37**, 445.
- Schenk, R.K., E. Hunziker, and W. Herrmann (1982). In: G.H. Nancollas (Ed.), *Biological Mineralization and Demineralization*, Springer, Berlin, p. 143.
- Shen, F.H., Q.L. Fend, and C.M. Wang (2002). *J. Cryst. Growth* **242**, 239.
- Siener, R., and A. Hesse (2002). *Eur. Urol.* **42**, 289.
- Sikirić, M., N. Filipović, V. Babić-Ivančić, N. Vdović, and H. Füredi-Milhofer (1999). *J. Colloid Interface Sci.* **212**, 384.
- Skrtić, M., H. Füredi-Milhofer, and M. Marković (1987). *J. Cryst. Growth* **80**, 113.
- Smith, L.H. (1982). In: G.H. Nancollas (Ed.), *Biological Mineralization and Demineralization*, Springer, Berlin, p. 259.

- Sparks, N.H.C. (1994). In: R.G. Board and R. Fuller (Eds.), *Microbiology of the Avian Eggs*, Chapman and Hall, London, p. 25.
- Sunagawa, I. (2005). *Crystals: Growth, Morphology and Perfection*, Cambridge University Press, Cambridge.
- Sutherland, J.W., J.H. Parks, and F.L. Coe (1985). *Miner. Electr. Metab.* **11**, 267.
- Teng, H.H., and P.M. Dove (1997). *Am. Mineral.* **82**, 878.
- Thongboonkerd, V., T. Semangoen, and S. Chitipongtanate (2006). *Clin. Chim. Acta* **367**, 120.
- Tsontos, A., and G.H. Nancollas (2002). *J. Colloid Interface Sci.* **250**, 159.
- Twetman, S. (2004). *Caries Res.* **38**, 223.
- van Nieuw Amerongen, A., J.G.M. Bolscher, and E.C.L. Veerman (2004). *Caries Res.* **38**, 247.
- Verma, A.R. (1953). *Crystal Growth and Dislocations*, Butterworth, London.
- Wada, N., and T. Umegaki (1993). *Gypsum Lime* **245**, 17.
- Wada, N., K. Yamashita, and T. Umegaki (1995). *J. Cryst. Growth* **148**, 297.
- Wada, N., K. Yamashita, and T. Umegaki (1998). *J. Colloid Interface Sci.* **201**, 1.
- Wada, N., K. Yamashita, and T. Umegaki (1999). *J. Colloid Interface Sci.* **212**, 357.
- Walters, D.A., B.L. Smith, A.M. Belcher, G.T. Paloczi, G.D. Stucky, D.F. Morse, and P.K. Hansma (1997). *Biophys. J.* **72**, 1425.
- Walton, R.C., J.P. Kavanagh, B.R. Heywood, and P.N. Rao (2005). *Biochim. Biophys. Acta* **1723**, 175.
- Wang, L., J.J. De Yoreo, X. Guan, S.R. Qui, J.R. Hoyer, and G.H. Nancollas (2006a). *Cryst. Growth Des.* **6**, 1768.
- Wang, L., W. Zhang, S.R. Qui, W.J. Zachowicz, X. Guan, R. Tang, J.R. Hoyer, J.J. De Yoreo, and G.H. Nancollas (2006b). *J. Cryst. Growth* **291**, 160.
- Webber, D., A.L. Rodgers, and E.D. Sturrock (2003). *J. Cryst. Growth* **259**, 179.
- Wei, H., Q. Shen, Y. Zhao, D.-J. Wang, and D.-F. Xu (2003). *J. Cryst. Growth* **250**, 516.
- Wesson, J.A., V. Ganne, A.M. Beshensky, and J.G. Kleinman (2005). *Urol. Res.* **33**, 206.
- Westin, K.-J., and A.C. Rasmussen (2005). *J. Colloid Interface Sci.* **282**, 359.
- Wilt, F.H. (2005). *Dev. Biol.* **280**, 15.
- Yang, Q., Y. Liu, A. Gu, J. Ding, and Z. Shen (2001). *J. Colloid Interface Sci.* **240**, 608.
- Yu, H., R. Sheikholeslami, and W.O.S. Doherty (2002). *Chem. Eng. Sci.* **57**, 1969.
- Yu, H., R. Sheikholeslami, and W.O.S. Doherty (2004). *J. Cryst. Growth* **265**, 592.

7

Morphology and Size Distribution of Crystals

Crystals are solid substances which may be obtained from the solid, liquid or vapor phase. Except for solid-phase and melt growths, other phases yield crystals with well-developed faces which represent the crystal–medium interface during their development from the growth medium. The essential requirement for the development of the faces of a crystal is the presence of a sufficient number of kinks on them. According to the classification of faces advanced by Hartman (see Section 3.2), K faces are entirely composed of kinks, but on S and K faces kinks are provided by statistical fluctuations. Since S faces are composed of ledges, the kink density on them is expected to be much higher than on F faces. A natural consequence of the structure of surfaces is that F faces are the slowest growing faces, S faces grow at a faster rate than the F faces by the displacement of ledges perpendicularly to the faces, and K faces are the fastest growing faces and are usually absent in the growth morphology. Microscopically, F faces remain smooth, whereas S faces show parallel ledges which appear to start from one of the neighboring F faces.

Among the F faces appearing in the growth form, their relative development (i.e. face area or morphological importance) is connected with the relative strength of the period bond chains (PBCs) in different faces. Faces endowed with strong PBCs are morphologically more important than those having relatively weak PBCs. This nature of the faces is due to the fact that weaker the PBC, the higher is the density of kinks that it can provide by edge nucleation and statistical fluctuations. Thus, due to a high density of kinks, an F face is essentially rough, although it can be composed of two or more PBCs. This type of roughening is called thermodynamic. A measure of thermodynamic roughness of an F face is the surface entropy factor α . An F face with α below about 3 is rough and grows by a continuous growth mechanism, whereas one with $\alpha > 3$ is smooth and grows by a layer growth mechanism. However, this criterion of thermodynamic roughening is valid at low supersaturations. An F face will develop only if a screw dislocation emerging on

it acts as a continuous source of steps or if an edge dislocation emerging on it facilitates repeated two-dimensional nucleation at its emergence point. Thus, the external appearance of a crystal and the topography of its F faces are related to the nature of solid–fluid interface and to the supersaturation available at the surface. However, under nonideal conditions such as high temperatures and/or high supersaturations, F faces no longer remain ideally flat. Instead, they become rough with a great number of kinks, and for all purposes they behave as S or K faces (i.e. kinetic roughening). These aspects were discussed in Chapter 3.

As-grown F faces of crystals exhibit a variety of spirals (simple spirals and macrospirals), macrosteps, hillocks of dislocation and nondislocation origin, and block structures, while growth striations appear on S faces. The crystals grow both as isolated entities and as aggregates. They can equally grow on substrates. Moreover, the size and the number of crystals growing in an experiment depend on experimental conditions such as solution supersaturation, growth temperature and impurities present in the growth medium. These aspects of growth of crystals are described and discussed in this chapter.

7.1 Growth Morphology of Crystals

7.1.1 General Concepts

The external form (growth habit or macromorphology, or simply growth morphology) of a freely growing crystal is a polyhedron bounded by faces of various surface areas. The rates R of displacement of different faces (called face growth rates or normal growth rates) determine the final growth morphology. To predict the growth morphology, it is assumed that the growth rates of the faces are proportional to perpendicular distances from the center of the crystal. This also implies that the morphological importance (i.e. surface area) of different faces is proportional to their growth rate. Therefore, slow-growing faces appear in the morphology at the expense of fast-growing faces.

There exists a relationship between morphology and structure of crystals. The first attempts to describe the morphology of crystals were formulated in terms of surface free energy per unit area (Hartman, 1973, 1987; Toschev, 1973). The surface free energy is calculated by using periodic bond chains, connected nets or Donnay–Harker analysis of a series of faces likely to be present in the morphology (Grimbergen *et al.*, 1998; Meekes *et al.*, 1998). In this case, the morphology of a polyhedral crystal is determined on the postulate that the surface free energies per unit area of different faces of the polyhedron are proportional to their perpendicular distances from the center of the crystal.

The equilibrium morphology obtained from relative surface free energies of different faces composing a polyhedral crystal is frequently different from the steady-state growth morphology obtained from relative growth rates of different faces. This difference is due to the fact that the normal growth rate R of a face is determined by the structure of crystal–medium interface where growth entities are incorporated into the crystal and depends on growth kinetics (i.e. on supersaturation, temperature, impurities, and mass and heat transport processes).

Figure 7.1 illustrates two different growth morphologies of a crystal composed of two types of faces, namely F{1} and F{2} faces. Let us consider that F{2} are S faces, and F{1} are F faces. In the first case, because of a relatively high density of kinks in comparison

with that on the F faces, the S faces are eliminated in the final growth form (Figure 7.1a). In the second case, the F{2} faces appear when their displacement rate is reduced due to, for example, hindered supply of solute to them (Figure 7.1b). Thus, depending on the supersaturation available on the surface, the growth morphology of a polyhedral crystal composed of two types of faces can undergo a change. Figure 7.2 shows the change in the morphology of a crystal composed of two types of flat faces F{1} and F{2} growing according to the BCF mechanism. Obviously, the crystal is bounded by F{1} faces below σ_1 , by F{2} faces above σ_2 , and by both F{1} and F{2} faces for $\sigma_1 < \sigma < \sigma_2$.

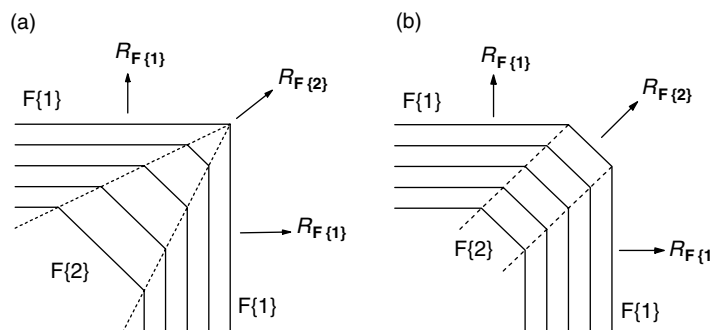


Figure 7.1 Schematic illustration of the difference in the development of F{1} and {2} faces lying in the same zone in terms of their relative displacement rates under different growth conditions, leading to the (a) elimination and (b) persistence of S face in the growth habit: (a) $R\{1\} < R\{2\}$ and (b) $R\{1\} > R\{2\}$

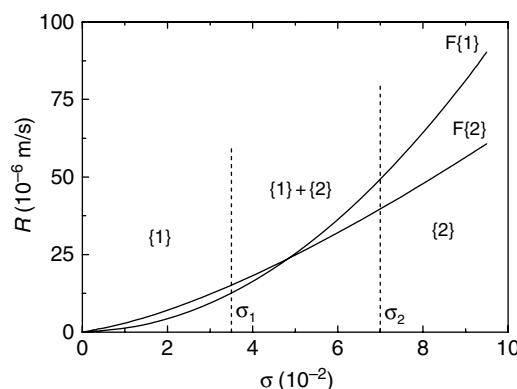


Figure 7.2 Growth morphology of a crystal composed of F{1} and F{2} faces in relation to supersaturation. Polyhedra {1} and {2} composed of F{1} and F{1} faces are formed at low and high supersaturations, respectively

While explaining the growth morphology changes in Figure 7.2 it was implicitly understood that the two types of faces remain smooth during the whole supersaturation interval. In fact, in view of this smooth nature of the interface, the BCF parabolic law

was used. However, as described in Section 3.3, a smooth interface may become rough with an increase in supersaturation. Thus, depending on the nature of the crystal–medium interface and the corresponding growth mechanisms, different morphologies may be anticipated. Figure 7.3 illustrates an excellent example of the changes in the morphology of NaHCO_3 crystals (monoclinic with $2/m$ symmetry) grown from aqueous solutions with increasing supersaturation. Isolated prismatic crystals are formed at $0 < \sigma < 12$, which show contact twinning in the supersaturation interval 12–23%. In the supersaturation interval 23–30%, the contact twinning turns into penetration twinning, which subsequently results in isolated dendritic branches in the supersaturation range 30–39%. In the range 39–49%, filling of dendritic branches results in twinned aggregates. At higher supersaturations, platy twins mutually overgrow, leading to the formation of spherulites. The main causes of the formation of contact twinning and dendrites, and filling of dendritic branches are associated with the formation of an increasing number of three-dimensional nuclei with increasing supersaturation and their subsequently aggregation to attain a configuration of lower surface free energy.

The evolution of growth morphology with supersaturation may be correlated with crystal growth processes (Sunagawa, 1981), as illustrated in Figure 7.4. Above σ^{**} the interface is rough and continuous (linear) growth occurs. Here crystals take dendritic to spherulitic morphology with increasing supersaturation. Below σ^{**} the interface is smooth and growth is possible by BCF or two-dimensional nucleation mechanism. In the region below σ^* , the BCF mechanism predominates and F faces grow by the outward motion of growth layers originating from dislocations. The crystal takes a polyhedral morphology bounded by flat faces. In the supersaturation region $\sigma^* < \sigma < \sigma^{**}$, growth by the two-dimensional nucleation mechanism predominates over the BCF mechanism. Since the probability of occurrence of two-dimensional nucleation is greater near the edges of faces, growth layers will advance inwards from edges and a hopper (skeletal) morphology will be produced.

It should be mentioned that growth from solution and vapor phases involves transport of crystallizing entities to the face of a crystal. Consequently, the supersaturation available on the surface may be smaller than that in the bulk of the medium (Section 3.8). In growth controlled by reactions and transport on a smooth surface (i.e. surface diffusion-controlled growth) the supersaturation on the surface approaches the bulk supersaturation, whereas in growth controlled by volume diffusion in the medium the supersaturation on the surface is lower than in the bulk. This supersaturation change also results in a supersaturation difference on the surface such that the supersaturation is the highest at edges and corners of the face, and is the lowest at the center of the face (Berg effect). Hopper growth of freely developing faces at high supersaturations and on faces in contact with the bottom of a crystallizer in solution growth even at moderate supersaturations is a consequence of this effect.

Experiments on the growth of crystals on self-nucleated seeds show a large number of faces in the initial stage of growth. On prolonged growth, some of the faces disappear whereas others grow in size, finally resulting in a steady-state growth morphology. It is also observed that, even when the crystals are sufficiently large and the final morphology is close to the steady-state morphology, new faces appear while the already-present faces disappear during their subsequent growth. According of the phenomenological approach of determination of growth morphology from relative growth rates of different faces,

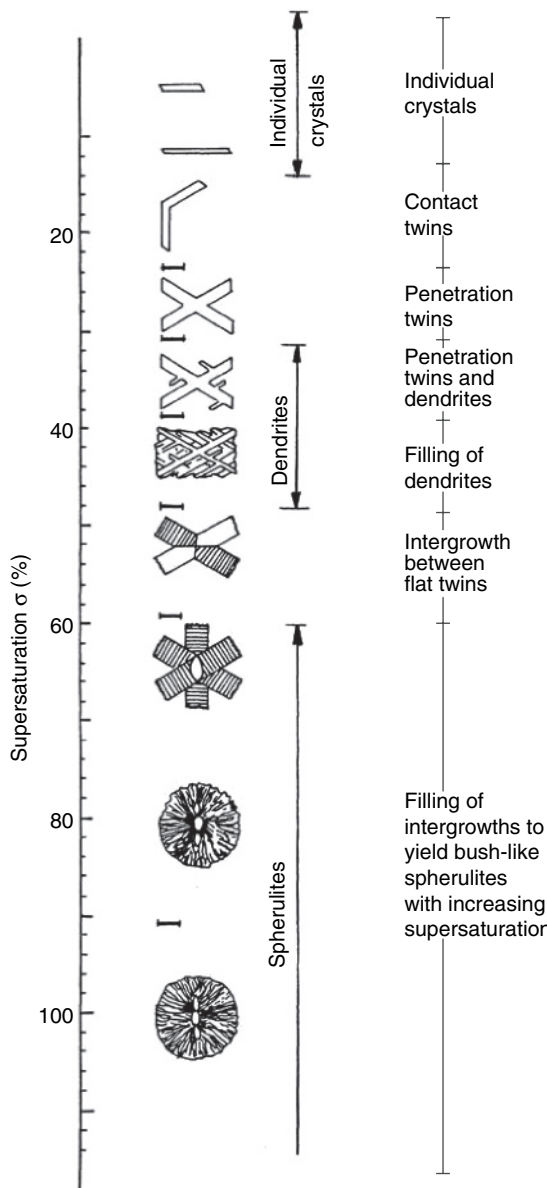


Figure 7.3 Schematic illustration of change in morphology of NaHCO_3 crystals with supersaturations. Adapted from S. Aslanian, I. Kostov, and H. Neels. *Krist. Tech.* **3**, 619. Copyright (1968), with permission from Wiley-VCH

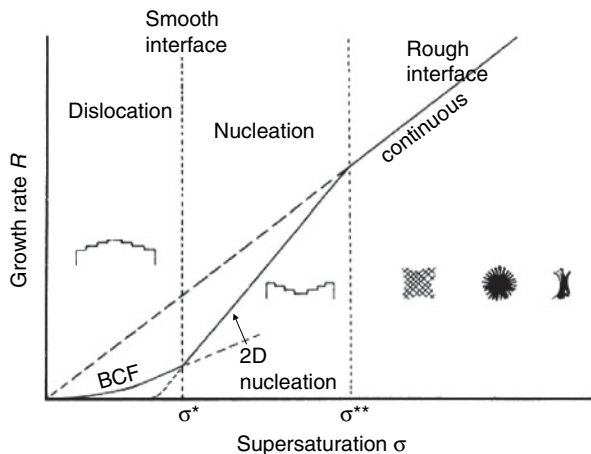


Figure 7.4 Schematic representation of the dependence of growth rate R on supersaturation σ for different growth mechanisms. Reproduced from I. Sunagawa. Crystals: Growth, Morphology and Perfection. Copyright (2005), with permission from Cambridge University Press

changes of this type in the growth morphology of crystals are caused by changes in growth conditions (i.e. on supersaturation, temperature, impurities, and mass and heat transport processes). Therefore, depending on the extent of fluctuations in growth conditions, some faces of the crystal may disappear, some other faces appear and still others simply remain present in the growth morphology. Conversely, since the evolution of growth morphology of crystals depends on growth rates, the above phenomenological concept that fast-growing faces disappear while slow-growing faces appear in the morphology still applies to predict the growth morphology.

Understanding of the causes of appearance and disappearance of faces during the evolution of crystal morphology is an active field of research (Rohl, 2003; Gadewar and Doherty, 2004; Prywer, 2005). In a series of papers during the last decade, Prywer (see Prywer, 2005) showed that (1) even fast-growing faces may increase their sizes and become morphologically important, whereas slow-growing faces may decrease their sizes and disappear from crystal morphology, and (2) the rate of change of cross-sectional size l_A of a given face A, defined as the tangential growth rate dl_A/dt , depends not only on its normal growth rate R_A but also on the growth rates of its neighbors 1 and 2 and their interfacial angles α and γ (see Figure 7.5). This implies that the crystallography of a crystal plays an important role in determining its morphology.

The starting point in the papers by Prywer (2005) and Gadewar and Doherty (2004) is the work of Kozlovskii (1957), who formulated a model to study the effect of two adjoining faces on the disappearance of a face in a two-dimensional crystal and derived the relation

$$l_A = \frac{R_1 \sin \gamma + R_2 \sin \alpha - R_A \sin(\alpha + \gamma)}{\sin \alpha \sin \gamma} t + l_0 \quad (7.1)$$

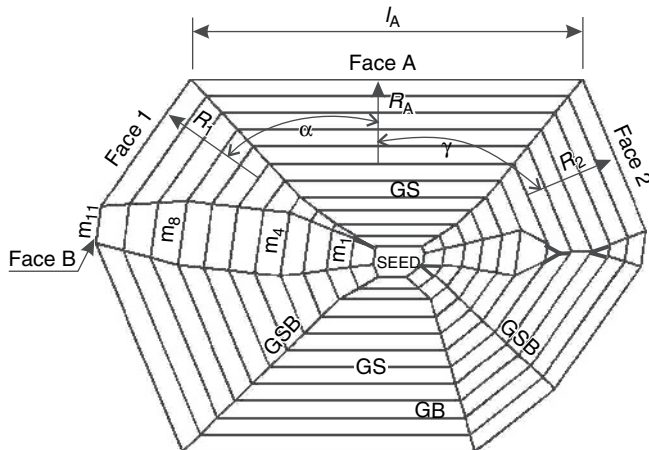


Figure 7.5 Cross-sectional size l_A of face A developing with time and its adjoining faces 1 and 2. Normal growth rates of faces A, 1 and 2 are R_A , R_1 and R_2 , respectively, α and γ are the interfacial angles between normals of faces, and GS and GSB denote growth bands and growth sector boundaries; m_1 – m_{11} are growth bands in the growth sector of face 1. Adapted from J. Prywer. Prog. Cryst. Growth Charact. Mater. **50**, 1. Copyright (2005), with permission from Elsevier

where R_A , R_1 and R_2 are the normal growth rates of faces A, 1 and 2, respectively, α and γ are the angles that a normal to the face A makes with faces 1 and 2, respectively, and l_0 is the initial size of the face at $t = 0$. The size l_0 is not indicated in Figure 7.5. From Equation (7.1) the critical growth rate R_A^{crit} , initially formulated by Borgström (1925), can be obtained by equating the numerator to zero (Szurgot and Prywer, 1991):

$$R_A^{\text{crit}} = \frac{R_1 \sin \gamma + R_2 \sin \alpha}{\sin(\alpha + \gamma)} \quad (7.2)$$

When $R_A > R_A^{\text{crit}}$, the size of the face decreases; when $R_A = R_A^{\text{crit}}$, the face maintains its size; but when $R_A < R_A^{\text{crit}}$, the face increases in size. For the analysis of the appearance and disappearance of face A in relation to the growth rates of faces 1 and 2, it is convenient to use the ratio R_A/R_A^{crit} expressed in the form (Prywer, 1996)

$$\frac{R_A}{R_A^{\text{crit}}} = \frac{\sin(\alpha + \gamma)}{(R_1/R_A) \sin \gamma + (R_2/R_A) \sin \alpha} \quad (7.3)$$

The physical meaning of the ratio R_A/R_A^{crit} is the following:

- (1) When $R_A/R_A^{\text{crit}} < 1$, face A increases. If it is not present initially, it will appear in the morphology.

- (2) When $R_A/R_A^{\text{crit}} = 1$, face A preserves its size. If it is not present initially, it will not appear in the morphology.
- (3) When $R_A/R_A^{\text{crit}} > 1$, face A decreases in size. If it is present initially, it will disappear in the morphology.

These situations are shown in Figure 7.5 by an increase, constancy and decrease in the length of growth bands in the growth sector of face 1.

From Equation (7.1) the instantaneous rate dl_A/dt of change of cross-sectional size (also called the tangential growth rate) of face A is given by (Prywer, 1999)

$$\frac{dl_A}{dt} = \frac{R_1 \sin \gamma + R_2 \sin \alpha - R_A \sin(\alpha + \gamma)}{\sin \alpha \sin \gamma} \quad (7.4)$$

Depending on whether $dl_A/dt > 0$, $dl_A/dt = 0$ or $dl_A/dt < 0$, the size of face A increases, remains unchanged or decreases. The higher the value of this rate, the larger is the corresponding face.

From Equation (7.4), it follows that the morphological importance of a given face is proportional to the value of the tangential rate dl_A/dt and is not directly proportional to the normal growth rate R_A of face A as stipulated in the determination of the steady-state growth morphology. The morphological importance of a face depends not only on its normal growth rate R , but also on the growth rates of the neighboring faces and on the crystal geometry represented by interfacial angles α and γ . Another consequence of this approach is that the geometry of the initial seed has a strong influence on the evolution of the growth morphology of crystals (Prywer, 2004; Gadewar and Doherty, 2004). However, except for the formulation of geometric conditions for the appearance and disappearance of face A surrounded by two neighboring faces 1 and 2, the basic mechanism of the role of adjoining faces in influencing the normal growth rate of face A in terms of sources of growth sites remains unexplained.

From an analysis of the existence of various faces in crystal morphology in relation to the relative normal growth rates and crystallographic structure of the crystal, Prywer (2003) concluded that faces for which $(\alpha + \gamma) \rightarrow \pi$ persist in growth morphology (stable faces) but those for which $(\alpha + \gamma) \ll \pi$ disappear (unstable faces). Therefore, the physical basis of the disappearance of a face in growth morphology may be attributed to the orientation of the neighboring faces with respect to the face A under consideration. If faces A are F faces, by their very nature it is expected that the inclined faces are S faces. Apart from ensuring their own growth, such faces can support edge nucleation in the vicinity of face A. Similarly, if the inclined face is a K face, its corners can serve as sources of nucleation for the face A. The basic mechanism is similar to that of the Berg effect discussed above.

The growth morphology of crystals may be determined by using connected net analysis carried out in two steps (Grimbergen *et al.*, 1998). First, direct chains are identified from the crystal structure as a sequence of strongly bonded possible growth units on the projection of different faces, and then from the direct chains surface graphs containing connected nets are found in the planes of these projections. In the case when individual growth units do not form direct parallel chains in a plane, one takes pairs of growth units lying in a particular direction to form the basic growth units. For example, this situation is encountered in Figure 4.32a where individual growth units, such as A and

B, form two half-layered connected nets such as $(200)_1$ and $(200)_2$, but AB pairs give monolayer connected nets $(100)_1$ and $(100)_2$ for the $\{010\}$ orientation (Sangwal *et al.*, 2003). Physically, two half-layered connected nets $(200)_1$ and $(200)_2$ for the $\{001\}$ and $\{010\}$ orientations, and the corresponding monolayer connected nets $(100)_1$ and $(100)_2$, are indistinguishable from each other in terms of bond energies, which are the same for a pair of two different half-layered nets and a pair of two different monolayer nets. A natural consequence of these requirements is that the relative concentrations of half-layered growth units (for example, A and B; Figure 4.31a) or monolayered growth units (for example, AB and BA; Figures 4.31a and 4.32a) available on the growing surface determine the rates of growth of parallel opposite $\{100\}$ and $\{010\}$ faces, leading to an anisotropy in their growth. In the case of stoichiometric composition of the two species, no preferred attachment of such growth units is expected on these faces. However, depending on the proportion of single and paired growth units in the growth medium, the growth rates of various faces of the morphology show different dependences on growth conditions such as supersaturation and temperature.

7.1.2 Effect of Additives on Surface Morphology

Interactions between additives and crystal interface are responsible for changes in the growth morphology of crystals. The nature of these interactions was discussed in Sections 4.11 and 4.12. Chemical interactions commonly occurring at the crystalline interface during adsorption of impurities are van der Waals, ionic, and hydrogen bonding. Among these interactions, van der Waals interactions are important both as an independent adsorption and as a supplementary mechanism in all types of adsorption. Formation of hydrogen bonds also plays an important role during the adsorption of impurities in the growth of both inorganic and ionic crystals. Ionic interactions are important in the crystallization of ionic salts from aqueous solutions.

Highly polarizable ions, such as Cr^{3+} , Al^{3+} and Fe^{3+} , have a pronounced effect on the growth of simple inorganic salts from aqueous solutions. In contrast, tailor-made additives are effective during the growth of both organic and inorganic crystals. They interact in specific ways with selected faces of crystalline materials, thereby inhibiting the growth of preselected faces, but the growth on other faces is not changed at all or only slightly. Thus, the morphology of the crystals is modified. For example, α -amino acids induce habit changes in sodium chloride (Fenimore and Thraikill, 1949) and gypsum ($\text{CaSO}_4 \cdot 2\text{H}_2\text{O}$) crystals (Cody and Cody, 1991). In the case of NaCl, the positive (NH_3^+) and negative (CO_3^-) charged moieties of α -amino acids fit at the $\{110\}$ faces but not at the $\{100\}$ and $\{111\}$ faces. Consequently, the less stable $\{110\}$ faces become more important in the growth morphology of NaCl crystals.

In terms of chemical interactions, polarizable cations are mobile and are expected to be adsorbed at kinks in the ledges on an F face. However, the molecules of tailor-made additives are immobile and adsorb on the surface terrace.

Direct observation of the velocity and morphology of monomolecular steps on the F faces of crystals in the presence of additives reveals that they decrease the growth rate and change the step morphology (Gratz and Hillner, 1993; Reyhani *et al.*, 2002; Dove *et al.*, 2004; Wang *et al.*, 2006a,b). As discussed in Section 4.3, additive molecules can lower the rate either by physically blocking the layers or by rendering kinks ineffective by adsorbing at them. Thus, the effects of additives on the morphology of growing surfaces

of bulk single crystals may be distinguished in accordance with the operative mechanism of adsorption (Sangwal, 1996). At low concentration of additives, the effects are reflected by changes in the configuration (overall shape) of growth structures (e.g. spirals and hillocks) and by changes in the thickness of layers composing them. The effectiveness of chemically different additives in changing the surface morphology is different.

Spirals and hillocks are composed of growth layers starting from growth centers and, consequently, their shapes reflect the shapes of growth layers composing them. Adsorption of additive particles at kinks in a growth ledge (layer) can reduce the rate of integration of growth units at them, and increase the average distance between kinks if the adsorbed impurity particles render them ineffective. The effect of both of these changes is to increase the polygonization of growth layers. However, in the case of adsorption at a surface terrace, the random distribution of impurity species and the curling tendency of layers between two adsorbed particles can lead to a rounding and roughening of growth layers. Both polygonization (Hottenhuis and Lucasius, 1986) and rounding of growth layers (Dunning and Albon, 1958; Dunning *et al.*, 1965; Dam and van Enckevort, 1984; Li *et al.*, 1990; Gratz and Hillner, 1993; Reyhani *et al.*, 2002; Sangwal *et al.*, 2003; Dove *et al.*, 2004; Wang *et al.*, 2006a,b) have been observed. In the case of the {010} faces of potassium hydrogenphthalate crystals, adsorption of different impurities at two different types of kinks has also been discerned (Hottenhuis and Oudenampsen, 1988). No observable effect on the morphology is found in some cases (Davey and Mullin, 1974; Chernov and Malkin, 1988).

Growth steps composing spirals and contours of steps formed by two-dimensional nucleation or initiated from edges and corners on different faces of crystals grown from pure solutions at low supersaturations usually correspond to the directions of connected nets obtained from crystal structure. For example, growth steps composing hexagonal macrospirals on the {010} face of AO crystals are parallel to the $\langle 001 \rangle$, $\langle 201 \rangle$ and $\langle 20\bar{1} \rangle$ directions (Sangwal *et al.*, 2003). These are precisely the directions of half-layered connected nets for this face. The contour of steps is altered by impurity particles because their adsorption at kinks of the steps leads to a change in the strength of the bonds of the connecting nets.

Growth layers emitted by an isolated source show that they are relatively thin and closely spaced near the source, but as one goes away from the source their height progressively increases (i.e. the layers become more and more bunched) and the distance between two neighboring layers increases (van der Eerden and Müller-Krumbhaar, 1986; Sangwal, 1998). This type of behavior of steps (i.e. bunching) results due to the deceleration of steps caused by the overlap of their diffusion fields (Chernov, 1961) and/or by the time-dependent adsorption of impurities (van der Eerden and Müller-Krumbhaar, 1986). An increase in the thickness of layers composing spiral layers has been observed both at low (Hottenhuis and Lucasius, 1986; Hottenhuis and Oudenampsen, 1988; Owczarek and Sangwal, 1990) and at relatively high impurity concentrations (Owczarek and Sangwal, 1990).

Adsorption of impurities on the steps of S faces may lead to the formation of bunched layers (called growth striations) (Sangwal and Rodriguez-Clemente, 1991). These growth striations are very similar to macrosteps on F faces (Sangwal and Rodriguez-Clemente, 1991).

7.1.3 Effect of Solvent on Crystal Morphology

The solvent has a strong influence on the habit of crystalline materials, because solvent molecules affect the growth rates of different faces appearing in the crystal morphology differently. The effect of solvent on the growth rates of different faces is associated with selective adsorption of solvent molecules on them. The effect of solvent on growth rates can be explained by two approaches (Weissbuch *et al.*, 1995). The first approach considers changes in the interfacial tension due to interactions between solvent and crystal molecules of the growing crystal face. An increase in the interfacial tension leads to a decrease in the growth rate, whereas a decrease in the interfacial tension leads to an increase in the growth rate. These effects may be explained in terms of surface entropy factor α (Section 3.3). The second approach is an extension of the role played by tailor-made impurities, where the growth rate of a crystal face is determined by the removal of solvent molecules adsorbed on the face. In this case, the face where solvent molecules are more strongly adsorbed than on other faces will grow more slowly than those where the solvent molecules are less strongly adsorbed.

An interesting example of the effect of solvents is the growth of *n*-alkanes (such as *n*-C₃₆H₇₄) from aliphatic solvents such as pentane, heptane and decane (Boistelle, 1980). The solubility of an *n*-alkane in each of these solvents is roughly the same, but the growth rate of the {110} faces of *n*-alkane crystals decreases drastically with increasing chain length of the solvent. The decreasing growth rate with increasing chain length of the solvents is due to the increasing adsorption energy of solvent molecules on the crystal surface as a result of van der Waals interactions.

Another example of the solvent-induced change in growth morphology is the organic compound alizarin (1,2-dihydroxy-9,10-anthraquinone), which crystallizes as long needles from the vapor and organic solvents such as acetone, acetonitrile, hexane, toluene and acetic acid, while flat triangular-shaped crystals are produced by alcohols such as ethanol, methanol and propanol (Algra *et al.*, 2005). In this case, the morphology change is not caused by the direct interaction of solvent molecules with the crystal surface itself, but by the interaction of partially deprotonated alizarin molecules with the solvent. This example demonstrates that a solvent can also play an indirect role in changing the morphology of a crystal. The solvent changes the structure of the solute molecules, which subsequently adsorb on several faces of the crystal, thereby blocking their normal growth.

The S and K faces usually appear at high supersaturations and from growth media containing impurities. The reduction in the displacement rate of S and K faces may be caused by a lack of supply of depositing material because the growth rate at high supersaturations is controlled by volume diffusion. In solution growth, the hindered supply of solute flux to the face by solvent molecules released from growth units during their integration into the crystal may also lead to a reduction in the growth rate of S and K faces. Moreover, if an S or K face contains a net charge, its normal growth rate may be reduced as a result of an increased adsorption on it of polar solvent molecules released from growth units. The reduction in the normal growth rate of S and K faces in the last case is associated with hindered solvation of solute ions adsorbed on the face due to a high charge density (i.e. net charge per unit area). The increasing morphological importance of the {111} face of crystals of rock-salt structure with increasing supersaturation is due to this effect (Hartman, 1973, 1987).

The stabilization of the {111} face of NaCl crystals from aqueous solutions containing formamide has been investigated using optical and atomic force microscopy (Radenović *et al.*, 2003). It was observed that (1) formamide and urea stabilize the {111} faces but larger molecules such as dimethylformamide and benzamide do not, (2) growth on the {111} faces proceeds by monomolecular, stabilized layers of height $d_{\{111\}} = \frac{1}{3}3^{1/2}a = 0.325$ nm (where $a = 0.563$ nm is the cell parameter), consisting of one Na^+ layer and one Cl^- layer, and (3) the steps originate from groups of dislocations as shallow growth hillocks with rounded tops and also from two-dimensional nucleation starting from the edges of the crystal. The authors suggested that growth of the {111} face of NaCl proceeds close to the roughening transition temperature, with monomolecular steps composed of the exposed layer of Na^+ ions on top of Cl^- ions, and the stabilization of the {111} faces is associated with better adsorption of formamide and urea molecules due to interaction of the negatively charged oxygen of these molecules with the Na^+ ion of the growing face.

In another study, Radenović *et al.* (2004) investigated the morphology of various alkali metal halide crystals from aqueous solutions containing formamide, and found that the stabilization of the {111} faces in the morphology of alkali metal halides occurs in the range of unit cell size between 0.462 and 0.628 nm and all the alkali metal halide crystals with unit cell size outside range are cubes. Apart from the effect of formamide described above, the effect of addition of solvents such as pyridine, aniline and glycine, molecules of which have positive charge concentrated on their nitrogen atoms, on the morphology of NaCl crystals was also investigated (Radenović *et al.*, 2004). It was observed that in the case of pyridine and aniline only {100} faces are formed but from solutions containing glycine well-developed faces with an average {110} orientation are produced. These results demonstrated that both the molecular size and fitting and the interaction between solvent molecules and surface ions are important for the stabilization of a K or S face. The interactions occur at the interface of a growing crystal in the double layer formed between the crystal and the bulk growth medium (Section 4.11).

7.1.4 Growth Morphodroms

The occurrence of a change in the growth mechanism of a face with a change in the supersaturation used for growth may result in a change in the relative growth rates of different faces appearing in the morphology. Since the overall morphology of a crystal, in general, consists of faces growing at the lowest rates, the morphology of a growing crystal may change with a change in the supersaturation. Similarly, the presence of an impurity in the growth system also leads to changes in the growth rates of various faces of the growing crystal. Crystals of alkali metal halides are well-known examples of such changes in growth morphology. The changes in the growth forms of crystals obtained by variations of both σ and c_i are described by (σ, c_i) curves, called growth morphodroms (Bienfait *et al.*, 1965; Kern, 1967). In the case of NaCl, at a supersaturation $\sigma > 0.23$, the growth habit changes from a cube with {100} faces to octahedra with {111} faces. It was also observed that certain impurities significantly lower the values of σ necessary for changing the external form, as shown in Figure 7.6. The value of supersaturation at which transition in the growth form takes place depends on the temperature of growth and the chemical properties of an impurity.

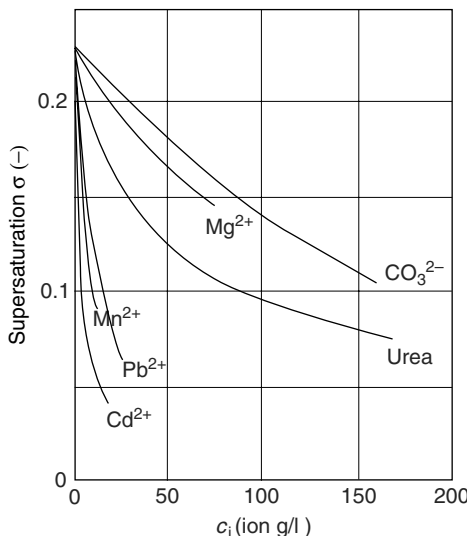


Figure 7.6 Morphodroms of NaCl in the presence of different impurities effective in changing the {100} form to the {111} form of NaCl crystals. The {100} and the {111} forms appear below and above the $\sigma(c_i)$ curve for an impurity. Reproduced from M.R. Bienfait, R. Boistelle and R. Kern. In: R. Kern (Ed.), Adsorption et Croissance Cristalline, p. 577. Copyright (1965), with permission from CNRS, Paris

The habit-modifying behavior of impurities in alkali metal halide crystals is caused by the formation of a two-dimensional adsorption layer composed of impurity particles, solvent molecules and crystal radicals/ions at the crystal–medium interface (Section 4.11). For example, in the case of growth of NaCl crystals from aqueous solutions containing Cd²⁺ ions, the {111} face is covered by an adsorption layer of CdCl₂·2NaCl·3H₂O (Boistelle and Simon, 1974; Radenović *et al.*, 2005). The adsorption layer is essentially a mixed monolayer of Cd²⁺ and water (with occupancies of 0.25 and 0.75, respectively) in direct contact with the top Cl⁻ layers of the {111} face underneath, such that the structure of the {111} faces is stabilized. The growth of the stabilized faces proceeds by monomolecular and higher steps originating from dislocations and crystal edges, implying that the {111} faces behave as F faces.

The effect of an impurity is not confined to changes in the growth rates R of different faces appearing in the growth habit, but the surface morphology of the faces is also altered. Figure 7.7 summarizes the results of the observation of growth forms and surface morphology of KCl crystals in relation to supersaturation and concentration of Pb²⁺ ions. It was suggested (Li *et al.*, 1990) that the habit change of KCl crystals from cubic to octahedral is due to the adsorption of Pb²⁺ ions as PbCl₂ crystallites preferentially along the ⟨110⟩ steps of growth layers on the {100} face. Preferential adsorption of PbCl₂ crystallites reduces the advancing velocity of the layers in perpendicular directions. The piling up of these ⟨110⟩ steps results in an S-type face, rather than the original K-type face consisting of only kinks. As a result, initially small hoppered {111} faces develop in the habit. The {111} faces become wavy as growth proceeds without distinguishable

growth steps on it. This is followed by the advancement of layers from the edges or corners of the face. Inhibition of the advancing steps by PbCl_2 precipitates, and coverage of the developing face by a PbCl_2 film, entirely block the normal growth of the face. At this stage the character of the face resembles that of an F face. After some time, growth spirals begin to appear from the central portion of the face. Growth spirals become circular and the step height increases with increasing impurity concentration. As shown schematically in Figure 7.7, both {100} and {111} faces become hoppered above certain values of supersaturation, but the transition from a flat {111} face to a hoppered one takes place at a Pb^{2+} concentration much higher than that for the {100} face.

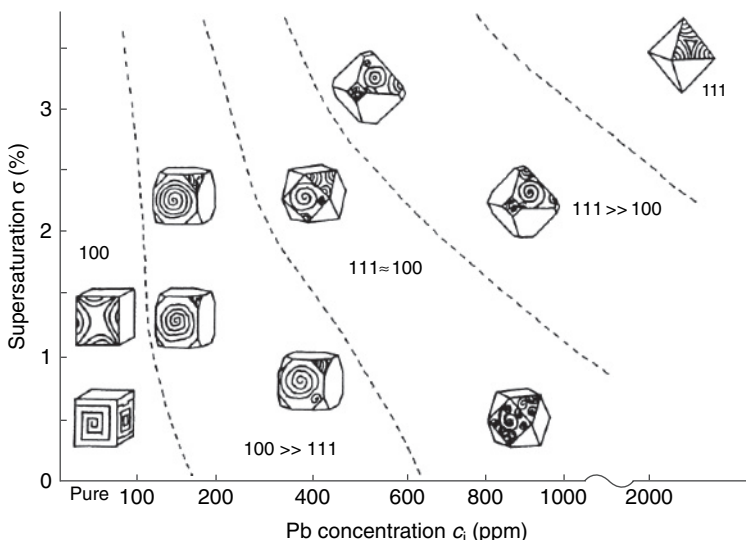


Figure 7.7 Growth forms and surface morphology of KCl crystals in relation to supersaturation and concentration of Pb^{2+} ions. Reproduced from L. Li, K. Tsukamoto, and I. Sunagawa. J. Cryst. Growth **99**, 150. Copyright (1990), with permission from Elsevier

The explanation of the effect of PbCl_2 impurity on the modification of the morphology of KCl crystals from aqueous solutions is not in conflict with the above concept of formation of a two-dimensional adsorption layer on the growth faces of alkali metal halide crystals. The contention essentially rests with the chemical composition of the two-dimensional adsorption layer.

The concept of the formation of a two-dimensional adsorption layer composed of a chemical compound resulting from the reaction of additive with the solution has frequently been used to explain the modification of the morphology of various crystals. For example, van Panhuys-Sigler *et al.* (1988) suggested that dominance of the {211} form over the {011} form of PbCl_2 crystals grown in the presence of different chlorides (KCl , NH_4Cl and CdCl_2) may be due to the formation of a two-dimensional adsorption layer of $\text{Pb}(\text{OH})\text{Cl}$. However, they also pointed out that preferential adsorption of OH^- ions on the {211} faces may be responsible for the formation of this $\text{Pb}(\text{OH})\text{Cl}$ layer, because addition of aqueous solution of a chloride such as NaCl to lead acetate solution

leads to the crystallization of $\text{Pb}(\text{OH})\text{Cl}$ instead of PbCl_2 . Addition of H^+ ions in the form of an acid (e.g. HCl) suppresses the inhibiting effect of OH^- ions because they start to compete with OH^- ions for the same adsorption sites. Therefore, the growth rate of the {211} faces is increased and PbCl_2 crystals become more elongated along the c axis, while the {011} faces appear as terminal faces in the PbCl_2 habit (see Figure 7.8b).

Figure 7.8a and b show the morphodroms of PbCl_2 crystals grown from aqueous supersaturated solutions in the presence of KCl , NH_4Cl and CdCl_2 additives and from solutions containing HCl, respectively. The dashed lines indicate approximately the boundary between regions of different habit. In Figure 7.8a, the dominant forms are shown, whereas in Figure 7.8b, different forms composed of combinations of the {010},

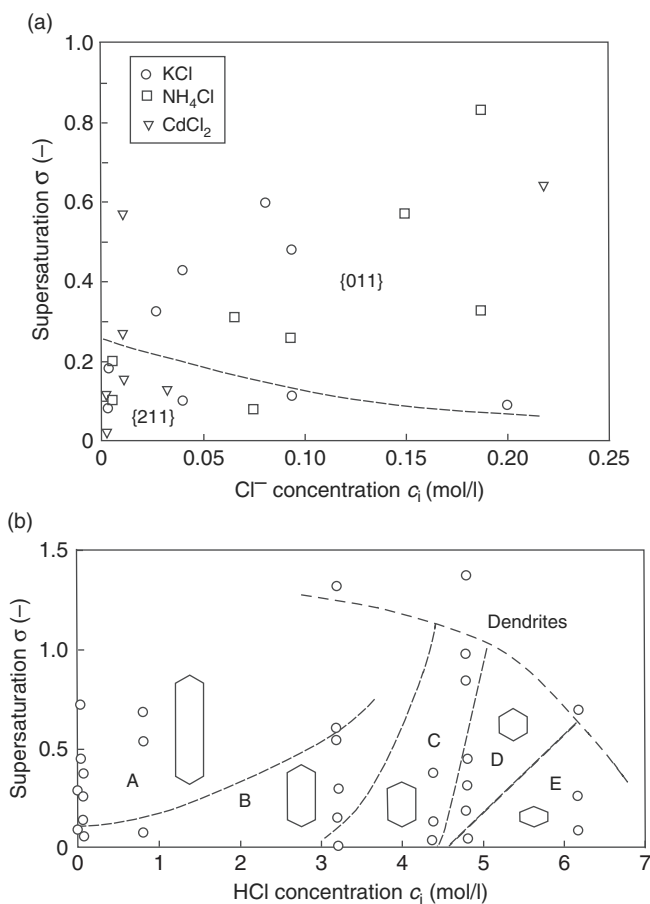


Figure 7.8 Morphodroms of PbCl_2 crystals grown from aqueous supersaturated solutions in the presence of different additives: (a) KCl , NH_4Cl and CdCl_2 additives and (b) HCl additive. In (a) the amount of the additive is expressed as moles of Cl^- ions per liter. Reproduced from M. van Panhuys-Sigler, P. Hartman, and C.F. Woensdregt. J. Cryst. Growth **87**, 554. Copyright (1988), with permission from Elsevier

{100}, {110} and {120} faces with the {111}, {011} and {121} as terminal faces are observed.

The above results may qualitatively be explained from the standpoint of the kinetic effects of impurities on the growth rates of different faces, without restriction to F, S or K faces. For example, when impurity adsorption occurs at kinks in steps on faces 1 and 2, one may write the relative growth rates $R_{\text{rel}} = R/R_0$ in the form [cf. Equation (4.28)]

$$R_{\text{rel}(1)} = 1 - (\sigma_1^0/\sigma)\theta_1 \quad (7.5)$$

$$R_{\text{rel}(2)} = 1 - (\sigma_2^0/\sigma)\theta_2 \quad (7.6)$$

respectively, where R and R_0 are the growth rates of a face in the presence and absence of the impurity, $\sigma^0 = \gamma_i a/kT x_0$ [cf. Equation (4.29)], and θ is the fractional coverage of the impurity. Using the Freundlich adsorption isotherm [see Equation (4.13)], one obtains the following relation between σ and c_i :

$$\sigma = K_1(1 - K_2 c_i^{m_2 - m_1}) \quad (7.7)$$

where the exponents m_1 and m_2 are less than unity, $K_1 = k_1 C_i^{m_1} / [R_{\text{rel}(1)} - R_{\text{rel}(1)}]$, and $K_2 = k_1/k_2$ with $k_1 = \sigma_1^0 m_1 / c_{i1}^{* m_1}$ and $k_2 = (\sigma_2^0 m_2 / c_{i2}^{* m_2})$. Different $\sigma(c_i)$ plots predicted by Equation (7.7) are illustrated in Figure 7.9.

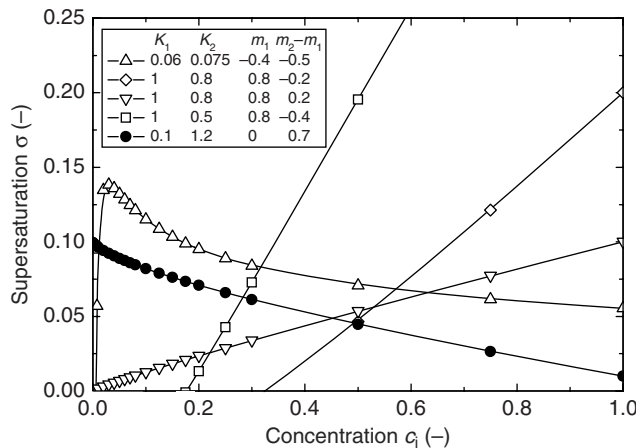


Figure 7.9 Different $\sigma(c_i)$ plots predicted by Equation (7.7). The values of constants K_1 , K_2 , m_1 and $(m_1 - m_2)$ are given in the inset

It can be seen from Figure 7.9 that with appropriate values of the constants in Equation (7.7), practically all types of experimentally determined $\sigma(c_i)$ boundaries are reproduced by the above relation. Another interesting feature follows from the plots. Certain combinations of the constants predict a peak at some value of c_i , although such maxima have not been reported in the $\sigma(c_i)$ morphodroms.

The growth morphology of crystals can also be changed when two impurities are simultaneously used in the growth medium. In such cases the concentration of one impurity required to bring about the same change in crystal morphology decreases at the expense of an increase in the concentration of the other impurity (Bienfait *et al.*, 1965). This behavior follows from the model of adsorption of two competing impurities (Section 4.3.6).

Morphodroms similar to Figure 7.9 with $\sigma(c_i)$ boundaries are observed for habit modification as a function of temperature (Inoue and Nishioka, 2000). Figure 7.10a and b show the growth morphology of NaBrO_3 crystals grown from pure aqueous solutions and from solutions containing 1.15 mol% acetic acid, respectively. The following features may be noted from this figure:

- (1) The domain of the {100} form (cubic habit) is located in a higher temperature region than the {111} form (tetrahedral habit) in a wide range of supersaturation σ for both pure and impurity-containing solutions.
- (2) The transition temperature delineating the boundary of the {111} to the {100} form decreases with an increase in supersaturation for both pure and impurity-containing solutions.
- (3) In contrast to growth from pure solutions, for growth from impurity-containing solutions the transition temperature decreases abruptly with increase in supersaturation, and the highest value of the transition temperature is shifted to a lower value of σ .
- (4) The transition temperature for habit modification from the {111} to the {100} form is higher for growth from impurity-containing solutions than that for growth from pure solutions.

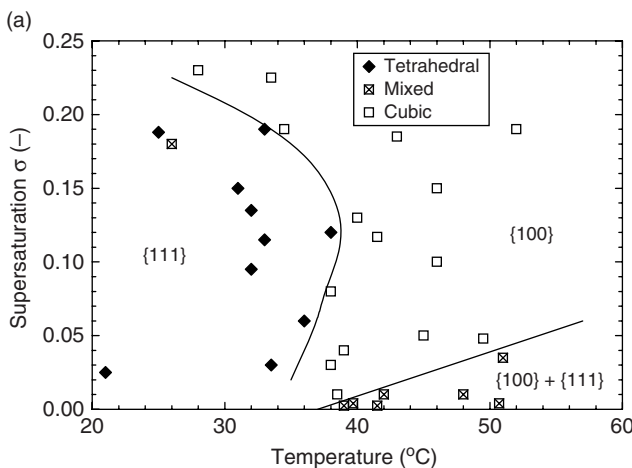
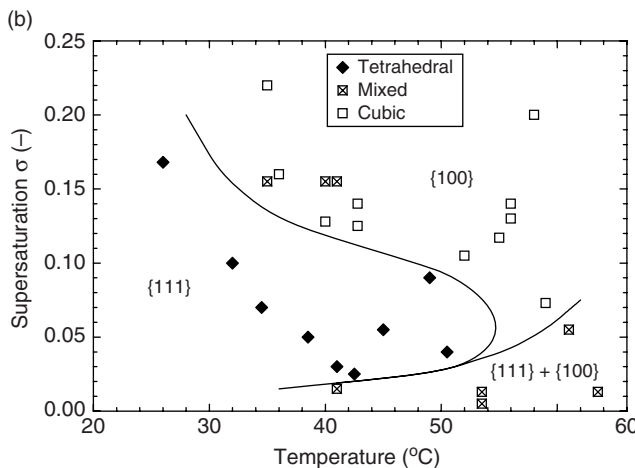


Figure 7.10 Growth morphodroms of NaBrO_3 crystals shown as plots of supersaturation as a function of temperature. Crystals were grown (a) from pure aqueous solutions and (b) from solutions containing 1.15 mol% acetic acid. Similarity between these morphodroms and those in Figure 7.8 may be discerned. Reproduced from T. Inoue and K. Nishioka. J. Cryst. Growth **212**, 507. Copyright (2000), with permission from Elsevier

**Figure 7.10** (Continued)

The above observations may be explained by considering the effects of both impurity and temperature. The influence of temperature is included in the growth rate R_{rel} and impurity adsorption processes [for example, the constants m_1 and m_2 in Equation (7.7)].

7.2 Ostwald Ripening and Crystal Size Dispersion

During the nucleation stage of a new phase, a large number of stable nuclei are formed either simultaneously or continuously, referred to as instantaneous or progressive nucleation (Section 2.4.2). In the latter nucleation, it is expected that the visible crystals are inherently of different sizes because the stable nuclei formed during a growth run grow for different durations. In the former case, however, since the stable nuclei are formed at the same time, one expects the visible crystals to be of the same size, provided that (i) the growth environment available for the growth of stable nuclei is the same and (ii) the crystal–medium interface ensures the same growth rate. In practice, both of these conditions may not be fulfilled because it is always possible that the growth conditions in the entire volume of the medium are not uniform and the defect structure of different growing crystals does not remain the same during an experiment. These factors lead to the formation of crystals of different sizes.

When crystals of different sizes grow in a system closed for mass transfer, the supersaturation available for growth decreases steadily with virtual cessation of growth. Then the crystalline solid with a particular crystal size distribution comes in contact with the saturated solution. The size distribution undergoes a change with time because the system tends to achieve a state corresponding to the minimum Gibbs free energy G according to the relation

$$dG = -SdT - Vdp + \sum \mu_i dn_i + \gamma dP \quad (7.8)$$

where S , T , V and p are the entropy, temperature, volume and pressure of the system, respectively, n_i is the number of species i , μ_i is their chemical potential, and γ and P are the surface free energy and the area of the solid particle, respectively. At given T , V and p conditions, the system tends to achieve the minimum energy state by changes in the surface area P of the crystalline particles. This occurs by changes in the solubility of the particles as a function of their size by the Gibbs–Thomson (also called Ostwald–Freundlich) relation

$$\ln[c(r)/c_0] = \gamma\Omega/rk_B T \quad (7.9)$$

where $c(r)$ is the solubility of the solid particle of radius r , c_0 is the equilibrium solubility, and Ω is the molecular volume. Thus, small particles dissolve and deposit on large particles, thereby decreasing the total surface area. This process is called Ostwald ripening.

Ostwald ripening is important in crystallization processes at high supersaturations, when crystallization is rapid and the crystal size is small. The role of Ostwald ripening is to change the crystal size distribution with time in a suspension of crystals in equilibrium with its saturated solution. It is an important phenomenon when one is concerned with obtaining fine particles or changes in crystal size distribution of the product before drying.

The size dependence of the solubility of crystalline particles results in a difference in supersaturation as a function of particle size. The smaller particles will be at a lower supersaturation than larger particles. Consequently, smaller particles grow at a lower rate than the larger ones. This is a case of size-dependent growth, but this mechanism becomes important when the crystal size is smaller than about 1 μm .

For larger crystals, size-dependent growth is also possible when the density of dislocations participating in growth increases as the crystal size increases. Thus, larger crystals growing by the BCF surface diffusion mechanism will grow faster than smaller crystals (see Section 3.6). In another situation, it is possible that smaller crystals are devoid of dislocations, but with an increase in size dislocations are developed in the growing surface. In this case also, smaller crystals growing by two-dimensional nucleation will grow at a lower rate than larger crystals which grow by the BCF surface diffusion mechanism. This results in the final product composed of crystals of different sizes.

Crystals of different sizes are frequently observed in mass crystallization, and this phenomenon is usually referred to as growth rate dispersion. By this term one understands that crystals of the same size and material exposed to identical conditions of supersaturation, temperature and hydrodynamics do not necessarily grow at the same rate. This is not the same as size-dependent growth in which crystals of different sizes grow at different rates.

Two different mechanisms have been proposed to explain growth rate dispersion (Söhnel and Garside, 1992; Myerson and Ginde, 1993). The first mechanism considers a distribution of growth rates for the crystal population for given growth conditions, but each individual crystal grows at a constant rate. This means that at steady-state conditions nuclei are formed with a distribution of growth rates and two nuclei in a crystallizer grow at a constant but different rates. Crystal fragments produced by attrition, secondary nuclei and single crystals produced by primary nucleation show this behavior. According to the second mechanism all crystals have the same time-averaged growth rate, but the growth

rates of individual crystals can fluctuate significantly with time. This means that two different crystals growing under identical conditions can have different growth rates at any time, but their time-averaged growth rate over a long time period remains the same.

Growth rate dispersion is usually explained from the standpoint of the BCF theory of crystal growth (Söhnel and Garside, 1992; Myerson and Ginde, 1993). According to the BCF theory, the growth rate of a crystal depends on the density of dislocations emerging on the growing surface. A higher density of screw dislocations leads to an increase in the growth rate. Collisions of growing crystals with the impeller, crystallizer walls and each other cause damage to them, resulting in new screw dislocations during growth. This type of behavior is especially expected for crystals grown by secondary nucleation. It should be mentioned that the growth rate of a crystal can also increase with an increase in the density of edge dislocations (see Section 3.6.4).

7.3 Crystal Size Distribution

The successful crystallization of a material on a large scale is intimately connected with the size, shape and size distribution of material particles, for various reasons. A small mean size of crystals causes problems with their centrifugation, washing and packaging. In some cases, a wide range of the size of product crystals ensures variations in time for their dissolution. Therefore, understanding of the genesis of the size and size distribution of crystals is of scientific and practical importance.

In every crystallization process occurring in a free volume over a long period of time, the final product is composed of a large number of crystalline particles in a wide range of sizes and, in many cases, the simultaneous presence of polymorphs or chemical phases of different shapes. Depending on the crystallization conditions, the crystals of different sizes formed in a growth run can also differ in shape. Figure 7.11 shows an excellent example, reported by Kitamura (2001), of the change in the size and morphology of calcium carbonate particles for two different addition rates of concentration $c = 0.05$ and 0.2 mol/l of sodium carbonate solutions to calcium chloride solutions of the same concentration. Similar observations have also been made more recently by Andreassen (2005). The crystals produced by 0.05 and 0.2 mol/l solutions are presented Figure 7.11a and c and Figure 7.11b and d, respectively. In these photographs, prismatic crystals are calcite and spherulites are vaterite. The following features may be noted from Figure 7.11:

- (1) The larger spherulites of vaterite are formed by the aggregation of smaller spherulites composed of small crystallites.
- (2) With an increase in solution concentration from 0.05 to 0.2 mol/l , the proportion of vaterite spherulites having relatively smooth surfaces increases while the crystal size decreases (see Figure 7.11a and c).
- (3) The vaterite spherulites are irregularly shaped at high solution concentration and small addition rate (Figure 7.11d), and their size is smaller than that at small addition rate (Figure 7.11b and d).

The above features are associated with (1) crystallization of metastable vaterite and its subsequent transformation to calcite in accordance with the Ostwald rule of stages and (2) the occurrence of secondary nucleation favored by small addition rates.

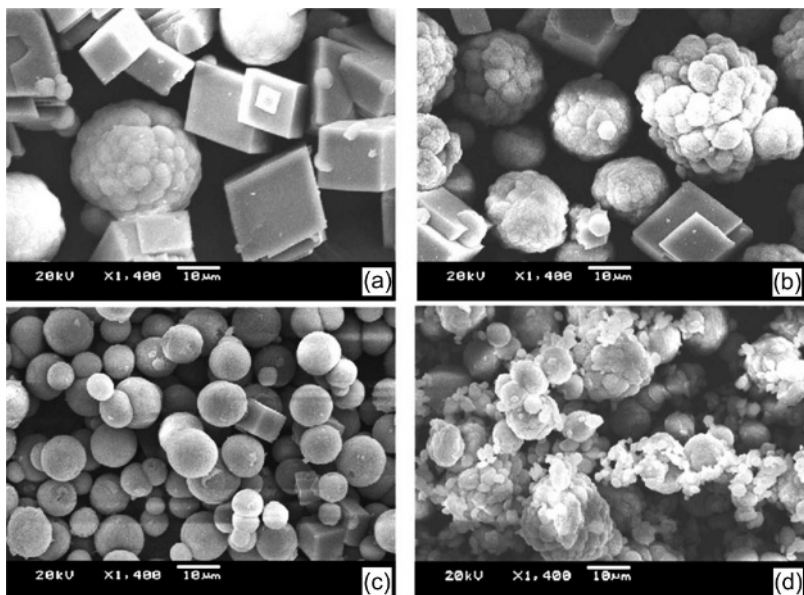


Figure 7.11 SEM photographs of calcium carbonate particles obtained by addition of sodium carbonate solutions to calcium chloride solutions at different addition rates: (a, c) 5 mol/s and (b, d) 0.05 mol/s. Concentration of reactants: (a, c) 0.05 mol/l and (b, d) 0.2 mol/l. Reproduced from M. Kitamura. J. Colloid Interface Sci. **236**, 318. Copyright (2001), with permission from Elsevier

The final product is a resultant of a variety of processes involving (1) formation of stable nuclei, (2) growth of the stable nuclei, (3) aggregation of nuclei, (4) Ostwald ripening, and (5) transformation of a metastable phase or polymorph into a stable one. Moreover, the processes of formation of stable nuclei and their subsequent growth may be complex. In the former case, the presence of trace amounts of unintentional impurities may lead to heterogeneous nucleation, whereas the presence of the already growing crystals in a crystallization run may lead to secondary nucleation. Similarly, depending on the growth conditions, the kinetics of the growth of the crystals may be controlled by volume diffusion or surface reactions and may depend on the size of the crystals and their defect density. Therefore, modeling of distribution of crystal size in terms of crystallization conditions is a formidable task.

Several approaches have been advanced to model crystal size distribution (CSD), which may be divided into three categories: (1) population balance approach, (2) balanced nucleation-growth approach and (3) size-dependent growth approach. These approaches are described below.

7.3.1 Population Balance Approach

The population balance approach was proposed by Randolph and Larson (1971, 1988) to predict the product CSD from a continuous stirred tank reactor (CSTR) (also referred to as

continuous mixed-suspension mixed product removal crystallizer; MSMPR) under steady-state conditions. The important assumptions involved in this model are the following:

- (1) CSD is the same as that found within the crystallizer.
- (2) The particles are formed only by nucleation and increase in size occurs by growth.
- (3) There is no breakage, attrition and agglomeration of growing particles.
- (4) The growing particles have the same shape.

According to the population balance approach, if the crystallization system under consideration follows McCabe's law that growth rate $R \neq R(L)$, the population density dn in the size range between L and $L + dL$ is given by

$$\frac{dn}{dL} = -\frac{n}{R\tau} \quad (7.10)$$

where n is the population density at size L and τ is the retention time, equal to the reaction volume V divided by the flow rate Q ($\tau = V/Q$). Integration of Equation (7.10) gives

$$n = n_0 \exp(-L/R\tau) \quad (7.11)$$

where n_0 is the population density for zero-sized crystals. Thus, according to Equation (7.11), a plot of $\ln n$ against L predicts a straight line with intercept $\ln n_0$ and slope $= 1/R\tau$, from which one can calculate the growth rate R for a known value of τ .

Figure 7.12 illustrates the plots of $\ln n$ against L for two different sets of experimental data reported for the sucrose–water system in MSMPR crystallizers by Belter *et al.* (1988) and Berglund and de Jong (1990). It can be seen that the data of Belter *et al.* (1988) are

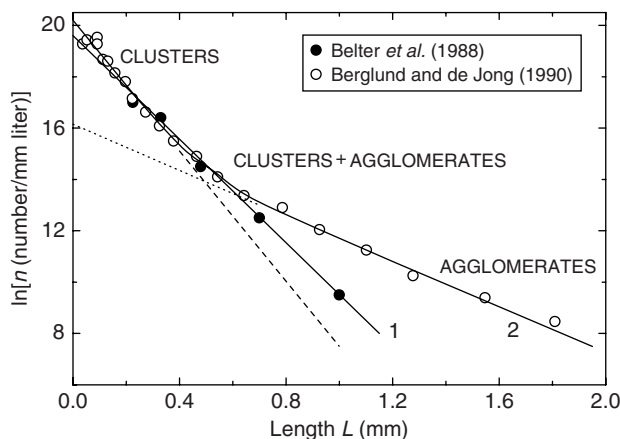


Figure 7.12 Plots of $\ln n$ against L for two different sets of experimental data for the sucrose–water system in MSMPR crystallizers. Note that data represented by filled circles (curve 1) can be fitted by a single growth rate distribution [i.e. in Equation (7.11) one value of R], whereas data denoted by open circles (curve 2) require two growth rate distributions (i.e. the sum of two exponentials). Adapted from K.A. Berglund. In: A.S. Myerson (Ed.), Handbook of Industrial Crystallization, p. 89. Copyright (1993), with permission from Elsevier

well described by Equation (7.11), but a single growth rate distribution is insufficient to explain the data of Berglund and de Jong (1990). In the latter case, a combination of two growth rates (i.e. the sum of two exponentials) is necessary to describe the data. It is interesting that the experimental data obtained in the two studies agree well for L smaller than about 0.4 mm. In fact, a strong upward curvature at smaller sizes of about 0.1 mm is observed in many cases in the plot of $\ln n$ against L (Berglund, 1993).

Another typical violation of Equation (7.11) of the conventional population balance is a relatively symmetrical size distribution around an average crystal size seen in Figure 7.13. Moreover, Equation (7.11) does not explicitly describe the dependence of crystal size distribution and average crystal size on experimental conditions such as temperature, solubility and molar addition rate (Leubner, 2000). The effect of additives on crystal size distribution, as observed by Kurutz *et al.* (2003) and Roque *et al.* (2004), also remains unexplained. The growth rate R in Equation (7.11) is a mass-balance variable and is not related to growth conditions.

The strong upward curvature, as seen in curve 2 in Figure 7.12, has been attributed to size-dependent growth, growth rate dispersion and agglomeration (Berglund, 1993). In the case of size-dependent growth, the following empirical dependence of growth rate R on crystal size L is assumed (Abegg *et al.*, 1968):

$$R = R_0(1 + fL)^b \quad (7.12)$$

where the empirical constants $f > 0$ and $b < 1$. Then, from the population balance, the following $n(L)$ dependence is obtained (Abegg *et al.*, 1968; Berglund, 1993):

$$n(L) = K n_0 (1 + fL)^{-b} \exp[-(1 + fL)^{1-b}/R_0 \tau f(1 - b)] \quad (7.13)$$

where $K = \exp[1/R\tau f(1 - b)]$ and $b < 1$. Obviously, when $f = 0$, there is no size-dependent growth and the situation corresponds to that given by Equation (7.11). Moreover, as expected from Equation (7.12), the upward curvature is obtained when $0 < b < 1$.

When growth rate dispersion occurs, the overall population balance yields an $n(L)$ relation which gives a linear plot of $\ln n$ against L with a large mean size than that predicted from the growth rate (Berglund, 1993). Agglomeration, as is commonly observed during the precipitation of proteins without intentionally added impurities and several ionic compounds both without and in the presence of additives (Figure 7.11), also results in a curvature similar to that found in size-dependent growth and growth rate dispersion (Hoyt, 1978; Hartel and Randolph, 1986). According to this approach, a higher slope at smaller size L is due to the growth of isolated clusters, whereas a smaller slope at larger size is caused by agglomerates. The regions of clusters and agglomerates are shown in Figure 7.12. However, Glatz *et al.* (1987) reported that agglomeration and breakup can lead to the appearance of a local maximum in the plots of $\ln n$ against L .

The rate of aggregation of particles is characterized by an aggregation kernel $\kappa(L, \lambda)$, which is a measure of the frequency of collisions between particles of size L and λ forming stable aggregates. The aggregation kernel is usually written in the form (Bramley *et al.*, 1996, 1997)

$$\kappa(L, \lambda) = \kappa_0 f(L, \lambda) \quad (7.14)$$

where κ_0 is size independent and depends on the operating conditions. The factor $f(L, \lambda)$ is some function of particle size and reflects the mechanism responsible for aggregation. Hartel and Randolph (1986) list several possible kernels. For more details on population balance approach and its modified versions, the reader is referred to Berglund (1993) and Randolph and Larson (1971, 1988).

It is frequently observed experimentally that the CSD is relatively complex. One of the common observations in a crystallization run is that, with an increase in their size L , the number of crystals n first increases and then decreases against L , showing thereby a local maximum in the plot of $\ln n$ against L (see, for example, Bramley *et al.*, 1996; Kile *et al.*, 2000; Gomez-Morales *et al.*, 2001; Hounslow *et al.*, 2001; Kurutz *et al.*, 2003; Roque *et al.*, 2004; Andreassen, 2005). It is also observed (Bramley *et al.*, 1996; Hounslow *et al.*, 2001) that the number of crystals decreases and the CSD broadens with an increase in crystallization time in a crystallization run, a phenomenon attributed to aggregation (Figure 7.13). These observations are difficult to explain from the standpoint of the traditional population balance approach.

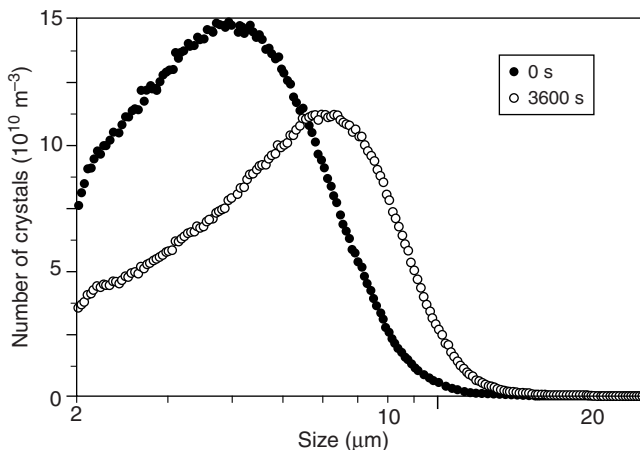


Figure 7.13 Crystal size distribution of calcium oxalate monohydrate (COM) at the beginning and the end of a crystallization run. Reproduced from A.S. Bramley, M.J. Hounslow, and R.L. Ryall (1996). J. Colloid Interface Sci. **183**, 155. Copyright (1996), with permission from Elsevier

Hounslow *et al.* (2001) proposed a micro-mechanical model for the rate of aggregation in terms of a collision rate constant $C_{L,\lambda}$ and segregation efficiency $\psi_{L,\lambda}$ during precipitation of inorganic salts from aqueous solutions, given by

$$\psi_{L,\lambda} = \kappa_{L,\lambda}/C_{L,\lambda} \quad (7.15)$$

They showed that the average efficiency ψ is related to a dimensionless parameter M , which depends on, among others, the yield strength σ_y of the crystallizing particles and their growth rate R . They also found that their model predicts peaks in the particle size

distribution and that, with an increase in time, the peaks decrease in height and shift to a larger value of particle size.

From the above discussion on the role of crystal agglomeration in CSD, it may be concluded that various process parameters that depend on the microscopic properties of specific crystal faces and their interaction with the solvent determine the influence of crystal agglomeration on CSD. Using molecular modeling, efforts have been made recently in this direction (Simons *et al.*, 2004; Brunsteiner *et al.*, 2005).

7.3.2 Balanced Nucleation-Growth Approach

The balanced nucleation and growth (BNG) model takes into account both nucleation and growth of stable crystals during the initial phase of their formation, and describes the number of crystals formed from the control variables of crystallization (Leubner, 2000, 2002). The main assumptions involved in BNG model are as follows:

- (1) In the initial phase only nucleation takes place and the nucleation process can be described by the classical nucleation theory [see Equation (2.22)], i.e.

$$J = J_0 \exp \left[-\frac{16\gamma^3 \Omega^2}{3k_B T^3 (\ln S)^2} \right] \quad (7.16)$$

where J_0 is a supersaturation independent constant, γ is the surface energy, Ω is the molecular volume, k_B is the Boltzmann constant, T is the temperature in kelvin, and S is the supersaturation ratio.

- (2) Formation of new nuclei and their subsequent growth compete until the end of nucleation.
- (3) During the nucleation period, all nuclei grow at a constant maximum growth rate R_m , but after this period the growth rate $R < R_m$. Thus, the existing crystal population grows with this maximum growth rate R_m until the end of nucleation.
- (4) Factors such as supersaturation as a function of time, molar addition rate during nucleation involving reactions and initial nucleation rate can be included in the model.

The growth rate R is determined by the material balance of added material and its consumption by growth, and is defined in terms of crystal size L by the relation

$$R = dL/dt = \delta_{\text{add}} \Omega / 3\beta_s L^2 N \quad (7.17)$$

where δ_{add} is the molar addition rate $d(\text{mol})/dt$, β_s is the shape factor for crystals and N is the number of crystals in the reactor. Since the growth rate R is obtained from material balance, this growth rate R is independent of temperature, solubility, diffusion and other reaction conditions. In contrast to R , the maximum growth rate R_m depends on temperature, solubility, type of material, and growth mechanism (i.e. diffusion or kinetically controlled growth). For diffusion or kinetically controlled growth conditions, the maximum growth rate is given by (Leubner, 2000)

$$R = \frac{2\gamma\Omega c_0 k_i (1 - L^*/L)}{R_G T L^* (1 - \varepsilon/L)} \quad (7.18)$$

with

$$\varepsilon = k_i/D\Omega \quad (7.19)$$

where k_i is a constant related with the integration of atoms/molecules in the crystal surface, c_0 is the solubility of the nucleating material, R_G is the gas constant, L^* is the critical crystal size when the crystal has the probability to grow or dissolve by Ostwald ripening such that $L > L^*$, and D is the diffusion coefficient.

Since the BNG model is based on the growth of crystal nuclei, the nucleation step is related to the growth mechanism. Depending on whether growth is controlled by volume diffusion or surface integration kinetics, two limiting cases can be distinguished from Equation (7.18).

When the nuclei grow under diffusion-controlled conditions, $D \ll k_i$ and $L + 1/\varepsilon \approx L$. Then the number of stable crystals is given by

$$N = \delta_{\text{add}} R_G / 2\beta_s \gamma \Omega c_0 D (L/L^* - 1) \quad (7.20)$$

where D is the diffusion coefficient of the reaction controlling reactant. Obviously, during a crystallization process when Z is constant, L/L^* is also constant, implying that L^* changes with L . L may be calculated if the value of supersaturation S is known.

From Equation (7.20) it follows that, for diffusion-controlled crystallization, the formation of stable crystals depends on the molar addition rate δ_{add} , material solubility c_0 and crystallization temperature, and is given by the following equations (Leubner, 2000):

$$d \ln N / d \ln \delta_{\text{add}} = 1 - [\delta_{\text{add}} / (L/L^* - 1)] [d(L/L^*) / d \delta_{\text{add}}] \quad (7.21)$$

$$d \ln N / d \ln c_0 = -\{1 - [c_0 / (L/L^* - 1)] [d(L/L^*) / d c_0]\} \quad (7.22)$$

$$d \ln N / d \ln T = -[T / (L/L^* - 1)] [d(L/L^*) / d T] \quad (7.23)$$

The above relations predict that plots of $\ln N$ against $\ln \delta_{\text{add}}$, $\ln c_0$ and $\ln T$ are linear, when the other two variables are kept constant.

When crystallization takes place under kinetically controlled growth conditions, $D \gg k_i$ and $L + 1/\varepsilon \approx 1/\varepsilon$. Then the number of stable nuclei is given by (Leubner, 2000)

$$N = \delta_{\text{add}} R_G T / 2\beta_s k_i c_0 L (L/L^* - 1) \quad (7.24)$$

or, by multiplying both sides by L , in the form

$$NL = \delta_{\text{add}} R_G T / 2\beta_s k_i c_0 (L/L^* - 1) \quad (7.25)$$

Equation (7.25) predicts that the product NL is constant when all reaction variables (i.e. δ_{add} and T) and L/L^* are constant.

The BNG model correlates the average crystal size L at steady state in the CSTR reactor with the retention time τ :

$$k_v L^3 R_G T - 2k_s \gamma D \Omega^2 c_0 (L/L^* - 1) - 3k_v R_m R_G T / L^2 \tau = 1 \quad (7.26)$$

where k_v is the volume constant which converts the crystal size into crystal volume, and k_s is the crystal surface factor which converts crystal size L to surface area. Equation (7.26) may be solved for τ in the form

$$\tau = L/3R_m - 2k_s \gamma D \Omega^2 c_0 (L/L^* - 1)/3k_v R_m R_G T/L^2 \quad (7.27)$$

Equation (7.27) predicts, *inter alia*, that for zero retention time $L > 0$. Moreover, this equation predicts that the average crystal size does not depend on reactant addition rate, suspension density and reaction volume. Thus, whereas the Randolph–Larson model deals with the crystal size distribution, Equation (7.26) of the BNG model describes the average crystal size.

7.3.3 Approach Based on Law of Proportionate Effect

The CSD of the type in Figure 7.13 is one of the four basic shapes observed in various experiments carried out under a variety of conditions. Following Kile *et al.* (2000), these four basic shapes are described as follows (see Figure 7.14):

- (1) Asymptotic CSD, in which the frequencies of the sizes of crystals in a growth run are greatest in the smallest size range and exponentially decrease with increasing size (Figure 7.14a). This shape has been traditionally discussed in the population balance approach.
- (2) Log-normal CSD, in which the logarithms of the crystal sizes are normally distributed, but the curve has a positive skew towards larger sizes in the plots of logarithm of frequencies of sizes against crystal size (Figure 7.14a).
- (3) Ostwald ripened CSD, usually referred to as universal steady-state shape, in which a negative skew in the plots of frequencies of sizes against crystal size is towards smaller sizes (Figure 7.14b). This shape is termed universal because it is approached during the ripening process, irrespective of the initial shape of the CSD. It is called a steady-state shape because its shape is constant, regardless of the mean size, in the plots of ratio of frequency to maximum frequency against the ratio of crystal size to mean size.
- (4) Bimodel CSD, in which two peaks of usually unequal height appear at two crystal sizes (Figure 7.14b).

The above four shapes of CSDs are discussed below from the standpoint of the law of proportionate effect.

According to Kile *et al.* (2000), asymptotic and log-normal CSDs can be derived mathematically by the law of proportionate effect (LPE) enunciated by Kapteyn (1903) and Gibrat (1930). According to this law, the growth rate is proportional to linear size times a random number, thereby making growth rate size dependent. The size-dependent growth takes place in two regimes, as described below.

The first regime deals with an exponential increase in mean crystal size and a linear increase in crystal size variance β^2 with time. Here growth occurs in systems far from equilibrium by surface-controlled reactions and not by mass transport. The growth rate of each crystal is governed by its size L_j and a random variable ϵ_j lying between 0 and 1. The range of ϵ_j indicates system variability and its values are evenly distributed:

$$L_{j+1} = L_j + \epsilon_j L_j. \quad (7.28)$$

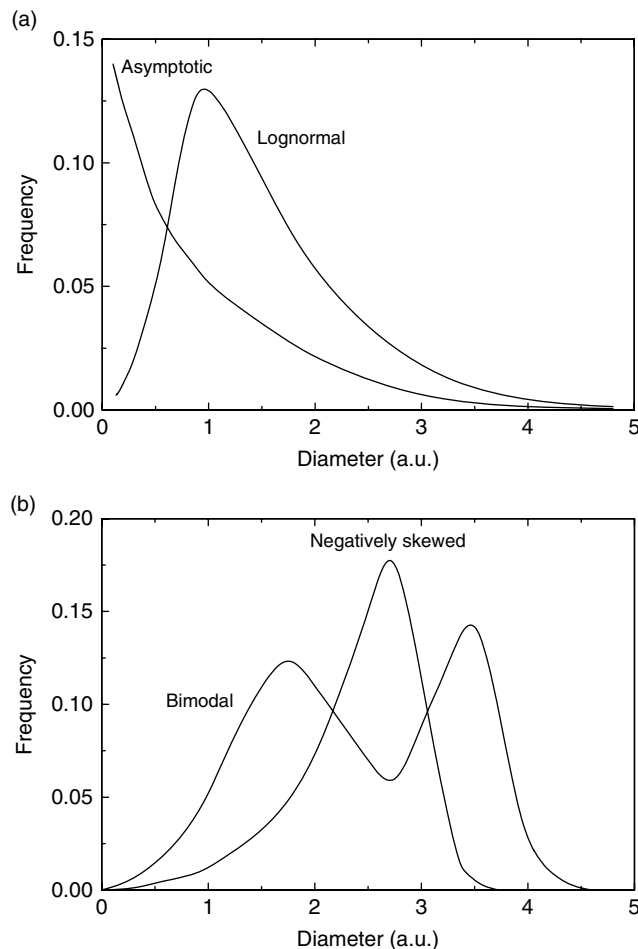


Figure 7.14 Four basic shapes of experimental CSDs observed under a variety of conditions: (a) asymptotic and log-normal CSDs, and (b) Ostwald ripened and bimodal CSDs. Adapted from Kile et al. (2000)

In a computer program such as Galoper (acronym for Growth According to the Law of Proportionate Effect and by Ripening), Equation (7.28) is iterated many times, with each iteration called a growth cycle. After several growth cycles involving many crystals, a log-normal CSD results. This implies that LPE requires an exponentially increasing amount of nutrients as the number of growth cycles increases, but due to limited supply of reactants growth becomes mass transport controlled.

During surface-controlled LPE growth, the term $\epsilon_j L_j$ in Equation (7.28) accounts for processes of size-dependent growth involving faster growth for larger crystals and growth rate dispersion due to different growth rates of crystals of the same initial size. L_j manifests size dependence and the range in ϵ_j describes dispersion.

An asymptotic CSD develops when there is a decay in the rate of formation of nuclei or new nuclei are added to a growth system at a constant rate. This means that nucleation gradually subsides while previously nucleated crystals continue to grow, and the nature of the CSD curve depends on the duration of growth following nucleation.

The second regime for size-dependent growth is governed by a supply-controlled mechanism. In this regime, crystals grow with a smaller tendency for growth rate dispersion (i.e. ϵ_j is in a small range). This type of growth leads to a decreasing rate of growth with increasing mean size and to a constant size variance ($\beta^2 = \text{constant}$). In this case, the growth rate can be approximated by (Kile *et al.*, 2000)

$$\frac{dL}{dt} = k_3 L \quad (7.29)$$

where k_3 is a constant. Equation (7.29) gives the exponential growth rate law:

$$L = L_0 \exp(k_3 t) \quad (7.30)$$

where L_0 is the crystal size at $t = 0$. Equation (7.30) is distinctly different from the traditional crystal growth rate $dL/dt = k_3$.

A negatively skewed shape of CSD is produced by diffusion-controlled Ostwald ripening (Lifshitz and Slyozov, 1961; Wagner, 1961; Kile *et al.*, 2000), where smaller crystals dissolve to provide material for the growth of larger crystals. The overall growth rate is determined by the rate of reactant supply to the larger crystals.

From the above, it follows that CSDs have three basic shapes: (1) asymptotic, (2) log-normal, and (3) Ostwald ripened. These three CSD shapes are related to four crystal growth processes (Kile *et al.*, 2000): (1) constant-rate nucleation accompanied by surface-controlled growth, thereby producing an asymptotic CSD, (2) decaying nucleation rate giving a log-normal CSD, (3) Ostwald ripening, where larger crystals grow at the expense of smaller crystals, thereby generating the negatively skewed CSD, and (4) mass transport-controlled growth, where the growth rate is determined by the activity of reactants at the surfaces of growing crystals.

Kile *et al.* (2000) and Roque *et al.* (2004) carried out experimental study of the shapes of CSDs for calcite growth by changing the nucleation conditions and solution concentrations. They found the following:

- (1) The asymptotic CSD is formed when additional reactants are added stepwise to the surface of solutions supersaturated with respect to calcite, thereby leading to continuous nucleation and growth of calcite crystals.
- (2) The log-normal CSDs result when reactants are added continuously below the solution surface, via a submerged tube, to similarly supersaturated solutions, thereby leading to a single nucleation event followed by surface-controlled growth.
- (3) The Ostwald CSDs are produced when concentrated reactants are rapidly mixed, leading initially to high levels of supersaturation, followed by the formation and subsequent dissolution of very small nuclei, thereby yielding CSDs with small crystal size variances.
- (4) The bimodal CSDs are produced as a consequence of two distinct nucleation events, which are possible for two reasons: (1) addition of one of the reactants to the initially supersaturated solution is carried out twice and is separated by a time interval, rather

than adding continuously (Kile *et al.*, 2000), and (2) nucleation and ripening of one phase, followed by dissolution of the first phase and nucleation and ripening of another more stable phase (Roque *et al.*, 2004).

Finally, it may be noted that the first three CSDs can be obtained by the empirical relation

$$n(L) = AL^n \exp[-B(L - L_0)^2] \quad (7.31)$$

where A , B , n and L_0 are constants. The CSD curves predicted by Equation (7.31) are shown in Figure 7.15 for various combinations of the constants such that the maximum value of the frequency of occurrence of the corresponding crystals is about 0.22. The constants are given in the insets. Figure 7.15a illustrates the effect of changes in n and B for $L_0 = 0$ and Figure 7.15b the effect of changes in L_0 for constant values of $n = 2$ and $B = 1$ on the trends of CSDs. The following features may be noted from these figures:

- (1) When $L_0 = 0$, an asymptotic CSD is obtained for $n = 0$. However, when $n > 0$, log-normal plots with positively skewed shapes of CSDs are produced. In the latter case, with increasing n the CSD becomes symmetrical and the value of L corresponding to the peak increases. For constant n and L_0 , A increases with increasing B .
- (2) When $L_0 = 0$, for $B = 0.5$ the crystal size lies in a relatively wide range, but the crystal size range becomes narrow with increasing B . For all values of B , the CSD has positively skewed shape.
- (3) For constant n and B , with an increase in L_0 the peak value of L also increases. However, for $L_0 < 0$ the CSD shape is negatively skewed. The value of A increases with decreasing L_0 .

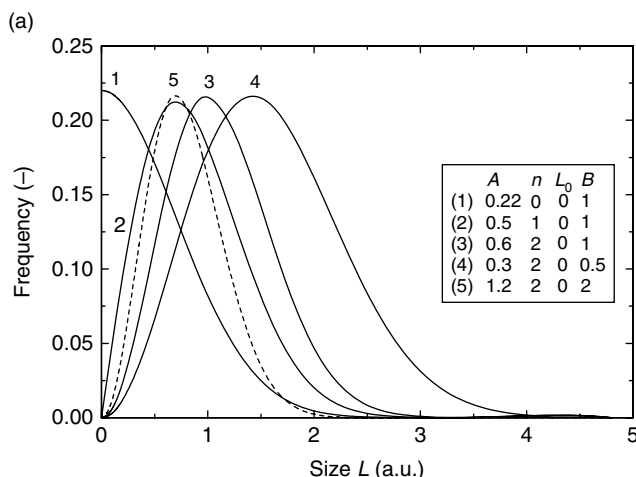


Figure 7.15 CSD curves predicted by Equation (7.31) for various combinations of the constants A , B , n and L_0 given in the insets. The value of A was chosen to give a maximum value of about 0.22 for the frequency of occurrence of the corresponding crystals

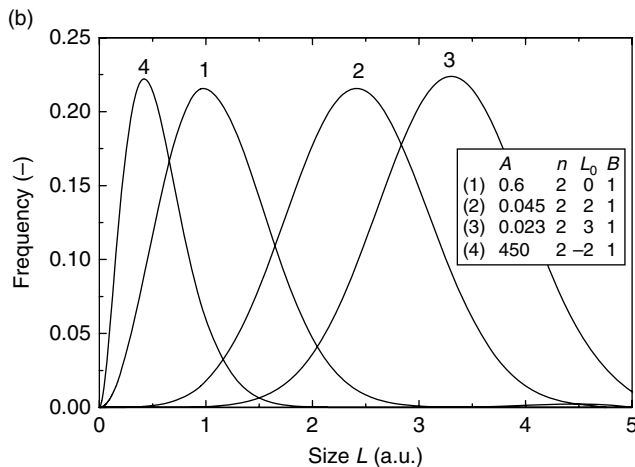


Figure 7.15 (Continued)

Equation (7.31) is very similar to Equation (7.16) of three-dimensional nucleation. Comparison of Equations (7.31) and (7.16) gives

$$B(L - L_0)^2 = 16\gamma^3 \Omega^2 / 3k_B T^3 (\ln S)^2 = (\gamma / 3k_B T) L_c^2 \quad (7.32)$$

$$AL^n = J_0 \quad (7.33)$$

where L_c is the diameter of the stable nucleus. Equation (7.31) suggests that the term in the exponential term is associated with the nucleation barrier while the pre-exponential term is connected with processes of development of stable nuclei. Physically, the constant A may be viewed as a kinetic parameter associated with the attachment of monomers or other basic growth units, L_0 is a correction factor associated with the attachment of basic units to the unstable nucleus in the initial stage, and the constant B is a measure of the effect of heterogeneous and secondary nucleation on nucleation rate. However, a precise interpretation of this expression with crystal growth processes is a matter of speculation.

7.3.4 Effect of Additives on Crystal Size Distribution

Additives present in a growth medium affect the formation of stable nuclei in the volume and also the growth of the stable nuclei to sizes detectable by experimental techniques. The usual effects of additives are (1) to lower the value of the nucleation barrier ΔG_{3D}^* whereby the process of nucleus formation is accelerated and (2) to inhibit the growth rate R of the stable nuclei. As seen above in Section 7.3.3, these two processes determine the shape of the CSD. Therefore, it is expected that, depending on the effect of an additive on these processes, the shape of the CSD curve and the crystal size range are changed. This type of behavior of CSDs has been reported for two popular crystallization systems of calcium carbonate and calcium oxalate.

Roque *et al.* (2004) investigated the crystallization of calcium carbonate produced by NH_3 and CO_2 diffusion in aqueous solutions CaCl_2 in the presence of soluble matrix

extracts (abbreviated hereafter as OMM, from organic matrix macromolecules) from *Mytilus edulis* and poly(aspartic acid) (abbreviated as Polyasp), and examined the crystals obtained at several intervals of time (1, 3 and 6 h) by optical microscopy and scanning electron microscopy (SEM) in different crystallization conditions. From SEM images, the authors observed three types of CSDs: asymptotic, log-normal and bimodal, depending on the experimental conditions. They made the following observations:

- (1) Asymptotic CSD occurs during crystallization from systems without additives. In the presence of OMM and Polyasp additives, both asymptotic and log-normal CSDs occur, but their occurrence depends on the time of crystallization, the type of the additive, the concentrations of OMM, Polyasp and CaCl_2 , and the OMM/ CaCl_2 and Polyasp/ CaCl_2 ratios.
- (2) In systems without additives and small amounts of OMM, asymptotic CSD appeared during the first hour, but bimodal CSDs appeared at 3 and 6 h.
- (3) The average crystal size showed that the growth rate R is the highest from solutions without additives, intermediate from solutions containing OMM and the lowest from solutions containing Polyasp.

The above results can be explained in terms of equilibrium between nucleation and growth of crystals. As judged from the length of the nucleation event, both OMM and Polyasp additives induce 3D nucleation, but increasing concentrations of OMM, Polyasp and CaCl_2 lead to longer nucleation events, thereby increasing the number of nuclei. However, the duration of the nucleation event is longer in OMM than in Polyasp. Consequently, the average size of crystals in OMM is longer than in Polyasp. This also means that OMM has a weaker inhibiting effect on the growth rate and a lower nucleation rate than Polyasp.

The bimodal CSD is a result of two different nucleation events associated with the initial precipitation of metastable vaterite followed by its transformation to calcite. When the transformation occurs rapidly, as in the case of additive-free systems or low concentrations of Polyasp, asymptotic or log-normal CSDs are obtained. However, when an additive stabilizes the nucleation of vaterite (i.e. suppresses its transformation to calcite), thereby increasing its lifetime during crystallization, bimodal CSD is produced. Obviously, the appearance of bimodal CSD is related with the type of the impurity.

Kurutz *et al.* (2003) investigated the growth of calcium oxalate in gelatin gels by slow diffusion in the presence of four isoforms of nephracalcin (referred to as NC-A, NC-B, NC-C and NC-D), a urinary protein proposed to inhibit the growth of kidney stones. NC-A and NC-B differ from NC-C and NC-D in their biochemical properties. For example, all four isoforms are phosphorylated, but NC-C and NC-D contain more phosphate groups than NC-A and NC-B. The additive was added to 5% gelatin aqueous solutions such that the final NC concentration was 740 nM, which is similar to that found in human urine. For the control growth experiment, no NC was added to the gel. Crystal growth was carried out at 4 °C for 30 days, and the size, morphology and surface morphology of the as-grown crystals were examined by optical microscopy, Coulter Counter measurements, SEM and AFM. It was found that all crystals were calcium oxalate monohydrate (COM), and the crystals formed in the presence of NC-A were smaller, those in NC-C and NC-D were larger and aggregated whereas those in NC-B were not different in size to the

crystals grown in control experiments. The CSDs for COM in the presence of different isoforms and in control experiment are shown in Figure 7.16.

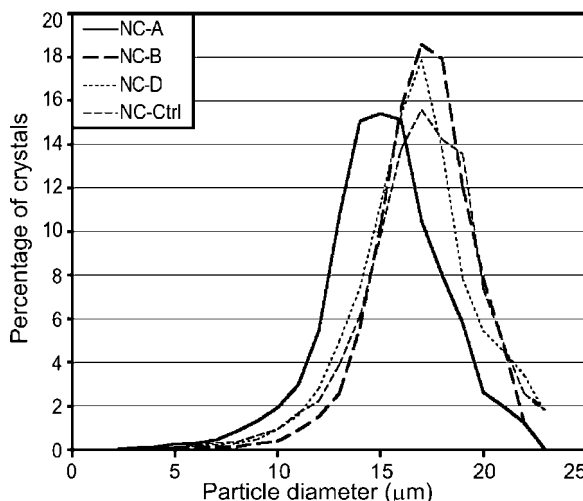


Figure 7.16 Distributions of size of crystals in the presence of NC-A, NC-B and NC-D and with no NC determined by Coulter Counter. Reproduced from J.W. Kurutz, M. Carvalho, and Y. Nakagawa. *J. Cryst. Growth* **255**, 392. Copyright (2003), with permission from Elsevier

Kurutz *et al.* (2003) attributed the above observations to the difference in their surface-active properties associated with the affinity of their hydrophilic sides to bind with the crystal surface. For example, NC-A and NC-B glycoproteins are amphiphilic, which enables their hydrophilic sides to interact with the surface, thereby exposing their hydrophobic sides to the saturated solution. Thus, the glycoprotein coating of NC-A and, perhaps, NC-B inhibits growth and prevents aggregation. However, because of their poor surface activity, NC-C and NC-D are not effective in suppressing aggregation.

The above results demonstrate that some additives promote growth and induce crystal aggregation, others inhibit growth and aggregation, and still others have no significant effect on growth and aggregation of crystals. Obviously, the kinetics of nucleation, growth and aggregation of crystals are complex, and the exact mechanisms of operation of different additives responsible for various processes during crystallization should take into account, on the molecular level, structural parameters of the growing crystals, their morphologies, and the stereochemistry of the additives. For a general understanding of the stereochemical correlation between the nucleating and growing crystal and the additive, specifically designed additives, called tailor-made additives, are used. The different aspects of crystallization in the presence of tailor-made impurities are described below.

7.4 Control of Shape and Size of Particles

Biological organisms are natural sophisticated crystal engineering systems for producing remarkable material properties of mineralized tissues such as bones and teeth, and the nacre of mollusks and abalone (Chapter 6). Consequently, inspired by the capabilities of Nature, scientists have synthesized and analyzed naturally occurring materials, examined Nature's processing strategies, and looked for engineering insight for producing ceramic components, films and composites (Campbell, 1999). Fabrication of advanced materials with anisotropic microstructures or with anisotropic particles uniformly dispersed in an isotropic matrix provides control over their structural, optical and electrical properties. Examples of such materials are structural composites, biomedical devices, and optical and electronic media, photographic films, and certain metal and ceramic alloys (Adair and Suvaci, 2000).

In recent years, the synthesis of anisotropic particles with predefined composition and physical characteristics (e.g. size distribution, shape and aspect ratio) has been an area of hectic scientific activity (Pozarnsky and Matijević, 1997; Goia and Matijević, 1998, 1999; Campbell, 1999; Adair and Suvaci, 2000; Cölfen, 2003; Li and Kaplan, 2003; Bosch *et al.*, 2004). It is well known that substances which yield single crystals usually produce anisotropic-shaped particles, and it is difficult to produce spherical particles for substances which crystallize in different polymorphs or phases. This is mainly because the processes that control shape uniformity, aspect ratio and phase composition of particles are insufficiently known. In general, control of the shape of particles requires the understanding of interactions between solute, solvent and additives, the nature of reactions at the solid–medium interface, and chemical kinetics. Moreover, during the synthesis of particles of controlled size, the processes of nucleation, growth and aggregation must be balanced with crystallization parameters (i.e. supersaturation, temperature, etc.).

There are two approaches for the control of shape and size of particles (Adair and Suvaci, 2000; Cölfen, 2003): (1) growth directed syntheses typical of precipitation processes and (2) template-directed syntheses where growth is induced by epitaxy via a pre-existing structure upon which nucleation and growth take place. These two approaches are briefly described below.

7.4.1 Growth-Directed Synthesis

Depending on the type of materials, growth-directed formation of particles may be divided into four groups: (1) precipitation of biominerals such as calcium carbonate and calcium oxalate, (2) precipitation of metals, (3) precipitation of inorganic compounds, including metal oxides and semiconductor compounds, and (4) precipitation of biologically active pharmaceutical compounds. The synthesis of a material is carried out by using specific growth-inducing agents. Recognition of template-induced growth has provided great interest in understanding the factors responsible for inducing morphologies, orientation and phases of biominerals such as calcium carbonate and oxalate. The morphological forms and phases of these compounds depend on the synthesis conditions, such as the concentration of reactants, temperature, aging time, mixing procedure, and the nature of additives (for calcium carbonate see Wang *et al.*, 1999; Raz *et al.*, 2000; Hardikar

and Matijević, 2001; Kitamura, 2001; Sondi and Matijević, 2001; Rudloff *et al.*, 2002; Cölfen, 2003; for calcium oxalate see Jung *et al.*, 2004, 2005; Yu *et al.*, 2005).

For the study of the shape and size of calcium carbonate particles, the particles are obtained by controlled reaction between two reactants which are sources of Ca^{2+} and CO_3^{2-} ions. The effect of an additive is investigated by adding the additive to the solution of calcium salt. A variety of additives, such as simple cations and anions, surfactants and polymers, have been used (for example, see Cölfen, 2003). The following methods are usually used:

- (1) An aqueous solution of CaCl_2 is reacted with an aqueous solution of Na_2CO_3 at a constant temperature (Kitamura, 2001; Rudloff *et al.* 2002).
- (2) The double-jet crystallization technique based on the injection of reactants via two capillaries to ensure nucleation of calcium carbonate particles at high supersaturation at the mixing spot, followed by transport of nucleated particles to regions of lower calcium carbonate concentration in the vicinity of a stabilizing polymer (Sedlak *et al.*, 1998; Rudloff *et al.*, 2002).
- (3) Aging aqueous solutions of calcium salts with urea at an elevated temperature (Wang *et al.*, 1999; Hardikar and Matijević, 2001; Sondi and Matijević, 2001).
- (4) Kitano technique based on bubbling CO_2 gas through CaCO_3 solution (Kitano *et al.*, 1962; Rudloff *et al.*, 2002).
- (5) Slow diffusion of $\text{NH}_4\text{HCO}_3 \cdot \text{NH}_2\text{COONH}_4$ vapor into cell-culture dishes containing CaCl_2 solution in a closed dessicator (Aizenberg *et al.*, 1997; Feng *et al.*, 2000; Raz *et al.*, 2000; Lee *et al.*, 2001; Jimenez-Lopez *et al.* 2003).

In the case of calcium carbonate crystallizing under the same experimental conditions, urea decomposition at elevated temperature results in acicular, prismatic, spherulitic and plate-like particles for different phases including aragonite, vaterite and calcite (Wang *et al.*, 1999; Hardikar and Matijević, 2001; Sondi and Matijević, 2001). However, it was found that at $0.5 \text{ mol}/\text{dm}^3$ CaCl_2 all the three phases are crystallized, but at $1.0 \text{ mol}/\text{dm}^3$ CaCl_2 vaterite and calcite phases are produced whereas at higher CO_3^{2-} concentrations achieved by preheating urea solution at 90°C for 3 h before mixing results in flower-like vaterite particles. Moreover, surfactants and polymers containing sulfate or sulfonate groups produce different types of calcium carbonate polymorphs in the presence of urea. Some typical morphologies of calcium carbonate particles are shown in Figure 7.17.

Using the Kitano method, Rudloff *et al.* (2002) observed that, depending on the degree of phosphorylation (i.e. conversion of protons of $-\text{OH}$ groups to $-\text{PO}_3\text{H}_2$ groups) of double-hydrophilic block copolymers with monophosphate ester moieties, spherical particles, fried-egg structure, flower-like structures, and aggregates of nanoparticles are produced (Figure 7.18). The complex morphologies result from temporarily stabilized nanoparticles, which begin to aggregate at CO_2 gas bubbles at the air/solution interface due to surface tension effects. Long experimental time and poor stirring favor this process of aggregation. This implies that temporarily stabilized nanoparticles are the building units for the aggregation processes which are controlled by external templates. This explanation also applies to the results in Figure 7.17 and to the observation that calcium carbonate nanoparticles are efficiently produced in the presence of block copolymers by the double-jet crystallization technique. The particles are predominantly composed

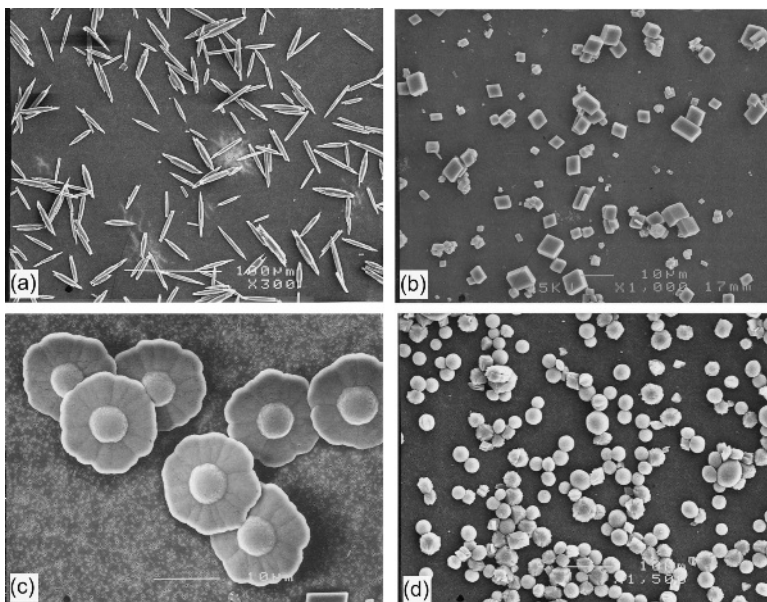


Figure 7.17 Some typical morphologies of calcium carbonate particles obtained by aging solutions containing CaCl_2 and urea at 90°C : (a) acicular aragonite particles obtained by aging a solution containing $0.25 \text{ mol}/\text{dm}^3$ CaCl_2 and $0.75 \text{ mol}/\text{dm}^3$ urea for 3 h, (b) rhombohedral calcite crystals obtained by aging a solution containing $0.25 \text{ mol}/\text{dm}^3$ CaCl_2 and $0.75 \text{ mol}/\text{dm}^3$ urea under magnetic stirring for 3 h, (c) flower-like morphology of vaterite particles obtained by separately preheating $0.25 \text{ mol}/\text{dm}^3$ CaCl_2 solution and $0.75 \text{ mol}/\text{dm}^3$ urea solution at 90°C for 3 h, followed by mixing at the same temperature, and (d) nearly spherical particles, composed of a mixture of vaterite and calcite, obtained by aging a solution containing $0.25 \text{ mol}/\text{dm}^3$ CaCl_2 and $0.75 \text{ mol}/\text{dm}^3$ urea at 90°C for 3 h in the presence of $0.5 \text{ g}/\text{dm}^3$ AVANEL S-150 impurity. Reproduced from L. Wang, I. Sondi, and E. Matijević. J. Colloid Interface Sci. **218**, 545. Copyright (1999), with permission from Elsevier

of metastable vaterite phase, which is stabilized by the strong and nonselective surface binding with the block polymers.

The above concept of deposition of metastable phase on templates is also consistent with the growth of vaterite particles with acid-terminated gold nanoparticles as nucleation templates, as reported by Lee *et al.* (2001). However, using the cooperative effect between Mg^{2+} ions and nanoparticles, these authors also observed the formation of needle-like aragonite crystals.

In order to understand the processes which form magnesian calcite skeletons with magnesium contents as high as 40 mol%, Raz *et al.* (2001) investigated the precipitation of calcium carbonate from solutions with Mg/Ca ratios ≥ 4 by the slow diffusion technique (i.e. method 5 above). It was found that the majority of the magnesian calcite precipitates, with 11–14 mol% magnesium, are composed of spherical particles up to $30 \mu\text{m}$ (Figure 7.19a) with surface morphologies reflecting the trigonal symmetry of calcite crystals (Figure 7.19b). Aragonite spherulites with much larger average sizes between 100 and $200 \mu\text{m}$, composed of needle-shaped crystallites, were also observed (Figure 7.19c), but

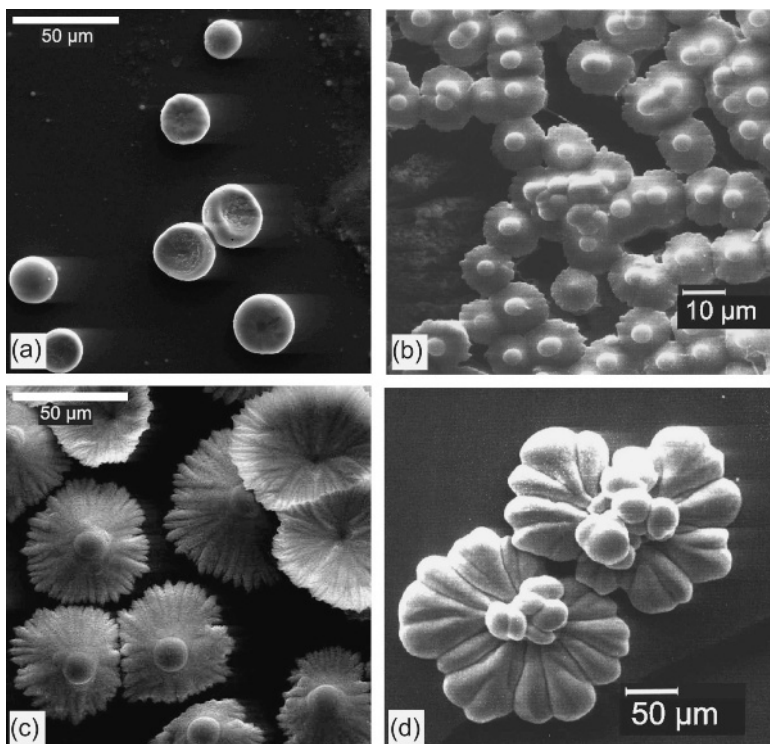


Figure 7.18 Formation of complex calcium carbonate morphologies with increasing surface activity as defined by degree of phosphorylation of block copolymers: (a) 10, (b) 34, (c) 40, and (d) 100%. Kitano technique based on bubbling CO_2 gas through CaCO_3 solution was used. Reproduced from J. Rudloff, M. Antonetti, H. Cölfen, J. Pretula, K. Kaluzynski, and S. Penczek. *Macromol. Chem. Phys.* **203**, 627. Copyright (2002), with permission from Wiley-VCH

in some cases the particles comprised a polycrystalline magnesian calcite core in an envelope of polycrystalline aragonite (Figure 7.19d). In this study perhaps another important observation was that less abundant calcite particles had distinct elongated morphologies (Figure 7.19e and f) and contained a higher magnesium content of up to 21 mol%. Addition of macromolecular matrix components suppressed the formation of aragonite phase and resulted in practically entirely the magnesian calcite.

The above study demonstrates that the formation of high magnesian calcite, both in the presence and absence of additives, takes place via a precursor amorphous phase. The presence of magnesium ions in the solution produces an increase in supersaturation, which results in the precipitation of particles composed of an amorphous phase. The spherical shape of the particles results from the liquid phase, which minimizes its surface contact with the surroundings. The amorphous phase subsequently transforms into more stable phases of calcite, aragonite and high magnesian calcite, depending on the crystallization conditions.

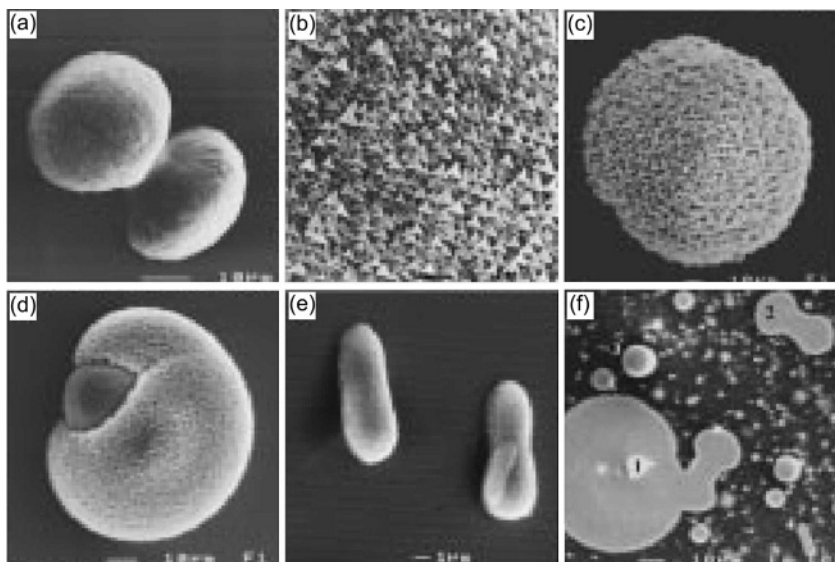


Figure 7.19 Scanning electron micrographs of calcium carbonate precipitates grown from solutions with $Mg/Ca = 4$: (a) magnesian calcite spherulite with dumb-bell morphology, (b) triangular morphology of crystallites on the surface of magnesian calcite spherulite of (a) observed at a higher magnification, (c) polycrystalline aragonite spherulites composed of needle-shaped crystallites, (d) a mixed particle with a core of polycrystalline magnesian calcite in an envelope of polycrystalline aragonite, (e) elongated magnesian calcite particles with high magnesium content, and (f) cross-sectional view of morphologies of different types of particles. In (f) spherulites marked 1 and 2 represent those in (c) and (a), respectively. Reproduced from S. Raz, S. Weiner, and L. Addadi. *Adv. Mater.* **12**, 38. Copyright (2000), with permission from Wiley-VCH

Interest in the controlled crystallization of calcium oxalate phases stems from our quest for understanding the processes responsible for their occurrence as the most common biomineral in higher plants and human kidney stones. Crystallization of calcium oxalate in buffer solutions similar to human urine showed (Jung *et al.*, 2004) that an increase in the initial supersaturation of the solution suppresses the formation of calcium oxalate dihydrate (COD) and favors the formation of calcium oxalate monohydrate (COM), while nonstoichiometric reactant conditions involving excess calcium or oxalate ions lead to changes in crystallized phase, and its morphology and crystal size. It has also been reported (Yu *et al.*, 2005) that variation in the concentration of CaC_2O_4 (produced by the reaction between $CaCl_2$ and $Na_2C_2O_4$ solutions with vigorous stirring) and additive poly(sodium 4-styrenesulfonate) (PSSS), added to $Na_2C_2O_4$ solution before the reaction, temperature of synthesis and pH have a significant influence on the crystallized phase, morphology and particle size. Plates and leaf-shaped structures composed mainly of COM, and pyramids and cylinders, composed mainly of COD, were produced, depending on the experimental conditions. A higher PSSS concentration favored the formation of COD in a pyramidal shape, whereas a high reaction temperature favored the formation of elongated COM particles. In the presence of the additive, roughly spherical particles

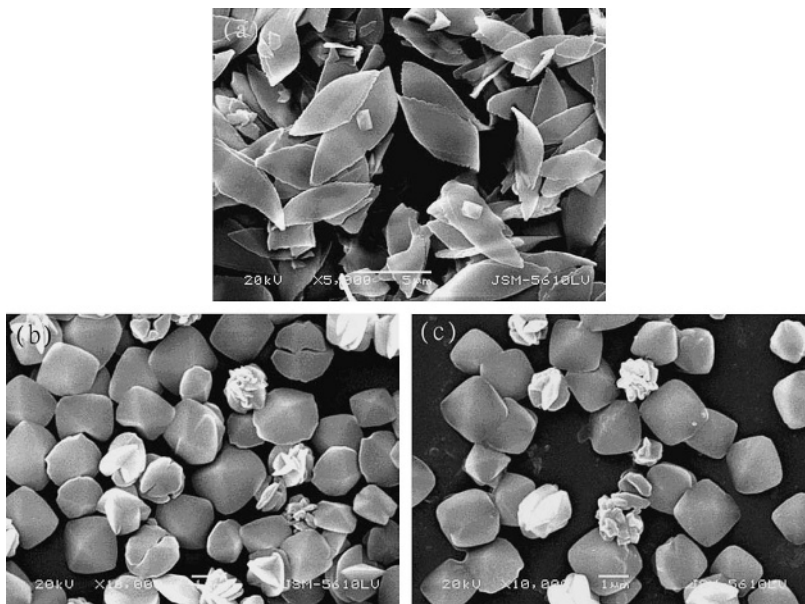


Figure 7.20 Examples of calcium oxalate particles obtained in the presence of 1 mM PSSS additive after 24 h aging of 0.1 g/l calcium oxalate solution at different pH: (a) 6, (b) 8, and (c) 10. Reproduced from J. Yu, H. Tang, and B. Chang. *J. Colloid Interface Sci.* **288**, 407. Copyright (2005), with permission from Elsevier

composed mainly of COD were produced at higher pH (Figure 7.20). This observation may be explained in terms of nonspecific interactions of calcium oxalate particles with the solvent and additive molecules under these experimental conditions. However, when specific interactions of the additives with the surfaces of a growing crystal phase occur, the resulting crystalline particles have well-developed faces, as reported by Kurutz *et al.* (2003), who studied the effect of four isoforms of nephrocalcin (NC), a urinary protein, on the morphology, growth and aggregation of calcium oxalate phases crystallizing from gelatin gels.

Control of the shape and size of metallic particles is important for their application in microelectronics. In a review, Goia and Matijević (1998) described different routes followed to produce monodispersed metal particles and the precipitation conditions to obtain uniform particles of various sizes for different applications. For example, Goia and Matijević (1999) used aqueous solutions of gold chloride and isoascorbic acid as reducing agent, in the presence of gum arabic as a protective colloid, to produce monodispersed, spherical gold particles, whereas Zhou *et al.* (1999) used ultraviolet radiation to promote the formation of nearly monodispersive gold particles of several different morphologies, depending on the reducing agent present during the synthesis. By manipulating the precipitation conditions, Goia and Matijević (1999) produced uniform gold particles of various sizes ranging in diameter from 80 nm to 5 µm. They concluded that the formation of spherical particles of metals involves the aggregation of subunits (primary

particles), and that the spherical particles of organic and inorganic compounds are also produced by this aggregation mechanism (for example, see Figure 7.19).

It should be mentioned that the concept of the formation and existence of primary particles or subunits in growth medium is fairly old. For example, about four decades ago Bulakh (1969) explained the various morphologies of CdS crystals grown from the vapor phase at different temperatures and Cd-to-S ratios in terms of formation of complexes of various types, depending on the growth conditions. Complexes were considered as the basic building units for nucleation and growth of CdS crystals as a result of their association. It was suggested that the association of the basic units yields larger geometric entities whose subsequent development leads to directional bonds in the crystal lattice. Similarly, Troost (1972) explained the difference in the growth rates of sodium triphosphate hexahydrate ($\text{Na}_5\text{P}_3\text{O}_{10} \cdot 6\text{H}_2\text{O}$) single crystals at the same supersaturation from aqueous solutions prepared from two different phases of sodium triphosphate ($\text{Na}_5\text{P}_3\text{O}_{10}$) from a consideration of the structure of the basic $[\text{Na}_2\text{P}_3\text{O}_{10}]^{3-}$ building units present in the solutions. Recent observations made by Onuma (2006) also indicate that the growth of hydroxyapatite crystals takes place by the integration of $[\text{Ca}_3(\text{PO}_4)_2]_3$ growth units (i.e. primary particles) of diameter about 1 nm, composed of $\text{Ca}_3(\text{PO}_4)_2$ complexes. In a review of the colloidal aspects of precipitation, Kind (2002) concluded that the newly precipitated primary particles, as a rule, are of nanometer size, and this behavior of colloidal particles in this size range is determined by interfacial forces. According to him, in most cases aggregation of primary particles leads to end-product particles, which are secondary ones.

Figure 7.21 shows the above aggregation behavior for gold particles, where the small primary particles (subunits) of about 30 nm diameter aggregate to form the final particle of about 3 μm diameter. Practically the same size of aggregates and small particles implies that the larger spherullite aggregates are produced by aggregation of nanosize primary precursor particles. The packing fraction of primary particles in the aggregates, about 56–58%, corresponds to random close packing, typical for rapidly assembled packing of equal spheres. X-ray diffraction analysis of the high-magnification image of aggregates in Figure 7.21b also shows the presence of a thin coating of protective organic matter (gum arabic) surrounding the primary particles. Various polymers are known to act as protective colloids during the synthesis of metal particles (Mayer and Antonietti, 1998).

There is a voluminous literature dealing with the morphological control of particles of a variety of inorganic compounds comprising different simple metal oxides (e.g. $\alpha\text{Al}_2\text{O}_3$, $\alpha\text{Fe}_2\text{O}_3$, $\gamma\text{Fe}_2\text{O}_3$ and ZnO) and complex metal oxides [e.g. PbTiO_3 , BTiO_3 and $\text{Pb}(\text{TiO}_3)_y(\text{ZrO}_3)_{1-y}$, and $\text{Pb}_x\text{La}_{1-x}(\text{TiO}_3)_y(\text{ZrO}_3)_{1-y}$ solid solutions] because of interest in their properties. Moon *et al.* (1999) and Adair and Suvaci (2000) surveyed the synthesis conditions for some of these compounds. A general feature of these systems is that both the solvent and the additive control the morphology of synthesized particles. However, in most cases the adsorption of the additives used for morphology control was found to be selective on specific faces of the synthesized oxide compound.

Drug materials exist in multiple polymorphic crystal forms and/or amorphous solids, but the most thermodynamically stable solid-state form of a drug determines its *in vivo* performance. Moreover, blending and compaction of crystallized drugs require appropriate morphology of the product. Therefore, it is an important task to develop methods to obtain drug particles of different shapes and internal structures. During

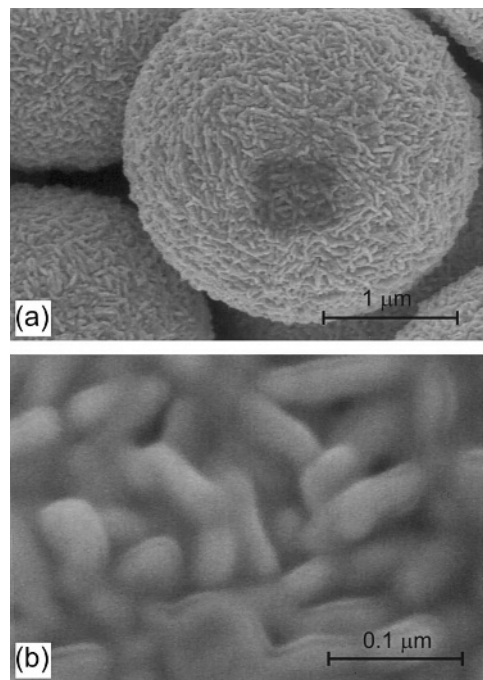


Figure 7.21 (a) Field emission micrograph of a spherical gold particles of about 3 μm diameter and (b) an enlarged part of surface of the particle of (a), showing small particles (subunits) of about 30 nm diameter. Reproduced from D.V. Goia and E. Matijević. *Colloids Surf. A* **146**, 139. Copyright (1999), with permission from Elsevier

the last decade, by simple precipitation in homogeneous solutions in the absence or presence of organic additives, Matijević and co-workers obtained as submicrometer sized particles of a variety of drug substances such as naproxen (Pozarnsky and Matijević, 1997), budesonide (Ruch and Matijević, 2000), cyclosporin (Joguet and E. Matijević, 2002), danazol and loratadine (Matijević and Škapin, 2004), and ethyl 3,5-di(acetylamino) 2,4,6-triiodobenzoate (Bosch *et al.*, 2004). These authors demonstrated that variation in the solubility of the same drug in different but miscible liquids, or variation of the pH of their aqueous solutions, can be used to control the size, shape and internal structure of the drug particles.

In summary, the control of the size, shape and phase of precipitating particles of different materials involves three stages: (1) depending on the experimental conditions, formation of complexes of specific constitution in the initial solution, (2) initial aggregation of complexes into nanometer-sized primary particles, and (3) aggregation of primary particles to form micrometer-sized final particles. Stages (1) and (2) represent the traditional nucleation and growth processes, where stable nuclei of critical size are formed by heterogeneous nucleation first and these nuclei subsequently grow to primary particles. Stage (3) may be considered as the growth of the primary particles into large particles by aggregation processes. Results on the crystallization of different systems in the

presence of organic additives show that interactions of additives with crystal surfaces are responsible for changes in shape, size and form of the crystallizing particles.

In an interesting review, Wu and Nancollas (1999) discussed the interfacial tension values between solutions and various sparingly soluble compounds, determined by precipitation (nucleation), crystallization and dissolution kinetics and compared these with values obtained from constant composition reaction kinetics and contact angle measurements involving thin-layer wicking techniques. It was found that (1) the nucleation data for different systems give interfacial tensions which suggest that the crystallizing phases are nucleated either on their own or foreign surfaces and (2) the interfacial tension values obtained from constant composition reaction kinetics are comparable to those determined from the contact angle method. Their review pointed out the issues involved in the interpretation of interfacial data obtained from contact angle measurements, and considered the surface free energy as a resultant of a number of components (surface tension component theory) involving Lewis acid–base (i.e. polar; AB) and intermolecular (Lifshitz–van der Waals or apolar; LW) interactions. Moreover, the surface tension component due to polar interactions has two contributions: acidic (or electron acceptor) and basic (or electron donor). Thus, according to the surface tension component theory, the interfacial tension for liquids is given by

$$\gamma_L = \gamma_{LW} + \gamma_{AB} = \gamma_{LW} + \gamma_{AB}^+ + \gamma_{AB}^- \quad (7.34)$$

The authors made the following inferences:

- (1) The Lewis acid–base contribution to the interfacial tension is negligible for most simple organic liquids such as heptane and its higher homologs (i.e. $\gamma_{AB} = 0$), but this contribution is relatively high for solvents such as water, ethylene glycol, formamide and glycerol ($\gamma_{AB} > 0$).
- (2) The basic component of the interfacial tension is higher than the acidic component for the organic liquids (i.e. $\gamma_{AB}^+ > \gamma_{AB}^-$ and $\gamma_{AB} > \gamma_{LW}$), but in the case of water $\gamma_{AB}^+ = \gamma_{AB}^-$ and $\gamma_{AB} > \gamma_{LW}$.

Inference (1) above implies that Lewis acid–base parameters are important for inducing crystal nucleation. Analysis of the mineralized structures of various organisms shows that the organic matrix present in them is composed of acidic amino acid residues, which are believed to induce mineral formation through the attraction of ionic species and then control the subsequent nucleation and growth (Campbell, 1999). For example, Feng *et al.* (2000) found that soluble mollusk shell proteins extracted from nacre forming aragonite/calcite control the morphology and phase of crystallizing calcium carbonate. The morphologies are determined by the soluble proteins rather than the insoluble matrix on which they are nucleated. This suggests that the role of the insoluble matrix is to serve as a specialized substrate for calcium carbonate nucleation while the soluble proteins control the crystal growth processes which determine the final crystal morphology. This conclusion is corroborated by several other natural organic macromolecules in affecting the crystallization behavior of calcium carbonate (Levi *et al.*, 2001).

Clark *et al.* (1999) investigated the relationship between the electrostatic distribution on protein surface and secondary calcium oxalate growth using 10 aspartic acid residues on its surface. They found that the surface properties of the protein interacting at the surface

of the crystal determine whether growth is inhibited or promoted. These observations appear to be corroborated by the inhibiting effect of aspartic acid on the spiral morphology on the surfaces of calcite (Teng *et al.*, 1998) and the normal growth rate of the (001) face of COM (Guo *et al.*, 2002). Bouropoulos *et al.* (2001) also observed that macromolecular extracts from tobacco and tomato leaves inhibit the growth of the (120) faces of COM crystals. Yang *et al.* (1988) reported that certain amphiphilic antifreeze proteins interact with ice crystal surfaces with their hydrophilic sides, leaving their hydrophobic sides exposed to inhibit growth. From a study of the growth of calcium oxalate crystals in the presence of four isoforms of nephrocalcin (NC), a urinary protein used to inhibit kidney stone growth, Kurutz *et al.* (2003) also arrived at a similar conclusion. They proposed that in the nucleation stage binding of calcium ions to NC maintains the amphiphilic character of the proteins and stabilizes them at air–water and crystal–water interfaces. However, during growth NC coats the hydrophilic faces of calcium oxalate crystals, leaving their exposed hydrophobic faces to inhibit subsequent growth. The ability of an NC isomorph to bind calcium ions during nucleation and to inhibit the growth of a face depends on the surface activity of the isomorph.

7.4.2 Template-Directed Synthesis

The techniques of template-directed synthesis mainly depend on the creation of functionalized interfaces for inducing heterogeneous nucleation and many of them use microemulsions as templates. Among the commonly used techniques for template directed synthesis are (Adair *et al.*, 1998; Campbell, 1999; Cölfen, 2003; Foo *et al.*, 2004) Langmuir monolayers, self-assembling monolayers, supramolecular assemblies, functionalized polymer substrates, immobilized biomolecules, and inorganic substrates derivatized with organic monolayers. The first three are briefly described below. Various template-directed techniques involving the fabrication of desired material within the pores or channels of a nanoporous template and suitable for applications in nanotechnology were reviewed by Huczko (2000). For more details, the reader is referred to the literature.

Langmuir monomolecular films are used to produce well-defined interfaces with desired charge densities and head group spacing (Figure 7.22a). The monolayers enable one to control the role of the polar head groups in binding the precipitating species and relative packing of the amphiphilic molecules in determining the epitaxial relationship between the template and the templated material. For example, Letellier *et al.* (1998) designed a model monolayer system to control the interfacial parameters (such as lattice matching, hydrogen bonding, stereochemistry and electrostatics) for the precipitation of calcium oxalate monohydrate (COM). It was found that (1) lattice matching or hydrogen bonding determines the control of COM crystal orientation, (2) stereochemistry (associated with monolayer head groups and crystal ions) determines the crystal morphology and nucleation, and (3) nonspecific electrostatic interactions control the growth of oriented COM crystals with well-defined morphologies. Mann *et al.* (1988, 1991) investigated the role of monolayer charge on calcium carbonate nucleation. They found that the growth of oriented calcite requires a negatively charged interface and electrostatic interactions between the monolayer and calcium ions stimulate calcite nucleation. Later studies showed (Heywood and Mann, 1994; Litvin *et al.*, 1997) that different CaCO_3 orientations nucleate under sulfate- and phosphate-terminated monolayers due to stereochemical relationships between the monolayer and the nucleating calcium carbonate form.

The use of Langmuir films is not confined to the precipitation of biominerals alone. Ravaine *et al.* (1998) studied the formation of gold particles on Langmuir films with several different amphiphilic head-group molecules. The nucleating species were obtained by photo-reduction of gold chloride in the system. It was found that binding between AuCl_4^- ions and positively charged polar head groups results in templating to form plate-like gold particles from 20 to 800 nm across the face. Uncharged and negatively charged polar head groups did not template the gold particles.

Unlike Langmuir films shown in Figure 7.22a, molecules of organic films can be attached to polymer, ceramic or metal substrates (Figure 7.22b). Such layers are called self-assembling monolayers (SAMs). Moreover, depending on the pattern in the substrate, patterned films can be obtained. The main advantage of these patterned films is that the crystallized structures can be easily separated and characterized. For example, Küther and Tremel (1998) studied the crystallization of calcium carbonate polymorphs on self-assembled monolayers of ω -substituted alkanethiols on gold surfaces.

Since 1990 there has been a lot of activity on the formation of inorganic minerals on SAMs (Campbell, 1999; Adair *et al.*, 1998; Li and Kaplan, 2003). Soluble inhibitors can be added to the solution to obtain a very thin layer of the deposit next to the promoting

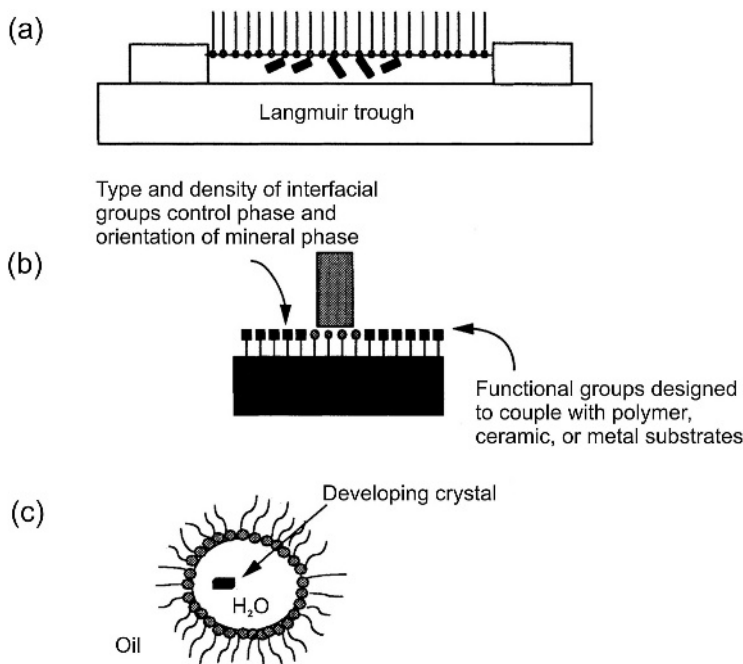


Figure 7.22 Schematic diagrams of two- and three-dimensional templates used for inducing heterogeneous nucleation of inorganic compounds: (a) Langmuir monomolecular film, (b) self-assembling monolayers, and (c) supramolecular templates such as reverse miscelle. Reproduced from A.A. Campbell. Curr. Opin. Colloid Interface Sci. **4**, 40. Copyright (1999), with permission from Elsevier

template. This so-called template-inhibition strategy has been used for the crystallization of CaCO₃ films on various substrates (for the literature, see Li and Kaplan, 2003).

Aizenberg *et al.* (1998) used patterned SAMs to produce ordered arrays of nucleation sites controlling calcite crystallization. The nucleation event was controlled by manipulation of the basal plane on which growth occurs and by manipulation of the mass transport of ions to nucleation sites. By patterning SAMs into domains of appropriate geometry and interfacial chemistry and by relying on the properties of mass transport, they demonstrated control of location and orientation of nucleation. It was found that nucleation domains are created by ‘stamping’ the surface with functional regions of a -CO₂H-, -OH- and -SO₃H-terminated SAM and back-filling the remaining surface with a -CH₃-terminated SAM. By careful manipulation of the density, size and functionality of the stamped region of the monolayer and the control of the solution conditions, it was possible to control the number of crystals nucleated within a region, the density of nucleation sites and the orientation of the growing crystallites.

Amphiphilic molecules of surfactants can self-assemble into different thermodynamically stabilized microstructures such as micelles, vesicles, liposomes, microtubules, and bilayers (Dickinson and McClements, 1995; Jones and Chapman, 1995; also see Section 1.4). These structures are physically, rather than chemically, associated, and the processes of their formation and evolution from one to another strongly depend on solution pH, ionic strength and temperature. Above a critical concentration (called the critical micelle concentration, CMC), the amphiphilic molecules of the surfactant associate to form aggregates (micelles) in polar solvents. When water is present together with the surfactant, the water molecules bind to the hydrophilic part of the amphiphilic surfactant molecules (polar heads), forming reverse micelles containing immobilized water molecules (Figure 7.22c). Additional solubilization of water results in aggregates containing small pools of water, and the system is referred to as a water-in-oil microemulsion (see Section 8.3.1). By providing size and geometric constraints and chemical stabilization, these microstructures serve as microreactors for the precipitation of organic and inorganic nanoscale clusters (Adair *et al.*, 1998).

For the investigation of biomineralization processes, gels have proved very useful, because they are less rigid than the templating insoluble organic matrix for the morphology control of biominerals. Moreover, by selecting an appropriate gelling medium and experimental conditions, they offer the possibility to mimic the growth of various biominerals in environments similar to natural biomineralization. Among the different gels, gelatin gels are of special interest because this polymer is a degradation product of collagen, which is an important part of the organic matrix of bones (see Chapter 6). Although fluoroapatite, hydroxyapatite, and calcium carbonate have been crystallized in gelatin gels, the majority of the publications have been devoted to the crystallization of calcium carbonate.

Falini *et al.* (1994, 1997, 1998) studied the controlled crystallization of calcium carbonate in gelatin gels without and with incorporated polypeptides (poly-L-aspartate and poly-L-glutamate) and observed that cross-linked gelatin with entrapped polypeptides provides a favorable environment for the controlled crystallization of calcium carbonate. In later work, Falini (2000) investigated the nature, density and structural geometry of the charged groups responsible for the crystallization of different calcium carbonate phases by changing the amount of poly-L-aspartate and poly-L-glutamate and also by

changing the structure of polypeptide–gelatin supramolecular assembly by mechanical deformation. It was found that the local supersaturation in the microenvironment where nucleation and growth occur determines the deposition of crystalline calcium carbonate polymorph inside cross-linked gelatin films and that a structured organic scaffold organizes the crystalline units in unusual habits. Figure 7.23 shows a schematic model of the oriented crystallization of calcium carbonate induced by interaction of the negatively charged groups of poly-L-aspartate in the β -structure with one of the most positively charged crystal plane of calcite, aragonite and vaterite.

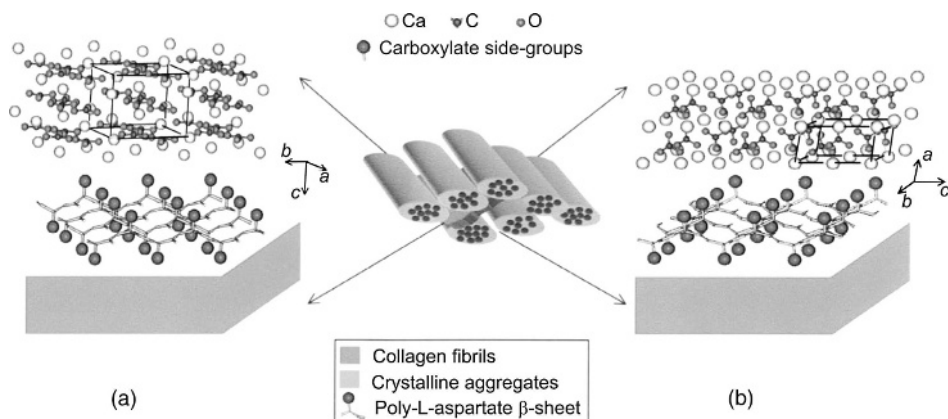


Figure 7.23 Schematic model of oriented nucleation of (a) aragonite and (b) vaterite in uniaxially deformed cross-linked gelatin film containing poly-L-aspartate. Different amounts of entrapped polypeptide induces one or the other polymorph. Reproduced from G. Falini. Int. J. Inorg. Mater. **2**, 455. Copyright (2000), with permission from Elsevier

Grassmann *et al.* (2003) reported that complex assemblies of oriented calcite subunits with microstructural similarities to natural mineralization can also be produced in a polyacrylamide hydrogel, indicating again the importance of physical network structures in mineralization processes. However, crystallization of calcium carbonate in polyacrylamide hydrogels modified with $-\text{SO}_3\text{H}$ groups (Grassmann and Löbmann, 2003) and $-\text{COOH}$ groups (Grassmann and Löbmann, 2004) showed significant differences in the calcium carbonate crystallization. In unmodified and $-\text{SO}_3\text{H}$ -modified polyacrylamide hydrogels, large precipitates with diameters exceeding $300\ \mu\text{m}$ after 1 week were formed, but the presence of $-\text{COOH}$ groups resulted only in turbidity due to a multitude of small precipitates after this period. The smaller precipitates are subsequently consumed by distinct larger calcite precipitates appearing as spherulites in the gel. These crystallization processes are represented schematically in Figure 7.24 as a function of time. The above results show that the stereochemical relationship between $-\text{COOH}$ moieties and the CO_3^{2-} ions of the crystalline phase dominates over purely electrostatic interactions.

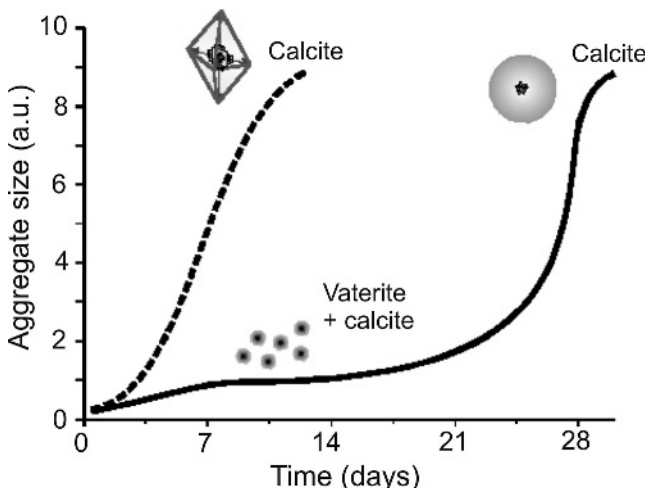


Figure 7.24 Schematic representation of the course of calcium carbonate crystallization in unmodified (dashed curve) and --COOH -modified polyacrylamide hydrogels (solid curve) as a function of time. Reproduced from O. Grassmann and P. Löbmann. Biomaterials **25**, 277. Copyright (2004), with permission from Elsevier

7.5 Biological Tissue Engineering

Mineralized tissues, such as bone, teeth and seashells, are usually formed at ambient temperature and in aqueous solutions. Although the dimensions of individual crystallites in these tissues are in the nanometer to micrometer range, these fine-scale structures are integrated into microscopic forms with excellent properties. As described in Chapter 6, calcium carbonates and calcium phosphates constitute these mineralized tissues and are two extensively studied biominerals. It is now known that crystallization of these biominerals usually starts on a template consisting of insoluble organic matrix, but nucleation and growth processes are regulated by the exposed acidic groups on the matrix (Section 7.4).

Cellular responses of mineralized tissues to materials depend on the structural properties of the materials at both the nano- and micrometer scale. However, there is a lack of general methods for controlling material properties on both of these scales. Therefore, the production of biomaterials for bone regeneration with complex structures having hierarchically organized features of different length scales is of increasing importance for biomedical applications.

Saito *et al.* (2003) investigated the effect of different additives, such as silicate, fluoride, calcium, phosphate, magnesium and silver, on the mineralization of dentin matrix *in vitro*. For the investigation, demineralized dentin matrix was incubated in a metastable calcium phosphate solution with or without the additive. It was found that silicate, fluoride, calcium and phosphate promoted whereas magnesium and silver inhibited the mineralization of dentin matrix. The above case is an example of tissue repair, yet it is difficult to implement the mineralization process *in vivo*.

The formation of an organic template for natural biomineralization involves complex cellular processes and it is difficult to duplicate template formation *in vitro*. Therefore, other approaches that mimic natural biomineralization processes have to be developed. Using the idea of microfabrication technology, widely used in semiconductor industry for making electronic materials, Tan and Saltzman (2004) synthesized nanostructured hydroxyapatite (HAP) minerals onto preset micrometer scale architectures following natural mineralization approaches. Figure 7.25 shows a schematic drawing of the fabrication steps. In this method, micropatterns were first created on silicon wafers using photolithography and reactive ion etching techniques (Figure 7.25b). Then nanostructured HAP were synthesized on the silicon microstructures. The procedure involved (a) surface modification of patterned silicon by attaching amine groups to silicon patterns (silanization) and obtaining carboxyl-terminated surface (succinylation) (see Figure 7.25c) and (b) deposition of HAP by immersing carboxyl-terminated patterned silicon chips in supersaturated calcium phosphate aqueous solutions of pH 7.4 at 37°C for desired periods (Figure 7.25d). Finally, the silicon chips were removed from calcium phosphate solutions

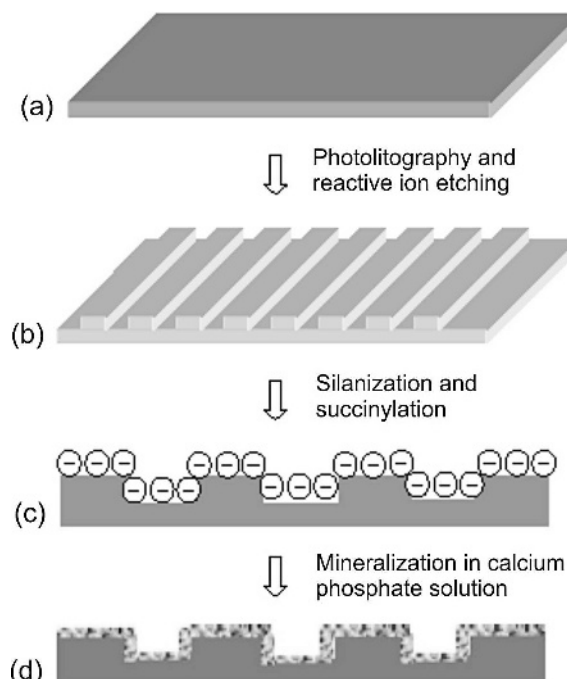


Figure 7.25 Schematic drawing of different fabrication steps for producing micro- and nanostructured material: (a) a clean silicon wafer, (b) micropatterns created by using photolithography and reactive ion etching techniques, (c) surface modification of patterned silicon by silanization and succinylation, and (d) deposition of HAP by immersing carboxyl-terminated patterned silicon chips in supersaturated calcium phosphate aqueous solutions. Reproduced from J. Tan and W.M. Saltzman. Biomaterials **25**, 3593. Copyright (2004), with permission from Elsevier

after different deposition periods, rinsed in water and dried, followed by examination of nanoscale structures with scanning electron and atomic force microscopes.

Figure 7.26 represents the phase diagram of calcium phosphate solutions at 37°C and ionic strength 0.15 mol/l, where the logarithm of the product of total calcium and phosphate concentrations is plotted as a function of solution pH. The tendency for precipitation of a calcium phosphate phase in the solution may be judged from this diagram. Most biological fluids fall into the box in the plot. Solutions A, B, C and D in the physiological range were tested to obtain uniform nanostructured HAP layer on the patterned silicon substrate. The thermodynamic driving force is the highest for solution A and decreases progressively from A to D. In solution A, dicalcium phosphate dihydrate (DCPD) and octacalcium phosphate (OCP), which are metastable phases, precipitated due to homogeneous nucleation within 6 h. In solution B, heterogeneous nucleation occurred in 8 h with the formation of plate-like morphology after 24 h, and the mineral layer was nearly uniform and continued to grow for periods up to 72 h. In solution C, heterogeneous nucleation took place after 24 h with the mineral having a plate-like morphology, but the growth ceased after 48 h. In solution D, no crystallization occurred within 24 h.

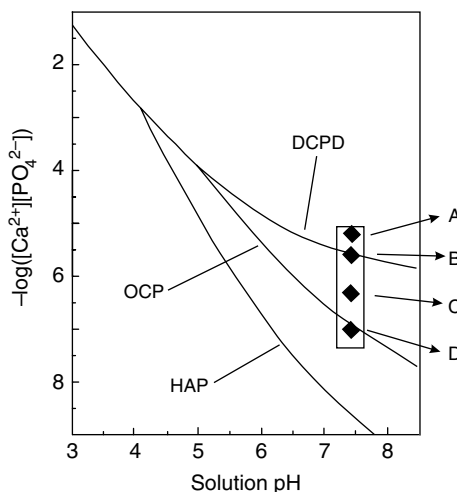


Figure 7.26 Plots of logarithm of the product of total calcium and phosphate concentrations against solution pH for calcium phosphate solutions at 37°C and ionic strength 0.15 mol/l. Most biological fluids fall into the box in the plot. Reproduced from J. Tan and W.M. Saltzman. Biomaterials **25**, 3593. Copyright (2004), with permission from Elsevier

On the basis of the above results, Tan and Saltzman (2004) selected solution B for the study of HAP structures at various times after the initiation of mineralization. Typical SEM images of the evolution of the mineralized structures on a patterned parallel ridges/channel silicon substrates are shown in Figure 7.27a–c. As can be seen, a nearly continuous mineral layer is formed on the patterned surface after 24 h (Figure 7.27b), and the mineral morphology changes to thin and plate-like. On prolonged growth, the mineral

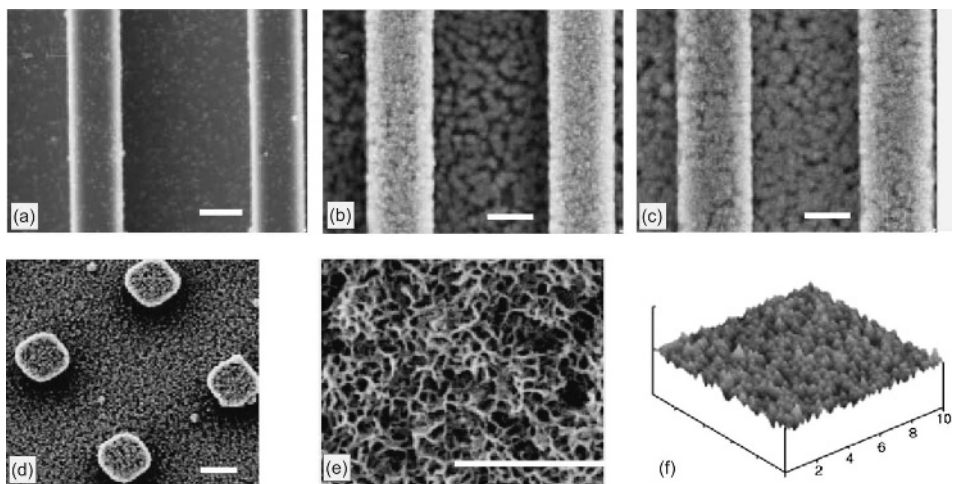


Figure 7.27 SEM images of mineralized structures on (a–c) patterned parallel ridges/channel and (d–f) pillared silicon substrates; scale bars represent 4 μm . In (a–c), evolution of structures is shown for different durations: (a) 8, (b) 24 and (c) 48 h, while (f) shows an AFM image of the structure. Reproduced from J. Tan and W.M. Saltzman. *Biomaterials* **25**, 3593. Copyright (2004), with permission from Elsevier

morphology essentially remains the same but the ridges become wider (Figure 7.27c). The results obtained for mineral formation on pillared structures are similar (Figure 7.27d). Detailed examination of thin plate-like morphology revealed nanometer-scale texture composed of thin plates of less than 100 nm on the patterned surface (Figure 7.27e), which remained practically unchanged with reaction time up to 3 days and had a mean size 55 ± 32 nm (Figure 7.27f). It was established that the mineral obtained has a structural texture and chemical composition similar to those of the bone mineral.

References

- Abegg, C.F., J.D. Stevens, and M.A. Larson (1968). *AIChE. J.* **14**, 118.
- Adair, J.H., and E. Suvaci (2000). *Curr. Opin. Colloid Interface Sci.* **5**, 160.
- Adair, J.H., T. Li, T. Kido, K. Havey, J. Moon, J. Mecholsky, A. Morrone, D.R. Talham, M.H. Ludwig, and L. Wang (1998). *Mater. Sci. Eng.* **R23**, 139.
- Aizenberg, J., J. Hanson, T.F. Koetzle, S. Weiner, and L. Addadi (1997). *J. Am. Chem. Soc.* **119**, 881.
- Aizenberg, J., A.J. Black, and G.M. Whitesides (1998). *Nature* **394**, 868.
- Algra, R.E., W.S. Graswinckel, W.J.P van Enckevort, and E. Vlieg (2005). *J. Cryst. Growth* **285**, 168.
- Andreassen, J.P. (2005). *J. Cryst. Growth* **274**, 256.
- Aslanian, S., I. Kostov, and H. Neels (1968). *Krist. Tech.* **3**, 619.
- Belter, P.A., E.L. Cussler, and W.-S. Hu (1988). *Bioseparations*, Interscience, New York.
- Berglund, K.A. (1993): In: A.S. Myerson (Ed.), *Handbook of Industrial Crystallization*, Butterworth-Heinemann, Boston, p. 89.

- Berglund, K.A., and E.J. de Jong (1990). *Sep. Technol.* **1**, 1.
- Bienfait, M.R., R. Boistelle and R. Kern (1965). In: R. Kern (Ed.), *Adsorption et Croissance Cristalline*, CNRS, Paris, p. 577.
- Boistelle, R. (1980). In: E. Kaldis (Ed.), *Current Topics in Materials Science*, Vol. 4, North-Holland, Amsterdam, p. 413.
- Boistelle, R., and B. Simon (1974). *J. Cryst. Growth* **26**, 140.
- Borgström, L.H. (1925). *Z. Kristalloge* **62**, 1.
- Bosch, H.W., S.D. Srečo, and E. Matijević (2004). *Colloids Surf. A* **250**, 43.
- Bouropoulos, N., S. Weiner, and L. Addadi (2001). *Chem. Eur. J.* **7**, 1881.
- Bramley, A.S., M.J. Hounslow, and R.L. Ryall (1996). *J. Colloid Interface Sci.* **183**, 155.
- Bramley, A.S., M.J. Hounslow, and R.L. Ryall (1997). *Chem. Eng. Sci.* **52**, 747.
- Brunsteiner, M., A.G. Jones, F. Pratola, S.L. Price, and S.J.R. Simons (2005). *Cryst. Growth Des.* **5**, 3.
- Bulakh, B.M. (1969). *J. Cryst. Growth* **5**, 243.
- Campbell, A.A. (1999). *Curr. Opin. Colloid Interface Sci.* **4**, 40.
- Chernov, A.A. (1961). *Usp. Fiz. Nauk* **73**, 277; Engl. Transl.: *Sov. Phys. Usp.* **4**, 116.
- Chernov, A.A., and A.I. Malkin (1988). *J. Cryst. Growth* **92**, 432.
- Clark, R.H., A.A. Campbell, L.A. Klumb, C.J. Long, and P.S. Stayton (1999). *Calcif. Tissue Int.* **64**, 516.
- Cody, A.M., and R.D. Cody (1991). *J. Cryst. Growth* **113**, 508.
- Cölfen, H. (2003). *Curr. Opin. Colloid Interface Sci.* **8**, 23.
- Dam, B., and W.J.P. van Enckevort (1984). *J. Cryst. Growth* **69**, 306.
- Davey, R.J., and J.W. Mullin (1974). *J. Cryst. Growth* **26**, 45.
- Dickinson, E., and D.J. McClements (1995). *Advances in Food Colloids*, Chapman and Hall, London.
- Dove, P.M., J.J. De Yoreo, and K.J. Davis (2004). In: X.Y. Liu and J.J. De Yoreo (Eds.), *Nanoscale Structure and Assembly at Solid–Fluid Interfaces, Vol. II: Assembly at Hybrid and Biological Systems*, Kluwer, Boston, Chap. 2, p. 55.
- Dunning, W.J., and N. Albon (1958). In: R.H. Doremus, B.W. Roberts, and D. Turnbull, (Eds.), *Growth and Perfection of Crystals*, John Wiley & Sons, Inc., New York, p. 411.
- Dunning, W.J., R.W. Jackson, and D.G. Mead (1965). In: R. Kern (Ed.), *Adsorption et Croissance Cristalline*, CNRS, Paris, p. 303.
- Falini, G. (2000). *Int. J. Inorg. Mater.* **2**, 455.
- Falini, G., M. Gazzano, and A. Ripamonti (1994). *Adv. Mater.* **6**, 46.
- Falini, G., S. Fermani, M. Gazzano, and A. Ripamonti (1997). *Chem. Eur. J.* **3**, 1807.
- Falini, G., S. Fermani, M. Gazzano, and A. Ripamonti (1998). *Chem. Eur. J.* **6**, 1408.
- Feng, Q.L., G. Pu, Y. Pei, F.Z. Cui, H.D. Li, and T.N. Kim (2000). *J. Cryst. Growth* **216**, 459.
- Fenimore, C.P., and A. Thraikill (1949). *J. Am. Chem. Soc.* **71**, 2714; cited by Weissbuch *et al.* (1995).
- Foo, C.W.P., J. Huang, and D.L. Kaplan (2004). *Trends Biotechnol.* **22**, 577.
- Gadewar, S.B., and M.F. Doherty (2004). *J. Cryst. Growth* **267**, 239.
- Gibrat, R. (1930). *Bull. Stat. Gen.* **19**, 469; cited by Kile *et al.* (2000).
- Glatz, C.E., M. Hoare, and J. Landa-Vertz (1987). *AIChE J.* **32**, 1196.
- Goia, D.V., and E. Matijević (1998). *New J. Chem.* **22**, 1203.
- Goia, D.V., and E. Matijević (1999). *Colloids Surf. A* **146**, 139.
- Gomez-Morales, J., J. Torrent-Burgues, and R. Rodriguez-Clemente (2001). *Cryst. Res. Technol.* **36**, 1065.
- Grassmann, O., and P. Löbmann (2003). *Chem. Eur. J.* **9**, 1310.
- Grassmann, O., and P. Löbmann (2004). *Biomaterials* **25**, 277.
- Grassmann, O., R. Neder, A. Putnis, and P. Löbmann (2003). *Am. Mineral.* **88**, 647.

- Gratz, A.J., and P.E. Hillner (1993). *J. Cryst. Growth* **129**, 789.
- Grimbergen, R.F.P., H. Meekes, P. Bennema, C.S. Strom, and L.J.P. Vogels (1998). *Acta Crystallogr. A* **54**, 491.
- Guo, S., M.D. Ward, and J.A. Wesson (2002). *Langmuir* **18**, 4284.
- Hardikar, V.V., and E. Matijević (2001). *Colloids Surf. A* **186**, 23.
- Hartel, R.W., and A.D. Randolph (1986). *AIChE J.* **32**, 1136.
- Hartman, P. (1973). In: P. Hartman (Ed.), *Crystal Growth: an Introduction* North-Holland, Amsterdam, p. 367.
- Hartman, P. (1987). In: I. Sunagawa (Ed.), *Morphology of Crystals, Part A*, Terrapub, Tokyo, Chap. 4.
- Heywood, B.R., and S. Mann (1994). *Chem. Mater.* **6**, 311.
- Hottenhuis, M.H.J., and C.B. Lucasius (1986). *J. Cryst. Growth* **78**, 379.
- Hottenhuis, M.H.J., and A. Oudenampsen (1988). *J. Cryst. Growth* **92**, 513.
- Hounslow, M.J., H.S. Mumtaz, A.P. Collier, J.P. Barrick, and A.S. Bramley (2001). *Chem. Eng. Sci.* **56**, 2543.
- Hoyt, R.C. (1978). *PhD Thesis*, Iowa State University, Ames, IA; cited by Berglund (1993).
- Huczko, A. (2000). *Appl. Phys. A* **70**, 365.
- Inoue, T., and K. Nishioka (2000). *J. Cryst. Growth* **212**, 507.
- Jimenez-Lopez, C., A. Rodriguez-Navarro, J.M. Dominguez-Vera, and J.M. Garcia-Ruiz (2003). *Geochim. Cosmochim. Acta* **67**, 1667.
- Joguet, L., and E. Matijević (2002). *J. Colloid Interface Sci.* **250**, 503.
- Jones, M.N., and D. Chapman (1995). *Micelles, Monolayers, and Biomembranes*, Wiley-Liss, New York.
- Jung, T., W.-S. Kim, and C.K. Choi (2004). *Mater. Sci Eng. C* **24**, 31.
- Jung, T., W.-S. Kim, and C.K. Choi (2005). *J. Cryst. Growth* **279**, 154.
- Kapteyn, J.C. (1903). *Skew Frequency Curves in Biology and Statistics*, Astronomical, Laboratory, Noordhoff, Groningen; cited by Kile *et al.* (2000).
- Kern, R. (1967). In: N.N. Sheftal (Ed.), *Rost Kristallov (Growth of Crystals)*, Vol. 8, Nauka, Moscow, 1967, p. 5.
- Kile, D.E., D.D. Eberl, A.R. Hoch, and M.M. Reddy (2000). *Geochim. Cosmochim. Acta* **64**, 2973.
- Kind, M. (2002). *Chem. Eng. Sci.* **57**, 4287.
- Kitamura, M. (2001). *J. Colloid Interface Sci.* **236**, 318.
- Kitano, Y., K. Park, and D.W. Hood (1962). *J. Geophys. Res.* **67**, 4873.
- Kozlovskii, M.I. (1957). *Kristallografiya* **2**, 760.
- Kurutz, J.W., M. Carvalho, and Y. Nakagawa (2003). *J. Cryst. Growth* **255**, 392.
- Küther, J., and W. Tremel (1998). *Thin Solid Films* **327/329**, 554.
- Lee, I., S.W. Han, H.J. Choi, and K. Kim (2001). *Adv. Mater.* **13**, 1617.
- Letellier, S.R., M.J. Lockhead, A.A. Campbell, and V. Vogel (1998). *Biochim. Biophys. Acta* **1380**, 31.
- Leubner, I.H. (2000). *Curr. Opin. Colloid Interface Sci.* **5**, 151.
- Leubner, I.H. (2002). *J. Dispers. Sci. Technol.* **23**, 577.
- Levi, Y., S. Albeck, A. Brack, S. Weiner, and L. Addadi (2001). *Chem. Eur. J.* **4**, 389.
- Li, C., and D.L. Kaplan (2003). *Curr. Opin. Solid State Mater. Sci.* **7**, 265.
- Li, L., K. Tsukamoto, and I. Sunagawa (1990). *J. Cryst. Growth* **99**, 150.
- Lifshitz, I.M., and V.V. Slyozov (1961). *J. Phys. Chem.* **19**, 35; Cited by Kile *et al.* (2000).
- Litvin, A.L., S. Viliyaveettil, D.L. Kaplan, and S. Mann (1997). *Adv. Mater.* **9**, 124.
- Mann, S., B.R. Heywood, S. Rajam, and J.D. Birchall (1988). *Nature* **334**, 692.
- Mann, S., B.R. Heywood, S. Rajam, and J.B. Walker (1991). *J. Phys. D* **3**, 154.
- Matijević, E., and S. Škapin (2004). *J. Colloid Interface Sci.* **272**, 90.
- Mayer, A., and M. Antonietti (1998). *Colloid Polym. Sci. (Kolloid-Z.)* **276**, 769.

- Meekes, H., P. Bennema, and R.F.P. Grimbergen (1998). *Acta Crystallogr. A* **54**, 501.
- Moon, J., M.L. Carasso, J.H. Adair, H.G. Krarup, and J.H. Kerchner (1999). *J. Mater. Sci.* **14**, 866.
- Myerson, A.S., and R. Ginde (1993). In: A.S. Myerson (Ed.), *Handbook of Industrial Crystallization*, Butterworth-Heinemann, Boston, p. 33.
- Onuma, K. (2006). *Prog. Cryst. Growth Charact. Mater.* **52**, 223.
- Owczarek, I., and K. Sangwal (1990). *J. Cryst. Growth* **99**, 827.
- Pozarnsky, G.A., and E. Matijević (1997). *Colloids Surf. A* **125**, 47.
- Prywer, J. (1996). *J. Cryst. Growth* **158**, 568.
- Prywer, J. (1999). *J. Cryst. Growth* **197**, 271.
- Prywer, J. (2003). *Cryst. Growth Des.* **3**, 593.
- Prywer, J. (2004). *Cryst. Growth Des.* **4**, 1365.
- Prywer, J. (2005). *Prog. Cryst. Growth Charact. Mater.* **50**, 1.
- Radenović, N., W. van Enckevort, P. Verwer, and E. Vlieg (2003). *Surf. Sci.* **523**, 307.
- Radenović, N., W. van Enckevort, and E. Vlieg (2004). *J. Cryst. Growth* **263**, 544.
- Radenović, N., W. van Enckevort, D. Kaminski, M. Heijna, and E. Vlieg (2005). *Surf. Sci.* **599**, 196.
- Randolph, A.D., and M.A. Larson (1971). *Theory of Particulate Processes*, Academic Press, New York.
- Randolph, A.D., and M.A. Larson (1988). *Theory of Particulate Processes*, 2nd ed., Academic Press, San Diego, CA.
- Ravaine, S., G.E. Fanucci, C.T. Seip, J.H. Adair, and D.R. Talham (1998). *Langmuir* **14**, 708.
- Raz, S., S. Weiner, and L. Addadi (2000). *Adv. Mater.* **12**, 38.
- Reyhani, M.M., A. Olivier, G.M. Parkinson, F. Jones, A.L. Rohl, and M.I. Ogden (2002). *Int. J. Mod. Phys.* **16**, 25.
- Rohl, A.L. (2003). *Curr. Opin. Solid State Mater. Sci.* **7**, 21.
- Roque, J., J. Molera, M. Vendrell-Saz and N. Salvado (2004). *J. Cryst. Growth* **262**, 543.
- Ruch, F., and E. Matijević (2000). *J. Colloid Interface Sci.* **229**, 207.
- Rudloff, J., M. Antonietti, H. Cölfen, J. Pretula, K. Kaluzynski, and S. Penczek (2002). *Macromol. Chem. Phys.* **203**, 627.
- Saito, T., H. Toyooka, S. Ito, and M.A. Crenshaw (2003). *Caries Res.* **37**, 445.
- Sangwal, K. (1996). *Prog. Cryst. Growth Charact. Mater.* **32**, 3.
- Sangwal, K. (1998). *Prog. Cryst. Growth Charact. Mater.* **36**, 163.
- Sangwal, K., and R. Rodriguez-Clemente (1991). *Surface Morphology of Crystalline Solids*, Trans Tech, Zurich.
- Sangwal, K., E. Mierniczek-Brzóska, and J. Borc (2003). *Cryst. Res. Technol.* **38**, 103.
- Sedlak, M., M. Antonietti, and H. Cölfen (1998). *Macromol. Chem. Phys.* **203**, 627.
- Simons, S.J.R., Y. Pratola, A.G. Jones, M. Brunsteiner, and S.L. Price (2004). *Parti. Part. Syst. Charact.* **21**, 276.
- Söhnel, O., and J. Garside (1992). *Precipitation: Basic Principles and Industrial Applications*, Butterworth-Heinemann, London.
- Sondi, I., and E. Matijević (2001). *J. Colloid Interface Sci.* **238**, 208.
- Sunagawa, I. (1981). *Bull. Mineral.* **104**, 81.
- Sunagawa, I. (2005). *Crystals: Growth, Morphology and Perfection*, Cambridge University Press, Cambridge.
- Szurgot, M., and J. Prywer (1991). *Cryst. Res. Technol.* **26**, 115.
- Tan, J., and W.M. Saltzman (2004). *Biomaterials* **25**, 3593.
- Teng, H.H., P.M. Dove, C.H. Orme, and J.J. De Yoreo (1998). *Science* **282**, 724.
- Toschev, S. (1973). In: P. Hartman (Ed.), *Crystal Growth: an Introduction*, North-Holland, Amsterdam, p. 328.
- Troost, S. (1972). *J. Cryst. Growth* **13/14**, 449.
- van der Eerden, J.P., and H. Müller-Krumbhaar (1986). *Electrochim. Acta* **31**, 1007.

- van Panhuys-Sigler, M., P. Hartman, and C.F. Woensdregt (1988). *J. Cryst. Growth* **87**, 554.
- Wagner, C. (1961). *Z. Elektrochem.* **65**, 561; cited by Kile *et al.* (2000).
- Wang, L., I. Sondi, and E. Matijević (1999). *J. Colloid Interface Sci.* **218**, 545.
- Wang, L., J.J. De Yoreo, X. Guan, S.R. Qui, J.R. Hoyer, and G.H. Nancollas (2006a). *Cryst. Growth Des.* **6**, 1768.
- Wang, L., W. Zhang, S.R. Qui, W.J. Zachowicz, X. Guan, R. Tang, J.R. Hoyer, J.J. De Yoreo, and G.H. Nancollas (2006b). *J. Cryst. Growth* **291**, 160.
- Weissbuch, I., L. Leiserowitz, and M. Lahav (1995). In: A. Mersmann (Ed.), *Crystallization Technology Handbook*, Marcel Dekker, New York, p. 401.
- Wu, W., and G.H. Nancollas (1999). *Adv. Colloid Interface Sci.* **79**, 229.
- Yang, D.S.C., M. Sax, A. Chakrabarty, and C.L. Hew (1988). *Nature* **333**, 232.
- Yu, J., H. Tang, and B. Chang (2005). *J. Colloid Interface Sci.* **288**, 407.
- Zhou, Y.C.Y., Y.R. Zhu, and Z.Y. Chen (1999). *Commun. Chem. Mater.* **11**, 2310.3.

8

Additives and Crystallization Processes in Industries

Various types of crystallization processes are encountered in industries, depending on the final product desired by the industry for marketing purposes. In the fertilizer industry, the important requirements that the crystallized solid-state product has to fulfill are its phase or polymorph, growth morphology and size distribution, because they ultimately determine the product solid-state properties such as separation, flow, compaction, dissolution and packing. The product should be stable during its storage life, and should have a solubility such that it is easily devoured by the earth and plants. In the pharmaceutical industry, the requirements are even more stringent, because the *in vivo* performance of a drug depends not only on the polymorph but also on its oral bioavailability. Dry powders, for example, are required for pulmonary administration, whereas it is desired to improve the performance of poorly water-soluble drugs by enhancing their oral bioavailability by increasing dissolution rates. The latter is possible by applying fine particle technology to develop dosage form in such a way that the ratio of surface area to substance mass is increased.

The above examples show that crystallization processes are the basis of the very existence of industries, where the role of crystallization conditions, including additives, is to ensure the formation of the desired end product. The end product is obtained by crystallization in the bulk medium or on some templates. Therefore, it is worthwhile to describe and discuss the main features of crystallization processes in common industries and the effects of additives on these crystallization processes. These issues are addressed in this chapter.

8.1 Pharmaceutical Industry

Solid-state properties of the active pharmaceutical components of drugs determine the product stability and the *in vivo* performance of the drugs. Since drug materials frequently exist in multiple polymorphic crystal forms and/or amorphous solids, it is always desirable to incorporate the most thermodynamically solid-state form of a dosage to avoid any transformation of the drug during its shelf-life. The morphology and the size of drug particles are also important factors during the formulation of development and manufacturing strategies. Because the morphology of crystallized particles determines their flow properties, appropriate morphology of the drug particles is essential in blending and compaction. Since the bioavailability of drugs is intimately connected with their solubility and dissolution rate, the size of drug particles is also an important consideration of development strategy. This factor is especially important when developing dosages of poorly water-soluble drugs. Therefore, it is an important task to develop methods to obtain drug particles of appropriate shape, size and internal structures for reproducible and maximized therapeutic efficacy.

The conventional batch or continuous crystallization processes yield relatively large particles in a wide range of size and morphology. This limitation requires an additional step to obtain suitable particle size characteristics using techniques such as microionization by air-jet milling. However, this processing does not lead to any significant control of the shape and morphology of the mechanically fractured crystals. Alternative methods for the production of solid drug particles of optimum particle size are based on the use of supercritical fluids in the precipitation of active material, spraying of solutions into liquid nitrogen, complex spray-drying of emulsion-based formulations, and conventional antisolvent precipitation-based techniques (Edwards *et al.*, 1997; York, 1999; Ruch and Matijević, 2000; Crowder *et al.*, 2002; Duddu *et al.*, 2002; Bosch *et al.*, 2004; Kaerger and Price, 2004; Rogers *et al.*, 2003). Other approaches in fine drug particle technology are based on adsorption of drug substances on uniform inorganic carriers, as exemplified by the encapsulation of nanosized alumina particles in naproxen and ketoprofen (Joguet *et al.*, 2002), and coating of drug particles by organic polymers such as polymethacrylates, to yield products of enhanced physical stability (Chang and Robinson, 1990; Wurster, 1990).

During the last decade, by simple precipitation in homogeneous solutions in the absence or presence of organic additives, Matijević and co-workers obtained submicrometer-sized drug particles of a variety of substances such as naproxen (Pozarnsky and Matijević, 1997), budesonide (Ruch and Matijević, 2000), cyclosporin (Joguet and Matijević, 2002), danazol and loratadine (Matijević and Škapin, 2004) and ethyl 3,5-di(acetylamino)-2,4,6-triiodobenzoate (Bosch *et al.*, 2004). They demonstrated that variation in the solubility of the same drug in different but miscible liquids, or variation of pH of their aqueous solutions, can be used to control the size, shape and internal structure of the drug particles.

The basic mechanisms of nucleation and growth of drug substances are the same as for other soluble compounds, and are discussed in Chapters 2 and 3. Similarly, the size distribution and morphology of drug particles shows features as presented in Chapter 7. Some general features of the morphology, size distribution and dissolution rate of drug particles are described below.

8.1.1 Nucleation, Growth and Morphology of Drug Crystals

One of the popular drug compounds investigated during the last decade is paracetamol (acetaminophen), which is a widely used analgesic and antipyretic drug. Paracetamol is fairly soluble in water and sparingly soluble in methanol and ethanol. Several workers have investigated the morphology and properties of paracetamol crystals grown from aqueous solutions both without additives and with additives such as *p*-acetoxyacetanilide (PAA), agar, gelatin, polyvinylpyrrolidone (PVP) and hydroxypropylmethylcellulose (HPMC) (Chow *et al.* 1985; Femi-Oyewo and Spring, 1994; Prasad *et al.*, 2001; Ristić *et al.*, 2001) and also the influence of a range of structurally similar additives on the nucleation kinetics and crystallization of paracetamol (Hendriksen and Grant, 1995; Hendriksen *et al.*, 1998; Prasad *et al.*, 2001).

Nucleation experiments on paracetamol crystals from aqueous solutions at a constant temperature as a function of supersaturation and impurity concentration reveal that, for a constant concentration of an impurity, the induction period τ for nucleation decreases with increasing supersaturation. These features can be seen in Figure 8.1, which illustrates the dependence of the induction period τ on supersaturation σ for different concentrations c_i of PAA additive. However, at a constant supersaturation, the induction time for nucleation increases with the concentration of a structurally similar additive. The supersaturation dependence of the induction period is consistent with the predictions of three-dimensional nucleation theory. In contrast, the increase in the induction period with additive may be explained in terms of competition of additive molecules with paracetamol molecules during the process of formation of critically sized stable nuclei of the latter. This possibility is logical because a PAA molecule is similar to a paracetamol molecule in both structure and size.

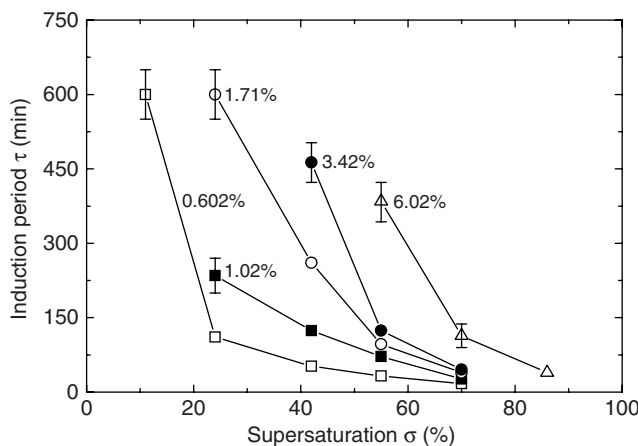


Figure 8.1 Dependence of induction period τ on supersaturation σ for different concentrations c_i of PAA additive. Reproduced from K.V.R. Prasad, R.I. Ristić, D.B. Sheen, and J.N. Sherwood. Int. J. Pharm. **215**, 29. Copyright (2001), with permission from Elsevier

Figure 8.2 illustrates the typical morphology of paracetamol grown from aqueous solutions at low ($<10\%$) and high ($>15\%$) supersaturation σ . The crystals grown at

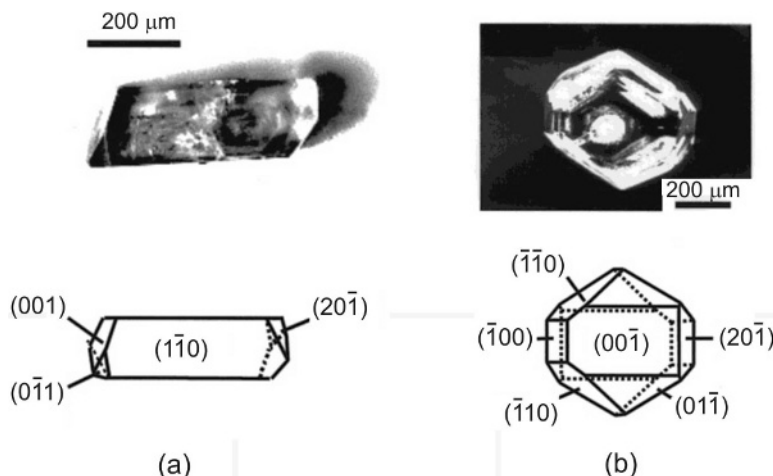


Figure 8.2 Typical morphology of paracetamol crystals grown from aqueous solutions at (a) low and (b) high supersaturation σ . Crystals were obtained by temperature lowering method. Reproduced from R.I. Ristić, S. Finnie, D.B. Sheen, and J.N. Sherwood. *J. Chem. Phys. B* **105**, 9057. Copyright (2001), with permission from American Chemical Society

low supersaturation have a columnar shape elongated along the [001] direction. They are bound by four dominant {110} faces and capped by {20 $\bar{1}$ }, {001} and two {011} type faces. At high supersaturation the crystals have a flat, tabular morphology in which the {001} faces become the most important morphologically while the morphological importance of the {110} faces is drastically reduced.

The change in the morphology of the crystals with supersaturation is directly connected with the supersaturation dependence of growth rates of different faces, as shown in Figure 8.3. The growth rates of {20 $\bar{1}$ }, {011} and {001} faces increase steadily with supersaturation, but the growth rate of the {001} face is lower than that of the former two faces. In contrast to the growth behavior of the {20 $\bar{1}$ }, {011} and {001} faces, the {110} face has virtually zero growth rate at $\sigma < 12\%$, but its growth rate increases steeply with σ such that at $\sigma > 17\%$ it is the fastest growing face. This unusual dependence of growth rate of the {110} face on supersaturation is due to a change in the growth mechanism of this face. For the other faces, the growth kinetics may be explained by the usual spiral growth mechanism for $\sigma < 15\%$, but for $15\% < \sigma < 20\%$ mass transport in the solution appears to give increasingly lower rates with increasing σ .

For the given concentration of an additive, the morphology of paracetamol crystals changes from columnar to plate-like with increasing supersaturation σ . Similarly, at a given supersaturation the morphology of the crystals changes from columnar to plate-like with the additive concentration c_i . These observations imply that there are transition values equal to σ_{tr} and $c_{i(tr)}$ corresponding to given values of experimental $c_{i(ex)}$ and σ_{ex} , respectively.

It was observed (Prasad *et al.*, 2001) that the change in the morphology of paracetamol crystals is accompanied by the formation of bunched steps on the morphologically dominant {110} face. This bunching of steps is a consequence of competition between

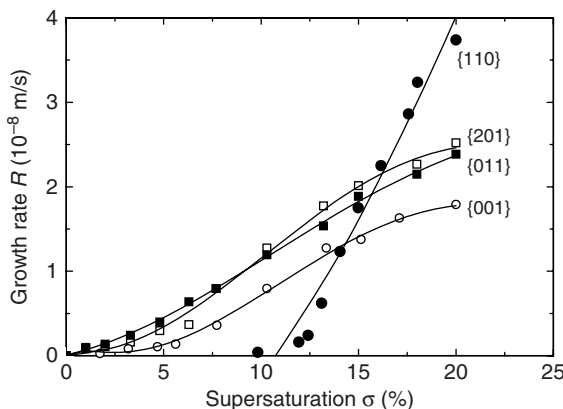


Figure 8.3 Supersaturation dependence of growth rates of dominant faces of paracetamol crystals in aqueous solutions. Reproduced from R.I. Ristić, S. Finnie, D.B. Sheen, and J.N. Sherwood. *J. Chem. Phys.* **105**, 9057. Copyright (2001), with permission from American Chemical Society

increased additive adsorption on the growing face and the supersaturation applied for growth. Bunching occurs at the transition supersaturation σ_t when impurity particles begin to be captured by the growing face. As discussed in Section 5.1, this transition supersaturation corresponds to the supersaturation threshold σ^* , the value of which increases with increasing additive concentration c_i .

The growth of paracetamol crystals also revealed that, for a given concentration of PAA additive, the crystal yield increases with increasing supersaturation and, for a given supersaturation, it decreases practically linearly with increasing additive. This feature is directly connected with the rate of formation of growth nuclei (see Figure 8.1) and the rate of their subsequent growth (see Figure 8.3), and is associated with the processes of adsorption of additive molecules on the aggregating and growing crystal nuclei. In the case of PAA additive, the rates of formation of nuclei and their growth into large crystals decrease with additive concentration.

Coalescence of elementary steps into bunched steps is a commonly observed phenomenon on growth surfaces of large crystals, and occurs for a variety of reasons, such as overlapping of diffusion fields of solute molecules, asymmetric supply of solute to advancing step from top and lower terraces (Schwobel effect), asymmetry of solution flow, and impurity effects (Sangwal and Rodriguez-Clemente, 1991; Sangwal, 1998). Once bunching of steps sets in, it continues to evolve, leading to unsteady layer propagation and reorganization of the bunched macrostep into sawtooth-like structures on the faces. Experiments with the growth of large crystals also reveal the formation of macrosteps and cavities near the central regions of their faces, which are caused by low solution/solid shear rates and also by the lack of alternative change of their flow directions. However, as growth proceeds, solution inclusions are trapped in the cavities and sawtooth structures, which subsequently lead to the generation of dislocations emerging in the growing face.

Inclusions decrease the chemical purity of the crystallized compound and may result in caking during their storage. Deterioration in the chemical purity and caking during storage of particles are direct consequences of the occurrence of interface instabilities. In the pharmaceutical industry, the problem of drug dosage controls in tabletting is another consequence of interface instability. Therefore, there is an increasing demand for the production of high-quality particles in specialty chemical and pharmaceutical industries.

The above causes of interfacial instability refer to a specific face of a preselected, relatively large crystal growing under controlled conditions of supersaturation and stirring. It is thus obvious that the overall control of interfacial instability of small crystalline particles in a batch crystallizer is complicated. This is mainly due to the movement of particles in the fluid and changes in the supersaturation available for their growth. Therefore, improvement of the quality of drug particles is a challenging subject for experimental investigation.

8.1.2 Preparation and Size Distribution of Drug Particles

Chew et al. (2004) investigated the influence of two different mixing mechanisms on bunch formation (interfacial instability) on the morphologically important {110} faces of paracetamol crystals. The paracetamol crystals (particles) were grown from aqueous solution in a conventional impeller-driven batch crystallizer (IDBC) and in an oscillatory baffled batch crystallizer (OBBC), in which, apart from hydrodynamics, all external conditions such as initial supersaturation and crystallization temperature were kept constant. In principle, the IDBC is the same as those used in industry but is smaller in size. Thus, it mimics the mixing mechanism involved in conventional industrial batch crystallization. However, OBBC offers an alternative mixing mechanism that generates intense eddy mixing by periodic oscillation of the fluid in a baffled column.

The results showed that paracetamol crystals precipitated in OBBC have smoother surfaces and significantly less evidence of crystals with cavities in their central regions than the crystals precipitated in IDBC. Paracetamol crystals precipitated in OBBC are of much higher quality than those produced in IDBC. This is because oscillation of solution with respect to the growing interface in OBBC provides a hydrodynamic environment in which interface instability is reduced.

Study of the volume-weighted median diameter of paracetamol particles as a function of initial supersaturation for crystals precipitated in IDBC and OBBC revealed the following features (*Chew et al.*, 2004):

- (1) The increase of agitation intensity in both IDBC and OBBC leads to the formation of smaller particles. The agitation intensity is related to operating parameters such as oscillation frequency, amplitude, and impeller speed.
- (2) Significantly smaller particles are grown in OBBC than in IDBC.
- (3) The size distribution of particles grown in OBBC is practically independent of the initial supersaturation.

All three features may be attributed to the a higher dynamic nucleation rate induced by the oscillatory mixing. Dynamic nucleation is defined as any nucleation event occurring

as a result of relative motion between different parts of the crystallization system, which includes the solution and any solid in contact with it.

Kaerger and Price (2004) produced paracetamol particles within a well-defined size range using solution atomization and crystallization by the sonication (SAXS) process. The process consists of three independent stages: (a) production of aerosol droplets of the solute from a carrier solvent using a suitable aerosol generator, (b) collection of the highly supersaturated droplets in a crystallization vessel containing a nonsolvent of the drug, and (c) application of ultrasonic waves to a crystallization vessel to induce controlled homogeneous nucleation and crystal growth. By combining these stages and controlling relevant parameters, high-purity micron-sized spherical particles are produced in a single step (solution to particle) operation. A major advantage of the technique is that any suitable aerosol generator can be used, and the entire process can be carried out under atmospheric pressure and ambient conditions.

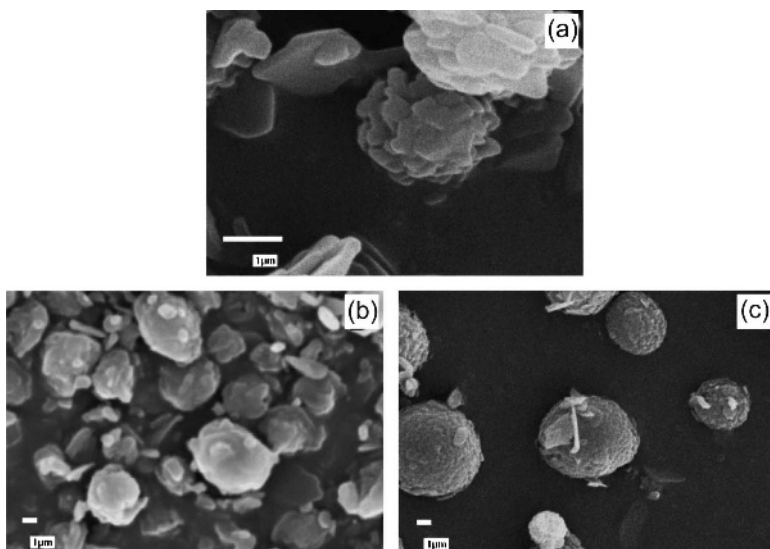


Figure 8.4 High-magnification scanning electron micrographs of particles obtained from air pressure atomization solutions of (a) 1, (b) 5 and (c) 10% (w/w) paracetamol in ethanol, at a constant atomizer-to-solution separation distance. Scale bar, 1 μm . Reproduced from J.S. Kaerger and R. Price. Pharm. Res. **21**, 372. Copyright (2004), with permission from Springer Science and Business Media

Figure 8.4 shows high-magnification scanning electron micrographs of particles obtained from air pressure atomization solutions of 1, 5 and 10% (w/w) paracetamol in ethanol, at a constant atomizer-to-solution separation distance (called Taylor cone conditions). It can be seen that at low solute concentration two different morphological forms, thin flake-like particles and particulates with a greater degree of sphericity, are formed (Figure 8.4a). The surfaces of the spherical particles are very rough. An increase in solute concentration leads to an increased formation of spherical particles such that at a

paracetamol concentration of 10% (w/w) the particles are highly spherical with surface roughness on the nanometer scale (Figure 8.4b and c). Figure 8.5 illustrates the cumulative particle size distribution of microionized, electrohydrodynamic (EHD)-sprayed and air-pressure atomized SAX-processed paracetamol particles obtained from 10% (w/w) paracetamol solution in ethanol. As can be seen from the particle size distribution, the monodispersed aerosol droplets formed through EHD spraying under stable Taylor cone conditions produce the narrowest particle size distribution.

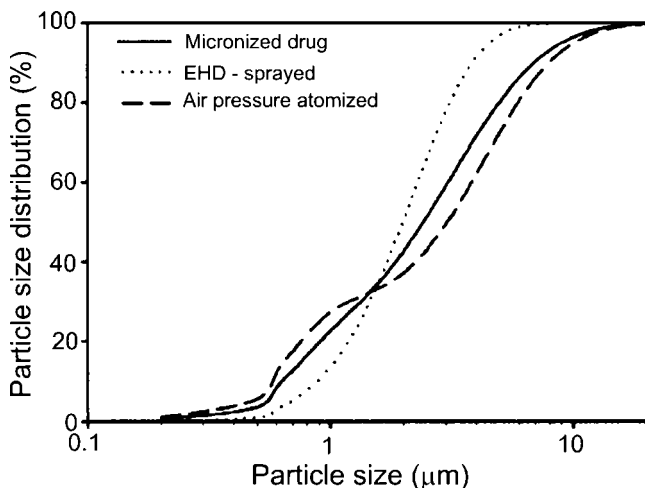


Figure 8.5 Cumulative particle size distribution of microionized, EHD-sprayed and air-pressure atomized SAX-processed paracetamol particles obtained from 10% (w/w) paracetamol solutions in ethanol. Reproduced from J.S. Kaerger and R. Price. Pharm. Res. **21**, 372. Copyright (2004), with permission from Springer Science and Business Media

The above results imply that variations in the aerosol formation of an air-pressure atomization system are the main causes of the broad dispersion in the SAXS-produced particles, and the air-pressure atomization SAXS process can be used to control the formation of spherical particles and their size distribution through variations in solute concentration in the initial solution. Since the concentration of the solute in the aerosol droplet is directly proportional to the mass m and volume V of the resulting particle and the diameter d of a sphere is proportional to $V^{1/3}$, it is expected that the average particle diameter is proportional to the concentration of the active solute. From an analysis of the particle diameter measured at the mode of each particle size distribution for different solute concentrations, Kaerger and Price (2004) indeed observed this type of relationship between particle size and the cube-root of solute concentration.

As mentioned above, the performance of a drug depends on its bioavailability, which, in turn, depends on its dissolution rate. Since the dissolution rate of a substance in a solvent is related to its solubility, many potential but poorly water-soluble drugs, especially several newly developed substances, have to be delayed or abandoned in pharmacological screening. Therefore, enhanced oral bioavailability of poorly water-soluble drugs is of great interest in the pharmaceutical industry.

The dissolution rate of particles of poorly water-soluble drugs may be increased by increasing the ratio of surface area to mass of the particles by decreasing their size (see Section 7.2). This may be achieved by producing particles of smaller sizes. Because of the disadvantages associated with the common milling techniques to reduce the particle size, optimal size of drug particle is directly obtained by suitable techniques.

An efficient way to micronize drug particles is to freeze atomized droplets rapidly in cryogenic nitrogen (Rogers *et al.*, 2003). In this technique, called spray freezing into liquid (SFL), aerosol droplets are passed into the cryogenic liquid and, as the solvent freezes, the solute becomes supersaturated in the unfrozen regions of the droplets, leading to the nucleation and growth of solute in them. The fast freezing rates lead to micron- and submicron-sized amorphous particles with large surface areas, depending on the experimental conditions. The frozen solvent is then removed by vacuum or atmospheric freeze-drying to obtain dry microionized SFL powders. Rogers *et al.* (2003) applied this technique to danazol. The main finding was that the residual water content in the danazol drug formulation after the atmospheric freeze-drying technique is comparable to that in the physical mixture of the drug components, but the dissolution rate of the former is about three times higher than in the latter due to differences in the size and morphology of the drug particles in the two cases.

Another novel method to produce nano- and micro-sized drug particles is *in situ* micronization of poorly water-soluble drugs by controlled crystallization using suitable additives (Rasenack and Müller, 2002). Crystallization is carried out using the solvent change method by instantaneously mixing two liquids in the presence of an additive. The first solution consists of the drug dissolved in an organic solvent that is miscible with water. The chosen concentration depends on the solubility of the drug. The additive is dissolved in water. By batch-wise mixing the two solutions in appropriate proportions, a dispersion is formed. The nonsolvent (*i.e.* the solution containing the additive) is poured rapidly into the drug solution with stirring. The stability of the dispersion depends on the additive used.

Rasenack and Müller (2002) investigated three poorly water-soluble drugs, ibuprofen, itraconazole and ketoconazole, in the presence of the following additives: agar, calcium caseinate, dextran 200, gelatin A, hydroxyethylcellulose (HEC), hydroxyethylstarch (HES), hydroxypropylcellulose (HPC), methylcellulose (MC), methylhydroxyethylcellulose (MHEC), hydroxypropylmethylcellulose (HPMC), sodium carboxymethylcellulose (NaCMC), sodium alginate, pectin, poly(vinyl alcohol) (PVA) and polyvinylpyrrolidone (PVP). The dispersion was formed by mixing drug and additive solutions in the ratio 1:4 in the case of ibuprofen and ketoconazole and 5:8 in the case of itraconazole. After spray drying the prepared dispersion during its stability, a micro- and nano-sized drug powder was obtained.

In pure water, a broad particle size distribution with a relatively large mean particle size is produced, but addition of several additives gives a narrow range of particle size distribution with a small mean particle size. Figure 8.6 illustrates this feature in the presence of HPMC additive on the particle size distribution of itraconazole after a stabilization period of 24 h. It can be seen that addition of HPMC resulted in a reduction in the mean particle size ($\times 50$) from 30 μm in pure water to about 600 nm. Obviously, HPMC additive inhibits the molecular association of drug molecules, as described above in the case of paracetamol nucleating in the presence of PAA additive.

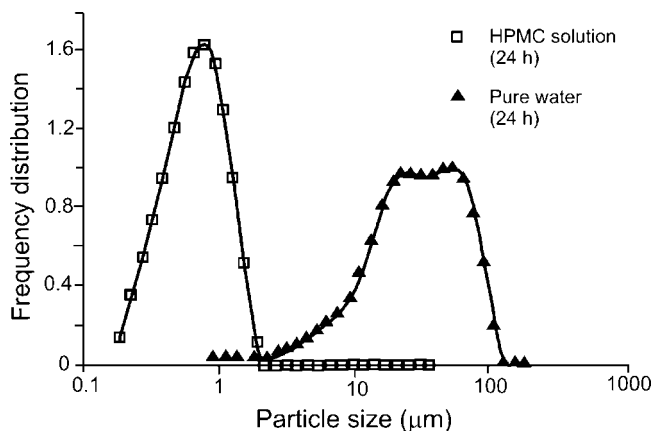


Figure 8.6 Particle size distribution of itraconazole with and without HPMC additive after a stabilization period of 24 h. Reproduced from N. Rasenack and B.W. Müller. Pharm. Res. **19**, 1894. Copyright (2002), with permission from Springer Science and Business Media

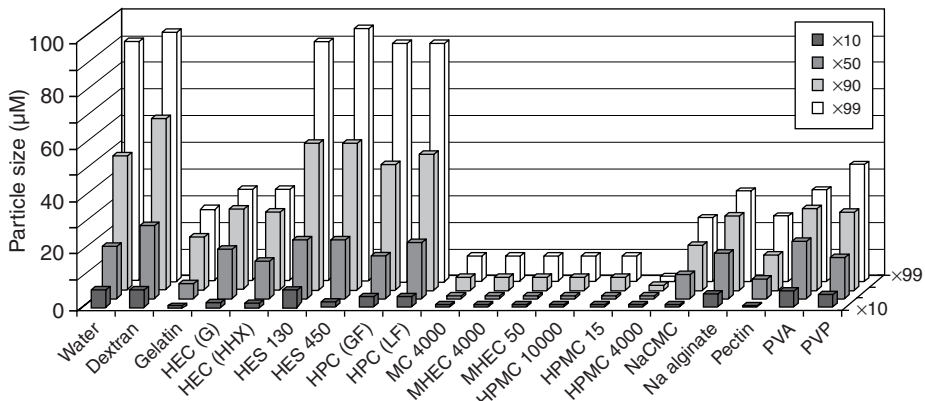


Figure 8.7 Particle size distribution of itraconazole with different additives after a stabilization period of 24 h; additive concentration 0.025% (mol/mol). Reproduced from N. Rasenack and B.W. Müller. Pharm. Res. **19**, 1894. Copyright (2002), with permission from Springer Science and Business Media

Since the stability of a dispersion depends on the additive used, the particle size distribution in the presence of different additives is also different. This behavior can be seen in Figure 8.7, which shows the particle size distribution of itraconazole with different additives after a stabilization period of 24 h corresponding to an additive concentration 0.025% (mol/mol). It can be seen that some of the additives such as cellulose ethers of alkyl substituents (for example: MC, MHEC and HPMC) reduce the particle size distribution enormously, but additives having a mainly hydrophilic molecule structures, such as dextran, hydroxyethylstarch (HEC) and cellulose ethers with polar substituents (HES), are practically ineffective in decreasing the particle size. This implies that the surface activity of the additives is associated with the adsorption of cellulose ethers with

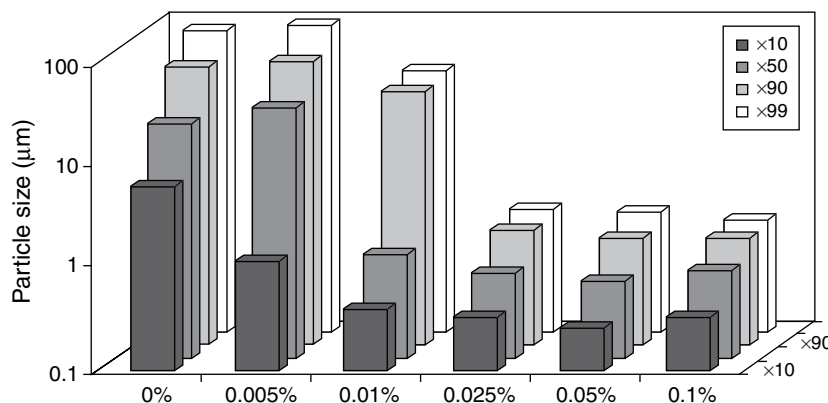


Figure 8.8 Effect of concentration of HPMC 4000 additive on the particle size of itraconazole in dispersion stabilized for 24 h. Reproduced from N. Rasenack and B.W. Müller. Pharm. Res. **19**, 1894. Copyright (2002), with permission from Springer Science and Business Media

methoxyl or hydroxypropyl groups. An additive was found to be effective in decreasing the particle size of a drug only above a certain additive concentration, as shown in Figure 8.8 for itraconazole stabilized in HPMC4000 for 24 h. Below this concentration, the particles grow and an increase in additive concentration does not produce smaller particles. Rasenack and Müller (2002) attributed this phenomenon to the formation of a protective layer around the growing drug particles. However, this explanation does not appear to be valid because even beyond the concentration when the particle size is drastically reduced, the mode of particle size distribution remains unchanged. This phenomenon is probably associated with the formation of micelles of the additive (see Sections 1.4 and 6.3.1).

A typical example of the difference between the morphologies of the common crystals of ibuprofen prepared by crystallization and micronized ibuprofen particles prepared from dispersion is presented in Figure 8.9. In the former case, the particles differ enormously

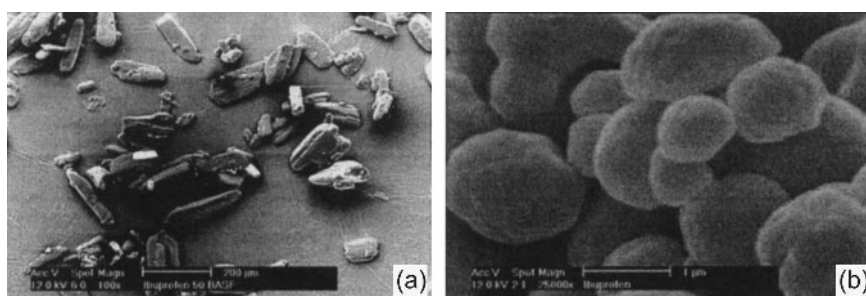


Figure 8.9 Morphology of ibuprofen: (a) prepared by crystallization and (b) micronized particles prepared from dispersion. Scale bar, 1 μm. Reproduced from N. Rasenack and B.W. Müller. Pharm. Res. **19**, 1894. Copyright (2002), with permission from Springer Science and Business Media

both in size and morphology, but particles obtained from the dispersion have spherical morphology with a relatively narrow size distribution.

Particle size is a critical parameter in the pharmaceutical industry because the physico-chemical and biopharmaceutical properties of drug supply dosages depend on the particle size. Therefore, selection of appropriate sizing techniques and cross-correlation between different techniques are important issues in the pharmaceutical industry. Shekunov *et al.* (2007) have recently reviewed the principles, methods and applications of particle size analysis in pharmaceutics.

8.2 Petroleum Industry

Petroleum, existing in the upper strata of various areas of the Earth's crust, consists of a complex mixture of various hydrocarbons, largely of the alkane series. It is used mostly for producing fuel oil, which is an important source of energy. Petroleum is also a raw material for many chemical products such as solvents, fertilizers, pesticides and plastics.

Diesel or diesel fuel is a specific fractional distillate of fuel oil, mostly of petroleum origin. However, diesel produced from petroleum is sometimes called petrodiesel when it is necessary to distinguish it from diesel from other sources such as wood, straw, corn and garbage. Petrodiesel is about 18% denser than gasoline (petrol). When burnt, diesel typically releases about 40.9 MJ/l, whereas gasoline releases 34.8 MJ/l heat energy (Wikipedia, 2006). Diesel usually costs less than gasoline. Petroleum-derived diesel is composed of about 75% saturated hydrocarbons (primarily alkanes including *n*-, *iso*- and cycloalkanes), and 25% aromatic hydrocarbons (including naphthalenes and alkylbenzenes). The average chemical formula for common diesel fuel is C₁₂H₂₆, ranging from approximately C₁₀H₂₂ to C₁₅H₃₂.

Diesel inherits its name from the inventor and designer of the original "diesel" engine, the German engineer Rudolf Diesel, more than 100 years ago. Rudolf Diesel used peanut oil to fuel his engine. However, with the advent of cheap petroleum, its appropriate fractions were refined to serve as fuel, and diesel fuels and diesel engines evolved together. In the 1930s and 1940s, vegetable oils were used as diesel fuels from time to time, but usually in emergency cases.

The energy crisis in the 1970s stirred enormous public and political concern about the supply levels and limited resources of fossil oil. This provided a strong impulse to use vegetable oils and animal fats to make biodiesel fuels. Since 2000, crude oil prices have been increasing steadily, reaching a record high of US\$74 in August 2006 from just about US\$20 in 2000. There are also environmental concerns such as global warming due to emission of carbon dioxide into the atmosphere, disturbances of the marine environment associated with offshore exploration and oil extraction, and damage to fragile ecosystems caused by spilling of crude oil and refined fuel from tanker ship accidents. Because of the increase in crude oil prices and environmental concerns, there is increasing focus on the use of ecologically friendly fuel such as biodiesel.

Biodiesel is defined as the monoalkyl esters of long-chain fatty acids derived from renewable feedstock, such as vegetable oil and animal fats, for use in compression-ignition engines. It is a possible substitute or extender for conventional diesel, and can be blended with it in any proportions. Because the carbon in the vegetable oils and animal

fats originates mostly from carbon dioxide in the air, biodiesel is considered to contribute much less to global warming than fossil fuels. Moreover, the exhaust emissions of carbon monoxide, unburnt hydrocarbons, particulate matter, and sulfur content are lower than with conventional diesel.

Although the use of vegetable oils as alternative fuels for diesel engines has been used in the past, it is again being promoted in many countries. For example, the European Union has a target to replace, by 2010, 5.75% of the yearly consumption of fossil fuel in its territory by biofuels (Prankl, 2002).

Depending on the climate and soil conditions, different countries are looking for different types of vegetable oils as substitutes for diesel fuels; for example, soybean oil (SBO) in the USA, rapeseed (RSO) and sunflower oils (SFO) in the European Union, palm oil (PMO) in Malaysia and Indonesia, and coconut oil in the Philippines. For the market introduction and commercialization of biodiesel, standards for quality assurance have been formulated in different countries (Prankl, 2002). Some important parameters taken into consideration when formulating a fuel standard include ester content, density, viscosity, lower heating value, flash point, pour point, sulfur content, carbon residue, cetane number, and oxidation stability.

8.2.1 Some Basic Concepts

Fats and oils are primarily water-insoluble, hydrophobic substances, commonly referred to as triglycerides, in the plant and animal kingdom, and are made up of one mole of glycerol and three moles of fatty acids. Vegetable oils contain 98% triglycerides and small amounts of mono- and diglycerides (Ma and Hanna, 1999; Barnwal and Sharma, 2005). Oils extracted from different vegetables contain different proportions of chemically distinct fatty acids. The fatty acids found in vegetable oils vary in carbon chain length and in the number of unsaturated bonds (double bonds). The chemical structure of common saturated fatty acids found in vegetable oils may be represented by the formula $C_nH_{2n}O_2$, where n is an even number varying from 12 to 24. They are lauric, myristic, palmitic, stearic, arachidic, behenic and lignoceric acids with $n = 12, 14, 16, 18, 20, 22$ and 24, respectively, and are solids at room temperature. Fatty acids with one unsaturated carbon bond have the chemical formula $C_nH_{2n-2}O_2$. They are oleic and erucic acids, and contain 18 and 22 carbon atoms, respectively. Fatty acids with two and three unsaturated carbon bonds are linoleic ($C_{18}H_{32}O_2$) and linolenic acids ($C_{18}H_{30}O_2$). The unsaturated fatty acids are liquids at room temperature. Some important properties of common vegetable oils are given in Table 8.1 (Barnwal and Sharma, 2005).

The molecular mass of vegetable oils lies in the range 600–900, which is about 20 times higher than that of diesel fuel. Due to this high molecular mass, the oils have high viscosity. The flash point of vegetable oils is very high (above 200 °C). Heating values and cetane numbers are lower than those of diesel fuel. Despite this, neat vegetable oils can be used as diesel fuels in conventional diesel engines. However, this causes a number of problems related to the type and grade of oil, and local climatic conditions. The injection, atomization and combustion characteristics of vegetable oils are markedly different from those of diesel. The high viscosity of vegetable oils causes problems with compression ignition. The inefficient mixing of oil with air contributes to incomplete combustion, leading to heavy smoke emission, and the high flash point results in poor volatility characteristics. For these reasons, diesel engines cannot operate trouble-free for

Table 8.1 Properties of some common vegetable oils (after Barnwal and Sharma, 2005)

Oil	Kinematic viscosity ^a (cSt)	Cetane number	Heating value (MJ/kg)	Cloud point (°C)	Pour point (°C)	Flash point (°C)	Density (kg/dm ³)
Corn	34.9	37.6	39.5	-1.1	-40	277	0.9095
Cottonseed	33.5	41.8	39.5	1.7	-15	234	0.9148
Linseed	27.2	34.6	39.3	1.7	-15	241	0.9236
Peanut	39.6	41.8	39.8	12.8	-6.7	271	0.9026
Rapeseed	37.0	37.6	39.7	-3.9	-31.7	246	0.9115
Sesame	35.5	40.2	39.3	-3.9	-9.7	260	0.9133
Soybean	32.6	37.9	39.6	-3.9	-12.2	254	0.9138
Sunflower	33.9	37.1	39.6	7.2	-15.0	274	0.9161
Palm	39.6	42.0	—	31.0	—	267	0.9180
Diesel	3.06	50	43.8	—	-16	76	0.885

^a At 38 °C.

long durations on vegetable oils. Therefore, vegetable oils are converted chemically to corresponding fatty esters by the transesterification reaction of their triglycerides.

8.2.2 Crystallization Behavior of Linear Long-Chain *n*-Alkanes

Crystallization of linear long-chain *n*-alkanes (paraffins), C_nH_{2n+2} , from solutions is of practical importance in the petroleum industry: paraffinic crude oils, asphalt, and diesel oil (Owen, 1989; Owen and Coley, 1995). Linear *n*-alkanes have limited solubility in the complex aromatic/aliphatic matrix and separate out from solutions either as thin rhombic plates or as long needles. The formation of *n*-alkane crystals of large size by uncontrolled crystallization leads to plugging of pipes, pumps, and filters or to gel formation. Therefore, these linear long-chain alkanes cause constant problems to both the oil industry and users in the storage, transport, and use of petroleum distillates at low temperatures.

The crystallization behavior of *n*-alkanes has been well investigated (for the literature, see Marie *et al.*, 2005). Depending on their length and evenness, pure *n*-alkanes crystallize in monoclinic (even-carbon *n*-alkanes with $n > 26$), triclinic (even-carbon *n*-alkanes with $n < 26$), or orthorhombic (odd-carbon *n*-alkanes) structure. *n*-Alkane mixtures crystallize as orthorhombic or hexagonal phases. The thermodynamic behavior of *n*-alkane mixture solutions resembles eutectics. Needle-shaped crystals are formed when the cooling rate of the mixture solution is fast, but plates are formed when the cooling rate is slow. The larger, flat faces of plates usually exhibit spiral growth.

In the petroleum industry, treatment with various chemical additives has drawn considerable attention because this method is the most convenient and economical way of improving the low-temperature flow properties of petroleum-based fuels and oils (Petinelli, 1979; Rätsch and Gebauer, 1989; Claudy *et al.*, 1993; Létoffe *et al.*, 1995; Srivastava *et al.*, 1995; El-Gamal and Al-Sabagh, 1996; El-Gamal *et al.*, 1998; Machado *et al.*, 2001; Zhang *et al.*, 2003; Marie *et al.*, 2005; Soriano *et al.*, 2005, 2006). The chemical additives are frequently referred to as pour-point depressants, flow improvers, paraffin inhibitors and wax modifiers. The molecular structure of these pour-point depressants for

conventional diesel fuel consists of a polymeric hydrocarbon chain with protruding polar groups.

The mechanism of action of the chemical additives often remains unclear, although in some cases a well-defined effect of the additive is observed. For example, in the presence of ethylene–vinyl acetate copolymer (EVA) the crystals formed from petroleum diesel are much smaller and more numerous, and exhibit a compact habit (Petinelli, 1979; Létoffe *et al.*, 1995; Machado *et al.*, 2001). Soluble complexes at low temperatures are formed when European diesel fuel is treated with a polymer prepared from linear α -olefins (C_{18} – C_{24}) with acrylic, vinylic and maleic unsaturated compounds, as a result of the interaction of the additive with the heavy *n*-alkane components of the diesel fuel (Claudy *et al.*, 1993; Létoffe *et al.*, 1995). These additives also lower the pour point of the diesel, i.e. they act as pour-point depressants.

The main obstacle to understanding the mechanism of action of additives is the strong interdependence between additive–alkane interactions due to the chemical structure of the additive and the complex composition of the diesel fuel. It is difficult to select an *n*-alkane and solvent matrix that would lead to generalization for different systems. Among the various additives used to improve the crystallization behavior of petroleum distillates at low temperatures, EVA copolymers has been reported to show good efficiency in diesel oils (Owen, 1989; Owen and Coley, 1995). The EVA copolymers have the maximum activity when the solvent has significant aromatic parts and the distribution of alkane chain lengths is broad.

For understanding the mechanism of action of additives on the properties of diesel fuel, it is necessary to investigate the crystallization behavior of *n*-alkanes with both narrow and broad distributions of their chain length in terms of size, phase (chemical composition) and morphology of crystallizing *n*-alkane in simple solvents. In this context, the findings of a recent study, carried out by Marie *et al.* (2005), devoted to the precipitation of four

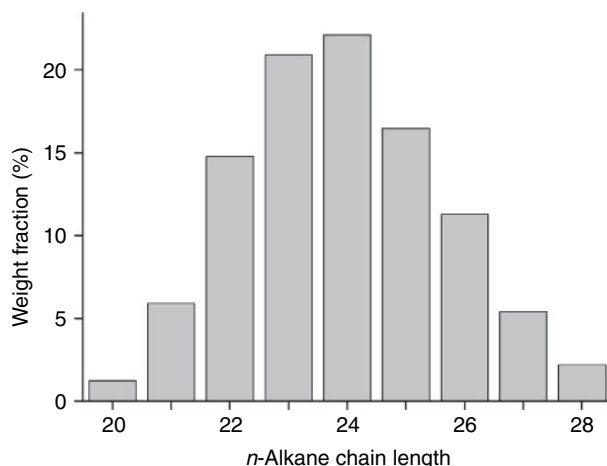


Figure 8.10 Distribution of different *n*-alkanes, as expressed by carbon chain length, in paraffin blend. Reproduced from E. Marie, Y. Chevalier, F. Eydoux, L. Germanaud, and P. Flores. J. Colloid Interface Sci. **290**, 406. Copyright (2005), with permission from Elsevier

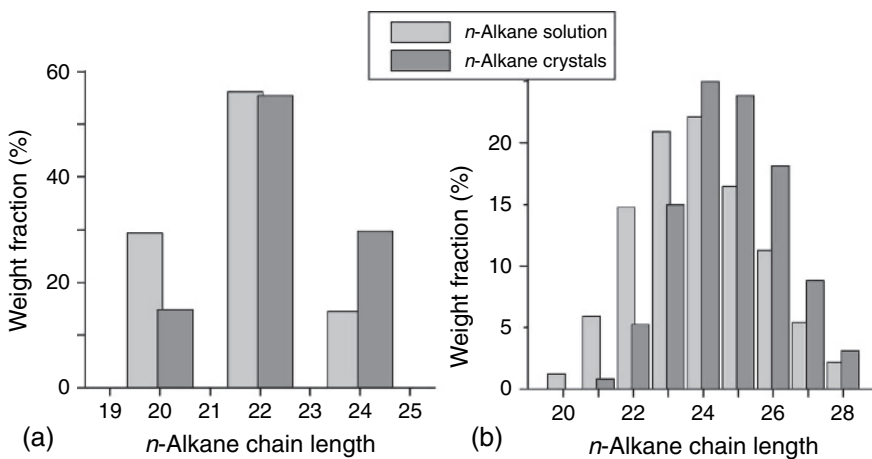


Figure 8.11 *n*-Alkane length distribution in initial solution and isolated crystals; solutions: (a) E1 and (b) K2. Note that in both cases the crystals are enriched in the higher molar mass *n*-alkane with respect to the original mixture composition. Reproduced from E. Marie, Y. Chevalier, F. Eydoux, L. Germanaud, and P. Flores. *J. Colloid Interface Sci.* **290**, 406. Copyright (2005), with permission from Elsevier

different systems comprising two *n*-alkane mixtures in two solvents, ethylbenzene and kerosene, in the presence of different concentrations of EVA copolymer are relevant and interesting. The *n*-alkane mixtures used were (1) a well-defined 1:2:1 mixture of eicosane ($C_{20}H_{42}$), docosane ($C_{22}H_{46}$), and tetracosane ($C_{24}H_{50}$), referred to as ‘paraffin mixture’, and (2) a commercially purchased mixture of both even- and odd-carbon *n*-alkanes with $20 < n < 28$, referred to as ‘paraffin blend’ (Figure 8.10), while the average length of the polyethylene segments was about 22 carbon atoms. The solutions were composed of 5 wt% paraffin mixture and 4 wt% paraffin blend, referred to as 1 and 2, in ethylbenzene and kerosene, denoted E and K, respectively. For example, solution K2 implies that it is composed of 4 wt% paraffin blend in kerosene. The interactions between pure *n*-alkane and the EVA additive were investigated by differential scanning calorimetry (DSC), infrared spectroscopy and X-ray diffraction, and the crystal size distribution was determined from optical microscope images.

Precipitation experiments were carried out in terms of (a) distribution of *n*-alkane chain length from pure solutions and (b) incorporation of the additive in the crystals as a function of initial concentration of the additive in the solution. The important results of these experiments are the following:

- (1) The crystals were enriched in the higher molar mass *n*-alkane with respect to the original mixture composition (Figure 8.11). This means that the distribution coefficient of higher *n*-alkanes in these solvents increases with increasing chain length.
- (2) In ethylbenzene the segregation coefficient k_{eff} (i.e. ratio of % EVA/*n*-alkane composition in crystals to that in solution) of EVA additive in the crystals is unity and does not depend on the initial additive concentration in the solution, whereas in kerosene it decreases with increasing additive concentration (see Section 9.1). These

observations mean that in ethylbenzene the EVA copolymer enters the growth sites with the same probability as the *n*-alkane units, whereas in kerosene there is a preference for EVA copolymer to enter the growth site over the *n*-alkane units.

- (3) The *n*-alkane crystals grown from pure solutions are needle-shaped with a length of about 5 mm, but addition of EVA leads to the formation of platelets. The crystal size distribution is typical log-normal (Figure 8.12).
- (4) Addition of EVA leads to a reduction in the mean crystal size (Figure 8.13). In ethylbenzene the platelets show complicated rounded shapes, but in kerosene the crystals remain regular rhombic-shaped, suggesting that the additive controls crystallization behavior in the two solvents in a different ways. In ethylbenzene the segregation coefficient k_{eff} is equal to unity for EVA and the irregular morphology of the crystals implies that EVA copolymer remains in the solution and inhibits crystal growth rather than nucleation of the *n*-alkane. However, in kerosene $k_{\text{eff}} > 1$, suggesting that the EVA copolymer acts as a nucleating agent in this case. The constant average size of *n*-alkane crystals in ethylbenzene and their decreasing size in kerosene are consistent with this concept (see Figure 8.13).

In the above study, the mean length of the polyethylene segments in the EVA additive is identical with the mean length of the *n*-alkanes. The same size of the additive gives it the maximum efficiency in controlling the crystallization of *n*-alkanes (Marie *et al.*, 2005). This means that van der Waals interactions are operative at the molecular level between these polyethylene moieties. These interactions can take place either in solution or at the surface of the crystal or inside the crystals formed by co-crystallization. However, complex situations may also arise when different mechanisms operate simultaneously, and the role of the solvent in these interactions is also important.

It is known (for the literature, see Marie *et al.*, 2005) that pure tetracosane crystallizes in the triclinic structure but it crystallizes in the orthorhombic structure when mixed with other *n*-alkanes, and that the triclinic structure undergoes a transition to the orthorhombic

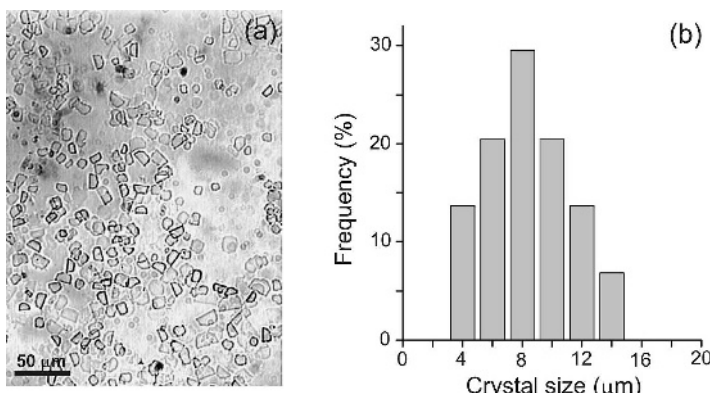


Figure 8.12 (a) *n*-Alkane crystals obtained from K2 solution containing 500 ppm EVA. (b) Crystal size distribution corresponding to the crystals of (a). Reproduced from E. Marie, Y. Chevalier, F. Eydoux, L. Germanaud, and P. Flores. J. Colloid Interface Sci. **290**, 406. Copyright (2005), with permission from Elsevier

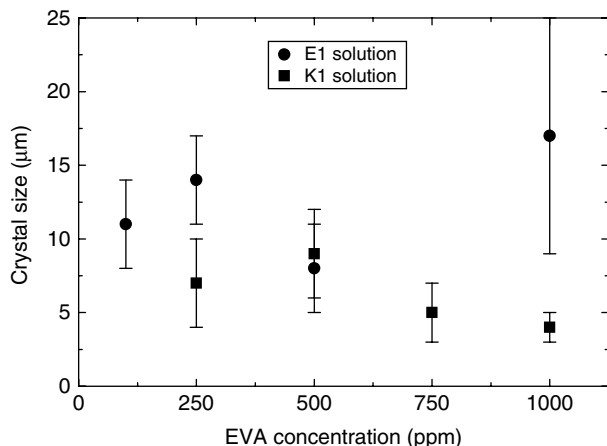


Figure 8.13 Dependence of mean crystal size of *n*-alkanes on EVA concentration in solution. Original data from Marie et al. (2005)

phase when the amount of the second component increases, with the two phases crystallizing as a solid solution. Keeping these facts in mind, using infrared spectroscopy and X-ray diffraction, Marie *et al.* (2005) studied the interactions between EVA and perdeuterated tetracosane ($C_{24}D_{50}$). In agreement with the earlier findings, the results revealed that the triclinic structure of pure tetracosane transforms into the orthorhombic structure when EVA co-crystallizes with it, corroborating the occurrence of van der Waals interactions between tetracosane and the linear alkane segments of the EVA additive.

Based on experimental observations that the structure of orthorhombic phase does not change with increasing EVA/tetracosane ratio in the *a* and *b* directions, and the fact that the paraffinic polyethylene moieties of tetracosane and EVA have the same lateral packing, Marie *et al.* (2005) proposed that co-crystallization occurs by lateral stacking of *n*-alkanes and the polyethylene segments of the EVA, as shown in Figure 8.14. Starting from the lamellar structure of semicrystalline EVA, where sheets of the crystalline part are separated by sheets of amorphous polymer, incorporation of *n*-alkanes into the crystalline parts leads to their lateral swelling. Because of this lateral swelling involving a constant amorphous content, the thickness of the amorphous sheets decreases as the *n*-alkane is added to the EVA. Assuming that the lateral stacking of the molecules is the same in the pure and mixed crystals such that each *n*-alkane and polyethylene segment occupies a constant area $A_{C_{24}}$ and A_{EVA} , from the ideal mixing relationship between the parameter c and the volume fraction Φ of EVA, one may write

$$c_{C_{24}} = V_{C_{24}} / A_{C_{24}} \quad (\text{in pure tetracosane}) \quad (8.1)$$

$$c_{EVA} = V_{EVA} / A_{EVA} \quad (\text{in pure EVA}) \quad (8.2)$$

$$\frac{1}{c} = \frac{\Phi}{c_{EVA}} + \frac{1 - \Phi}{c_{C_{24}}} = \Phi \left(\frac{1}{c_{EVA}} - \frac{1}{c_{C_{24}}} \right) + \frac{1}{c_{C_{24}}} \quad (\text{in co-crystals}) \quad (8.3)$$

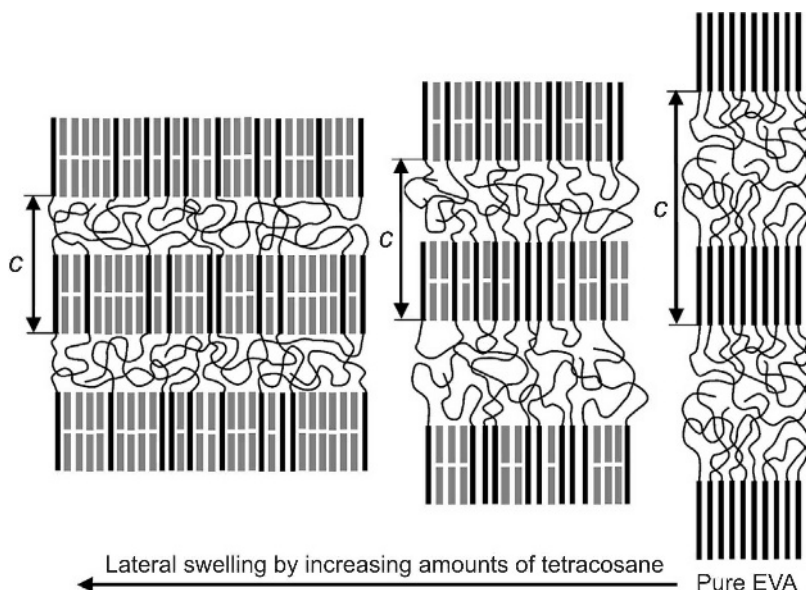


Figure 8.14 Schematic presentation of structural modification of semicrystalline EVA due to co-crystallization with increasing amounts of tetracosane. Amorphous parts of the polymer are represented by thin curved lines, and EVA and tetracosane segments of the co-crystallized phase by black and gray straight bold lines, respectively. Lateral swelling of the crystalline lamellae at a constant content of amorphous materials results in a decrease in the lattice parameter c . Reproduced from E. Marie, Y. Chevalier, F. Eydoux, L. Germanaud, and P. Flores. J. Colloid Interface Sci. **290**, 406. Copyright (2005), with permission from Elsevier

where $V_{C_{24}}$ and V_{EVA} are the volumes of pure tetracosane and EVA, respectively, and $c_{C_{24}}$ and c_{EVA} are the corresponding c parameters of pure tetracosane and EVA. Figure 8.15 shows the plot of the experimental values of the inverse of the parameter c of the co-crystallized tetracosane/EVA phase against the volume fraction Φ of EVA, according to Equation (8.3). The plot is linear for the monophase orthorhombic samples, and extrapolation of the linear plot to pure tetracosane (i.e. $\Phi = 0$) gives $c = 6.15 \text{ nm}$. This value of c for pure tetracosane is in good agreement with a value of $c = 6.485 \text{ nm}$ obtained from extrapolation of the parameters c of odd-carbon n -alkane crystals, which have the orthorhombic structure.

The intersection of the linear plot in Figure 8.15 with the horizontal line at $1/c = 0.73 \text{ nm}^{-1}$ (i.e. $c = 13.7 \text{ nm}$) gives the limiting value of the chemical composition of the orthorhombic phase coexisting with the triclinic crystals of pure tetracosane in the binary phase. This value is $\Phi = 0.65$, which corresponds to an EVA/tetracosane ratio of about 2. The parameter c for the hypothetical orthorhombic phase of tetracosane fits the experimental data for the co-crystallized tetracosane/EVA phase through Equation (8.3). The EVA concentration $\Phi = 0$ corresponds to the hypothetical orthorhombic crystal of pure tetracosane with $c = 6.48 \text{ nm}$ ($1/c = 0.155 \text{ nm}^{-1}$). This suggests that the paraffinic lamellae in the tetracosane/EVA co-crystals incorporate pairs of tetracosane molecules aligned end-to-end in the orthorhombic crystals. Since the average lengths of EVA

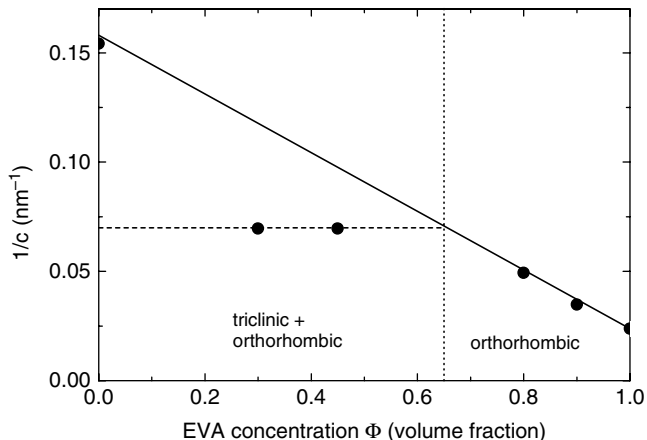


Figure 8.15 Dependence of $1/c$ of co-crystallized tetracosane/EVA on the volume fraction Φ of EVA. The solid line shows the linear swelling behavior of monophase orthorhombic samples according to Equation (8.3). Adapted from E. Marie, Y. Chevalier, F. Eydoux, L. Germanaud, and P. Flores. *J. Colloid Interface Sci.* **290**, 406. Copyright (2005), with permission from Elsevier

and tetracosane segments are similar, one expects that the thickness of the crystalline lamellae of EVA would match a single tetracosane molecule. However, the hypothetical orthorhombic structure of pure tetracosane with $c/2$ as the parameter along the c direction does not fit to the linear dependence in the region $\Phi < 0.65$. In the case of co-crystallized *n*-tetracosane and ethylene–butene copolymers, the thickness of the crystalline lamellae is 3.2 nm, corresponding to a single sheet of tetracosane molecules. This observation suggests that the lamellae of the crystalline part of EVA is about 6 nm because the crystalline fraction alone incorporates the longer polyethylene segments of the EVA additive.

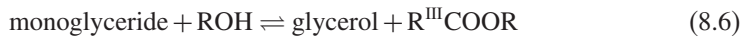
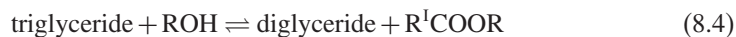
8.2.3 Biodiesels and their Crystallization Behavior

Biodiesel is a potential substitute for conventional diesel fuel (Carraretto *et al.*, 2004; Barnwal and Sharma, 2005). Due to the great similarities of biodiesel to paraffinic diesel fuel, it can maintain the engine performance with essentially no engine modifications. Moreover, biodiesel fuels have environmental advantages over diesel fuels: they are biodegradable, nontoxic and show low emissions of SO_2 , CO_2 , CO, hydrocarbons, polycyclic aromatic hydrocarbons, and aromatics during combustion.

As mentioned above, direct use of vegetable oils is not satisfactory in diesel engines because of their high viscosity, which causes problems with compression ignition. There are also problems associated with fatty acid composition, free fatty acid content and gum formation due to oxidation and polymerization during storage and combustion, carbon deposits and lubricating oil thickening. Therefore, fatty oils are converted into biodiesel by breaking chemical bonds to yield relatively small-chain molecules using pyrolysis and transesterification of triglycerides of an oil or fat (Ma and Hanna, 1999). For example, pyrolysis (or thermal cracking) of vegetable oils carried out over a standard

$\text{SiO}_2/\text{Al}_2\text{O}_3$ petroleum catalyst at 450 °C produces gases, liquids and solids with lower molecular weights (Pioch *et al.*, 1993). The condensed organic phase yields biogasoline and biodiesel fuels, and the chemical composition of the diesel fractions is similar to that of fossil diesel fuels. It also produces some low-value materials and, sometimes, more gasoline than biodiesel fuel. However, this method is expensive.

The overall transesterification reaction of glycerides in vegetable oils with an alcohol occurs in three consecutive and reversible reactions (see, for example, Ma and Hanna, 1999; Demirbas, 2002; Barnwal and Sharma, 2005):



where R^{I} , R^{II} and R^{III} are long-chain hydrocarbons which may be the same or different. Among the alcohols used in the transesterification process are methanol, ethanol, propanol, butanol, and amyl alcohol. However, methanol is frequently used in view of its low cost and its physical and chemical advantages associated with being polar and the shortest chain alcohol. It readily reacts with triglycerides, and NaOH is readily dissolved in it. A 3:1 molar ratio of alcohol to glycerides is required to complete transesterification stoichiometrically, but excess alcohol is used to shift the equilibrium to the product side because the reaction is reversible. For a 95–98% yield of ester a 5:1 molar ratio alcohol to glycerides is needed. Several parameters, such as molar ratio of oil to alcohol, reaction temperature, time and water content of the reactants, affect the reaction. A catalyst is usually used to improve the reaction rate and yield. Alkalies (NaOH, KOH, carbonates and sodium alkoxides), acids (sulfuric acid, sulfonic acids and hydrochloric acid), and enzymes (lipases) are used as catalysts. Alkali-catalyzed transesterification takes place much faster than acid-catalyzed transesterification and is often used commercially.

The transesterification process requires mixing of vegetable oil with a mixture prepared by dissolving KOH catalyst in methanol and heating the entire content at a relatively low temperature with vigorous stirring. The mixture is then allowed to settle under gravity. Glycerin, being heavier, settles down in the bottom layer while the upper layer constitutes biodiesel (esters). The glycerin is separated and the esters are washed with water for catalyst recovery. Thus, the overall process of catalytic transesterification has a high production cost. Moreover, vigorous stirring required for the mixing of the two-phase oil–alcohol mixture and separation of catalyst after the reaction are two problems in this transesterification technique.

The non-catalytic production of biodiesel from soybean, rapeseed, and sunflower oils in supercritical alcohols has aroused great interest in recent years (Diasakov *et al.*, 1998; Saka and Kusdiana, 2001; Demirbas, 2002; Madras *et al.* 2004; Cao *et al.*, 2005). The main advantages of this technique are the following:

- (1) Nearly complete conversions can be achieved in a very short time (2–4 min) because supercritical alcohol and oil exist as one phase.
- (2) Because of the non-catalytic process, purification of products after the transesterification reaction is much simpler and environmentally friendly in comparison with the common method in which all the catalyst and saponified products have to be removed for biodiesel fuels.

The conversion of triglycerides into methyl or ethyl esters through a transesterification process reduces the molecular weight to about one-third, reduces the viscosity by about one-eighth, and increases the volatility insignificantly (Barnwal and Sharma, 2005). The properties of biodiesel fuels from some oils and fossil diesel fuel are given in Table 8.2. As can be seen, biodiesel fuels have properties similar to those of fossil fuel.

Table 8.2 Properties of biodiesels from different vegetable oils^a

Biodiesel	Kinematic viscosity (cSt)	Cetane number	Heating value (MJ/kg)	Cloud point (°C)	Pour point (°C)	Flash point (°C)	Density (kg/dm ³)
Peanut	4.9	54	33.6	5	—	176	0.883
Rapeseed	— (4.43)	—	—	(−4) —	(−13) —	(178) —	(0.871)
Soyabean	4.5 (4.12)	45	33.5	1 (1)	−7 (−2)	178 (186)	0.885 (0.870)
Sunflower	4.6 (4.3)	49	33.5	1 (1)	1 (−5)	183 (181)	0.860 (0.873)
Palm	5.7 (5.15)	62	33.5	13 (18)	— (12)	164 (179)	0.880 (0.842)
Diesel	3.06	50	43.8	—	−16	76	0.855

^aData without and in parentheses are from Barnwal and Sharma (2005) and Soriano *et al.* (2006), respectively, and the corresponding data for viscosity were obtained at 38 or 40 °C.

Biodiesel consists of fatty acid methyl esters (FAMEs). Therefore, the structures of fatty acids and the ester moiety derived from the alcohol affect the fuel properties of biodiesel. Since the transesterification reaction of an oil or fat results in a biodiesel fuel, biodiesel is a mixture of fatty acid esters with each ester component contributing to the biodiesel properties (Knothe, 2005; Soriano *et al.*, 2006). Figure 8.16 shows the dependence of pour points, cloud points, flash points and viscosities of FAMEs on their chain length and unsaturation. The linear regressions of the properties of saturated esters against carbon number are also included, where *y* and *x* denote the physical properties and the carbon number of the saturated esters, respectively. The analysis shows that the viscosity, flash point, pour point and cloud point of saturated FAMEs increase essentially linearly with the carbon chain length, but the presence of unsaturated bonds leads to a decrease in these properties. A highly pronounced effect of chain length and unsaturation of bonds occurs with pour point and cloud point. The relationship between the physical properties of FAMEs and their chain length is due to the increasing intermolecular attractive interactions with increasing chain length. However, the presence of double bonds disrupts the attractive interaction between the molecules along the hydrocarbon chain, thereby leading to a decrease in the above physical properties.

The properties of different FAMEs of vegetable oils are mainly determined by the composition and structure of the corresponding oils (Table 8.3). Corresponding to a given carbon number of an ester molecule, the effective size of the molecule decreases with the number of unsaturated bonds in the molecule. This ensures weakened interactions between molecules, thereby resulting in poorer internal molecular packing in the volume.

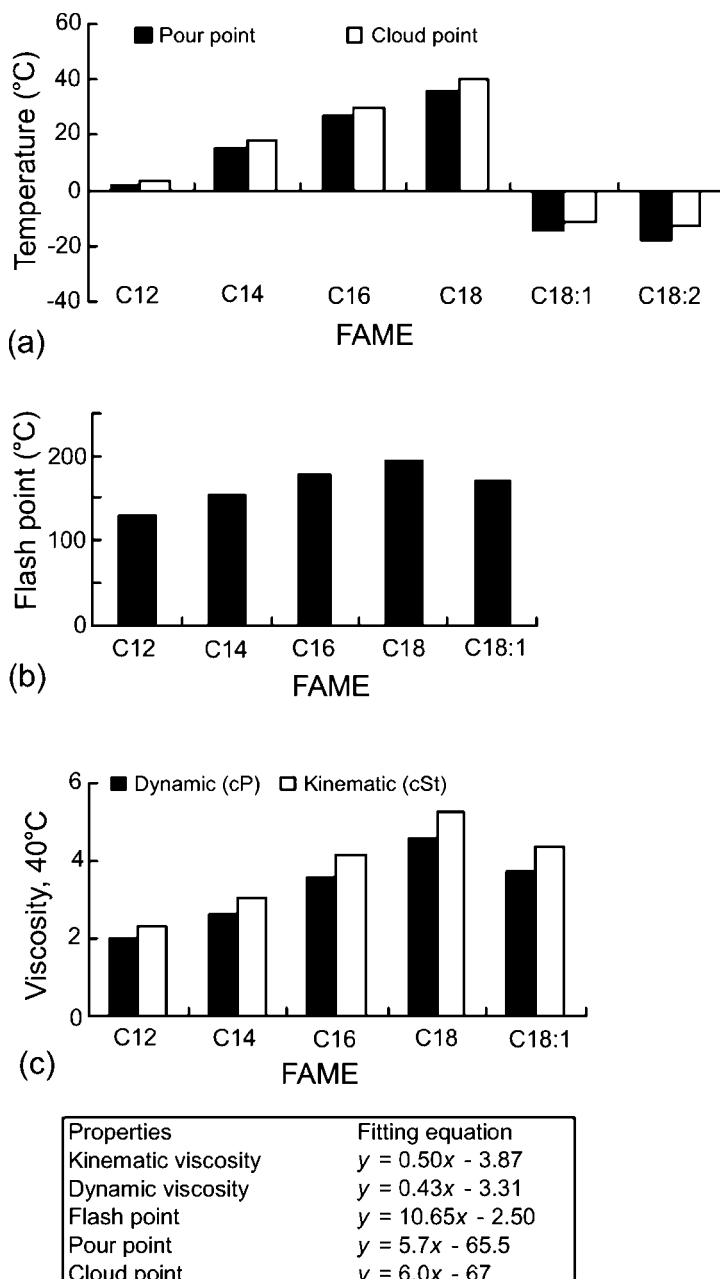


Figure 8.16 Dependence of (a) pour point and cloud point, (b) flash point and (c) viscosity of FAMEs on their chain length and unsaturation. In all cases the regression coefficient was better than 0.99. Adapted from N.U. Soriano Jr, V.P. Migo, and M. Matsumura. Fuel **85**, 25. Copyright (2006), with permission from Elsevier

Table 8.3 Composition profile of different vegetable oils

Vegetable oil	Fatty acid composition (% by weight)							Ref. ^a
	16:0	18:0	20:0	22:0	18:1	18:2	18:3	
Peanut	11.4	2.4	1.3	2.5	48.3	32.0	0.9	(a)
Rapeseed (RSO)	3.5	0.9	—	—	64.4	22.3	8.2	(a)
Soyabean (SBO)	11.8	3.2	—	—	23.3	55.5	6.3	(a)
Sunflower (SFO)	6.1	3.3	—	—	16.3	73.7	—	(a)
Palm (PMO)	45	4	—	—	40	10	—	(b)

^a (a) Ma and Hanna (1999); (b) Soriano *et al.* (2006).

However, because of the unsaturated bond(s), the internal friction between successive molecular layers (i.e. steric hindrance) is enhanced. Consequently, the density of the unsaturated ester is higher and its viscosity is higher than those of a saturated ester of the same carbon number. The relatively low density and high viscosity of palm oil (PMO) in comparison with those of other oils is due to large amounts of saturated fatty acids.

The biodiesel properties determined by the structure and composition of its fatty ester components are ignition quality, heat of combustion, cold flow, oxidative stability, viscosity and lubricity (Knothe, 2005). The ignition quality is related to the ignition delay time and is indicated by the cetane number: the shorter the ignition delay time, the higher is the cetane number. Generally, cetane number decreases with decreasing chain length and increasing branching. The cetane scale is arbitrary and usually lies between 15 and 100. Gross heat of combustion is a measure of the suitability of fatty compounds as diesel fuel. The heat of combustion of fatty acid esters and triglycerols lie between about 1300 to 3500 kg cal/mol for C₈–C₂₂ fatty acids and esters. Cloud point and pour point are related to the flow properties of biodiesel fuel at low temperatures. The cloud point is the temperature at which a liquid fatty material becomes cloudy due to the formation of crystals and solidification of saturated fatty compounds. Solids and crystals subsequently grow and agglomerate, thereby clogging fuel lines and filters. With decreasing temperature, the liquid ceases to flow at a particular point. The lowest temperature at which the liquid still flows is the pour point. Saturated fatty compounds have significantly higher melting points than unsaturated fatty compounds, and in a mixture the saturated fatty compounds crystallize at higher temperatures than the unsaturated compounds. Therefore, biodiesel fuels produced from fats and oils with larger amounts of unsaturated fatty compounds have lower cloud points and pour points. This behavior is connected with the hampered internal molecular packing in the liquid volume (Lee *et al.*, 1995).

It should be mentioned that, as in the case of other liquids, the temperature dependence of viscosity of biodiesels follows an Arrhenius-type relationship (Kerschbaum and Rinke, 2004):

$$\eta = A \exp(E_\eta / R_G T) \quad (8.7)$$

where η is the dynamic viscosity in mPa·s, A is a constant, E_η is the activation energy for viscous flow, R_G is the gas constant and T is the absolute temperature in kelvin. Both A and E_η depend on the composition of the biodiesel and the temperature range

of measurements. For example, in the case of biodiesels derived from rapeseed oil and waste cooking oil, Equation (8.1) is followed with two different sets of values of A and E_η , corresponding to two different temperature intervals: (1) above the cloud point and (2) between the cloud point and pour point. It was found that the values of A and E_η for various biodiesels in the temperature range between the pour point and cloud point are about twice those above the cloud point. Obviously, these differences are associated with differences in the chemical composition of the samples. This feature is discussed below in more detail.

Biodiesel contains 10–11% by weight of oxygen, thereby promoting the combustion process in an engine. Biodiesel has about 12% lower heating values, a higher cetane number and a higher flash point than fossil diesel fuel. The cloud points and pour points of biodiesels are higher than those of diesel, depending on the nature of vegetable oil from which the biodiesel is derived. In general, however, the problems associated with using diesel fuels at low temperatures also apply to biodiesel.

Several approaches have been adopted to solve the problems associated with using biodiesel at low temperatures, including blending with conventional diesel fuel, winterization, additives, branched-chain esters, and bulky substituents in the chain (Knothe, 2005). Blending diesel fuel with biodiesel (at 20–30% by volume) does not improve the pour point. On the contrary, higher addition of saturated ester components in the biodiesel somewhat increases the cloud point and pour point of the blend. Winterization is based on the lower pour and cloud points of unsaturated FAME components than those of saturated components. This process leads to the formation of solidified masses of saturated ester components during cooling of the vegetable oil ester, thereby increasing the contents of unsaturated components remaining in the ester. Thus, winterization leads to a reduction in the pour point of biodiesel by lowering its saturated components (Dunn *et al.*, 1996; Lee *et al.*, 1996; Gomez *et al.*, 2002). However, to achieve a significant reduction in the pour point, several winterization steps are required. This process results in a low biodiesel yield and makes winterization economically less acceptable.

Several investigations have been carried out to improve the low-temperature flow properties of neat biodiesel prepared from different vegetable oils by using chemical additives (Du Plessis *et al.*, 1985; Dunn, 2002; Mittelbach and Schober, 2003; Soriano *et al.*, 2005, 2006). Among the additives, several antioxidants, such as TBHQ (*tert*-butylhydroquinone), pyrogallol, *n*-propyl gallate, BHA (3-*tert*-butyl-4-hydroxyanisole) and BHT (2,6-di-*tert*-butyl-4-methylphenol), and different types of synthetic phenolic antioxidants have been reported to be effective in improving the stability of biodiesels derived from vegetable oils and fats (Du Plessis *et al.*, 1985; Dunn, 2002; Mittelbach and Schober, 2003; Schober and Mittelbach, 2004). It was found that all antioxidants significantly improve the oxidation stability, and in the case of phenolic additives the improvement occurs at additive concentrations as low as 0.01% by weight (Schober and Mittelbach, 2004). However, not all additives influence the stability to the same level. For example, antioxidants DTBHQ (2,5-di-*tert*-butylhydroquinone), Ionox 220 [4,4'-methylenebis(2,6-di-*tert*-butylphenol)], Vulkanox ZKF [2,2'-methylenebis(4-methyl-6-cyclohexylphenol)], Vulkanox BKF (2,2'-methylenebis(4-methyl-6-*tert*-butylphenol)], and Baynox (20% 2–6-di-*tert*-butyl-4-methylphenol dissolved in biodiesel) increase the stabilization factor, defined as the ratio of the induction period in the presence of an additive to that without the additive, between 1.89 and 13.07, depending on the origin

of the biodiesel. Moreover, as expected, the stabilization factor, as indicated by the induction period, increases with increasing additive concentration between 0.01 and 0.1% by weight, as can be seen in Figure 8.17.

The dependence of the induction period on the concentration of different additives (Figure 8.17) is associated with the reduction in active aggregation/growth centers required for the formation of critically sized three-dimensional nuclei in the bulk medium (see Chapter 2). The role of the additive molecules is to bind the saturated ester components, thereby suppressing the onset of three-dimensional nucleation. This results in an increase in the metastable zone width of the biodiesel for three-dimensional nucleation (see Sections 2.3 and 2.6.3). A decrease in the cloud point and, perhaps, pour point of biodiesel is a consequence of this process, as discussed below.

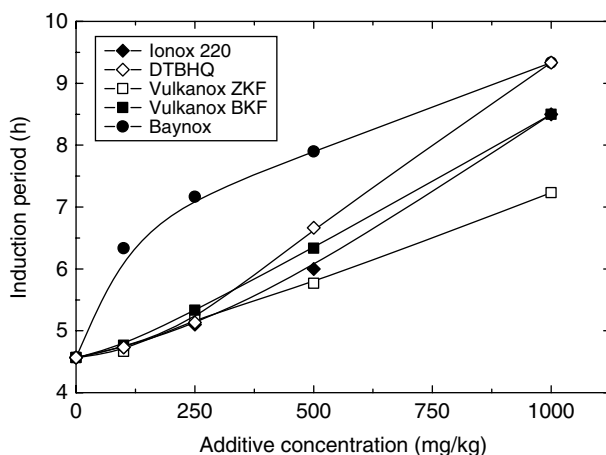


Figure 8.17 Dependence of induction period for instability (as determined by pour point) of rapeseed oil methyl ester on the concentration of some selected additives. Adapted from S. Schober and M. Mittelbach. Eur. J. Lipid Sci. Technol. **106**, 382. Copyright (2004), with permission from Elsevier

Several studies have demonstrated that the addition of branched-chain esters to biodiesel leads to products with lower pour points (Lee *et al.*, 1995; Lang *et al.*, 2001) and the presence of relatively high amounts of mono- and diglycerides as a result of transesterification of oils increases the viscosity of the product (Soriano *et al.*, 2006). In line with the explanation given above, these effects are due to reduced nucleophilicity and increased steric hindrance of the alkyl groups adjacent to the carbon atom bearing the –OH of the secondary alcohols (Lang *et al.*, 2001). However, addition of different antioxidants has no significant effect on viscosities, densities, carbon residues, pour point and sulfated ash components of different biodiesel samples (Schober and Mittelbach, 2004). Therefore, it is necessary to develop additives with specifically designed molecular structure to improve the low-temperature flow properties of biodiesel.

As described above, the molecular structure of known pour-point depressants for conventional diesel fuel consists of a polymeric hydrocarbon chain with protruding polar groups. The widely accepted mechanisms of action of these additives include adsorption, co-crystallization, nucleation and improved wax solubility (Dunn *et al.*, 1996; El-Gamal

and Al-Sabagh, 1996; El-Gamal *et al.*, 1998; Machado *et al.*, 2001; Zhang *et al.*, 2003; Marie *et al.*, 2005). However, vegetable oils and their FAMEs do not have polar groups. Therefore, to design effective pour-point depressants, polar groups have to be introduced in their structure. Soriano *et al.* (2003, 2005, 2006) reported that ozonized vegetable oils are effective pour-point depressants for neat biodiesel derived from different vegetable oils [sunflower (SFO), soybean (SBO), palm (PMO) and rapeseed oil (RSO)].

Figure 8.18 shows the effect of 1% (by weight) of ozonized SFO, SBO, PMO and RSO on the cloud points (black bars) and pour points (white bars) of biodiesels prepared from different vegetable oils. Ozonization was carried out by passing an ozone–oxygen mixture into a bubbling reactor. The ozonized oils contained about 0.18 g/ml of O₃ in SFO, SBO and RSAO and about 0.06 g/ml of O₃ in PMO. In PMO, the lower ozone content absorbed is due to the high amounts of saturated hydrocarbon chains. It can be seen that all ozonized oil additives lead to a decrease in the pour points of different biodiesels. However, ozonized SFO, SBO and RSO lead to significant decreases in the pour points of SFO, SBO and RSO biodiesels, whereas the effect of ozonized PMO is minor for PMO biodiesel and insignificant for other biodiesels. The pour points and cloud points of all samples treated with ozonized SFO do not vary significantly from each other. These observations suggest that the reduction in the pour points of different biodiesel samples is associated with interactions between molecules of FAME and ozonized oils. As inferred from the maximum reduction in the pour point of SFO in the presence of ozonized SFO, the strongest interactions occur when the additive and the biodiesel are prepared from the same vegetable oil. In other words, a pour-point depressant is most effective when the average length of its hydrocarbon chain is the same as that of the main components of the biodiesel being treated with the additive (Soriano *et al.*, 2006).

Soriano *et al.* (2006) found that ozonized additives have a relatively insignificant effect on the cloud points of different FAMEs (see Figure 8.18). Ozonized PMO reduced the cloud points of SFO, SBO and RSO biodiesel by 2–3 °C and that of PMO biodiesel by 12–18 °C. However, as reported by Schober and Mittelbach (2004), small amounts of ozonized vegetable oils do not result in a significant increase in the density and viscosity of different biodiesel samples, but addition of ozonized oils to PMO diesel always leads to the upper limit of 5.00 cSt kinematic viscosity for the commercial use of this biodiesel being exceeded, regardless of the additive concentration. The additives also decrease the flash points of different biodiesel samples from 178–186 °C by about 20 °C. These values of flash point are within American and European standards.

In order to establish the factors affecting the interactions of the ozonized vegetable oils and the biodiesel components, Soriano *et al.* (2005) carried out an investigation of pour points and cloud points of pure saturated and unsaturated FAMEs and their binary and ternary mixtures containing 1% ozonized SFO. The results for pure FAMEs and FAMEs treated with 1% ozonized SFO as a function of FAMEs chain length are shown in Figure 8.19. Obviously, the pour points and the cloud points increase with increasing chain length of the saturated FAMEs, but the presence of unsaturation in the FAMEs considerably improves these properties. The unsaturation of FAMEs involves the *cis* configuration, resulting in a bent geometry due to 1,2,4-trioxolane rings. In contrast to the straight chain of saturated FAMEs, the bent geometry of FAMEs weakens the intermolecular interactions and loosens the molecular packing, thus resulting in a lower pour point. Therefore, improvements in the flow properties of saturated FAMEs by the

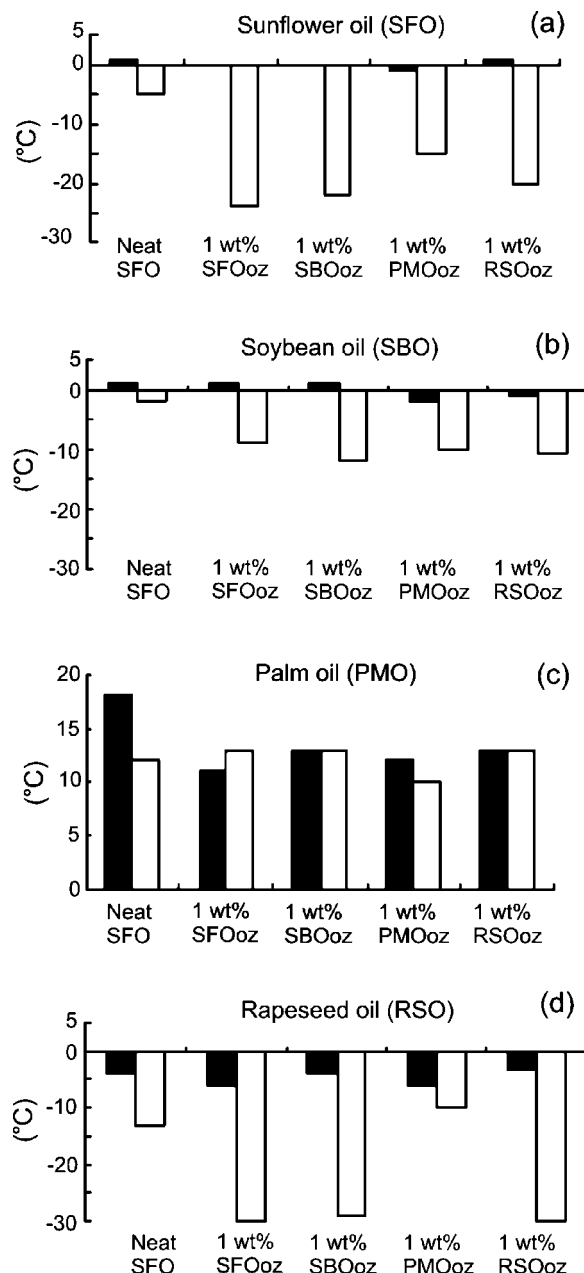


Figure 8.18 Effect of 1% (by weight) of ozonized vegetable oils on the cloud point (black bars) and pour point (white bars) of biodiesels prepared from different vegetable oils. Reproduced from N.U. Soriano Jr, V.P. Migo, and M. Matsumura. Fuel 85, 25. Copyright (2006), with permission from Elsevier

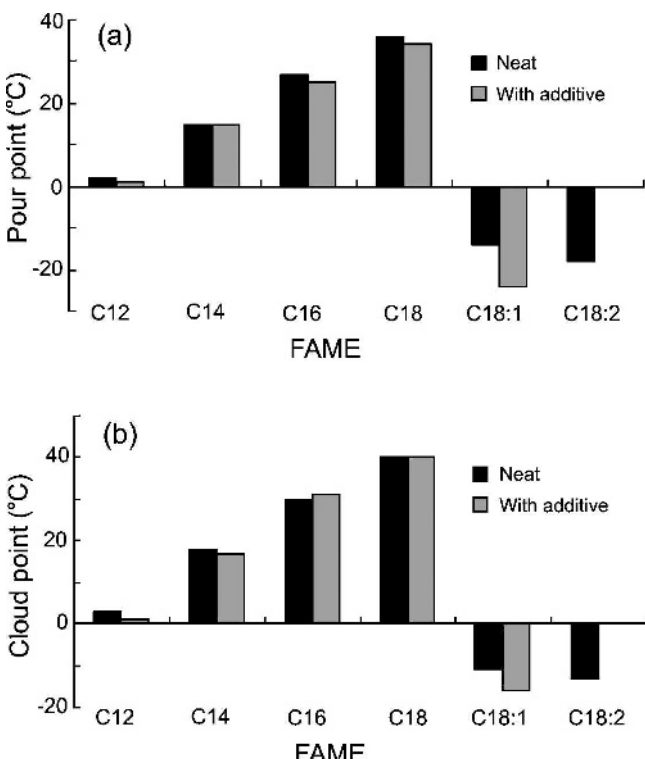


Figure 8.19 (a) Pour points and (b) cloud points of pure FAMEs and FAMEs treated with 1% ozonized SFO as a function of FAME chain length. Reproduced from N.U. Soriano Jr, V.P. Migo, K. Sato, and M. Matsumura. Eur. J. Lipid Sci. Technol. **107**, 689. Copyright (2005), with permission from Wiley-VCH

addition of ozonized vegetable oil are due to the introduction of polar moieties (i.e. 1,2,4-trioxolane rings) during their ozonation.

Investigation of pour points and cloud points of binary mixtures of C18:1 with C16:0 and C18:0 without and with 1% ozonized SFO showed the following (Soriano *et al.*, 2005):

- (1) In the absence of ozonized SFO, at equal amounts of unsaturated and saturated FAMEs, the effect of C18:0 in increasing the pour point and cloud point of the binary mixture is greater than that of C16:0.
- (2) Ozonized vegetable oil becomes less effective as a pour-point depressant with increasing amount of saturated components, especially C18:0.
- (3) Ozonized vegetable oil leads to a considerable reduction in the pour point when the saturated component is less than 10%. In the case of saturated FAMEs, the cloud point remains unaffected.

Studies of ternary mixtures of C16:0, C18:0 and C18:1, with the total amount of saturated components not exceeding 10%, revealed (Soriano *et al.*, 2005) that (1) the cloud

and pour points increase with increasing amount of the high melting-point component C18:0 but the additive has no effect on the pour point and cloud point of the mixture containing equal amounts of the saturated components, and (2) the additive decreases the cloud point more than the pour point, the former decreasing by 6 °C and the latter by a maximum of 3 °C.

As pointed out above, the cloud point of a biodiesel is associated with the formation of three-dimensional nuclei of saturated FAMEs in the bulk solution. Further cooling of the biodiesel leads the growth of the nuclei of saturated FAMEs and formation of new nuclei of low-melting unsaturated components and their subsequent growth into agglomerates. The pour point is reached when these agglomerates restrict the biodiesel flow. However, since additives mainly decrease the pour points of different FAMEs and have insignificant effect on their cloud points (see Figure 8.18), it may be concluded that additives practically do not disturb the initial stage of formation of nuclei but suppress the development of agglomerates and promote the continuous formation of new three-dimensional nuclei during the cooling of the biodiesel below the cloud point. Figure 8.20 presents polarized light micrographs showing the morphology and size distribution of crystalline agglomerates obtained from different biodiesel samples cooled down to –30 °C from 40 °C at a rate of 10 °C/min without and with 1% ozonized SFO additive. Obviously, SBO, SFO and RSO biodiesel samples yield very similar agglomerates composed of rod-shaped crystals but the additive forms more numerous but much smaller rod-shaped crystalline aggregates. However, the additive does not significantly modify the morphology and number of agglomerates in palm oil biodiesel.

The effect of ozonized vegetable oil on the difference in the morphology and size distribution of different biodiesel samples may be explained by considering the physical blocking of the existing active growth sites. When the growth of faces of a crystal is blocked, nucleation becomes favorable to ease the supercooling (i.e. supersaturation) caused by decreasing temperature during cooling. This leads to more numerous and smaller crystals. The physical blocking of growth sites occurs by adsorption of additive molecules, and depends on interactions between molecules composing the adsorption site and adsorbing molecule. These interactions are essentially determined by the functional groups present in them. This is illustrated in Figure 8.21. Because saturated FAMEs are composed of linear hydrocarbon chains, they assume flat surfaces. However, since the carbon–carbon double bonds in unsaturated FAMEs have bent geometry, they change the flat geometry of the surfaces into a bent form. Thus, due to the ample space available for their accommodation, 1,2,4-trioxolane moieties of ozonized vegetable oil are easily adsorbed in the bent geometry of the surface. Once these moieties have been adsorbed, they inhibit the growth of unsaturated FAMEs, thereby enhancing nucleation. Adsorption of additive molecules can also lead to a decrease in the interfacial free energy of the three-dimensional nuclei, thereby increasing the nucleation rate (see Section 2.2).

8.3 Food Industry

Food products are usually composed of fats, proteins, and carbohydrates existing together in the presence of water. Only minor components of binary or ternary mixtures are present in such systems as true solutions. These products are viewed as assemblies of

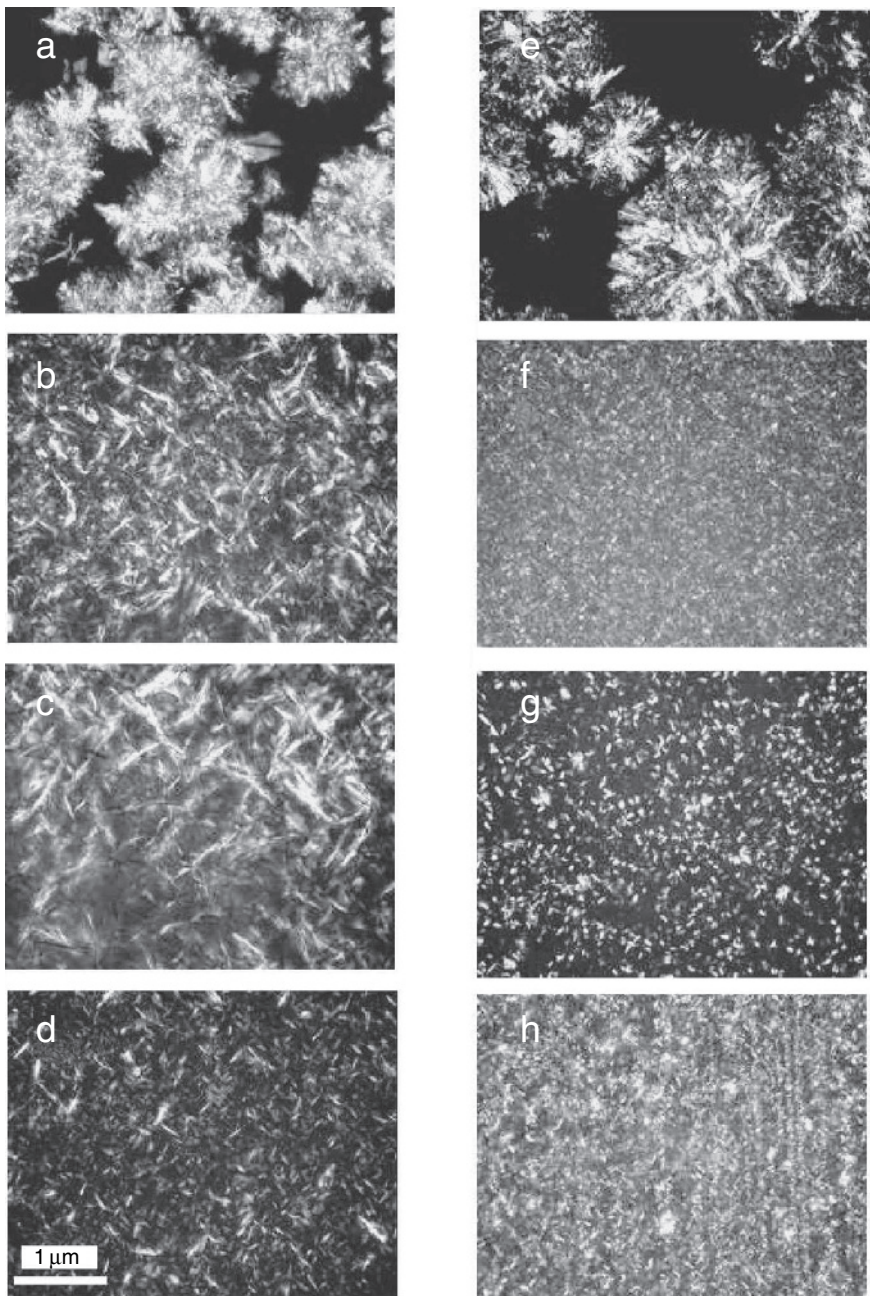


Figure 8.20 Polarized light micrographs showing the morphology and size distribution of crystalline agglomerates obtained from different biodiesel samples: (a, e) PMO diesel, 10°C; (b, f) SBO diesel, 10°C; (c, g) SFO diesel, -20°C; (d, h) RSO biodiesel, -30°C. (a-d) neat biodiesel and (e-h) biodiesel with 1% ozonized SFO additive. Reproduced from N.U. Soriano, V.P. Migo, K. Sato, and M. Matsumura. Eur. J. Lipid Sci. Technol. **107**, 689. Copyright (2005), with permission from Wiley-VCH

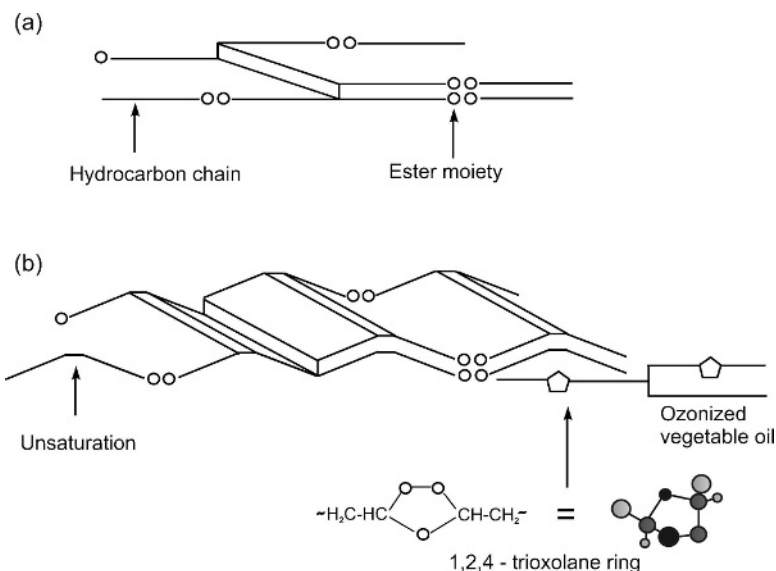


Figure 8.21 Schematic illustration of the geometry of lateral surfaces of (a) saturated and (b) unsaturated FAMEs. Note that unsaturation provides enough space to accommodate 1,2,4-trioxolane moieties of ozonized vegetable oil. Reproduced from N.U. Soriano, V.P. Migo, K. Sato, and M. Matsumura. Eur. J. Lipid Sci. Technol. **107**, 689. Copyright (2005), with permission from Wiley-VCH

Table 8.4 Some examples of food colloids. Adapted from N. Garti and J. Yano. In: N. Garti and K. Sato (Eds.), *Crystallization Processes in Fats and Lipid Systems*, Chap. 6, p. 211. Copyright (2001), with permission from Taylor and Francis

Food	Type of emulsion	Method of preparation	Mechanism of stabilization
Milk Cream	O/W A + O/W	Natural product Centrifugation	Protein membrane Protein membrane + particle stabilization of air
Ice-cream	A + O/W	Homogenization	Protein membrane + particle stabilization of air + ice network
Butter and margarine Sauces	W/O O/W	Churning High-speed mixing and homogenization	Fat crystal network Protein and polysaccharide
Fabricated meat products	O/W	Low-speed mixing and chopping	Gelled protein matrix
Bakery products	A + O/W	Mixing	Starch and protein network

particles and macromolecules in various states of organization, and are referred to as food colloids or colloidal foods. Food products such as milk, butter, margarine, cheese, ice-cream, mayonnaise and yoghurt are examples of food colloids. Among these, margarine is the simplest example of a water-in-oil (W/O) emulsion stabilized by a blend of food emulsifiers such as lecithin and monoglyceride with fat acids. In this case, solid fat particles along with liquid water droplets are dispersed in a continuous oil phase. In the case of ice-cream, fat particles are dispersed in a continuous water phase. In chocolate, however, a mixture of fat, sugar and cocoa powder is dispersed in liquid oil. Table 8.4 gives some examples of food colloids.

8.3.1 Some Basic Concepts

The main chemical constituents of edible fats and oils are triglycerides, which are esters of glycerol and three fatty acid molecules. The fatty acids have different numbers of carbon atoms, and have different degrees of unsaturation and branching. Most of the fatty acids in foods have an even number of carbon atoms, usually lying between 12 and 24, and are straight chained. Food oils are composed of mixture of triglycerides, but stearic, palmitic, lauric, oleic and linoleic acids are usually predominantly present. Apart from triglycerides, food oils also contain diglycerides, monoglycerides, free acids and various other lipid components.

As in the case of alkanes (Section 8.2.2), the melting point of an individual pure triglyceride depends on the chain length, the chain branching and the degree of unsaturation of its constituent fatty acids, and also on their relative position along the glycerol molecule (Table 8.5). The melting points of individual pure triglyceride usually lie between -40 and 80°C . The melting point of triglycerides increases with increase in their chain length

Table 8.5 Chemical structure of common fatty acids and their melting points (data from Lide, 1996/1997)

Fatty acid	Systematic name	Structure (xx:y)	Formula	Melting point ($^{\circ}\text{C}$)
Caprylic acid	Octanoic acid	8 : 0	$\text{C}_8\text{H}_{16}\text{O}_2$	16
Capric acid	Decanoic acid	10 : 0	$\text{C}_{10}\text{H}_{20}\text{O}_2$	32
Lauric acid	Dodecanoic acid	12 : 0	$\text{C}_{12}\text{H}_{24}\text{O}_2$	43
Myristic acid	Tetradecanoic acid	14 : 0	$\text{C}_{14}\text{H}_{28}\text{O}_2$	54
Palmitic acid	Hexadecanoic acid	16 : 0	$\text{C}_{16}\text{H}_{32}\text{O}_2$	62
Stearic acid	Octadecanoic acid	18 : 0	$\text{C}_{18}\text{H}_{36}\text{O}_2$	69
Arachidic acid	Eicosanoic acid	20 : 0	$\text{C}_{20}\text{H}_{40}\text{O}_2$	75
Behenic acid	Docosanoic acid	22 : 0	$\text{C}_{22}\text{H}_{44}\text{O}_2$	81
Lignoseric acid	Tetracosanoic acid	24 : 0	$\text{C}_{24}\text{H}_{48}\text{O}_2$	84
Palmitoleic acid	<i>cis</i> -9-Hexadecenoic acid	16 : 1	$\text{C}_{16}\text{H}_{30}\text{O}_2$	0
Oleic acid	<i>cis</i> -9-Octadecenoic acid	18 : 1	$\text{C}_{18}\text{H}_{34}\text{O}_2$	13
Linoleic acid	<i>cis</i> -9, <i>cis</i> -12-Octadecadienoic acid	18 : 2	$\text{C}_{18}\text{H}_{32}\text{O}_2$	-9
Linolenic acid	<i>cis</i> -9, <i>cis</i> -12, <i>cis</i> -15-Octadecatrienoic acid	18 : 3	$\text{C}_{18}\text{H}_{30}\text{O}_2$	-17
Erucic acid	<i>cis</i> -13-Docosenoic acid	22 : 1	$\text{C}_{22}\text{H}_{42}\text{O}_2$	34

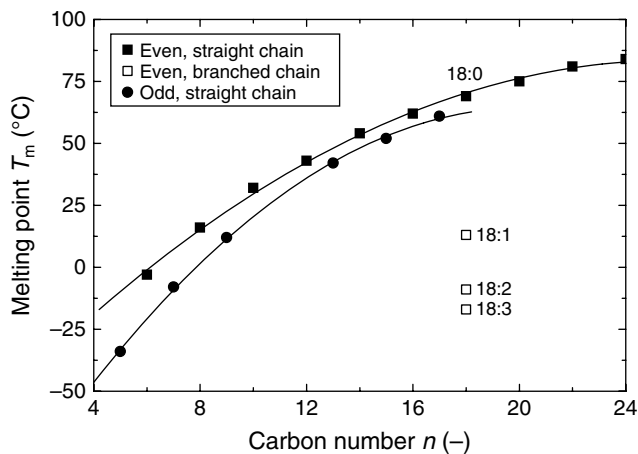


Figure 8.22 Dependence of melting point of triglycerides on their chain length. The constants are $T_m(0) = -59.9^\circ\text{C}$, $a = 11.1^\circ\text{C}$ and $b = 0.215^\circ\text{C}$ for triglycerides with even n ; $T_m(0) = -107.8^\circ\text{C}$, $a = 17.1^\circ\text{C}$ and $b = 0.422^\circ\text{C}$ for triglycerides with odd n . In both cases the regression coefficient was better than 0.997. Data from Lide (1996/1997)

and number of carbon atoms in the chain (see Figure 8.22 and Table 8.5) but, for the triglycerides of a given carbon number, it decreases with the degree of chain branching and unsaturation. The dependence of melting point T_m on the number n of carbon atoms in the linear chain may be described by the empirical relation (Figure 8.22)

$$T_m = T_m(0) + an - bn^2 \quad (8.8)$$

where $T_m(0)$ is the extrapolated value of T_m for $n = 0$, and a and b are empirical constants, the values of which depend on whether the chain has an even or odd number of carbon atoms. The important point here is that the curve for odd n is lower than that for even n , but the gap in the two curves decreases with increase in n . These trends are associated with the packing of the molecules in the crystalline state, a higher melting point corresponding to more effective packing.

Food oils are composed of a complex mixture of triglyceride molecules, each triglyceride having a different melting point in the pure state. Therefore, instead of melting at a single distinct temperature, a food oil melts over a wide interval of temperature (Figure 8.23). However, high melting-point triglycerides are soluble in lower melting-point glycerides. Consequently, the melting-point of a fat is not a simple weighted sum of its component triglycerides. In general, if the solid and liquid components have widely differing melting points, the solubility of the solid component can be determined reasonably well by using ideal solubility thermodynamics [see Equation (2.68)].

The solidification behavior of complex mixtures of triglycerides in oils depends on the cooling rate and the temperature of solidification. When an oil is cooled rapidly, all the component triglycerides solidify practically simultaneously producing a *solid solution* composed of a system of homogeneous crystals in which the triglycerides are mixed together. However, when the same oil is cooled slowly, the higher melting-point triglycerides solidify (i.e. crystallize) first, yielding *mixed crystals* in which some regions are rich

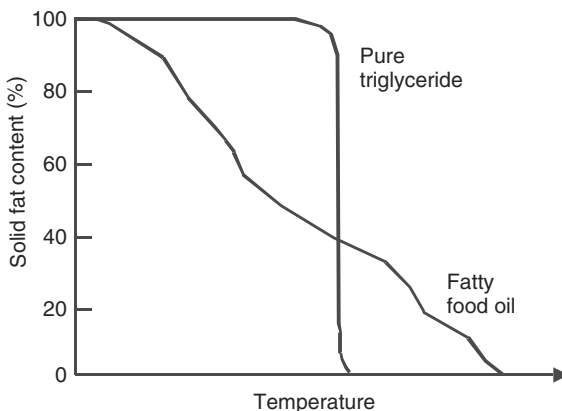


Figure 8.23 Schematic illustration of solid fat content against temperature for a pure triglyceride and a fatty food. Reproduced from E. Dickinson and D.J. McClements, Advances in Food Colloids. Copyright (1995), with permission from Springer Science and Business Media

and others are depleted in high melting-point components. The physico-chemical properties of the solidified phase depend on whether mixed crystals or a solid solution is formed.

Triglycerides exist in a number of polymorphs characterized by differing crystalline structures with different states of molecular packing (Sato, 1996, 2001). The commonly occurring polymorphs in triglycerides are hexagonal, orthorhombic and triclinic, usually referred to as α , β' and β , respectively. The thermodynamic stability of these three forms increases in the order: $\alpha > \beta' > \beta$. Although the β form is the most stable thermodynamically, triglycerides frequently crystallize initially in one of the other metastable forms because a lower value of activation energy is required for their nucleation. However, with time, crystals of the α and β' forms transform to the β form at a rate determined by the environmental conditions (e.g. temperature and pressure) and the nature of impurities present in the growth medium. The kinetic behavior of crystallization of polymorphs of fats and lipids is briefly described in Section 8.3.3.

After the initial crystallization of a fat, its individual crystals may subsequently undergo aggregation to form three-dimensional crystal networks and also Oswald ripening. Weak van der Waals forces and reduction in the surface energy between the solid fat and liquid oil phases, adhesive forces between crystals arising from water bridges and crystal-crystal interaction forces, and dependence of solubility on crystal size are responsible for these processes (Dickinson and McClements, 1995). Although the total solid fat content during these processes remains constant, they can result in changes in the physico-chemical properties of the fat with time.

The polymorphic forms of a fat differ in melting point, solubility, crystal morphology and network, rheology, particle flow, etc. However, the physical properties of stable polymorphs are usually not preferable in fat products because of, *inter alia*, their high melting point, slow crystallization and large crystalline sizes. Moreover, polymorphic transformation can lead to phase separation in fat products by destroying the fine-grained network between the fat crystals themselves and/or between fats and other constituents.

Therefore, control of polymorphic transformation of triglycerides and modification of the physical properties of fats and their rheological behavior are of scientific and technological interest.

Crystallization of fats can take place not only in bulk liquid or solution but also in confined spaces called emulsions. Emulsions are metastable dispersion phases of one liquid in a second immiscible liquid. Common examples are water-in-oil (W/O) and oil-in-water (O/W) emulsions (Figure 8.24). Small-molecule surfactants are commonly used in the food industry to modify the properties of the fat surface and the fat crystallization process, leading thereby to a changed solid fat content and crystal size. The small-molecule surfactants allowed for use in food are usually called emulsifiers. Food emulsifiers are long-chain molecules having two parts, hydrophobic (nonpolar) and hydrophilic (polar) moieties (see Chapter 1). In contrast, fats are neutral lipids with minimized hydrophilic nature. Consequently, two different effects operate for the interactions between two molecules. Hydrophobic moieties have attractive forces with fat molecules. Depending on the chain length of and the presence of double bonds in the fatty acid moiety, emulsifiers are physically adsorbed at the fat crystal surface or incorporated in fat crystals. Hydrophilic groups of the emulsifiers, however, result in repulsive forces, which depend on the volume and chemical formula of the hydrophilic moieties of emulsifiers. Adsorption of emulsifiers also reduces the oil/water interfacial energy, which improves the stability of emulsions as a result of the formation of small emulsion droplets with diameters ranging from 10^{-5} to 10^{-7} m to be dispersed in the bulk volume.

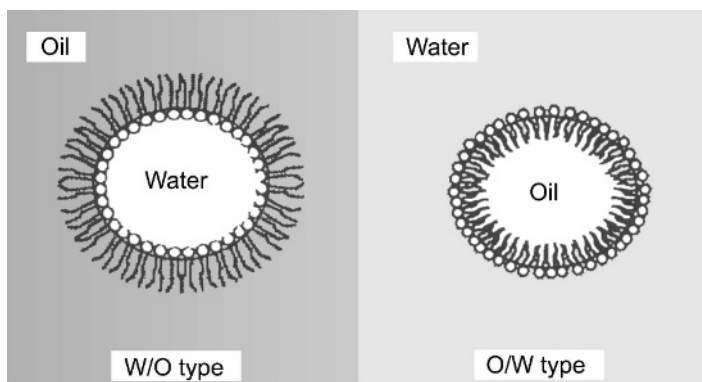


Figure 8.24 Two types of emulsion systems. Adapted from N. Garti and J. Yano. In: N. Garti and K. Sato (Eds.), Crystallization Processes in Fats and Lipid Systems, Chap. 6, p. 211. Copyright (2001), with permission from Taylor & Francis

Structures and properties of commonly used food emulsifiers have been reviewed by Garti and Yano (2001). The common emulsifiers are lecithins, mono- and monodiglycerides, polyglycerol polyricinoleate (PGPR), sorbitan esters, and sugar esters. Lecithins are naturally occurring amphiphiles extracted from soya and egg, mono- and monodiglycerides are glycerol fatty acid esters, PGPR is a synthetic compound produced by esterification between polycondensed ricinoleic acid and polyglycerol, sorbitan esters

are obtained by reaction between sorbitol and various fatty acids, and sugar esters are produced by esterification of fatty acids or transestrification of fats with sugar. The commonly used food emulsifiers and the levels of their use are given in Table 8.6. Most food emulsifiers have fatty acyl chains, such as stearic, palmitic and oleic/linoleic as hydrophobic/lipophilic moieties, in their structures.

Table 8.6 Common food emulsifiers and their legal status. Adapted from N. Garti and J. Yano. In: N. Garti and K. Sato (Eds.), *Crystallization Processes in Fats and Lipid Systems*, Chap. 6, p. 211. Copyright (2001), with permission from Taylor & Francis

Emulsifier	Abbreviation	ADI value ^a	EEC No.	US FDA 21 CFR
Lecithin	—	Not limited	E322	\$182.1400
Monodiglycerides	MG	Not limited	E471	\$182.4505
Acetic acid esters of monodiglyceride	AMG (ACETEM)	Not limited	E472a	\$172.828
Lactic acid esters of monodiglyceride	LMG (LACTEM)	Not limited	E472b	\$172.852
Citric acid esters of monodiglyceride	CMG (CITREM)	Not limited	E472c	—
Diacetyltauric acid esters of monodiglyceride	DATEM	50	E472e	\$182.4101
Succinic acid esters of monodiglyceride	SMG	—	—	\$172.830
Salts of fatty acids (Na, K)	—	Not limited	E470	\$172.863
Polyglycerol esters of fatty acids	PGE	0–25	E475	\$172.856
Propylene glycol esters of fatty acids	PGMS	0–25	E477	\$172.856
Sodium stearoyl lactylate	SSL	0–20	E481	\$172.846
Calcium stearoyl lactylate	CSL	0–20	E482	\$172.844
Sucrose esters of fatty acids	—	0–10	E473	\$172.859
Sorbitan monostearate	SMS	0–25	E491	\$172.842
Polysorbate-60	PS 60	0–25	E435	\$172.836
Polysorbate-65	PS 65	0–25	E436	\$172.838
Polysorbate-80	PS 80	0–25	E433	\$172.840

^a Acceptable daily dose in mg/kg body weight per day.

Food oils contain a large number of different chemical components. Consequently, they exhibit complex physico-chemical properties. Therefore, experimental investigations devoted to the understanding of the factors affecting the crystallization of oil droplets in emulsions have usually been carried out on individual single triglycerides or simple hydrocarbons rather than complex food oils. Since food oils can be present as a single liquid phase (for example, different oils used for cooking) and as complex emulsion

systems (for example, milk and butter), crystallization of food oils, present either as single bulk phases or as emulsions, has been a subject of enormous scientific interest. These studies essentially deal with the kinetics of overall solidification of the oil at different temperatures and in the absence and presence of emulsifiers. The basic issues addressed in these investigations are nucleation, crystal growth and identification of crystallizing polymorphic forms, and the role of additives/emulsifiers in these processes.

Differential scanning calorimetry, differential thermal analysis, X-ray diffraction, neutron diffraction, ultrasonic velocity measurements, and density measurements are the commonly employed techniques to study the kinetics of crystallization in emulsions. These techniques enable one to obtain, directly or indirectly, experimental data on the fraction of crystallized volume of the droplets as a function of time. However, these techniques do not enable one to obtain experimentally data of the number density N (i.e. number of droplets per unit volume) of crystallized droplets of different sizes as a function of time t to verify theoretical models of kinetics of crystallization of droplets in emulsion systems. For this purpose, *in situ* isothermal crystallization in emulsion droplets is more suited.

This section briefly describes the effect of emulsifiers on the crystallization behavior of fatty acids. For more details the reader is referred to, among others, Dickinson and McClements (1995), Garti and Yano (2001), Povey (2001), and Sato (2004), where the experimental methods for the study of crystallization kinetics in model and natural food systems are also presented.

8.3.2 Crystallization of Food Fats in the Bulk

Crystallization of triglycerides is a complex phenomenon characterized by fairly slow growth rates and polymorphic transitions of their crystallized phases. The crystallization of triglycerides is also complicated by the presence of minor components frequently contained in them. For example, milk fat consists of 95–98% triglycerides, but also contains diglycerides, free fatty acids, monoglycerides, phospholipids and sterols as minor components. All of these minor components are amphiphilic compounds consisting of molecules having a polar and an apolar part in their chemical structure. Diglycerides and sterols have the lowest hydrophile–lipophile balance (HLB) number, whereas phospholipids have the highest HLB.

Investigation of the effect of minor components and additives on the crystallization behavior of food fats in the bulk has been an active area of scientific interest. For these studies, palm oil and anhydrous milk fat (AMF) have been selected as model fats. The selection of these substances is motivated by the fact that they are common fat resources for the food industry and cooking purposes. Moreover, among the different cooking oils, palm oil has high thermal and oxidative stability at room temperature.

Most research has been carried out on diglycerides because they are the most abundant minor components, constituting up to 3 wt%, in triglyceride fats (Siew and Ng, 1999; Kaneko *et al.*, 1999; Katsuragi *et al.*, 2001; Foubert *et al.*, 2004). However, the influence of monoglycerides, which are more polar and present in smaller quantities in fats than their diglyceride counterparts, has also been studied (Smith *et al.*, 1994; Foubert *et al.*, 2004). For the study of the crystallization behavior of bulk food oils, palm oil has been selected as a model compound. Investigations of the fatty oils have been carried out by isothermal crystallization, where a sample in a conducting vessel is first held at a

sufficiently high temperature for several minutes and is then cooled at a fast rate of 5–100 °C/min to a predefined temperature of crystallization. A typical example of the effect of additives on the crystallization behavior of fats is shown in Figure 8.25. The experimental data were generated from the original plots of crystallized mass Φ of anhydrous milk fat (AMF) at 26 °C as a function of crystallization duration for monostearin (MS) and distearin (DS) additives, and the curves were plotted with the best-fit parameters obtained by using Equation (2.50) from the generated data (Table 8.7). The crystallization behavior was determined using differential scanning calorimetry (Foubert *et al.*, 2004).

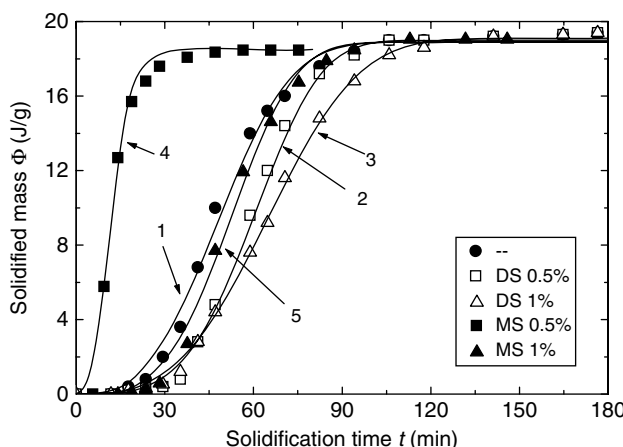


Figure 8.25 Effects of two different additives on the crystallization behavior of milk fat at 26.5°C: (1) no impurity, (2, 3) MS, and (4, 5) DS. Additive concentration: (2, 4) 0.5% and (3, 5) 1%. Adapted from I. Foubert, B. Vanhoutte, and K. Dewettinck. Eur. J. Lipid Sci. Technol. **106**, 531. Copyright (2004), with permission from Wiley-VCH

Table 8.7 Constants Φ_0 , Θ and q for overall crystallization of anhydrous fat milk in the presence of additives

Additive	Concentration (wt%)	Φ_0 (J/m)	Θ (min)	q
None		18.9 ± 0.2	54.6 ± 0.9	3.1 ± 0.2
MS	0.5	18.7 ± 0.3	57.9 ± 0.9	3.7 ± 0.2
	1.0	18.0 ± 0.1	13.6 ± 0.5	2.8 ± 0.3
DS	0.5	19.0 ± 0.1	64.9 ± 0.5	4.0 ± 0.2
	1.0	19.1 ± 0.1	73.1 ± 0.6	3.2 ± 0.1

As described in Chapter 2, crystallization in bulk systems occurs by nucleation and growth of crystallites in the entire volume. In an ideally pure liquid, nucleation is homogeneous. However, when the liquid contains nanoparticles and/or impurity particles, which act as nucleation centers in the volume or at the surface of the droplets, nucleation is

heterogeneous, which occurs in the volume or at the surface of the droplets, respectively. Crystallization can occur by a mononuclear or polynuclear mechanism involving the formation of one or many nuclei in the volume, respectively. Therefore, overall crystallization in the liquid may involve both mononuclear and polynuclear mechanisms. In the case of the polynuclear mechanism, the nuclei may be formed instantaneously or successively. Moreover, when crystallization of different polymorphs occurs under the experimental conditions, one has to take into account the phase transformation of the metastable phase into a more stable phase. The theoretical expressions due to the above mechanisms are different and are given in Chapter 2.

From Table 8.7, it follows that, with increasing concentration of additive, the value of the time constant (or induction period) Θ increases regularly in the case of distearin (DS). However, it increases with 0.5% and then decreases with 1% monostearin (MS). This means that the nucleation rate is increased by the addition of DS, but MS exhibits a reversed trend. For both additives, the exponent q lies between 3 and 4, suggesting that growth occurs by the polynuclear mechanism and is not altered by the presence of the additive.

The entire process of crystallization in the bulk may also be considered to occur in two steps, as shown in Figure 8.26. The first step is associated with the crystallization of the metastable α polymorph, and the second step involves the transformation of the α polymorph into the stable β' polymorph (Herrera *et al.*, 1999; Foubert *et al.*, 2004, 2006). However, when the crystallized mass Φ_{m1} is small, one observes only the second step in the crystallization experiment. Physically, this situation is possible when the crystallizing unstable phase transforms simultaneously into a more stable phase. The crystallization behavior in this one-step mechanism is given by (Foubert *et al.*, 2004)

$$\Phi = \Phi_{m2} \exp \left\{ -\exp \left[\frac{2.3R_2}{\Phi_{m2}} (\Theta - t) + 1 \right] \right\} \quad (8.9)$$

where Φ_{m2} is the maximum solidified mass, R_2 is the growth rate, and Θ is a time constant related to induction period. These symbols are explained in Figure 8.26. In the

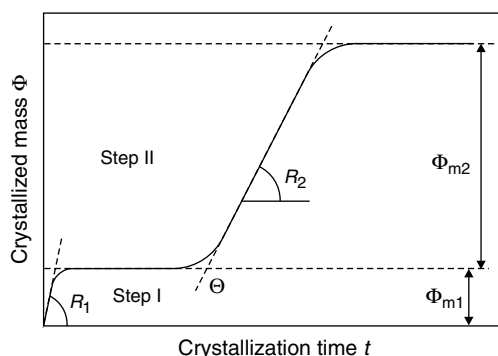


Figure 8.26 Schematic illustration of the two-step model of crystallization in the bulk. Meanings of different symbols are defined. Adapted from I. Foubert, B. Vanhoutte, and K. Dewettinck. Eur. J. Lipid Sci. Technol. **106**, 531. Copyright (2004), with permission from Wiley-VCH

case of the two-step model of crystallization, the two steps are represented as a sum of two reaction steps (Foubert *et al.*, 2004; see also Section 6.3.4):

$$\Phi = \Phi_{m1} \left[1 - \exp \left(-\frac{2R_1}{\Phi_{m1}} t \right) \right] + \Phi_{m2} \exp \left\{ -\exp \left[\frac{2.3R_2}{\Phi_{m2}} (\Theta - t) + 1 \right] \right\} \quad (8.10)$$

where Φ_{m1} is the total mass of the metastable phase and R_1 is its growth rate.

Foubert *et al.* (2004) investigated the effects of the addition of 0.5 and 1% of two diglycerides (distearin and diolein) and two monoglycerides (monostearin and monoolein) on the crystallization behavior of AMF at four temperatures, 22, 23.5, 25 and 26.5 °C, using pulsed nuclear magnetic resonance and differential scanning calorimetry. They observed the following features:

- (1) Two-step crystallization occurs at 22 °C for a pure AMF sample and also for all samples containing partial glycerides.
- (2) One-step crystallization occurs at 25 and 26 °C for pure and additive-containing samples.
- (3) At 23 °C, the crystallization behavior depends on the type of partial triglyceride. The two-step process occurred when distearin, monostearin or monoolein was added, but the pure fat sample showed only one-step crystallization. Addition of 0.5% diolein followed one-step crystallization but addition of 1% diolein changed the crystallization behavior into a two-step process.

From Figure 8.25, illustrating the crystallization kinetics of AMF at 26 °C it can be seen that distearin (DS) increases the induction period Θ for nucleation but the growth rate R_2 is not altered significantly with increase in the additive concentration. Monostearin (MS), on the other hand, exhibits a reversed trend in crystallization. Addition of 0.5% of MS increases the induction period Θ but 1% of the additive markedly decreases Θ . At both concentrations there is an increase in the growth rate R_2 , the rate increasing with increasing additive concentration. The crystallization kinetics of AMF at 26 °C in the presence of monoolein and diolein additives, however, revealed an increase in the rates of nucleation (decrease in induction period Θ) and crystal growth R_2 .

The above results show that the effect of the minor components on the crystallization behavior of fats from melts depends on the temperature of crystallization (i.e. applied undercooling ΔT), the type and concentration of the minor component, and the polar head of its amphiphilic molecules. Due to their more polar nature, monoglycerides are more effective than diglycerides. Both di- and monoglycerides have an influence on the processes of nucleation and crystal growth. Moreover, the nature of the polar head of the molecules of a minor component and the insolubility of the minor component in the bulk melt determine its overall effect on these processes.

Figure 8.27 demonstrates the effect of 1% DDB-750 (polyglycerol-10 dodecabehenate; melting point 69 °C) additive on the isothermal crystallization of palm oil (T_m between 34 and 40 °C) at 20 and 27 °C for 60 min. DDB-750 additive is composed of polymerized 10 glycerol molecules with an average degree of esterification with behenic acid of 12. The photographs show that the palm oil crystals exhibit two types of crystal morphology: (1) tiny individual crystals, randomly distributed in the liquid, having an average diameter of up to several micrometers, and (2) spherulites of an average diameter up to 100 μm. The crystals formed in the presence of the additive differ from those without the additive

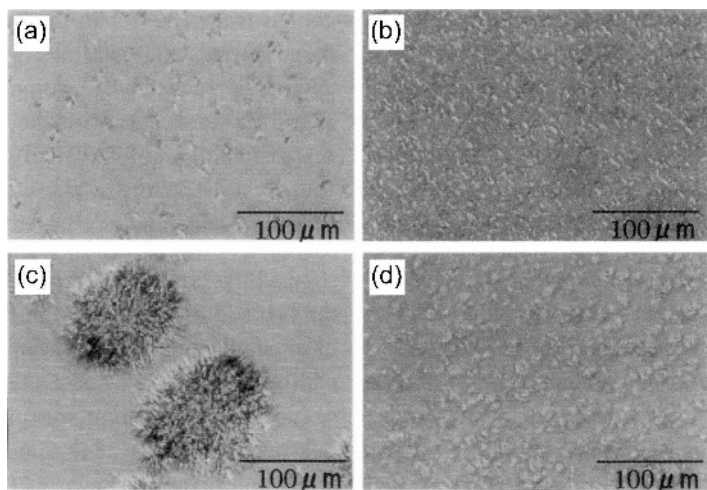


Figure 8.27 Isothermal crystallization of palm oil at (a, b) 20°C and (c, d) 27°C for 60 min; (a, c) no additive and (b, d) 1% DDB-750 additive. Reproduced from M. Sakamoto, K. Maruo, J. Kuriyama, M. Kouno, S. Ueno, and K. Sato. *J. Oleo Sci.* **52**, 639. Copyright (2003), with permission from Japan Oil Chemists' Society

in morphology, size and density (i.e. number per unit area). The difference in the crystal morphology and the density of crystals is better seen in the case of crystals formed at 27 °C. These results show that the addition of DDB-750 increases the nucleation rate of palm oil crystals and inhibits their growth rate. It is a common observation that nucleation-promoting additives have higher melting points than those of the crystallizing compounds. During the crystallization of a fat, such additives remain insoluble in the medium and act as nucleation centers.

Figure 8.28 shows the growth rate R of *n*-hexadecane from bulk liquid at constant crystallization temperature T_c as a function of concentration of P-170 and O-170 additives. The effect of S-170 and L-195 additives was comparable to that of O-170, hence, their data are not shown. These additives are highly hydrophobic sucrose oligoesters (SOEs) having sucrose molecules and fatty acid moieties of palmitic (P-170), stearic (S-170), lauric (L-195) and oleic (O-170) acids. The average degree of esterification of each SOE was about 5.5.

In Figure 8.28, the curves were drawn with the parameters listed in Table 8.7. The parameters were determined by the best-fit plots of the data according to Equation (4.30) of the Kubota–Mullin model. It can be seen from Table 8.7 that:

- The value of R_0 for pure system is higher when the undercooling ΔT is larger for the P-170 additive.
- The value of the impurity effectiveness parameter α , equal to about 2, is practically independent of ΔT for P-170 additive but α is lower by a factor of 10 for O-170 additive.
- The value of the Langmuir constant K depends on the type of additive and also on the value of undercooling ΔT .

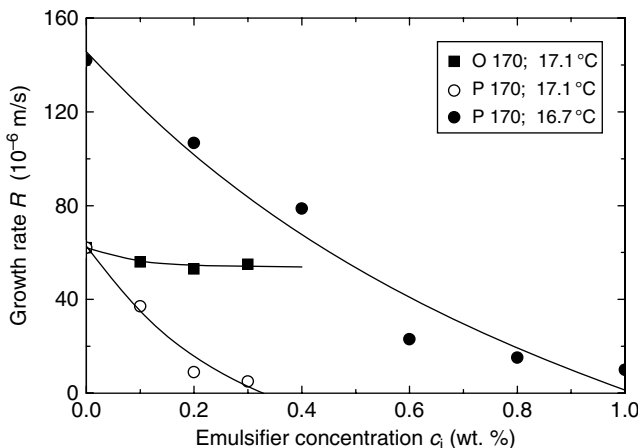


Figure 8.28 Growth rate of *n*-hexadecane from bulk liquid at constant crystallization temperature T_c as a function of concentration of P-170 and O-170 additives. Best-fit plots of the data according to Equation (4.30) of the Kubota–Mullin model are shown for the parameters listed in Table 8.8. Original experimental data from Kaneko *et al.* (1999) and Katsuragi *et al.* (2001)

Observation (i) is consistent with the crystal growth theories, whereas observation (ii) may be explained in terms of the effect of additive molecules on the value of interfacial energy γ [see Equations (4.29) and (4.42)]. Observation (iii) implies that the value of the differential heat of adsorption Q_{diff} for O-170 additive is higher than that for P-170, and the value of Q_{diff} decreases with increase in ΔT . These features may be understood if the heat of adsorption ΔG_{ad} of adsorbing molecules and the heat of desorption ΔG_{des} of adsorbed molecule are taken into account (see Section 4.2).

Table 8.8 Constants R_0 , α and K for *n*-hexadecane growth

Additive	T_c (°C)	R_0 (μm/s)	α	K (wt% $^{-1}$)
O-170	17.1	62.0	0.15	25.9
P-170	17.1	62.7	2.02	3.04
P-170	16.7	145.6	2.27	0.78

8.3.3 Crystallization of Polymorphs

All long-chain compounds, including fats and lipids, crystallize in different polymorphic forms. The crystallization of these compounds is determined by internal factors related to their molecular structure and by various external factors such as temperature, pressure, solvent, supercooling or supersaturation and presence of additives. For example, during an investigation of the crystallization behavior of commercial palm oil (melting point T_m between 34 and 40 °C) by X-ray diffractometry, the following features were revealed (Sakamoto *et al.*, 2003):

- (1) Without additives such as DDB-750 (polyglycerol-10 dodecabehenate; $T_m = 69^\circ\text{C}$) and HB-750 (polyglycerol-10 heptabehenate; $T_m = 65^\circ\text{C}$), palm oil crystallizes in the α form after rapid quenching the liquid palm oil at 10°C . However, during heating from 10 to 40°C , the α form transforms to the more stable β' form at about 15°C , and the β' form changes to the most stable β form.
- (2) Addition of the above additives leads to the crystallization of the β' form at 10°C , but this form does not transform to the β form during heating.
- (3) The additives promote the crystallization of the β' form at 20 and 25°C , but inhibits it at 28°C .

In this section, the kinetic aspects of the crystallization behavior of polymorphs of fats are briefly discussed. The description is confined to polymorphs in two popular fats: tripalmitoylglycerol (PPP) and 1,3-distearoyl-2-oleoyl-*sn*-glycerol (SOS), and is mainly based on a recent review by Sato (2001). For more details, the reader is referred to the literature (Sato *et al.*, 1999; Sato, 2001).

Figure 8.29 illustrates the typical characteristics of polymorphism of a triacylglycerol (TAG) fat. The nature and composition of three acid moieties (denoted R_1 , R_2 and R_3) of a TAG molecule determine the chemical properties of the fat, as shown in Figure 8.29a. Figure 8.29b illustrates the three polymorphs α , β' and β , which are based on subcell structures defined by cross-section packing modes of the zigzag aliphatic chains as seen in Figure 8.29c. Figure 8.29c shows the crystal structure of β form of tricaprin. The chain-length structure produces a sequence of acyl chains stacking a unit cell lamella along the long-chain axis (Figure 8.29d). A double chain-length structure is formed when the chemical properties of the three chain moieties are the same or similar, as in the case

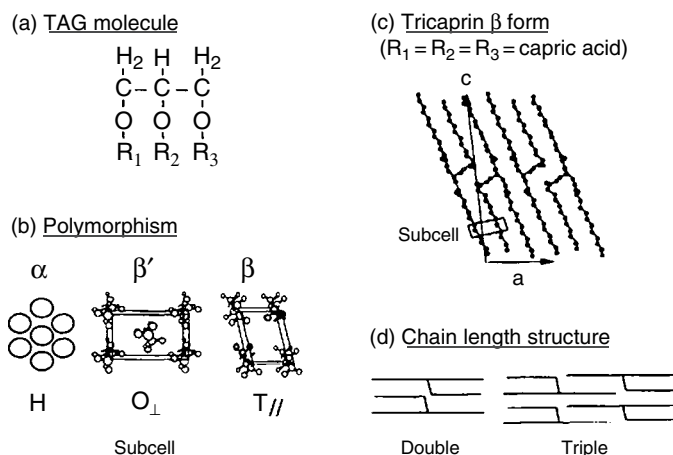


Figure 8.29 Typical characteristics of polymorphism of a triacylglycerol (TAG) fat: (a) a triacylglycerol molecule, (b) packing modes of different polymorphs, (c) crystal structure of β form of tricaprin, and (d) chain-length structure representing the unit cell of tricaprin β form. Reproduced from K. Sato. Chem. Eng. Sci. **56**, 2255. Copyright (2001), with permission from Elsevier

of the β form of tricaprin (see Figure 8.29c). However, when the chemical properties of one or two of the three chain moieties are significantly different from each other, a triple chain-length structure is formed. The mixing behavior of different types of TAGs in solid phases is determined by the chain-length structure.

When the three chain moieties are the same (i.e. $R_1 = R_2 = R_3$), the fatty acids have homogeneous compositions and are called monoacid triacylglycerols. For example, in the case of palmitic acid, the homogeneous composition gives tripalmitoylglycerol (PPP). The structural and crystallization properties of PPP have been well investigated as a model fat substance. The molecular structures of the three forms of PPP are disordered aliphatic chain conformation in the α form, intermediate packing in the β' form and the most dense packing in the β form. These structures are shown schematically at the top of Figure 8.30, which illustrates the relationship between Gibbs energy G and temperature T for the three polymorphs of PPP. Due to the specificity of the structure, the Gibbs energy G is the highest in α , intermediate in β' and the lowest in β . As a consequence of the combined effects of the molecular structures and the rate of crystallization, the crystal morphology is amorphous-like for the α phase, tiny bulky crystals for the β' phase and needle-like for the β phase.

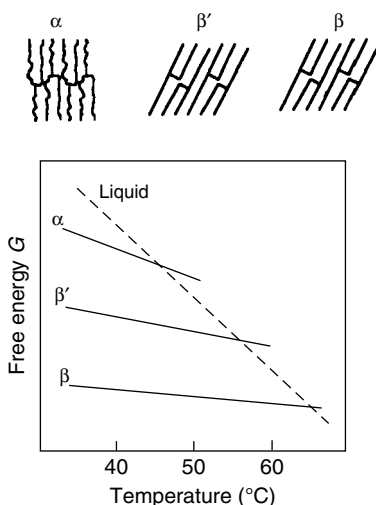


Figure 8.30 Structure models, and relationship between Gibbs free energy (G) and temperature (T) for the three polymorphs of PPP. Reproduced from K. Sato. Chem. Eng. Sci. **56**, 2255. Copyright (2001), with permission from Elsevier

The polymorphic properties of other fats of homogeneous compositions are similar to those of PPP. However, when the fatty acid compositions of the three moieties are not homogeneous such that one or two of the moieties differ from each other, either the β form is absent and the β' form becomes more stable, or two β forms appear. For example, in the case of 1,3-distearoyl-2-oleoyl-*sn*-glycerol (SOS), in which R_1 and R_3 are stearic acid moieties and R_2 is an oleic acid moiety, five forms are present: α , γ , β' , β_1 and β_2 (Sato *et al.*, 1999). In this case, the γ form has a structure which is a

compromise between the structures of the α and β' forms. In the liquid state, two liquid crystalline phases, called LC1 and LC2, have also been identified. The presence of these two liquid crystalline phases affects the crystallization properties of the SOS polymorphic phases. The β_2 form is equivalent to Form V of cocoa butter, which is the most favorable polymorph for use in confectionery.

Fats and lipids present in natural resources are mixtures of different types of TAGs. Therefore, the complex behavior of melting, crystallization and transformation, crystal morphology and aggregation of the real fat systems is partly due to the physical properties of the components of TAGs and partly to the phase behavior of the mixtures. In general, when two components of a binary TAG mixture are miscible in all proportions in the liquid state, three phases may occur: solid solution, eutectic phase and compound formation. Polymorphism and chain-chain interactions are the factors affecting the crystalline behavior of TAG mixtures.

Crystallization of polymorphs of a TAG is determined by thermodynamic and kinetic factors (see Section 2.4). According to the Ostwald rule of stages, a crystallized phase transforms successively to more stable phases step by step. Thus, as is usually observed, the metastable form nucleates prior to the nucleation of the most stable form when the process is induced by large kinetic factors, e.g. large supercooling or supersaturation (see Figure 8.30). However, when the effect of kinetic factors is suppressed, for example, by temperature fluctuation, ultrasonic stimulation, additives and seeding, the more stable form can be nucleated.

Figure 8.31 shows the induction period τ for the crystallization of different polymorphs of tripalmitoylglycerol (PPP) as a function of crystallization temperature T . The induction period was determined as the time when the occurrence of a crystal was detected optically after attaining a predefined temperature of the melt during isothermal crystallization

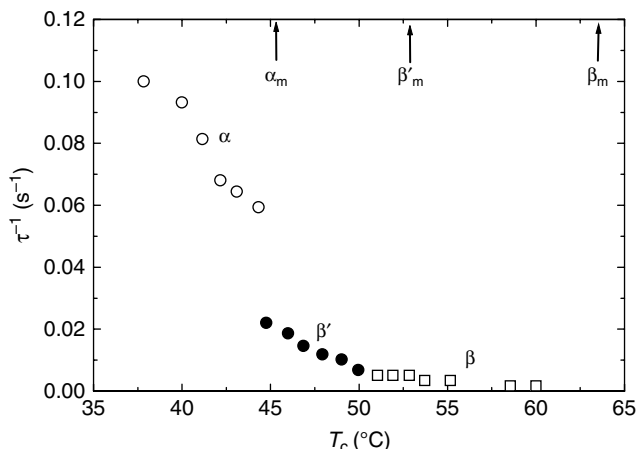


Figure 8.31 Induction period τ for crystallization of different polymorphs of tripalmitoylglycerol (PPP) as a function of crystallization temperature T . Melting points of the polymorphs are also indicated. Reproduced from K. Sato (2001). Chem. Eng. Sci. **56**, 2255. Copyright (2001), with permission from Elsevier

(Sato and Kuroda, 1987). As can be seen, τ is the shortest for the α form, intermediate for the β' form and the longest for the β form. However, when the temperature of cooling was fluctuated around the melting point of the α or β' form, nucleation of the more stable form was accelerated due to melt-mediated transformation of the metastable form.

Figure 8.32a and b show the experimental $\tau(T)$ data of Figure 8.31 replotted as dependences of $\ln \tau$ on ΔT^{-2} and $\ln \tau$ on T for the crystallization of different polymorphs of PPP, according to classical nucleation and atomistic theories, respectively; see Equations (2.65) and (2.66) and Equation (2.67). In Figure 8.32a, the supercooling

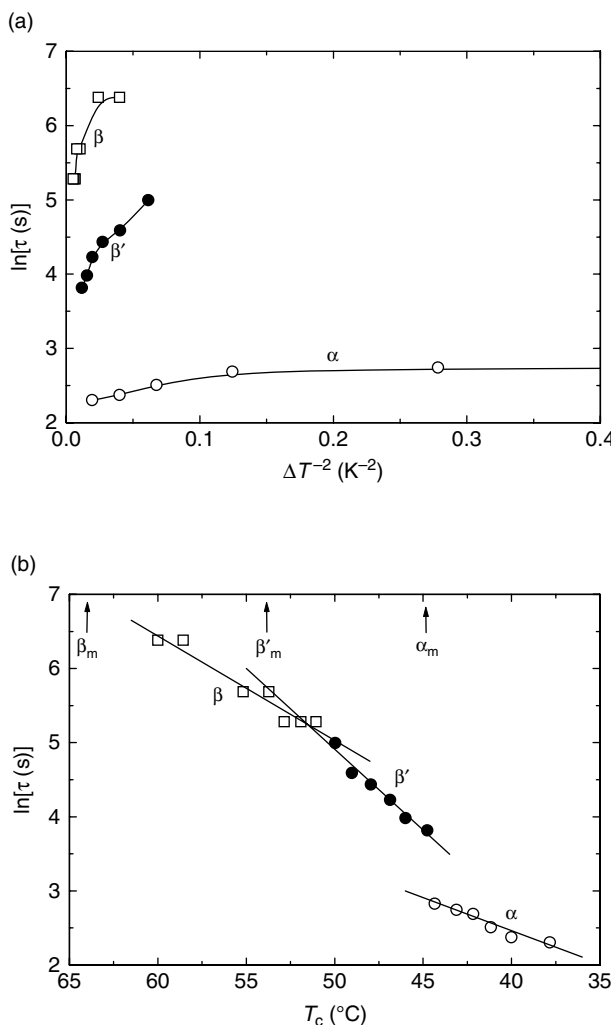


Figure 8.32 Experimental $\tau(T)$ data of Figure 8.31 replotted according to classical nucleation and atomistic theories [Equations (2.65) and (2.66), and Equation (2.67), respectively]. Dependence of (a) $\ln \tau$ on ΔT^{-2} and (b) $\ln \tau$ on T for crystallization of different polymorphs of tripalmitoylglycerol (PPP). In (a), supercooling $\Delta T = T - T_m$

$\Delta T = T - T_m$ was calculated by taking into account their corresponding T_m . The supercooling ΔT is related to supersaturation $\ln S$ by the relation (see Section 2.1):

$$\Delta T = nk_B \ln S / \Delta H_m \quad (8.11)$$

where ΔH_m is the enthalpy of melting, k_B is the Boltzmann constant and the number of molecules n in the formula unit of the fat is unity. As is frequently observed for small-molecule compounds, in the case of PPP also the $\ln \tau(\Delta T^{-2})$ plot is not a single straight line. This implies that a single nucleation mechanism, heterogeneous or homogeneous, cannot explain the $\tau(\Delta T)$ data for different PPP polymorphs (see Figure 8.32a). Instead, the trends of the $\ln \tau(\Delta T^{-2})$ plots suggest that heterogeneous and homogeneous nucleation mechanisms occur in the range of small and high supercooling ΔT , respectively. However, the linear dependences of the $\ln \tau(\Delta T)$ data in the entire range of ΔT for different polymorphs suggest that the atomistic theory of nucleation is applicable. The slopes of the plots are 0.09, 0.22 and 0.14 for the α , β' and β forms, respectively. Since the slope is equal to the number i of molecules in the critical nucleus, the values of $i < 1$ indicate that only a small part of the polymorph molecules is active in their nucleation.

As mentioned above, the mixed-acid triacylglycerol SOS has five polymorphs: α (23.5 °C), γ (35.4 °C), β' (36.5 °C), β_2 (41.0 °C) and β_1 (43.0 °C), where the melting points are given in the parentheses. Experiments revealed that direct chilling of liquid at various crystallization temperatures leads to a reduction in the temperature interval for the occurrence of the α , γ and β' forms, while rapid or slow heating of the crystallized polymorphs leads to a reduction in the temperature range for the occurrence of more stable β' and β_2 forms. This means that polymorphic control of the solidification and subsequent transformation depends strongly on the type of temperature variation and is related to whether the polymorphic transformation is melt-mediated or solid-mediated.

8.3.4 Crystallization of Fats and Oils in Emulsion Droplets

Crystallization of fats and oils in oil-in-water emulsion droplets determines their physical properties such as stability, whippability, rheology and texture (for the literature, see Sakamoto *et al.*, 2004). Consequently, control of fat crystallization is an important process in various technologies where emulsion is subjected to thermal thaw, causing crystallization and melting of the dispersed oil phase. In the food industry, crystallization in O/W emulsions contributes to de-emulsification in whipped cream, freezing of ice-cream and coagulation of oil droplets of mayonnaise in chilled states (Dickinson and McClements, 1995). Crystallization in O/W emulsions is a complex phenomenon influenced by a variety of factors such as emulsion droplet size, type of emulsifiers, droplet–droplet interaction, polymorphism of fat, cooling rate and subsequent temperature variations (Coupland, 2002).

The nucleation-promoting effect of additives is not confined to bulk crystallization alone, but is equally encountered during the crystallization of droplets in emulsion systems. However, the effect is somewhat reduced in emulsion systems because the nucleation-promoting particles are distributed into many droplets. Consequently, the effect of additives on the nucleation rate in emulsion systems is expected to be lower than that in bulk systems. The nucleation-promoting effect of additives is associated with

an increase in the crystallization temperature T_c (Kaneko *et al.*, 1999; Awad and Sato, 2001, 2002; Awad *et al.*, 2001; Katsuragi *et al.*, 2001; Sakamoto *et al.*, 2004). In these studies, the effect of the following additives was investigated: (a) various polyglycerol fatty acid esters (PGEs), synthesized by reaction between polyglycerol and fatty acids (palmitic, stearic and behenic acids) at an acid/polyglycerol molar ratio of 3, 6, 9 and 12, (b) sucrose fatty acid esters, also called sucrose oligoesters (SOEs), synthesized by reactions of polar sucrose molecules with fatty acid moieties of palmitic stearic, lauric, oleic acids (referred to as P-170, S-170, L-195 and O-170), and (c) diacylglycerols (DAGs) having different fatty acid moieties.

As an example, Figure 8.33 illustrates the dependence of crystallization temperature T_c in *n*-hexadecane–water emulsions on the concentration of four sucrose oligoester additives: P-170, S-170, L-195 and O-170 (see above). Among these additives, the greatest effect is observed for S-170 and P-170. The addition of S-170 and P-170 in fact shows similar profiles of increasing T_c to *n*-hexadecane and is characterized by two stages. The first stage involves an increase in T_c from about 2 to 10 °C up to an additive concentration of about 0.3 wt%, and a subsequent increase up to about 13 °C in the concentration range between 0.5 and 0.8 wt%. Probably similar two-stage processes are also followed in the case of L-195, but O-170 has no detectable effect on the T_c of *n*-hexadecane. Similar trends were found in the crystallization of emulsions of (a) palm oil mid-fraction in the presence of polyglycerol fatty acid esters (Sakamoto *et al.*, 2004) and sucrose oligoesters P-170 and S-170 (Awad and Sato, 2001), (b) *n*-hexadecane in the presence of diacylglycerols (Awad *et al.*, 2001), and (c) palm kernel oil in the presence of sucrose oligoesters P-170 and S-170 (Awad and Sato, 2002).

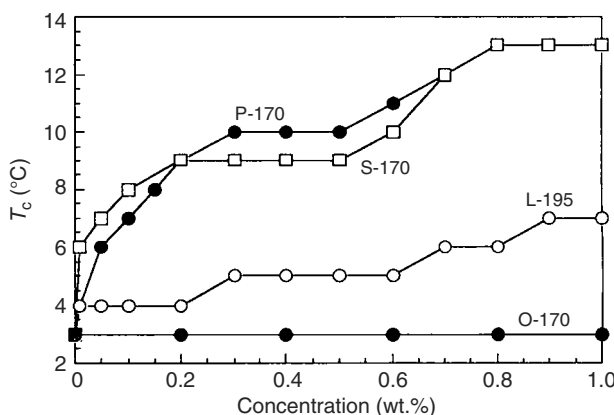


Figure 8.33 Dependence of crystallization temperature T_c in *n*-hexadecane–water emulsions on the concentration of different additives. Adapted from T. Katsuragi, N. Kaneko, and K. Sato. Colloids Surf. B **20**, 229. Copyright (2001), with permission from Elsevier

The above observations are associated with the adsorption of additive molecules at the oil–water interface of the emulsion system and the formation of a reversed micelle phase in the system (Katsuragi *et al.*, 2001; Sakamoto *et al.*, 2004). This is illustrated in

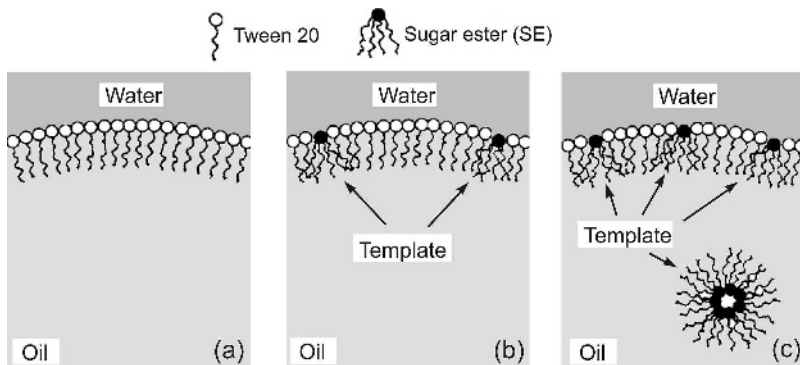


Figure 8.34 Model of interface heterogeneous nucleation in O/W emulsions containing different concentrations of SOE additives: (a) no additive, (b) low SOE concentration, and (c) high SOE concentrations. Adapted from T. Katsuragi, N. Kaneko, and K. Sato. *Colloids Surf. B* **20**, 229. Copyright (2001), with permission from Elsevier

Figure 8.34. In the absence of additive, the oil–water interface is covered with Tween 20 (Figure 8.34a). With the addition of the additive, the additive molecules rupture the Tween 20 layer and are adsorbed at the oil–water interface (Figure 8.34b). Due to the repulsive interaction between the oils and the additive units, the additive molecules, although highly hydrophobic, are not solubilized in the oil phase. Thus, when the O/W emulsion is cooled, additive molecules adsorbed at the interface are crystallized due to their higher melting point. These crystallized fatty acid chains of the adsorbed additive molecules form a template for heterogeneous nucleation of the oil phase at the surface of droplets. With an increase in the additive concentration, the oil–water interface becomes saturated with the adsorbed additive molecules and the excess additive molecules form inverse micelles (Figure 8.34c). The solidified chains in the inverse micelles during the cooling process also act as templates for heterogeneous nucleation in the oil phase. Thus, the initial increase in T_c at lower additive concentration is due to heterogeneous nucleation at the template film formed at the oil–water interface, while the subsequent increase in T_c is caused by nucleation due to inverse micelles in the bulk oil phase.

The above investigations demonstrated that additives having a short chain length of the fatty acid moieties do not accelerate the nucleation of fatty oil crystals in O/W emulsion systems, whereas those with a long chain length of the fatty acid moieties accelerate nucleation. This means that heterogeneous nucleation in O/W emulsion systems is associated with the freezing of the long-chain fatty acid molecules of the additives. The longer the chain length of the additive molecule, the higher is the nucleation-promoting effect of the additive. The temperature of chain crystallization of saturated and unsaturated fatty acid moieties increases and decreases, respectively, with increasing chain length (see Figure 8.22). Therefore, additives such as S-170, P-170 and fully esterified polyglycerol fatty acid esters (PGEs) show a profound increase in T_c , whereas additives such as L-195, O-170 and partially esterified PGEs show an insignificant change in T_c .

Additive particles present in O/W emulsion droplets not only catalyze nucleation in the droplets, but also lead to the crystallization of structures which are usually not observed during bulk crystallization at room temperature. For example, even-carbon *n*-alkanes with

$n < 26$ always crystallize in a triclinic structure (Figure 8.35a) but, depending on the temperature, odd-carbon n -alkanes crystallize in an orthorhombic or pseudo-hexagonal structure (Figure 8.35b); see also Section 8.2.2. However, using synchrotron radiation X-ray diffraction of small-angle and wide-angle areas combined with differential scanning calorimetry, Ueno *et al.* (2003) reported that, when certain additives, such as sucrose palmitic acid ester (P-170), decaglycerin decastearate (DAS-750), and dibehenoylglycerol (DB), are mixed with the emulsion droplets, even n -alkanes nucleate into pseudo-hexagonal and orthorhombic structures, a behavior similar to that of odd-carbon n -alkanes. These structures are crystallized at relatively high supercooling for C_{16} , C_{18} , C_{20} , and C_{22} emulsions containing additives. In a review of the kinetics of liquid–solid transformations in emulsion droplets, Sato (2004) discussed these results. The mechanism of these phase transformations are summarized below.

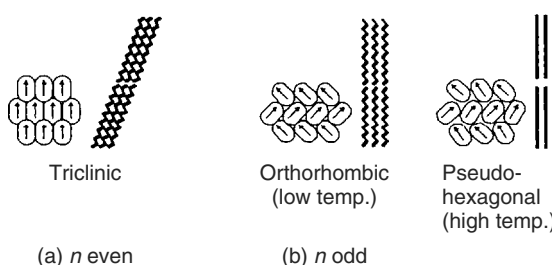


Figure 8.35 Structure of polymorphs of even- and odd-carbon n -alkanes. Reproduced from S. Ueno, Y. Hamada, and K. Sato. Cryst. Growth Des. 3, 935. Copyright (2003), with permission from American Chemical Society

Figure 8.36a shows the temperatures of melting (T_m), crystallization (T_c), and transformation (T_t) for different polymorphs observed in the emulsion droplets of even-carbon n -alkanes without and with the additive DAS-750, and for odd-carbon n -alkanes in the absence of the additive. The temperature T_t refers to transformation from orthorhombic to pseudo-hexagonal polymorphs in the crystals of odd-carbon n -alkanes, and in the additive-induced crystals of even-carbon n -alkanes.

It may be noted from Figure 8.36a that even-carbon n -alkanes crystallize in the triclinic structure in both pure and additive-containing emulsion droplets, but the additive induces the crystallization of the pseudo-hexagonal form. The values of T_m and T_t of all crystalline forms increase with increase in the carbon number n of the alkanes. This is due to the fact that the latent heats of melting and transformation of the n -alkanes increase with increasing chain length. However, the important result is that the values of T_m of the pseudo-hexagonal forms are somewhat lower than or roughly the same as those of the triclinic forms, although crystallization of the pseudo-hexagonal forms occurs at higher temperatures than that of the triclinic forms. For $n < 22$, this trend of the melting points T_m of odd- and even-carbon n -alkanes is similar to that shown by fatty acids (see Figure 8.22).

The above results mean that the additive-induced pseudo-hexagonal forms of the even-carbon n -alkanes are thermodynamically less stable than the triclinic forms, while

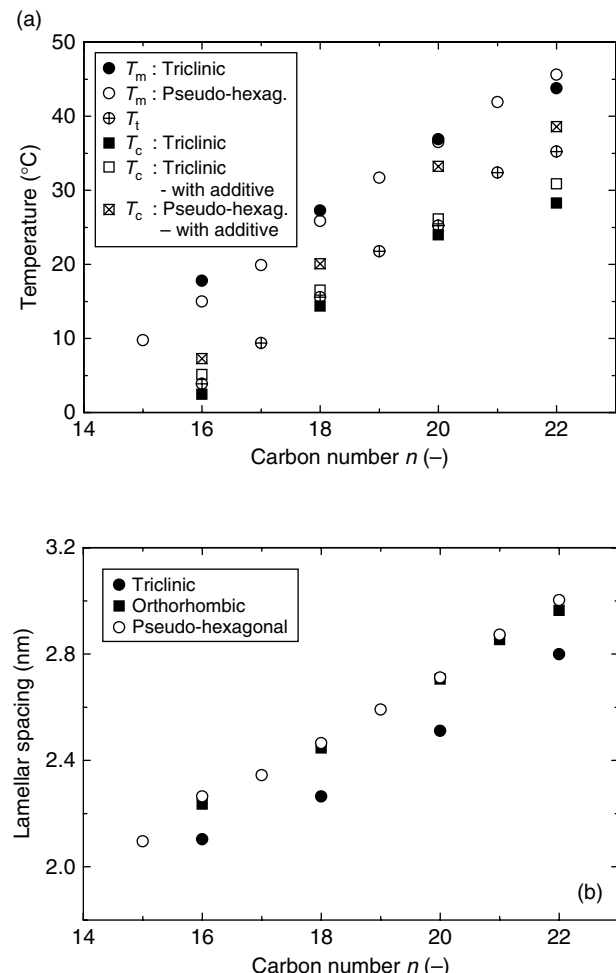


Figure 8.36 (a) Temperatures of melting (T_m), crystallization (T_c), and transformation (T_t) from pseudo-hexagonal to orthorhombic form, and (b) lamellar spacing of different forms of *n*-alkanes in the presence and absence of additive. Reproduced from S. Ueno, Y. Hamada, and K. Sato. Cryst. Growth Des. 3, 935. Copyright (2003), with permission from American Chemical Society

the nucleation rate of the former form is higher than that of the latter. The aliphatic chain axis of the pseudo-hexagonal and orthorhombic forms of odd-carbon *n*-alkanes is perpendicular to the lamellar plane. Therefore, the lamellar spacing of odd- and even-carbon *n*-alkanes increases with increasing length of the carbon chain (Figure 8.36b). This suggests that the additive with a high melting point contained in the O/W emulsion droplets of even-carbon *n*-alkanes leads to the crystallization of new metastable polymorphs at a higher nucleation rate than the basic triclinic polymorph.

The results of acceleration of nucleation and formation of metastable polymorphs of even-carbon *n*-alkanes may be explained in terms of their nucleation rates by considering the Gibbs free energy difference ΔG between the liquid and the solid phases and the activation energy for nucleation ΔG_{3D}^* , as illustrated in the inset of Figure 8.37. Since the melting point T_m of the pseudo-hexagonal form is lower than that of the triclinic form, it can be argued that ΔG for the former is lower than that of the latter. This means that the nucleation rate of the pseudo-hexagonal polymorph is higher than that of the triclinic form. The higher nucleation rate of the pseudo-hexagonal form means that ΔG_{3D}^* is lower for the pseudo-hexagonal form than that for the triclinic form. A lower value of ΔG_{3D}^* implies that the interfacial energy γ for the pseudo-hexagonal form is lower than that of the triclinic form [see Equation (2.17)].

A lower value of the interfacial energy γ for the pseudo-hexagonal form than that of the triclinic form suggests that attractive interactions occur between the crystalline *n*-alkane molecules and an additive film or additive crystals at the interface. These interactions can result due to the freezing of aliphatic chains of the high melting-point additive molecules that are adsorbed on the oil–water interface due to their amphiphilic character. Figure 8.37 shows the oil–water interface delineated by polar head groups of additive molecules as dark ovals and aliphatic chains of the additive and *n*-alkane as zig-zag lines. Cooling of the droplet results in the formation of a template film composed of an array of additive particles crystallized at the oil–water interface with their aliphatic chains aligned normally to their lamellar plane. Crystallization of the additive template at

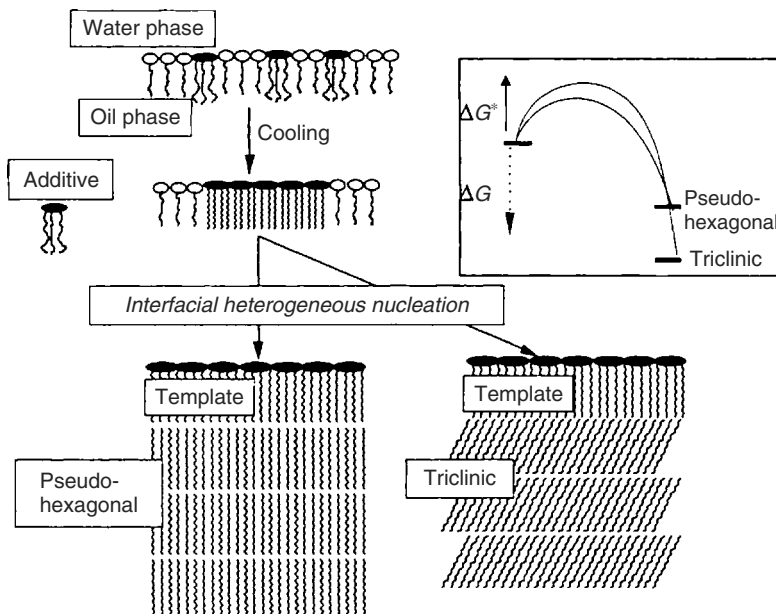


Figure 8.37 Schematic illustration of interfacial heterogeneous nucleation of pseudo-hexagonal and triclinic forms of even-carbon *n*-alkanes with additives. Reproduced from S. Ueno, Y. Hamada, and K. Sato. Cryst. Growth Des. **3**, 935. Copyright (2003), with permission from American Chemical Society

the oil–water interface occurs because the temperatures in the experiments are below the melting point of the additive. This template results in a larger decrease in γ in contact with the pseudo-hexagonal form than that for the triclinic form, which contains tightly and obliquely arranged aliphatic chains (see Figure 8.35).

8.3.5 Number of Nucleation Centers and Overall Crystallization in Emulsion Systems

Crystallization in emulsion systems occurs by nucleation and growth of crystallites in the emulsion droplets, each droplet behaving as a closed system. Since emulsion droplets usually contain nanoparticles and/or impurity particles, heterogeneous nucleation dominates in emulsion systems. Depending on the size of emulsion droplet, crystallization in the droplets occurs by a mononuclear or polynuclear mechanism involving the formation of one or many nuclei in the droplet, respectively. Since the probability of inclusion of nanoparticles and/or impurity particles increases with the size of droplets, mononuclear and polynuclear mechanisms can occur in droplets of relatively small and large sizes, respectively. Moreover, when crystallization occurs by a polynuclear mechanism in a closed system, many nuclei may be formed by instantaneous and progressive nucleation mechanisms.

Emulsions are usually polydisperse, consisting of droplets of various sizes lying in a particular range. Therefore, overall crystallization in a polydisperse emulsion system involves both mononuclear and polynuclear mechanisms, the former being dominant in small droplets and the latter in large droplets.

Theoretical expressions for the number of crystallizing droplets N and the fraction y of crystallized volume Φ of the droplets as functions of time t have been derived on the assumption that emulsion droplets have the same size (i.e. monodisperse emulsions). Since polydisperse emulsions are composed of some size distribution of droplets, this assumption holds for a narrow droplet size distribution. For a wide distribution of droplet size in polydisperse emulsion systems, Kashchiev *et al.* (1998) derived expressions relating N and Φ with crystallization time t and analyzed the experimental data for the change in the ultrasonic velocity during isothermal crystallization of the droplets in palm oil-in-water and *n*-hexadecane-in-water emulsions. This study revealed that crystallization in these emulsion systems occurs by the mononuclear mechanism.

Assuming that the average time required for a nucleation event is much longer than the time required for the droplet to achieve complete crystallization and the nucleation is catalyzed by active sites at the droplet surface or in the bulk volume, the volume of droplets involved in crystallization may be given by (Povey, 2001)

$$\Phi = \Phi_0 [1 - 1/(1 + J_0 V_p t)] \quad (8.12)$$

where Φ_0 is the maximum volume of crystallized droplets, J_0 is the kinetic coefficient for three-dimensional nucleation and is associated with the frequency of attachment of growth units to growth nuclei, and V_p is the volume of the material in the droplet. It should be noted that the fraction y of the crystallized volume of emulsion droplets is simply the ratio of Φ to Φ_0 , i.e. $y = \Phi/\Phi_0$.

The maximum volume of crystallized droplets Φ_0 is given by

$$\Phi_0 = \Phi'_0 [1 - \exp(-V_p N_c)] \quad (8.13)$$

where Φ'_0 is the total volume for crystallization and N_c is the number density of active centers in a droplet. Since the droplets in polydisperse emulsion systems are of different dimensions and the number of catalytic impurities varies according to the droplet size, the kinetic coefficient J_0 (and the corresponding nucleation rate J) depends on droplet size D , implying that the time dependence of the number N of droplets of various sizes cannot be described by a single expression. Therefore, Equation (8.12) may be considered to be a crude approximation. The values of the constants J_0 and N_c are calculated from the experimental $\Phi(t)$ data.

For polydisperse emulsion systems containing droplets of different diameters, following the ‘gamma distribution’, the expressions for the time dependence of N and Φ may be given by (Kashchiev *et al.*, 1998)

$$N(t) = N_0[1 - 1/(1+t/A)^p] \quad (8.14)$$

$$\Phi(t) = \Phi_0[1 - 1/(1+t/A)^b] \quad (8.15)$$

where N_0 is the total number of crystallized droplets when $t = \infty$ and Φ_0 is the corresponding crystallized volume, $A = a/3J_m$ (a is a numerical parameter describing the width of the droplet size distribution and J_m is the rate of nucleation in a droplet of diameter D_m), and for nucleation in the droplet volumes the exponents $p = 4/3$ and $b = 7/3$. According to Equations (8.12), (8.13) and (8.15), larger droplets are expected to crystallize first.

Not all droplets in an emulsion system contain active nucleation centers. Therefore, the number of active nucleation centers in a droplet is exhausted progressively during its crystallization. Consequently, the total number of crystallizing droplets N_0 in an emulsion system cannot exceed the total number N'_0 of droplets present in the system. The maximum number density N_0 of crystallized droplets is determined by the concentration and activity of nucleation centers in the droplets and is described by an expression similar to Equation (8.14).

We assume that (1) nucleation of crystallites in each droplet occurs by the polynuclear mechanism, (2) all active nucleation centers have the same activity, and (3) the nucleation rate in the drops is independent of size. Then, in the case of non-stationary nucleation, for $\tau > 4t$ the number of droplets crystallized in the emulsion per unit volume (i.e. number density of crystallized droplets) can be written in the approximate form (see Section 2.4)

$$N(t) = N_0\{1 - \exp[-(t/\tau)^m]\} \quad (8.16)$$

where the constant $m > 3/2$. In the case of stationary nucleation, the exponent $m = 1$. For progressive stationary nucleation, following Kashchiev (2000), the crystallized volume in overall crystallization is given by

$$\Phi(t) = \Phi_0\{1 - \exp[-(t/\Theta)^q]\} \quad (8.17)$$

where Φ_0 is the total volume for crystallization, Θ is a time constant [see Equation (2.51)] and the exponent q has a value between 1 and 4 [see Equation (2.52)].

It should be noted that, for $b = 1$, Equation (8.15) reduces to Equation (8.12) and the constant $1/J_0 V_p = A$. According to Equations (8.12), (8.13) and (8.15), for small t the

plots of the number N of crystallized droplets and the volume Φ of crystallized droplets increase linearly with increasing crystallization period t , and pass through the origin. In contrast, according to Equations (8.16) and (8.17) the plots of N and Φ against t show an exponential increase with t even for small t . However, the time constants τ and Θ are roughly equal to $1/J_0 V_p = A$.

The validity of theoretical expressions for crystallization in emulsion droplets can be verified, provided that reliable $N(t)$ and $\Phi(t)$ data are obtained experimentally (Sangwal *et al.*, 2007). For this purpose, *in situ* recording of crystallization of emulsion droplets in a specially designed cell at a predefined temperature can be used. Figure 8.38 illustrates a typical example of the sequence of images of crystallization in emulsion droplets of

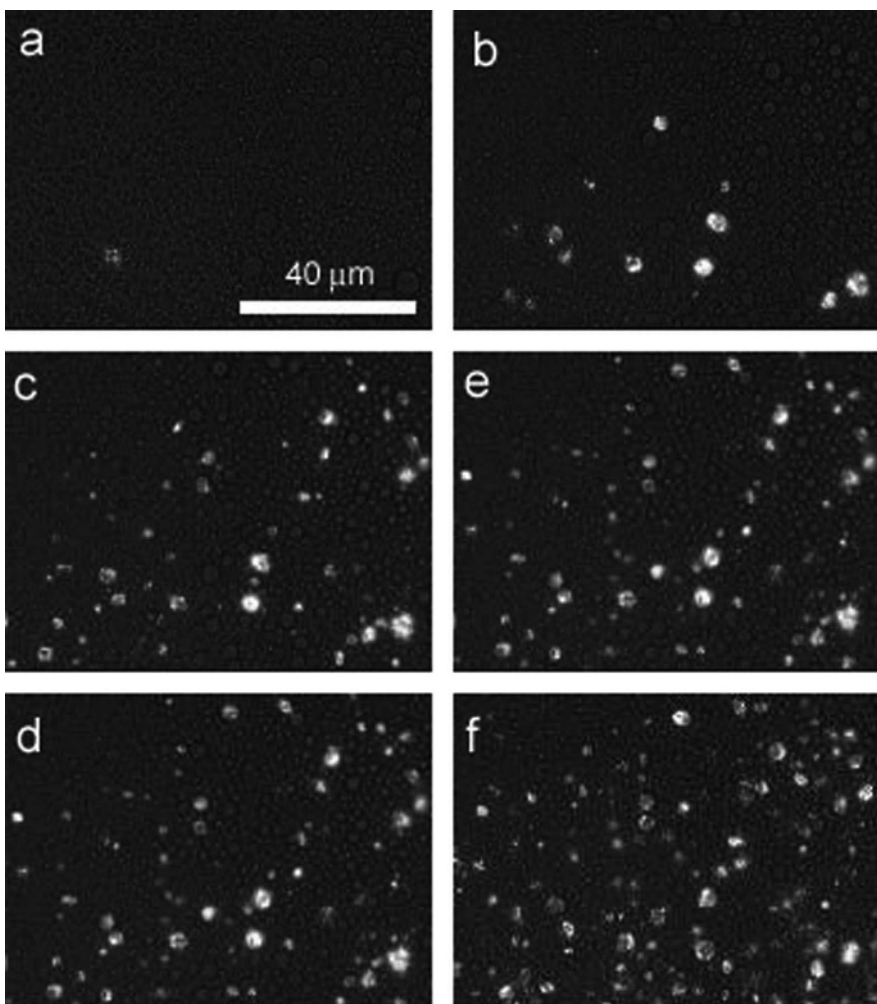


Figure 8.38 Example of the sequence of images of crystallization in emulsion droplets of mean diameter $1.73 \mu\text{m}$ observed after different durations: (a) 10, (b) 30, (c) 100, (d) 160, (e) 240 and (f) 375 s. In the inset, 1 mm droplet dimension = $2.75 \mu\text{m}$. After Sangwal *et al.* (2007)

mean diameter $1.73 \mu\text{m}$ observed after different durations. The oil-in-water emulsion was composed of 20% *n*-hexadecane, 78% water and 2% Tween 20 as emulsifier (by volume), and supercooling $\Delta T = 22.7^\circ\text{C}$.

Examination of crystallized droplets in emulsion systems reveals that (a) the initiation of crystallization occurs in droplets of various sizes and large droplets are not always preferential, and (b) different active centers in the volume of a large-sized droplet produce crystallites progressively (see Figure 8.38). These observations suggest that nucleation in our emulsion systems occurs by the progressive polynuclear mechanism.

From the printed images, the crystallized droplets in the total image area were counted in different diameter groups as a function of time, and from these data the total of crystallization volume Φ was determined as the sum of volumes of all droplets according to the relation

$$\Phi = \frac{\pi}{6} \sum_{i=2}^7 N_i D_i^3 \quad (8.18)$$

where N_i is the number of emulsion droplets of diameter D_i . When calculating the total volume, the mean diameter of droplets in each diameter group was taken into account. It was found that (a) the number of crystallized droplets decreases with increase in their diameter, the lowest number being for the largest droplets, and (b) the time dependence of droplets in different diameter groups shows similar trends. Since the volume Φ of droplets is proportional to D^3 , this observation suggests that the smallest droplets can be omitted in the calculation of total crystallized volume. However, the omission of the smallest droplets gives a much lower value for the maximum number N_0 of crystallized droplets.

Figures 8.39 and 8.40 show the dependences of N and Φ on t for cycle I of one of the isothermal crystallization experiments for an O/W emulsion sample of average diameter $2.18 \mu\text{m}$, respectively. The curves in Figure 8.39 were drawn according to Equations (8.14) and (8.16) and in Figure 8.40 according to Equations (8.15) and (8.17). The fitting parameters are included in the insets. Curve 1 and curves 2 and 3 in both figures are indicated as ‘exponential’ and ‘inverse’, respectively. Regardless of the chosen values of the fitting parameters N_0 or Φ_0 and A to describe the experimental $N(t)$ and $\Phi(t)$ data, Equations (8.14) and (8.15) are less satisfactory than Equations (8.16) and (8.17). The main discrepancy occurs at low t . Equations (8.16) and (8.17) describe the data perfectly well for low and high t values. This analysis of the experimental $N(t)$ and $\Phi(t)$ data on crystallization kinetics for the O/W emulsion is consistent with the progressive polynuclear mechanism following from the examination of sequence of images of crystallized droplets in Figure 8.38.

In Figure 8.39, one can distinguish three time intervals in which the $N(t)$ plots exhibit well-defined differences. The first period, lasting up to about 100 s, shows an $N(t)$ dependence passing through the origin, and is characteristic of stationary nucleation. In the second period, lying between about 100 and 400 s, the number of nuclei shows a rapid increase with increasing time. The third period, lasting between about 400 and 700 s, is characterized by a constant value of the maximum number N_0 of nuclei. In some cases, a fourth period, beyond about 700 s, again exhibiting a small increase in the number of active centers with time, was observed. The first three periods are connected with

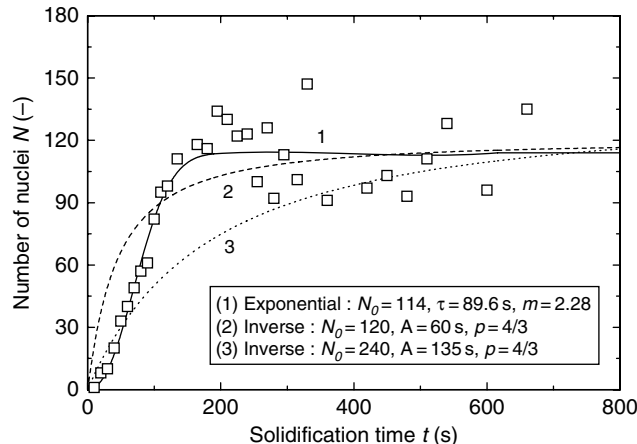


Figure 8.39 Dependence of total number N of crystallized droplets on the crystallization period t for an O/W emulsion sample of average diameter $2.18\text{ }\mu\text{m}$; Curves: (1) Equation (8.16) and (2, 3) Equation (8.14). The fitting parameters are given in the insets. 1 mm droplet dimension = $2.75\text{ }\mu\text{m}$. After Sangwal et al. (2007)

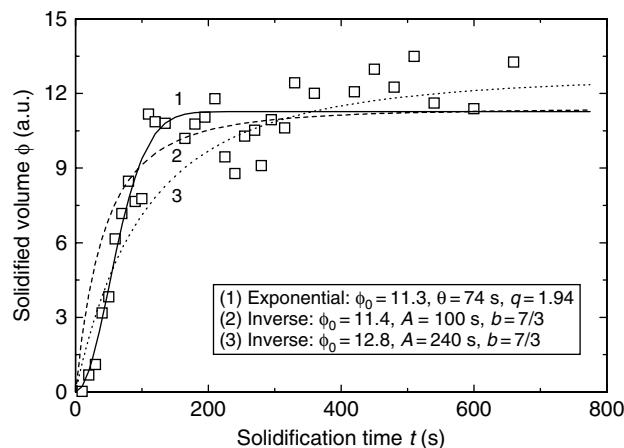


Figure 8.40 Dependence of total volume Φ of crystallized droplets on the crystallization period t for an O/W emulsion sample of average diameter $2.18\text{ }\mu\text{m}$; Curves: (1) Equation (8.17) and (2, 3) Equation (8.15). The fitting parameters are given in the insets. 1 a.u. of volume $\approx 2 \times 10^{-17}\text{ m}^3$. After Sangwal et al. (2007)

nucleation and growth processes, whereas the last period is connected mainly with the growth of nuclei in the emulsion droplets. Due to the geometric shapes of the growing nuclei in spherical emulsion droplets, their growth results in relatively irregular shapes of the droplets and an increase in their dimensions.

References

- Awad, T., and K. Sato (2001). *J. Am. Oil Chem. Soc.* **78**, 837.
- Awad, T., and K. Sato (2002). *Colloids Surf. B* **25**, 45.
- Awad, T., Y. Hamada, and K. Sato (2001). *Eur. J. Lipid Sci. Technol.* **103**, 735.
- Barnwal, B.K., and M.P. Sharma (2005). *Renew. Sustain. Energy Rev.* **9**, 363.
- Bosch, H.W., S.D. Srećo, and E. Matijević (2004). *Colloids Surf. A* **250**, 43.
- Cao, W., H. Han, and J. Zhang (2005). *Fuel* **84**, 347.
- Carraretto, C., A. Macor, A. Mirandola, A. Stoppato, and S. Tonon (2004). *Energy* **29**, 2195.
- Chang, R.K., and J.R. Robinson (1990). In: H.A. Liberman, L. Lachman, and J.B. Schwartz (Eds.), *Particle Coating Methods – Pharmaceutical Dosage Forms: Tablets*, 2nd ed., Vol. 3, Marcel Dekker, New York, p. 199.
- Chew, C.M., R.I. Ristić, R.D. Dennehy, and J.J. De Yoreo (2004). *Cryst. Growth Des.* **4**, 1045.
- Chow, A.H.L., P.K.K. Chow, W. Zhongshan, and D.J.W. Grant (1985). *Int. J. Pharm.* **24**, 239.
- Claudy, P., J.M. Letoffe, B. Bonardi, D. Vassilakis, and B. Damin (1993). *Fuel* **72**, 821.
- Coupland, J.N. (2002). *Curr. Opin. Colloid Interface Sci.* **7**, 445.
- Crowder, T.M., J.A. Rosati, J.D. Schroeter, A.J. Hickey, and T.B. Martonen (2002). *Pharm. Res.* **19**, 239.
- Demirbas, A. (2002). *Energy Convers. Manage.* **43**, 2349.
- Diasakov, M., A. Loulodi, and N. Papayannakos (1998). *Fuel* **77**, 1297.
- Dickinson, E., and D.J. McClements (1995). *Advances in Food Colloids*, Chapman and Hall, London.
- Duddu, S.P., S.A. Sisk, Y.H. Walter, T.E. Tarara, K.R. Trimble, A.R. Clark, M.A. Eldon, R.C. Elton, M. Pickford, P.H. Hirst, S.P. Newman, and J.G. Weers (2002). *Pharm. Res.* **19**, 689.
- Dunn, R.O. (2002). *J. Am. Oil Chem. Soc.* **79**, 915.
- Dunn, R.O., M.W. Shockley, and M.O. Bagby (1996). *J. Am. Oil Chem. Soc.* **73**, 1719.
- Du Plessis, L.M., J.B.M. de Villiers, and W.H. van der Walt (1985). *J. Am. Oil Chem. Soc.* **62**, 748.
- Edwards, D.A., J. Hanes, G. Caponetti, J. Hrkach, A. Ben-Jebria, M.L. Eskew, J. Mintzes, D. Deaver, N. Lotan, and R. Langer (1997). *Science* **276**, 1868.
- El-Gamal, I.M., and A.M. Al-Sabagh (1996). *Fuel* **75**, 743.
- El-Gamal, I.M., T.T. Khidr, and F.M. Ghuiba (1998). *Fuel* **77**, 375.
- Femi-Oyewo, M.N., and M.S. Spring (1994). *Int. J. Pharm.* **112**, 17.
- Foubert, I., B. Vanhoutte, and K. Dewettinck (2004). *Eur. J. Lipid Sci. Technol.* **106**, 531.
- Foubert, I., K. Dewettinck, G. Janssen, and P.A. Vanrolleghem (2006). *J. Food Eng.* **75**, 551.
- Garti, N., and J. Yano (2001). In: N. Garti and K. Sato (Eds.), *Crystallization Processes in Fats and Lipid Systems*, Marcel Dekker, New York, Chap. 6, p. 211.
- Gomez, M.E.G., R. Howard-Hildige, J.J. Leahy, and B. Rice (2002). *Fuel* **81**, 33.
- Hendriksen, B.A., and D.J.W. Grant (1995). *J. Cryst. Growth* **156**, 252.
- Hendriksen, B.A., D.J.W. Grant, P. Meenan, and D.A. Green (1998). *J. Cryst. Growth* **183**, 629.
- Herrera, M.L., M. De Léon Gatti, and R.W. Hartel (1999). *Food Res. Int.* **32**, 289.
- Joguet, L., and E. Matijević (2002). *J. Colloid Interface Sci.* **250**, 503.
- Joguet, L., I. Sondi, and E. Matijević (2002). *J. Colloid. Interface Sci.* **251**, 284.
- Kaerger, J.S., and R. Price (2004). *Pharm. Res.* **21**, 372.
- Kaneko, N., T. Horie, S. Ueno, J. Yano, T. Katsuragi, and K. Sato (1999). *J. Cryst. Growth* **197**, 263.
- Kashchiev, D. (2000). *Nucleation: Basic Theory and Applications*, Butterworth-Heinemann, Oxford.
- Kashchiev, D., N. Kaneko, and K. Sato (1998). *J. Colloid Interface Sci.* **208**, 167.
- Katsuragi, T., N. Kaneko, and K. Sato (2001). *Colloids Surf. B* **20**, 229.
- Kerschbaum, S., and G. Rinke (2004). *Fuel* **83**, 287.

- Knothe, G. (2005). *Fuel Process. Technol.* **86**, 1059.
- Lang, X., A.K. Dalal, N.N. Bakhshi, M.J. Reaney, and P.B. Hertz (2001). *Bioresource Technol.* **80**, 53.
- Lee, I., L.A. Johnson, and E.G. Hammond (1995). *J. Am. Oil Chem. Soc.* **72**, 433, 1155.
- Lee, I., L.A. Johnson, and E.G. Hammond (1996). *J. Am. Oil Chem. Soc.* **73**, 631.
- Létoffe, J.-M., P. Claudy, D. Vassilakis, and B. Damin (1995). *Fuel* **74**, 1830.
- Lide, D.R. (Ed.) (1996/1997). *Handbook of Chemistry and Physics*, 77th ed., CRC Press, Boca Raton, FL.
- Ma, F., and M.A. Hanna (1999). *Bioresource Technol.* **70**, 1.
- Machado, A.L.C., E.F. Lucas, and G. Gonzalez (2001). *J. Pet. Sci. Eng.* **32**, 159.
- Madras, G., C. Kolluru, and R. Kumar (2004). *Fuel* **83**, 2029.
- Marie, E., Y. Chevalier, F. Eydoux, L. Germanaud, and P. Flores (2005). *J. Colloid Interface Sci.* **290**, 406.
- Matijević, E., and S. Škapin (2004). *J. Colloid Interface Sci.* **272**, 90.
- Mittelbach, M., and S. Schober (2003). *J. Am. Oil Chem. Soc.* **80**, 817.
- Owen, K. (1989). *Gasoline and Diesel Fuel Additives*, John Wiley & Sons, Inc., New York.
- Owen, K., and T. Coley (1995). *Automotive Fuels Reference Book*, 2nd ed., SAE, Warrendale, PA.
- Petinelli, J.C. (1979). *Rev. Inst. Fr. Pet.* **34**, 791–811.
- Pioch, D., P. Lazano, M.C. Rasoanantoandro, J. Graille, P. Geneste, and A. Guida (1993). *Oleagineux* **48**, 289.
- Povey, M.J.W. (2001). In: N. Garti and K. Sato (Eds.), *Crystallization Processes in Fats and Lipid Systems*, Marcel Dekker, New York, Chap. 7, p. 251.
- Pozarnsky, G.A., and E. Matijević (1997). *Colloids Surf. A* **125**, 47.
- Prankl, H. (2002). *Eur. J. Lipid Sci. Technol.* **104**, 371.
- Prasad, K.V.R., R.I. Ristić, D.B. Sheen, and J.N. Sherwood (2001). *Int. J. Pharm.* **215**, 29.
- Rasenack, N., and B.W. Müller (2002). *Pharm. Res.* **19**, 1894.
- Rätsch, M., and M. Gebauer (1989). *Erdöl Kohle* **42**, 238.
- Ristić, R.I., S. Finnie, D.B. Sheen, and J.N. Sherwood (2001). *J. Chem. Phys. B* **105**, 9057.
- Rogers, T.L., A.C. Nelsen, M. Sarkari, T.J. Young, K.P. Johnston, and R.O. Williams (2003). *Pharm. Res.* **20**, 485.
- Ruch, F., and E. Matijević (2000). *J. Colloid Interface Sci.* **229**, 207.
- Saka, S., and D. Kusdiana (2001). *Fuel* **80**, 225.
- Sakamoto, M., K. Maruo, J. Kuriyama, M. Kouno, S. Ueno, and K. Sato (2003). *J. Oleo Sci.* **52**, 639.
- Sakamoto, M., A. Ohba, J. Kuriyama, K. Maruo, S. Ueno, and K. Sato (2004). *Colloids Surf. B* **37**, 27.
- Sangwal, K. (1998). *Prog. Cryst. Growth Charact. Mater.* **36**, 163.
- Sangwal, K., and R. Rodriguez-Clemente (1991). *Surface Morphology of Crystalline Solids*, Trans Tech, Zurich.
- Sangwal, K., S. Arima, K. Sato, S. Ueno, and Y. Takata (2007). Unpublished results.
- Sato, K. (1996). In: F. Padley (Ed.), *Advances in Applied Lipid Research*, Jai Press, Greenwich, CT, p. 213.
- Sato, K. (2001). *Chem. Eng. Sci.* **56**, 2255.
- Sato, K. (2004). In: X.Y. Liu, and J.J. De Yoreo (Eds.), *Nanoscale Structure and Assembly at Solid–Fluid Interfaces, Vol. II: Assembly at Hybrid and Biological Systems*, Kluwer, Boston, Chap. 3, p. 83.
- Sato, K., and T. Kuroda (1987). *J. Am. Oil Chem. Soc.* **64**, 124.
- Sato, K., S. Ueno, and J. Yano (1999). *Prog. Lipid Res.* **38**, 91.
- Schober, S., and M. Mittelbach (2004). *Eur. J. Lipid Sci. Technol.* **106**, 382.
- Shekunov, B.Y., P. Chattopadhyay, H. Tong, and H.L. Albert (2007). *Pharm. Res.* **24**, 203.
- Siew, W.L., and W.L. Ng (1999). *J. Sci. Food Agric.* **79**, 722.

- Smith, P.R., D.J. Cebula, and M.J.W. Povey (1994). *J. Am. Oil Chem. Soc.* **71**, 1367.
- Soriano, N.U., Jr, V.P. Migo, and M. Matsumura (2003). *J. Am. Oil Chem. Soc.* **80**, 997.
- Soriano, N.U., Jr, V.P. Migo, and M. Matsumura (2006). *Fuel* **85**, 25.
- Soriano, N.U., Jr, V.P. Migo, K. Sato, and M. Matsumura (2005). *Eur. J. Lipid Sci. Technol.* **107**, 689.
- Srivastava, S.P., R.S. Tandon, P.S. Verma, D.C. Pandey, and S.K. Goyal (1995). *Fuel* **74**, 928.
- Ueno, S., Y. Hamada, and K. Sato (2003). *Cryst. Growth Des.* **3**, 935.
- Wikipedia (2006). <http://en.wikipedia.org/wiki/petroleum>.
- Wurster, D. (1990). In: H.A. Liberman, L. Lachman, and J.B. Schwartz (Eds.), *Particle Coating Method – Pharmaceutical Dosage Forms: Tablets*, 2nd ed., Vol. 3, Marcel Dekker, New York p. 161.
- York, P. (1999). *Pharm. Sci. Technol.* **2**, 430.
- Zhang, J., C. Wu, W. Li, Y. Wang, and Z. Han (2003). *Fuel* **82**, 1419.

9

Incorporation of Impurities in Crystals

Impurity particles present in a growth medium can induce crystallization by acting as three-dimensional (3D) substrate nuclei which subsequently develop into large polyhedral crystals composed of well-developed faces. The impurities can equally suppress nucleation if some parts of their particles are unfavorable for the aggregation of solute molecules during the formation of stable 3D nuclei in the bulk medium. The impurity particles also change the growth rates of the developing faces of polyhedral crystals by adsorbing on them during growth. Usually, the impurities lead to a reduction in the face growth rates. These effects of impurities on crystallization processes of different types of materials were discussed previously. However, since crystal growth is a statistical process involving the aggregation of growth units into 3D stable nuclei and the incorporation of growth units into growth sites at the crystal–medium interface, impurity particles joined with solute particles and adsorbed on the growing face also have the probability to be captured in the crystal. Therefore, there is an intimate relationship between the effect of impurities on nucleation as well as growth kinetics of crystals and on their incorporation in the crystals because both are the result of interactions between solute and impurity particles.

Phenomena and processes associated with the capture of impurities, inherently present in or intentionally added to the growth medium, in crystallizing solids are, *inter alia*, purification of materials by repeated crystallization from solutions and zone refining in melt growth, coloration of crystals of gemstones and laser materials by different dopants, prediction of depositional and diagenetic environments of carbonate rocks from their impurity content (Rimstidt *et al.*, 1998), and development of geochemical engineering methods to seclude, or at least suppress, the migration of, toxic and/or radioactive elements using carbonate rocks (Rimstidt *et al.*, 1998). Therefore, understanding of the

mechanisms of capture of impurities in crystals has interesting applications in different domains of our everyday life.

The process of capture of impurities in crystals during their growth from the liquid phase is a combined effect of several factors, such as the chemical composition of the liquid phase, relative solubilities of host and impurity phases, interactions between host and impurity molecules, relative dimensions of substituting (impurity) and substituted (host phase) ions/molecules, the similarity in crystallographic structure of the two phases, and crystallization conditions (Chernov, 1984; Kirkova *et al.*, 1996). There is voluminous literature devoted to investigations of the effects of different factors on the capture of impurities in crystals, and this has been reviewed (Brice, 1973; Chernov, 1984; Klug, 1993; Kirkova *et al.*, 1996). The main aim of the present chapter is to review briefly the progress made since 1990 in the area of capture of impurities in crystals, but earlier approaches involving diffusion of impurity particles in the bulk medium and relaxation of captured impurity particles in the surface are also presented for the sake of completeness and an overview on the subject.

9.1 Types of Impurity Incorporation and the Segregation Coefficient

The incorporation of impurity species in a crystal results in the creation of point defects in the otherwise perfect crystal lattice. This is illustrated schematically in Figure 9.1 for the two-dimensional lattice of an element. If the impurity atoms are similar in size and chemical properties of the atoms of the host crystal lattice, the impurity atoms replace the host atoms at the lattice sites, without creating much disturbance and strain in the lattice. If the impurity atoms are chemically similar to those of the host lattice but are much smaller than those of the latter, they enter interstitial sites in the host lattice. However, if the impurity atoms differ substantially in size or chemical properties from those of the host, they can enter the crystal lattice only by distorting the lattice, thereby increasing the total free energy of the system. Consequently, in order to accommodate such impurity atoms, the host lattices attains a lower energy by creating vacancies in the lattice.

The incorporation of impurity ions in ionic crystal lattices occurs in a similar manner, but the entire crystal as whole remains neutral. If the cations or anions are of sizes and charges similar to those of the ions of the crystal, they substitute the host cations or anions. Smaller ions enter the interstitial sites. If the impurity cations or anions differ in charge from that of the host lattice, depending on their size, they not only enter the lattice substitutionally or interstitially but also create vacancies in order to maintain charge neutrality of the crystal. Different sets of point defects resulting from the charge compensation, called color centers, often produce color changes in the crystals.

In an EPR investigation of the incorporation of Cu^{2+} ions in ammonium oxalate monohydrate (AO) single crystals grown from aqueous solutions, it was found (Mielniczek-Brzóska *et al.*, 2000) that Cu^{2+} ions enter the lattice as a substitutional impurity in highly doped crystals (i.e. at high effective segregation coefficient k_{eff}), but Cu^{2+} ions enter the lattice as interstitial and substitutional impurity in crystals with low Cu^{2+} incorporation (i.e. for low k_{eff}). In the former case, Cu^{2+} complexes in the crystals are monomeric. However, in the latter case, they form dimeric systems with oxalate anions as a bridge between them.

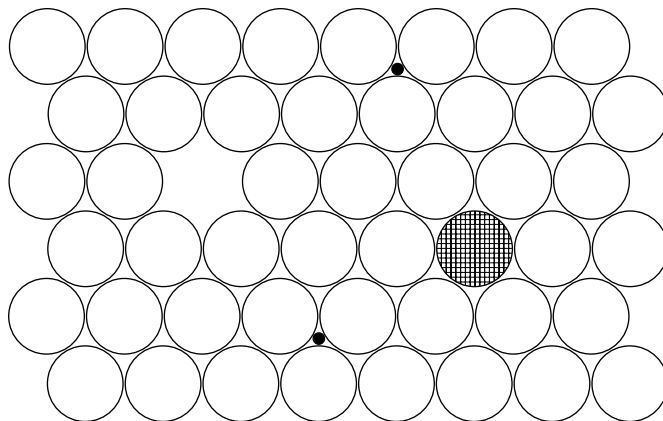


Figure 9.1 Different types of point defects involved during impurity incorporation: vacant site, substituted atom (hatched circle), and interstitial atoms (small black circles)

Incorporation of metal cations (e.g. Co^{2+} , Zn^{2+} , Pb^{2+} , Ba^{2+} , and Mg^{2+}) and complex anions such as SO_4^{2-} and SeO_4^{2-} in calcite has attracted much attention. Using different spectroscopic techniques such as XAFS, it has been shown (Lamble *et al.*, 1997; Reeder *et al.*, 1994, 1998) that trace metal ions substitute in Ca^{2+} ions and form dilute solid solutions, whereas anions substitute in CO_3^{2-} sites. Both cations and anions introduce local distortion.

A recent computer modeling study of the structure of defects (Figure 9.1) introduced in potassium dihydrogenphosphate (KDP) crystal by the incorporation of bi- and trivalent metal (M) ions differing widely in their ionic radii revealed (Rak *et al.*, 2005) the following features:

- (1) M^{3+} ions can occupy interstitial sites, with simultaneous removal of two nearest K^+ ions and one proton.
- (2) M^{2+} ions of ionic radii $r_i > 0.1 \text{ nm}$ substitute K^+ ions with simultaneous K^+ vacancy formation, whereas M^{2+} ions of ionic radii $0.075 \text{ nm} < r_i < 0.1 \text{ nm}$ occupy chains of interstitial sites connected by unoccupied interstitial positions.
- (3) Incorporation of cations distort the crystal structure and introduce local lattice stresses. Trivalent cations create weaker lattice stresses than bivalent cations.

It should be noted that large distortions caused in the crystals by incorporation of impurity species are energetically unfavorable. Consequently, impurities that create large distortions in the lattice of the host phase are captured in insignificant amounts.

An impurity present in the growth medium is usually captured by the growing crystal both in the form of individual atoms, ions, molecules or molecular-size complexes such as dimers and trimers and in the form of colloidal inclusions of one to several micrometer dimensions or macroscopic inclusions. The former and the latter are referred to as *homogeneous* and *heterogeneous* capture of impurities, respectively. Homogeneous capture results in the formation of solid solutions in which the impurity concentration is either equal to or differs from the thermodynamic equilibrium concentration at the growth temperature, and depends on growth kinetics. They are usually called

thermodynamic equilibrium and *nonequilibrium* capture, incorporation or segregation of impurities. Thermodynamic equilibrium capture of impurities is determined by factors such as the chemical composition of the liquid phase, relative solubilities of host impurity phases, interactions between host and impurity molecules, relative dimensions of substituting (impurity) and substituted (host phase) ions/molecules, the similarity in crystallographic structure of the two phases, whereas nonequilibrium capture is governed by crystallization conditions. By its very nature, heterogeneous impurity capture is always nonequilibrium.

The concentration and the distribution of the homogeneously and heterogeneously captured impurities usually vary in the crystal bulk. This nonuniform distribution of impurities is associated with thermodynamic nonequilibrium at the growth interface. The nonuniform impurity distribution is of three main types: sectorial, zonal, and structural.

In order to explain the causes of formation of the above nonuniformities, we refer to Figure 7.5, which illustrates a polyhedral crystal formed by successive deposition of elementary growth layers on different faces developed on a growing three-dimensional crystal nucleus or seed. In the two-dimensional cross-section of the crystal, each of these growth faces may be represented by its growth sector defined by the displacement of the face in a direction away from the initial nucleus or seed. Growth sectors of different faces appearing in the morphology are separated by growth sector boundaries, while parallel lines of increasing, decreasing or constant length l representing the position of the face at different moments of crystal growth appear in a growth sector.

Different growth faces appearing in the morphology of a crystal are structurally different and follow different growth kinetics. Therefore, the capture of impurity particles in different growth sectors of a growing crystal is different. This type of nonuniform distribution of impurities in the crystal bulk is called *sectorial nonuniformity*. However, if the growth rate of the same face fluctuates around a constant value at different moments of crystal growth, the incorporation of impurities in the depositing growth layers of the face at different moments of growth is also nonuniform. This type of nonuniformity in the distribution of impurities, appearing as parallel lines in a growth sector, is called *zonal nonuniformity*. Zonal nonuniformity is usually referred to as growth bands in solution growth and impurity striations in melt growth. In contrast to the above nonuniformities, the concentration of a captured impurity can be increased or decreased at the boundaries of growth sectors, twins and grains, and in the vicinity of dislocations, inclusions and other structural defects of a crystal.

The ability of incorporation of an impurity i into the main host or crystallizing solute s is described by its segregation coefficient k_d , which is defined as the ratio of concentration of the impurity phase i in the crystalline solid phase S to that in the liquid growth medium L i.e.

$$k_d = c_{iS}/c_{iL} \quad (9.1)$$

where the concentrations c_{iS} and c_{iL} are expressed in atom/ion fractions, weight fractions or weight per unit volume. The segregation coefficient is also referred to as distribution or partition coefficient, and is usually denoted by \mathcal{D} . In terms of the concentrations of i and s , k_d may be written in the form

$$k_d = \frac{c_{iS}}{c_{iS} + c_{sS}} \times \frac{c_{iL} + c_{sL}}{c_{iL}} \quad (9.2)$$

Since $c_i \ll c_s$, Equation (9.2) can be written as

$$k_d = \frac{c_{iS}}{c_{iL}} \times \frac{c_{sL}}{c_{sS}} \quad (9.3)$$

When the concentrations of components i and s are expressed in mole fractions, one has

$$k_d = k x_{sL} \quad (9.4)$$

where the nonequilibrium segregation coefficient

$$k = x_{iS}/x_{iL} \quad (9.5)$$

In Equation (9.3), the ratio $x_{sL}/x_{sS} \leq 1$, and depends on the type of system and the crystallizing compound. At the usual crystallization temperatures, in the case of fairly soluble inorganic compounds crystallizing from aqueous solution, its value lies between 0.1 and 0.5. In the case of proteins, this ratio is much lower and lies between 10^{-3} and 10^{-2} . If the system is composed of a crystal and its melt, the ratio $x_{sL}/x_{sS} \approx 1$. Then the segregation coefficient

$$k_d = k = x_{iS}/x_{iL} \quad (9.6)$$

Note that k_d is the so-called thermodynamic segregation coefficient, which can be described in terms of chemical potentials (Section 9.2.2), but the nonequilibrium segregation coefficient is described by the concentration of the impurity in the solid and liquid phases. However, in this chapter the symbol k_d is used to denote the experimental segregation coefficient which is considered to be close to the equilibrium state.

In order to illustrate the physical meaning of segregation coefficient, it is advantageous to rewrite Equation (9.2) in the form

$$k_d = \frac{x_{iS}/x_{sS}}{x_{iL}/x_{sL}} \quad (9.7)$$

where x_{iS} and x_{sS} are, respectively, the concentrations of impurity i and solute s, expressed in mole fraction, in the solid solution, and x_{iL} and x_{sL} are their corresponding concentrations in the solution. In the solutions of fairly or highly soluble ionic salts, the concentrations are frequently expressed in molalities (i.e. moles of substance in 1 kg of solvent). We consider only the processes at the crystal–medium interface, where the impurity is incorporated into the growing crystal at a rate faster or slower than the rate of incorporation of the solute (Figure 9.2). Then the ratio x_{iL}/x_{sL} in the bulk medium is either smaller or larger than that in the bulk medium. The enrichment or depletion of the impurity at the crystal–medium interface depends on the value of the segregation coefficient k_d and the rate of transport of the impurity and solute species from the bulk solution to the crystal–medium interface and their incorporation into the growing surface. When the process of incorporation of impurity and solute particles is controlled by material transport from the bulk, the diffusion coefficient D of the species and the thickness δ of the diffusion layer determine the value of k_d (Section 9.3.1). However, when the incorporation of impurity and solute particles is controlled by integration processes at the surface, integration kinetics determine the value of k_d (Section 9.3.2).

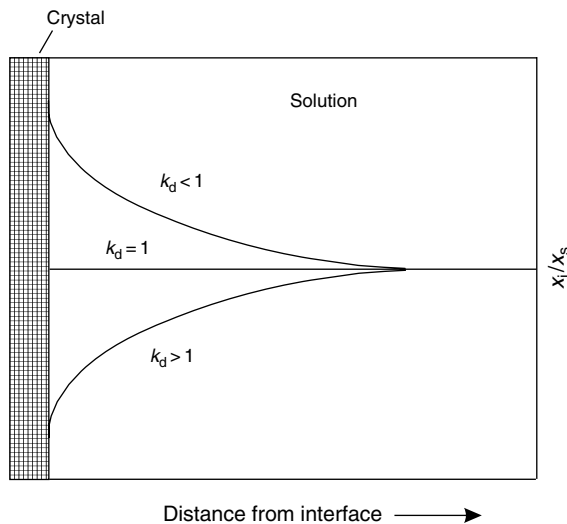


Figure 9.2 Schematic illustration of the dependence of x_{iL}/x_{sL} on distance from the crystal–solution interface, and relationship between x_{iL}/x_{sL} at the crystal–medium interface and the segregation coefficient k_d . Adapted from Rimstidt et al. (1998)

In summary, enrichment of the impurity at the crystal–medium interface means that $k_d > 1$, whereas depletion means that $k_d < 1$. In the case when $k_d > 1$, the crystal–medium interface acts as a sink for impurity particles, and successive crystallization will lead to increasingly impure material. When $k_d < 1$, the crystal–medium interface serves as a filter for impurity particles, and successive crystallization will lead to improvement in the purity of the material. However, when $k_d = 1$, no impurity segregation takes place, i.e. there is no purification of the material by repeated crystallization. Obviously, purification of the material by repeated crystallization is possible only when $k_d < 1$. There are other consequences of the value of k_d . When $k_d < 1$, the impurity is accumulated at the interface, which leads to lower quality and smaller crystals. However, when $k_d > 1$, the opposite effect is expected: the crystals are of better quality and larger size.

9.2 Equilibrium Segregation Coefficient

9.2.1 Binary Mixture Approach

In this approach, it is assumed that the impurity atoms i replace the host atoms s in the crystalline (i.e. solid solution) phase. When no interactions occur between impurity and solute atoms, then, as in the case of ideal solutions (Section 2.6.1), at the equilibrium temperature T the segregation of the impurity across both phases is given by

$$\ln k_0 = \ln \left(\frac{x_{iS}}{x_{iL}} \right) = \frac{\Delta H_{m,i}}{R_G} \left(\frac{1}{T} - \frac{1}{T_{m,i}} \right) \quad (9.8)$$

where x_{iS} and x_{iL} are the concentrations of the impurity i in the solid and the liquid phases, respectively, $\Delta H_{m,i}$ is the heat of melting of the impurity i , $T_{m,i}$ is its melting point, and R_G is the gas constant. Because an ideal solution does not take into account the chemical interactions between the impurity and the solute in the solid phase, it is rarely encountered in practice. Therefore, in the case of actual systems, it is realistic to assume that both the solid and the liquid phases behave as regular solutions. Then the equilibrium segregation coefficient may be expressed by (Brice, 1973)

$$\ln k_0 = \frac{\Delta H_{m,s}}{R_G} \left(\frac{1}{T} - \frac{1}{T_{m,s}} \right) - \frac{\Delta H_{m,i}}{R_G} \left(\frac{1}{T} - \frac{1}{T_{m,i}} \right) \quad (9.9)$$

or, in a more familiar form,

$$\ln k_0 = \frac{1}{R_G} \left(\frac{T_{m,s} \Delta H_{m,i} - T_{m,i} \Delta H_{m,s}}{T_{m,s} T_{m,i}} \right) - \frac{\Delta H_{m,s} - \Delta H_{m,i}}{R_G T} \quad (9.10)$$

where $\Delta H_{m,s}$ is the heat of melting of the solute s and $T_{m,s}$ is its melting point. When the entropy and heat of mixing are considered, one has (Brice, 1973; Klug, 1993)

$$\ln k_0 = \frac{\Delta H_{sol,iL} - \Delta H_{sol,iS}}{R_G T} + \frac{\Delta H_{m,i}}{R_G T} \left(\frac{1}{T} - \frac{1}{T_{m,i}} \right) \quad (9.11)$$

where $\Delta H_{sol,iL}$ and $\Delta H_{sol,iS}$ are the heats of solution of the impurity in the liquid and the solid state, respectively. According to Equation (9.11), the incorporation of the impurity in the solid solution decreases with increase in the heat of solution in the solid state.

According to the above equations, the logarithm of the segregation coefficient decreases linearly with increase in the inverse of absolute temperature. Figure 9.3 illustrates the plot of $\ln k_0$ of copper in silicon crystals as a function of $1/T$. From the slope of the plot and the known value of the heat of melting of the impurity, the heat of dissolution of the impurity in the solid solution can be calculated.

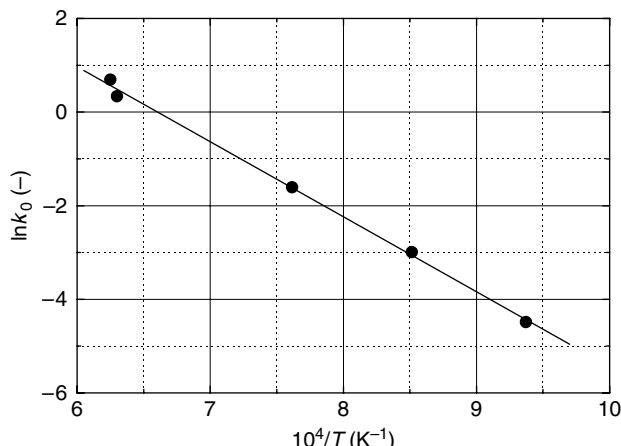


Figure 9.3 Dependence of $\ln k_0$ on $1/T$ for copper in silicon crystals. After Thurmond and Struthers (1953)

From Equations (9.9) and (9.11), the relationship between the segregation coefficient k_0 of an impurity in the solid solution and its concentration x_{iL} in the liquid solution can be obtained, using the ideal solubility [Equation (9.9)] for the solute s in the form:

$$\begin{aligned} \frac{\Delta H_{m,s}}{R_G} \left(\frac{1}{T} - \frac{1}{T_{m,s}} \right) &= \ln x_{sS} - \ln x_{sL} \\ &= \ln(1 - x_{iS}) - \ln(1 - x_{iL}) \\ &\approx x_{iL}(1 - k_0) \end{aligned} \quad (9.12)$$

Then, for example, from Equation (9.9) one can write

$$\ln k_0 = \ln k_0(0) - x_{iL} \left(1 + \frac{\Delta H_{m,i}}{\Delta H_{m,s}} \right) \quad (9.13)$$

where $k_0(0)$ is the value of k_0 for $x_i \rightarrow 0$. However, discussion on the relationship between $\ln k_0$ and x_{iL} is deferred to the following sections.

9.2.2 Thermodynamic Approach

The thermodynamic approach to the segregation coefficient has been developed essentially for crystallization from solution. The main advantage of this approach is that the description of the segregation coefficient is general and is not restricted to ideal solutions. Considering the thermodynamics of solid and liquid solutions, the segregation coefficient of an impurity in crystals grown from solutions may be given by (Klug, 1993)

$$k_0 = \frac{\gamma_{iL}^{sat} x_{sL}^{sat} x_{iL}}{\gamma_{iL}^{sat} x_{iL}^{sat} x_{sL}} \exp \left(-\frac{\Delta H_{sol,iS} + T \Delta S_{therm,iL}}{R_G T} \right) \quad (9.14)$$

where γ_{iL}^{sat} and γ_{iL} are the activity coefficients of the impurity at its equilibrium (solubility) and actual concentrations in the solutions corresponding to concentrations x_{iL} and x_{iL}^{sat} , respectively, $\Delta H_{sol,iS}$ is the heat of solution of the impurity in the solid state, and $\Delta S_{therm,iL}$ is the change in the thermal entropy of the impurity caused by its transfer from the solution to the crystal. When $\gamma_{iL}/\gamma_{iL}^{sat} = 1$ and $\Delta S_{therm,iL} = 0$, Equation (9.14) may be written in the form

$$k_0 = \frac{x_{sL}^{sat} x_{iL}}{x_{iL}^{sat} x_{sL}} \exp \left(-\frac{\Delta H_{sol,iS}}{R_G T} \right) \quad (9.15)$$

This relationship applies to undissociated compounds, such as metals and organic compounds, in which the same atoms and molecules form the crystal lattice while impurity species differing in size, shape, and chemical behavior are incorporated into the solid solution. In metals, for example, the host and the guest atoms can differ in both size and electronic configuration in their outermost orbits. In organic compounds, on the other hand, the impurity molecules can differ in size and geometry (and hence charge distribution) from those of the molecules of the host compound.

In the case of crystallization from aqueous solutions of dissociated ionic compounds with a common anion or cation of the impurity, one has to take into account three types

of ions: cations and anions of the host compound, and cations or anions of the impurity that enters the lattice of the host compound. Let us consider that the host compound s and the impurity i are dissociative such that $s = s_{\nu_+}^+ s_{\nu_-}^-$, and $i = i_{\nu_+}^+ i_{\nu_-}^-$, where s^+ and i^+ are cations and s^- and i^- are anions, ν_+ and ν_- are the numbers of cations and anions, respectively, in a molecule of s or i, and the total number of ions in a molecule is $\nu = \nu_+ + \nu_-$. Then the general expression for the segregation coefficient is given in the form (Chernov, 1984)

$$k_0 = \left(\frac{\gamma_{iL} \gamma_{sL}^{\text{sat}}}{\gamma_{sL} \gamma_{iL}^{\text{sat}}} \right)^\nu \left(\frac{\gamma_{s+S}}{\gamma_{i+S}} \right)^{\nu_+} \left(\frac{x_{sL}^{\text{sat}}}{x_{iL}^{\text{sat}}} \right)^{\nu/\nu_+} \exp \left(-\frac{\Delta\mu_i - \Delta\mu_s}{k_B T} \right) \quad (9.16)$$

where $\Delta\mu_s$ and $\Delta\mu_i$ are the changes in the chemical potentials of the solute s and the impurity i, respectively, during their transfer from the solution to the solid solution. When $\gamma_L/\gamma_L^{\text{sat}} = 1$ for solute s and impurity i, and the changes in the chemical potentials $\Delta\mu_s$ and $\Delta\mu_i$ are expressed in terms of corresponding changes in their Gibbs free energies ΔG_s and ΔG_i , respectively, Equation (9.16) simplifies to the form

$$k_0 = \left(\frac{\gamma_{s+S}}{\gamma_{i+S}} \right)^{\nu_+} \left(\frac{x_{sL}^{\text{sat}}}{x_{iL}^{\text{sat}}} \right)^{\nu/\nu_+} \exp \left(-\frac{\Delta G_{is}}{R_G T} \right) \quad (9.17)$$

where ΔG_{is} denotes the overall change in the Gibbs free energy of the system, which may be identified with the heat of solution ΔH_{sol} in Equation (9.15). In Equations (9.15) and (9.17), the terms $(x_{sL}^{\text{sat}}/x_{iL}^{\text{sat}})$ and $(\gamma_{s+S}/\gamma_{i+S})$ account for dissimilarity in the substituting impurity and the substituted host species.

In the case of sparingly soluble salts, the segregation coefficient of impurity cations is given by (Rimstidt *et al.*, 1998)

$$k_0 = \left(\frac{\gamma_i}{\gamma_s} \right)^{1/\nu_c} \left(\frac{K_s}{K_i} \right)^{1/\nu_c} \exp \left(-\frac{\Delta\mu_{is}}{\nu_a k_B T} \right), \quad (9.18)$$

where K_s and K_i are the solubility products of s and i, respectively, γ_s and γ_i are their corresponding activity coefficients, $\Delta\mu_{is}$ is the difference in the chemical potentials of impurity i in its pure crystal and its solid solution with the solute, and the ratio $\nu_a = \nu_-(i)/\nu_-(s)$ and $\nu_c = \nu_+(i)/\nu_+(s)$. Here ν_+ and ν_- are the number of cations and anions, respectively, in a salt molecule.

9.2.3 Theoretical Predictions and their Comparison with Experimental Data on Segregation Coefficient

The theoretical expressions for the thermodynamic segregation coefficient k_0 , given above, are derived on the assumption that the impurity–solute system is in thermodynamic equilibrium, i.e. the chemical potential of a component is the same in all phases of the system. They contain at least three quantities: (1) the ratio of concentrations of solute and impurity in the solution, (2) the ratio of activity coefficients of solute and impurity, and (3) the solid-state thermodynamics. The first two quantities are associated with solution thermodynamics. Therefore, the equilibrium segregation coefficient of an impurity in a solute is a function of solution thermodynamics and solid-state thermodynamics.

With reference to the solid-state thermodynamics, one finds that the segregation of an impurity is determined by dissimilarities between the impurity and the host. The dissimilarities are associated with mismatches in molecular volume, ionic/atomic radii or unfavorable steric interactions, for example, due to the shape of molecules/ions. The mismatches lead to an increase in the energy and entropy of incorporation of impurity species, which results in a reduced probability of their incorporation in the host lattice. For a given impurity–solute system, temperature is the only parameter, related to solid-state thermodynamics, that reduces the effect of mismatches, thereby increasing the impurity incorporation with an increase in temperature. In the case of growth from the melt for example, this is the situation [see Equation (9.15)].

In crystallization from solutions, apart from the solid-state thermodynamics, the solubility of both impurity and solute can change enormously with temperature. Consequently, in growth from solutions, temperature can play an even greater role in impurity incorporation by changing the solution thermodynamics, i.e. by changing the pre-exponential terms in Equations (9.15) and (9.17). It should also be noted that, according to Equations (9.15) and (9.17), impurity incorporation increases with a decrease in the concentration x_{iL}^{sat} of an impurity and an increase in the concentration x_{sL}^{sat} of solute in the solution. These relationships show that the purity of a material is improved by crystallization from solutions composed of solvents in which impurities are more soluble relative to the product material in the temperature range of crystallization.

In order to verify the validity of different models and their limitations, it is convenient to recast the different equations given above by taking logarithms on their both sides. For example, in the case of segregation of cations in calcite, Equation (9.18) gives

$$\ln k_0 = \frac{1}{\nu_c} \ln \left(\frac{\gamma_i}{\gamma_s} \right) + \frac{1}{\nu_c} \ln \left(\frac{K_s}{K_i} \right) - \frac{\Delta\mu_{is}}{\nu_a k_B T} \quad (9.19)$$

Figure 9.4 shows a plot of experimental $\ln k_d$ of different bivalent cations in calcite as a function of $\ln(K_{\text{calcite}}/K_{\text{imp}})$ in the presence of cationic carbonates. The data for $\ln k_d$ against $\ln(K_{\text{calcite}}/K_{\text{imp}})$ reveal two trends. Cations Mg^{2+} , Co^{2+} , Fe^{2+} , Mn^{2+} , Cu^{2+} , Zn^{2+} , and Cd^{2+} , which have ionic radii r_i smaller than that of Ca^{2+} and which form rhombohedral carbonates, fit the solid line of the highest k_d values, whereas cations Sr^{2+} , Ra^{2+} and Ba^{2+} , which have ionic radii larger than that of Ca^{2+} and form orthorhombic carbonates, follow the dashed line of lower k_d values. UO_2^{2+} ion, which is still larger than Sr^{2+} , Ra^{2+} and Ba^{2+} , deviates enormously from the above trends. The increasingly deviating trend of cations with larger radii than that of Ca^{2+} may be attributed to strain caused in the calcite lattice by the ions of larger sizes during their incorporation. This inference follows from the fact that the solid line gives a chemical potential difference $\Delta\mu_{is}$ equal to -1.1 kJ/mol , whereas the dashed line gives $\Delta\mu_{is}$ equal to about 9.5 kJ/mol (cf. Rimstidt *et al.*, 1998).

The slope $1/\nu_c$ of the solid line is about 0.6 rather than the 1.0 expected for the stoichiometry 2:2. The main reason of this lower value of the slope is the experimental method used to determine k_d . The k_d values are usually determined during growth and not in equilibrium. Therefore, the segregation of impurities is affected by growth kinetics. Differences in the incorporation of an impurity in different faces of a crystal are a typical example of the influence of growth kinetics.

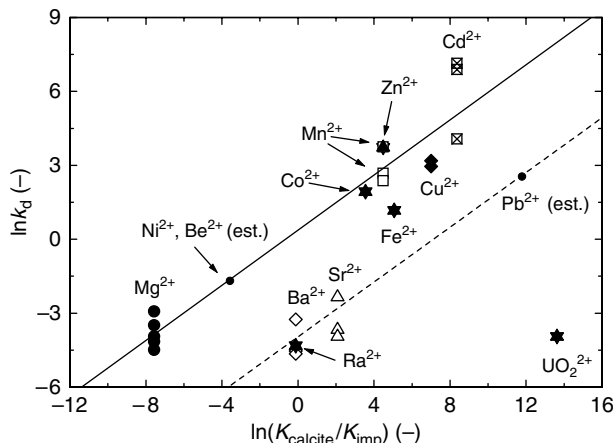


Figure 9.4 Dependence of experimental $\ln k_d$ of different bivalent cations in calcite on $\ln(K_{\text{calcite}}/K_{\text{imp}})$ in the presence of cationic carbonates. Adapted from Rimstidt et al. (1998)

It may be noted that Equations (9.10), (9.15) and (9.18) are very similar in form and if, all quantities before the pre-exponential term are combined and denoted by $k_0(0)$, one may write the above-mentioned relations in the general form

$$k_0 = k_0(0) \exp(-\Delta G/R_G T) \quad (9.20)$$

where $k_0(0)$ is the segregation coefficient k_0 of a solute of radius r_i equal to the radius r_s of the lattice site, and the free energy change ΔG denotes changes in the free energy difference $\Delta H_{m,s} - \Delta H_{m,i}$, the heat of solution ΔH_{sol} , and difference in the chemical potentials $\Delta \mu_{is}$ in Equations (9.10), (9.15) and (9.18), respectively. Dissimilarities associated with mismatches in the sizes of impurity and solute species lead to changes in the free energy change ΔG . The simplest relation between k_0 and ionic/atomic radii r_i is given by (Brice, 1973)

$$\ln k_0 = A + B\Delta V/V_0 = A - B + B(r_i/r_s)^3 \quad (9.21)$$

where A and B are constants, $\Delta V/V_0$ is the fractional volume misfit of the solute in the lattice due to incorporation of the impurity, and $r_i/r_s > 1$. For different impurities in group IV and III-V compounds, the constant $B = 1.43$, but $A = 0$ for chemically similar impurities whereas $A = -0.59$ for dissimilar impurities. Obviously, the fractional volume misfit is proportional to ΔG . In Equation (9.21), when $r_i/r_s < 1$, $B < 0$. When r_i/r_s does not differ significantly from unity (e.g. by about 10%), from Equation (9.21) one can write

$$\ln k_0 = (A - B) + \frac{B}{3} \frac{r_i}{r_s} \quad (9.22)$$

and when $\ln k_0 \approx k_0 - 1$, one has

$$k_0 = (A - B + 1) + \frac{B}{3} \frac{r_i}{r_s} \quad (9.23)$$

Obviously, under certain conditions, simple relationships between k_0 and r_i are expected.

Assuming that the only change in the free energy ΔG of the system caused by the misfit ($r_i - r_s$) in the radii of ions/atoms of impurity i and host solute s is in the strain energy, from Equation (9.20) one may write (Brice, 1975; Römer *et al.*, 1994)

$$\ln k_0 = \ln k_0(0) - \frac{4\pi EN_A}{R_G T} \left[\frac{1}{2}r_s(r_i - r_s)^2 - \frac{1}{3}(r_i - r_s)^3 \right] \quad (9.24)$$

where E is Young's modulus of the host lattice and N_A is Avogadro's number.

Figure 9.5 illustrates the plot of the logarithm of equilibrium segregation coefficient k_0 of various rare earths in cubic ZrO_2 stabilized with Y_2O_3 as a function of $\frac{1}{2}r_s(r_i - r_s)^2 + \frac{1}{3}(r_i - r_s)^3$, as reported by Römer *et al.* (1994). The plot is drawn according to Equation (9.24) with the 'experimental' k_0 data for Er^{3+} , Sm^{3+} , and Nd^{3+} ions, while the k_0 values for Lu^{3+} and Ce^{3+} ions were calculated from the best-fit plot. In the calculations the cationic radii r_i of the additives due to Shannon, with coordination number 8, were used. The k_0 values for the additives were obtained by using graphical solutions of Equation (9.26), of the Burton–Prim–Slichter (BPS) theory (Burton *et al.*, 1953), with the experimentally determined values of effective segregation coefficient k_{eff} as a function of growth rate R (see also Section 9.4).

The slope of the linear dependence in Figure 9.5 gives a value of Young's modulus $E = 10.8 \times 10^{10} \text{ N/m}^2$, which is comparable to the literature values of $E_{110} = 17.9 \times 10^{10} \text{ N/m}^2$ and $E_{111} = 15.6 \times 10^{10} \text{ N/m}^2$, but lower than $E_{100} = 34.3 \times 10^{10} \text{ N/m}^2$ (Römer *et al.*, 1994). The model of the lattice strain caused by impurity species assumes that the crystal is isotropic. The comparison of the values of Young's modulus suggests that the condition of an isotropic crystal is worse fulfilled by low-index planes and directions.

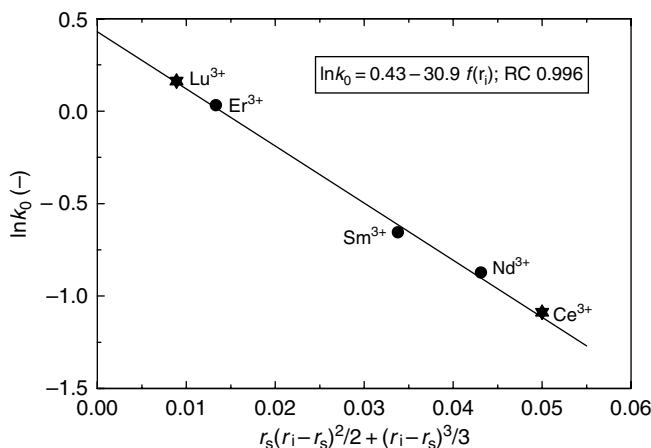


Figure 9.5 Logarithm of equilibrium segregation coefficient k_0 of various rare earths in cubic ZrO_2 stabilized with Y_2O_3 as a function of $\frac{1}{2}r_A(r_i - r_s)^2 + \frac{1}{3}(r_i - r_s)^3$. Data for Er^{3+} , Sm^{3+} , and Nd^{3+} are experimental, whereas those for Lu^{3+} and Ce^{3+} are calculated from Equation (9.24). Adapted from Römer *et al.* (1994).

The dependence of $\ln k_0$ of various chemically similar impurity ions in a variety of inorganic crystals on the strain introduced in the host lattice, as defined by the function $f(r_i)$ of the ionic radii of the impurities, is a consequence of the change in the volume ΔV of the lattice site. Therefore, if it is assumed that the volume change ΔV results due to changes in the impurity ionic radius, Equations (9.22) and (9.23) should hold. Figure 9.6 presents the plots of $\ln k_0$ of various rare earths in cubic ZrO_2 stabilized with Y_2O_3 against additive cationic radii r_i and r_i^3 . The values of k_0 for all cations, other than Er^{3+} , Sm^{3+} and Nd^{3+} , were calculated by using Equation (9.24) with Shannon's radii r_i , of coordination number 8 (Römer *et al.*, 1994). As has been observed in different systems, relatively good linear fits for the $\ln k_0(r_i)$ and $\ln k_0(r_i^3)$ data are obtained. It can be seen that a better fit is obtained when the data are analyzed separately for $r_i < r_s$ and $r_i > r_s$. However, in general, one finds that the constants $B \approx -2.5$ and $A \approx 0$.

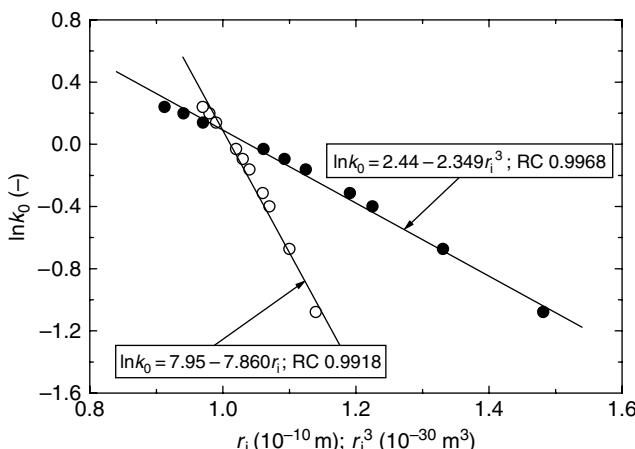


Figure 9.6 Logarithm of equilibrium segregation coefficient k_0 of various rare earths in cubic ZrO_2 stabilized with Y_2O_3 against additive cationic radii r_i and r_i^3 . The cationic radii r_i and r_i^3 are due to Shannon, with coordination number 8. Data from Römer *et al.* (1994)

Figure 9.7 illustrates the plots of $\ln k_d$ for various bivalent cations in calcite against r_i^3 of their Shannon radii r_i with coordination number 6. It can be seen that the $\ln k_d(r_i^3)$ data for all cations, other than Mg^{2+} , having radius r_i smaller than r_s of Ca^{2+} , and for cations Sr^{2+} , Ra^{2+} and Ba^{2+} , with $r_i > r_s$, reveal the expected trends. However, in contrast to the experimental results, the concept of lattice strain predicts two symmetrical plots of increasing and decreasing slope B exhibiting a maximum at $r_i = r_s$.

Figure 9.8 shows the dependence of $\ln k_d$ on r_i^3 of trivalent rare earth metal cations. In this case, $\ln k_d$ increases fairly linearly with increasing r_i^3 up to $r_i = r_s$, but later, in the interval $r_s < r_i < 1.07$, k_d attains a saturation value of $\ln k_d \approx 8.2$. The anomalous behavior in the dependence of $\ln k_d$ on r_i^3 is associated with the difference in the influence of impurities with $r_i < r_s$ and $r_i > r_s$ on the growth kinetics of the crystals. For $r_i < r_s$, here $B = 13.5$ and $A = 8.6$. Another example of the relation between segregation coefficient k_d of different impurity particles and their size is shown in Figure 9.9, which presents a plot

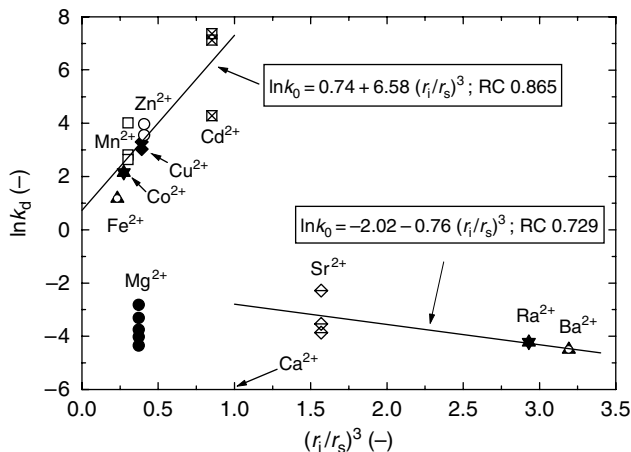


Figure 9.7 Plots of $\ln k_d$ for various bivalent cations in calcite against $(r_i/r_s)^3$. Data from Rimstidt et al. (1998)

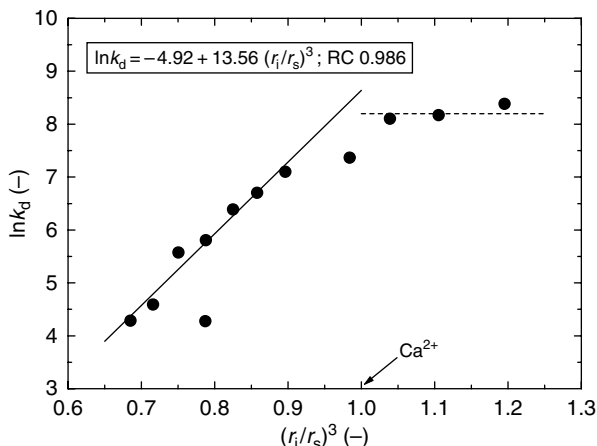


Figure 9.8 Logarithm of k_d for various trivalent rare earth metal ions in calcite as a function of $(r_i/r_s)^3$. The effective ionic radius, due to Shannon, is in six-fold coordination. The extremely deviating point for $(r_i/r_s)^3 = 0.78$ was excluded while fitting the data. Data from Rimstidt et al. (1998)

of effective segregation coefficient k_{eff} of lanthanide ions against their radii r_i for gypsum crystals. Obviously, except for La^{3+} ions, all additive cations follow Equation (9.23) with $B = 8.73$ and $A = 6.89$. An interesting feature of Figures 9.8 and 9.9 is that $A < B$ in both cases and $A \neq 0$.

Evidence in support of the explanation that growth kinetics influence the incorporation of an impurity are the experimental data on the segregation coefficient k_d of different ions in some alkali metal halides grown from the melt and from aqueous solutions as

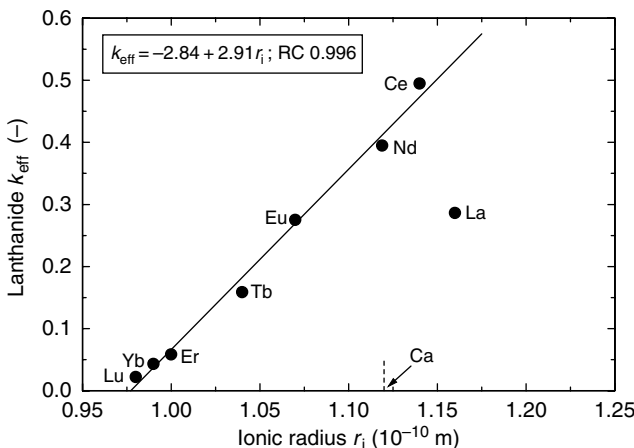


Figure 9.9 Plot of k_{eff} for various lanthanide ions in gypsum crystals against their radii r_i . Data from de Vreugd et al. (1994)

a function of ratio r_i/r_s of ionic radii shown in Figure 9.10. It can be seen that practically the entire available $k_d(r_i/r_s)$ data obtained in the interval $0.8 < r_i/r_s < 1.2$ from melt growth fit the concept of formation of symmetrical plots with positive and negative slopes $B = 5$. The $k_d(r_i/r_s)$ data obtained from solution growth, although relatively sparse and sporadic, also follow the dependence of Equation (9.23), as seen for $r_i > r_s$ with a much lower slope $B \approx 0.7$. The value of B is directly connected with the nature of the

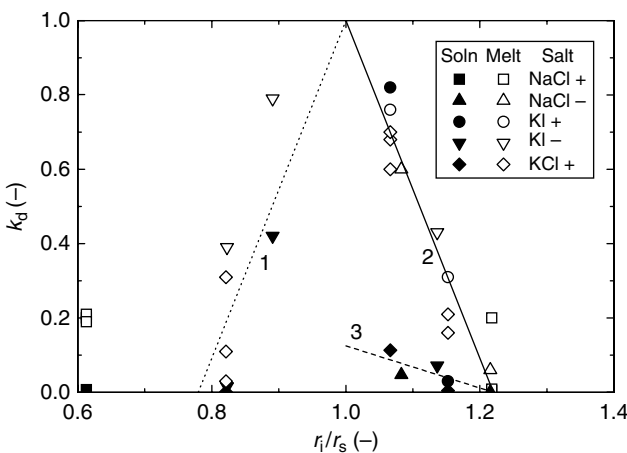


Figure 9.10 Dependence of segregation coefficient k_d of cations and anions in different alkali metal halides grown from aqueous solutions and from the melt on their Shannon radii r_i , with coordination number 8 or 9. Data from Brice (1973). Additive cations and anions are denoted by + and -, respectively, in the inset

crystal–medium interface. The greater the roughness of the interface, the higher is the impurity incorporation.

9.3 Effective Segregation Coefficient

9.3.1 Volume Diffusion Model

In the preceding section, the segregation coefficient k_d was defined as the ratio of impurity concentration in the crystal to its average concentration in the bulk medium. Based on this definition, different relationships of the equilibrium segregation coefficient k_0 with thermodynamic parameters were discussed. However, when studying the incorporation of impurities one measures the effective segregation coefficient k_{eff} , which is the ratio of impurity concentration in the crystal to its average concentration at the crystal–medium interface. This concentration at the interface is different from that in the bulk medium because the growth interface acts either as a source ($k_0 < 1$) or as a sink ($k_0 > 1$), as shown in Figure 9.2. The removal of the impurity from the growth interface or its transport to the interface is affected by volume diffusion in the bulk medium. Assuming that the volume diffusion occurs through a boundary layer of thickness δ , the interface grows at a rate R , and the impurity concentration satisfies the diffusion equation

$$D \frac{\partial^2 x_i}{\partial z^2} + R \frac{\partial x_i}{\partial z} = 0 \quad (9.25)$$

then one obtains (Burton *et al.*, 1953; Chernov, 1984)

$$k_{\text{eff}} = \frac{k_0}{k_0 + (1 - k_0) \exp(-R\delta/D)} \quad (9.26)$$

When $k_0 \ll 1$, Equation (9.26) can be written in the form

$$k_{\text{eff}} = k_0 \exp(R\delta/D) \quad (9.27)$$

However, when $R\delta/D \ll 1$, Equation (9.27) simplifies to

$$k_{\text{eff}} = k_0 + k_0(R\delta/D) \quad (9.28)$$

Equation (9.27) predicts that k_{eff} increases exponentially with growth rate R , whereas Equation (9.28) predicts that k_{eff} increases linearly with increase in growth rate R .

Figure 9.11 shows the effective segregation coefficient k_{eff} of Sb in Ge crystals as a function of growth rate R for different stirring conditions. The solid curves are drawn according to Equation (9.26) with $k_0 = 3 \times 10^{-3}$ (Burton *et al.*, 1953), whereas the dashed lines are according to the best fit of the data by the linear dependence [Equation (9.28)]. The values of δ/D for the linear dependence are given in parentheses. Obviously, as inferred from the decreasing value of δ/D with increasing rate of stirring, this is a case of impurity incorporation controlled by volume diffusion. However, in view of the sparse data, it seems that the linear relation better represents the experimental data than does the original exponential relation in Equation (9.26).

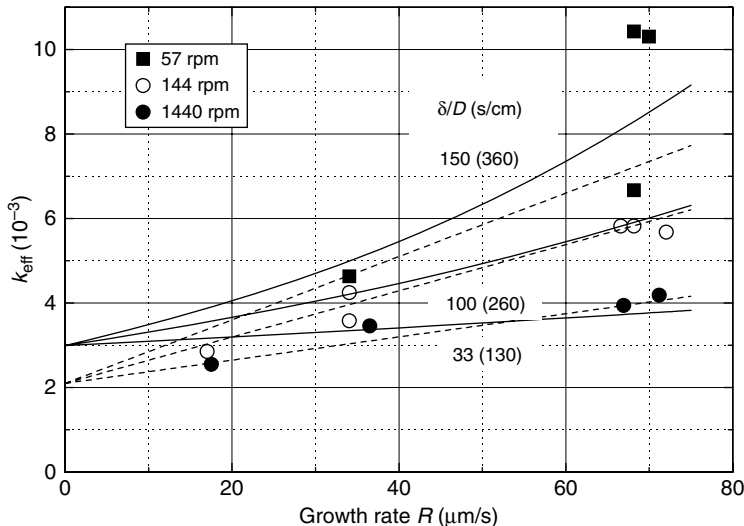


Figure 9.11 Dependence of segregation coefficient k_{eff} of Sb in Ge crystals on growth rate R for different stirring conditions. Solid curves were drawn according to the BPS Equation (9.26) due to Burton et al. (1953), and dashed lines are according to the linear dependence in Equation (9.28). The values of δ/D for the linear dependence are given in parentheses. Adapted from Burton et al. (1953)

From the values of δ/D lying between 30 and 150 s/cm (cf. Figure 9.11) and the value of D of about $10^{-12} - 10^{-9}$ cm²/s (Chernov, 1984), one finds a diffusion layer thickness δ between 0.3 and 1.5 nm for the highest value of D . This is the correct order of the magnitude of δ .

9.3.2 Diffusional Relaxation Approach

The main idea of this approach rests on the presence of an adsorption layer at the crystal–medium interface. This adsorption layer contains $k_{\text{ads}}x_{iL}$ atoms/molecules per unit volume. When a growth layer is deposited, it completely buries the adsorbed layer in the crystal, but after incorporation the concentration relaxes to the equilibrium value k_0x_{iL} until a new growth layer is deposited after a time τ . Because the concentration of impurity particles is different in the deposited layer of the crystal and in the adsorption layer, the incorporated impurity particles diffuse from the surface layer to the bulk medium at a rate D/h , where D is the corresponding diffusion coefficient of the impurity and h is the thickness of the deposited layer. This process of the diffusion flow of impurity particles is known as *diffusional relaxation*. Relaxation of impurity particles in the surface layer may occur in kinks in step ledges, in step ledges or in the surface terrace, depending on the sites of incorporation of the impurity particles (Figure 9.12). The probability of removal of captured impurity particles from the surface layer before the arrival of the next growth layer is $\exp(-h/R\tau)$, where $\tau = h^2/D$. Therefore, one has (Hall, 1953; Kitamura and Sunagawa, 1977; Chernov, 1984)

$$k_{\text{eff}} = k_0 + (k_{\text{ads}} - k_0) \exp(-R_i/R) \quad (9.29)$$

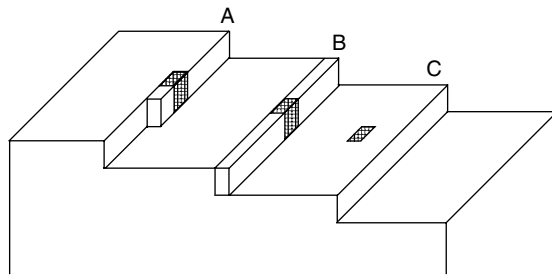


Figure 9.12 Different positions of trapped impurity particles: (A) trapped in a kink, (B) trapped in a step ledge by solute particles from both sides, and (C) trapped in the surface terrace

where the growth rate constant $R_i = h/\tau = D/h$. When $k_0 \ll 1$, Equation (9.29) simplifies to

$$k_{\text{eff}} = k_{\text{ads}} \exp(-R_i/R) \quad (9.30)$$

and when $R_i/R \ll 1$

$$k_{\text{eff}} = k_{\text{ads}} + k_{\text{ads}}(-R_i/R) \quad (9.31)$$

According to these relations, k_{eff} decreases exponentially or linearly with the inverse of growth rate R .

Figure 9.13 presents a plot of $\ln(k_{\text{eff}} - k_0)$ of Pb^{2+} ions in the {111} faces of BaNO_3 crystals against the inverse of face growth rate R , as predicted by Equation (9.29). From the plot one finds $\ln(k_{\text{ads}} - k_0) = -1.846$ and $R_i = h/\tau = D/h = 0.0743 \text{ nm/s}$. Since the value of the equilibrium segregation constant $k_0 = 0.08$ (see Figure 9.14), one

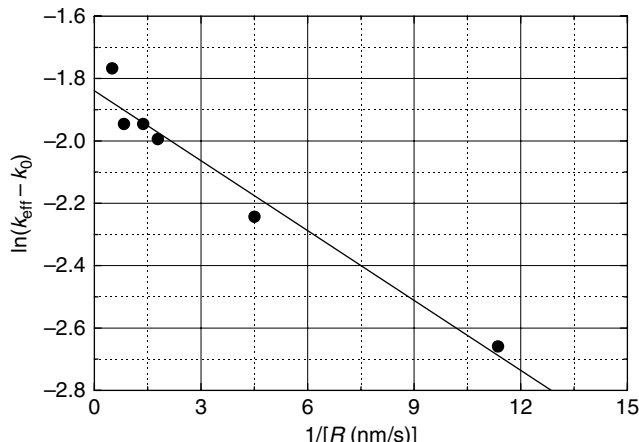


Figure 9.13 Plot of $\ln(k_{\text{eff}} - k_0)$ of Pb^{2+} ions in BaNO_3 crystals against $1/R$; impurity concentration c_i in the solution about 10 mol%. Adapted from Tsuchiyama et al. (1981)

obtains $k_{\text{ads}} = 0.24$. This k_{ads} is the limiting value of k_{eff} when $R \rightarrow \infty$. Between the {111} planes the spacing $h = 0.469 \text{ nm}$. This gives $\tau = 6.3 \text{ s}$ and $D = 3.5 \times 10^{-20} \text{ m}^2/\text{s}$ (i.e. $3.5 \times 10^{-16} \text{ cm}^2/\text{s}$). This value of D for the diffusion coefficient of Pb^{2+} impurity in $\text{Ba}(\text{NO}_3)_2$ is realistic at room temperature.

The relationships between the effective segregation coefficient k_{eff} of impurities and interface or face growth rate R were discussed above. In fact, it is well known that the segregation coefficient k_{eff} of an impurity always changes with the rate of growth of fairly soluble compounds and the rate of precipitation of sparingly soluble compounds. For impurities with equilibrium segregation coefficient $k_0 > 1$, the effective segregation coefficient $k_{\text{eff}} < k_0$, and approaches k_0 when the crystallization rate R approaches zero. However, for impurities with $k_0 < 1$, $k_{\text{eff}} > 0$, and k_{eff} approaches k_0 when $R \rightarrow 0$. As an example, Figure 9.14 shows the effective segregation coefficient k_{eff} of Pb^{2+} ions in the {111} faces of BaNO_3 crystals as a function of temperature difference $\Delta T = (T_0 - T)$ used for growth from aqueous solutions containing about 10 mol% Pb^{2+} ions. Here T_0 is the temperature corresponding to solution saturation and T is the growth temperature. The temperature difference ΔT is a measure of supersaturation for growth and determines the growth rate R , because $R \propto (\Delta T)^n$, where $1 < n < 2$. Consequently, the experimental $k_{\text{eff}}(\Delta T)$ data in Figure 9.13 may be described by Equation (9.29). The data can equally well be represented by Equation (9.43) or (9.48) of the surface adsorption approach, with $k_0 = 0.08$, $B_2 = B'' = 0.05$, and $(1 - n_2) = 0.46$ (Section 9.4).

Figure 9.15a and b show examples of somewhat different behavior of the dependences of effective segregation coefficient k_{eff} of CrO_4^{2-} and Ni^{2+} ions in K_2SO_4 and $\text{ZnK}_2(\text{SO}_4)_2 \cdot 6\text{H}_2\text{O}$ crystals grown from aqueous solutions on supersaturation σ . The k_{eff} values were measured in the (110) and (031) faces of K_2SO_4 crystals and in the (001) and (110) faces of $\text{ZnK}_2(\text{SO}_4)_2 \cdot 6\text{H}_2\text{O}$ crystals.

It can be seen that, for $k_{\text{eff}} < 1$, the trend of the $k_{\text{eff}}(\sigma)$ data in Figure 9.15a is different from that in Figure 9.14. The k_{eff} value increases steeply at low σ , thus showing a strong

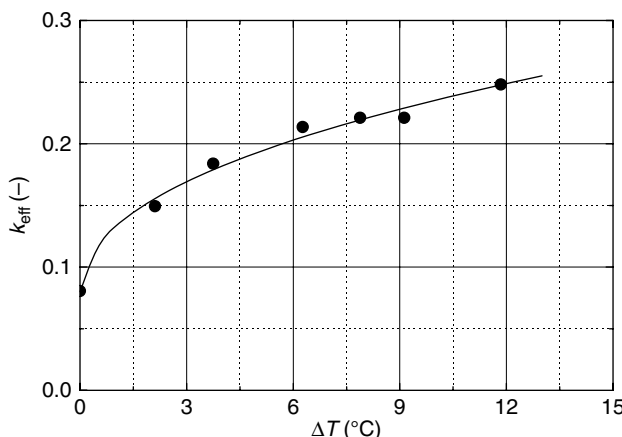


Figure 9.14 Dependence of effective segregation coefficient k_{eff} of Pb^{2+} ions in BaNO_3 crystals on temperature difference $\Delta T = (T_0 - T)$. The curve was drawn according to Equation (9.43) with $k_0 = 0.08$, $B_2 = 0.05$, and $1 - n_2 = 0.46$. Adapted from Tsuchiyama et al. (1981)

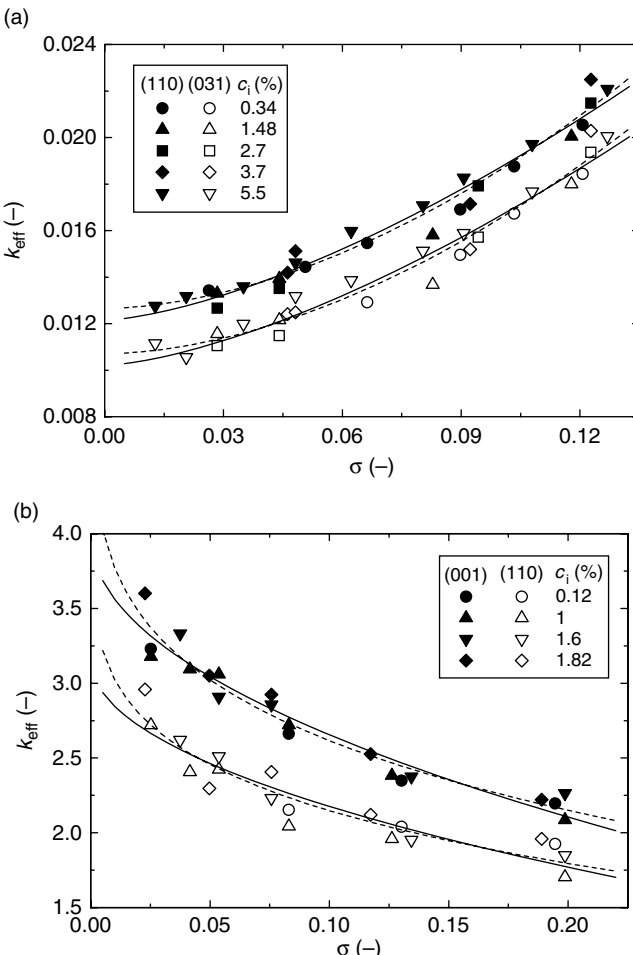


Figure 9.15 Dependence of effective segregation coefficient k_{eff} of additive ions for two different faces of crystals grown from aqueous solutions on supersaturation σ : (a) CrO_4^{2-} ions in the (110) and (031) faces of $K_2\text{SO}_4$ crystals and (b) Ni^{2+} ions in the (001) and (110) faces of $\text{ZnK}_2(\text{SO}_4)_2 \cdot 6\text{H}_2\text{O}$ crystals. Curves were drawn according to Equation (9.43) with different values of n_2 : (a) $n_2 = -0.5$ (continuous curve) and -0.8 (dashed curve), and (b) $n_2 = 0.5$ (continuous curve) and 0.8 (dashed curve). Original data are from Zhmurova and Khaimov-Mal'kov (1970b). Adapted from Sangwal and Pałczyńska (2000).

upward curvature in the $k_{\text{eff}}(\sigma)$ plot in Figure 9.14, in contrast to the relatively weak upward curvature in the $k_{\text{eff}}(\sigma)$ data of Figure 9.15a. Similarly, for $k_{\text{eff}} > 1$, trends with a curvature opposite to that of Figure 9.15b are observed (for example, see Rimstidt *et al.*, 1998). The nature of the $k_{\text{eff}}(\sigma)$ data in Figure 9.14 is associated with the diffusional relaxation mechanism of impurity incorporation, as explained above, whereas that of the $k_{\text{eff}}(\sigma)$ data in Figure 9.15 is due to a different impurity incorporation mechanism in

which competition between impurity and solute molecules/ions plays an important role for their integration into kinks in step ledges. This mechanism is described in Section 9.3.4.

9.3.3 Statistical Selection Approach

The capture of impurity particles in the surface occurs by building up of new atomic/molecular rows of solute atoms/molecules during the movement of the kinks and trapping of impurity particles in the kinks of the advancing rows perpendicular to the direction of the advancing steps (see Figure 9.12). The impurity particle is captured in the kink if the time of its stay there is longer than the time of joining a solute particle with the new kink formed by the trapped impurity particle. These stay times depend on the energy of adsorption and desorption of these impurity particles at the kink site, and on the relative concentration of impurity and solute particles. The higher the energy of adsorption of impurity particles and the lower the concentration of impurity particles, the higher is the probability of capture of the impurity particle in the kink. Consequently, the process of incorporation of the impurity in the crystal is essentially a statistical selection process of impurity particles by kinks, and is determined by the probability of attachment and detachment of impurity particles. Then the effective segregation coefficient may be given by (Voronkov and Chernov, 1967; Chernov, 1984)

$$k_{\text{eff}} = \frac{k_0}{1 + \sigma/\sigma^*} \quad (9.32)$$

where σ is the actual supersaturation at the surface, and σ^* is some constant depending on the elementary frequencies of attachment and detachment of host and impurity particles. The value of σ^* is positive for an impurity adsorbing more strongly in kinks than the solute, and is negative in the opposite case. For $\sigma/\sigma^* \ll 1$, Equation (9.32) can be written in the linear form

$$k_{\text{eff}} = k_0 - k_0 \sigma/\sigma^* \quad (9.33)$$

From these equations, it follows that, with increasing σ , k_{eff} decreases in the former case and increases in the latter.

The trends of the experimental $k_{\text{eff}}(\sigma)$ data for impurity ions in K_2SO_4 and $\text{ZnK}_2(\text{SO}_4)_2 \cdot 6\text{H}_2\text{O}$ crystals are consistent with the above approach. However, it was observed (Zhmurova and Khaimov-Mal'kov, 1970a) that, for $\sigma > 0.12$, the values of k_{eff} predicted by Equation (9.32) are lower than those obtained experimentally, with the deviation between the experimental and predicted values increasing with increasing σ . According to Zhmurova and Khaimov-Mal'kov (1970a), this deviation is associated with the influence of mass transport processes in the bulk solution.

It should be noted that, in the examples presented in Figure 9.15, there is an insignificant effect of impurity concentration c_i on the values of k_{eff} at a given σ . However, as shown below, the impurity concentration usually has a strong influence on the $k_{\text{eff}}(\sigma)$ dependence. The above statistical selection approach qualitatively predicts the dependence of the concentration of an impurity on k_{eff} through the ratio of frequencies of attachment and detachment of host and impurity particles, and through changes in the binding energy between the nearest neighbors on the surface and energy of adsorption for the impurity

molecules. According to this approach, no simple theoretical expression describing the effect of concentration c_i of an impurity on its segregation coefficient k_{eff} has been obtained.

9.3.4 Surface Adsorption Approach

In order to describe the combined effect of solution supersaturation σ and impurity concentration c_i on the effective segregation coefficient k_{eff} , a model based on competitive adsorption of solute and impurity molecules has been proposed (Sangwal and Pałczyńska, 2000; Sangwal *et al.*, 2002). The model is based on the postulate that the effect of an increase in solution supersaturation is to increase the density of kinks in ledges of the F faces of crystals whereas that of the impurity is to adsorb and occupy the kink sites which would otherwise have been available to the host solute. Physically, this means that the solution contains two types of particles, solute s and impurity i, which adsorb simultaneously on the surface to extents θ_s and θ_i , respectively. Then the total surface coverage

$$\theta = \theta_s + \theta_i \quad (9.34)$$

If f_{kink} is the fraction of kink sites on the surface of a crystal growing at supersaturation σ with respect to a perfect surface at $\sigma \rightarrow 0$ (i.e. equilibrium surface) and $(1 - \theta)/\theta$ is the relative fractional coverage of the sites, the effective segregation coefficient may be expressed as a sum of equilibrium segregation coefficient k_0 and a contribution due to the effect of supersaturation, i.e.

$$k_{\text{eff}} = k_0 + f_{\text{kink}}(1 - \theta)/\theta \quad (9.35)$$

The fractional coverage θ_j of the surface by the component j (where j denotes the solute s or the impurity i) is given by (Eggers *et al.*, 1964; see Section 4.2)

$$\theta_j = m_j(c_j/c_j^*)^{m_j} \quad (9.36)$$

for the Freundlich isotherm. The constant m_j in Equation (9.36) is given by

$$m_j = k_B T / \varepsilon_{mj} \quad (9.37)$$

and c_j and c_j^* are the concentrations of j corresponding to θ_j and $\theta_j = 1$, respectively. In Equation (9.37), ε_{mj} is a measure of the distribution of energies of adsorption sites. The energy constant ε_{mj} is related to the differential heat of adsorption $Q_{\text{diff},j}$ by

$$Q_{\text{diff},j} = -\varepsilon_{mj} \ln \theta_j \quad (9.38)$$

In Equation (9.36), the concentration ratio c_j/c_j^* of the component j is always less than unity. Therefore, the maximum value of the fractional coverage $\theta_{\max,j} = m_j \leq 1$.

We consider that crystal growth occurs by the displacement of steps emitted by a spiral, N_{kink} is the density of kinks in a step per unit length, y_0 is the spacing between a

successive steps of the spiral, and a is the diameter of atoms/molecules in the step. Then the fraction f_{kink} of kinks in the steps on the surface may be written as

$$f_{\text{kink}} = N_{\text{kink}} a^2 / y_0 = a^2 / x_0 y_0 = B \sigma^{1-n_2} \quad (9.39)$$

with the constant

$$B = \frac{1}{19(\gamma_l/k_B T)(1-n_2) \exp(W_0/k_B T)} \quad (9.40)$$

In Equation (9.40), W_0 is the activation energy for growth molecules to enter the step in the absence of supersaturation effects, the constant n_2 is a measure of the barrier due to supersaturation effects, and γ_l is the linear edge free energy ($\gamma_l \approx \gamma a^2$, where γ is the surface free energy). The fraction f_{kink} of kinks is a dimensionless quantity and is always less than unity.

Substituting for f_{kink} from Equation (9.39) and θ from Equation (9.36), Equation (9.35) may be written in the form

$$k_{\text{eff}} = k_0 + B \sigma^{1-n_2} \left[\frac{1}{m_s(c_s/c_s^*)^{m_s} + m_i(c_i/c_i^*)^{m_i}} - 1 \right] \quad (9.41)$$

where s and i denote the solute and the impurity, respectively. Equation (9.41) is the key expression relating k_{eff} with σ , n_2 and c_i . However, depending on the values of σ and n_2 , whether $[m_s(c_s/c_s^*)^{m_s} + m_i(c_i/c_i^*)^{m_i}]^{-1} \gg 1$, and the relative values of $m_s(c_s/c_s^*)^{m_s}$ and $m_i(c_i/c_i^*)^{m_i}$, several cases can be predicted.

Since m_j is a measure of adsorption of species on a surface and impurities adsorb preferentially on it, it may be supposed that $m_i(c_i/c_i^*)^{m_i} \gg m_s(c_s/c_s^*)^{m_s}$. Usually, the fractional coverage $\theta_i = m_i(c_i/c_i^*)^{m_i} < 0.1$. Therefore, Equation (9.41) may be rewritten in the form

$$k_{\text{eff}} = k_0 + B_1 \sigma^{1-n_2} / c_i^m \quad (9.42)$$

where $m = m_i$ and $B_1 = B m / c_i^{*m}$. Equation (9.42) shows that k_{eff} depends on n_2 , σ and c_i . However, when $m_i(c_i/c_i^*)^{m_i} \ll m_s(c_s/c_s^*)^{m_s}$, Equation (9.41) takes the form

$$k_{\text{eff}} = k_0 + B_2 \sigma^{1-n_2} \quad (9.43)$$

where $B_2 = B / m_s(c_s/c_s^*)^{m_s}$. Obviously, in this case k_{eff} depends on σ and n_2 .

When the fractional surface coverage θ_j for the component j is given by the Langmuir adsorption isotherm, i.e.

$$\theta_j = K_j c_j / (1 + K_j c_j) \quad (9.44)$$

Equation (9.35) is given by

$$k_{\text{eff}} = k_0 + \frac{B \sigma^{1-n_2}}{K_s c_s + K_i c_i} \quad (9.45)$$

In Equation (9.45) the constant B is given by Equation (9.40), and the Langmuir constant

$$K_j = \exp(Q_{\text{diff},j}/R_G T) \quad (9.46)$$

When $K_s c_s \ll K_i c_i$, one obtains

$$k_{\text{eff}} = k_0 + B' \sigma^{1-n_2} / c_i \quad (9.47)$$

where $B' = B/K_i$. However, when $K_s c_s \gg K_i c_i$,

$$k_{\text{eff}} = k_0 + B'' \sigma^{1-n_2} \quad (9.48)$$

where $B'' = B/K_s c_s$. Note that Equations (9.42) and (9.43) transform, respectively, to Equations (9.46) and (9.48) when $m = 1$.

The predictions of the theoretical equations may be verified by constructing plots of k_{eff} against σ by arbitrarily taking different values of k_0 , $B'' = B_2$, and n_2 such that the $k_{\text{eff}}(\sigma)$ plots reproduce situations observed experimentally when $k_0 < 1$ and $k_0 > 1$. An example of the predicted plots of the dependence of k_{eff} on σ for $B_2 > 0$ in Equation (9.43) is illustrated in Figure 9.16 for different values of n_2 . The plots reveal that k_{eff} increases linearly when $n_2 = 0$. However, they show positive deviations (i.e. downward curvatures) from linearity when $n_2 < 0$, and negative deviations (i.e. upward curvatures) when $n_2 > 0$. Moreover, as seen from the positive deviations, the nature of the $k_{\text{eff}}(\sigma)$ plots is very sensitive to the value of n_2 for $-\frac{1}{2} < n_2 < \frac{1}{2}$, and also depends on the value of B_2 .

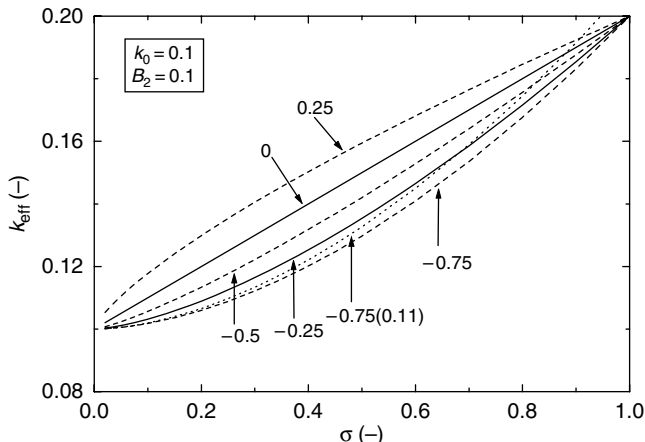


Figure 9.16 Illustrative plots of the dependence of k_{eff} of additive in an imaginary crystal on supersaturation σ predicted from Equation (9.43) for different values of n_2 with constant $B_2 > 0$. This case represents $k_0 < 1$. Adapted from Sangwal and Pałczyńska (2000)

Figure 9.16 presents the experimental situation when $k_0 < 1$; then $B_2 > 0$. However, when $k_0 > 1$, k_{eff} decreases with an increase in σ , i.e. $B_2 < 0$. Then the trends of n_2 are also reversed. In the situation of $k_0 > 1$, the downward curvature is represented by

positive values of n_2 , while the upward curvature by negative n_2 . These trends are seen in Figure 9.15. Thus, the constant n_2 is a measure of deviation of the $k_{\text{eff}}(\sigma)$ plot from linearity, which occurs when $n_2 = 0$. It may be argued (Sangwal and Pałczyńska, 2000) that when $k_0 < 1$ (i.e. $B_2 > 0$), $n_2 < 0$ is a consequence of depletion of solute molecules in the vicinity of kinks. Then k_{eff} increases with increase in σ . However, when $k_0 > 1$ (i.e. $B_2 < 0$), $n_2 > 0$ is a result of the accumulation of solute molecules in the vicinity of kinks. In this case, k_{eff} decreases with increase in σ .

The predicted trends of the $k_{\text{eff}}(\sigma)$ plots in Figure 9.16 are consistent with the linear $k_{\text{eff}}(\sigma)$ dependences observed for Cd^{2+} and several lanthanide ions in gypsum (de Vreugd *et al.*, 1994), Fe^{3+} and Ce^{3+} ions in potassium acid phthalate (Hottenhuis and Oude-nampsen, 1988), and Cu^{2+} , Fe^{3+} and Cr^{3+} ions in ammonium oxalate monohydrate crystals (Mielińczek-Brzóska *et al.*, 2000; Sangwal *et al.*, 2002), and also with the curvatures in the $k_{\text{eff}}(\sigma)$ plots for CrO_4^{2-} ions in potassium sulfate and Ni^{2+} ions in zinc potassium sulfate hexahydrate crystals; see Figure 9.15 (Zhmurova and Khaimov-Mal'kov, 1970b).

The upward curvature in the plot of k_{eff} of Pb^{2+} impurity as a function of σ observed in the case of barium nitrate crystals (Figure 9.14) is unusual, because the best fit of the data gives $1 - n_2 \approx 0.46$, i.e. $n_2 = 0.54$. Since in the $\text{Ba}(\text{NO}_3)_2(\text{Pb}^{2+})$ system $k_0 < 1$, the positive value of n_2 for this system is unexpected. The reason of this anomalous behavior is associated with a different impurity incorporation mechanism, as discussed in Section 9.3.2.

In Figure 9.15a and b, the best-fit plots of the $k_{\text{eff}}(\sigma)$ data are shown by continuous and dashed curves for two different values of n_2 . It can be seen that, except for the $k_{\text{eff}}(\sigma)$ data at very low values of σ (below about 0.02), both values of n_2 fit the data satisfactorily. However, the best fit, with least variations in both k_0 and B_2 , is observed when $0.3 < n_2 < 0.6$. This suggests that $n_2 \approx |0.5|$, and $K_s c_s \gg K_i c_i$ in Equation (9.45).

Figure 9.17 shows a typical example of the dependence of the effective segregation coefficient k_{eff} of Cu^{2+} impurity in AO crystals on supersaturation σ for different

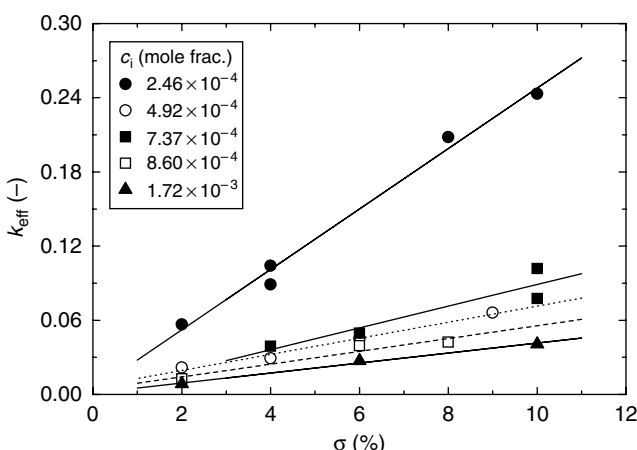


Figure 9.17 Segregation coefficient k_{eff} of Cu^{2+} ions in AO crystals as a function of supersaturation σ for different impurity concentrations c_i . Reproduced from E. Mielińczek-Brzóska, K. Giełzak-Koćwin, and K. Sangwal. J. Cryst. Growth **212**, 532. Copyright (2000), with permission from Elsevier

concentrations c_i of the impurity. It can be seen that the plots essentially pass through the origin (i.e. $\sigma = 0$), and k_{eff} increases linearly with increasing σ for all concentrations c_i of the impurity. This observation means that the thermodynamic segregation coefficient in this case is close to zero. A similar behavior was found for Fe^{3+} impurity. In the case of Cr^{3+} impurity, however, although the plots of k_{eff} against σ were linear as for Cu^{2+} and Fe^{3+} impurities, the origin was shifted to a supersaturation value $\sigma \approx 0.03$. This different behavior of Cr^{3+} impurity is due to the existence of a threshold supersaturation barrier σ_d (i.e. dead supersaturation zone) during the growth of AO crystals in the presence of this impurity (see Section 9.4).

Figure 9.18 shows the plots of segregation coefficient k_{eff} of various lanthanides and Cd^{2+} in gypsum crystals as a function of supersaturation σ . Irrespective of the charge on a cation, the value of k_{eff} for an impurity increases practically linearly with increasing σ . Despite the steep slopes of the plots for lanthanides, the equilibrium segregation coefficient k_0 cannot be obtained from the extrapolation of the plots mainly because of large scatter in the data at low σ (also see Section 9.5).

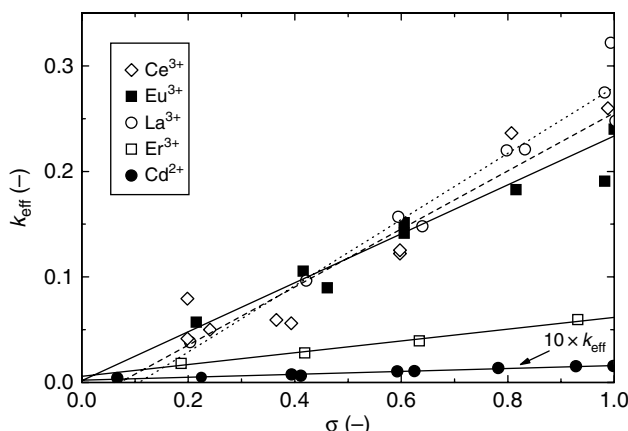


Figure 9.18 Segregation coefficient k_{eff} of various lanthanides in gypsum crystals as a function of supersaturation σ . Impurity concentration: 3×10^{-4} M lanthanides and 4.4×10^{-4} M Cd^{2+} . Adapted from de Vreugd et al. (1994)

As can be seen from Figure 9.18, the k_{eff} values for the lanthanides in gypsum crystals are typically of the order of 0.1, and about 100 times larger than that for Cd^{2+} . A higher value of k_{eff} than that of Cd^{2+} is also expected for lanthanides because their sulfates have lower solubility than that of cadmium sulfate. The high values of k_{eff} of lanthanides in gypsum may also be associated with their strong electrostatic interaction with sulfate ions at the surface due to their charge.

A general feature of the $k_{\text{eff}}(\sigma, c_i)$ results is that, at a given supersaturation σ , k_{eff} of an impurity decreases with increasing c_i of the impurity (see Figure 9.17). It is observed that the value of k_{eff} of an impurity also decreases with an increase in its concentration c_i , when the growth system contains another impurity having k_{eff} lower than that of the investigated impurity. As an example, Figure 9.19 shows the dependence of the

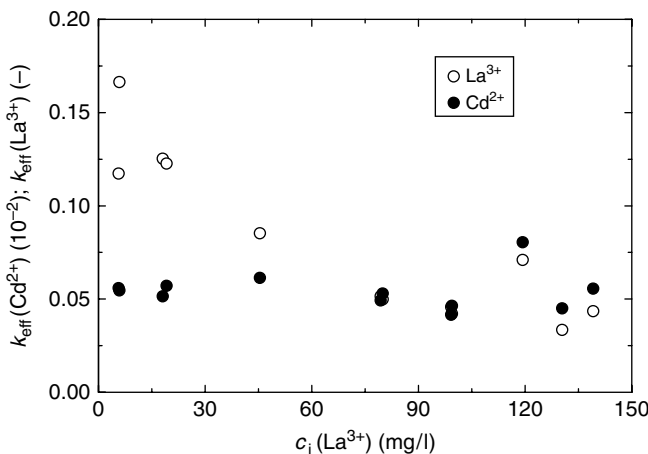


Figure 9.19 Segregation coefficient k_{eff} of Cd^{2+} and La^{3+} in gypsum crystals from solutions containing $4.4 \times 10^{-4} \text{ M } \text{Cd}^{2+}$ as a function of concentration c_i of La^{3+} ; growth supersaturation $\sigma = 0.4$. Adapted from de Vreugd et al. (1994)

segregation coefficient k_{eff} of La^{3+} ions in gypsum crystals grown at a σ of 0.4 from aqueous solutions containing $4.4 \times 10^{-4} \text{ M } \text{Cd}^{2+}$ as a function of concentration c_i of La^{3+} . The figure shows that, in the entire investigated interval of La^{3+} concentration up to 10^{-3} M (i.e. 150 mg/l), the value of k_{eff} of La^{3+} decreases with increase in c_i of La^{3+} ions. A plot of growth rate R as a function of c_i of La^{3+} also shows a similar trend, which can be described by a linear dependence of $R_0/(R_0 - R)$ on $1/c_i$, as expected from the Kubota–Mullin model of adsorption of impurity particles at kinks [see Equation (4.43); Section 4.3]. These observations are consistent with the general concept that incorporation of impurities is connected with growth kinetics, and both are determined by the adsorption behavior of the impurities on growing surfaces.

As mentioned above, the k_{eff} value for Cd^{2+} in gypsum is about 100 times lower than that of La^{3+} ions. Figure 9.19 shows that, in the investigated interval of La^{3+} concentration, the value of k_{eff} of Cd^{2+} remains practically constant at 6×10^{-4} . This implies that the presence of La^{3+} ions in the solution has an insignificant effect on the k_{eff} value of Cd^{2+} . This is probably due to the fact that, at the given supersaturation value, the value of k_{eff} of Cd^{2+} ions is already close to its thermodynamic value of 3×10^{-4} .

A decrease in the value of k_{eff} of an impurity with an increase in its concentration c_i is also observed in *n*-alkane mixtures crystallized by rapid cooling of their solutions in organic solvents. Figure 9.20 illustrates the plots of segregation coefficients k_{eff} of ethylene–vinyl acetate (EVA) copolymer in crystals of two *n*-alkane mixtures as a function of EVA concentration c_i in ethylbenzene and kerosene solvents. The first crystals were obtained from a 5 wt% solution of 1:2:1 mixture of eicosane, docosane and tetracosane in ethylbenzene, and the second crystals from a 4 wt% solution of a tetracosane-centered *n*-alkane mixture in kerosene. It can be seen that the value of k_{eff} decreases rapidly with an increase in the concentration c_i of EVA in kerosene, but an insignificant decrease with an increase in c_i of EVA occurs in ethylbenzene. Since the solubility of EVA in kerosene is much lower than that in ethylbenzene, the observed

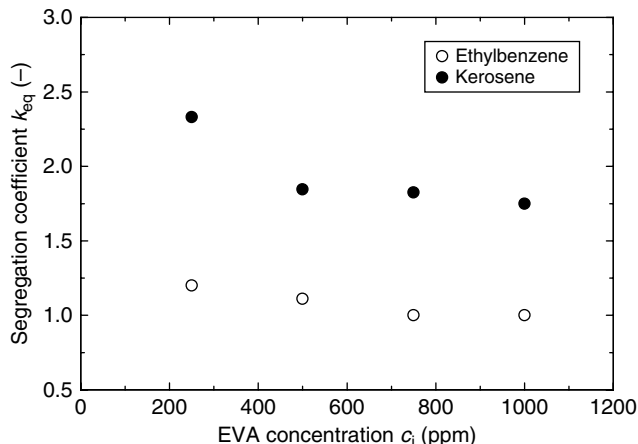


Figure 9.20 Segregation coefficient k_{eff} of EVA copolymer in *n*-alkane crystals as a function of EVA concentration c_i in ethylbenzene and kerosene solvents. See text for details. Data from Marie et al. (2005)

difference in the $k_{\text{eff}}(c_i)$ dependence may be explained in terms of the ratio $x_{iL}^{\text{sat}}/x_{sL}^{\text{sat}}$, as expected for the equilibrium segregation coefficient k_0 [see Equation (9.14)].

The original $k_{\text{eff}}(\sigma_{\text{eff}})$ data for Cu^{2+} and Fe^{3+} in AO crystals are illustrated in Figure 9.21 in the form of plots of k_{eff} as a function of σ/c_i^m [see Equation (9.42)]. Note that $k_0 \approx 0$ for the two impurities, because the $k_{\text{eff}}(\sigma)$ plots practically pass through the origin with $\sigma = 0$. This enables one to compare qualitatively the incorporation behavior of the two impurities from the values of the differential heat of adsorption Q_{diff} obtained

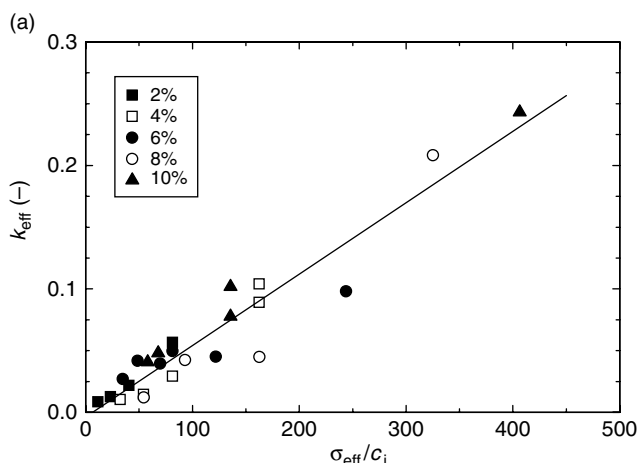


Figure 9.21 Plots of k_{eff} for (a) Cu^{2+} and (b) Fe^{3+} in AO crystals against $\sigma_{\text{eff}}/c_i^m$. Reproduced from K. Sangwal, E. Mielniczek-Brzóska, and J. Borc. *J. Cryst. Growth* **244**, 183. Copyright (2002), with permission from Elsevier

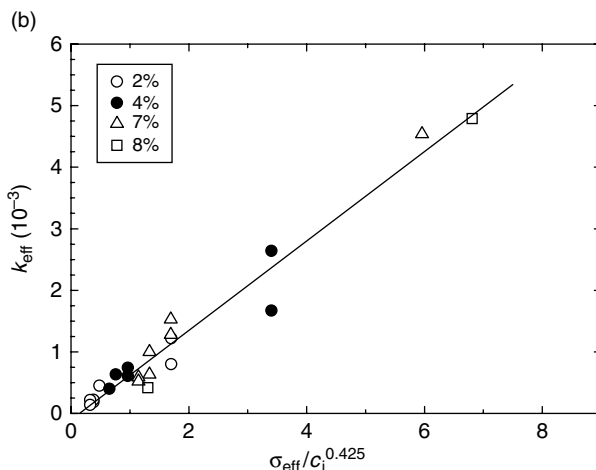


Figure 9.21 (Continued)

from the slope B_1 and the exponent m of the plots of their k_{eff} as a function of σ/c_i^m . This may be done by assuming that the fractional coverage θ by different impurities is the same. The value of coverage θ may be calculated for an impurity for which $m = 1$, and hence the Langmuir constant $K = B/B_1$ and Q_{diff} [cf. Equations (9.42), (9.45) and (9.46)]. The constant $B = 0.02$ may be estimated from Equation (9.40) by taking $n_2 = 0$ and $\gamma_l/k_B T = W_0/k_B T = 1$. For Cu^{2+} , one finds $\theta = 0.029$. The calculated values of Q_{diff} are 8.9 and 20.8 kJ/mol for Cu^{2+} and Fe^{3+} impurities, respectively. This suggests that the higher the value of Q_{diff} for an impurity, the lower is its incorporation capability in the crystal. Thus, the observed trends of the incorporation of different impurities may be discussed from the standpoint of processes of adsorption of impurities.

During the growth of crystals from solutions containing impurities, the adsorbing species form bonds with the solute molecules/ions in the crystal plane (Section 4.11). The stability of the complex formed between the adsorbing complex and the surface molecules/ions determines the growth kinetics. The higher the stability of the adsorbed complex, the greater is its effectiveness in reducing growth rates. However, the process of removal of the adsorption complex determines the capability of incorporation of the impurity particles ions in the crystal. These two processes determine the differential heat of adsorption (Section 4.2.1)

$$Q_{\text{diff}} = Q_{\text{ad}} - Q_{\text{des}} \quad (9.49)$$

where Q_{ad} is the heat of adsorption of impurity species adsorbed on the surface and Q_{des} is the heat of dissolution (dissociation) of the adsorbed impurity species. The values of Q_{ad} and Q_{des} determine the values of k_{eff} of different impurities in crystals. Since the values of Q_{ad} and Q_{des} determine the frequencies of attachment and detachment of host and impurity particles (Section 4.1), one sees a connection between surface adsorption and statistical selection approaches.

9.4 Relationship Between Effective Segregation Coefficient and Face Growth Rate

Volume diffusion and diffusional relaxation approaches of capture of impurities describe the dependence of effective segregation coefficient k_{eff} on the interface or face growth rate R , but statistical selection and surface adsorption approaches relate k_{eff} to supersaturation σ . Since the growth rate R depends on σ , the $k_{\text{eff}}(R)$ dependences of the former approaches can equally be represented by $k_{\text{eff}}(\sigma)$ dependences, and the $k_{\text{eff}}(\sigma)$ dependences of the latter approaches by $k_{\text{eff}}(R)$ relations. In this section, some features of the experimental $k_{\text{eff}}(R)$ data for different growth systems are presented. However, when discussing the nature of the $k_{\text{eff}}(\sigma)$ dependences of different approaches, it is assumed that $k_0 < 1$ (i.e. $B_2 > 0$) in Equation (9.43), $\delta/D > 0$ in Equation (9.26), and $k_{\text{ads}} > k_0$ in Equation (9.29).

The supersaturation dependence of the face growth rate of a crystal in the presence of an impurity follows the empirical relation [see Equation (5.18); Section 5.2.2]

$$R \approx A(\sigma - \sigma_c)^n \quad (9.50)$$

where A is a constant, σ_c is a supersaturation barrier beyond which growth kinetics may be described by $R(\sigma)$ relations for pure system, and the exponent n lies between 1 and 2. Substituting the value of σ from Equation (9.50) in Equation (9.42), one obtains

$$k_{\text{eff}} = \left(k_0 + \frac{B_1 \sigma_c}{c_i^m} \right) + \frac{B_1}{A^{1/n} c_i^m} R^{1/n} \quad (9.51)$$

Equation (9.51) predicts that a plot of k_{eff} against $R^{1/n}$ gives slope $B_1/A^{1/n} c_i^m$ and intercept $(k_0 + B_1 \sigma_c/c_i^m) \geq 0$. The values of the slope $B_1/A^{1/n} c_i^m$ and the intercept $(k_0 + B_1 \sigma_c/c_i^m)$ increase with decreasing c_i . The important prediction of Equation (9.51) is that k_{eff} increases linearly with R when $n = 1$ (i.e. $R \propto \sigma$), but it approaches a constant value asymptotically when $n = 1/2$ (i.e. $R \propto \sigma^2$). Depending on the value of n , other intermediate cases are also possible.

Here it should be recalled that $R \propto \sigma$ (i.e. $n = 1$) when the growth interface is rough or a cooperating source of screw dislocations is operative. The former situation is usually encountered in melt growth and in growth from solutions at high σ as a result of either creation of bundles of dislocations by liquid inclusions or kinetic roughening due to high σ (see Sections 3.3, 3.4 and 3.6). The latter situation, on the other hand, occurs when the growth interface is smooth and the supersatuation for growth is low (Section 3.6).

According to the volume diffusion approach, there are two extreme cases (Section 9.3.1): (1) k_{eff} of an impurity increases linearly with R and (2) k_{eff} increases practically exponentially with increasing R , implying that k_{eff} increases progressively with increasing R , as shown in Figure 9.11. The main feature of this approach is that the value of k_{eff} decreases with increase in stirring rate. The diffusional relaxation approach also predicts an increase in k_{eff} of an impurity with increasing R , but stirring does not alter the value of k_{eff} .

Figure 9.22 illustrates an example of the dependence of effective segregation coefficient k_{eff} of three rare earth ions (Nd^{3+} , Sm^{3+} and Er^{3+}) in cubic zirconium dioxide crystals

grown by the scull melting technique on their growth rate R controlled with a precision of 1 mm/h by reduction of the radiofrequency (RF) heating combined with crucible lowering out of the RF field. Irrespective of the scatter in the data, a linear dependence of k_{eff} on R for the three impurities, with the extrapolated values of the equilibrium segregation coefficient k_0 equal to 0.446 ± 0.014 , 0.571 ± 0.017 and 1.091 ± 0.005 for Nd^{3+} , Sm^{3+} and Er^{3+} ions, respectively, may be noted. These extrapolated values of k_0 agree well with those obtained by the graphical solutions of the BPS Equation (9.26) (Burton *et al.*, 1953) by Römer *et al.* (1994). Therefore, it may be concluded that, when the BPS volume diffusion approach applies, it is sufficient to use the simplified linear $k_{\text{eff}}(R)$ dependence to estimate k_0 for these impurities.

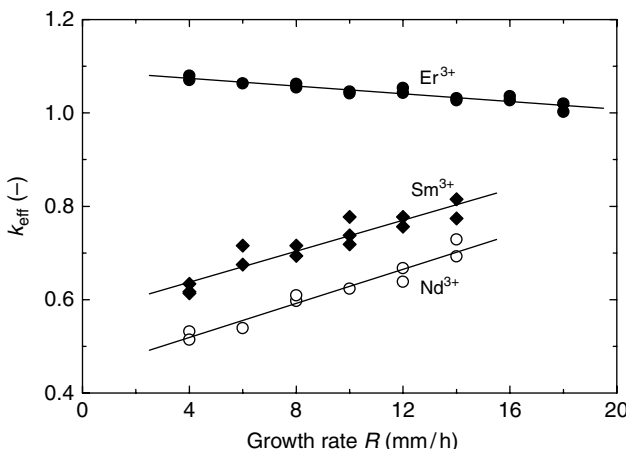


Figure 9.22 Dependence of effective segregation coefficient k_{eff} of three rare earth ions in cubic zirconium dioxide crystals on growth rate R . The crystals were grown by the scull melting technique. Data from Römer *et al.* (1994)

Assuming that the BPS equation applies, one finds that $\delta/D = 1475$, 1045 and 140 s/cm for Nd^{3+} , Sm^{3+} and Er^{3+} ions, respectively. As before in Section 3.3.1, if one takes $D \approx 10^{-9} \text{ cm}^2/\text{s}$, one obtains $\delta \approx 15$, 10 and 1.4 nm for the above three ions, respectively. These values of δ are reasonable for the capture of impurity ions by bulk diffusion during the growth of ZrO_2 in the scull crucible.

The radii r_i of Nd^{3+} , Sm^{3+} and Er^{3+} ions are 0.112, 0.109 and 0.100 nm, respectively. This implies that the diffusion layer thickness δ increases with increasing ionic radius r_i , and is associated with the mobility of ions in the melt. The higher the mobility of ions in the melt, the smaller is the thickness of the diffusion layer.

Examples of the linear dependence of k_{eff} of impurities in crystals having enormously different solubilities in water on their growth rate R are illustrated in Figures 9.23 and 9.24. Figure 9.23 shows the plot of k_{eff} of La^{3+} ions in crystals of sparingly soluble gypsum as a function of the overall growth rate R . A linear $k_{\text{eff}}(R)$ dependence is evident, but extrapolation of the plot to $R = 0$ does not enable one to calculate the value of k_0 due to a large scatter in the data.

Fig. 9.24 shows the plots of the effective segregation coefficient k_{eff} of $\text{Fe}(\text{III})$ impurity in crystals of fairly soluble ammonium oxalate monohydrate at different impurity

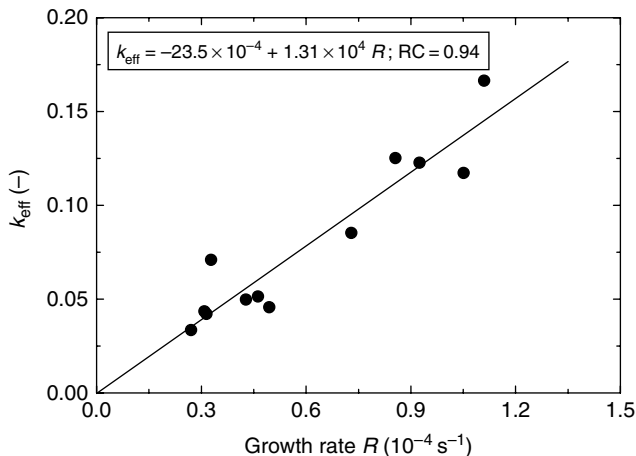


Figure 9.23 Dependence of k_{eff} of La^{3+} ions in gypsum crystals on growth rate R . Original data from de Vreugd et al. (1994)

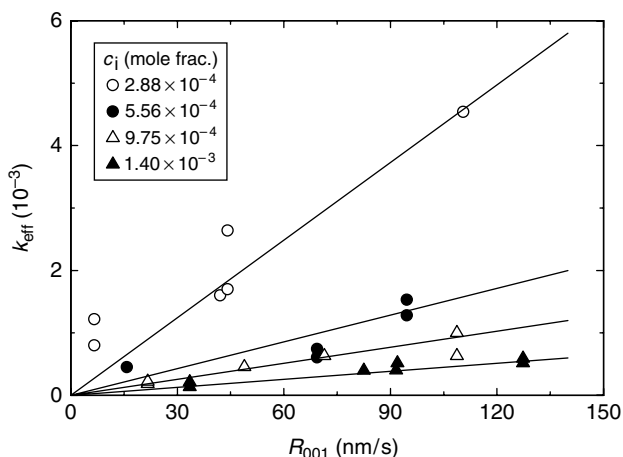


Figure 9.24 Plots of effective segregation coefficient k_{eff} of Fe^{3+} impurity at different impurity concentration c_i against growth rate R of AO crystals along the $\langle 001 \rangle$ direction. Reproduced from K. Sangwal and E. Mielniczek-Brzóska. J. Cryst. Growth **257**, 185. Copyright (2003), with permission from Elsevier

concentrations c_i against the growth rate R along the $\langle 001 \rangle$ direction. The $k_{\text{eff}}(R)$ data indicate that the value of k_{eff} corresponding to $R = 0$ decreases with increase in impurity concentration c_i . However, because of scatter in the k_{eff} values, as in the case of La^{3+} ions in gypsum, it is difficult to determine the equilibrium segregation coefficient k_0 from the $k_{\text{eff}}(R)$ plots for different c_i , and the plots practically pass through the origin.

Results of the dependence of k_{eff} of Cu^{2+} impurity in AO crystals on growth rate R along the $\langle 001 \rangle$ direction have also been reported and analyzed (Mielniczek-Brzóska

et al., 2000). These results are similar to those in Figure 9.24. Analysis of these $k_{\text{eff}}(R)$ data for Cu²⁺ ions according to the BPS Equation (9.26) suggested that the values of k_0 and δ/D are not constant, and that k_0 increases whereas δ/D decreases with increase in supersaturation σ . A decrease in the value of δ/D with increasing supersaturation implies that either the diffusion-layer thickness δ decreases or the diffusion constant D increases. This inference is contrary to the known behavior of δ and D with increasing solute concentration in solutions (Myerson, 1993). Moreover, in contrast to the inference made from analysis of the $k_{\text{eff}}(R)$ data using the BPS Equation (9.26), k_0 should be a constant quantity independent of σ . Thus, it may be concluded that, in the case of fairly soluble AO crystals, the $k_{\text{eff}}(R)$ dependence for Cu²⁺ and Fe³⁺ impurities on growth rate cannot be described by the BPS model based on mass transport involving volume diffusion.

According to the diffusional relaxation approach, k_{eff} increases either exponentially or linearly with inverse of R [see Equations (9.29) and (9.31)]. However, in AO crystals the experimental data for Cu²⁺ and Fe³⁺ impurities do not support such dependences. Hence this model also can be excluded.

In the above examples of the dependence of k_{eff} of impurities in zirconium dioxide, gypsum and AO crystals, it was implied that the incorporation of an impurity in the crystal and its growth rate are isotropic. This situation is true in the first two crystals. In the case of AO, however, the values of k_{eff} are for global impurity capture, whereas the growth rate data are for different faces. Therefore, the behavior of the $k_{\text{eff}}(R)$ plots for growth of different faces of AO crystals differs from each other (Sangwal and Miśniczek-Brzóska, 2003).

9.5 Threshold Supersaturation for Trapping of Impurities During Growth

The dependence of the effective segregation coefficient k_{eff} of different impurities in the crystals of even the same compound on supersaturation σ exhibits different trends. For instance, in the case of the growth of AO crystals, the values of k_{eff} of Cu(II) and Fe(III) impurities increases linearly with σ and all the $k_{\text{eff}}(\sigma)$ plots essentially pass through the origin (i.e. $\sigma_0 = 0$). Cr(III) impurity also exhibits a similar behavior, but the linear $k_{\text{eff}}(\sigma)$ plots showed a threshold supersaturation $\sigma_0 > 0$. In contrast to the above impurities, a completely different behavior was noted for Mn(II) impurity. In this case, irrespective of impurity concentration c_i , the plots of k_{eff} against σ show two distinct dependences, as illustrated in Figure 9.25.

In the range $k_{\text{eff}} < 5 \times 10^{-4}$, the $k_{\text{eff}}(\sigma)$ data for different c_i appear to follow practically the same linear plot. This implies that the slope $\Delta k_{\text{eff}}/\Delta\sigma$ of the $k_{\text{eff}}(\sigma)$ plots in this region practically does not depend on impurity concentration c_i , although the existence of a threshold supersaturation σ_d cannot be excluded in this k_{eff} range. In contrast to the low k_{eff} range of Mn(II) impurity, in the range $k_{\text{eff}} > 5 \times 10^{-4}$ the $k_{\text{eff}}(\sigma)$ data for different c_i follow different linear plots, which intersect the σ -axis at different threshold values σ_0 . In this k_{eff} range, the $k_{\text{eff}}(\sigma)$ data follow the empirical relation

$$k_{\text{eff}} = p(\sigma - \sigma_0) \quad (9.52)$$

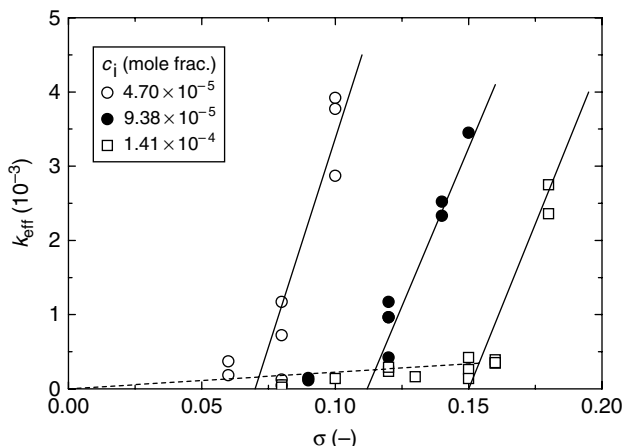


Figure 9.25 Plots of k_{eff} of Mn(II) ions in AO crystals against σ for different c_i . Note two distinct linear dependences in the ranges $k_{\text{eff}} < 5 \times 10^{-4}$ and $k_{\text{eff}} > 5 \times 10^{-4}$. Reproduced from K. Sangwal and E. Mielniczek-Brzóska. J. Cryst. Growth **257**, 185. Copyright (2003), with permission from Elsevier

where p is the slope of the $k_{\text{eff}}(\sigma)$ plot and σ_0 is the threshold supersaturation when k_{eff} shows an abrupt increase with σ . The value of the threshold supersaturation σ_0 increases with increasing concentration c_i of Mn(II) impurity, but the slope p of the plots is practically constant at $(9.6 \pm 1.1) \times 10^{-2}$, and does not depend on impurity concentration c_i . This value of the slope is about four times higher than that at low k_{eff} .

The dependence of σ_0 on c_i is similar to that of supersaturation barriers σ_d and σ^* observed during the growth of crystals from solutions (see Section 5.3). In fact, it is observed that, for a given concentration c_i of an impurity, the threshold supersaturation $\sigma_0 = \sigma^*$. This means that strong incorporation of impurities during crystal growth from solutions is associated with the onset of time-dependent impurity adsorption, and occurs when there is a sudden increase in the face growth rate R . As discussed in Section 5.3, when the Langmuir adsorption isotherm applies for an impurity, the relationship between threshold barrier σ^* and impurity concentration c_i may be written in the form [see Equation (5.23)]

$$\frac{1}{\sigma^*} = \frac{1}{\sigma^0} \left(1 + \frac{1}{Kc_i} \right) \quad (9.53)$$

where σ^0 is given by

$$\sigma^0 = \gamma_l a / kT\lambda \quad (9.54)$$

γ_l is the linear step free energy and λ is the average distance between possible adsorption sites. Figure 9.26 shows the plot of $1/\sigma_0$ and $1/\sigma^*$ versus $1/c_i$ of Mn²⁺ impurity according to Equation (9.53). The best fit for the $\sigma^*(c_i)$ data gives $\sigma^0 = 0.24$, $K = 8525$ and $Q_{\text{diff}} = 22.8 \text{ kJ/mol}$. Assuming that γ_l/kT , one finds $\lambda \approx 4a$ as the upper limit for the surface coverage when time-dependent adsorption sets in.

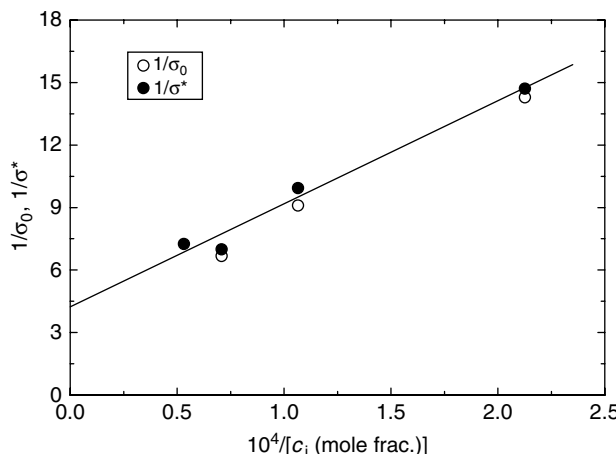


Figure 9.26 Dependence of $1/\sigma_0$ and $1/\sigma^*$ on $1/c_i$ of Mn^{2+} impurity according to Equation (9.53). The plot was drawn for $\sigma^*(c_i)$ data. Reproduced from K. Sangwal and E. Mielniczek-Brzóska. J. Cryst. Growth 257, 185. Copyright (2003), with permission from Elsevier

Two different types of $k_{\text{eff}}(R)$ dependences for $\sigma < \sigma^*$ and $\sigma > \sigma^*$ are associated with steady-state and time-dependent adsorption of impurities, respectively. These regions of supersaturation σ are also distinguished by the surface morphology. For $\sigma < \sigma^*$, the growing surface remains relatively smooth, but for $\sigma > \sigma^*$ a change in the mechanism of impurity adsorption leads to the bunching of growth steps (Rashkovich and Kronsky, 1997). This bunching of steps favors intense incorporation of the adsorbed impurity.

As described in Section 9.3, the stability of the surface complex formed between an adsorbing complex and surface ions determines the crystal growth kinetics, while the process of removal of the surface complex determines the capability of incorporation of M^{z+} ions in the crystal. These two processes determine the differential heat of adsorption Q_{diff} , which is equal to the heat of adsorption Q_{ad} of impurity species adsorbed on the surface minus the heat of their dissolution Q_{des} . The relative values of Q_{ad} and Q_{des} determine the values of k_{eff} of an impurity adsorbing according to two different adsorption mechanisms for $\sigma < \sigma^*$ and $\sigma > \sigma^*$.

Rashkovich and Kronsky (1997) proposed that the appearance of σ^* is associated with the burial of adsorbed impurity particles as a result of curling of advancing steps around them. According to these authors, when the depth of the bent step (indentation) reaches a value d , the indentation collapses and the advancing step covers the impurity particle. This happens at $\sigma = \sigma^*$ when the critical nucleus diameter $2r_{2D}^* \propto \sigma^{-1}$ becomes equal to the average distance l^* between the adsorbed impurity particles (Section 5.3). The number of particles in the indentations per unit length $c_{l^*} = c_i d$, and the average distance l^* between them is $c_{l^*}^{-1}$. Therefore, $\sigma^* \propto c_i d$. Since the relationship between indentation depth d and σ is of the type $d \propto \sigma^{-m}$ (where $0 < m < 1$), one has $\sigma^* \propto c_i^{1/(1+m)}$. This feature is consistent with the experimental dependence of σ^* on c_i in terms of Freundlich adsorption isotherm (Section 9.3.4).

It should be mentioned that the capture of impurity particles associated with their time-dependent adsorption on the surface of a growing crystal provides a chemical picture of the incorporation process. However, the collapse of bent step and trapping of impurity particles adsorbed on the surface is a physical picture of the segregation process.

9.6 Effective Segregation Coefficient and Internal Stresses Caused by Impurities

Impurity and solute species are usually different in size and coordination and/or charge, but they can also differ in their shape. These dissimilarities are the causes of distortion in the lattice of the host crystal. There are at least two side-effects of the lattice distortions by captured impurities: (1) they increase the solubility of the host and (2) they increase the chemical potential of the host in the deformed region. The basis of these effects is explained below.

When lattice strain associated with impurity capture changes the chemical potential μ_s of the crystal in the vicinity of a kink site, the overall chemical potential difference $\Delta\mu_{is}$ is decreased [cf. Equation (9.18)]. This results in an increase in the inhibiting effect of the impurity, thereby increasing the segregation coefficient k_d .

It is well known (Dove *et al.*, 2004) that greater the amount of Mg^{2+} present in the calcite lattice, the higher is the solubility of calcite. Since the mechanism of inhibition of calcite growth involves the adsorption of Mg^{2+} ions at kink sites prior to dehydration and incorporation, this means that the higher energy required for the dehydration of Mg^{2+} at the kinks in the calcite surface is the rate-controlling step in calcite growth. The main tenet of this mechanism is that dehydration of growth units is usually the rate-limiting step in the crystallization of ionic compounds. In any case, the increase in solubility leads to an increase in the segregation coefficient k_d [see Equation (9.18)].

Lattice strain in small crystals may be determined from asterism associated with radial spread of reflections in Laue diffraction patterns. The radial spread in the Laue spots from a crystal at different reflections enables one to obtain the so-called average mosaic spread for the crystal (Ristić *et al.*, 1988). Prasad *et al.* (2001) reported experimental data on the effective segregation coefficient k_{eff} of PAA (*p*-acetoxyacetanilide), mosaic spread η of paracetamol (acetaminophen) microcrystals, and interfacial tension γ (from the dependence of the induction period on σ) for different concentrations c_i of PAA. It was found that (1) the effective segregation coefficient k_{eff} of PAA lies between 0.14 and 0.18, with a slight increase with increase in supersaturation σ and an increase followed by a decrease in k_{eff} with increase in c_i , and (2) the degree of lattice distortion increases with increase in c_i of PAA, the increase being more pronounced at lower than at higher c_i . The relationship between the effective segregation coefficient k_{eff} of PAA additive in paracetamol crystals with mosaic spread η is shown in Figure 9.27. Obviously, not only is the dependence complex, but also the maximum impurity incorporation occurs at a particular value of c_i of about 3 wt%.

The PAA molecule is 1.24 times larger in volume than a paracetamol molecule. A natural consequence of the incorporation of a PAA molecule in paracetamol crystals is the introduction of lattice strain in them. An average effective segregation coefficient

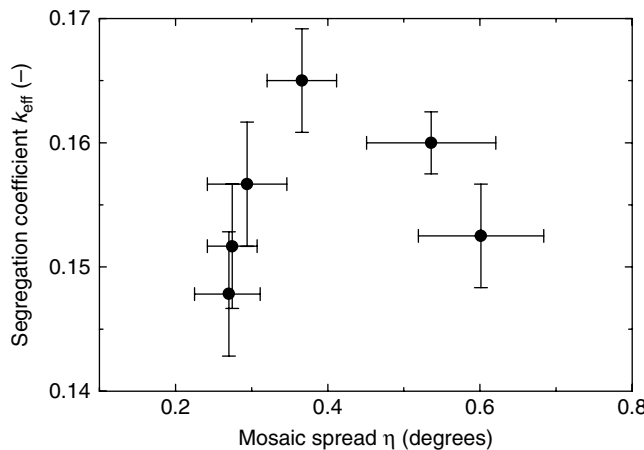


Figure 9.27 Relationship between effective segregation coefficient k_{eff} of PAA additive in paracetamol crystals and mosaic spread η . Data from Prasad et al. (2001)

k_{eff} of 0.16 means that one PAA molecule occupies the position occupied by a paracetamol molecule in its solid solution. These facts mean that the incorporation of PAA in paracetamol crystals results in 3–4% lattice distortion. Unlike in plastic materials, where lattice strain can be released by plastic deformation, the strain in paracetamol crystals is retained because they are brittle. This results in a significant increase in the mosaic spread.

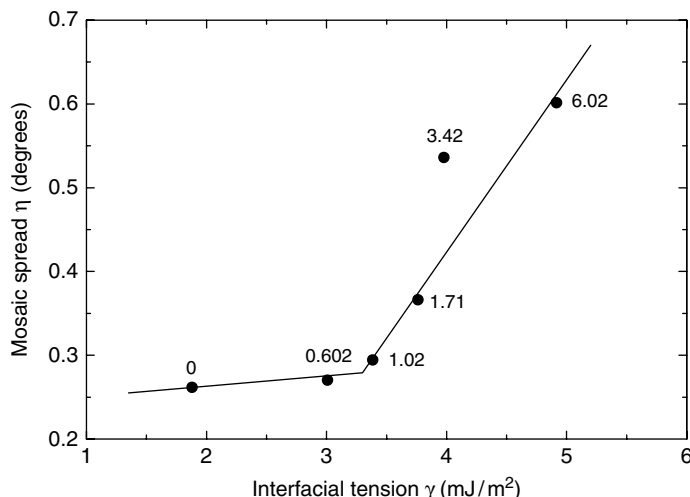


Figure 9.28 Dependence of mosaic spread η in paracetamol crystals containing PAA additive on interfacial tension γ obtained from induction period data. PAA concentration for different data is in wt%. Data from Prasad et al. (2001)

Figure 9.28 shows the dependence of mosaic spread η in paracetamol crystals containing PAA additive on their interfacial tension γ obtained from induction period data. Obviously, for PAA concentration $c_i > 0.6 \text{ wt\%}$ (i.e. for $\gamma > 3 \text{ mJ/m}^2$), the mosaic spread increases practically linearly with increasing γ . This dependence is associated with the inhibition of the development of 3D paracetamol nuclei to their critical sizes r_{3D}^* by PAA molecules. This is due to the fact that PAA molecules differ from paracetamol molecules by the substitution of the phenolic hydroxyl groups with acetyl groups. During nucleation, similar parts of PAA and paracetamol molecules join to form nuclei but dissimilar parts do not, thereby suppressing the nucleation rate, increasing the induction period, and increasing the interfacial tension (see Section 2.2). However, a relatively small mosaic spread for $c_i < 1 \text{ wt\%}$ is probably due to lower incorporation of PAA in the crystals.

References

- Brice, J.C. (1973). *The Growth of Crystals from Liquids*, North-Holland, Amsterdam.
- Brice, J.C. (1975). *J. Cryst. Growth* **28**, 249.
- Burton, J.A., R.C. Prim, and W.P. Slichter (1953). *J. Chem. Phys.* **21**, 1987.
- Chernov, A.A. (1984). *Modern Crystallography III: Crystal Growth*, Springer, Berlin.
- de Vreugd, C.H., G.J. Witkamp, and G.M. van Rosmalen (1994). *J. Cryst. Growth* **144**, 70.
- Dove, P.M., J.J. De Yoreo, and K.J. Davis (2004). In: X.Y. Liu and J.J. De Yoreo (Eds.), *Nanoscale Structure and Assembly at Solid–Fluid Interfaces, Vol. II: Assembly at Hybrid and Biological Systems*, Kluwer, Boston, Chap. 2, p. 55.
- Eggers, D.F., N.W. Gregory, G.D. Halsey, and B.S. Rabinovitch (1964). *Physical Chemistry*, John Wiley & Sons, Inc., New York.
- Hall, R.N. (1953). *J. Phys. Chem.* **57**, 836.
- Hottenhuis, M.H.J., and A. Oudenampsen (1988). *J. Cryst. Growth* **92**, 513.
- Kirkova, E., M. Djarova, and B. Donkova (1996). *Prog. Cryst. Growth Charact. Mater.* **32**, 111.
- Kitamura, M., and I. Sunagawa (1977). In: *Collected Abstracts of the 5th International Conference on Crystal Growth, Cambridge, MA, 1977*, p. 92; cited by Tsuchiyama *et al.* (1981).
- Klug, D.L. (1993). In: A.S. Myerson (Ed.), *Handbook of Industrial Crystallization*, Butterworth-Heinemann, Boston, p. 65.
- Lamble, G.M., R.J. Reeder, and P.A. Northrup (1997). *J. Phys. IV* **7**, C2, 793.
- Marie, E., Y. Chevalier, F. Eydoux, L. Germanaud, and P. Flores (2005). *J. Colloid Interface Sci.* **290**, 406.
- Mielniczek-Brzóska, E., K. Giełzak-Koćwin, and K. Sangwal (2000). *J. Cryst. Growth* **212**, 532.
- Myerson, A.S. (1993). In: A.S. Myerson (Ed.), *Handbook of Industrial Crystallization*, Butterworth-Heinemann, Boston, p. 1.
- Prasad, K.V.R., R.I. Ristić, D.B. Sheen, and J.N. Sherwood (2001). *Int. J. Pharm.* **215**, 29.
- Rak, M., N.N. Eremin, T.A. Eremina, V.A. Kuznetsov, T.M. Okhrimenko, N.G. Furmanova, and E.P. Efremova (2005). *J. Cryst. Growth* **273**, 577.
- Rashkovich, L.N., and N.V. Kronsky (1997). *J. Cryst. Growth* **182**, 434.
- Reeder, R.J., G.M. Lamble, J.-F. Lee, and W.J. Staudt (1994). *Geochim Cosmochim. Acta* **58**, 5639.
- Reeder, R.J., G.M. Lamble, and P.A. Northrup (1998). *Am. Mineral.* **84**, 1049.
- Rimstidt, J.D., A. Balog, and J. Webb (1998). *Geochim. Cosmochim. Acta* **62**, 1851.
- Ristić, R.I., J.N. Sherwood, and K. Wojciechowski (1988). *J. Cryst. Growth* **91**, 163.
- Römer, H., K.-D. Luther, and W. Assmus (1994). *J. Cryst. Growth* **141**, 159.
- Sangwal, K., and E. Mielniczek-Brzóska (2003). *J. Cryst. Growth* **257**, 185.

- Sangwal, K., and T. Pałczyńska (2000). *J. Cryst. Growth* **212**, 522.
- Sangwal, K., E. Mielniczek-Brzóska, and J. Borc (2002). *J. Cryst. Growth* **244**, 183.
- Thurmond, C.D., and J.D. Struthers (1953). *J. Chem. Phys.* **57**, 831.
- Tsuchiyama, A., M. Kitamura, and I. Sunagawa (1981). *J. Cryst. Growth* **55**, 510.
- Voronkov, V.V., and A.A. Chernov (1967). *Kristallografiya* **12**, 222.
- Zhmurova, Z.I., and V.Ya. Khaimov-Mal'kov (1970a). *Kristallografiya* **15**, 135.
- Zhmurova, Z.I., and V.Ya. Khaimov-Mal'kov (1970b). *Kristallografiya* **15**, 142.

List of Symbols

a	activity of super- or undersaturated solution
a	dimension of growth species
a	interionic distance in the solid state
a	lattice parameter in x direction
a_0	activity of saturated solutions
a_0	distance between ions in crystalline lattice
A	constant
A	kinetic parameter
A	specific capillary activity
A_s	parameter characterizing dependence of solubility of a solute on additive concentration
A_0	constant
A_1, A_2, A_3	constants
A'	constant
A'	pre-exponential term
b	constant
b	lattice parameter in y direction
b_l	empirical constant
b'	constant
B	constant
B_1, B_2	constants
c	actual solute concentration in solution
c	lattice parameter in z direction
c_g	shape factor for crystal nucleus
c_i	concentration of additive
c_{light}	velocity of light.
c_0	equilibrium solute concentration in solution

C	constant
C_1, \dots, C_8	constants
C^*	constant
d	dimensionality of growth
d	interplanar distance
D	bulk diffusion constant of the solute
e	elementary charge
E	Young's modulus
E_{ad}	energy of adsorption of the molecules/atoms on the surface
f	activity coefficient of super- or undersaturated solution
f	constant
f_i	fraction of sites i corresponding to the coverage θ_i
f_0	activity of saturated solution
f_1	constant
F	electrostatic force between ions
F, F_0	constants
F^*	effective excess energy of the nucleus
ΔG	Gibbs free energy change
ΔG	thermodynamic potential difference
ΔG_{att}	attachment energy for growth unit
ΔG_{dehyd}	dehydration energy of molecule/atom
ΔG_S	surface excess free energy
ΔG_V	volume excess free energy
ΔG_v	free energy change per unit volume
ΔG_{2D}^*	activation barrier for 2D nucleation
ΔG_{3D}^*	activation barrier for 3D nucleation
h	average hydration number per ion
h	height of step
h_P	Planck's constant
H	enthalpy of a phase
ΔH_m	enthalpy of melting
ΔH_{mix}	enthalpy of mixing
ΔH_s	heat of solution of the electrolyte
ΔH_{solv}	heat of solvation of ions
i	number of dislocations of unit Burgers vector
I	light intensity
J	nucleation rate (number of nuclei per unit volume per unit time)
$J_{\text{a,s}}$	stationary nucleation rate per active center
J_s	rate of stationary nucleation
J_0	kinetic coefficient for three-dimensional nucleation
k	growth constant
k_{ads}	adsorption layer contains
k_B	Boltzmann constant
k_d	thermodynamic segregation coefficient
k_{eff}	effective segregation coefficient of impurity

k_m	rate constant corresponding to dissolution of metastable phase m
k_s	rate constant corresponding to nucleation of stable phase s
k_1, k_2	constants
k_0	equilibrium segregation coefficient
K	Langmuir constant
K_s	solubility product
K_1	hydrolysis constant
K_1, K_2	constants
l	size, length of a line containing equally spaced screw dislocations
l_A	cross-sectional size of face A
l_d, l^*, l^{**}	average distances between the adsorbed impurity particles
l_0	initial cross-sectional size of face at $t = 0$
L	average distance between adsorbed particles
L	size range, size
L	length of a line containing equally spaced screw dislocations
L^*	critical crystal size when the crystal grows or dissolve by Ostwald ripening
m, m_u	constants, exponents
M	molecular weight
n	exponent, Born exponent
n	number
n	population density at size L
n_{ad}	number of adsorption sites occupied per unit area on the surface
n_{max}	number of sites available for adsorption per unit area of a surface
n_0	concentration of growth units in the bulk
n_0	population density for zero-sized crystals
n_1	concentration of adsorbed molecules/atoms (i.e. the number of molecules/atoms per unit area)
n_1, n_2, \dots, n_i	number of moles of components
n'	exponent
N	number of stable crystals
N_a	total number of active nucleation centers in a system
N_A	number of ions per mole, Avogadro's number
N_c	number density of active centers in a droplet
N_k	density of kinks (i.e. the number of kinks per unit area)
N_0	concentration of growth units on a surface
N_0	number of nuclei per unit area on a surface
N_0	total number of nuclei in a system
p	actual vapor pressure
p	slope (inclination) of spiral hillock

p_0	saturation vapor pressure
p_1, p_2	constants
P	surface area
q	parameter
q	exponent
Q	parameter
Q_{ad}	heat of adsorption
Q_{des}	heat of dissolution of adsorbed molecules
Q_{diff}	differential heat of adsorption
Q_{diff}^0	initial heat of adsorption when $\theta \rightarrow 0$
ΔQ_{smig}	activation energy for surface migration
r	average distance between ions, radius of curvature
r_i, r_s	radii of ion, water molecule
r_{2D}^*	critical radius of 2D stable disc-shaped nucleus
r_{3D}^*	critical radius of 3D stable spherical nucleus
R	face growth rate
R_i	face growth rate in the presence of impurity
R_i	growth rate constant
R_i	ratio of reactants
R_A^{crit}	critical growth rate
R_G	gas constant
R_m	maximum growth rate
R_{rel}	relative growth rate
R_s	radius of foreign substrate body (s)
R_0	face growth rate in the absence of impurity
R'	parameter
s	constant
S	supersaturation ratio ($= p/p_0$ or c/c_0)
S	entropy of a phase
S_c	critical supersaturation
S_{max}	maximum supersaturation ratio
S_i	initial supersaturation ratio
t	time
t_i	induction period or induction time for nucleation
T	temperature in kelvin
T_c	crystallization temperature
T_m	melting point of compound in kelvin
T_R	roughening temperature
T_t	transformation temperature for a polymorph
U	lattice energy
v	step velocity
v_{min}	minimum velocity of curved step
v_r	advancement velocity of a curved step
v_0	step velocity in the absence of impurity
V	volume
$w(t)$	mass crystallized in volume V at time t

w_0	maximum mass of the crystallizing phase
W	activation energy for growth
$W_{\text{I-D}}$	work of interaction between ions and water molecules
x	solute concentration expressed in mole fraction
x_0	solubility expressed in mole fraction
x_0	limiting value of variable x
y	fraction of crystalline phase or overall crystallization of a phase
y_0	interstep distance
z_i	valency of ion
Z	number of nearest neighbors
α	angle
α	surface entropy factor
α_l	impurity effectiveness parameter for kink adsorption
α_m	Madelung constant
α_s	impurity effectiveness factor for surface adsorption
β	equilibrium dissociation constant
β, β'	retardation factor related with density of kinks in steps
β_l	kinetic coefficient of step
β_{l0}	kinetic coefficient of step for pure system
$\beta_1, \beta_2, \beta_3$	first- and second-order equilibrium dissociation constants
γ	angle
γ	interfacial energy, surface free energy between solid–liquid interface
γ_{eff}	effective interfacial energy
γ_l	linear step free energy
γ_0	surface free energy of pure liquid (solvent)
δ	thickness of unstirred diffusion layer at the surface
ϵ_j	a random variable lying between 0 and 1
ε	dielectric constant of solvent or solution
ε	parameter
ε_{abs}	absorptivity of solution
ε_m	measure of distribution of energies of adsorption sites
η	average mosaic spread for the crystal
θ	equilibrium wetting (contact) angle
θ	fractional coverage by adsorbed impurity particles
θ_{eq}	fractional coverage corresponding to equilibrium adsorption
θ_l	fractional coverage by impurity particles in kink adsorption
θ_s	fractional coverage by impurity particles in surface adsorption
Θ_m, Θ_{m_u}	time constant for transformation of metastable phase
Θ_s	time constant for the transformation of stable phase
κ	correction factor
κ	constant
$\kappa(L, \lambda)$	aggregation kernel
λ	wavelength of absorbed light

λ_s	surface diffusion distance for the adsorbed atoms/molecules
Λ	step retardation factor
μ	chemical potential of a phase
μ_s	dipole moment of a water molecule
$\Delta\mu$	difference in chemical potentials of a given phase
ν	frequency of vibration of atom/molecule
ν	number equal to 1/2 and 1 for growth
ξ	crystallographic anisotropy factor
ρ	density of crystal or solution
ρ	exponent
σ	supersaturation
σ_b	bulk supersaturation
σ_c	threshold supersaturation
σ_d	value of supersaturation up to which $v = 0$ and $R = 0$
σ_s	surface supersaturation
σ_y	yield strength
σ^*	threshold supersaturation when v and R abruptly increase with σ
σ^*	supersaturation for transition from homogeneous to heterogeneous nucleation
σ^{**}	threshold supersaturation when v and R attain values corresponding to pure solutions
τ	induction period
τ	retention time
τ	deposition time for a new growth layer
τ_{ad}	time of adsorption
τ_0	time of oscillation of the molecules in the adsorbed state
τ_{smig}	average time of surface migration of a molecule
ϕ	a numerical factor connected with contact angle
ϕ_b	bond energy between atoms, ions or molecules
Φ	volume fraction of additive
Φ	volume of droplets involved in crystallization
Φ	activity factor related with numerical factor ϕ
Φ_0	maximum volume of crystallized droplets
$\psi_{L,\lambda}$	segregation efficiency during precipitation
w_m	constant
Ω	specific molecular volume of molecules/atoms

Subject Index

Note: Page numbers in *italic* refer to figures.

- Abnormal mineralization, *see* Pathological mineralization
- Acetaminophen, *see* Paracetamol
- p*-acetoxyacetanilide 416–18
- Additive defined xiii
- Adenosine diphosphate (ADP) 143–4
- Admixture defined xiii
- Adsorption of impurities 89, 109–74
- available surface sites 112–13
 - and effective segregation coefficient 402–9
 - growth promoting effects 146–57
 - isotherms 112–14, 193–7
 - kinetic models 115–16
 - correlation with experimental data 127–32
 - impurity effectiveness factor 118, 120, 121–4
 - kinks in steps: Kubota–Mullin model 118–19, 179
 - surface terrace: Cabrera–Vermilyea model 119–21
 - velocity of curved steps 116–17
 - mobile and immobile impurities 109–12
 - on rough faces 157–8
 - and solution supersaturation 197–8
 - surface free energy 115
- and tapering of KDP-type crystals 143–6, 161, 170–2
- time-dependent 132–6
- two competing impurities 113, 124–7
- two-dimensional adsorption layer 158–60
- Aggregation 288–9
- control of particle shape and size 303–4
- Air-jet milling 320
- Air-pressure atomization processes 325–6
- Alcohols 3
- Alizarin 275
- Alkali metal halides
- morphodroms 277
 - and segregation coefficient 395
- N*-alkanes 275
- crystallization behavior 332–8, 360–1, 367
 - in emulsions 368–72
 - paraffin crystals 138, 139
 - and segregation coefficient 407–8
- Amino acids 233–4
- Ammonium oxalate complexes 10–14
- and dead supersaturation zone 178, 195–7
 - dissociation 168
 - growth-promotion by iron (III) ions 148–52
 - impurities and growth rate 85–6

- Ammonium oxalate (*Continued*)
 impurity–crystal interface interactions
 161–6
 complex adsorption 166–72
 metastable zone width 58–62
 rough face stabilization 160
 and segregation coefficient 405–6, 408–9,
 412–13
 structure 148, 162, 164, 167
 threshold supersaturation/impurity trapping
 413–14
- Ammonium sulfate crystals 139, 141–2
- Amorphous phases 38
- Anhydrous milk fat 356, 357–60
- Animal biominerization 206–9
- Antimony 396, 397
- Aqueous electrolyte solutions, *see* Electrolyte
 solutions, structure of
- Aquo complexes
 additive containing solutions 10–13
 formation 8–10
 impurity–crystal interactions 166–72
 spatial structures 15–16
 speciation analysis 13–15
- Aragonite 212, 213, 214–15, 239, 240–1,
 300, 302
- Atomic force microscopy 100–1
- Atomic force spectroscopy 105
- Avian eggshell 212
- Barium nitrate 86–7, 93–4
 and segregation coefficient 398–9
- BCF surface diffusion model 80–1, 111, 149
- Benzamide 173–4
- Benzoic acid 173–4
- Biodiesel 330–1, 338–48
 additives 343–8, 349
 fatty acid methyl esters 340–1, 345–8
 properties 342–3
 transesterification 338–40
- Biogenic opals 210
- Biological tissue engineering 311–14
- Biologically active additives (mineralization)
 222
 overall growth kinetics 230–42
 acidic amino acids 233–4
 dentin collagen 241–2
 polycarboxylic acids 230–3, 239
 polyphosphates 235–8
 simple ions 238–41
- overall precipitation kinetics 222–30
 overall crystallization 224–5
 sparingly soluble salts 222, 225–9
 surfactants 229–30
- phases and polymorphs of calcium
 salts 242–6
- polyphosphate inhibitors 235–9
- transformations of metastable phases
 247–58
- Biominerization 205–6, 298
- animal/human
 avian eggshell 212
 bone 207–8
 mollusk shell 211, 212–16
 teeth 208–9, 217–18
- inhibitors 219
- pathological mineralization 216, 217
 dental caries and saliva 216–18
 kidney stones 218–22
 plants 209–11
- Bone, mineralization of 207–8, 314
- Brushite 99–100
- Bulk diffusion growth models 80–2
- Bunched steps 322–4
- Cabrera–Vermilyea adsorption model
 111–12, 119–21
 and threshold supersaturations 179
- Cadmium ions 405, 406, 407
- Calcite 101, 102, 212, 300, 302
 crystal size distribution 293–5
 ion incorporation 383
 and polycarboxylic acids 230–3, 239
 and polyphosphate inhibitors 235–8
 and segregation coefficient 390–2,
 393, 394
 and simple ions 238–41
- Calcium carbonate 50–1
 as biomineral 206–7, 209–10,
 212, 222
 control of particle shape and
 size 299–302
- crystal size distribution 284–5, 295–6
- phases and polymorphs 242–4, 246
 scale formation 258–60
see also Aragonite; Calcite
- Calcium oxalate 39–40, 43–6
 as biomineral 206, 209, 222
 control of particle shape and
 size 302–3, 306–7

- crystal size distribution 296–7
 crystallization of metastable phases 39–41,
 43–6
 kidney stones 218–22
 phases and polymorphs 245–6
 precipitation kinetics 225–6, 227–9
 and surfactants 229–30
 scale formation 260
- Calcium phosphate
 as biomineral 206, 222
 phases and polymorphs 245
 precipitation and surfactants 229–30
- Calcium salts
 phases and polymorphs 242–7
 sparingly soluble 225–9
 transformation of metastable phases
 247–58
 see also specific salts
- Calcium sulphate, *see* Gypsum
- Capture of impurities, *see* Incorporation of
 impurities in crystals
- Chernov's bulk diffusion model 81–2
- Cloud point 335–8, 341
- Collagen 208
- Colloidal inclusions 383
- Colloids, food 350
- Competitive absorption 113, 124–7
- Complexes in solutions 1–19
 see also Aquo complexes
- Copper (II) complexes 9–10
 oxalate solutions 10–14
- Critical micelle concentration 17–18
- Critical nucleus 21
- Critical radius 26–7
- Crystal defects/distortions 382–3, 416–18
- Crystal faces
 described and classified 67–9
 growth morphology 266–7, 270–3
 roughening 69–72
- Crystal growth, *see* Growth kinetics; Growth
 mechanisms
- Crystal shape and size, control of
 growth-directed synthesis 298–307
 template-directed synthesis 307–14
- Crystal size dispersion 282–4
- Crystal size distribution 284–5
 balanced nucleation-growth approach
 289–91
 basic shapes 291–2
 effect of additives 295–7
- law of proportionate effect approach 291–5
 population balance approach 285–9
- Crystal–impurity interactions, *see*
 Impurity–crystal interactions
- Crystal–medium interface
 and diffusional relaxation 397, 398
 face types described and classified 67–9
 ionic crystal 3, 98, 161
 and segregation coefficient 386
 structure of interfacial layer 96–100
 see also Impurity–crystal interactions
 Crystallization 65–6
 induction period 47–52
 metastable phases 38–41
 overall 41–6, 223–4, 372–6
 see also Growth kinetics; Growth
 mechanisms
- Curved steps 116–17
- Cystoliths 209–10, 211
- Danazol 327
- DDB-750 359–60
- Dead supersaturation zone 83, 166–7,
 177–8, 197
 see also Threshold supersaturations
- Dentin collagen 241–2
- Dentine 208–9, 311
- Dexamethasone sodium phosphate 49–50
- 1,3-diastearoyl-2-oleoyl-*sn*-glycerol 362–6
- Diesel 330
 additives 332–8
 see also Biodiesel
- Diffusion layer 97, 160
- Diffusional relaxation 397, 398
- Diglycerides 356, 359
- Diolein 359
- Direct integration growth model 80
- Dissociation 7
- Distearin 358, 359
- Drugs
 nucleation and growth morphology 321–4
 particle size and shape 304–5
 preparation and size distribution 321–30
 air-pressure atomized processes 325–6
 impeller and oscillatory crystallization
 324–5
 micronization 327–30
- Edge dislocations 84–5
- Effective interfacial energy 30–1

- Effective segregation coefficient
definitions 384–6
diffusional relaxation approach 397–401
lattice strain caused by impurities 416–18
relationship to face growth rate 410–13
statistical selection approach 401–2
surface adsorption approach 402–10
volume diffusion model 396–7
- Effectiveness factor (adsorption) 118, 120, 121–4
- Eggshell, avian 212
- Electrical double layer 96–7, 98, 100, 160–2
- Electrolyte solutions, structure of
aquo complexes 8–10
concentrated and saturated solutions 6–8
dilute solutions 4–6
effect of additive 10–16
- Emulsifiers, food 354–6
- Emulsion droplets 354
crystallization of fats and oils 366–72
nucleation centers/overall crystallization 372–6
- Enamel, tooth 208–9
- Equilibrium adsorption 132–3
- Equilibrium segregation coefficient
binary mixture approach 386–8
defined and described 384–6
experimental data correlated with theory
bivalent ions in calcite 390–2, 393–4
lanthanides in gypsum 394, 395
metal halides 394–5
rare earths in zirconium oxide 392–4
thermodynamic approach 388–9
- Ethylene–vinyl acetate copolymer 333–8
and segregation coefficient 407–8
- Face growth rate
displacement time-dependence 141–2
and effective segregation coefficient 410–13
- Fats and oils 331–2, 348, 350–6
crystallization
bulk 352–4, 356–61
in emulsion droplets 354, 366–76
of polymorphs 361–6
physical properties of oils 332, 340, 342
see also Triglycerides
- Fatty acid methyl esters
and biodiesel 340, 345–8
properties 341
saturated and unsaturated 350
- Fatty acids 351
- Flat crystal faces 68, 69
- Food colloids 350, 351
- Food emulsifiers 354–6
- Food industry 348–77
bulk crystallization of fats 356–61
polymorphs 361–6
- emulsion systems
crystallization of fats and oils 361–6
nucleation centers and overall crystallization 372–6
- Foreign substance
classified 2
defined xiii
nucleation on foreign substrate 30–5
see also Impurity
- Free energy, *see* Gibbs free energy
- Freundlich isotherm 114, 119, 120
and threshold supersaturations 187–90, 196
- Gels 309–11
- Germanium 396, 397
- Gibbs free energy
crystallization 22–5, 38–9
growth on rough interface 75, 147
and nuclear radius 26–7
- Gibbs–Thomson relation 27
- Gibbs–Wolf plot 67
- Gold particles 303, 304, 305
- Growth-directed synthesis 298–307
- Growth-inhibition
biomineralization 219
inhibitor defined xiii
polycarboxylic acids 230–3, 239
polyphosphates 235–8
simple ions 238–40
surfactants 229–30
two-dimensional adsorption layer 158–60
- Growth kinetics
foreign substances/impurities
basic kinetic equations 136–41

- general effects/considerations 85–90
 heterogeneous two-dimensional nucleation 90–6
 step kinetic coefficient 142
 time-dependence of face displacement 141–2
see also Growth-promotion
 imperfect smooth face 78
 bulk diffusion models 80–2
 and cooperating screw dislocations 82–4, 185
 direct integration model 80
 and edge dislocations 84–5
 surface diffusion model 78–9
 perfect smooth face 75–8
 rough faces 73–5
 and segregation coefficient 394–6
 techniques for studying 104–5
see also under Biologically active additives (mineralization)
- Growth layers 274
- Growth mechanisms
 experimental techniques 104–5
 growth steps 100–4
 interfacial layer 96–100
see also Growth-promotion
- Growth morphodroms 276–82
- Growth morphology, *see* Morphology of crystals
- Growth-promotion 146–7
- impurity macroclusters 153–7
 step free energy and roughening 147–52
- Growth rate dispersion 283–4
- Growth steps, *see* Steps and surfaces
- Gypsum 394, 395, 405, 406–7, 411, 412
- Heat of solution 5–6
- Helmholtz–Stern layer 97, 160
- Henry's equation 113
- Heterogeneous capture (impurities) 383, 384
- Heterogeneous nucleation 30–5
 additives and solubility 52–6
 induction period 48–50
 interfacial in emulsions 366–72
 metastable zone width 56–62
 nucleation rate 56
 two-dimensional nucleation 90–1
 surface diffusion-control 91–2
 volume diffusion-control 92–3
- N*-hexadecane 360–1, 367
- Homogeneous capture (impurities) 383–4
- Homogeneous nucleation 21–30
 correction factors 29–30
 driving force for phase transition 22–5
 growth kinetics of smooth faces 75, 76
 induced period for crystallization 47–52
 metastable phases 38–46
 metastable zone width 21, 35–8
 nucleation rate 25–30
 two-dimensional nucleation 92–3, 96
- Human biomineratization 206–9
- Hydration number 4
- Hydration, *see* Solvation
- Hydrogen bonding
 adsorption of impurities 161
 structure of water 2–3
 and tailor-made additives 19
- Hydroxyapatite 226, 227
 amino acids and growth rate 233–4
 nanostructured minerals 312–14
- Ibuprofen 327, 329–30
- Ice 2
- Idioblasts 209, 210
- Immobile impurities 109–12
- Impeller-driven batch crystallizer 324–5
- Impurity
 clusters 146, 152–7
 defined xiii
 distance between particles 182–3
 general effects on growth rates 85–7
 and growth kinetics 136–42
 and heterogeneous two-dimensional nucleation 90–6
see also Incorporation of impurities in crystals
- Impurity–crystal interactions 19, 160–6
 chemical aspects 166–72
- Inclusions 383
- Incorporation of impurities in crystals
 381–6
 effective segregation coefficient 396–410
 relationship with face growth rate 410–13
 equilibrium segregation coefficient 386–96
 lattice strain 416–18
 threshold supersaturation 413–16
- Induction period 21, 47–52
- Inhibitor, *see* Growth-inhibition
- Instantaneous adsorption 132–3, 134, 136
 distance between impurity particles 182–3

- Interfacial energy 30–1
 and foreign substances 90
 and metastable zone width 35–8
- Interfacial heterogeneous nucleation 366–72
- Interfacial instability 324
- Interfacial layer, *see* Crystal–medium interface
- Interfacial tension 306
- Ion-dipole forces 4
- Ions
 aquo complexes 8–10
 crystal interface 98, 161
 electrostatic force between 6
 ion pairs and clusters 6–8
 solvation 4–6
 thermodynamic properties of trivalent 170
- Isotherms, adsorption 112–14
 correlation with experimental data 127–31
 and threshold supersaturation 193–7
- Itraconazole 327–9
- KDP crystals 98–9, 140
 dead supersaturation zone 177–8, 186–7,
 191–5, 199–202
 growth-promoting impurities 156–7
 point defects 383
 tapering 143–6, 161, 170–2
- Ketocanazole 327
- Ketoprofen 320
- Kidney stones 218–22
- Kinetic roughening 72–3, 92–3, 152
- Kink site 66
 crystal faces 68, 69
 growth promotion/impurity absorption 152
 and threshold supersaturation 190–3
- KJMA theory 223
- Kubota–Mullin adsorption model 111,
 118–19
 and threshold supersaturations 179
- Langmuir isotherm 113–14, 118, 120
 experimental correlations 127, 128,
 129–30
 and threshold supersaturations 187–90, 196
- Langmuir monomolecular films 307–8
- Lanthanide ions 394, 395, 405, 406–7,
 411–12
- Lattice strain and defects 382–3, 416–18
- Law of proportionate effect 291–5
- Lead chloride 278–80
- Lead ions 398, 399
- Ledge site 66
- Ligands
 aquo complex formation 8–10
 polydentate 18–19, 235–8
 spatial coordination 15–16
 stability constants and dead
 supersaturation zones 166–7
- Liquid-lattice models 3
- Literature overview xiv–xv
- Macroclusters, surface impurity
 146, 152–7
- Macromolecular crystals 102, 103, 104
- Macroscopic inclusions 383
- Macrosteps 101, 102–3
- Metastable equilibrium 21
- Metastable phases
 crystallization 38–41
 overall crystallization 41–6
 transformation of 247–58
- Metastable zone width 21, 35–8
 effect of additives 56–7
 transition metal cations 58–60
 effect of solubility 57, 60–2
- Micelles 17–18
 reversed micelle phase 367–8
- Michelson interferometry 105
- Microemulsion templates 307
- Microgravity 50–2
- Micronization of drugs 320, 327–30
- Mineralization, *see* Biologically active
 additives (mineralization);
 Biomineralization
- Mobile impurities 109–12
- Molecular additives 18–19
- Molecular dynamic models 3
- Mollusk shell, mineralization of 211,
 212–16
- Monoglycerides 356, 359
- Mononuclear growth mechanism 41, 42,
 47–8
 perfect smooth faces 75–8
- Monostearin 358, 359
- Morphology of crystals 265–6
 basic concepts 266–73
 control of particle size and shape
 298–311
 effects of additives 273–4
 growth morphodroms 276–82
 solvent effects 275–6

- Mosaic spread 416, 417, 418
Mother-of-pearl, see Nacre
 Multiple nucleation model
 impurity growth-promotion 147,
 149–51
 perfect smooth faces 75–8, 147
- Nacre 212–14, 213, 216, 306
 Nanostructured hydroxyapatite minerals 312–14
 Naphthalene 73
 Non-equilibrium capture 383–4
 Non-stationary nucleation 41, 42–3
 Nucleation, *see* Heterogeneous nucleation;
 Homogeneous nucleation;
 Two-dimensional nucleation
 Nucleation rate 25–30
 crystallization of metastable phases 38–41
 dependence on supersaturation 34, 35,
 36–7
 effect of additives 56
 heterogeneous nucleation 31–5
 homogeneous nucleation 27–9
- Oil–water interface 367–72
 Oils, *see* Fats and oils
 Opal 210
 Organic compounds
 adsorption isotherms 130–2
 solvents, structure of 3
 Organophosphates 18
 Oscillator-baffled batch crystallizer 324–5
 Osteopontin 172
 Ostwald ripening 282–4, 292
 Oswald rule of stages 43
 Overall crystallization 41–6, 223–4
 emulsion systems 372–6
 sparingly soluble salts 225
 Ozonized oils 345–8
- Palm oil 356, 359, 360
 Paracetamol
 nucleation and morphology 321–4
 preparation and particle size distribution 324–6
 and segregation coefficient 416–18
 Paraffin crystals 138, 139
 Pathological mineralization 216
 Pearls 214–16
 Petroleum industry 330–8
 biodiesel 338–48
 long chain *n*-alkanes 332–8
 pH
 aqueous ammonium oxalate 10–11
 aqueous sodium oxalate 7–8
 Pharmaceutical industry 299, 320–30
 crystal growth and morphology 321–4
 particle preparation and size 324–30
 Phase transitions 22–5
 solution-mediated transformation 40–1
 Phosphate complexes, structure of 15–16
 Phosphonic acids 16, 161
 Phytoliths 210
 Plant mineralization 209–11
 Platy crystals 214–15, 216
 Point defects 382, 383
 Poison defined *xiii*
 Polycarboxylic acids 16, 161,
 230–3, 239
 Polydentate ligands 18–19, 235–8
 Polyelectrolytes 16–18, 230–3, 233
 Polyglycerol-10 dodecabehenate 359–60
 Polymorphs 38
 triglycerides 353–4, 361–6
 Polynuclear growth mechanism 41, 42,
 47–8
 perfect smooth faces 75–8
 Polyphosphates 18, 235–8
 Polysaccharides 16
 Polysulfonic acids 16, 161
 Potassium chloride 277–8
 Potassium dihydrogen phosphate, *see* KDP
 crystals
 Potassium sulfate 399–400, 401–2
 Pour points 332–3, 341, 344–8
 Power-law 185
 Precipitation-based techniques (drugs) 320
 Precipitation kinetics (mineralization) 222–30
 Promoter defined *xiii*
 Proportionate effect, law of 291–5
 Proteins 16
 Rare earth ions 392–4, 410–11
 Renal stones 218–22
 Residence time 4–5
 Rough crystal interface 68
 impurity adsorption on 157–8

- Roughening
 and growth promotion 147–52
 kinetic 72–3, 152
 thermodynamic 70–2
- Saliva 216–18
 Salt weathering 260
 SAXS process 325–6
 Scale formation 258–60, 258–61
 Screw dislocations 82–4, 149
 Sectorial nonuniformity 384
 Segregation coefficients
 defined and described 384–6
see also Effective segregation coefficient;
 Equilibrium segregation coefficient
 Self-assembling monolayers 3–7, 308–9
 Shells, mineralization of 211–16
 Silicon bodies 210
 Silicon dioxide 210, 259
 Singular crystal faces 67–8
 Size distribution, *see* Crystal size distribution
 Smooth crystal interface 68
 Sodium bromate 281–2
 Sodium carbonate 269
 Sodium chlorate 89–90, 95
 adsorption on rough faces 157–8
 dithionate impurity and step velocity
 127–9
 Sodium chloride
 face stabilization 276
 morphodroms 276, 277
 two-dimensional adsorption layer 158–60
 Sodium nitrate 155–6
 Sodium oxalate 7–8
 Solid–fluid interfacial energy 35–8
 Solubility
 crystal size dependence 283
 effects of additives 52–6, 166
 and heat of solution 5–6
 and metastable zone width 60–2
 sparingly soluble biominerals 222
 sparingly soluble drugs 326–30
 Soluble polymers 16
 Solution atomization 325
 Solution–crystal phase change 22, 23
 Solution-mediated phase transformation 40–1
 Solvate phases 38
 Solvation
 concentrated/saturated electrolyte 6–8
 dilute electrolyte 4–6
- Solvents
 choice of 1
 effect on growth morphology 275–6
 organic 3
 structure of 2–3
 water 1, 2–3
 Sparingly soluble salts 222, 225–9
 Speciation analysis 13–15
 Spiral growth 100, 101–2,
 103, 274
 Spray freezing 327
 Stationary nucleation 41, 42–3
 Step kinetic coefficient 142
 Steps and surfaces 69–70
 bunched steps 322–4
 distance between impurity particles
 182–3
 growth promotion and roughening
 147–52
 kinetic roughening 72–3, 92–3, 152
 and morphology 274
 sources of growth steps 100–4
 step curling and impurities 415
 thermodynamic roughening 70–2
 velocity of curved steps 116–17
 Stern layer 97
 Sucrose 191, 192
 Sucrose oligoesters 367
 Supersaturation
 barriers 177–8
 and impurity adsorption 197–8
 Supramolecular assemblies 307,
 308, 309–11
 Surface coverage parameter 112
 Surface diffusion growth model 78–9,
 83, 111
 heterogeneous two-dimensional
 nucleation 91–2
 Surface entropy factor 71–2
 Surface free energy 115
 Surface macroclusters 146, 152–7
 Surface tension 115, 306
 Surfaces, *see* Steps and surfaces
 Surfactants 16–18, 161
 defined xiii
 as selective inhibitors 229–30
 stable molecular aggregates 18
 and surface free energy 115
 Symbols, list of 421–6

- Tailor-made additives 19, 89, 112, 130, 273
 discussed and exemplified 172–4
- Tapering of crystals 143–6, 161, 170–2
- Teeth
 dental caries 217
 mineralization of 208–9
- Temkin isotherm 113–14, 118–19, 120
 experimental correlations 127, 128,
 129–30
- Template-directed synthesis 307–14
- Terrace site 66
- Tetracosane 335–8
- Thermodynamic equilibrium capture 383–4
- Thermodynamic roughening 70–2
- Three-dimensional nucleation, *see*
 Heterogeneous nucleation; Homogeneous
 nucleation
- Threshold supersaturations 177–202
 basic kinetic equations 179–81
 dependence of ratios σ_d/σ^* and σ^*/σ^{**} on
 c_i 198–202
 determination from $v(\sigma)$ and $R(\sigma)$ data
 184, 186–7
 cooperating spirals/power-law relationship
 185
 empirical expression/power-law
 relationship 185–6
- distances between impurity particles 182–3
- impurity adsorption and supersaturation
 197–8
 impurity concentration dependence 187–90
 impurity trapping during growth 413–16
 interpretation of experimental data
 adsorption at kinks and terraces 190–3
 impurity adsorption isotherms 193–7
- Time-dependence
 adsorption 132–5, 136, 183
 of face displacement 141–2
- Tissue engineering 311–14
- Tooth, *see* Teeth
- Transesterification 338–40
- Transition metal cations
 complexes 12–13
 impurity crystal interactions 166–72
 and metastable zone width 58–60
- Triglycerides 351–2
 bulk crystallization 356–61
 melting points 351–2
 polymorphic crystallization 353–4, 361–6
 transesterification 338–40
- Tripalmitoylglycerol 362–6
- Tween 20 368
- Two-dimensional adsorption layer 158–60
- Two-dimensional nucleation 90–6, 100, 101,
 102, 103
 and impurity growth-promotion 147
- Urine and urinary stones 218–22
- Van der Waals interactions 160–1
- Vapor-crystal phase change 22, 23
- Vegetable oils, *see* Fats and oils
- Vicinal crystal faces 68
- Volume diffusion-controlled growth 92–3
- Water
 solvent properties 1
 structure 2–3
 see also Electrolyte solutions, structure of
- Water-oil interface 367–72
- Weddellite 209
- Whewellite 209
- Wilson–Frenkel law 74
- Work of interaction 5
- Zinc potassium sulfate 399–400, 401–2
- Zirconium dioxide 393–4, 410–11

Author Index

Note: Normal numerals denote the page where an author is cited in the text whereas the numerals in bold indicate the pages where the author appears in the list of references of chapters. Different authors with same surnames and initials have separate entries. Same authors with different initials are also listed in separate entries.

- Abdel-Aal, N. 243, 262
Abegg, C.F. 287, 314
Abegunasekara A., *see* Chandrajith, R. 218,
219, 262
Ackermann, D., *see* Brown, P. 220, 262
Adair, J.H. 298, 299, 304, 307–9, 314
Adair, J.H., *see* Moon, J. 304, 317
Adair, J.H., *see* Ravaine, S. 308, 317
Adams, C., *see* Clarkson, J.R. 243, 262
Addadi, L. 173, 174
Addadi, L., *see* Aizenberg, J. 222, 262, 299,
314
Addadi, L., *see* Berkovitch-Yellin, Z. 172,
173, 174
Addadi, L., *see* Bouropoulos, N. 307, 315
Addadi, L., *see* Levi, Y. 306, 316
Addadi, L., *see* Levi-Kalisman, Y. 214, 263
Addadi, L., *see* Raz, S. 298–300, 302, 317
Affolter, B. *see* Baumann, J.M. 245, 262
Aikawa, N., *see* Kawano, J. 243, 244, 246,
254, 263
Aizenberg, J. 222, 262, 299, 309, 314
Al-Sabagh, A.M., *see* El-Gamal, I.M. 332,
344, 377
Albeck, S., *see* Levi, Y. 306, 316
Albert, H.L., *see* Shekunov, B.Y. 330, 378
Albon, N. 193, 202
Albon, N., *see* Dunning, W.J. 274, 315
Alexeev, I.V., *see* Malkin, A.I. 86, 94, 107,
152, 175
Algra, R.E. 275, 314
Allegri, F., *see* Guerra, A. 218, 219, 262
Amatavivadham, A., *see* Mullin, J.W. 143,
144, 156, 176
Ando, K., *see* Guzman, L.A. 138, 175
Andreassen, J.P. 284, 288, 314
Antonietti, M., *see* Mayer, A. 304, 317
Antonietti, M., *see* Rudloff, J. 299, 301, 317
Antonietti, M., *see* Sedlak, M. 299, 317
Arends, J. 208, 262
Arias, J.L. 212, 262
Arima, S., *see* Sangwal, K. 374, 376, 378
Arnott, H.J. 209, 211, 262
Arsié, J. 99, 105
Aslanian, S., *see* Aslanian, S. 269, 314
Assmus, W., *see* Römer, H. 392, 393,
411, 418

- Astier, J.P., *see* Boistelle, R. 69, 106
 Atanassova, S., *see* Atanassova, S. 225, 226, 262
 Awad, T. 367, 377
- Babić-Ivančić, V., *see* Sikirić, M. 227, 228, 263
 Bagby, M.O., *see* Dunn, R.O. 343, 344, 377
 Bakhshi, N.N., *see* Lang, X. 344, 378
 Balicka, A., *see* Frej, H. 61, 63
 Balog, A., *see* Rimstidt, J.D. 381, 386, 389–91, 394, 400, 418
 Barnwal, B.K. 331, 332, 338–40, 377
 Barrick, J.P., *see* Hounslow, M.J. 288, 316
 Barsukova, M.I. 88, 105
 Bartles, G., *see* van Erk, W. 86, 107
 Baumann, J.M. 245, 262
 Bauser, E. 84, 106
 Belcher, A.M., *see* Walters, D.A. 235, 264
 Belter, P.A. 286, 314
 Ben-Jebria, A., *see* Edwards, D.A. 320, 377
 Bennema, P. 35, 61, 62, 70, 72, 78, 82, 84, 106, 123, 174
 Bennema, P., *see* Grimbergen, R.F.P. 164, 175, 266, 272, 316
 Bennema, P., *see* Meekes, H. 266, 317
 Bennema, P., *see* van der Eerden, J.P. 72, 107
 Bennema, P., *see* van Rosmalen, G.M. xv, 2, 20
 Berg, E.W. 52, 54, 62
 Berglund, K.A., *see* Chu, Y.D. 89, 106
 Berglund, K.A., 286–8, 314, 315
 Berkovitch-Yellin, Z. 172, 173, 174
 Berkovitch-Yellin, Z., *see* Addadi, L. 173, 174
 Beshensky, A.M., *see* Wesson, J.A. 219, 264
 Biala, N., *see* Manne, J. 245, 246, 263
 Bienfait, M.R. 158, 174, 276, 277, 281, 315
 Birchall, J.D., *see* Mann, S. 307, 316
 Black, A.J., *see* Aizenberg, J. 309, 314
 Black, S.N. 89, 106, 130, 174
 Bliznakov, G.M. 88, 106, 116, 130, 131, 174, 175
 Bloem, J., *see* van der Putte, P. 133, 176, 183, 203
 Bockris, J.O'M. 5, 7, 19, 100, 106
 Boistelle, R., *see* Bienfait, M.R. 158, 174, 276, 277, 281, 315
 Boistelle, R., *see* Simon, B. xv, 130, 138, 147, 176, 185, 203
 Boistelle, R. xv, 41, 62, 69, 106, 158, 159, 175, 275, 277, 315
 Bolscher, J.G.M., *see* van Nieuw Amerongen, A. 216, 264
 Bonardi, B., *see* Claudy, P. 332, 333, 377
 Booth, N.A. 104, 106
 Borc, J. 60, 62
 Borc, J., *see* Sangwal, K. 113, 160–2, 164, 166, 167, 176, 273, 274, 317, 402, 405, 408, 419
 Borghi, L., *see* Guerra, A. 218, 219, 262
 Borgström, L.H. 271, 315
 Bosch, H.W. 298, 305, 315, 320, 377
 Bouropoulos, N. 307, 315
 Brack, A., *see* Levi, Y. 306, 316
 Bramley, A.S. 287, 288, 315
 Bramley, A.S., *see* Hounslow, M.J. 288, 316
 Braybrook, A.L. 172, 175
 Brecević, Lj. 245, 262
 Bredikhin, V.I. 138, 175, 177, 185, 191, 192, 197, 202
 Brice, J.C. 66, 74, 106, 382, 387, 391, 392, 395, 418
 Broul, M., *see* Nývlt, J. 62, 63
 Brown, P. 220, 262
 Brunsteiner, M. 289, 315
 Brunsteiner, M., *see* Simons, S.J.R. 289, 317
 Buckley, H.E. xiv
 Bulakh, B.M. 304, 315
 Burton, J.A. 392, 396, 397, 411, 418
 Burton, W.K. 68, 71, 76, 78, 82, 106, 116, 117, 133, 175
 Cabrera, N. 117, 133, 175, 183, 202
 Cabrera, N., *see* Burton, W.K. 68, 71, 76, 78, 82, 106, 116, 117, 133, 175
 Cahn, J.W. 68, 106
 Campbell, A.A., 298, 299, 306, 307, 308, 315
 Campbell, A.A., *see* Clark, R.H. 306, 315
 Campbell, A.A., *see* Letellier, S.R. 307, 316
 Cao, W. 339, 377
 Caplan, A.I., *see* Arias, J.L. 212, 262
 Caponetti, G., *see* Edwards, D.A. 320, 377
 Caprez, U., *see* Baumann, J.M. 245, 262
 Carasso, M.L., *see* Moon, J. 304, 317
 Carraretto, C. 338, 377
 Carvalho, M., *see* Kurutz, J.W. 218, 263, 287, 288, 296, 297, 303, 307, 316

- Cebula, D.J., *see* Smith, P.R. 356, 378
 Chakarov, V., *see* Katz, J.L. 29, 63
 Chakrabarty, A., *see* Yang, D.S.C. 307, 318
 Chakraborty, M., *see* Mullin, J.W. 143, 144, 156, 176
 Chandrajith, R. 218, 219, 262
 Chang, B., *see* Yu, J. 299, 302, 303, 318
 Chang, R.K. 320, 377
 Chapman, D., *see* Jones, M.N. 17, 19, 309, 316
 Charlot, G. 54, 62
 Chateigner, D. 212, 262
 Chattopadhyay, P., *see* Shekunov, B.Y. 330, 378
 Chauvet, M.C., *see* Ryall, R.L. 219, 222, 245, 263
 Chen, Z.Y., *see* Zhou, Y.C.Y. 303, 318
 Chernov, A.A., *see* Booth, N.A. 104, 106
 Chernov, A.A., *see* Malkin, A.I. 86, 94, 107, 152, 175
 Chernov, A.A., *see* Voronkov, V.V. 401, 419
 Chernov, A.A., *see*, Rashkovich, L.N. 104, 105, 107
 Chernov, A.A. xv, 66, 69, 70, 71, 76, 77, 80, 82, 84, 89, 106, 116, 149, 175, 177, 202, 274, 315, 382, 389, 396, 397, 400, 418
 Cherpanova, T.A., *see* van der Eerden, J.P. 72, 107
 Cheung, W.H. *see* Doherty, W.O.S. 260, 262
 Chevalier, Y., *see* Marie, E. 332, 338, 345, 378, 408, 418
 Chew, C.M. 324, 377
 Chitipongtanate, S., *see* Thongboonkerd, V. 218, 264
 Choi, C.K., *see* Jung, T. 40, 63, 218, 245, 262, 263, 299, 302, 316
 Choi, H.J., *see* Lee, I. 299, 300, 316
 Chow, A.H.L. 321, 377
 Chow, P.K.K., *see* Chow, A.H.L. 321, 377
 Chu, Y.D. 89, 106
 Chujo, Y., *see* Naka, K. 246, 263
 Clark, A.R., *see* Duddu, S.P. 320, 377
 Clark, R.H. 306, 315
 Clarkson, J.R. 243, 262
 Claudy, P. 332, 333, 377
 Claudy, P., *see* Létoffe, J.-M. 332, 333, 378
 Cody, A.M. 174, 175, 273, 315
 Cody, R.D., *see* Cody, A.M. 174, 175, 273, 315
 Coe, F.L., *see* Sutherland, J.W. 218, 264
 Coley, T., *see* Owen, K. 332, 333, 378
 Cölfen, H. 298, 299, 307, 315
 Cölfen, H., *see* Rudloff, J. 299, 301, 317
 Cölfen, H., *see* Sedlak, M. 299, 317
 Collier, A.P., *see* Hounslow, M.J. 288, 316
 Costa-Bauza, A., *see* Grases, F. 218, 219, 262
 Coupland, J.N. 366, 377
 Crenshaw, M.A. 212, 262
 Crenshaw, M.A., *see* Saito, T. 209, 241, 242, 263, 311, 317
 Crowder, T.M. 320, 377
 Cui, F.Z., *see* Feng, Q.L. 222, 262, 299, 306, 315
 Cussler, E.L., *see* Belter, P.A. 286, 314
 Dabringhaus, H., *see* Gutjahr, A. 239, 241, 243, 262
 Dalal, A.K., *see* Lang, X. 344, 378
 Dalas, E., *see* Koutsopoulos, S. 222, 233, 263
 Dalas, E., *see* Manali, F. 231, 237, 239, 263
 Dalbey, E.R., *see* Grey, W.A. 130, 132, 175
 Dam, B. 274, 315
 Damin, B., *see* Claudio, P. 332, 333, 377
 Damin, B., *see* Létoffe, J.-M. 332, 333, 378
 Davey, R.J., *see* Black, S.N. 89, 106, 130, 174
 Davey, R.J. xv, 87, 89, 106, 113, 175, 274, 315
 Davis, K.J., *see* Dove, P.M. 100, 106, 177, 202, 238, 239, 262, 273, 274, 315, 416, 418
 de Boer, J.H. 109, 175
 de Jong, E.J., *see* Berglund, K.A. 287, 287, 315
 De Léon Gatti, M., *see* Herrera, M.L. 358, 377
 de Villiers, J.B.M., *see* Du Plessis, L.M. 343, 377
 de Vreugd, C.H. 395, 405, 406, 407, 412, 418
 De Yoreo, J.J., *see* Chew, C.M. 324, 377
 De Yoreo, J.J., *see* Dove, P.M. 100, 106, 177, 202, 238, 239, 262, 273, 274, 315, 416, 418
 De Yoreo, J.J., *see* Wang, L. 171, 176, 222, 235, 264, 273, 274, 318
 De Yoreo, J.J., *see*, Land, T.A. 100, 105, 107
 De Yoreo, J.J., *see*, Teng, H.H. 100, 101, 102, 105, 107, 307, 317

- Deaver, D., *see* Edwards, D.A. 320, 377
 Deij, M.A., *see* Kaminski, D. 98, 98, 99,
 100, 106
 Dekker, A.J. 53, 62
 Demirbas, A. 339, 377
 Deng, F., *see* Ouyang, J.-M. 244, 245, 263
 Deng, Y., *see* Hu, Z. 243, 262
 Dennehy, R.D., *see* Chew, C.M. 324, 377
 Dewettinck, K., *see* Foubert, I. 356–8, 359,
 377
 Deyl, Z. *see* Mikšík, I. 212, 263
 Diasakov, M. 339, 377
 Dickinson, E. 17, 18, 19, 309, 315, 353, 355,
 356, 377
 DiMasi, E., *see* Fenter, P. 98, 106
 Ding, J., *see* Yang, Q. 258, 260, 261, 264
 Dissanayake, C.B., *see* Chandrajith, R. 218,
 219, 262
 Djarova, M., *see* Kirkova, E. 382, 418
 Doehe, E., *see* Rodriguez-Navarro, C. 260,
 263
 Doherty, M.F., *see*, Gadewar, S.B. 270, 272,
 315
 Doherty, W.O.S. 260, 262
 Doherty, W.O.S., *see* Yu, H. 258, 264
 Doki, N., *see* Kubota, N. 138, 175
 Dominguez-Vera, J.M., *see* Jimenez-Lopez, C.
 299, 316
 Donkova, B., *see* Kirkova, E. 382, 418
 Dove, P.M. 100, 106, 177, 202, 238, 239,
 262, 273, 274, 315, 416, 418
 Dove, P.M., *see* Teng, H.H. 100, 101, 102,
 105, 107, 235, 264, 307, 317
 Du Plessis, L.M. 343, 377
 Duan, L., *see* Ouyang, J.-M. 244, 245,
 248, 263
 Duddu, S.P. 320, 377
 Dunn, R.O. 343, 344, 377
 Dunning, W.J. 274, 315
 Dunning, W.J., *see* Albon, N. 193, 202

 Eberl, D.D., *see* Kile, D.E. 291–4, 316
 Edwards, D.A. 320, 377
 Efremova, E.P., *see* Eremina, T.A. 148, 175
 Efremova, E.P., *see* Rak, M. 383, 418
 Eggers, D.F. 52, 63, 113–15, 124, 175,
 402, 418
 Eiden-Assman, S. 245, 262
 El-Gamal, I.M. 332, 344, 345, 377
 Eldon, M.A., *see* Duddu, S.P. 320, 377

 Elfil, H. 242, 262
 Elton, R.C., *see* Duddu, S.P. 320, 377
 Elwenspoek, M. 35, 61, 63, 72, 73, 106
 Emons, H.H., *see* König, A. 18, 19
 Eremin, N.N., *see* Eremina, T.A.
 148, 175
 Eremin, N.N., *see* Rak, M. 383, 418
 Eremina, T.A. 148, 175
 Eremina, T.A., *see* Rak, M. 383, 418
 Ershov, V.I., *see* Bredikhin, V.I. 138,
 175, 177, 185, 191, 192, 197, 202
 Eskew, M.L., *see* Edwards, D.A.
 320, 377
 Eydoux, F., *see* Marie, E. 332, 338,
 345, 378, 408, 418

 Falini, G. 309, 310, 315
 Falini, G., *see* Levi-Kalisman, Y.
 214, 263
 Fanucci, G.E., *see* Ravaine, S. 308, 317
 Fawcett, W.R. 100, 106
 Fellows, C.M., *see* Doherty, W.O.S.
 260, 262
 Felsche, J., *see* Eiden-Assman, S. 245, 262
 Femi-Oyewo, M.N. 321, 377
 Fend, Q.L., Shen, F.H. 222, 263
 Feng, Q.L. 222, 262, 299, 306, 315
 Fenimore, C.P. 174, 175, 273, 315
 Fenter, P. 98, 106
 Fermani, S., *see* Falini, G. 309, 315
 Fernandez-Diaz, L., *see* Prieto, M. 222, 263
 Fernandez, M.S., *see* Arias, J.L. 212, 262
 Fiaccadori, E., *see* Guerra, A. 218, 219, 262
 Fila, W., *see* Davey, R.J. 89, 106
 Filipović, N., *see* Füredi-Milhofer, H. 229,
 262
 Filipović, N., *see* Sikirić, M. 227, 228, 263
 Finlayson, B., *see* Brown, P. 220, 262
 Finnie, S., *see* Ristić, R.I. 320, 323, 378
 Firoozabadi, A., *see* Kashchiev, D. 56, 63
 Fisk, J.A., *see* Katz, J.L. 29, 63
 Flores, P., *see* Marie, E. 332, 338, 345, 378,
 408, 418
 Foo, C.W.P. 206, 262, 307, 315
 Foubert, I. 356, 358, 359, 377
 Fovet, Y., *see* Gal, J.Y. 243, 262
 Fox, P.C. 217, 262, 307, 315
 Frank, F.C. 84, 106, 133, 175, 183, 202
 Frank, F.C., *see* Burton, W.K. 68, 71, 76, 78,
 82, 106, 116, 117, 133, 175

- Frej, H. 61, 63
Frolow, F., see Weisinger-Lewin, Y. 172, 176
Fujiwara, K., see Sazaki, G. 105, 107
Füredi-Milhofer, H., see Sikirić, M. 227, 228, 263
Füredi-Milhofer, H., see Skrtić, M. 245, 263
Füredi-Milhofer, H. xv, 16, 19, 225, 229, 245, 262
Furmanova, N.G., see Eremina, T.A. 148, 175
Furmanova, N.G., see Rak, M. 383, 418
- Gache, N., *see Gal, J.Y.* 243, 262
Gadewar, S.B. 270, 272, 315
Gal, J.Y. 243, 262
Ganne, V., see Wesson, J.A. 219, 264
Garcia-Ruiz, J.M., see Jimenez-Lopez, C. 299, 316
Garside, J., see Brecević, Lj. 245, 262
Garside, J., see Davey, R.J. 89, 106
Garside, J., see Söhnel, O. 283, 284, 317
Garti, N. 350, 354–6, 377
Garti, N., see Füredi-Milhofer, H. 229, 262
Gazzano, M., see Falini, G. 309, 315
Gebauer, M., see Rätsch, M. 332, 378
Geissbühler, P., see Fenter, P. 98, 106
Geneste, P., see Pioch, D. 339, 378
Germanaud, L., see Marie, E. 332, 338, 345, 378, 408, 418
Ghuiba, F.M., see El-Gamal, I.M. 332, 345, 377
Gibrat, R. 291, 315
Giełzak-Koćwin, K., see Mielniczek-Brzóska, E. 123, 175, 178, 202, 382, 405, 412, 418
Giling, L.J., see van der Putte, P. 133, 176, 183, 203
Gilmer, G.H. 70, 106
Gilmer, G.H., see Bennema, P. 70, 78, 82, 84, 106
Ginde, R., see Myerson, A.S. 283, 284, 317
Glatz, C.E. 287, 315
Goia, D.V. 298, 303, 305, 315
Gomez-Morales, J. 48, 49, 63, 222, 225, 262, 288, 315
Gomez, M.E.G. 343, 377
Gonzalez, G., see Machado, A.L.C. 332, 333, 335, 378
Gorjian, S., see Doherty, W.O.S. 260, 262
Goudie, A.S. 260, 262
- Goyal, S.K., see Srivastava, S.P.* 332, 379
Graille, J., see Pioch, D. 339, 378
Grant, D.J.W., see Hendriksen, B.A. 321, 377
Grant, D.J.W., see, Chow, A.H.L. 321, 377
Grases, F. 218, 219, 262
Grassi, A., see Simon, B. 130, 138, 147, 176, 185, 203
Grassmann, O. 310, 311, 315
Graswinckel, S., see Radenović, N. 100, 107
Graswinckel, W.S., see Algra, R.E. 275, 314
Gratz, A.J. 235, 262, 273, 274, 316
Green, D.A., see Hendriksen, B.A. 321, 377
Gregory, N.W., see Eggers, D.F. 52, 63, 113–15, 124, 175, 402, 418
Grey, W.A. 130, 132, 175
Grimbergen, R.F.P. 164, 175, 266, 272, 316
Grimbergen, R.F.P., see Meekes, H. 266, 317
Grover, P.K. 206, 219, 245, 262
Grover, P.K., see Ryall, R.L. 219, 222, 245, 263
Gryte, C.C., see Manne, J. 245, 246, 263
Gu, A., see Yang, Q. 258, 260, 261, 264
Guan, X., see Wang, L. 171, 176, 222, 235, 264, 273, 274, 318
Guerra, A. 218, 219, 262
Guida, A., see Pioch, D. 339, 378
Guo, S. 307, 316
Gürbüz, H. 56, 57, 60, 63
Gutjahr, A. 239, 241, 243, 262
Gutzov, I., see Atanassova, S. 225, 226, 262
Guzman, L.A. 113, 138, 175
Guzman, L.A., see Kubota, N. 138, 175
- Halcrow, M., see Black, S.N.* 89, 106, 130, 174
Hall, R.N. 397, 418
Halsey, G.D., see Eggers, D.F. 52, 63, 113–15, 124, 175, 402, 418
Hamada, Y., see Awad, T. 367, 377
Hamada, Y., see Ueno, S. 369, 371, 379
Hammond, E.G., see Lee, I. 342, 344, 378
Han, H., see Cao, W. 339, 377
Han, S.W., see Lee, I. 299, 300, 316
Han, Z., see Zhang, J. 332, 345, 379
Hanes, J., see Edwards, D.A. 320, 377
Hanna, M.A., see Ma, F. 331, 338, 339, 342, 378
Hansma, P.K., see Walters, D.A. 235, 264
Hanson, J., see Aizenberg, J. 222, 262, 299, 314

- Hao, H. 50, 63
 Hardikar, V.V. 298, 299, 316
 Hartel, R.W. 287, 288, 316
 Hartel, R.W., *see* Herrera, M.L. 358, 377
 Hartman, P. 68, 106, 158, 175, 266, 275, 316
 Hartman, P., *see* van Panhuys-Sigler, M. 278, 318
 Havey, K., *see* Adair, J.H. 307, 309, 314
 Hedegaard, C., *see* Chateigner, D. 212, 262
 Hejna, M., *see* Radenović, N. 159, 160, 176, 277, 317
 Heiss, A., *see* Eiden-Assman, S. 245, 262
 Hendriksen, B.A. 321, 377
 Henze, U., *see* Baumann, J.M. 245, 262
 Herrera, M.L. 358, 377
 Herrmann, W., *see*, Schenk, R.K. 206, 207, 263
 Hertz, P.B., *see* Lang, X. 344, 378
 Hesse, A., *see* Siener, R. 218, 263
 Heuer, A.H., *see* Arias, J.L. 212, 262
 Hew, C.L., *see* Yang, D.S.C. 307, 318
 Heywood, B.R. 307, 316
 Heywood, B.R., *see* Braybrook, A.L. 172, 175
 Heywood, B.R., *see* Mann, S. 307, 316
 Heywood, B.R., *see* Walton, R.C. 206, 245, 264
 Hickey, A.J., *see* Crowder, T.M. 320, 377
 Hillner, P.E., *see* Gratz, A.J. 235, 262, 273, 274, 316
 Hirota, S., *see* Guzman, L.A. 113, 175
 Hirst, P.H., *see* Duddu, S.P. 320, 377
 Hoare, M., *see* Glatz, C.E. 287, 315
 Hoch, A.R., *see* Kile, D.E. 291, 292, 293, 294, 316
 Hoch, A.R., *see* Reddy, M.M. 230, 232, 239, 243, 263
 Hoetzer, K.A., *see* Eiden-Assman, S. 245, 262
 Holán, V., *see* Mikšík, I. 212, 263
 Hood, D.W., *see* Kitano, Y. 299, 316
 Horie, T., *see* Kaneko, N. 356, 361, 367, 377
 Hottenhuis, M.H.J. 274, 316, 405, 418
 Hounslow, M.J. 288, 316
 Hounslow, M.J., Bramley, A.S. 287, 288, 315
 Howard-Hildige, R., *see* Gomez, M.E.G. 343, 377
 Hoyer, J.R., *see* Wang, L. 171, 176, 222, 235, 264, 273, 274, 318
 Hoyt, R.C. 287, 316
 Hrkach, J., *see* Edwards, D.A. 320, 377
 Hu, W.-S., *see* Belter, P.A. 286, 314
 Hu, Z. 243, 262
 Huang, J., *see* Foo, C.W.P. 206, 262, 307, 315
 Huczko, A. 307, 316
 Hunter, G.K. 206, 262
 Hunziker, E., *see* Schenk, R.K. 206, 207, 263
 Idelson, M., *see* Berkovitch-Yellin, Z. 173, 174
 Ikemoto, K., *see* Kitamura, M. 138, 175
 Inoue, T. 281, 316
 Ito, A., *see* Onuma, K. 105, 107
 Ito, S., *see* Saito, T. 209, 241, 242, 263, 311, 317
 Izmailov, N.A. 6, 19, 52, 63
 Jackson, K.A. 71, 106
 Jackson, K.A., *see* Gilmer, G.H. 70, 106
 Jackson, R.A., *see* Braybrook, A.L. 172, 175
 Jackson, R.W., *see* Dunning, W.J. 274, 315
 Jakubczyk, M., *see* Frej, H. 61, 63
 Janicki, J., *see* Arias, J.L. 212, 262
 Janssen, G., *see* Fouber, I. 358, 377
 Jimenez-Lopez, C. 299, 316
 Joguet, L. 305, 316, 320, 377
 Johnson, L.A., *see*, Lee, I. 342, 343, 344, 378
 Johnston, K.P., *see* Rogers, T.L. 320, 327, 378
 Jones, A.G., *see* Brunsteiner, M. 289, 315
 Jones, A.G., *see* Simons, S.J.R. 289, 317
 Jones, F., *see* Reyhani, M.M. 235, 236, 263, 273, 274, 317
 Jones, M.N. 17, 19, 309, 316
 Jung, T. 40, 63, 218, 245, 262, 263, 299, 302, 316
 Kachalov, O.V., *see* Barsukova, M.I. 88, 105
 Kaerger, J.S. 320, 325, 326, 377
 Kaldis, E. 68, 106
 Kaluzynski, K., *see* Rudloff, J. 299, 301, 317
 Kameyama, T., *see*, Onuma, K. 86, 104, 105, 107
 Kaminski, D. 98, 100, 106
 Kaminski, D., *see* Arsić, J. 99, 105
 Kaminski, D., *see* Radenović, N. 100, 107, 159, 160, 176, 277, 317
 Kaneko, N. 356, 361, 367, 377
 Kaneko, N., *see* Kashchiev, D. 372, 373, 377

- Kaneko, N., *see* Katsuragi, T. 356, 361, 367, 368, 377
 Kaplan, D.L., *see* Foo, C.W.P. 206, 262, 307, 315
 Kaplan, D.L., *see* Li, C. 298, 308, 309, 316
 Kaplan, D.L., *see* Litvin, A.L. 307, 316
 Kapteyn, J.C. 291, 316
 Kashchiev, D. 30, 35, 42, 43, 47, 48, 56, 63, 223, 263, 372, 373, 377
 Kashchiev, D., *see* Verdos, D. 48, 63
 Katsifaras, A. 222, 243, 263
 Katsuragi, T. 356, 361, 367, 368, 377
 Katsuragi, T., *see* Kaneko, N. 356, 361, 367, 377
 Katz, J.L. 29, 63
 Kavanagh, J.P., *see* Walton, R.C. 206, 245, 264
 Kawamura, Y., *see* Kitamura, M. 138, 175
 Kawano, J. 243, 244, 246, 254, 263
 Keller, K.W. 84, 106
 Kerchner, J.H., *see* Moon, J. 304, 317
 Kern, R. 87, 106, 276, 316
 Kern, R., *see* Bienfait, M.R. 158, 174, 276, 277, 281, 315
 Kerschbaum, S. 342, 377
 Khaimov-Mal'kov, V.Ya., *see* Zhmurova, Z.I. 400, 401, 405, 419
 Khidr, T.T., *see* El-Gamal, I.M. 332, 345, 377
 Khlyunev, N.V., *see* Bredikhin, V.I. 138, 175, 177, 185, 191, 192, 197, 202
 Kido, T., *see* Adair, J.H. 307, 308, 309, 314
 Kile, D.E. 291, 292, 293, 294, 316
 Kim, K., *see* Lee, I. 299, 300, 316
 Kim, T.N., *see* Feng, Q.L. 222, 262, 299, 306, 315
 Kim, W.-S., *see* Jung, T. 40, 63, 218, 245, 262, 263, 299, 302, 316
 Kind., M. 304, 316
 Kipp, S. 105, 107
 Kirkova, E. 382, 418
 Kirkova, E.K. 88, 107, 155, 156, 175
 Kirkova, E.K., *see* Bliznakov, G.M. 88, 106, 116, 130, 131, 174, 175
 Kitamura, M. 138, 175, 238, 243, 244, 246, 252–5, 263, 284, 285, 299, 316, 397, 418
 Kitamura, M., *see* Kawano, J. 243, 244, 246, 254, 263
 Kitamura, M., *see* Tsuchiyama, A. 398, 399, 419
 Kitano, Y. 299, 316
 Kleinman, J.G., *see* Wesson, J.A. 219, 264
 Klimova, A.Yu., *see* Barsukova, M.I. 88, 105
 Klug, D.L. xv, 161, 175, 382, 387, 388, 418
 Klumb, L.A., *see* Clark, R.H. 306, 315
 Knothe, G. 340, 342, 343, 377
 Koetzel, T.F., *see* Aizenberg, J. 222, 262, 299, 314
 Koetzel, T.F., *see* Weisinger-Lewin, Y. 172, 176
 Kolluru, C., *see* Madras, G. 339, 378
 Kolybaeva, M.I., *see* Barsukova, M.I. 88, 105
 Komatsu, H., *see* Kurihara, K. 105, 107
 König, A. 18, 19
 Konno, H., *see* Kitamura, M. 244, 263
 Koretsky, C.M., *see* Prapaipong, P. 9, 20
 Koretsky, C.M., *see* Shock, E.L. 9, 20
 Korolikhin, V.V., *see* Bredikhin, V.I. 138, 175, 177, 185, 191, 192, 197, 202
 Kostov, I., *see* Aslanian, S. 269, 314
 Kouno, M., *see* Sakamoto, M. 360, 361, 378
 Koutsopoulos, S. 222, 233, 263
 Kozlovskii, M.I. 270, 316
 Kralj, D., *see* Brecević, Lj. 245, 262
 Krarup, H.G., *see* Moon, J. 304, 317
 Kronsky, N.V., *see* Rashkovich, L.N. 138, 140, 176, 177, 183, 184, 186, 193, 194, 202, 415, 418
 Kubota, N., *see* Guzman, L.A. 113, 138, 175
 Kubota, N. xv, 117, 118, 123, 133–5, 138–42, 175, 177, 181, 183, 186, 187, 202
 Kumar, R., *see* Madras, G. 339, 378
 Kurihara, K. 105, 107
 Kuriyama, J., *see* Sakamoto, M. 360, 361, 367, 378
 Kuroda, T., *see* Sato, K. 365, 378
 Kurutz, J.W. 218, 263, 287, 288, 296, 297, 303, 307, 316
 Kusdiana, D., *see* Saka, S. 339, 378
 Küther, J. 308, 316
 Kuznetsov, V.A. 148, 175
 Kuznetsov, V.A., *see* Barsukova, M.I. 88, 105
 Kuznetsov, V.A., *see* Eremina, T.A. 148, 175
 Kuznetsov, V.A., *see* Rak, M. 383, 418
 Kuznetsov, Y.G., *see* Malkin, A.J. 96, 100, 105, 107
 Kuznetsov, Yu.G. 101, 104, 107

- Kuznetsov, Yu.G., *see* Chernov, A.A. 89, 175, 177, 202, 106, 149
- Kuznetsov, Yu.G., *see* McPherson, A. 100, 105, 107
- Lacmann, R. *see* Kipp, S. 105, 107
- Lacmann, R., *see* Gutjahr, A. 239, 241, 243, 262
- LaFemina, P., *see* McCoy, J.M. 235, 263
- Lahav, M., *see* Addadi, L. 173, 174
- Lahav, M., *see* Berkovitch-Yellin, Z. 172, 173, 174
- Lahav, M., *see* Weisinger-Lewin, Y. 172, 176
- Lahav, M., *see* Weissbuch, I. 161, 172, 173, 176, 275, 318
- Lakshmana Perumal, C.K., *see* Rajesh, N.P. 56, 57, 63
- Lamble, G.M. 383, 418
- Lamble, G.M., *see* Reeder, R.J. 383, 418
- Land, T.A. 100, 105, 107
- Landa-Vertz, J., *see* Glatz, C.E. 287, 315
- Lang, X. 344, 378
- Langer, R., *see* Edwards, D.A. 320, 377
- Laraia, V.J. *see* Arias, J.L. 212, 262
- Larson, M.A., *see* Abegg, C.F. 287, 314
- Larson, M.A., *see* Randolph, A.D. 285, 288, 317
- Lazano, P., *see* Pioch, D. 339, 378
- Leahy, J.J., *see* Gomez, M.E.G. 343, 377
- Lee, I. 299, 300, 316
- Lee, I. 342, 344, 378
- Lee, J.-F., *see* Reeder, R.J. 383, 418
- Lee, J.D., *see* Land, T.A. 100, 105, 107
- Leiserowitz, L., *see* Addadi, L. 173, 174
- Leiserowitz, L., *see* Berkovitch-Yellin, Z. 172, 173, 174
- Leiserowitz, L., *see* Weisinger-Lewin, Y. 172, 176
- Leiserowitz, L., *see* Weissbuch, I. 161, 172, 173, 176, 275, 318
- Letellier, S.R. 307, 316
- Létoffe, J.-M. 332, 333, 378
- Letoffe, J.M., *see* Claudio, P. 332, 333, 377
- Leubner, I.H. 287, 290, 316
- Levi-Kalisman, Y. 214, 263
- Levi, Y. 306, 316
- Li, C. 298, 308, 309, 316
- Li, H.D., *see* Feng, Q.L. 222, 262, 299, 306, 315
- Li, L. 159, 175, 274, 277, 278, 316
- Li, T., *see* Adair, J.H. 307, 308, 309, 314
- Li, W., *see* Zhang, J. 332, 345, 379
- Lide, D.R. 15, 19, 351, 352, 378
- Lifshitz, I.M. 293, 316
- Linares-Fernandez, L., *see* Rodriguez-Navarro, C. 260, 263
- Litvin, A.L. 307, 316
- Liu, X.Y. 32, 34, 51, 63, 90, 91, 94, 107
- Liu, Y., *see* Yang, Q. 258, 260, 261, 264
- Lizyakina, V.N., *see* Bredikhin, V.I. 138, 175, 177, 185, 191, 192, 197, 202
- Löbmann, P., *see* Grassmann 310, 311, 315
- Lockhead, M.J., *see* Letellier, S.R. 307, 316
- Long, C.J., *see* Clark, R.H. 306, 315
- Lopez-Andres, S., *see* Prieto, M. 222, 263
- Loste, E. 238, 263
- Lotan, N., *see* Edwards, D.A. 320, 377
- Loulodi, A. and *see* Diasakov, M. 339, 377
- Lucas, E.F., *see* Machado, A.L.C. 332, 333, 335, 378
- Lucasius, C.B., *see* Hottenhuis, M.H.J. 274, 316
- Ludwig, M.H., *see* Adair, J.H. 307, 309, 314
- Luquet, G., *see* Marin, F. 212, 214, 263
- Luther, K.-D., *see* Römer, H. 392, 393, 411, 418
- Ma, F. 331, 338, 339, 342, 378
- Machado, A.L.C. 332, 333, 335, 378
- Macor, A., *see* Carraretto, C. 338, 377
- Madras, G. 339, 378
- Madura, J.D., *see* Wierzbicki, A. 172, 176
- Maeda, K., *see* Guzman, L.A. 113, 175
- Maiwa, K., *see* Liu, X.Y. 90, 91, 94, 107
- Maiwa, K., *see* Sunagawa, I. 97, 100, 107
- Makino, D.L., *see* Kuznetsov, Yu.G. 101, 104, 107
- Malkin, A., *see* McPherson, A. 100, 105, 107
- Malkin, A.I. 86, 94, 96, 100, 105, 107, 152, 175
- Malkin, A.I., *see* Chernov, A.A. 89, 106, 149, 175, 177, 202, 274, 315
- Malkin, A.J., *see* Kuznetsov, Yu.G. 101, 104, 107
- Manali, F. 231, 237, 239, 263
- Mandel, I.D. 216, 263
- Mann, S. 307, 316
- Mann, S., *see* Heywood, B.R. 307, 316
- Mann, S., *see* Litvin, A.L. 307, 316
- Manne, J. 245, 246, 263

- Margolis, E.J. 54, 63
 Marie, E. 332, 338, 345, 378, 408, 418
 Marin, F. 212, 214, 263
 Marković, M., *see* Skrtić, M. 245, 263
 Marshall, V.R., *see* Grover, P.K. 219, 245, 262
 Martins, P.M. 113, 175
 Martonen, T.B., *see* Crowder, T.M. 320, 377
 Maruo, K., *see* Sakamoto, M. 360, 361, 367, 378
 Masuoka, H., *see* Kitamura, M. 244, 263
 Matijević E., *see* Pozarnsky, G.A. 298, 317, 320, 378
 Matijević, E. 305, 316, 332, 378
 Matijević, E., *see* Bosch, H.W. 298, 305, 315, 320, 377
 Matijević, E., *see* Goia, D.V. 298, 303, 305, 315
 Matijević, E., *see* Hardikar, V.V. 298, 299, 316
 Matijević, E., *see* Joguet, L. 305, 316, 320, 377
 Matijević, E., *see* Ruch, F. 305, 317, 320, 378
 Matijević, E., *see* Sondi, I. 299, 317
 Matijević, E., *see* Wang, L. 298, 300, 318
 Matsui, T., *see* Sazaki, G. 105, 105, 107
 Matsumura, M., *see* Soriano, N.U., Jr 332, 340–7, 350, 378, 379
 Matuchova, M., *see* Nývlt, J. 62, 63
 Mayer, A. 304, 317
 McClements, D.J. *see* Dickinson, E. 17, 18, 19, 309, 315, 353, 355, 356, 377
 McCoy, J.M. 235, 263
 McMullan, R.K., *see* Weisinger-Lewin, Y. 172, 176
 McPherson, A. 100, 105, 107
 McPherson, A., *see* Kuznetsov, Yu.G. 101, 104, 107
 McPherson, A., *see* Malkin, A.J. 96, 100, 105, 107
 Mead, D.G., *see* Dunning, W.J. 274, 315
 Mecholsky, J., *see* Adair, J.H. 307, 308, 309, 314
 Meekes, H. 266, 317
 Meekes, H., *see* Grimbergen, R.F.P. 164, 175, 266, 272, 316
 Meenan, P., *see* Hendriksen, B.A. 321, 377
 Meera, K., *see* Rajesh, N.P. 56, 57, 63
 Meera, K., *see* Srinivasan, K. 56, 57, 63
 Meldrum, F.C., *see* Loste, E. 238, 263
 Mersmann, A. 36, 50, 63
 Meschi, T., *see* Guerra, A. 218, 219, 262
 Mielniczek-Brzóska, E. 9, 19, 85, 107, 123, 140, 148, 175, 177, 178, 195, 196, 202, 382, 405, 412, 418
 Mielniczek-Brzóska, E., *see* Sangwal, K. 10, 14, 20, 52, 55–61, 63, 113, 136, 138, 140, 141, 147–52, 160–2, 164, 166, 167, 176, 177, 178, 195, 196, 203, 273, 274, 317, 402, 405, 408, 412–15, 418, 419
 Migo, V.P., *see* Soriano, N.U., Jr 332, 340–7, 350, 378, 379
 Mikšík, I. 212, 263
 Mintzes, J., *see* Edwards, D.A. 320, 377
 Mirandola, A., *see* Carraretto, C. 338, 377
 Misztal, R. 8, 20, 52, 63
 Mittelbach, M. 343, 378
 Mittelbach, M., *see* Schober, S. 343, 345, 378
 Miyashita, S., *see* Kurihara, K. 105, 107
 Mkrtchyan, A.A., *see* Chernov, A.A. 80, 82, 89, 106, 149, 175, 177, 202
 Mkrtchyan, A.A., *see* Rashkovich, L.N. 104, 105, 107
 Molera, J., *see* Roque, J. 287, 288, 293–5, 317
 Moon, J. 304, 317
 Moon, J., *see* Adair, J.H. 307, 309, 314
 Morrone, A., *see* Adair, J.H. 307, 309, 314
 Morse, D.F., *see* Walters, D.A. 235, 264
 Müller-Krumbhaar, H., *see* van der Eerden, J.P. 274, 318
 Müller, B.W., *see* Rasenack, N. 327, 328, 329, 378
 Mullin, J.W. 143, 144, 156, 176
 Mullin, J.W., *see* Davey, R.J. 113, 175, 274, 315
 Mullin, J.W., *see* Kubota, N. 117, 118, 133–5, 139–42, 175, 181, 183, 186, 187, 202
 Mumtaz, H.S., *see* Hounslow, M.J. 288, 316
 Myerson, A.S. 283, 284, 317, 413, 418
 Naka, K. 246, 263
 Nakada, T., *see* Kurihara, K. 105, 107
 Nakagawa, Y., *see* Kurutz, J.W. 218, 263, 287, 288, 296, 297, 303, 307, 316
 Nakai, T., *see* Kitamura, M. 138, 175
 Nakajima, K., *see* Sazaki, G. 105, 105, 107, 107

- Nakata, P.A. 209, 210, 263
 Nancollas, G.H. 44, 63, 222, 245, 255, 263
 Nancollas, G.H., *see* Tsortos, A. 222, 227, 228, 264
 Nancollas, G.H., *see* Wang, L. 171, 176, 222, 235, 264, 273, 274, 318
 Nancollas, G.H., *see* Wu, W. 306, 318
 Naumov, V.S., *see* Barsukova, M.I. 88, 105
 Neder, R., *see* Grassmann, O. 310, 315
 Neels, H., *see* Aslanian, S. 269, 314
 Nelsen, A.C., *see* Rogers, T.L. 320, 327, 378
 Newman, S.P., *see* Duddu, S.P. 320, 377
 Neykov, K., *see* Atanassova, S. 225, 226, 262
 Ng, W.L., *see* Siew, W.L. 356, 378
 Nielsen, A.E. 36, 63, 181, 202
 Nikolaeva, R.D., *see* Kirkova, E.K. 88, 107, 155, 156, 175
 Nishioka, K., *see* Inoue, T. 281, 316
 Northrup, P.A., *see* Lamble, G.M. 383, 418
 Northrup, P.A., *see* Reeder, R.J. 383, 418
 Nouvenne, A., *see* Guerra, A. 218, 219, 262
 Nývlt, J. 62, 63
- Ogden, M.I., *see* Reyhani, M.M. 235, 236, 263, 273, 274, 317
 Ohara, M. 77, 87, 107
 Ohba, A., *see* Sakamoto, M. 367, 378
 Ohtaki, H. 4, 19
 Okhrimenko, T.M., *see* Barsukova, M.I. 88, 105
 Okhrimenko, T.M., *see* Eremina, T.A. 148, 175
 Okhrimenko, T.M., *see* Kuznetsov, V.A. 148, 175
 Okhrimenko, T.M., *see* Rak, M. 383, 418
 Olivier, A., *see* Reyhani, M.M. 235, 236, 263, 273, 274, 317
 Omar, W. 56, 57, 60, 63
 Onuma, K. 86, 104, 105, 107, 245, 263, 304, 317
 Onuma, K., *see* Sunagawa, I. 97, 100, 107
 Orme, C.H., *see* Teng, H.H. 307, 317
 Oćcik, J. 113, 115, 124, 176
 Oudenampsen, A., *see* Hottenhuis, M.H.J. 274, 316, 405, 418
 Ouyang, H.M. 245, 263
 Ouyang, J.-M. 244, 245, 248, 263
- Owczarek, I. 143, 144, 147, 148, 154, 156, 176, 274, 317
 Owen, K. 332, 333, 378
 Özdemar, B., *see* Gürbüz, H. 56, 57, 60, 63
- Pak, C.Y.C. 218, 263
 Pałczyńska, T., *see* Sangwal, K. 113, 176, 400, 402, 404, 419
 Paloczi, G.T., *see* Walters, D.A. 235, 264
 Pandey, D.C., *see* Srivastava, S.P. 332, 379
 Papayannakos, N., *see* Diasakov, M. 339, 377
 Parello, J., *see* Grases, F. 218, 219, 262
 Park, K., *see* Kitano, Y. 299, 316
 Parkinson, G.M., *see* Reyhani, M.M. 235, 236, 263, 273, 274, 317
 Parks, J.H., *see* Sutherland, J.W. 218, 264
 Pataki, L. 54, 63
 Pei, Y., *see* Feng, Q.L. 222, 262, 299, 306, 315
 Penczek, S., *see* Rudloff, J. 299, 301, 317
 Perdok, W.G., *see* Hartman, P. 68, 106
 Petinelli, J.C. 332, 333, 378
 Pickford, M., *see* Duddu, S.P. 320, 377
 Piöch, D. 339, 378
 Pitt, K., *see* Braybrook, A.L. 172, 175
 Plomp, M., *see* McPherson, A., 100, 105, 107
 Poodt, P., *see* Arsić, J. 99, 105
 Potapenko, S.Yu. 121, 176
 Potapenko, S.Yu., *see* Bredikhin, V.I. 138, 175, 177, 185, 191, 192, 197, 202
 Povey, M.J.W. 356, 372, 378
 Povey, M.J.W., *see* Smith, P.R. 356, 378
 Pozarnsky, G.A. 298, 317, 320, 378
 Prankl, H. 331, 378
 Prapaipong, P. 9, 20
 Prasad, K.V.R. 321, 322, 378, 416, 417, 418
 Prati, B., *see* Guerra, A. 218, 219, 262
 Pratola, F., *see* Brunsteiner, M. 289, 315
 Pratola, Y., *see* Simons, S.J.R. 289, 317
 Pretula, J., *see* Rudloff, J. 299, 301, 317
 Price, R. *see* Kaerger, J.S. 320, 325, 326, 377
 Price, S.L., *see* Brunsteiner, M. 289, 315
 Price, S.L., *see* Simons, S.J.R. 289, 317
 Price, T., *see* Clarkson, J.R. 243, 262
 Prieto, M. 222, 263
 Prim, R.C., *see* Burton, J.A. 392, 396, 397, 411, 418
 Prockop, D.J. 206, 263
 Prywer, J. 270, 272, 317
 Prywer, J., *see* Szurgot, M. 271, 317

- Pu, G., *see* Feng, Q.L. 222, 262, 299, 306, 315
 Putnis, A., *see* Grassmann, O. 310, 315
- Qui, S.R., *see* Wang, L. 171, 176, 222, 235, 264, 273, 274, 318
- Rabinovitch, B.S., *see* Eggers, D.F. 52, 63, 113–15, 124, 175, 402, 418
 Radenović, N. 100, 107, 159, 160, 176, 276, 277, 317
 Radenović, N., *see* Kaminski, D. 98, 100, 106
 Rajam, S., *see* Mann, S. 307, 316
 Rajesh, N.P. 56, 57, 63
 Rak, M. 383, 418
 Rak, M., *see* Eremina, T.A. 148, 175
 Rak, M., *see* Kuznetsov, V.A. 148, 175
 Ramasamy, P., *see* Rajesh, N.P. 56, 57, 63
 Ramasamy, P., *see* Srinivasan, K. 56, 57, 63
 Randolph, A.D. 285, 288, 317
 Randolph, A.D., *see* Hartel, R.W. 287, 288, 316
 Rao, M.S. 257, 263
 Rao, P.N., *see* Walton, R.C. 206, 245, 264
 Rasenack, N. 327, 328, 329, 378
 Rashkovich, L.N. 104, 105, 107, 138, 140, 176, 177, 183, 184, 186, 193, 194, 202, 415, 418
 Rashkovich, L.N., *see* Chernov, A.A. 80, 82, 89, 106, 149, 175, 177, 202
 Rasmuson, A.C., *see* Westin, K.-J. 222, 239, 264
 Rasoanantoandro, M.C., *see* Pioch, D. 339, 378
 Rätsch, M. 332, 378
 Ravaine, S. 308, 317
 Raz, S. 298, 300, 302, 317
 Reaney, M.J., *see* Lang, X. 344, 378
 Reddy, A.K.N., *see* Bockris, J.O'M. 5, 7, 19, 100, 106
 Reddy, M.M. 230, 232, 239, 243, 263
 Reddy, M.M., *see* Kile, D.E. 291, 294, 316
 Reeder, R.J. 383, 418
 Reeder, R.J., *see* Lamble, G.M. 383, 418
 Reid, R.C., *see* Ohara, M. 77, 87, 107
 Rein, P.*see* Martins, P.M. 113, 175
 Reyhani, M.M. 235, 236, 263, 273, 274, 317
 Rice, B., *see* Gomez, M.E.G. 343, 377
 Rimstidt, J.D. 381, 386, 389–91, 394, 400, 418
 Rinke, G., *see* Kerschbaum, S. 342, 377
 Ripamonti, A., *see* Falini, G. 309, 315
 Ristić, R.I. 89, 90, 95, 107, 127, 128, 157, 176, 320–3, 378, 416, 418
 Ristić, R.I., *see* Chew, C.M. 324, 377
 Ristić, R.I., *see* Prasad, K.V.R. 321, 322, 378, 416, 417, 418
 Robertson, W.G. 218, 263
 Robinson, J.R., *see* Chang, R.K. 320, 377
 Rocha, F.A., *see* Martins, P.M. 113, 175
 Rodgers, A.L., *see* Webber, D. 218, 221, 245, 264
 Rodriguez-Clemente, R., *see*, Gomez-Morales, J. 48, 49, 63, 222, 225, 262, 288, 315
 Rodriguez-Clemente, R., *see*, Sangwal, K. 84, 100, 107, 274, 317, 323, 378
 Rodriguez-Clemente, R., *see*, Veintemillas-Verdaguer, S. 15, 20, 170, 176
 Rodriguez-Navarro, A., *see* Jimenez-Lopez, C. 299, 316
 Rodriguez-Navarro, C. 260, 263
 Rogers, T.L. 320, 327, 378
 Rogues, H., *see* Elfil, H. 242, 262
 Rohl, A.L. 270, 317
 Rohl, A.L., *see* Reyhani, M.M. 235, 236, 263, 273, 274, 317
 Römer, H. 392, 393, 411, 418
 Roque, J. 287, 288, 293, 294, 295, 317
 Rosati, J.A., *see* Crowder, T.M. 320, 377
 Ruch, F. 305, 317, 320, 378
 Rudloff, J. 299, 301, 317
 Ryall, R.L. 219, 222, 245, 263
 Ryall, R.L., *see* Bramley, A.S. 287, 288, 315
 Ryall, R.L., *see* Grover, P.K. 206, 219, 245, 262
 Saito, T. 209, 241, 242, 263, 311, 317
 Saka, S. 339, 378
 Sakamoto, M. 360, 361, 367, 378
 Salo, V.I., *see* Barsukova, M.I. 88, 105
 Saltzman, W.M., *see* Tan, J. 312, 313, 314, 317
 Salvado, N., *see* Roque, J. 287, 288, 293, 294, 295, 317
 Sanchis, P., *see* Grases, F. 218, 219, 262
 Sangwal, K., *see* Borc, J. 60, 62

- Sangwal, K., *see* Mielniczek-Brzóska, E. 85, 107, 123, 140, 148, 175, 177, 178, 195, 196, 202, 382, 405, 412, 418
- Sangwal, K., *see* Owczarek, I. 143, 144, 147, 148, 154, 156, 176, 274, 317
- Sangwal, K. xv, 10, 14, 20, 35, 52, 55–61, 63, 66, 76, 77, 83, 84, 100, 104, 107, 109, 111, 113, 116, 118–23, 128–30, 136, 137, 138, 140, 141, 143–5, 147–52, 160–2, 164, 166, 167, 176, 177, 178, 185, 186, 189–91, 194–7, 200–2, 203, 273, 274, 317, 323, 374, 376, 378, 400, 402, 404, 405, 408, 412–15, 418, 419
- Santhana Raghavan, P., *see* Rajesh, N.P. 56, 57, 63
- Sarig, S.*see* Füredi-Milhofer, H. xv, 16, 19, 225, 245, 262
- Sarkari, M., *see* Rogers, T.L. 320, 327, 378
- Sasaki, S.*see* Kubota, N. 138, 175
- Sasaki, T. 143, 176
- Sassani, D.C. 9, 20
- Sato, A., *see* Guzman, L.A. 138, 175
- Sato, K.*see* Kaneko, N. 356, 361, 367, 377
- Sato, K., *see* Awad, T. 367, 377
- Sato, K., *see* Kashchiev, D. 372, 373, 377
- Sato, K., *see* Katsuragi, T. 356, 361, 367, 368, 377
- Sato, K., *see* Sakamoto, M. 360, 361, 367, 378
- Sato, K., *see* Sangwal, K. 374, 376, 378
- Sato, K., *see* Soriano, N.U., Jr 332, 343, 345–7, 350, 379
- Sato, K., *see* Ueno, S. 369, 370, 371, 379
- Sato, K.. 343, 353, 356, 362, 363, 365, 369, 378
- Sawada, K., *see*, Abdel-Aal, N. 243, 262
- Sax, M., *see* Yang, D.S.C. 307, 318
- Sayan, P. 56, 57, 63
- Sazaki, G. 105, 105, 107, 107
- Sazaki, G., *see* Kurihara, K. 105, 107
- Schenk, R.K. 206, 207, 263
- Schneeweiss, M.A., *see* Kipp, S. 105, 107
- Schober, S. 343, 345, 378
- Schober, S., *see* Mittelbach, M. 343, 378
- Schroeter, J.D., *see* Crowder, T.M. 320, 377
- Sebastian, E., *see* Rodriguez-Navarro, C. 260, 263
- Sedlak, M. 299, 317
- Seip, C.T., *see* Ravaine, S. 308, 317
- Semangoen, T., *see* Thongboonkerd, V. 218, 264
- Senogles, E., *see* Doherty, W.O.S. 260, 262
- Shah, I., *see* Radenović, N. 100, 107
- Sharma, M.P., *see* Barnwal, B.K. 331, 332, 338–40, 377
- Sheen, D.B., *see* Prasad, K.V.R. 321, 322, 378, 416, 417, 418
- Sheen, D.B., *see* Ristić, R.I. 320, 323, 378
- Sheikholeslami, R., *see* Yu, H. 258, 264
- Shekunov, B.Y. 330, 378
- Shekunov, B.Yu., *see* Rashkovich, L.N. 177, 202
- Shekunov, B.Yu., *see* Ristić, R.I. 89, 90, 95, 107, 127, 128, 157, 176
- Shen, F.H. 222, 263
- Shen, Q., *see* Wei, H. 222, 243, 264
- Shen, Z., *see* Yang, Q. 258, 260, 261, 264
- Sherwood, J.N. 84, 107
- Sherwood, J.N., *see* Prasad, K.V.R. 321, 322, 378, 416, 417, 418
- Sherwood, J.N., *see* Ristić, R.I. 89, 90, 95, 107, 127, 128, 157, 176, 320–3, 378, 416, 418
- Sheshadri, R., *see* Loste, E. 238, 263
- Shiau, L.D., *see* Chu, Y.D. 89, 106
- Shimobayashi, N., *see* Kawano, J. 243, 244, 246, 254, 263
- Shimomura, O. 56, 57, 60, 63
- Shinoda, K., *see* Kawano, J. 243, 244, 246, 254, 263
- Shock, E.L. 9, 20
- Shock, E.L., Prapaipong, P. 9, 20
- Shock, E.L., *see* Sassani, D.C. 9, 20
- Shockley, M.W., *see* Dunn, R.O. 343, 344, 377
- Shripathi, T., *see* Sherwood, J.N. 84, 107
- Siener, R. 218, 263
- Siew, W.L. 356, 378
- Sikirić, M. 227, 228, 263
- Simon, B., *see* Boistelle, R. 158, 159, 175, 277, 315
- Simon, B. xv, 130, 138, 147, 176, 185, 203
- Simons, S.J.R. 289, 317
- Simons, S.J.R., *see* Brunsteiner, M. 289, 315
- Sisk, S.A., *see* Duddu, S.P. 320, 377
- Škapin, S., *see* Matijević, E. 305, 316, 332, 378
- Skirić, M., *see* Füredi-Milhofer, H. 229, 262
- Skrtić, M. 245, 263

- Slichter, W.P., *see* Burton, J.A. 392, 396, 397, 411, 418
- Slyozov, V.V., *see* Lifshitz, I.M. 293, 316
- Smagala, T.G., *see* Fawcett, W.R. 100, 106
- Smith, A.D., *see* Manne, J. 245, 246, 263
- Smith, B.L., *see* Walters, D.A. 235, 264
- Smith, L.H. 217, 263
- Smith, P.R. 356, 378
- Smol'ski, I.L., *see* Chernov, A.A. 89, 106, 149, 175, 177, 202
- Söhnle, O. 36, 63, 283, 284, 317
- Söhnle, O., *see* Nielsen, A.E. 36, 63
- Söhnle, O., *see* Nývlt, J. 62, 63
- Sondi, I. 299, 317
- Sondi, I., *see* Jouget, L. 320, 377
- Sondi, I., *see* Wang, L. 298, 300, 318
- Sorai, M., *see* Liu, X.Y. 32, 34, 51, 63
- Sorensen, L.B., *see* Fenter, P. 98, 106
- Soriano, N.U., Jr 332, 340–7, 350, 378, 379
- Spanos, N., *see* Katsifaras, A. 222, 243, 263
- Sparks, N.H.C. 212, 264
- Spring, M.S., *see* Femi-Oyewo, M.N. 321, 377
- Srajer, G., *see* Fenter, P. 98, 106
- Srećo, S.D., *see* Bosch, H.W. 298, 305, 315, 320, 377
- Srinivasan, K. 56, 57, 63
- Srinivasan, K., *see* Rajesh, N.P. 56, 57, 63
- Srivastava, S.P. 332, 379
- Stanojev, B., *see* Booth, N.A. 100, 106
- Staudt, W.J., *see* Reeder, R.J. 383, 418
- Stayton, P.S., *see* Clark, R.H. 306, 315
- Stevens, J.D., *see* Abegg, C.F. 287, 314
- Stoppato, A., *see* Carraretto, C. 338, 377
- Strom, C.S. 164, 176, 212, 215, 216, 264, 268, 270, 317
- Strom, C.S., *see* Grimbergen, R.F.P. 164, 175, 266, 272, 316
- Strunk, H., *see* Bauser, E. 84, 106
- Struthers, J.D., *see*, Thurmond, C.D. 387, 419
- Stucky, G.D., *see* Walters, D.A. 235, 264
- Sturchio, N.C., *see* Fenter, P. 98, 106
- Sturrock, E.D., *see*, Webber, D. 218, 219, 220, 221, 245, 264
- Sunagawa, I. 97, 100, 107
- Sunagawa, I., *see* Kitamura, M. 397, 418
- Sunagawa, I., *see* Li, L. 159, 175, 274, 277, 278, 316
- Sunagawa, I., *see* Onuma, K. 86, 107
- Sunagawa, I., *see* Tsuchiya, A. 398, 399, 419
- Sutherland, J.W. 218, 264
- Suvaci, E., *see* Adair, J.H. 298, 299, 304, 314
- Suzuki, M., *see* Shimomura, O. 56, 57, 60, 63
- Suzuki, Y., *see* Kurihara, K. 105, 107
- Szurgot, M. 271, 317
- t'Velt, M.I., *see* Radenović, N. 100, 107
- Takata, Y., *see* Sangwal, K. 374, 376, 378
- Talham, D.R., *see* Adair, J.H. 307, 308, 309, 314
- Talham, D.R., *see* Ravaine, S. 308, 317
- Tan, J. 312, 314, 317
- Tandon, R.S., *see* Srivastava, S.P. 332, 379
- Tang, H., *see* Yu, J. 299, 302, 303, 318
- Tang, R., *see* Wang, L. 171, 176, 222, 235, 264, 273, 274, 318
- Tarara, T.E., *see* Duddu, S.P. 320, 377
- Tateishi, T., *see* Onuma, K. 105, 107
- Teng, H.H. 100, 102, 105, 107, 235, 264, 307, 317
- Thongboonkerd, V. 218, 264
- Thraikill, A., *see* Fenimore, C.P. 174, 175, 273, 315
- Thurmond, C.D. 387, 419
- Tieke, B., *see* Ouyang, J.-M. 245, 248, 263
- Tomson, M.B., *see*, Nancollas, G.H. 222, 263
- Tong, H., *see* Shekunov, B.Y. 330, 378
- Tonon, S., *see* Carraretto, C. 338, 377
- Torrent-Burgues, J., *see* Gomez-Morales, J. 48, 49, 63, 222, 225, 262, 288, 315
- Toschev, S. 266, 318
- Toyooka, H., *see* Saito, T. 209, 241, 242, 263, 311, 317
- Tremel, W., *see* Küther, J. 308, 316
- Trimble, K.R., *see* Duddu, S.P. 320, 377
- Troost, S. 304, 318
- Tsortos, A. 222, 227, 228, 264
- Tsuchiya, A. 398, 399, 419
- Tsukamoto, K., *see* Li, L. 159, 175, 274, 277, 278, 316
- Tsukamoto, K., *see* Liu, X.Y., 32, 34, 51, 63, 90, 91, 94, 107
- Tsukamoto, K., *see* Onuma, K. 86, 104, 107
- Tsukamoto, K., *see* Sazaki, G. 105, 107

- Tsukamoto, K., *see* Sunagawa, I. 97, 100, 107
- Tunik, L., *see* Füredi-Milhofer, H. 229, 262
- Twetman, S. 217, 264
- Ueno, S., 369, 371, 379
- Ueno, S., *see* Kaneko, N. 356, 361, 367, 377
- Ueno, S., *see* Sakamoto, M. 360, 361, 367, 378
- Ueno, S., *see* Sangwal, K. 374, 376, 378
- Ueno, S., *see* Sato, K. 363, 378
- Ujihara, T., *see* Sazaki, G. 105, 107
- Ulrich, R., *see* Omar, W. 56, 57, 60, 63
- Ulrich, R., *see* Sayan, P. 56, 57, 63
- Umegaki, T., *see* Wada, N. 222, 240, 241, 245, 252, 256, 257, 264
- Usami, N., *see* Sazaki, G. 105, 105, 107, 107
- van der Eerden, J.P., *see* Bennema, P. 35, 61, 62, 72, 106, 123, 174
- van der Eerden, J.P., *see* Elwenspoek, M. 73, 106
- van der Erden, J.P. 66, 72, 107, 274, 318
- van der Putte, P. 133, 176, 183, 203
- van der Walt, W.H., *see* Du Plessis, L.M. 343, 377
- van Dolah, R.W., *see* Grey, W.A. 130, 132, 175
- van Enckevort, W., *see* Radenović, N. 100, 107, 159, 160, 176, 276, 277, 317
- van Enckevort, W.J.P. 100, 107
- van Enckevort, W.J.P., *see* Algra, R.E. 275, 314
- van Enckevort, W.J.P., *see* Dam, B. 274, 315
- van Enckevort, W.J.P., *see* Kaminski, D., 98, 100, 106
- van Enckevort, W.J.P., *see* van der Putte, P. 133, 176, 183, 203
- van Erk, W. 86, 107
- van Hoek-Martens, H.J.G.J., *see* van Erk, W. 86, 107
- van Mil, J., *see* Berkovitch-Yellin, Z. 172, 174
- van Nieuw Amerongen, A. 216, 264
- van Panhuys-Sigler, M. 278, 318
- van Rosmalen, G.M., *see* de Vreugd, C.H. 395, 405–7, 412, 418
- van Rosmalen, G.M., *see* Kashchiev, D. 47, 48, 63
- van Rosmalen, G.M., *see* Verdos, D. 48, 63
- van Rosmalen, G.M. xv, 2, 20
- Vanhoutte, B., *see* Foubert, I. 356, 359, 377
- Vanrolleghem, P.A. *see* Foubert, I. 358, 377
- Vassilakis, D., *see* Claudy, P. 332, 333, 377
- Vassilakis, D., *see*, Létoffe, J.-M. 332, 333, 378
- Vdović, N., *see* Sikirić, M. 227, 228, 263
- Veerman, E.C.L., *see* van Nieuw Amerongen, A. 216, 264
- Veintemillas-Verdaguer, S. 15, 20, 98, 107, 143, 170, 171, 176
- Vekilov, P.G., *see* Booth, N.A. 104, 106
- Vendrell-Saz, M., *see* Roque, J. 287, 288, 293–5, 317
- Verdoes, D., *see* Kashchiev, D. 47, 48, 63
- Verdos, D. 48, 63
- Verma, A.R. 84, 107, 215, 264
- Verma, P.S., *see* Srivastava, S.P. 332, 379
- Vermilyea, D.A., *see* Cabrera, N. 117, 133, 175, 183, 202
- Verwer, P., *see* Radenović, N. 159, 160, 176, 276, 317
- Viertelhaus, M., *see* Eiden-Assman, S. 245, 262
- Viles, H., *see* Goudie, A.S. 260, 262
- Viliyaveettil, S., *see* Litvin, A.L. 307, 316
- Vlieg, E. *see* Kaminski, D. 98, 100, 106
- Vlieg, E. *see* Radenović, N. 100, 107, 159, 160, 176, 276, 277, 317
- Vlieg, E., *see* Algra, R.E. 275, 314
- Vlieg, E., *see* Arsić, J. 99, 105
- Vogel, V. *see* Letellier, S.R. 307, 316
- Vogels, L.J.P., *see* Grimbergen, R.F.P. 164, 175, 266, 272, 316
- Voronkov, V.V. 401, 419
- Wada, N. 222, 240, 241, 245, 252, 256, 257, 264
- Wagner, C. 293, 318
- Walker, J.B., *see* Mann, S. 307, 316
- Walter, Y.H., *see* Duddu, S.P. 320, 377
- Walters, D.A. 235, 264
- Walton, R.C. 206, 245, 264
- Wang, C.M., *see* Shen, F.H. 222, 263
- Wang, D.-J., *see* Wei, H. 222, 243, 264
- Wang, J., *see* Hao, H. 50, 63
- Wang, L. 171, 176, 222, 235, 264, 273, 274, 298, 299, 300, 318
- Wang, L., *see* Adair, J.H. 307, 308, 309, 314
- Wang, Y., *see* Hao, H. 50, 63

- Wang, Y., *see* Zhang, J. 332, 345, 379
 Ward, M.D., *see* Guo, S. 307, 316
 Webb, J.*see* Rimstidt, J.D. 381, 386, 389–91,
 394, 400, 418
 Webber, D., 218, 221, 245, 264
 Weers, J.G., *see* Duddu, S.P. 320, 377
 Wei, H. 222, 243, 264
 Weiner, S., *see* Aizenberg, J. 222, 262, 299,
 314
 Weiner, S., *see* Bouropoulos, N. 307, 315
 Weiner, S., *see* Levi-Kalisman, Y. 214, 263
 Weiner, S., *see* Levi, Y. 306, 316
 Weiner, S., *see* Raz, S. 298, 300, 302, 317
 Weisinger-Lewin, Y. 172, 176
 Weissbuch, I. 161, 172, 173, 176, 275, 318
 Weissbuch, I., *see* Addadi, L. 173, 174
 Wenk, H.-R., *see* Chateigner, D. 212, 262
 Wesson, J.A. 219, 264
 Wesson, J.A., *see* Guo, S. 307, 316
 Westin, K.-J. 222, 239, 264
 Whitesides, G.M., *see* Aizenberg, J. 309, 314
 Wierzbicki, A. 172, 176
 Wijewardana, G., *see* Chandrajith, R. 218,
 219, 262
 Williams, C.J., *see* Prockop, D.J. 206, 263
 Williams, R.O., *see* Rogers, T.L. 320, 327,
 378
 Wilson, R.M., *see* Loste, E. 238, 263
 Wilt, F.H. 206, 264
 Witkamp, G.J., *see* de Vreugd, C.H. 395,
 405–7, 412, 418
 Woensdregt, C.F., *see* van Panhuys-Sigler, M.
 278, 318
 Wojciechowski, K. *see* Ristić, R.I. 416, 418
 Wu, C., *see* Zhang, J. 332, 345, 379
 Wu, W. 306, 318
 Wurster, D. 320, 379
 Xu, D.-F., *see* Wei, H. 222, 243, 264
 Yamashita, K., *see* Wada, N. 222, 240, 241,
 245, 252, 256, 257, 264
 Yang, D.S.C. 307, 318
 Yang, Q. 258, 260, 261, 264
 Yano, J.*see* Sato, K. 363, 378
 Yano, J., *see* Garti N. 350, 354–6, 377
 Yano, J., *see* Kaneko, N. 356, 361, 367, 377
 Yasui, A., *see* Kitamura, M. 244, 263
 Yokota, M., *see* Guzman, L.A. 138, 175
 Yokota, M., *see* Kubota, N. 118, 133–5,
 138–42, 175, 181, 183, 186, 187, 202
 Yokotani, A., *see* Sasaki, T. 143, 176
 York, P. 320, 379
 Young, T.J., *see* Rogers, T.L. 320, 327, 378
 Yu, H. 258, 264
 Yu, J. 299, 302, 303, 318
 Zachowicz, W.J., *see* Wang, L. 171, 176,
 222, 235, 264, 273, 274, 318
 Zapp, E., *see* Pataki, L. 54, 63
 Zhang, J. 332, 345, 379
 Zhang, J., *see* Cao, W. 339, 377
 Zhang, W., *see* Wang, L. 171, 176, 222, 235,
 264, 273, 274, 318
 Zhao, Y., *see* Wei, H. 222, 243, 264
 Zhmurova, Z.I. 400, 401, 405, 419
 Zhongshan, W., *see* Chow, A.H.L. 321, 377
 Zhou, N., *see* Ouyang, J.-M. 245, 248, 263
 Zhou, Y.C.Y. 303, 318
 Zhu, Y.R., *see* Zhou, Y.C.Y. 303, 318